Controls of reservoir quality in Carboniferous tight gas sandstone

WASIELKA, NATALIA

Controls of reservoir quality in Carboniferous tight gas sandstone

Natalia Wasielka

This thesis is submitted in partial fulfilment of the requirements for the degree of Doctor of Philosophy at Durham University

Department of Earth Sciences

Durham University

2021

Abstract

The UK Continental Shelf is one of the most mature offshore basins in the world, yet the existing Namurian tight gas reservoirs are still largely unexplored since permeability differences of several orders of magnitude over small areas of reservoir are a key exploration risk. It is therefore important to be able to identify sandstones with sufficient reservoir quality to optimize the drilling process and minimize exploration costs.

This study integrates sedimentological logging, quantitative petrographic data, burial history modelling, and quantitative analysis of the pore network using microCT to understand the controls on reservoir quality in Copernicus discovery and Cavendish fields of the Southern North Sea. These two fields display different reservoir qualities despite the fact that both lie on the same structure and show similar present day burial depths.

This study shows that a combination of multiple factors was responsible for reservoir quality distribution. The best reservoirs are associated with quartz rich sandstones that are less prone to adverse effects of diagenesis than the predominant, more feldspathic and more kaolinitised sandstones, which were sourced from a different area. Next, depositional environment was responsible for differences in detrital composition, grain size and different initial pore water chemistry that led to varying diagenetic pathways. Furthermore, differences in burial histories created better conditions for quartz cement development in Copernicus field, ultimately rendering it an economically non-viable resource.

Mapping of the pore networks with microCT on micron scale shows how small variations in diagenetic style result in permeability differences of several orders of magnitude over small areas of reservoir. An integrated approach utilising burial history modelling, analysis of diagenetic processes, 3D modelling of pore architecture, and modelling changes in pore connectivity through time, offer a methodology that allows reconstructing permeability evolution and the timing and mechanisms of reservoir tightening throughout the geological history.

Table of Contents

Declaration

I declare that this thesis, which I submit for the degree of Doctor of Philosophy at Durham University, is my own work, except where acknowledgement is made in the text, and not substantially the same as any work which has previously been submitted at this or any other university for any degree, diploma or other qualification.

April 2021

Acknowledgements

First and foremost, I would like to thank my supervisory team: Andy Aplin, Jon Gluyas, and Stuart Jones. I am very grateful for being given the opportunity to do this PhD back in 2016, and for your support, all the discussions and advice you gave me over the years. Furthermore, I would like to thank Kate Dobson for teaching me all I know about microCT, always having time to help, and the all the stimulating discussions which helped me greatly to develop this project.

I would also like to thank Sam Allshorn and Fabian Wadsworth for your help and your input in this project.

Many thanks go to my colleagues from the Department of Earth Sciences - thanks for making this a very enjoyable time.

Huge thanks must also go to all the climbers I met while working on my PhD. There are too many to name, but a special 'thank you' goes to Bevan, Ollie, Ian and Marek. You have played such an important role in keeping my sanity, and it was climbing with you that helped me stay positive throughout this difficult adventure that was doing a PhD.

I would also like to thank my parents for always supporting and believing in me.

Finally, thank you to my husband Karol. Thank you for going on core-logging trips with me, for reading all my work, and offering your help whenever I needed it. And thank you for always being by my side. I could not have done it without you.

CHAPTER 1:

Introduction

1.1 Research context

1.1.1 World tight gas potential

Tight reservoirs are major resource of gas worldwide. Many tight gas reservoirs have been developed and successfully producing in multiple countries, including USA, Canada, Australia, Mexico, Venezuela, Argentina, Indonesia, China, Russia, Egypt, Saudi Arabia, Oman, Jordan and Germany (Holditch, 2006; Khlaifat et al., 2011; Becker et al., 2017; Wulandari et al., 2018). New reserves have been discovered, but not yet developed, e.g. in Pakistan or Poland (Polish Geological Institute, 2015; Dahraj et al., 2018;). Estimated resources of gas in tight sands are 7405 Tcf as of 2001 (Kawata and Fujita, 2001). The success of the tight gas potential is best illustrated by the U.S. example, where about 20% of the country's total gas production comes from tight reservoirs (Holditch, 2006). A lot of interest has been directed towards unconventional reservoirs in recent years, but whilst it was onshore shale gas has grabbed the public's attention, offshore tight gas represents a potentially more readily recoverable resource (Holditch, 2003).

1.1.2 Tight gas definition

The term tight gas reservoir refers to low permeability reservoirs, typically <0.1 mD, that require hydraulic fracturing, horizontal drilling or multilateral wells in order to produce economic volumes of gas (Holditch, 2006). Tight reservoirs vary in shape, depositional environments, depths, thicknesses and age, although are generally found in strongly cemented Palaeozoic deposits (e.g. US Permian Basin, UK Southern North Sea, Chinese Ordos Basin). Tight gas reservoirs can develop in conventional structural or stratigraphic traps as well as basin-centred type of reservoirs which can occupy large areas compared to conventional reservoirs (Law and Curtis, 2002; Kiersnowski et al., 2010).

Due to relatively low production from tight gas wells compared to conventional reservoir wells, more wells need to be drilled to produce commercial amounts of gas. Also, most tight gas reservoirs are not homogeneous; some are naturally fractured, layered and have anisotropic permeabilities (Khlaifat et al., 2011). It is therefore important to be able to identify sandstones with sufficient reservoir quality to optimize the drilling and gas recovery process. To be able to develop these low porosity and low permeability sandstones predictive reservoir quality and porosity distribution models are necessary. Especially with the current low gas prices, for the tight gas reserves to be produced economically, it is even more important to be able

to predict the best reservoir quality sandstone distribution to minimize production costs.

1.1.3 North Sea prospects

The UK Continental Shelf is one of the most mature offshore basins in the world but still has interesting frontier areas and new exploration plays, such as the Carboniferous deposits in the North Sea (Wood, 2014). The Namurian tight gas reservoirs in the Southern North Sea are largely unexplored gas prospects, despite the fact that their gas potential has been proven by a number of wells that successfully produce gas (e.g. in Trent and Cavendish fields). Prospectivity studies across the Carboniferous fairway have proven the presence of undeveloped prospects within the Namurian strata (Cameron et al., 2005; Monaghan et al., 2017; Wood, 2014). According to estimates by Robertson Research International, the Namurian and Westphalian A sandstones of the Millstone Grit accounted for more than 50% of estimated reserves in the undeveloped Carboniferous discoveries (Cameron et al., 2005). BGS Carboniferous fairway mapping has led to creation of 279 undrilled prospects greater than 500 acres (Cameron et al., 2005).

Mature source rock is present in the Southern North Sea basin, traps and seals are provided at the base Permian unconformity and by intra-Carboniferous closures (Monaghan et al., 2017). Any new development in this mature gas province could benefit from the existing infrastructure. Despite this, the Namurian deposits still remain relatively poorly documented, as reservoir effectiveness remains a key exploration risk (Cameron et al., 2005). This is caused by variations in depositional and diagenetic style, which can result in permeability differences of several orders of magnitude over small areas of reservoir (O'Mara et al., 2003; Besly, 2018; Wasielka et al., 2020). It is therefore important to be able to identify sandstones with sufficient reservoir quality to optimize the drilling and gas recovery process and minimize exploration costs.

United Kingdom, as well as the rest of the European Union, depends on oil and gas import from non-EU member countries. In 2017 Oil and Gas Authority, UK, issued a Southern North Sea Tight Gas Strategy (Oil & Gas Authority, 2017) to promote further development within the SNS area and to extend the economic life of the existing infrastructure. Reassessing the potential of the Upper Carboniferous deposits of the North Sea in terms of oil and gas exploration may bring new, recoverable resources to the UK enhance the security of energy supply. Revitalisation

of exploratory drilling in the Carboniferous fairway of the SNS is required to enable the fairway to continue as a major gas-producing region of the UK (Cameron et al., 2005).

1.1.4 Reservoir quality

Reservoir quality of deeply buried sandstones is a cumulative product of depositional processes and subsequent shallow and deep-burial diagenesis and tectonic movement (Ajdukiewicz and Lander, 2010; Wang et al., 2017). Sedimentological factors such as provenance, transport and depositional processes, as well as climate affect the initial texture, composition, and porosity, which control the fluid flow and geochemical reactions in the rock (Ramm, 2000; Worden and Burley, 2003; Ajdukiewicz and Lander, 2010; Bjørlykke, 2014). Interaction of the sediment with meteoric waters (<2000 m; Morad et al. (2000)) results in the formation of early diagenetic cements. Those early diagenetic cements can have a profound effect on reservoir quality preservation, as they can lead to reservoir quality loss or can significantly affect later diagenetic processes. In buried reservoirs temperature and time are critical components in diagenetic reactions (Morad et al., 2000; Worden and Burley, 2003). In tight reservoirs burial diagenesis is the key factor leading to the tightening of the reservoir and reduction of permeability. The most common cements in tight reservoirs include quartz and carbonates (e.g. Xi et al., 2015; Oluwadebi et al., 2018), although the latter can also precipitate at lower temperatures..

Initial variations in sedimentological factors and in the distribution of diagenetic alterations throughout the reservoir result in reservoir heterogeneity (Morad et al., 2010). Diagenetic processes are generally not basin-wide but more local, reflecting the sediment composition, temperature history and effective stress (Bjørlykke, 2014). High heterogeneity, as well as low porosity, low permeability and commonly well-developed fractures are typical characteristics of most tight gas reservoirs (Khlaifat et al., 2011; Yue et al., 2018). The heterogeneity and the presence of natural fractures can result in spatial variability in productivity, therefore a better understanding of the factors controlling reservoir quality distribution is required to successfully develop such reservoirs. Reservoir unit shape and dimensions can be predicted to an extent from seismic data and sedimentological models (Bjørlykke, 2014). To understand porosity and permeability distribution it is important not only to be able to link them to depositional environments where the sandstone units formed, but also to understand how depositional processes and meteoric pore water chemistry affected sediment mineralogy, textures, and early cement development. Then, burial history

and pore fluid chemistry evolution during burial diagenesis, and sometimes also telogenesis, need to be understood to analyse diagenetic phases that formed throughout the basin history. Yet, the ultimate goal for anyone interested in reservoir quality is understanding of how all these sedimentological and diagenetic factors affect pore network architecture and, consequently, permeability.

This is a big undertaking as it involves field-scale predictions down to micron-scale models, particularly in tight reservoirs where permeability values are typically in the low mD scale or lower, and pore throats are only microns wide. A thorough investigation would involve numerous techniques to appropriately characterise the reservoir, starting from reservoir-scale seismic and depositional models, m- to cm-scale sedimentary facies and sedimentary structure analysis, mm-scale petrographic descriptions, down to techniques that allow pore structure analysis at a micron-scale, such as X-ray micro-tomography (XMT) or mercury injection capillary pressure (MICP).

1.2 Aims

The focus here is on poorly documented, low porosity, low permeability Carboniferous sandstones, in which small variations in depositional and diagenetic style can result in permeability differences of several orders of magnitude over small areas of reservoir. In order to develop these sandstones permeability and porosity distribution models are necessary. These will enable forecasting the reservoir quality distribution ahead of drilling and planning well placement and identification of key zones for perforation or frack locations, reducing risks and costs. To create such models, it is necessary to understand the controls on reservoir quality on multiple-scales. This project aims to investigate the sedimentological and diagenetic controls on reservoir quality distribution and link measurements of permeabilities, pore structures and diagenetic minerals in order to understand and thus predict how differences in diagenesis control flow properties in those low permeability sandstones. A multidisciplinary approach comprising sedimentological characterisation, petrographic analysis, SEM, CL, burial history modelling, and 3-D X-ray micro-tomography modelling of pore structures and mineral distribution was applied.

The study investigates:

-The relationship between sedimentological and diagenetic controls on reservoir quality;

-Reservoir quality evolution of tight reservoirs throughout the basin history;

-The relationship between diagenesis, pore architecture and reservoir quality.

1.3 Thesis outline

This thesis is made up of seven chapters, with the outlines of Chapters 2-7 described individually below.

Chapter 2: Geological setting.

This chapter presents a summary of the geology of the Southern North Sea, basin evolution, depositional system during the Namurian period, and hydrocarbon system of the study area, based on published references.

Chapter 3: Sedimentary and diagenetic controls on reservoir quality in tight Namurian sandstone reservoirs of Copernicus discovery and Cavendish field, Southern North Sea.

This chapter discusses the influence of depositional factors on reservoir quality preservation and links them to diagenetic factors to establish main controls on reservoir quality.

Chapter 4: Burial modelling and petroleum system development in Copernicus discovery and Cavendish field, Southern, North Sea.

One-dimensional basin modelling is used to investigate how burial and pore water chemical evolution shape diagenetic processes.

Chapter 5: Diagenetic evolution and reservoir quality of Upper Carboniferous fluviodeltaic systems.

Chapter 5 expands on work done in Chapter 3, using various petrographic techniques and basin modelling to investigate the diagenetic paragenesis and reservoir quality evolution.

Chapter 6: Characterization and quantitative analysis of pore architecture and permeability modelling in tight gas sandstones utilizing X-ray computed microtomography.

This chapter deals with pore network architecture and permeability modelling on X-ray computed microtomography models to determine micron-scale controls on reservoir quality.

Chapter 7: Permeability evolution of sandstones using X-ray tomography and quartz cement modelling.

This chapter exploits the capability of X-ray micro-tomography to quantify complex pore structures, and presents a novel method of forward-modelling of quartz cementation and simulation of changes in the pore network, to estimate sandstone permeability development through geological time.

CHAPTER 2:
Geological setting

2.1 Study area

2.1.1 Introduction

The study focuses on the Namurian deposits drilled in quadrants 43- 44 of the Southern North Sea (Anglo-Dutch Basin). The Namurian strata, which subcrop the Permian and Westphalian deposits, were penetrated and, in some cases, cored in numerous wells in Quadrants 42-48. The reservoirs investigated in this study comprise the Copernicus gas discovery in Quadrant 44, wells 44/16-1, 44/16-1Z and 44/16-2, and Cavendish gas field, wells 43/19-1, 43/19-2 and 43/19a-4Z (Figure 2.1.).

The Namurian deposits in the selected wells occur at a wide range of present burial depth (3710 – 4850.6 m TVDSS; base Namurian not penetrated) and different estimated maximum burial depths, and are therefore a suitable material to study varying degrees of diagenesis depending on burial depths. The cores penetrated through the Yaedonian (Namurian C) to Pendleian (Namurian A) deposits, thus representing most of the Namurian strata. The studied material represents different depositional environments, ranging from basinal muds through to delta and fluvial environment. None of the wells analysed in this study were fracked, therefore the measured flow rates were not artificially affected.

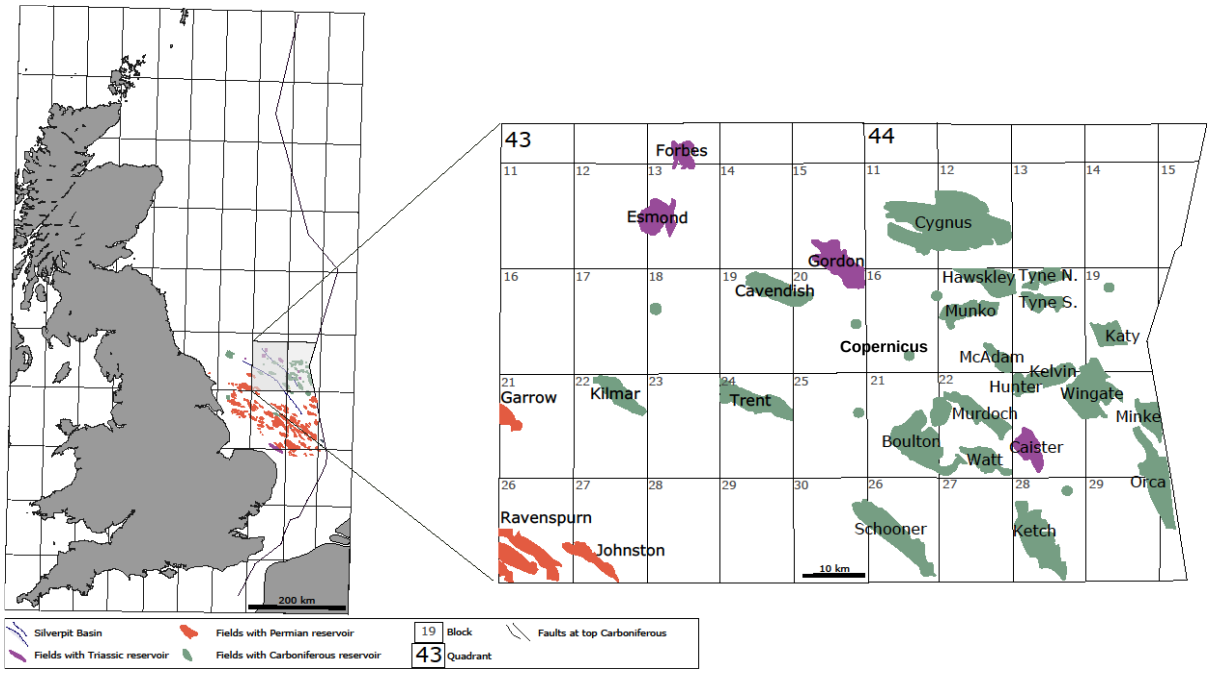

Figure 2.1. Study area

2.1.2 Southern North Sea drilling history, resources, and gas production

Success in the early onshore hydrocarbon exploration of the Carboniferous deposits in the UK encouraged the oil and gas companies to move offshore in the early 1960s to look for further resources to develop. A number of wells were drilled in the southern North Sea, however they proved to be rather unprospective due to very strong cementation. The rapid development of Rotliegend plays halted the interest in Carboniferous exploration, and the latter became regarded as economic basement in the North Sea (Besly, 1990, 2018). With the new knowledge, technology development and need for more gas production, Carboniferous once again gained interest in the 1980s. 143 exploration wells were drilled to test Carboniferous objectives period between 1984 and 2014 (Besly, 2018). Three more exploration wells with Carboniferous targets were drilled in the UK sector between 2015 and 2018 (44/23g-14; 44/19a-8; & 49/25b-11A; Discovery Digest United Kingdom, 2019). In 2017 UK Oil and Gas Authority issued Southern North Sea Tight Gas Strategy to promote further development in the SNS area (Oil & Gas Authority, 2017).

The results of a USGS World Petroleum Assessment show that estimated mean values of undiscovered resources of the Carboniferous-Rotliegend total petroleum system in the onshore and offshore areas of the Anglo-Dutch Basin and adjacent parts of Northwest German Basin are about 144 MMBO and over 26 tcf of natural gas (Gautier, 2003). By the end of 2012, Southern North Sea gas province had produced around 45.8 tcf of gas from 140 gas fields, 7% of which was from the Carboniferous fluvial sandstones (Gray, 2013). According to Oil and Gas Authority, UK, the Southern North Sea contains estimated 3.8 tcf of remaining gas accessible in tight gas reservoirs (Oil & Gas Authority, 2017). Cameron et al. (2005) estimated that Namurian and Westphalian A sandstones of the Millstone Grit Formation account for more than 50% of estimated reserves in the undeveloped discoveries.

2.1.3 Copernicus gas discovery

The Copernicus discovery is located in UKCS Southern North Sea block 44/16 about 150 km NE of the Lincolnshire coast Figure 2.1. It is located in the Silverpit Basin, in the northern part of the Southern North Sea gas province. The Copernicus structure is a NW-SE oriented dip and fault closed anticline, with the crest of the anticline eroded by the Base Permian Unconformity (BPU). A series of NW-SE and WSW-ENE faults cut across the anticline giving a series of tilted fault blocks and grabens (ENGIE, 2015; Figure 2.2.). The seal is provided by the Permian Silverpit shales and

Zechstein salt. The most likely source rocks are the Westphalian aged coals occurring downdip of the structure. Reservoir rock comprises Namurian fluviodeltaic sediments of the Millstone Grit Formation (ENGIE, 2015). Copernicus discovery lies within the same structure as several other fields producing gas from the Upper Carboniferous strata (Cavendish, Caister, Murdoch; (Cameron et al., 2005)). It was discovered in 1991 by Lasmo well 44/16-1 and flowed gas at 32 mmscf/d, yet it was assessed as economically non-viable (ENGIE, 2015).

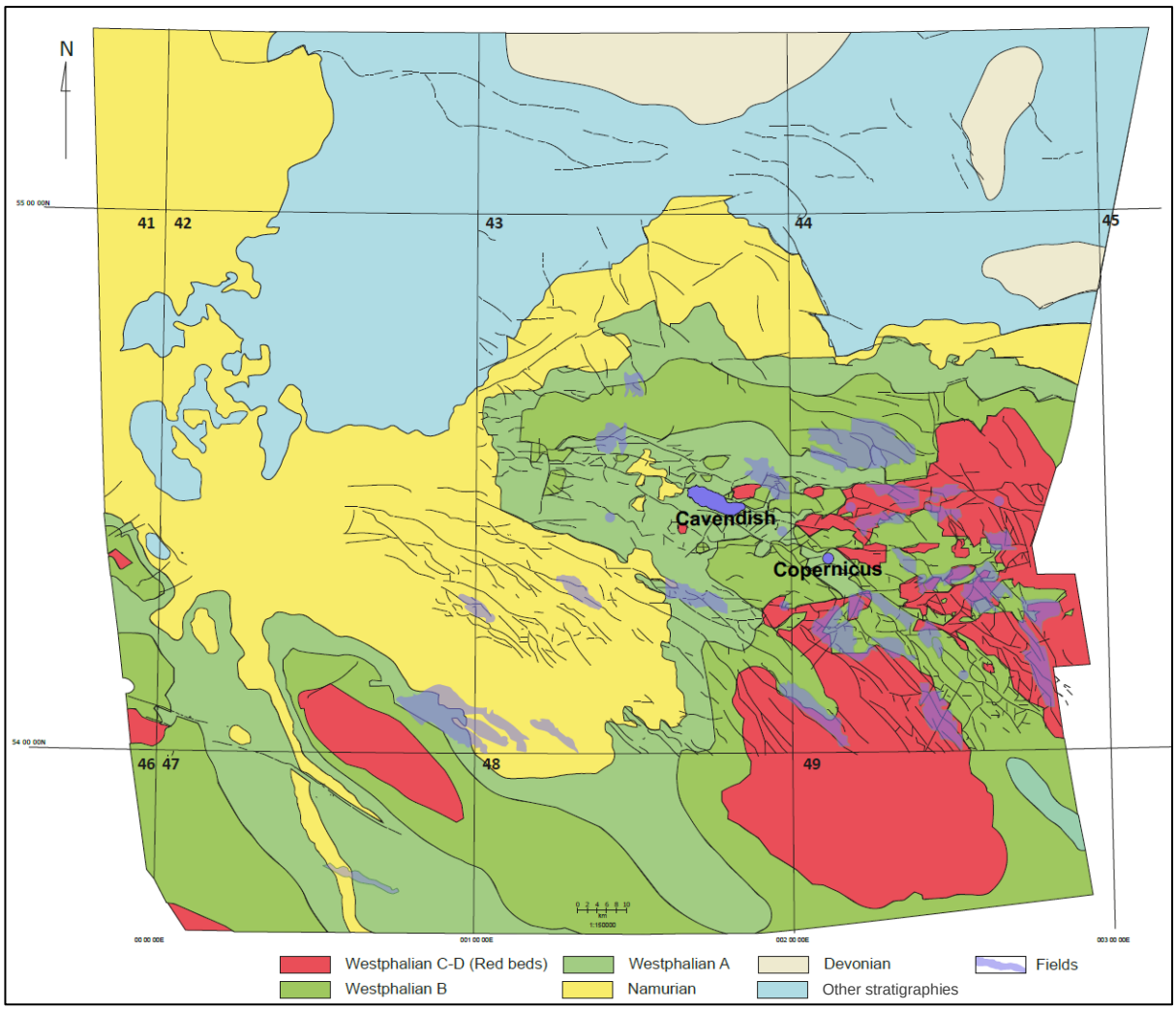

Figure 2.2. Pre-Permian subcrop map. Adapted by Gluyas from (Underhill, 2003).

2.1.4 Cavendish gas field

The Cavendish Field, currently operated by Ineos UK SNS Limited, is located within UKCS Block 43/19a (Figure 2.1.). The block is located on the Northern margin of the Outer Silverpit Basin of the Southern North Sea, 140 km north-east of the Lincolnshire coast in a water depth of 18.9 m. The field is approximately 12 km (7.5 miles) long and covers an area of 35.5 sq km (13.7 sq miles). Reservoir rock comprises

Namurian (Millstone Grit Formation) to Westphalian A (Caister Coal Formation) fluvial sandstones deposited by a southward prograding fluviodeltaic system infilling a deep basin, which formed in the Dinantian times. The Cavendish lies on the same structure as the Copernicus discovery, a NW-SE orientated anticline truncated to the SE by a WSW-ENE trending fault and to the north by a major NW-SE trending reverse fault with the crest of the anticline is eroded by the Base Permian Unconformity (BPU) (Figure 2.2.).

The field was discovered in 1989 by Britoil well 43/19 1. Production started in 2007 and ceased in 2018. Gas initially in place was 184 bcf and at end of field life 98 bcf had been produced (Wasielka et al., 2020; provided as Appendix 8).

2.2 Regional context

2.2.1 Tectonic history of the Carboniferous of the Southern North Sea

The Variscan collisional episode in Europe that commenced in the Devonian and ended in the Early Permian, resulted in the convergence of the southern continent of Gondwana with the northern continent of Laurussia (Laurentia, Baltica and Avalonia), to form the supercontinent of Pangaea (Warr, 2012). The subduction of the Theic oceanic plate towards the north resulted in a phase of back-arc extension within the Avalonia plate in the Late-Devonian-Early Carboniferous (Waters and Davies, 2006). The Northwest European Carboniferous Basin, a precursor of the Southern Permian Basin, formed as a result of those events (Kombrink et al., 2010). The N-S rifting resulting from the extension caused a series of grabens and half-grabens to develop, separated by platforms and tilted block highs to the north of the Wales-Brabant High (Besly, 1990; Leeder and Hardman, 1990; Ziegler, 1990; Waters and Davies, 2006). The location of those highs and grabens was largely controlled by the emplacement of granite plutons and tectonic structures inherited from earlier orogenic events (Besly, 1990).

By late Dinantian the regional extension had greatly reduced and gave way to thermal subsidence by early/mid Namurian, although some reactivation of the faults occurred in the Namurian (Fraser and Gawthorpe, 1990; Waters and Davies, 2006). All this was coincidental with a major climatic change probably forced by glacial expansion in Gondwanaland (Leeder and Hardman, 1990). The sedimentary facies development in the Namurian and their thickness were still largely controlled by the relic Dinantian highs (Besly, 1990). Those blocks had a much lower subsidence rate than the surrounding basins and thus accumulated thinner sediment sequences. They

also acted as baffles for sediment distribution, with turbidite front-deltas developing in basins around those uplifted blocks.

2.2.2 Basin evolution

The Southern North Sea Basin experienced a complicated geological history, involving multiple episodes of uplift and subsidence. From Carboniferous times the basin was bounded in the south by the Anglo-Brabant Massif and in the north by the Mid North Sea High/Ringkøping-Fyn High (Cameron et al., 1993)(Cameron, 1993), with over 6000 m of sediments deposited in parts of the basin (Besly, 2018). The Variscan Orogeny resulted in faulting and folding of the Carboniferous rocks and a subsequent erosion of much of the Upper Carboniferous strata. In the Permian the subsidence of the Variscan foreland renewed, resulting in deposition of a thick sequence of mainly clastic and evaporate strata in continental (initially) and restricted marine (subsequently) environments, which were for short periods connected to the ocean through constricted seaways resulting in hypersaline conditions (Ziegler, 1990; Cameron et al., 1993). Crustal extension at the end of the Triassic times and in Early Jurassic caused rapid subsidence, and a major transgression in the Jurassic times marked the onset of deposition of deep-water muds. This period of subsidence was interrupted by thermal doming in the Central North Sea, which caused uplift and erosion of much of the Jurassic sequence in the region. Crustal extension continued after the uplift until mid-Cretaceous times providing accommodation space for a thick, predominantly marine sequence. An episode of uplift at the end of the Cretaceous caused basin inversion in many fault-bounded basins. Paleogene marine deposits unconformably overlie the Cretaceous Chalk deposits. Tectonic uplift linked to the Alpine Orogeny in Miocene times removed part of the Palaeogene sequence. Resumption of subsidence led to the development of a major deltaic system. Sea level fluctuated during several periods of glaciation in Pleistocene with the fully marine conditions established after Holocene transgression (Cameron et al., 1993).

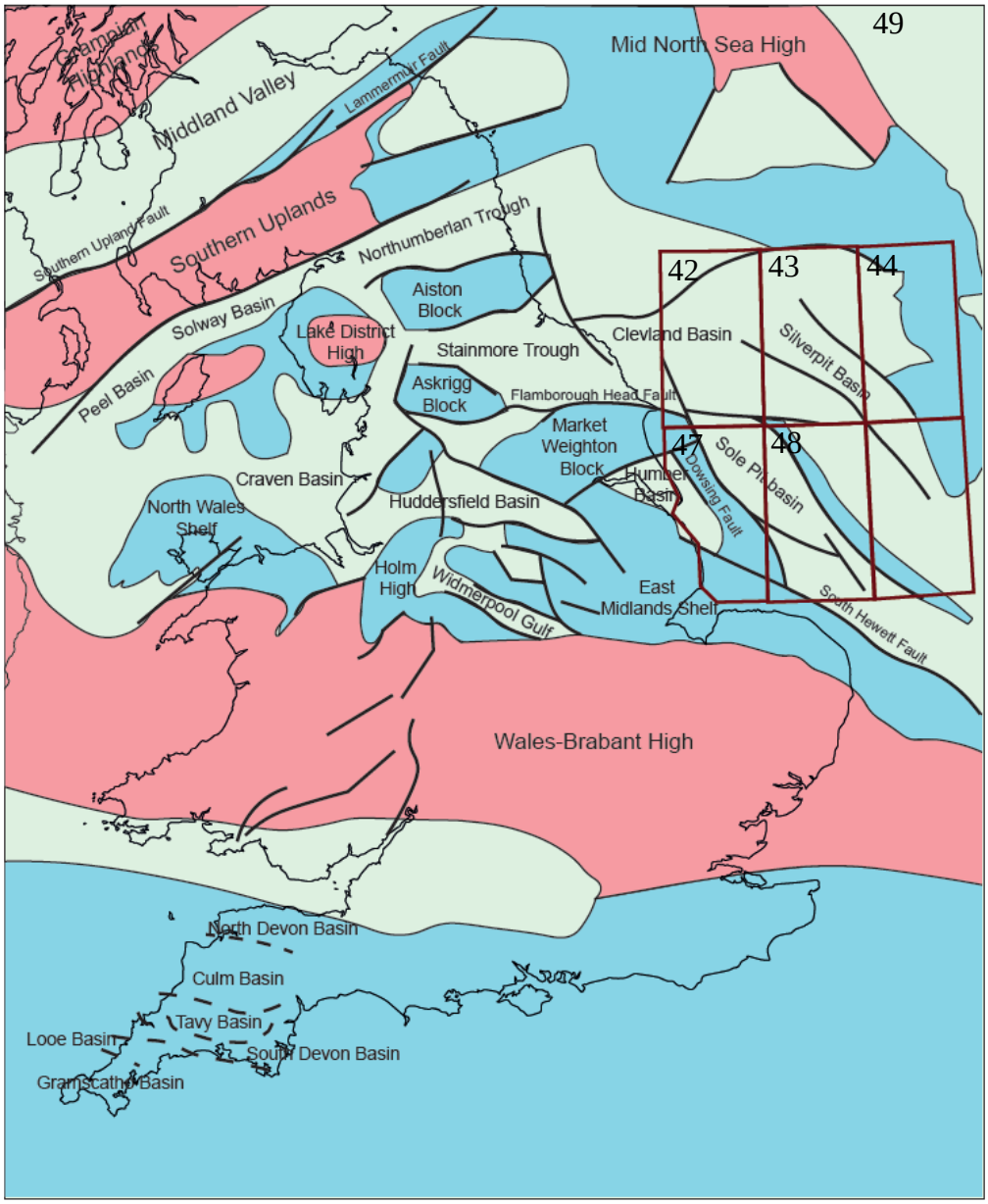

Figure 2.3. Structural map of the UK during Carboniferous times. Adapted from Waters & Davies, (2006).

2.3 Namurian depositional system and palaeoenvironment

The Namurian deposits in the Southern North Sea and onshore England are represented by Yoredale Formation, Bowland Shale Formation and Milstone Grit Formation. Yoredale and Miltstone Grit facies comprise siliciclastic turbidite and fluviodeltaic sequences, whilst the Bowland shale is composed of basinal mudstones. The base boundary is diachronous and the underlying strata comprise mainly Dinantian deposits and Lower Palaeozoic sediments towards the south. The Namurian sediments are conformably overlain by Westphalian deposits and have an unconformable boundary with Permian deposits in the north. The characteristic

feature of the Millstone Grit Formation is its cyclicity. Such cycles are commonly about 50 m thick, have mudstone intervals containing marine bands at their base, and display coarsening upwards trends (Cameron, 1993). The main source of the clastic material was from the north (Collinson et al., 1993), likely sourced from the Laurentian block, north of the Scottish or Scandinavian massifs (Hallsworth and Chisholm, 2000). Minor other sources were also active during the Carboniferous times, particularly during the Westphalian times. These are a south-eastern source, responsible for a thicker sand sequence in and around the Netherlands, and a third source from the Anglo-Brabant Massif (Collinson et al., 1993).

A major drainage system which developed in the north gave rise to a large fluviodeltaic system gradually migrating southwards and progressively infilling basin topography (Figure 2.4). Sedimentation in the south occurred on carbonate platforms in a shelf setting. The fluviodeltaic system was interrupted numerous times by marine transgressions. Cyclical growth and waning of polar ice sheets in Gondwanaland resulting from Milankovitch cycles caused glacio-eustatic sea-level changes that were likely responsible for the bands preserved within the Namurian deposits (Leeder, 1988). On a large scale, the Namurian deposits record a coarsening upwards sequence, from black shales deposited under periodically anoxic conditions in a deep basin, through delta-front turbidites, delta slope deposits, to fluviodeltaic deposits(Leeder and Hardman, 1990). The turbidite feeder channels are restricted to early Namurian (Collinson et al., 1993). By Marsdenian times the deltas had reached the northern margin of the Wales-Brabant High (Waters and Davies, 2006). The sandstone-dominated multi-storey fluvial channels act as the best reservoirs within the Namurian strata (Besly, 2018). In terms of reservoir continuity, Collinson et al. (1993) suggested that the channel sandbodies are up to about 40 m thick and probably over 10 km wide, with majority of the thinner channels (<10 m) having widths of 100 m or less. This is largely consistent with thicknesses reported by Hampson et al. (1999) who suggested that incised valley fill sandstone bodies are 20 to 45 m thick, and 5 - 25 km wide. Collinson et al. (1993) also suggest that the sandbodies that are over 20 m thick are most likely multi-storey channels.

Closing of the Theic Ocean and collision of Gondwanaland with Laurussia had a great impact on climate and thus facies development during the Carboniferous. The resulting growth of a Variscan mountain range, cyclic expansion of ice sheets in Gondwana and the latitudinal shift of the landmasses were all controlling the Carboniferous climate, which was becoming increasingly more humid and wet throughout most of the Carboniferous. The huge fluvial system that developed during

the Namurian times likely drained continental-scale areas, with the Pennine river-delta system possibly comparable to modern Amazon in size (Leeder, 1988).

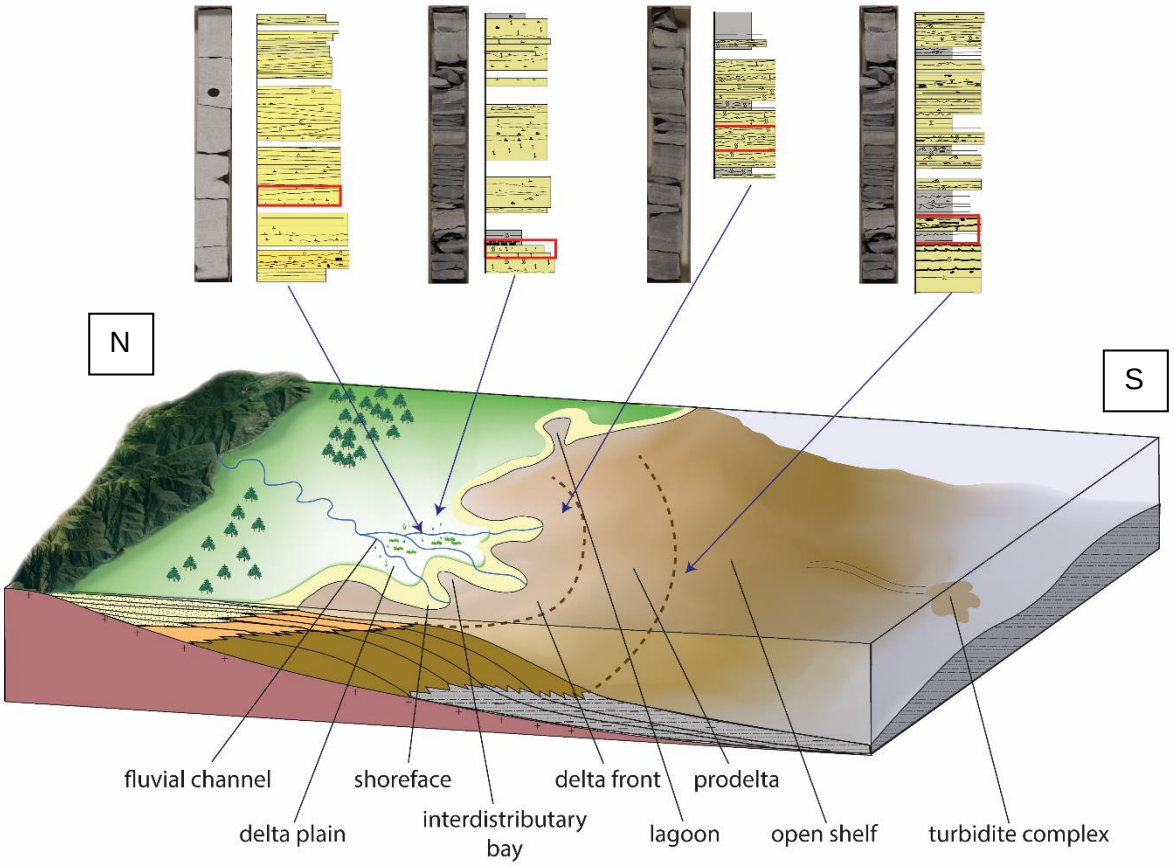

Figure 2.4. Deposition during the Namurian occurred through large fluviodeltaic systems infilling pre-existing basin topography. Sedimentary log fragments of several examples of facies associations described in cores are shown above, with photos showing 1 m core fragments that are marked in red boxes on the logs.

2.4 Upper Carboniferous stratigraphy of the study area

The Carboniferous succession in the Southern North Sea, deposited between 360 and 300 Ma, has likely originally consisted of over >6 km of sediment (Besly, 2018) yet much of it has been eroded as a result of the late Carboniferous inversion.

The Upper Carboniferous succession in the Southern North Sea, deposited during the Pennsylvanian times, consists of Namurian and Westphalian A sediments belonging to Whitehurst Group, which is overlain conformably by Westphalian Conybeare Group or unconformably by Permian sediments of the Rotliegend Silverpit Formation (Figure 2.5). The group lies on sediments of Dinantian to Early Namurian Yoredale Formation (Fame Group) or Dinantian carbonates of Zeeland Formation (Carboniferous Limestone Supergroup; British Geological Survey, 2019; Cameron,

1993). The Whitehurst Group comprises the Bowland Shale Formation and Millstone Grit Formation, which are offshore equivalents of the Bowland Shale and Millstone Grit groups defined formally for onshore England (Cameron, 1993). The Whitehurst Group is widespread in the central part of the Southern North Sea, with its thicknesses locally reaching over 1600 m (although this figure might be higher as the base have rarely been penetrated) (Cameron, 1993). The Bowland Shale Formation is composed of basinal mudstones. Millstone Grit, which is the subject of this study, consists of an upward coarsening succession of marine black shales, siltstones and mudstones, passing upwards into fluviodeltaic fine to very coarse-grained sandstones, with thin coal seams (Waters and Davies, 2006), and occasional conglomeratic beds. Mudstone–dominated intervals are up to 100 m thick (Cameron, 1993).

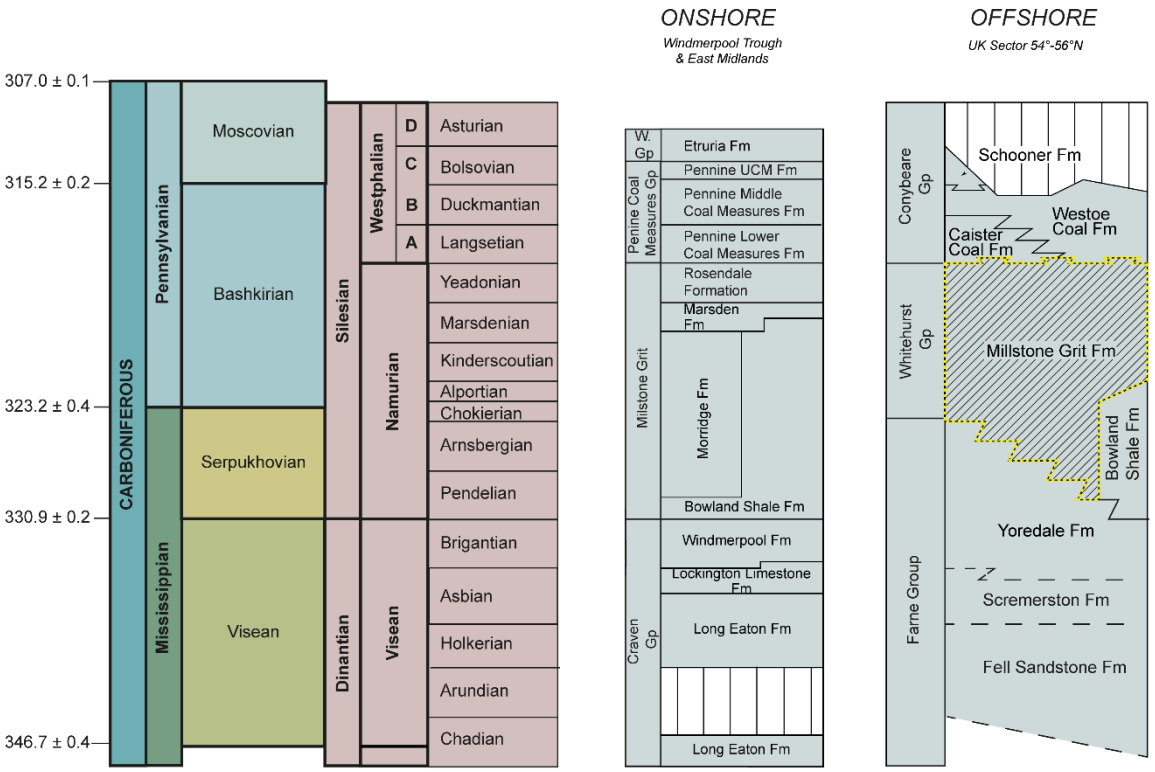

Figure 2.5. Carboniferous stratigraphy of the Southern North Sea and onshore UK. Upper Carboniferous deposits, which are the subject of this study, were deposited during the Pennsylvanian times, whilst the Lower Carboniferous belongs to the Mississippian times Adapted from Cameron, 1993. Samples in this study are from the Millstone Grit Formation.

2.5 Hydrocarbon system of the study area and drilling history

2.5.1 Reservoir rocks

Reservoir rocks within the Westphalian and Namurian intervals occur in stacked fluvial channels, in incised valley fills and in laterally extensive sheet-like multi-storey complexes(Besly, 2018; Hampson et al., 1999; Wasielka et al., 2020). The

percentage of sandstone in the Namurian is generally higher in Quadrants 42 and 43 (up to 60%) than in Quadrant 44 (37%), with individual channel thickness at 10-25 m in Quadrants 42 and 43 compared to 8-20 m in Quadrant 44 (Bailey et al., 1993). According to Hampson et al. (1999) incised valley fill sandstone bodies have a mean thickness of 20-25 m, with a maximum thickness of 30- 45 m locally, and are 5 -25 km wide, whereas the extensive sheet sandstone bodies are similar in mean and maximum thickness to the valley fills (10-30 m and 20-45 m, respectively), but exceed 35-70 km in width. The percentage of sand and channel thicknesses show a decrease from north to south consistent with sediment provenance from the north, according to Bailey et al. (1993).

Besly (2018) suggested that sand bodies of probable turbidite origin found in the lower part of the Namurian may form a viable exploration objective, however Cameron et al. (2005) claims that these are unlikely to provide attractive exploration targets. Turbidite sands analysed in this study do not present good quality reservoirs.

2.5.2 Seal rocks

A northward drift of Pangaea into more arid latitudes during Permian time resulted in deposition of alluvial, fluvial and aeolian sequences, with sabkha and desert-lake evaporates and claystones of Silverpit Claystone Formation. A later sea level rise causing marine transgression across the Rotliegend desert resulted in deposition of carbonates and claystones, with evaporates at basin margins and in playa lakes (Zechstein Group) (Gautier, 2003). These evaporates, claystones and some tight carbonates form an effective regional topseal to the underlying Carboniferous and Rotliegend reservoirs (Figure 2.6; (Monaghan et al., 2017; Cameron et al., 2005)). There is evidence that mudstone intervals within the Westphalian potentially act as an intraformational topseal in some locations, including the Copernicus and Cavendish fields (e.g. Wasielka et al., 2020). Both intra-Carboniferous and Permian shales and evaporates can act as a lateral seal by fault juxtaposition against them (e.g. Conway and Valvatne, 2003; Bailey et al., 1993).

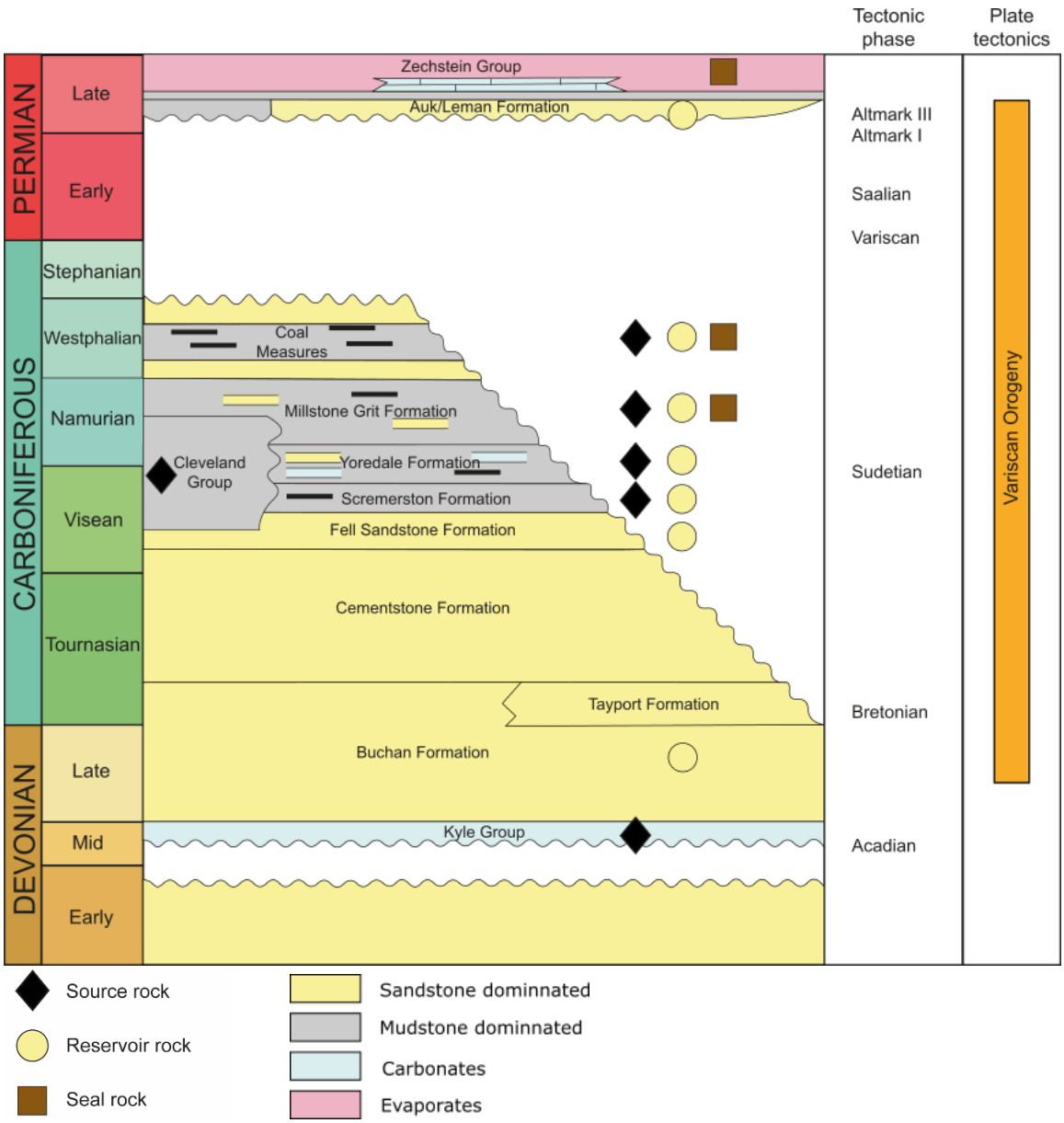

Figure 2.6. Overview of late Palaeozoic stratigraphy and plays. Includes proven and inferred play elements. Modified from Monaghan et al. (2015) and Doornenbal and Stevenson (2010).

2.5.3 Source rocks

Westphalian and Namurian coals (Westoe Coal Formation, Caister Coal Formation, Millstone Grit Formation) are considered to be a source rock for gas for many of the Carboniferous Fields in the region (Cameron and Ziegler, 1997; Cornford, 1998; Gerling et al., 1999; Figure 2.6). Also, Dinantian basinal marine mudstones are a potential source rocks for the Namurian reservoirs (Cameron et al., 2005). Coals and carbonaceous shales in the upper part of the Namurian are typically 0.5-5 m thick and have an average TOC of around 10-20% and consist of gas-prone woody organic matter. The mudstones from the middle section of the Namurian contain a mixture of oil and gas prone inertinite with amorphous and woody kerogen, whilst the lower part

is mainly composed of marine shale with TOCs ranging from 2 to 5% and organic matter with a reduced potential for gas generation (predominantly inertinite and wood) (Bailey et al., 1993).

Marine shales and shallow lacustrine shales have oil potential, particularly onshore (e.g. Fraser et al., 1990), however there is local evidence for offshore oil as well (Besly, 2018; Cornford, 1998).

2.5.4 Traps

Structural and dip traps for Carboniferous reservoirs occur in faulted blocks and small-scale folds superimposed on major anticlines and synclines (Besly, 2018; Monaghan et al., 2017), (Figure 2.7). The traps are commonly in areas that have been modified by Mesozoic or Cenozoic transpression. Most of the Carboniferous drilling targets tested so far are defined by structural closure on the base Permian unconformity (Gray, 2013). Many of the largest traps occur along the crests of ridges bounded by NW-SE trending reverse faults, including Caister, Murdoch (Westphalian reservoirs) and Cavendish Field (Namurian reservoir) on the Murdoch ridge (Cameron et al., 2005).

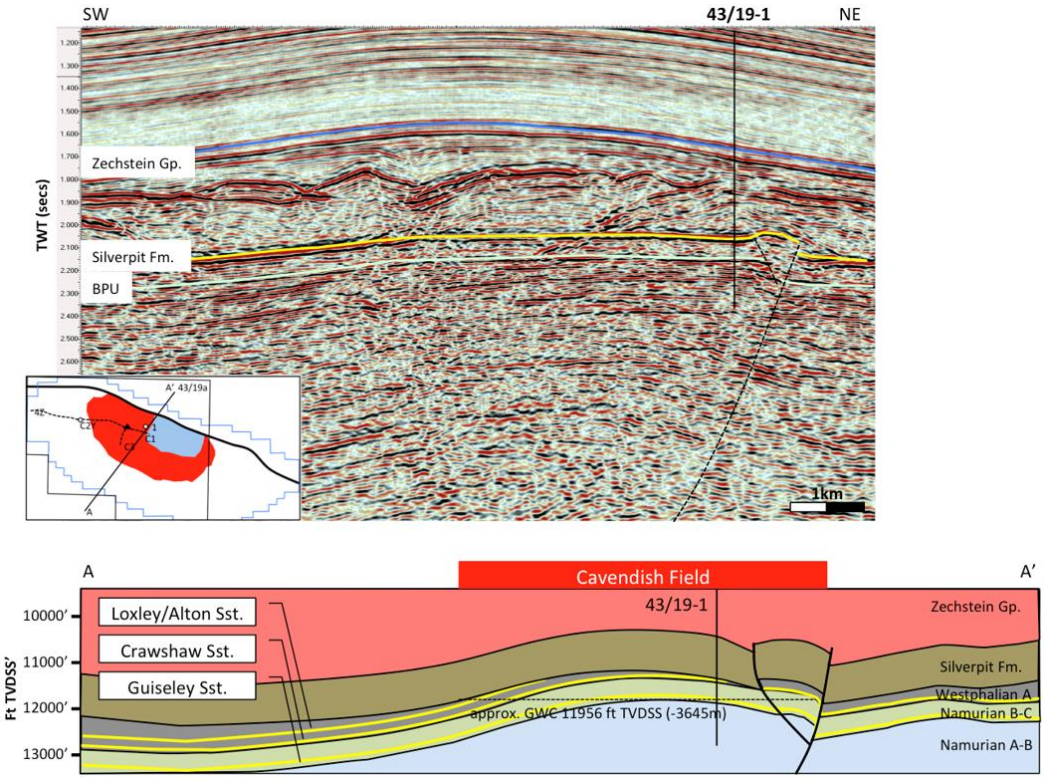

Figure 2.7. An example of a structural trap in the Southern North Sea from the Cavendish Field. Figure shows 2D time-migrated dip-line BN 43/87-107 (image form seismic data acquired for Britoil in 1982) through discovery 43/19-1 and schematic cross section along line. Location shown on inset map, where pale blue area denotes crestal absence of Crawshaw Sandstone. From Wasielka et al. (2020).

2.5.5 Overburden

The Permian deposits above the Base Permian Unconformity comprise mudstones and halite within the Silverpit Formation and halite with anhydrite beds in the Zechstein Group formations (Figure 2.8). The overlying Triassic Bacton Group comprises Bunter Shale Formation and Bunter Sandstone Formation, consisting of red-brown mudstones and sandstones respectively. The next unit up, the Haisborough Group, comprises mudstones, halite and dolomite in the Dowsing Dolomitic Formation, followed by Dudgeon Saliferous Formation, Triton Anhydritic Formation and Winterton Formation composed of claystones with minor anhydrite. The Jurassic

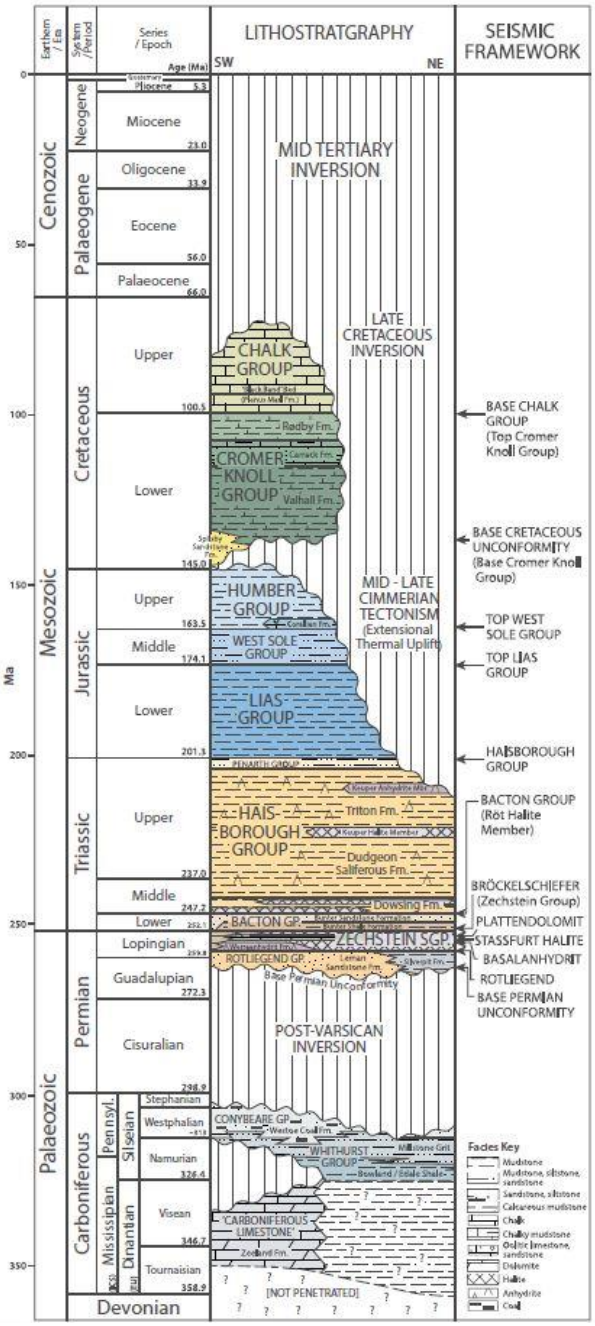

Figure 2.8. Overburden in the southwest margin of the Southern Permian Basin. From Grant et al., 2019.

Lias Group comprises a thick claystone sequence. Most of the Middle and Upper Jurassic sequence was removed by erosion during a domal uplift. The Liassic sequence is unconformably overlain by claystones and limestones of the Cretaceous Cromer Knoll Group and limestones of the Chalk Group. Another period of uplift which begun in the Paleogene removed the latest Cretaceous-Palaeocene deposits. During the subsequent burial a sequence of shales was deposited. A renewed phase of uplift during Late Palaeogene removed the youngest, Late Paleogene and Neogene deposits (Wasielka et al., 2020).

2.5.6 Hydrocarbon generation and migration

The deep lying parts of the Carboniferous sequence entered the oil generation window already during the Carboniferous burial phase in some areas of the SNS (Figure 2.9). Any oil, however, that was generated at this time has likely escaped during the Variscan inversion (Besly, 2018). In other areas, where Carboniferous burial was much shallower, oil generation did not commence until the Mesozoic times (see e.g. well 48/3-3 in Leeder and Hardman (1990)). Carboniferous source rocks entered the gas generation window during the phase of deep burial in the Mesozoic times, between Jurassic and Cretaceous times (Jurassic or Cretaceous by Besly (2018); Cretaceous by Bailey et al. (1993)) in parts of the basin, although some areas never reached depths and temperatures high enough for gas generation. Thermal maturity data show that currently the Upper Carboniferous deposits in Cavendish Field are in oil generation window, with vitrinite reflectance (Vr) values from 0.65-0.72% Ro (well 43/19-1, Millstone Grit Fm.; British Geological Survey (2016), and Copernicus deposits are partially within the oil window, and those buried below c. 4200 m are currently in the gas window (this study). Vr values in the Copernicus well 44/16-1 are from 0.9– 2.0% Ro (Millstone Grit Fm., British Geological Survey (2016). Hydrocarbon migration distances of the Carboniferous sourced gas were relatively short and occurred along porous and permeable sandstones, as well as along fractures in fine-grained sedimentary rocks (Gautier, 2003).

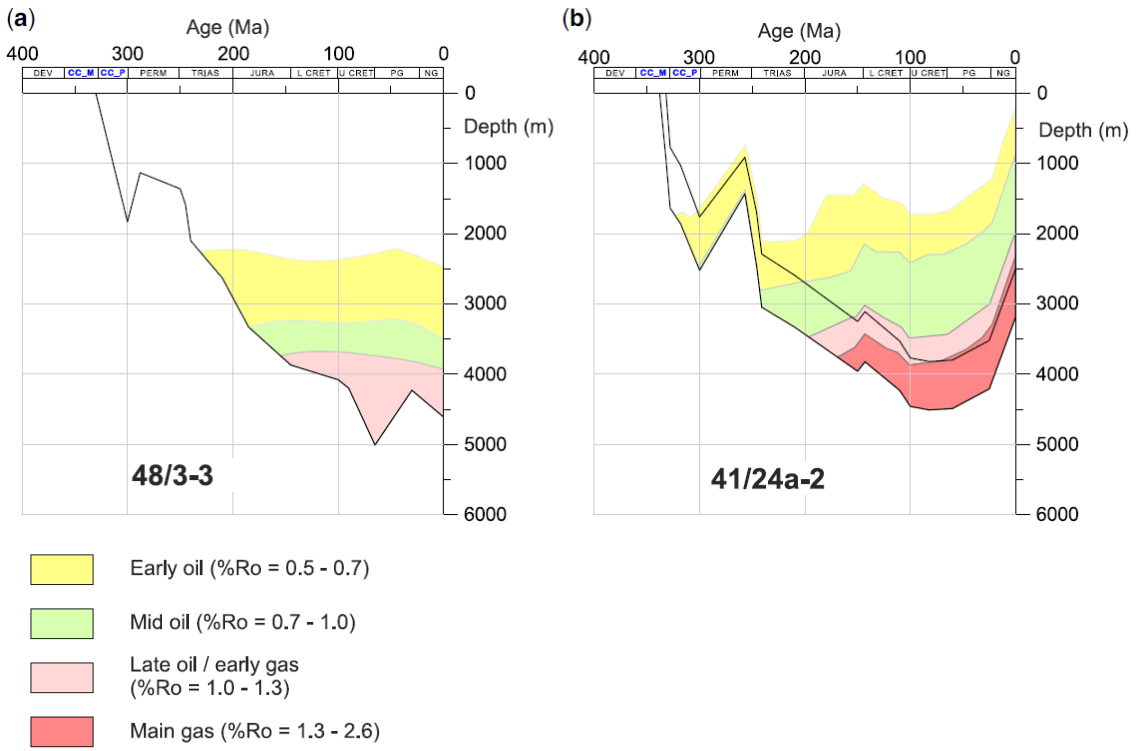

Figure 2.9. Examples of burial history plots illustrating varied burial and maturation histories in different parts of the Southern North Sea. From Besly, 2018.

CHAPTER 3:
Sedimentary and diagenetic controls on reservoir quality in tight Namurian sandstone reservoirs of Copernicus discovery and Cavendish field, Southern North Sea

3.1 Introduction

Reservoir quality of deeply-buried sandstones is a cumulative product of depositional processes and subsequent shallow and deep-burial diagenesis and tectonic movement (Ajdukiewicz and Lander, 2010; Wang et al., 2017). Sedimentological factors such as provenance, transport and depositional processes affect the initial texture, composition, and porosity, which control the fluid flow and geochemical reactions in the rock (Ajdukiewicz and Lander, 2010). Climate and relative sea level changes also have an effect on eogenetic alterations (Morad et al., 2000). Interaction of the sediment with meteoric waters results in the formation of early diagenetic cements and dissolution. Those early diagenetic cements can have a profound effect on reservoir quality preservation, as they can lead to reservoir quality loss or can significantly affect pore water chemistry and subsequently the later diagenetic processes.

Initial variations in sedimentological factors and in the distribution of diagenetic alterations throughout the reservoir result in reservoir heterogeneity (Morad et al., 2000). High heterogeneity, as well as low porosity, very low permeability and commonly well-developed fractures are typical characteristics of most tight gas reservoirs (Khlaifat et al., 2011; Yue et al., 2018). The heterogeneity and the presence of natural fractures can result in spatial variability in productivity, therefore a better understanding of the factors controlling reservoir quality distribution is required to successfully develop such reservoirs.

The Southern North Sea is a mature gas province with numerous gas fields producing from the Upper Carboniferous strata. Yet, Copernicus discovery was drilled and tested for gas, and although gas bearing, was deemed economically non-viable and was never developed. Reservoir quality is considered as one of the most limiting factors in the exploration of the Carboniferous of the Southern North Sea (Cameron et al., 2005). Cementation during deep burial resulted in the formation of tight reservoirs.

Tight gas reservoir refers to a reservoir with permeabilities of <0.1 mD, which requires hydraulic fracturing, multilateral wellbores or horizontal drilling in order to produce economic quantities of gas (Holditch, 2006). Due to technological difficulties tight reservoirs offshore are more expensive to develop that conventional ones. Reservoir heterogeneity additionally makes the development more risky and difficult. It is therefore important to understand what controls reservoir quality distribution

for accurate assessment of reservoir effectiveness, rick reduction, and successful reservoir development.

In this study we analyse what factors were responsible for reservoir quality loss by linking diagenesis to sedimentary facies and pore water chemistry to understand reservoir quality distribution in those tight, heterogeneous sandstones.

3.2 Geological setting and stratigraphy

This study focuses on the Namurian Millstone Grit deposits drilled in Copernicus discovery (block 44/16) and Cavendish Field (block 43/19) in the Southern North Sea (Anglo-Dutch Basin; Figure 3.1). The fields are located about 140-150 km north-east of the Lincolnshire coast in the Silverpit Basin. The structure is a NW-SE oriented dip and fault closed anticline, with the crest of the anticline eroded by the Base Permian Unconformity (BPU). The BPU is underlain by Westphalian A in all wells, except for well 44/16-2, where a short section of Westphalian B is preserved. The Cavendish Field was discovered in 1989 by well 43/19-1 and was put into production in 2007. From then till 2018 when production ceased it produced 98 bcf of gas plus associated condensate (Wasielka et al., 2020). Copernicus was drilled in 1991 and was classed as gas discovery, however it was assessed as economically non-viable and was never put into production (ENGIE, 2015).

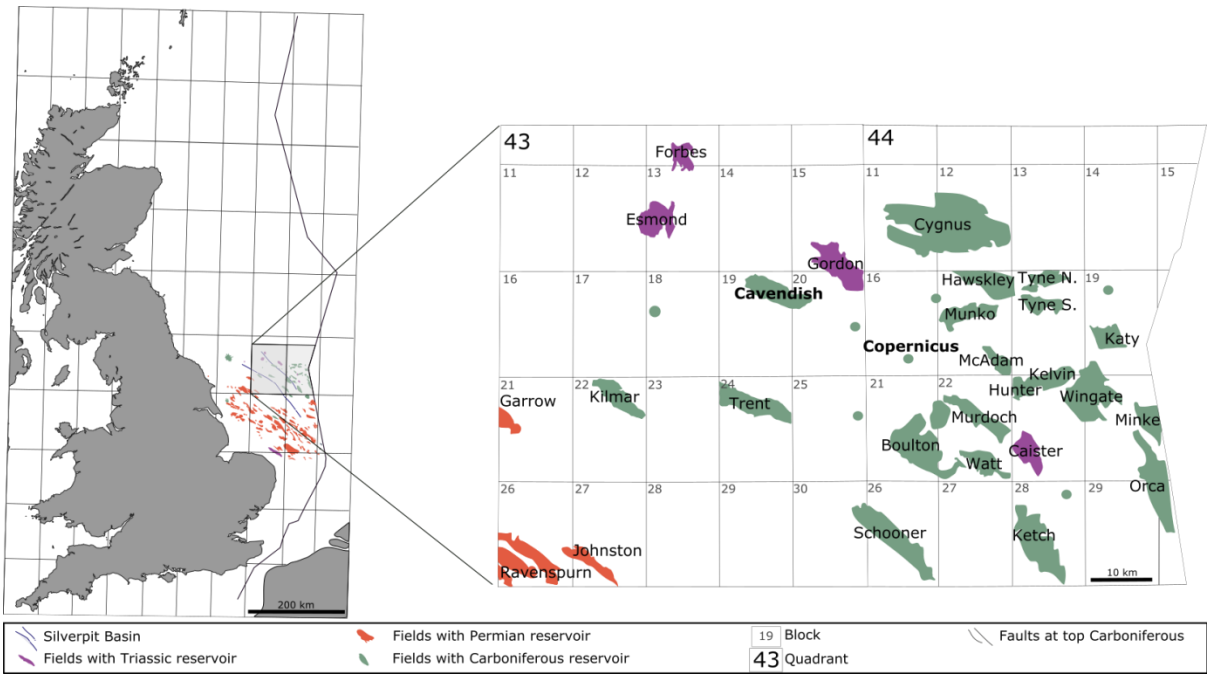

Figure 3.1 Study area.

During Late Carboniferous times the British Isles were located in equatorial latitudes, with warm and humid climate (Waters and Davies, 2006). Closing of Theic

Ocean and collision of Gondwanaland with Laurussia had a great impact on facies development at that time. As a result of growing of a Variscan mountain range, cyclic expansion of ice sheets in Gondwana and the latitudinal shift of the continent, all controlling the Carboniferous climate, a huge fluvial system had developed (Leeder, 1988). It has likely drained continental-scale areas, with the Pennine river-delta system possibly comparable to modern Amazon in size (Leeder, 1988). Cyclical growth and waning of polar ice sheets in Gondwanaland resulting from Milankovitch cycles caused glacio-eustatic sea-level changes that were likely responsible for the bands preserved within the Namurian deposits (Leeder, 1988). On a large scale, the Millstone Grit Formation deposits record a coarsening upwards sequence, from black shales deposited under periodically anoxic conditions in a deep basin, through delta-front turbidites, delta slope deposits, to very coarse-grained fluviodeltaic deposits, and delta plains with coal seams (Leeder and Hardman, 1990; Waters and Davies, 2006). The turbidite feeder channels are restricted to early Namurian (Collinson et al., 1993). By Marsdenian times the deltas had reached the northern margin of the Wales-Brabant High (Waters and Davies, 2006). Lithological cycles of the Millstone Grit in the North Sea are commonly about 50 m thick, but their thickness can reach hundreds of metres (Cameron, 1993).

The Millstone Grit Formation is widespread between the Anglo-Brabant Massif and the Mid North Sea Hugh in Quadrants 40, 41, 43 and 44, with an outlier in Quadrant 39 (Cameron, 1993; Kearsey et al., 2015). Its thickness is highly variable, reaching 1308 m in well 43/25-1.

3.3 Methods

Six exploration wells were logged in detail (scale 1:100), including grain size, sorting, sedimentary structures, bioturbation index, cements, colour, lithofacies and facies associations (Appendices 1 and 2). Lithofacies classification is based on modified Miall's (1996) facies classification with G, S, M representing dominant grain size (gravel, sandstone, mudstone/siltstone). Where macroscopic identification of grain size was impossible, the more generic term of mudstone was applied. A suffix '(M)' and 'M' added after sandstone refers to 'slightly silty' and 'highly silty' respectively. A suffix 'S' after siltstone/mudstone refers to sandy siltstone/mudstone (Table 3.1). Grain size is followed by the sedimentary structure type. Bioturbation index was described using the method of Taylor and Goldring (1993).

Lithology	Percentage Sand	Facies code	Heterolith facies code
'Clean' sandstone	95 - 100	S	-
Silty sandstone	80 - 95	S(M)	S(M)s
Highly silty sandstone	50 -80	SM	SMs
Sandy siltstone	30 - 50	MS	MSs
Siltstone	0 - 30	M	Ms
Conglomerate	0 - 100	G	-
Coal	-	C	-

Structure qualifiers	
m	massive/structureless
l	laminated (mudstones)
p	planar laminated (sandstones, heteroliths)
x	cross-stratified
r	ripple cross-laminated
w	wavy lamination
fla	flaser lamination
hcs	hummocky cross stratification
b	bioturbated
ped	pedogenically modified

d	deformed
g	pebbly
i	injected
c	clast supported (conglomerates)
m	matrix supported (conglomerates)

Table 3.1. Lithofacies classification.

One hundred and eighteen sandstone samples were collected from six wells (Appendix 1) representing Millstone Grit Formation from the Southern North Sea. The samples were selected at or as close as possible to core plugs depths where poroperm data was readily available. The samples from five wells (43/19-1, 43/19-2, 44/16-1, 44/16-1Z, 44/16-2) were selected to be statistically random representing the porosity distribution for the whole set of measured core plugs (99.5% confidence limits). Extra samples from the most permeable intervals were added to help with analysis of the factors controlling reservoir quality distribution. Well 43/19a-4Z was sampled to cover the main reservoir units. All samples were then impregnated with blue resin before petrographic thin sections were made to highlight pores. Carbonate minerals were stained with Alizarin Red S and Potassium ferricyanide to identify varieties of calcite and dolomite. The samples from five wells were selected to be statistically random representing the porosity distribution for the whole set of measured core plugs. Sampling in well 43/19a-4Z was targeted at the most permeable intervals. One hundred point grain size measurements and three hundred point counts were undertaken on all thin sections using Conwy Valley Consultants stepping StageTM connected to PETROG software. A subset of samples representing a range of diagenetic patterns was selected for SEM analyses. They were analysed using Hitachi SU-70 field emission gun scanning electron microscope equipped with an energy-dispersive detector (EDS). Mineral and elemental maps were collected and processed using AZtecEnergy EDS Microanalysis software. Cathodoluminescence analysis has been undertaken using Gatan MonoCL system with a panchromatic imaging mode, and blue, red or green filter.

3.4 Results

3.4.1 Lithofacies and facies associations

The analysed intervals within the Namurian Millstone Grit Formation represent a siliciclastic system dominated by fine-grained sediments (claystones and siltstones) with lesser sandstones, and subordinate contribution of granulestones and conglomerates. The six logged wells (Appendices 1 and 2) show that the Millstone Grit Formation is highly heterolithic, and hence highly heterogeneous, with variable reservoir quality. The net:gross of the Upper Carboniferous strata ranges from 17-36% (Table 3.2; data from Amoco (U.K.) (1989) and Unknown (n.d.), Well 44/16-1 and 44/16-1ST Final Well Report).

Despite a limited amount of cored section in the Namurian strata in the studied wells patterns of coarsening-upwards cycles can be seen (i.e. claystone → siltstone → sandstone → conglomerate). These patterns are particularly well seen on the wireline logs (Gamma-ray and density logs; Figure 3.2), with cycles typically 30 – 60 m (100 – 200 ft) thick. The lateral extent of individual lithofacies is difficult to infer due to fragmentary record and distance between the wellbores. The multiple cycles of sea level change during delta progradation resulted in the development of multiple facies associations, from deep water muds to continental deposits, which are well represented in the cored sections (Figure 3.3 and 3.4). These facies are characterised by different lithology, grain size, sedimentary structures and depositional processes that led to their development. The 1:100 core descriptions charts are presented in Appendix 2.

Field	Well	Net:gross	Cut off	Interval
Cavendish	43/19-1	17%	porosity >7% which relates to 0.1mD permeability, gamma ray response <50 API	Carboniferous
	43/19-2	22%	porosity >8% which relates to 0.1mD permeability, gamma ray response <50 API	Carboniferous
	43/19a-4Z			

	44/16-1			
Copernicus	44/16-1Z	36%	Porosity >8%, 40%Vshale cutoff	Intervals: 12118 - 12187, 14174 - 14234, 14708 - 14849
	44/16-2			

Table 3.2. Net:gross values of the Upper Carboniferous section from operators reports: data from (Amoco (U.K.), 1990, 1989); Unknown (n.d.), Well 44/16-1 and 44/16-1ST Final Well Report. Greyed out areas indicate no available data.

The lithofacies identified in the studied area have been grouped into twelve facies associations. These include multi-storey fluvial channels (MSFC), distributary channels, delta plains and swamps representing the proximal parts of the system, shoreface and interdistributary bays in the medial parts, and proximal and distal delta front and prodelta, prodelta turbidite complex and offshore muds representing the distal setting. Facies associations, which are described in detail in Table 3.3, were used as a baseline for further analysis of potential impact of the sedimentary environments and processes into diagenetic patterns recognised in thin sections. Special attention was placed on sandstone intervals as they form the main exploration target.

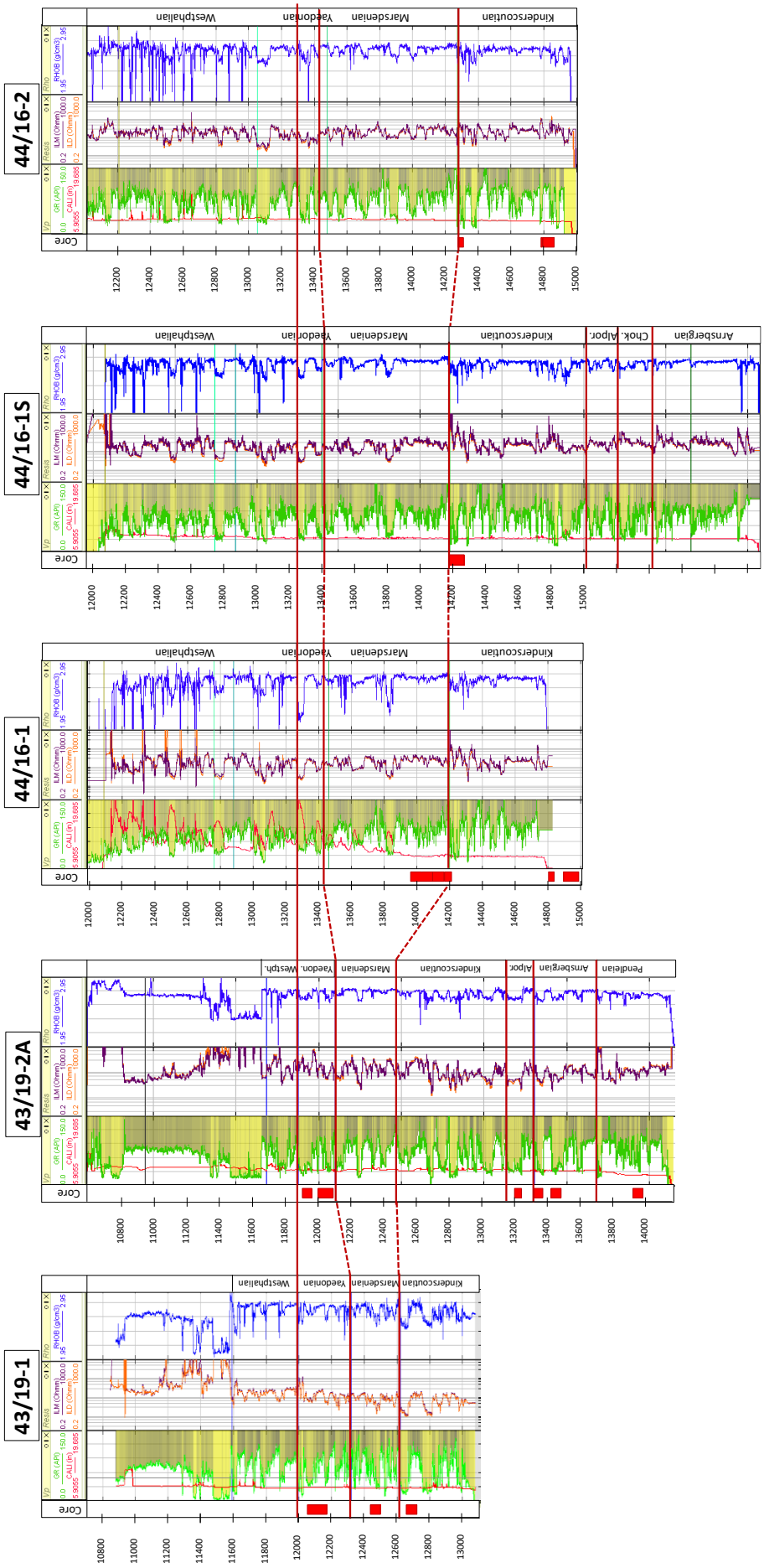

Figure 3.2 Well correlation panel of wells in Cavendish field and Copernicus discovery, flattened on top Namurian. Multiple coarsening upwards cycles are reflected in the upwards-decreasing gamma-ray responses. The gamma-ray maxima at the base of each cycle represent basin muds, while the gamma-ray minima represent clean, fluvial sandstones. Alpor = Alportian, Chok = Chokierian.

Conglomerates and granulestones (lithofacies 'G) are matrix- or clast-supported and form relatively thin (up to 25 cm) beds composed of granule to pebble sized grains of mudstones, quartz and lithic grains. Lower boundaries are erosive whereas upper boundaries are sharp or gradational. No clear stratification is observed, however clasts are locally aligned parallel to each other, picking out crude low angle cross-stratification. Conglomerates are found in high-energy environments such as basal part of the multi-storey fluvial channels, likely representing channel lags. Cross bedded sandstones were deposited as longitudinal bars suggesting downstream bar migrations although lateral accretion cannot be ruled out. The dominant depositional process suggests deposition from bedload.

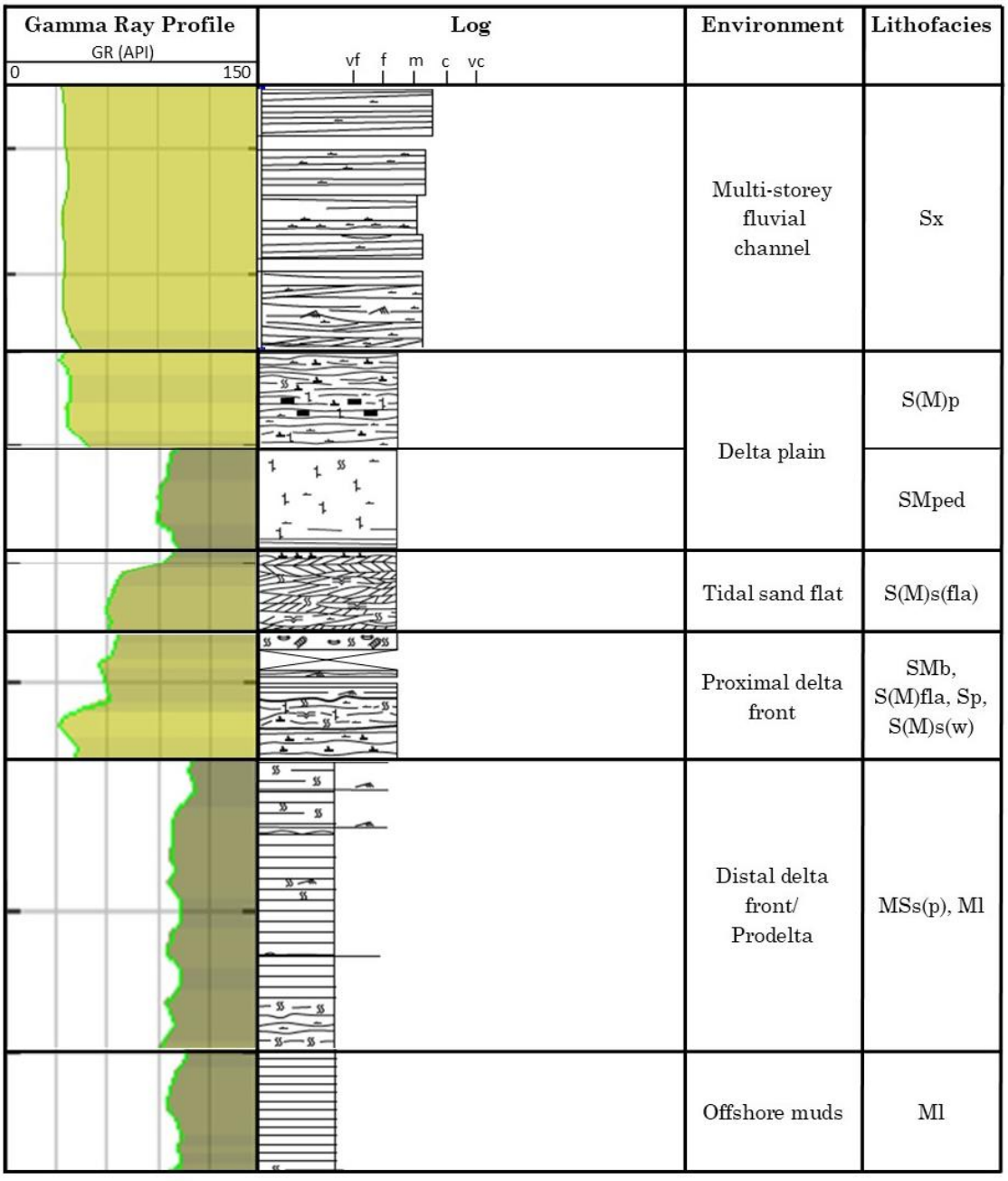

Figure 3.3. Facies association characteristics. Refer to Table 3.1 for abbreviations.

Sandstones (lithofacies 'S') dominate through the cored sections. These are commonly fine to medium grained, and locally coarse grained with occasional very coarse-grained beds. They are well cemented with no- or very low visible porosity. Sandstones are typically moderately well sorted but reveal a variety of sedimentary structures including sets with tabular and trough cross stratification, low-angle cross stratification, horizontal stratification, ripple-cross lamination or hummocky cross-stratification and wavy lamination. Lamination is highlighted by grain size variation, mud content, and carbonaceous plant debris. Locally, sandstone primary structures are heavily obliterated by bioturbations and pedogenic processes. Sandstone intervals were deposited in various proximal to distal environments with varying discharge energies. Cross stratification and ripple cross-lamination indicate aggradation and migration of small to medium size micorforms as well as deposition and reworking by turbulent sub-critical flows that generated 2D/3D dunes (Ielpi and Ghinassi, 2015). Sandstones associated with turbidite complex in distal part of the system were transported in turbulent/cohesive flows (such as debris flows and turbidites). Sandstones dominate in following environments: multi-storey fluvial channels, distributary channels delta plain, shoreface and proximal delta front, however matrix content in sandstones increases towards the basin (Figure 3.3 and 3.4; Table 3.3)

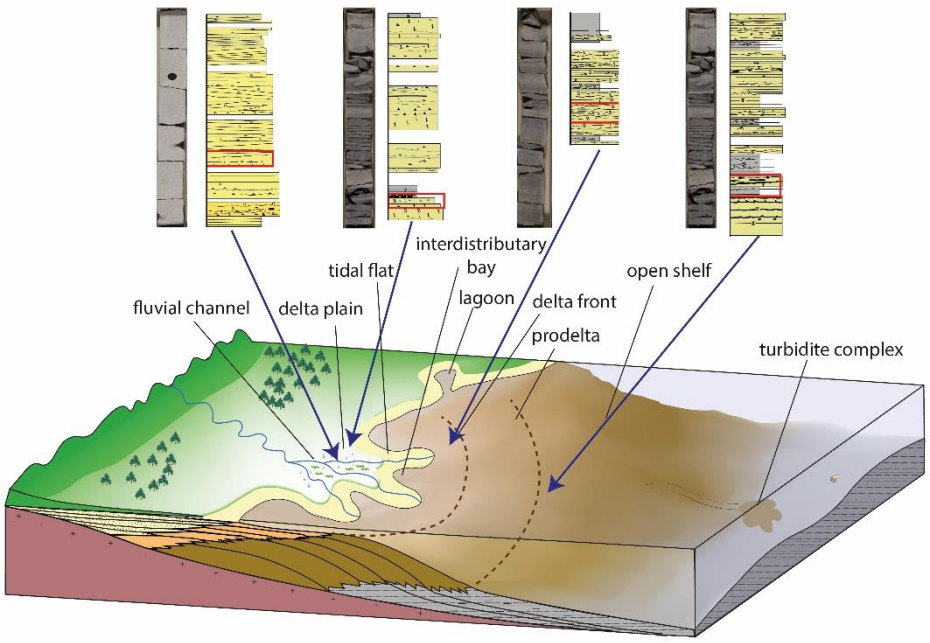

Figure 3.4. Deposition during the Namurian occurred through largo fluviodeltaic systems infilling pre-existing basin topography. Sedimentary log fragments of several examples of facies associations described in cores are shown above, with photos showing 1 m core fragments that are marked in red boxes on the log.

Mudstones (here comprising both siltstone and claystone fraction) are represented by grey to dark grey intervals, often with preserved fauna and bioturbation structures. Within the mudstones thin (up to 5 cm) siderite bands are present. Mudstone intervals were deposited mostly in tranquil settings such as offshore muds etc. (for details see Table 3.3). The lateral extends of some claystone/siltstone intervals allowed to use them as intrabasinal stratigraphic markers.

Facies described in the cored sections from the Copernicus and Cavendish fields generally show similar development in both areas (Table 4.3), however a notable difference lies within the multi-storey fluvial channels, which show coarser grain size in Cavendish Field, where they range from upper fine to lower very coarse grain size, compared with upper fine to upper coarse grain size in Copernicus. The coarse-grained sections also have bigger thicknesses in Cavendish than in Copernicus. Amalgamated sandstone intervals are also thicker in Cavendish than in Copernicus as seen in core (24.5 m and 15 m (or 80 and 50 ft) respectively; Appendix 2) and on the wireline logs, where clean sandstone intervals of likely fluvial origin are thicker in the Cavendish respectively reaching up to 30 m (100 ft; Figure 3.2)

Facies association	Description	Interpretation	Main lithofacies	Subordinate lithofacies
Offshore muds	Dark grey, fissile, parallel-laminated m-scale claystone/siltstone intervals with occasional dark grey or brown very fine-grained sandstone stringers and lenses that are millimetre to 20 cm thick. Goniatites, and undifferentiated calcitic bioclasts are locally preserved. Siderite bands and nodules are common, with pyrite nodules also locally present. Bioturbation is largely absent, with sparse burrow mottling and *Chondrites* observed locally within claystones/siltstones and burrow mottling within sandstones.	Low-energy, suspension fallout well below the storm wave base was the main depositional process. General lack of bioturbation and dark colour suggests anoxic conditions. Thin sandstone beds indicate that sediment transport also occurred, possibly caused by storms, major river floods or gravity-induced sedimentary instability. In the Namurian of Millstone Grit facies the marine shales with goniatites represent the transgressions (Ramsbottom, 1977).	Ml	SMp, Sr
Prodelta turbidite complex	Light grey-brown moderately well sorted mid very fine to upper fine-grained sandstones arranged into packaged up to 5 ft thick interbedded with dark grey siltstones. Siltstone intervals are up to 15 ft thick, but are interrupted by frequent sandstone stringers. Sedimentary structures observed within sandstone beds and stringers comprise horizontal stratification, low-angle cross stratification and ripple cross lamination. Thick (up to 5 ft), massive intervals are also present. Occasionally pebble-size mudclasts occur within sandstone beds. Sandstones commonly show sharp bed bases, with locally erosive surfaces evident. Siltstones are predominantly	Upward-fining, laminated or normally graded sandstone to mudstone beds with *flame structures*, flat or erosive bases are a characteristic product of surge-type turbidity currents (Sultan and Plink-Björklund, 2006). Massive sandstones reflect high rates of sediment accumulation, while the ripple cross laminated intervals were deposited under waning flow (Collinson et al., 1991). Loading structures form when sand beds are deposited above mud layers resulting in a density inversion with the denser sand	S(M)p, Ml, SMs(p), SMs(r)	Sm, SMp, Ms(p), SMs(x), S(M)r, SMs(w), S(M)s(p), S(M)s(r), Sx, S(M)x, S(M)d, SMs(d), MSs(p), MSs(p), MSs(d), SMx, Md, Sp, Sr,

Facies association	Description	Interpretation	Main lithofacies	Subordinate lithofacies
cont. Prodelta turbidite complex	planar stratified, with occasional ripple cross-lamination and sandstone injections. Sandstones and siltstones are locally arranged into dm-scale fining upwards packages. Loading structures and flame structures are common at bed bases, soft sediment deformed beds and occasional synaeresis cracks are also observed. Rare weak bioturbation structures include *Zoophycos* traces and burrow mottling. Carbonaceous debris scattered in sandstones.	sinking into an underlying muddy substrate. In response mud is often displaced upwards into forming flame structures (Southern et al., 2014). Synaeresis cracks, carbonaceous matter and low abundance trace fossil suite are interpreted as evidence of fresh water input (MacEachern and Pemberton, 1994; Pattison, 2005).		S(M)s(g), MSs(r), S(M)g, S(M)d, Ms(p), MS(r), Ms(p), Ms(r), Sg, SMr, Mr, MSs(p)
Distal prodelta	This heterolithic facies predominantly consists of dark grey, cm- to dm-scale horizontally, and less commonly ripple-cross laminated siltstones and sandy siltstones, interbedded with minor mm- to lower dm-scale, mid very fine to mid fine-grained, moderately-well sorted silty sandstone beds, stringers or lenses. Some beds show soft sediment deformation. Sandstones show planar stratification, low angle cross stratification and ripple-cross lamination. Occasional thin siderite bands and mm-scale pyrite nodules are present. Bioturbation is absent to moderate, comprising *Chondrites*, *Teichichnus*, *Zoophycos* and general burrow mottling. Occasional small bioclasts are observed. Carbonaceous debris is scattered throughout.	This facies records deposition in generally poorly oxygenated, low energy conditions and slow sedimentation rate suggested by low ichnodiversity and simple tiering structure. Suspension fallout is the dominant depositional process, at times interrupted by tractive sand deposition (Carmona et al 2009). The presence of carbonaceous matter coupled with the low abundance trace fossil suite, is interpreted as evidence of fresh water input (Pattison, 2005).	Ml, Mr	MSr, Ms(p), SMs(p), SMs(r), S(M)x

Facies association	Description	Interpretation	Main lithofacies	Subordinate lithofacies
Proximal prodelta	Heterolithic succession consisting of mm to dm-scale siltstones and sandy siltstones interbedded with cm- to dm-scale mid very fine to upper fine grained silty sandstone bed and stringers. Siltstones are typically horizontally laminated, while sandstones are horizontally and ripple cross-laminated and occasionally deformed by slumping. Interbedded sandstones commonly show sharp bed bases. Some sandstone beds show soft sediment deformation. Occasional thin siderite bands, mm-scale pyrite nodules, or small bioclasts are present. Bioturbation is absent to moderate with *Teichichnus*, *Planolites*, *Chondrites, Zoophycos*, resting traces and general burrow mottling. Carbonaceous debris is scattered throughout.	Increase in grain size suggests a more proximal setting compared to the above facies, but its heterolithic nature still indicates a position within the prodelta setting. Deposition of sandy silt and silt interbedded with very fine and fine sand laminae represents the occurrence of alternating high- and low-energy sedimentary processes, with silt deposition occurring mainly from suspension fallout and sandstone deposited by current action (Carmona et al., 2009). The presence of synaeresis cracks indicates reduced salinity (MacEachern and Pemberton, 1994). Slumps formed on slopes due to downslope gravitational instability, where sediments were rapidly deposited and easily liquefied (Bhattacharya and Davies, 2004).	Ml, SMs(p), MSs(p)	MSs(r), Mb, Ml, SMb, SMd, SMp, SMs(p), MSs(p),Ms(p), SMs(w), S(M)p, Msp
Distal delta front	Light grey brown and light grey, moderately well sorted, lower fine to fine/medium 'clean' to silty sandstones form cm- to lower m-scale packages, interbedded with minor dark grey siltstones millimetre to metre thick horizontally laminated beds. Sandstones are horizontally stratified, low-angle cross-stratified, ripple-cross laminated, and locally wave cross	This sand dominated facies is results from deposition on a distal part of delta front. Cross stratification and ripple cross lamination suggest the dominance of unidirectional flow, but the occasional wavy bedding indicates wave influence and relatively shallow water conditions. Soft-sediment deformation features suggests sedimentary loading due to rapid	S(M)p, SMs(r), SMs(p), Ml	Sm, SMp, Ms(p), SMs(x), S(M)r, SMr, S(M)s(r), Sx, S(M)x, S(M)s(p), S(M)d, SMd, MSs(p), Md,

Facies association	Description	Interpretation	Main lithofacies	Subordinate lithofacies
cont. Distal delta front	stratified. Sandstone beds show sharp, locally erosive bases. Some intervals are deformed and contain sandstone injections. Occasional thin siderite bands and mm-scale pyrite nodules are present. Carbonaceous debris is common. Elongated mud clasts up to cobble grade are locally present within sandstone beds. Bioturbation within both sandstones and siltstones is absent to moderate and comprises *Planolites* and unidentified burrow mottling.	deposition probably along relatively steep slopes (Buatois et al., 2008). Sandstone intrusions which are associated with the deformed intervals have likely formed due to localized excess pore fluid pressures generated by deposition related processes such as slumping, the passage of storm waves or channel switching, but can also result from seismicity-induced liquefaction, tectonic stress, or the influx of an overpressured fluid from deeper within the basin into a shallow sand body (Jolly and Lonergan, 2002).		MSs(r), SMs(w), MSr, MSs(p)
Proximal delta front	Light grey, moderately well sorted, very fine/ fine to mid fine grained, silty to 'clean' sandstones organised into m-scale packages, interrupted in places by mm- to cm-scale dark grey siltstone laminae. Sandstones are mainly ripple-cross laminated, low angle cross-stratified and occasionally hummocky cross-stratified or display wave ripples. Sandstone is locally penetrated by roots. Some intervals are weakly deformed. Carbonaceous debris is scattered throughout. Local weak bioturbation comprises escape burrows and unidentified burrow mottles.	This facies was deposited on the proximal portion of fluvial dominated delta front. Hummocky cross stratification and wave ripples indicate wave influence in a shallow water setting. The presence of possible root structures suggests that current and wave energy became less prominent at times. Soft-sediment deformation features suggests sedimentary loading due to rapid deposition probably along relatively steep slopes (Buatois et al., 2008).	S(M)r	Sp, S(M)x, S(M)hcm, Sx, Shcm, S(M)p, S(M)s(w), Ml, MSs(p), SMs(p)

Facies association	Description	Interpretation	Main lithofacies	Subordinate lithofacies
Inter-distributary bay	Highly heterolithic facies composed of light grey, moderately well sorted, mid very fine to upper fine-grained sandstones and dark grey siltstones, mostly arranged into dm- to m-scale coarsening upward sequences. Sedimentary structures in sandstones are represented mainly by ripple cross lamination, wavy and planar stratification. Some sandstone beds show erosive bases. Sandstone beds are commonly pedogenically modified with numerous root traces and contain plant debris. Siltstones are planar or ripple cross-laminated. Bioturbation is absent to locally high. Trace fossils is represented by *Teichichnus, Diplocraterion*, *Planolites, Asterosoma* and burrow mottling. Siderite bands and nodules are present. Carbonaceous debris is observed locally.	Coarsening upward sequences reflect repeated infilling of the bays, commencing with muds deposited from suspension during river flood periods, passing into sands during levee progradation (Elliott, 1974; Reading, 1995). Sandstones with erosive bases may indicate development of crevasse splays. Wave reworking produces symmetrical ripples (Reading, 1995). Pedogenically modified intervals with plant fragments represents the proximal facies of the bay filling and abandonment phase, resulting in marsh development (Elliott, 1976).	SMr, Ml, SMp	SMw, Mm, S(M)p, MSs(r), MSs(p), Ms(p), S(M)r, S(M)w, SMs(r), SMs(p), SM(d), Sp, Sr, S(M)fla, SMfla
Shoreface	Light grey, moderately well sorted, mid to upper fine, 'clean' to slightly silty sandstones interbedded with minor cm-to dm-scale dark grey siltstone beds. Sedimentary structures observed in sandstones comprise current and wave ripple cross-lamination, horizontal stratification, low angle-cross stratification, hummocky cross-stratification, and wavy bedding. Bed bases are either gradational or abrupt. Siltstones are	Combination of hummocky cross-stratification and current ripples records deposition under the influence of mixed wave and current activity. Hummocky cross-stratification records deposition from powerful oscillatory and/or unidirectional flows with high suspended sediment loads (Hampson, 1998) whereas the current ripple structures suggest rapid deposition by	S(M)r	S(M)p, MSr, MSs(r), Sx, Ml, S(M)x, Sr, S(M)w, S(M)s(hcs), S(M)hcs, MSs(len), Shcs

Facies association	Description	Interpretation	Main lithofacies	Subordinate lithofacies
cont. Shoreface	horizontally or ripple cross-laminated. None to moderate bioturbation comprises escape structures and unidentified burrow mottling, and sparse pedogenic modification are observed in places. Scattered carbonaceous debris is present.	unidirectional tractional flows. The mixed character of unidirectional and oscillatory flow might be a result of deposition or reworking by storm events (Hampson, 1998). Deposition took place in relatively shallow water, above the storm wave base, and close to shoreline, as suggested by the local presence of pedogenic modification.		
Delta plain	Light brown-grey and mid grey, lower fine to fine/medium grained, 'clean' to silty sandstones, interbedded with dark grey siltstone intervals. Sandstone bodies up to 25 ft thick. They are massive, low angle cross-stratified, crinkly, or flat horizontally laminated or ripple cross-laminated. Root structures are common in paleosoil intervals. Primary structures are often obliterated by the strong pedogenic alternations. Mm- to cm-scale coal seams and occasional mudclasts up to pebble grade are present, with carbonaceous debris common throughout. Sparse bioturbation is seen in places. Siderite bands and nodules are present. This facies is typically developed on top of fluvial channel facies.	This facies records deposition on a delta plain, recording channel abandonment, infill, and overbank flooding. Interchannel areas starved of coarse sediment supply for long periods were sites of pedogenesis. Coals record prolific plant growth and preservation of organic matter in reducing conditions (Reading, 1995).	S(M)x, SMped, S(M)ped, S(M)p	S(M)m, Sx, SMs(w), Sm, Ml, Sped, Sp, SMp, Ms(p), coal, MSped

Facies association	Description	Interpretation	Main lithofacies	Subordinate lithofacies
Swamp	Dark grey planar laminated claystones and mudstones with occasional mm-thick sandstone laminae. Occasional sparse bioturbation within claystones/siltstones. Siderite nodules and bands, and mm-thick coals seams are present. This facies is always developed on top of delta plain.	Deposition on waterlogged swamp areas from suspension of mud and organic-rich fine sediment on a flood plain, in a reducing environment (Reading, 1995).	Ml	Ms(p)
Distributary channel	Mid grey-brown, light grey, moderately well sorted, mid to upper fine m-scale 'clean' sandstone beds, interbedded with mm-to cm-scale muddrapes. Sandstones are mainly low-angle cross stratified or less commonly horizontally stratified, ripple cross laminated or massive. Fine carbonaceous debris is common, mudclasts up to pebble size and pedogenic alterations are observed in places.	This facies represents single-storey distributary channels. Low angle cross bedding, flat lamination and ripple cross lamination reflect unidirectional traction currents with fluctuating strength (Reading, 1995). Channel avulsion led to deposition of finer grained ripple cross-laminated beds, siltstones and pedogenic alterations.	Sx	Sm, Sp, S(M)p, MSs(p)
Multi-storey fluvial channel	Light grey to light grey-yellowish, moderately to moderately well sorted, upper fine to very coarse grained, 'clean' to slightly silty sandstones, interbedded with occasional cm- to dm-scale siltstone beds and cm- to dm-scale granulestone and conglomerate beds. Dm- to m-scale fining upward conglomerate, granulestone and sandstone profiles are amalgamated into up to 80 ft packages. Individual beds locally show erosional bed bases with pebble lags	Based on the coarse grain size and cross-stratification style this facies is interpreted as deposits of a braided fluvial system. The presence of multiple sets fining-upwards sequences beginning with erosion surfaces suggests that these sandstone bodies are multi-storey, with each set inferred to represent a single-storey	Sx	S(M)x, Sp, Sr, MSp, Sm, S(M)g, MSs(p), Sg, Sd, GSm, GSc, SMp, S(M)p, S(M)r, S(M)w, Sr, Ms(d), Ms(p),

Facies association	Description	Interpretation	Main lithofacies	Subordinate lithofacies
cont. Multi-storey fluvial channel	consisting of mudclasts and rigid grains. Sandstone bodies are predominantly low angle cross-stratified, trough cross stratified, or horizontally stratified, but massive sandstones are also developed. Ripple cross-lamination is largely limited to fine-grained sandstone intervals. The less abundant conglomerates (GSm and GSc lithofacies) are limited to the Cavendish Field. Conglomerates are matrix- and clast-supported and comprise red brown mudclasts, quartz and lithic fragments. Outsized mudclasts and rigid grains up to a pebble grade are present within the medium and coarse grained sandstones in both Copernicus and Cavendish. Fragments of carbonaceous debris are scattered throughout. Moderate bioturbation is observed within siltstone intervals	channel (Hampson, 1995). Siltstone beds represent temporary channel abandonment. Fining upwards sequences result either from infilling of the channel by diminishing flow possibly leading to channel abandonment, or lateral migration of the channel (Reading, 1995).		SMs(r)

Table 3.3. Sedimentary facies of Cavendish field and Copernicus discovery.

The facies association that shows overall best reservoir quality is multi-storey fluvial channels (Figure 3.5c). The highest recorded macroporosity values, as well as the highest average porosity values are recorded in the multi-storey fluvial channels (max 7.7%, average 3.1%) and delta plain (max 8.0%, average 2.9%) in the Copernicus discovery, and in multi-storey fluvial channels (max 21.7%, average 6.1%) in Cavendish Field. Similarly, multi-storey fluvial channels have the highest geomean permeability values in both areas (0.8 mD and 1.2 mD in Copernicus and Cavendish respectively) (Appendix 5, Figure 3.5). The maximum permeability value of 691 mD is in Cavendish well 43/19a-4Z in multi-storey fluvial channel (Figure 3.5a). The highest measured permeability value in the Copernicus discovery (61 mD) is in the sample from a delta plain facies. Depositional facies are strongly related to grain size, with the coarsest grains recorded within multi-storey fluvial channel (compare (Figures 3.5 b and c).

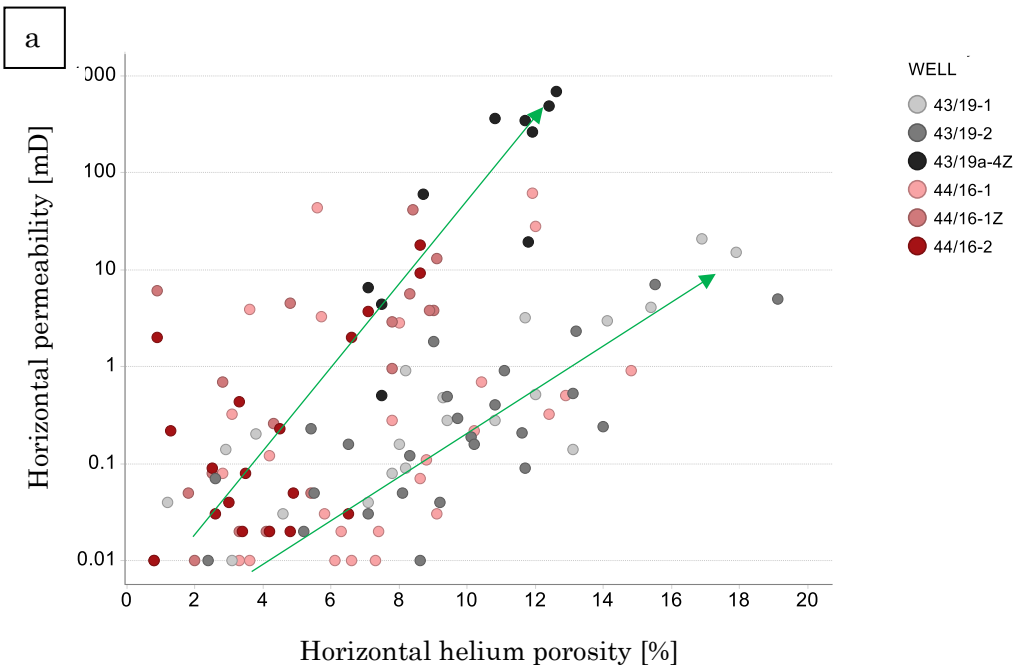

Figure 3.5. Porosity – permeability plots coded by a) well; b) grain size; c) facies association. Note the two separate poroperm trends indicated by arrows.

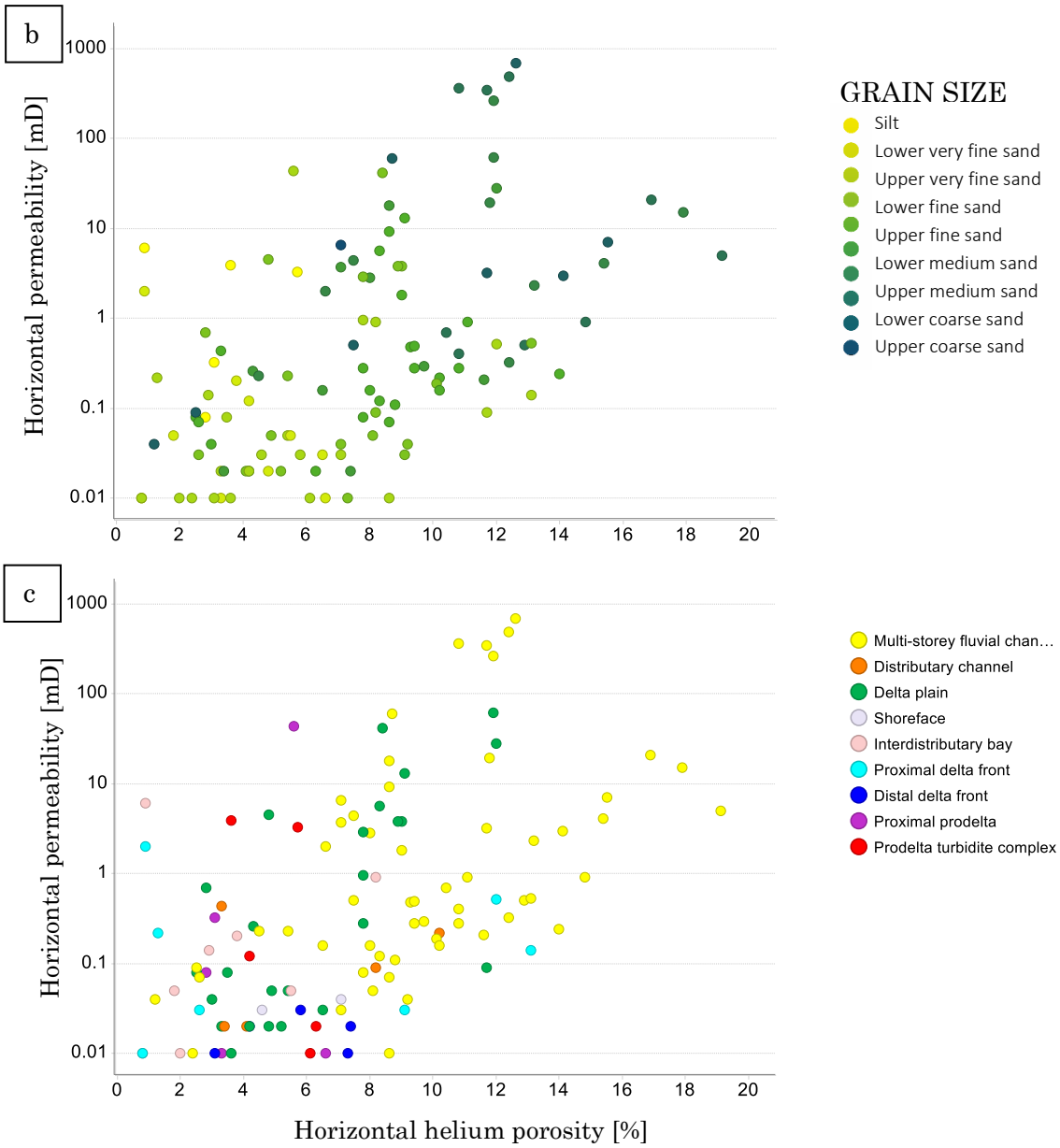

Figure 3.5. Porosity – permeability plots coded by a) well; b) grain size; c) facies association.

3.4.2 Petrography and diagenesis

3.4.2.1 *Detrital mineralogy and textures*

Analysed samples from the Namurian in the Copernicus discovery can be classified as 34 quartz arenites, 10 sublithic arenites, 7 sublithic wackes, 7 feldspathic arenites, 2 lithic arenites, 2 lithic wackes and 1 subfeldspathic arenite (based on Folk's (1980) sandstone classification scheme; Appendix 3). Thirty-one of those sandstones are further classified as siliceous, since they contain >10% quartz cement, seven as dolomitic, seven as sideritic, two as dolomitic/sideritic. Samples from Cavendish field are significantly more quartz rich and cleaner, comprising 28 sublithic arenites and 27 quartz arenites. Notably, no feldspathic or subfeldspathic arenites are recorded in

Cavendish. Eighteen samples are further classified as siliceous, five as dolomitic, three as sideritic and one as dolomitic/siliceous. Grain size ranges from silt grade to upper coarse-grained sand in Copernicus and lower very fine to lower very coarse-grained sand in Cavendish (Appendix 3). The sediments are primarily moderately well sorted, with mainly subrounded and subangular grains. The coarse- to very coarse-grained sandstones occur only within the multi-storey fluvial facies.

Sandstone classification plots show that the detrital composition does not vary significantly by well (Figure 3.6a), with the exception of well 44/16-1, where the shallowest sandstones contain higher proportion of feldspars and lithic fragments. Quartz, feldspar and lithic proportions show that the greatest variability in grain composition is exhibited by samples from the most distal facies: prodelta turbidite complex, proximal prodelta and distal delta front, in the Copernicus discovery (Figure 3.6b). In Cavendish Fields, distal delta front facies and some of the multi-storey fluvial channels show the biggest variation in composition (Figure 3.6c). The 'clean' sandstones (lithofacies S) are quartz arenites, whilst the silts and silty sandstones (lithofacies M, MS and SM) are typically feldspathic, lithic and sublithic in composition in Copernicus (Figures 3.6 d & e). Composition is also associated with grain size, with the coarse-grained sandstones being more quartz rich than the silts which contain more feldspar in Copernicus, and lower very fine grained sandstones containing more lithic fragments in Cavendish (Figures 3.6 f & g). This is, however, facies controlled, with the cleanest and coarsest sandstones deposited within the fluvial channels (Figures 3.6 b & c). Sorting does not have a big influence on sandstone composition (Figures 3.6 h & i).

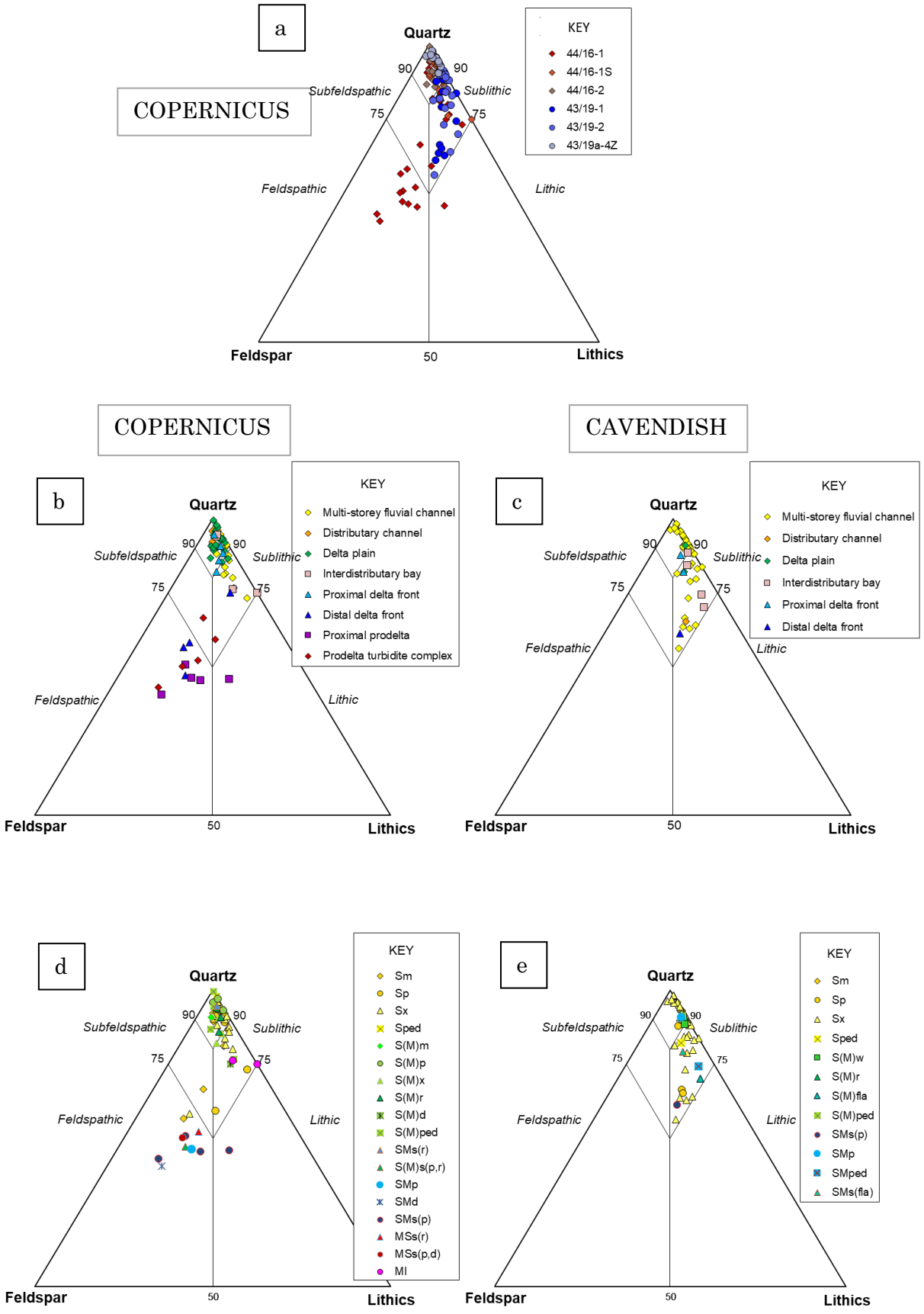

Figure 3.6 continued: Detrital composition of sandstones (QFL plots) split by a) well; b-c) facies association; d-e) lithofacies; f-g) petrographically-derived grain size; h-i) petrographically-derived sorting. Copernicus field is shown on the left, Cavendish on the right.

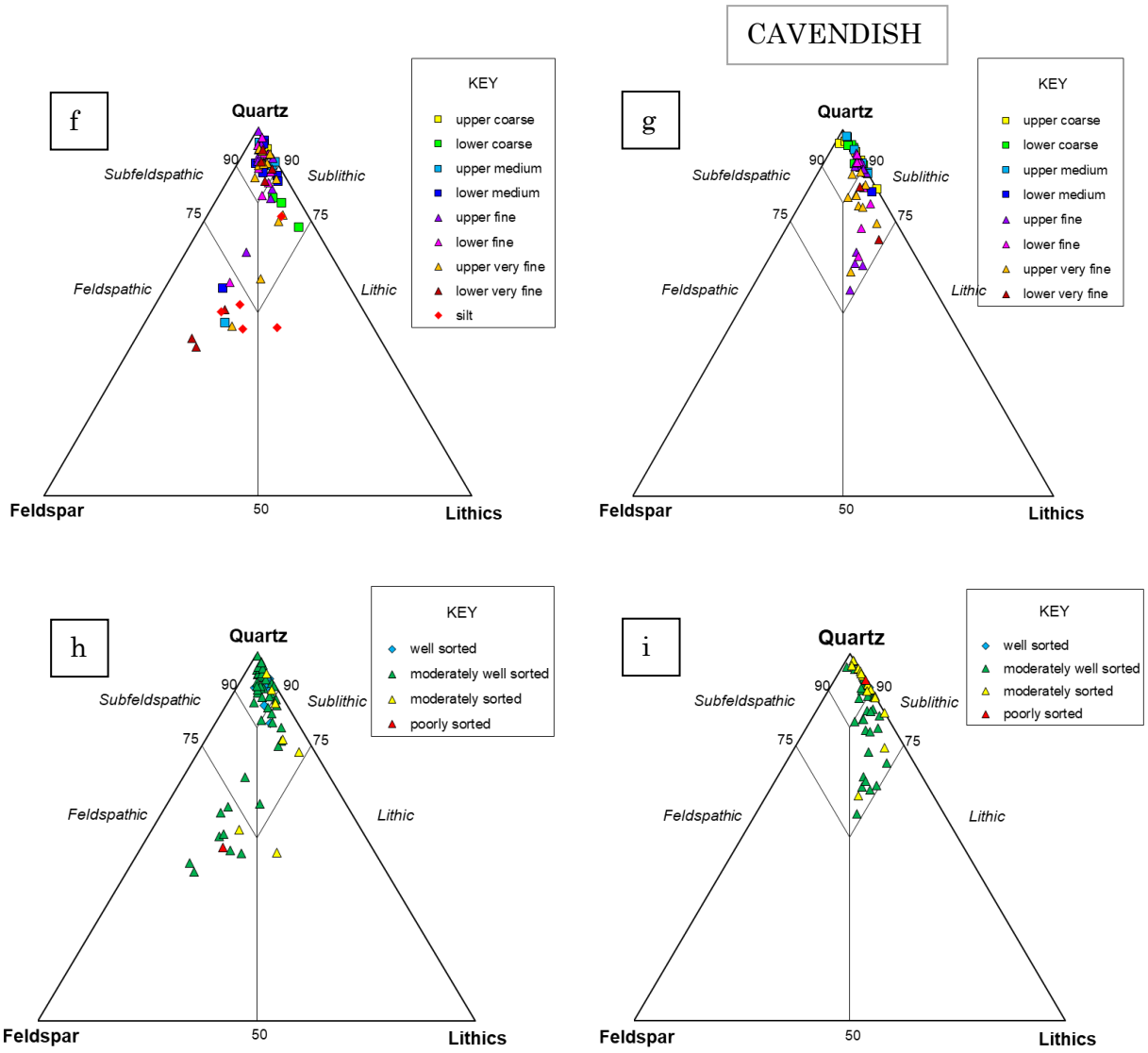

Figure 3.6 continued: Detrital composition of sandstones (QFL plots) split by a) well; b-c) facies association; d-e) lithofacies; f-g) petrographically-derived grain size; h-i) petrographically-derived sorting. Copernicus field is shown on the left, Cavendish on the right.

It is important to note that due to diagenetic processes some of the feldspars were dissolved, resulting in secondary porosity formation, or were replaced by kaolinite, and therefore present-day composition is not equivalent of the depositional composition. Assuming that all secondary porosity and all replacive kaolin occupy space occupied by feldspar at the time of deposition, then QFL plots show a significant shift from quartz arenite and sublithic arenite fields towards subfeldspathic field in each well. (Figure 3.7 a-f). This shift is particularly pronounced in the multi storey-fluvial facies (Figure 3.7 g & h), but less pronounced in delta plain, and virtually unnoticeable in the distal delta front, proximal prodelta and prodelta turbidite, due to the fact that initial carbonate cementation in the delta front and prodelta did not allow for dissolution and kaolinitisation of feldspar in those samples. The original feldspar content would have been on average 7.5% (range 0.3- 25.0%), that is 3.6%

higher than at present day (Appendix 3). Feldspars which are replaced by kaolin form on average 2.3% of the rocks, and those dissolved are 0.6% in the Copernicus discovery, while in the Cavendish Field these values are on average 1.6% and 2.6% respectively. This higher secondary porosity, combined with the higher primary porosity in Cavendish, is an important factor in the better reservoir quality in Cavendish.

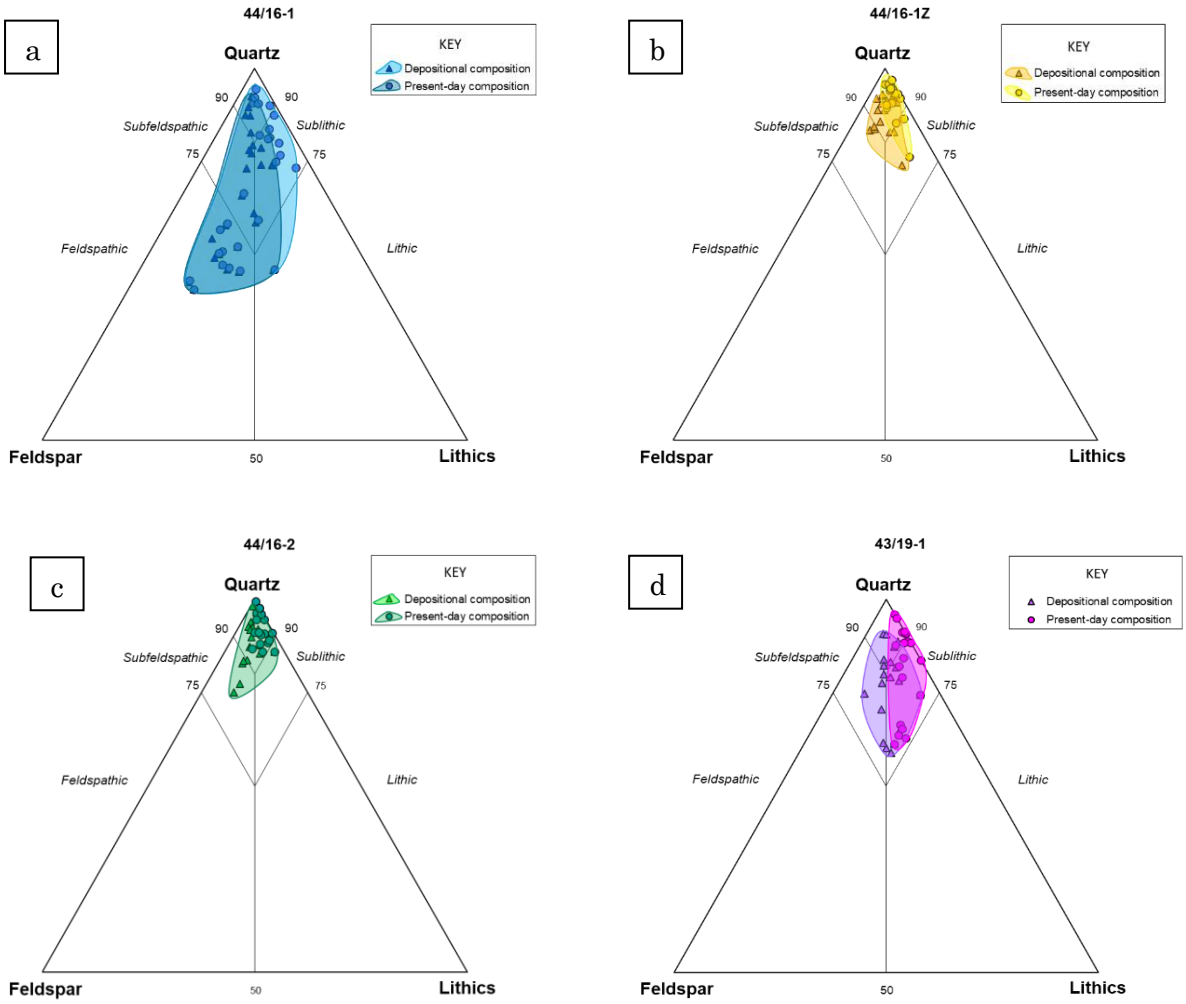

Figure 3.7. Detrital composition of sandstones during deposition and at present day. a) well 44/16-1; b) well 4/16-1Zl c) well 44/6-2; d) well 43/19-1; e) well 43/19-2; f) well 43/19a-4Z; g) Multi-storey fluvial channel facies, Copernicus discovery; h) Multi-storey fluvial channel facies, Cavendish field.

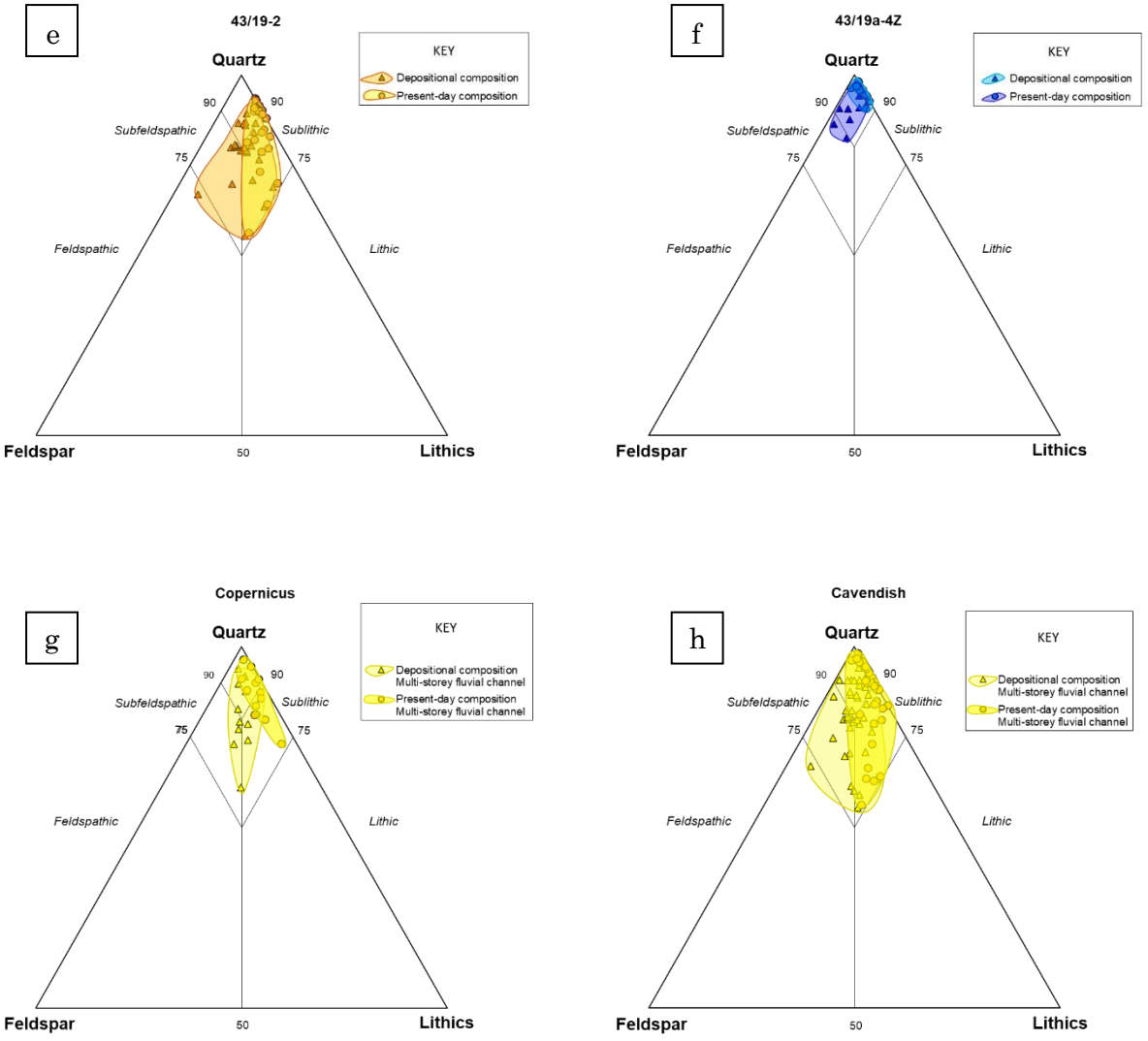

Figure 3.7 continued: Detrital composition of sandstones during deposition and at present day. a) well 44/16-1; b) well 4/16-1Zl c) well 44/6-2; d) well 43/19-1; e) well 43/19-2; f) well 43/19a-4Z; g) Multi-storey fluvial channel facies, Copernicus discovery; h) Multi-storey fluvial channel facies, Cavendish field.

Present day detrital mineralogy is dominated by quartz in both Copernicus and Cavendish, averaging 56.6% in all samples (ranging from 1% to 78%) (Appendices 3 and 4). Quartz comprises monocrystalline grains (average 47.1%) and polycrystalline grains (average 9.5%). The ratio of polycrystalline grains to monocrystalline grains is the highest in the coarsest grained samples of the multi-storey fluvial facies. Rigid rock fragments form on average 4.2% of the analysed sandstones (range 0 – 15.0%), but are more abundant in the Cavendish (average 4.9%) that in Copernicus (3.6%). These are primarily of igneous origin, with occasional metamorphic and sedimentary grains. Metamorphic grains comprise schistose quartz ± mica grains. Feldspars are only a minor component, averaging 3.9%, and are more common in Copernicus (average 5.3%) than Cavendish (average 2.3%). They comprise both plagioclase

(average 2.9%) and K-feldspar grains (average 1.1%). The most feldspar-rich facies are distal delta front, prodelta turbidite complex and proximal prodelta, which likely results from their high preservational potential, due to early carbonate precipitation. Where present, feldspar grains are typically well preserved or only weakly dissolved. Plagioclase feldspars show lamellar twinning and are weakly sericitised. Micas form on average 1.6% of the sandstones (range 0 - 9.7%), with muscovite being the dominant component, and biotite occurring in trace amounts. Micas flakes range from pristine, where early carbonate cementation allowed their preservation, to strongly degraded and replaced by kaolin and other clays. Organic fragments, ductile rock fragments and heavy minerals each form <1% of the sandstones. Ductile rock fragments are lithic grains typically partially composed of clays and are therefore susceptible to ductile deformation and can accommodates shape change in the rock during mechanical compaction filling intergranular spaces. These fragments comprise degraded igneous fragments and mudclasts. Mudclasts are, however, commonly strongly compacted between rigid grains and filling intergranular areas, resulting in the formation of pseudomatrix, which accounts on average for 2.0% of all samples (up to 11.7%), and is mainly concentrated within proximal and distal delta front (Appendix 5). Heavy mineral assemblage comprises apatite, monazite, rutile, tourmaline, zircon opaque minerals, and garnet. Detrital clays on average account for 4.9% of the analysed sandstones (range 0 – 48.3%), but the content is strongly facies related. The lowest detrital clay content is noted in distributary channels in both analysed areas (0% in Copernicus and average of 0.3% in Cavendish), and the highest amounts are recorded in interdistributary bay (average 17.7% in Copernicus and 27.2% in Cavendish) (Appendix 5). Detrital clays are generally more concentrated within the marine facies (shoreface, proximal delta front, distal delta front, interdistributary bay, proximal prodelta, prodelta turbidite complex) than in the continental facies (multi-storey fluvial channel, distributary channel, delta plain). SEM EDS data suggest an illitic or illitic-smectitic composition of detrital clays.

3.4.2.2 *Authigenic mineralogy*

Authigenic minerals in analysed sandstones consist mainly of quartz, dolomite, kaolin and siderite. Other cements and clays occur only in minor amounts and generally have little effect on reservoir quality. The major cement and clay types, important for the reservoir quality of the Copernicus and Cavendish sandstones, are discussed in more detail below in order of decreasing average modal abundance.

3.4.2.2.1 Quartz overgrowths

Quartz overgrowths are the most common authigenic mineral in the analysed sandstones and form on average 8.9% of the rocks (range 0 – 21.7%; based on point counting results under optical microscope), and the amount of quartz is similar in both Copernicus and Cavendish (Appendices 3 and 4). There is however, a big difference in quartz overgrowths between different facies associations. Overall, the continental facies associations contain abundant quartz cement, on average 12.1% in Copernicus and 9.2% in Cavendish, whilst the marine facies contain 3.9% and 5.5% in those two areas respectively. Distributary channels contain the highest amounts of quartz in all facies (15.8% in Copernicus and 11.0% in Cavendish). Quartz preferentially precipitated in this facies due to their very low detrital clay content, which is known to inhibit quartz nucleation where coating detrital grains (Hansen et al., 2017; Porten et al., 2019). Syntaxial quartz cements commonly form continuous overgrowths around detrital quartz grains (Figure 3.8a) and, where abundant, they interlock to form mosaics that occlude most of the primary porosity (Figure 3.8b). Locally, quartz overgrowths are delineated from their host grain by a line of micron-scale fluid inclusions, however commonly the boundary between detrital grains and overgrowths can only be precisely identified on CL images. The overgrowths reach up to 100 µm in fluvial and delta plain facies, where primary pores are 'clean' and detrital and authigenic clays are absent. The fact that quartz overgrowths thin, or terminate completely, at long grain contacts, suggests that they largely precipitated after the main period of compaction (Figure 3.8a). Quartz overgrowths enclose earlier kaolin booklets (Fig 3.8c), siderite, pyrite and some of the illite (Figure 3.8d) and dolomite, however they are also locally observed enclosed by dolomite (Figure 3.8e) and draped by illite (Figure 3.8f).

In the Copernicus discovery two generations of quartz overgrowths are well defined, being separated by a thin layer of residual oil (Figure 3.8g). The presence of two generations of quartz is confirmed by cathodoluminescence in both Copernicus and Cavendish (Figure 3.8 h and i), albeit the two generations are not visible in all overgrowths. A complex pattern that is in fact observed within the overgrowths might result from more than two phases of quartz formation, or changing chemistry during quartz growth. Locally quartz surfaces observed in SEM are weakly etched (Figure 3.8f).

3.4.2.2.2 Dolomite

Dolomite forms 3.8% of the analysed sandstones and comprises mainly ferroan dolomite (3.1%) and lesser non-ferroan dolomite (0.7%). Most of the ferroan dolomite

occurs within primary pores (2.8%) and a lesser amount in the secondary pores (0.3%). Non-ferroan dolomite is also primarily found in primary pores (0.6%), with a minor amount in secondary pores (0.1%). Dolomite is mainly concentrated within marine facies (Appendix 5), forming 7.8% of the sandstones in Copernicus and 4.4% in Cavendish (whilst in continental facies it forms 1.1% and 4.1%. for the two areas respectively). Dolomite forms rhomb-shaped crystals, locally showing darker core, or occurs as pore-filling patches or pervasive cement. Textural observations suggest that much of the dolomite in marine sandstones precipitated during eogenesis prior to mechanical compaction, as detrital grains show point contacts or locally appear to be floating in the dolomite cement (Figure 3.8j). Some ferroan and non-ferroan dolomite formed later during diagenesis, as it locally encloses quartz overgrowths (Figure 3.8e).

3.4.2.2.3 Kaolin

Kaolin (average 3.6%, range 0 – 13.7%) comprises replacive kaolin (average 2.0%, up to 10.7%) and pore-filling (average 1.7%, up to 11.3). Kaolin shows a patchy distribution filling primary and secondary pores. Two morphologies of vermicular kaolin are observed: finely crystalline, thin to commonly blocky booklets which are 5 - 15 µm wide (Figure 3.8c), and coarser, 30 - 50 µm wide, thin to blocky booklets (Figure 3.8k). Residual hydrocarbons are observed staining kaolin booklets in all Copernicus wells, but not in Cavendish. Kaolin is more common in continental facies (average 3.4% and 4.9% in Copernicus and Cavendish respectively) than in marine ones (average 2.4% and 1.7% in Copernicus and Cavendish respectively; Appendix 5), and consists primarily of replacive kaolin in Copernicus, and primary-pore filling kaolin in Cavendish (Appendix 5).

3.4.2.2.4 Siderite

Siderite (average 3.4%, range 0 – 48.7%) fills primary pores. It is commonly associated with early dolomite and shows a similar distribution pattern, occurring primarily within marine facies associations (10.6% and 4.9% in Copernicus and Cavendish respectively, whilst it forms 0.6% and 1.8% in continental facies in the two areas respectively). Siderite forms lozenge shape crystals, nodules of finely-crystalline siderite, or sphaerosiderite crystals in pedogenically modified deposits.

3.4.2.2.5 Optically non-resolvable clay

Optically-non resolvable clay comprises pore-lining clay (average 0.8%, range 0-9.3%) and replacive clay (average 0.4%, range 0 – 3.7%). Based on SEM and EDAX, these clays are composed of illite, illite-smectite and some illitised kaolin. Replacive clay is

seen altering degraded ductile grains and is composed of illite, suggested by its high birefringence in XPL and EDS data, and illitised kaolin.

3.4.2.2.6 Illite and illite-smectite

Illite and illite-smectite (average 0.1%, up to 2.7%) forms ribbon-like strands that developed as primary pore-filling phase as well as grain-replacing phase. SEM shows that illite strands drape over quartz overgrowths and are locally also enclosed by quartz (Figure 3.8 f and d).

3.4.2.2.7 Pyrite

Pyrite (average 0.2%, up to 3.3%) forms framboids and cubic crystals which occur within primary pores or replacing mudclasts and organic fragments. Pyrite is also seen outlining root traces in samples from delta plain facies association. Pyrite generally only occurs in minor amounts and is slightly more common in marine facies.

3.4.2.2.8 Other cements

Other cements are volumetrically insignificant and have little effect on reservoir quality. These comprise Na-feldspar overgrowths, K-feldspar overgrowths, barite, anhydrite, anatase, possible zeolite and iron oxides, which occur only in minor to trace amounts and have little effect on reservoir quality.

3.4.2.2.9 Residual oil

Residual oil (average 0.1%, up to 3.7% in Copernicus discovery only) is seen enclosed within isolated primary pores, between quartz overgrowth layers in the Copernicus discovery (Figure 3.8g) and staining kaolin booklets. Residual oil is observed at depths 14065.8- 14917 ft MDBRT.

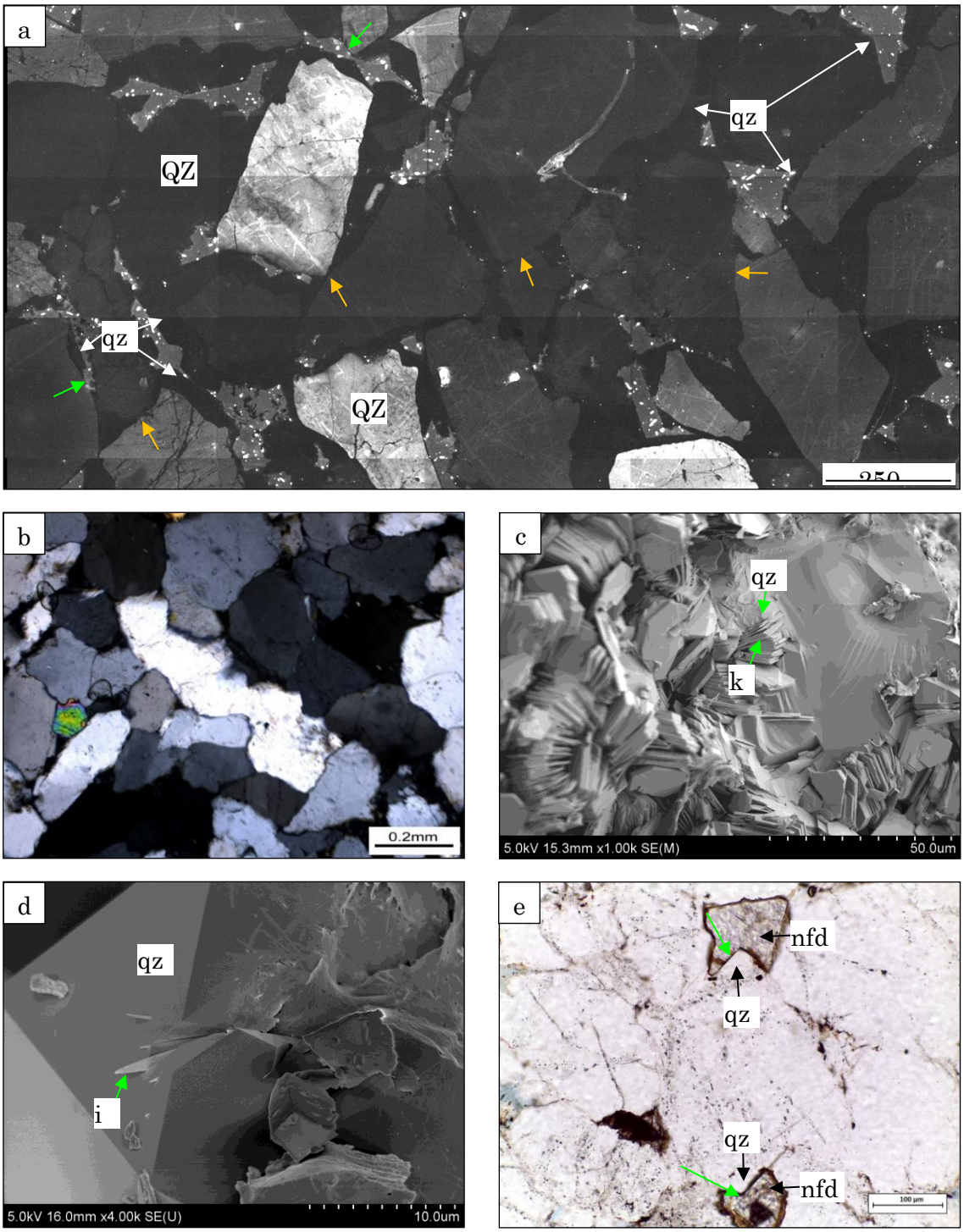

Figure 3.8. a) Quartz overgrowths (dark grey) are typically continuous around detrital grains, although local gaps are present (green arrows). Quartz overgrowths thin, or terminate completely, at long grain contacts (orange arrows), suggesting that they largely precipitated after the main period of compaction; CL image, well 44/16-1, depth 14190 ft, b) Abundant quartz overgrowths interlock, occluding primary porosity; photomicrograph, well 44/16-1, depth 14189.1 ft; c) Kaolin booklets are enclosed by quartz overgrowths; SEM image, well 44/16-1, depth 14922 ft; d) Ribbon-like illite crystals are enclosed by quartz overgrowths; SEM image, well 43/19-1, depth 12475.9 ft; e) Euhedral quartz overgrowths are enclosed by late non-ferroan dolomite (arrowed); photomicrograph, well 44/16-2, depth 14270.9.

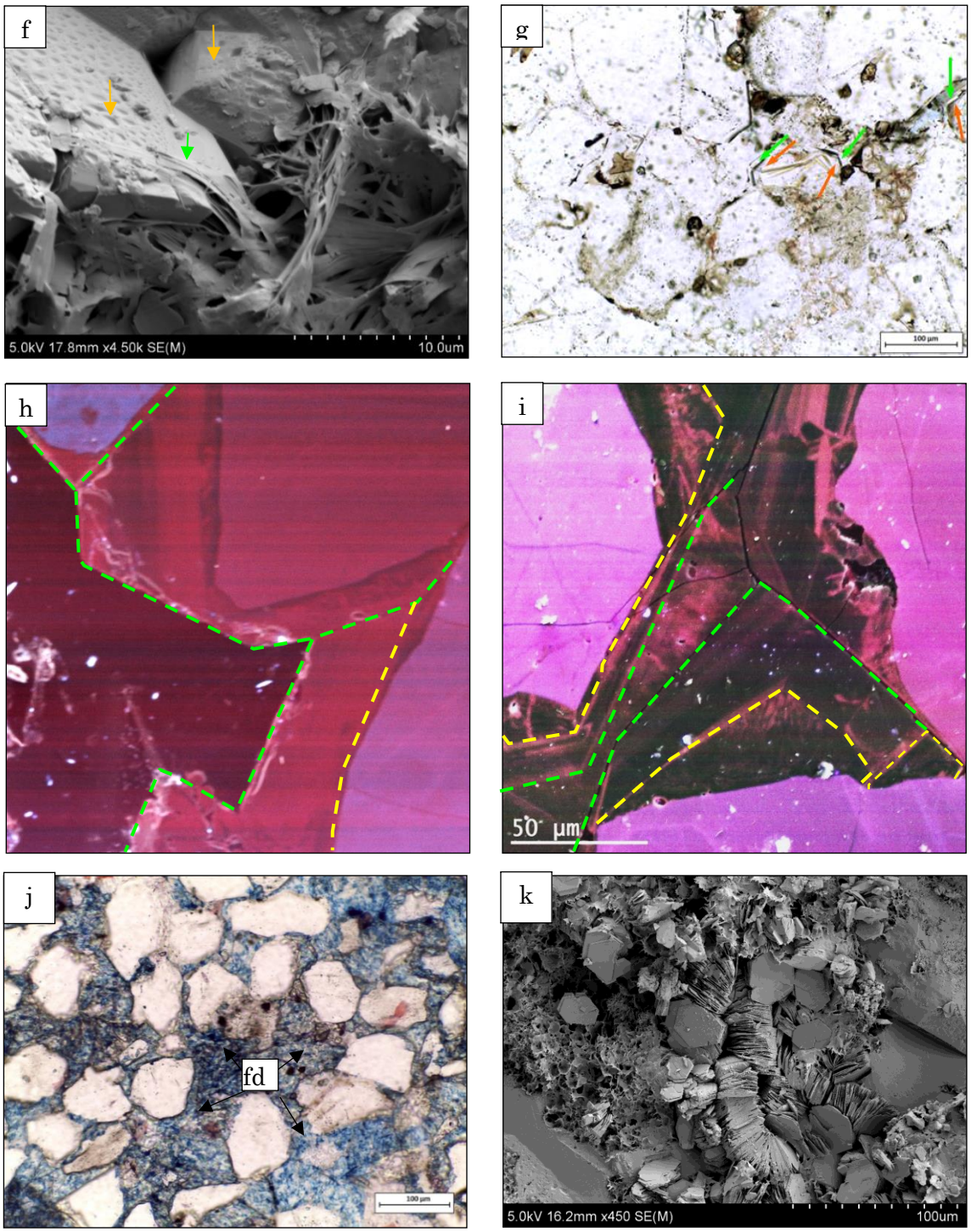

Figure 3.8 continued. f) Quartz overgrowths, which locally show pitted surfaces (orange arrows) are draped over by authigenic illite (green arrows); SEM image, well 43/19-1, depth 12164 ft; g) Multiple episodes of quartz cementation have occurred during the diagenesis diagenetic history. Two generations of quartz overgrowths can be observed in the thin sections (see green and orange arrows) separated by a black layer of residual oil; photomicrograph, well 44/16-1Z, 14194.0 ft; h,i) CL images showing two phases of quartz cementation. First phase is outlined in yellow, second in green; CL images, well 44/16-1, depth 14189 ft and well 43/19-1, 4037.26 m; j) showing extensive dolomite cementation. Pervasive ferroan dolomite (fdm) precipitated during early diagenesis, prior to mechanical compaction; photomicrograph, well 44/16-2, depth 14822.90 ft; k) Large, 30 µm wide, kaolin booklets filling a secondary pore and surrounded by illite. SEM image, well 43/19-1, depth 12659 ft.

3.4.3 Reservoir quality

3.4.3.1 *Mechanical and chemical compaction*

Grain to grain contacts vary significantly in the suite of samples studied, however patterns are evident. By applying Taylor's (1950) grain contact classification, we note that in samples with pervasive early dolomite and siderite cements point (tangential) and long contacts are predominant, indicating only weak to moderate mechanical compaction (Figure 3.9a). In one sample with >50% dolomite (well 44/16-2, depth 14822.90 ftMD; Figure 3.8j) detrital grains show only point contacts or appear to be floating within dolomite cement. This results from very early dolomite formation, before the onset of mechanical compaction, as well as some grain dissolution and replacement by dolomite. Dolomite and siderite are primarily associated with marine environments in the analysed samples. The presence of detrital clay increases grain-to-grain dissolution leading to formation of concave-convex and sutured contacts between grains (Figure 3.9b), and formation of stylolites where clay is concentrated along thin laminae (Figures 3.9 c and d). Samples where none or only minor early cements occur show significantly higher levels of mechanical compaction (Figure 3.10a). Under transmitted light long and concave-convex contacts are observed in those samples. CL images confirm that the concave-convex contacts occur between detrital grains, rather than between quartz overgrowths (Figure 3.9e). Samples with concave-convex and sutured contacts experienced strong levels of compaction.

The total cement volume was used to calculate porosity loss by mechanical compaction and the porosity loss by cementation using the method of Lundegard (1992). The initial (depositional) porosity values are assumed to be 45% (Lundegard, 1992). The COPL/CEPL plots (compactional porosity loss vs. cementational porosity loss) show that COPL is generally higher than CEPL in both Copernicus and Cavendish fields (Figure 3.10b), indicating that mechanical compaction is the primary cause of porosity reduction in the analysed sandstones. However, the dominance of mechanical compaction is more pronounced in Copernicus, where 60 of 61 sandstones show higher COPL than CEPL, than in Cavendish where this proportion is 47 to 55. COPL ranges from 0% to 44.6% (mean 32.7%) in the Copernicus discovery, and 0 to 43.7% (mean 28.6%) in the Cavendish. While mechanical processes alone are thought to only reduce porosity down to 26% in well sorted sandstones (Paxton et al., 2002), pressure solution and ductile grain deformation can increase the compactional porosity loss value (Lundegard, 1992). CEPL values range from 0.7% to 45% (mean 12.0%) in the

Copernicus discovery, and 1.3% to 45% (mean 14.8%) in the Cavendish field (Appendix 4).

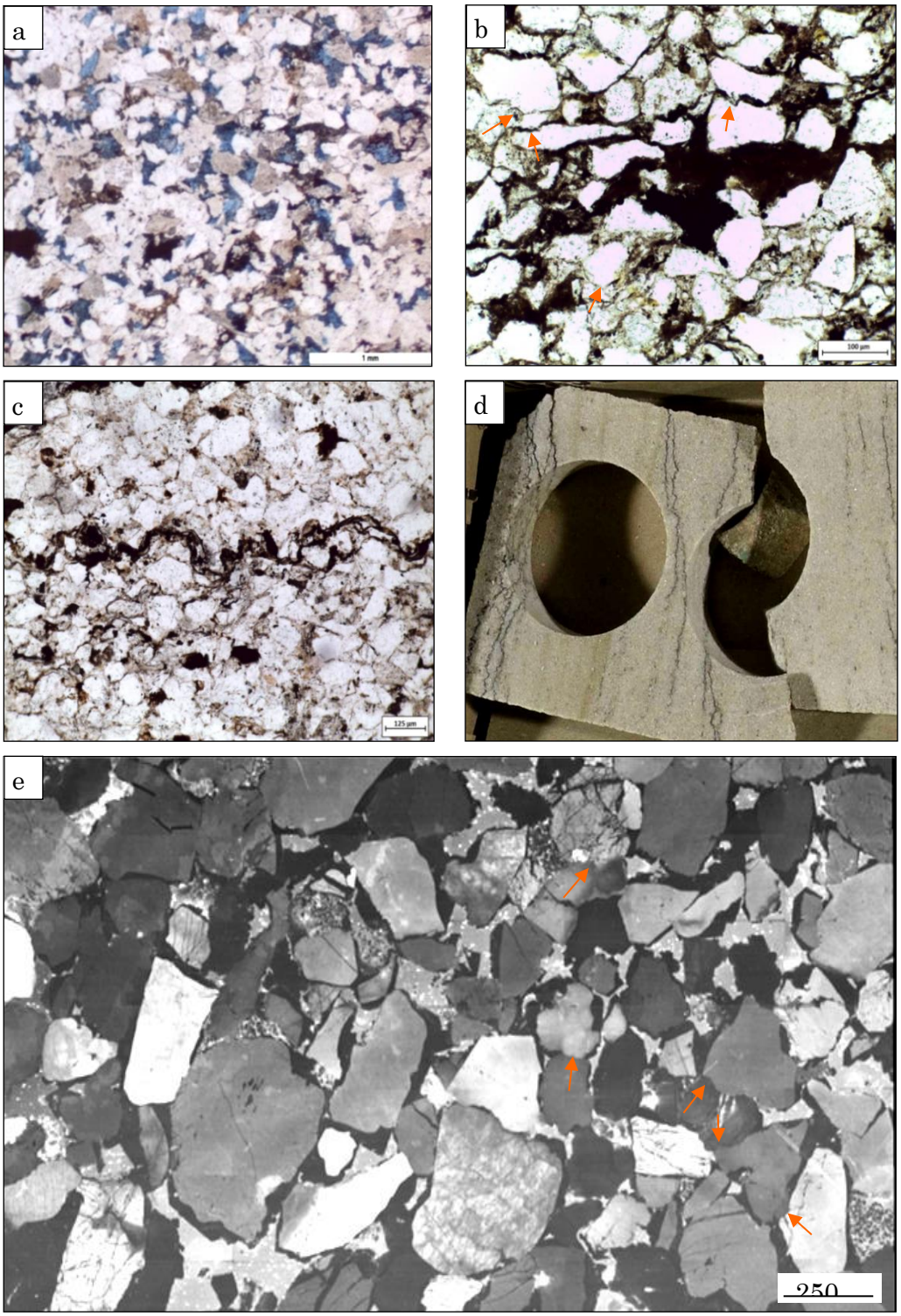

Figure 3.9. a) Grains show point and long contacts where early pore-filling dolomite stabilised grain framework and impeded mechanical compaction; photomicrograph, well 44/16-1, depth 14065.8 ft; b) Detrital clay increases grain-to grain dissolution leading to formation of concave-convex and sutured contacts between grains (orange arrows); photomicrograph, well 44/16-2, depth 14824.1.90ft; c & d) Stylolites form where detrital clay is concentrated along thin laminae; photomicrograph, well 44/16-2, depth 14828 ft and core photograph, well 43/19a-4Z, depth 16258 ft; e) CL shows that the concave-convex contacts (orange arrows) occur between detrital grains, rather than quartz overgrowths, CL image, well 44/16-1m, depth 14837.9 ft.

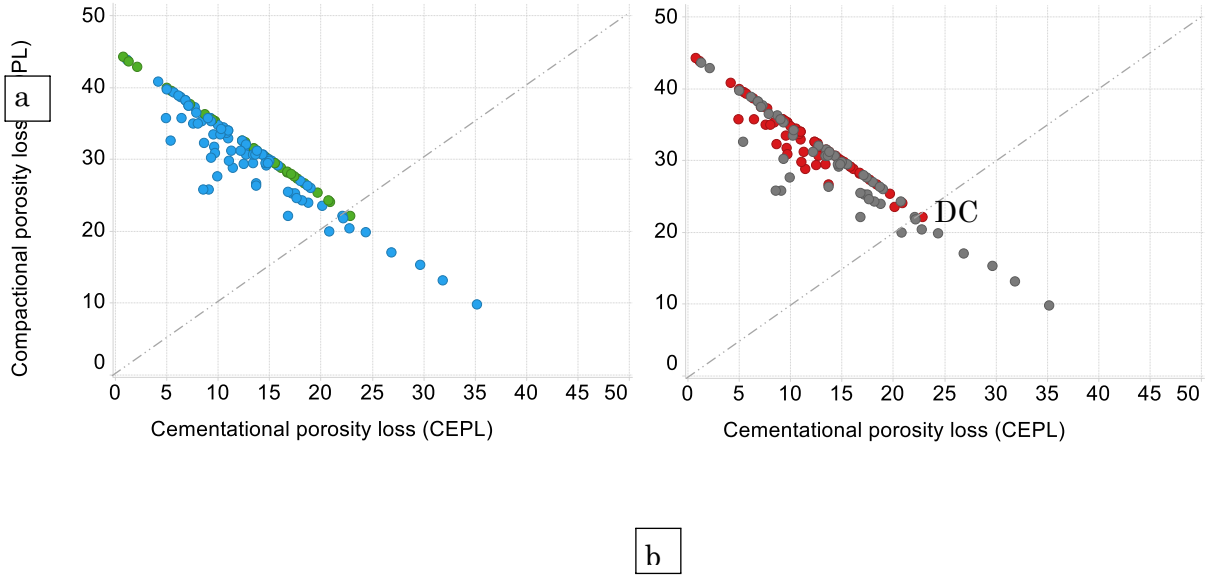

Figure 3.10. a) Cementational porosity loss (CEPL) and compactional porosity loss (COPL) for the marine (blue) and continental (green) deposits in the Copernicus and Cavendish fields; b) COPL/CEPL plot for the Copernicus discovery (red) and Cavendish field (grey); c) COPL/CEPL pot coded by the proportion of quartz overgrowths; d) COPL/CEPL pot coded by the proportion of kaolin. Calculated after Lundegard (1992).

In the Copernicus discovery the only sample with higher CEPL than COPL was deposited in proximal delta front and contain abundant early dolomite which inhibited mechanical compaction. In Cavendish samples that have higher CEPL than

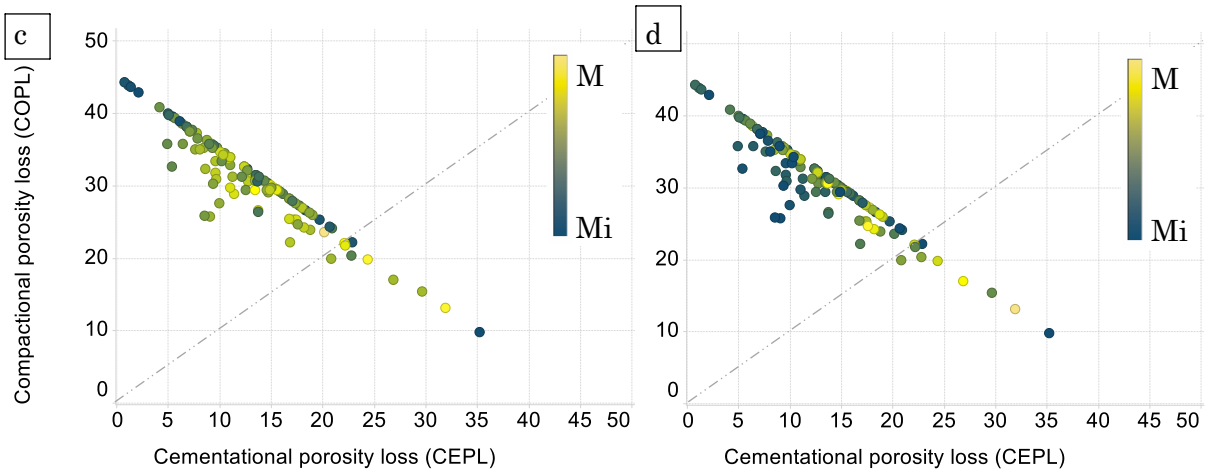

COPL belong to the multi-storey fluvial channels and distributary channel facies. The multi-storey fluvial channel samples which show higher CEPL than COPL are those that contain the most abundant quartz overgrowths and kaolin, with the addition of some early and late dolomite (Figure 3.10 c and d).

Precipitation of early cements, although preventing mechanical compaction, had a profoundly detrimental effect on porosity and permeability preservation, due to pervasive nature of those cements (Figure 3.8j and 3.9a).

3.4.3.2 *Porosity and permeability controls*

Modal porosity comprises primary porosity (modal porosity average 1.7%, range 0 – 14.3%), secondary porosity (average 1.6%, range 0- 24.3%) and microporosity (average 4.7%, range 0-13.3%) (Appendices 3 and 4). Secondary pores are divided into intragranular porosity (which forms on average 0.2% of the samples) and the more common 'oversized' porosity (average 1.4%). Intragranular porosity occurs within degraded ductile grains and partially dissolved rigid rock fragment and feldspars. 'Oversized' porosity results from complete dissolution of grains, presumably mainly feldspars, or perhaps packing flaws, both leading to a formation of large pores.

Recorded modal primary and secondary porosity values are higher in the continental facies (2.0% average primary porosity plus 0.9% secondary porosity in Copernicus, and 2.6% primary plus 3.2% secondary porosity in Cavendish), compared to no macroporosity in marine facies in Copernicus and only minor porosity in Cavendish (average 0.4%; Appendix 5). Cavendish samples show overall higher secondary porosity than the Copernicus sandstones, however sampling in well 43/19a-4Z was biased towards multi-storey fluvial channel facies, which generally show the highest porosity values. However, when comparing the multi-storey fluvial channel samples only from both fields, there is still a difference in porosity values, primarily in the secondary porosity. While Copernicus shows 1.8% primary porosity and 1.2% secondary porosity, Cavendish has 1.6% primary porosity and 2.6% secondary porosity. The QFL plots showing depositional composition show, that initial composition was the same in both fields. The difference between the amounts of secondary porosity is therefore likely to be a diagenetic effect.

Microporosity was calculated as the difference between helium porosity and point counted macroporosity, and it is likely to be largely located within clays and degraded grains. While microporosity might be considered largely ineffective in oil reservoirs, in gas reservoirs it might at least partially contribute towards the effective porosity. Microporosity values in the Copernicus range from 0 – 11.8% (mean 4.1%, and 0 – 13.3% (mean 5.5%) in Cavendish.

The reservoir quality of the sandstones varies from the Copernicus discovery is very low to high (0.01- 61mD, geomean 0.26 mD) and very low to very high (0.01 – 744 mD, geomean 0.66 mD) in the Cavendish Field (Figure 3.11). A combination of multiple factors controls permeability in those two areas, some of the most important ones being depositional facies (see section 3.4.1) and associated detrital composition and grain size. But there is a lot of variation in reservoir quality within each depositional facies and within each grain size mode, which is caused by other factors which are investigated in this section.

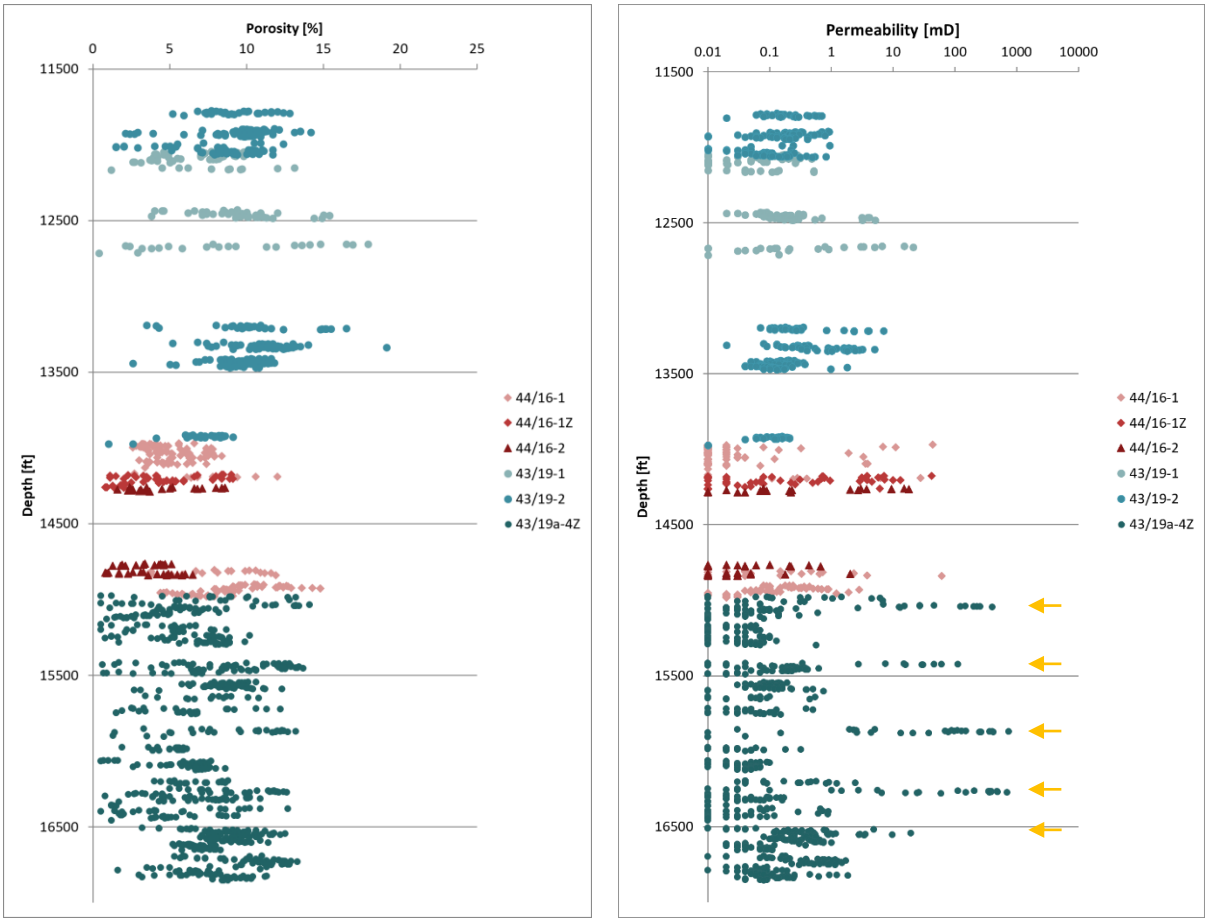

Figure 3.11. Porosity and permeability versus depth for wells drilled in the Upper Carboniferous deposits of Copernicus discovery and Cavendish field, Southern North Sea. High permeability streaks in the Cavendish well 43/19a-4Z marked with arrows.

Notably, there are four layers of exceptionally high permeability sandstones (up to 744 mD) preserved at high depths in well 43/19a-4Z (Figure 3.11). One of those very high permeability streaks, plus one with a moderate permeability (Figure 3.11, orange arrows) are of Namurian age and have been logged and analysed petrographically (depths 16260 – 16277 and 16517 – 16553 ft). Both these high permeability streaks are in the multi storey-fluvial channels, characterised by upper fine to coarse grain size.

While the high permeability streaks are limited to one depositional facies (multi-storey fluvial channels) the high variability in reservoir quality which exists within each of those beds, and within the fluvial channel facies overall, indicates that reservoir quality preservation is not only controlled by depositional environment, and multiple factors need to be considered to unravel factors controlling reservoir quality in the Namurian sandstones in the analysed areas.

Porosity-permeability plot on Figures 3.12a shows two trends on poroperm plot. Coding the plot by detrital clay and kaolin content reveals that the difference between the two trends arises from the different clay content. The steeper of the two trends, with higher permeability values, is associated with lower kaolin and detrital clay content (Figure 3.12 a and b). The highest permeabilities lie within the 43/19a-4Z well, however samples from wells 44/16-1, 44/16-1Z and 44/16-2 also lie along the same trend (Figure 3.12a). Sandstones from these three wells are characterised by finer grain size than those from the 43/19a-4Z well (Figure 3.12b). Importantly quartz overgrowths, although volumetrically most important cement, do not affect the two poroperm trends (Figure 3.12c).

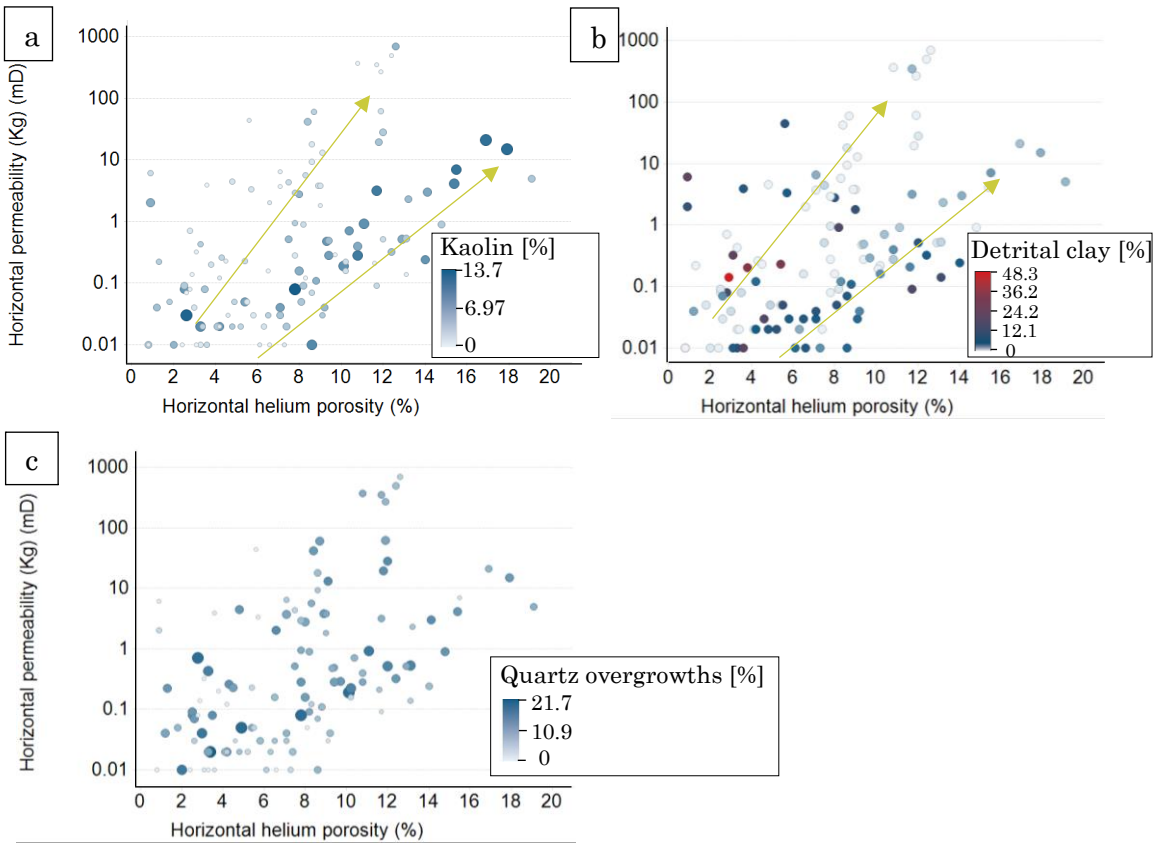

Figure 3.12. a) Poroperm plot showing kaolin content coded by colour and point size. The steeper of the two visible trends (arrowed) is associated with lower kaolin content; b) Poroperm plot coded by detrital clay content. The steeper of the two visible trends is associated with lower detrital clay content; c) Poroperm plot coded by quartz overgrowth content shows that quartz cement, despite being volumetrically most significant, is not responsible for the development of different porosity-permeability trends in the analysed wells.

QFL plots on Figures 3.7 f-h, show that the original mineralogical composition of multi-storey fluvial sandstones in well 43/19a-4Z differs from the composition of the same facies in other well, initially having a more quartz-rich and less feldspathic composition. The lack of feldspar during deposition inhibited kaolinite formation in primary and secondary pores, resulting in the preservation of the highest primary porosity of all analysed wells and facies.

Of authigenic cements, quartz overgrowths are volumetrically most important, however the relationship between porosity/permeability and quartz cement content is not a straightforward one. As Figure 3.12c and 3.13 show, there is no direct relationship between the amount of quartz overgrowths and porosity and permeability. Yet, since quartz cement forms on average 8.9% of the analysed sandstones, and is commonly seen occluding pore throats, it most certainly has a profound effect on reservoir quality, as do other cements. The significance of authigenic cements is discussed in more detail in Chapters 5 and 6. The reason why there is no observed trend in authigenic quartz and porosity and permeability relationship is because multiple other factors are in play thus obscuring any trends related to an isolated element.

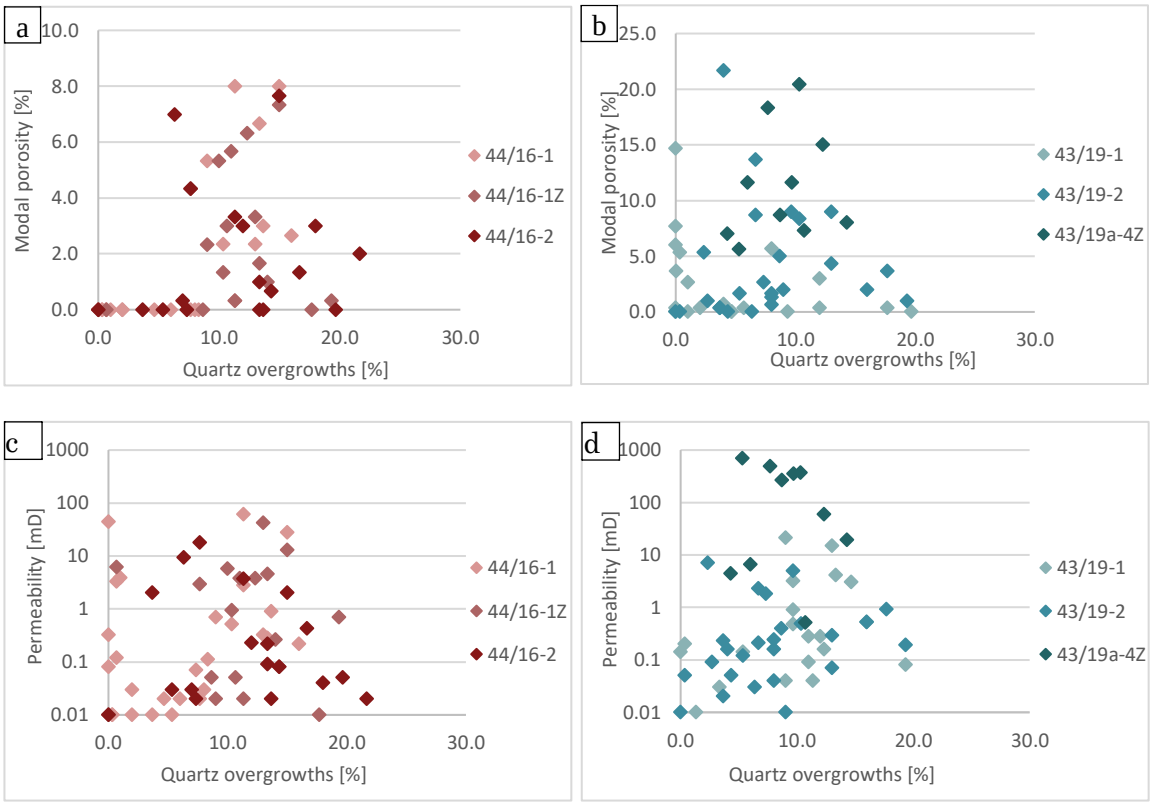

Figure 3.13. Relationship between the amount of a -b) quartz overgrowths and modal porosity and permeability, and c-d) quartz overgrowths and permeability.

3.4.4 Distribution of diagenetic alterations

Porosity and permeability in the analysed sandstones are in part a function of grain size, sorting, and detrital clay content, which are controlled by depositional facies (Figure 3.5 b and c), and diagenesis. Macroporosity increases with 'shallowing' of the depositional environment (Figure 3.14 a and b), which is generally associated with increasing grain size and decreasing detrital clay content, and also with a changing type of authigenic cement. The marine facies, which show virtually no macroporosity, mainly contain abundant dolomite and siderite (Figure 3.14 c-f), whilst the continental facies, contain predominantly quartz overgrowths and kaolin (Figure 3.14 g-j). Although these trends are not as clear in Cavendish as they are in Copernicus, it must be noted that each of the marine facies in the Cavendish only comprises one to four samples, and is therefore statistically much less representative (Appendix 5). Helium porosity values are not facies dependant, due to the high detrital content in the marine facies, which contains high microporosity.

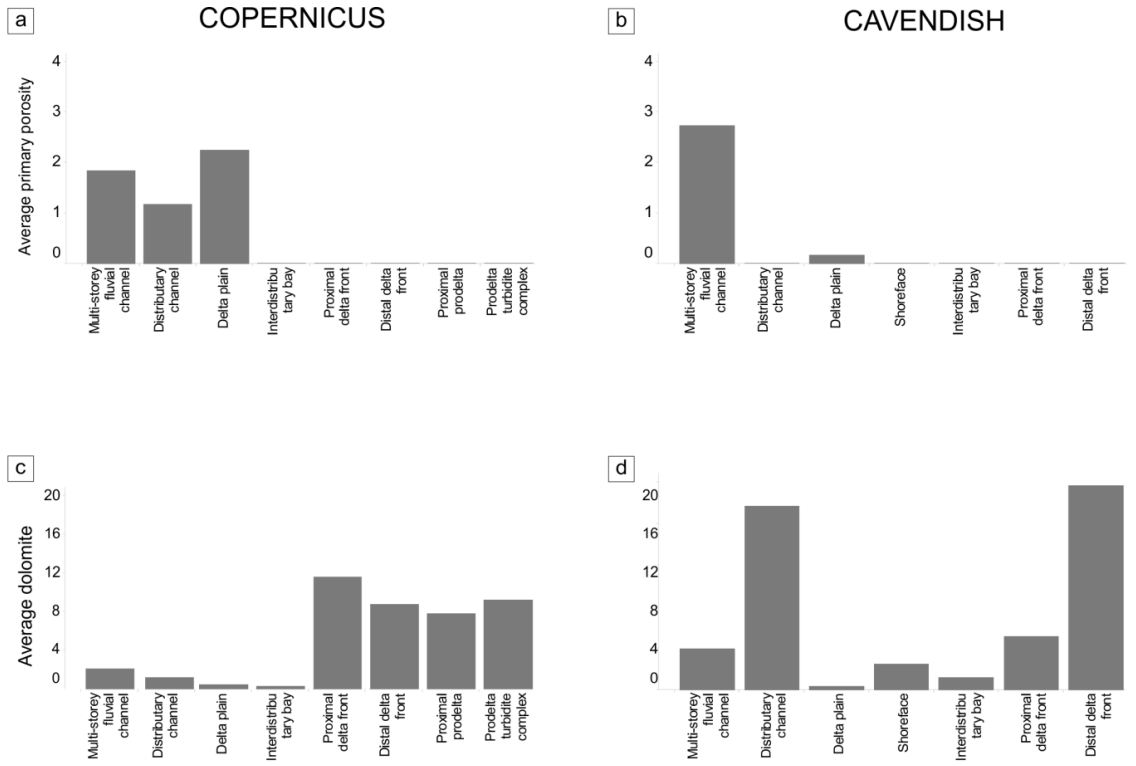

Figure 3.14. a-b) Macroporosity increases with 'shallowing' of the depositional environment; c-d) dolomite is more abundant in marine environment; e-f) siderite is more abundant in marine environment; g-h) quartz cement is more abundant in continental environment; i-j) kaolin is more abundant in continental environment Copernicus discovery is shown on the left, Cavendish on the right.

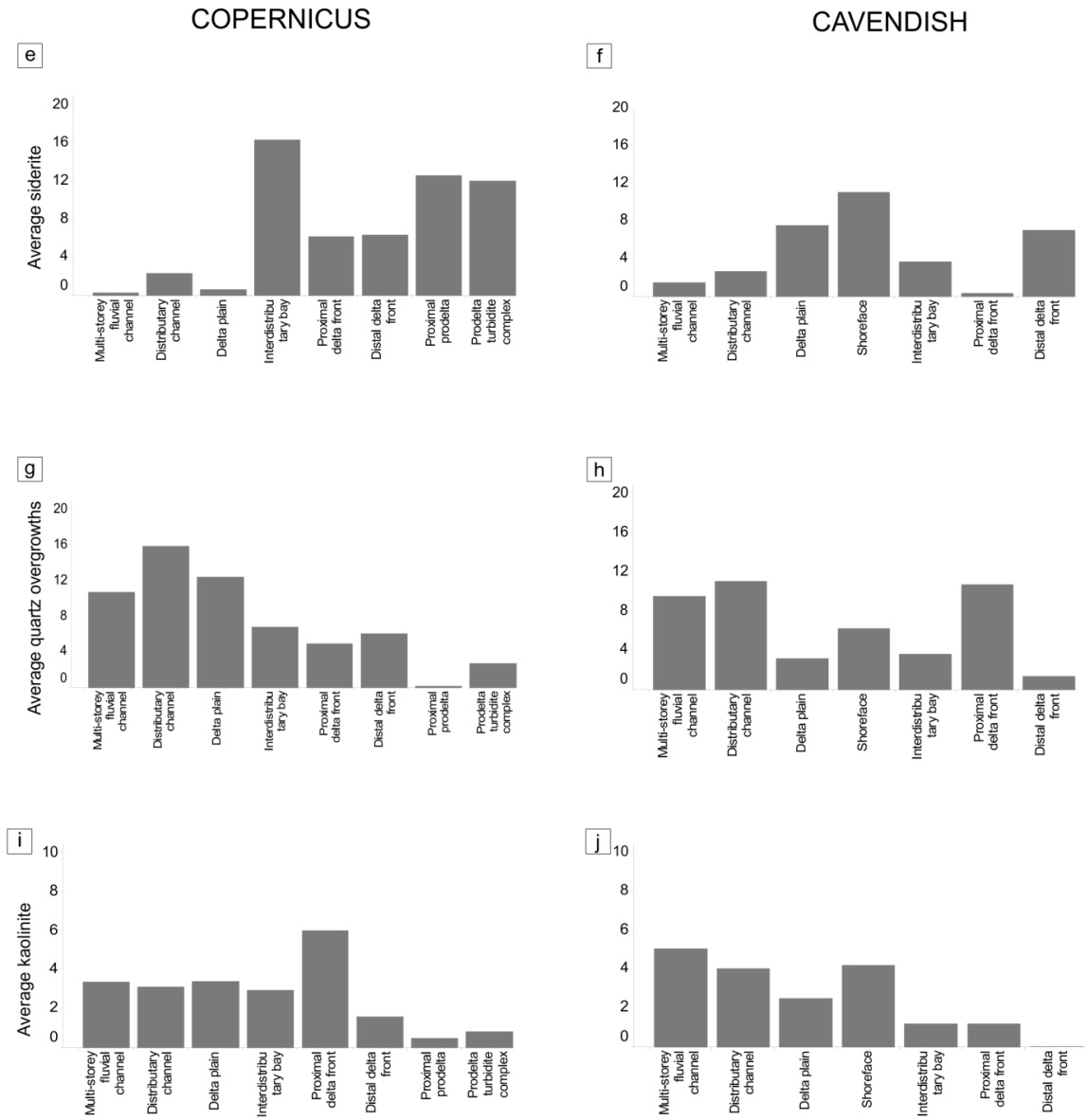

Figure 3.14 continued. a-b) Macroporosity increases with 'shallowing' of the depositional environment; c-d) dolomite is more abundant in marine environment; e-f) siderite is more abundant in marine environment; g-h) quartz cement is more abundant in continental environment; i-j) kaolin is more abundant in continental environment Copernicus discovery is shown on the left, Cavendish on the right.

3.4.5 Depositional feldspar content and provenance

In Copernicus discovery and Cavendish field the highest permeabilities are also recorded in quartz-rich sandstones, which were deposited as multi-storey fluvial channels. By far the best reservoir properties are recorded in well 43/19a-4Z. Petrographic analysis shows that the quartz-rich nature of those sandstones does not reflect the original composition during deposition. Most sandstones from the multi-storey fluvial channel facies contain some secondary porosity and/or replacive kaolin, which originated from dissolution or alteration of feldspar. The QFL plots on Figure

3.7 show how sandstone composition has changed between deposition and present day, after feldspathic component was removed during diagenesis. The initial (depositional) composition spanned feldspathic, subfeldspathic, sublithic and quartz arenite fields in all but one well (44/16-1, which also spans the lithic field), and has shifted toward exclusively sublithic and quartz arenite fields at present. However, sandstones from well 43/19a-4Z were much more quartz rich during deposition than all other sandstones (Figures 3.7 a-f), which might suggest that these high quality samples are a depositional feature, rather than diagenetic, and result either from a different provenance or better feldspar removal during transport. However, it is important to note that this might also be a result of sampling bias, as sampling in well 43/19a-4Z was targeted towards high quality samples, whilst all other wells comprise a range of facies and permeability values. Depositional feldspar content is so important as it is responsible for the supply of ions necessary for kaolinite precipitation during diagenesis. The lack of supply source made the quartz rich-sandstones less prone to kaolinite formation, allowing for preservation of high reservoir quality. Two poroperm trends observed on Figure 3.12a clearly show that the higher permeability trend is associated with low kaolin content.

To lessen the effect of sampling bias in well 43/19a-4Z, we analysed only the multi-storey fluvial channel facies (MSFC) from all wells. The content of feldspar at deposition, as well as the content of rigid rock fragments was still the lowest in well 43/19a-4Z, along with well 44/16-2 (Appendix 6). Depositional feldspar content in MSFC is on average 3.8% in 43/19a-4Z and 2.9% in well 44/16-2, whilst in wells 43/19-1, 43/19-2 and 44/16-1 it accounts for 7.5-9.1% of the rock. No multi-storey fluvial channel facies was cored in well 44/16-1Z. Rigid rock fragments are least abundant in well 43/19a-4Z (2.6%), followed by 4.8% in well 44/16-2, and 5.7-7.0% in the remaining three wells. Despite some similarities between the framework composition in wells 43/19a-4Z and 44/16-2, the present-day porosity and permeability values are significantly higher in well 43/19a-4Z. The amounts of the most abundant cements (quartz overgrowths, dolomite and siderite) and detrital clay are comparable in both wells. Different levels of early mechanical compaction, and different grain size might partially account for this effect. MSFC from well 43/19a-4Z are composed of slightly coarser grains, ranging from upper medium to lower very coarse, compared to upper fine to upper coarse-grained sand in well 44/16-2. Furthermore, more differences between the two wells emerge when analysing the proportions of lithic fragments (Figure 3.15). The recognised rock fragments include granitic and schistose rock fragments, but these are not uniformly distributed in

studied sequence. In well 43/19a-4Z metamorphic fragments are appreciably more abundant than in other analysed wells, whilst igneous fragments are clearly least abundant.

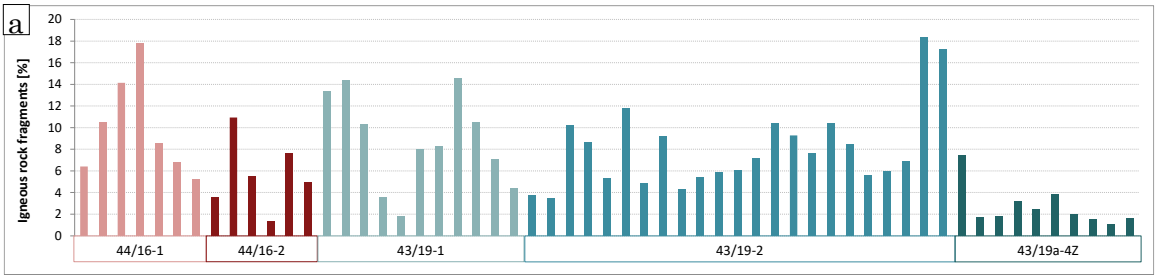

Count	7	6	11	23	10
Average	9.9	5.7	8.7	8.1	2.6
Outliers	0	0	0	2	1

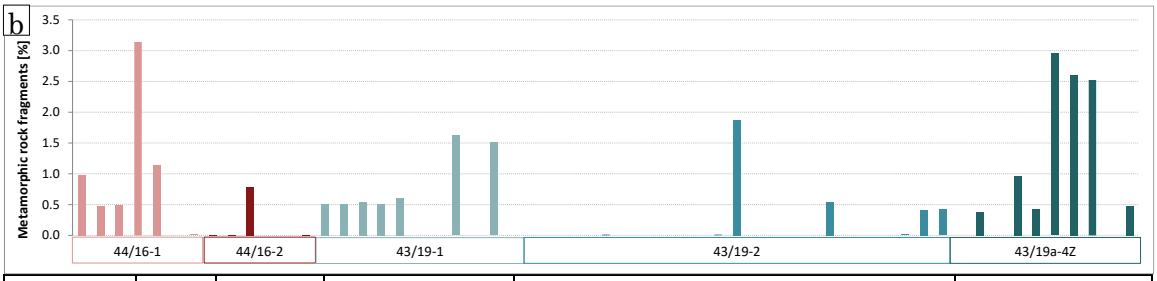

Count	7	6	11	23	10
Average	0.89	0.14	0.53	0.14	1.03
Outliers	1	1	2	4	0

Figure 3.15. Proportion of a) igneous and b) metamorphic rock fragments in the detrital framework.

3.5 Discussion

3.5.1 Sedimentary environment and reservoir quality distribution

Twelve facies associations were identified in the cored sections of the Millstone Grit Formation from the Copernicus discovery and Cavendish field. The facies comprise siliciclastic deposits dominated by mudstones and sandstones, with minor granulestones and conglomerates. Net:gross ranges from 17% to 36%. Despite the limited amount of cored sections, some cyclicity is observed within the analysed deposits. A typical full cycle comprises offshore muds, followed by turbidite complexes or prodelta deposits, which shallow up into delta front deposits and interdistributary bay fills overlain by fluvial channel fills or delta plain deposits. However, contacts between the fluvial and underlying facies are commonly sharp, where the erosion of fluvial channels locally reaches into the offshore mud deposits, therefore full cyclicity

cannot always be observed. Delta plain facies are typically deposited on top of fluvial channels after channel abandonment, and are overlain by clay and coal-rich swamp deposits.

The successive progradation of the deep water turbidite and prodelta into delta front and fluvial channel resulted in progressive infilling of existing basin topography, starting from the north and prograding southwards (Collinson, 2005). As the deep basin progressively infilled, more shallow water conditions were established producing a cyclic succession driven by eustatic fluctuations in sea level (Leeder, 1988).

Collinson (2005) suggests that some of the multi-storey fluvial channels are a result of filling of incised palaeovalleys, based on the fact that they are out of scale with the associated cyclothems, cutting down to the underlying marine bands, as well as having coarser grained fills than distributary channels. The incised valleys were created in response to a rapid fall in relative sea level, allowing the rivers to create regional scale, valley-like features that are significantly larger than the river itself, that develop in the lower reaches of the river (Hampson et al., 1997). Laterally extensive, sheet-like multi-storey complexes deposited in non-confined settings, possibly fluvial braidplains, were described e.g. by Bristow (1993). The valley fill sandstone bodies have a mean thickness of 20-25 m reaching 80 m locally and variable width of 5-25 km. Sheet-like sandstone bodies have similar mean and maximum thicknesses to the valley fills with mean thicknesses 10-30 m, reaching up to 20-45 m, but exceed 35-70 km in width (Hampson et al., 1999). The incised valley fills are rarely vertically connected despite their deep incision.

The medium and coarse grained multi-storey fluvial channels observed in Copernicus and Cavendish in particular, which locally erode the underlying sections down to the offshore muds, are likely to have been deposited as incised valley fills. Most of the recorded multi-storey-fluvial channels, however, are most likely deposited through stacking of distributary channels on a fluvial braidplain, rather than through deep incision, as their lower thicknesses, and fine to medium grain size, do not meet the incised valley fill criteria.

The multi-storey incised valley fills as well as single storey distributary channels form gas reservoirs in the nearby Trent field. In general, it is the multi-storey fluvial facies of the Millstone Grit that are described as the having the best reservoir properties, making them the potential exploration targets (e.g. Hampson et al., 1999; Besly, 2018). Multi-storey fluvial channels in both Copernicus and Cavendish have better

reservoir properties than single storey distributary channels, or any other facies association, and present the best reservoir potential. Identification of multi-storey fluvial sandstones is therefore important during exploration to increase the chance of finding potential reservoirs.

The depositional environment is a fundamental factor controlling reservoir quality in the analysed Copernicus and Cavendish fields. The low-energy sedimentary environment produced fine to very fine-grained sandstones with high matrix contents, which have a damaging effect on porosity and permeability (Figure 3.5 b & c). The marine environments are characterised by high salinities, slightly alkaline waters and are dominated by Na^+, Cl^- and subordinate SO_4^{2-}, HCO_3^-, Ca^{2+} and Mg^{2+} (R. H. Worden and Burley, 2003). The interaction of such waters with the reducing organic matter and bacterial activity produces a suite of authigenic minerals, which commonly pervasively occlude primary porosity. The minerals precipitated in marine environments in the Copernicus and Cavendish include various carbonate cements: ferroan dolomite, non-ferroan dolomite and siderite, and pyrite. These cements, combined with abundant detrital clay and typically fine grain size, render the marine sandstones ineffective as potential reservoirs. Common interbedding of mudstone and sandstone beds, ductile grains compacted between rigid grains, mica and organic fragments concentrated along mud laminae and siderite nodules cause high heterogeneity of the marine deposits. Additionally, colonization by fauna may further increase the heterogeneity through mixing of mud into the sandstone beds.

The continental pore waters in a warm and humid climate, which characterised the late Carboniferous times, typically have low salinity and are slightly to moderately acidic due to the presence of decaying organic material (R. H. Worden and Burley, 2003). Reducing conditions caused by bacterial decay of organic matter, in the presence of ferric iron, formed some sphaerosiderite and siderite nodules on the delta plain. Fluvial channels, with their fresh waters and high current, are not an environment where cements can easily precipitate, and therefore avoided the fate of marine sands and high porosity and permeability were preserved until mechanical compaction started. In the low salinity, undersaturated pore waters, feldspars can also be easily dissolved, initially increasing porosity, but the released ions can be utilised for kaolinite formation, which has a detrimental effect on porosity and permeability.

3.5.2 Mechanical and cementational porosity loss

Reduction of depositional porosity and permeability starts very early after deposition, either through detrital clay infiltration or through diagenetic mechanisms such as mechanical compaction and cementation. Reservoir quality can also be increased during diagenesis through dissolution of unstable detrital and authigenic minerals. The combined effects of all these processes will shape the final reservoir properties. Mechanical compaction reduces porosity by reorientation and repacking of brittle grains and by plastic deformation of ductile grains (Houseknecht, 1987), and can reduce porosity from the initial values of over 40% down to 26%, which corresponds to about 1500 m depth in the absence of cement or matrix (Paxton et al., 2002). Cementation may further reduce porosity. With increasing burial and temperature, authigenic minerals such as quartz, illite and zeolite might precipitate, while some unstable detrital grains (e.g. feldspar) or early cements (e.g. carbonates) might dissolve, increasing porosity.

In the analysed 113 sandstone samples, mechanical compaction was the main mechanism leading to porosity loss, with eighty-four samples experiencing more porosity loss due to mechanical compaction than to cementation. Porosity loss by cementation was typically higher in samples that contain abundant early carbonate cements, i.e. dolomite and siderite, and detrital clay which stabilised grain framework thus impeding mechanical compaction. The dominance of mechanical compaction indicates that most porosity loss occurred during early diagenesis. Strong mechanical compaction can be explained by the burial history of the Southern North Sea sandstones, which experienced rapid burial reaching 4000 m in some areas in the Late Carboniferous, shortly after deposition (Vincent, 2015). Despite the stabilisation of grain framework by early carbonate cements, due to their pervasive nature carbonate cements occluded virtually all intergranular porosity, rendering the reservoir ineffective for hydrocarbon flow therefore sandstones devoid of early carbonates, that experiences strong mechanical compaction show a better reservoir quality.

This strong effect of mechanical compaction on porosity reduction has been somewhat overlooked in the past. Many works that focus on reservoir quality of Upper Carboniferous sandstones predominantly concentrate on the influence of sedimentary environment and the effects of authigenic cements and grain dissolution (e.g. Cowan, 1989; Cowan and Shaw, 1991; O'Mara et al., 2003). Others, although note the importance of severe mechanical compaction and its effects of porosity loss, do not attempt to quantify the effects of mechanical compaction vs chemical cementation

(e.g. Besly et al., 1993; Leeder and Hardman, 1990). Yet, understanding of mechanical compaction and the processes that lead to it, i.e. rapid, early burial (see Chapter 4) is of high importance for understanding of the basin history and its reservoir quality preservation potential. Besly et al. (1993) notes that the detection of red-coloured Westphalian sandstones, which are associated with strong compaction in the Silverpit area, may be a useful rapid visual way of identifying sandstones from which hydrocarbon production can be expected to be unfavourable.

3.5.3 Depositional feldspar content and provenance

Quartz-rich sandstones are found to be the best reservoirs within the Namurian deposits in onshore UK and the Southern North Sea (e.g. Trent Field, O'Mara et al., 2003, 1999; Cavendish Field, Wasielka et al., 2020). O'Mara et al. (2003) proposed that in the Trent Field, which is located nearby the analysed here Copernicus and Cavendish fields, feldspar removal is responsible for the origin of the quartz-rich sandstones and the single most important factor controlling reservoir quality. Understanding the origin of the quarzitic sandstones might therefore be crucial to unravel what controls reservoir quality distribution in the analysed deposits of the Cavendish and Copernicus fields.

O'Mara et al. (2003) suggested that the key role in reservoir quality preservation is played by the depositional environment. Firstly, the environments with higher hydraulic energy levels (incised valley fills, marginal marine environments and distributary channels) provide some of the best reservoirs as detrital clay and feldspar removal during transportation and reworking in those environments increased sediment textural and mineralogical maturity, which in turn made them less prone to adverse effects of diagenesis (such as authigenic clay formation). Secondly, tidal reworking of the estuarine/tidal channels resulted in most effective cleaning-up of sandstones producing the best reservoirs in the Trent Field, with permeabilities reaching up to 1000 mD. Such cleaning up of feldspars and clay minerals was also observed in shallow marine sandstones by Percival (1992), who reported that reworking of deltaic sands with a significant proportion of feldspar by wave and storm action resulted in formation of a texturally and mineralogically mature quartz arenite sandstones.

Bristow (1988) suggested another theory for the observed increasing proportion of quartz to feldspar from north to south in age equivalent Rough Rock fluvial sandstones from onshore UK. He postulates that this resulted from both increasing

maturity of the sediment further from the source, as well as extra sediment supply from a quartz rich source to the south.

Framework composition of deeply buried sandstones is a function of provenance, transport, weathering processes and diagenesis (e.g. Weltje and von Eynatten, 2004). Although this study did not concentrate on recognising potential sources of the detritus, it is important to highlight that the observed differences in framework composition of the studied sediments have likely resulted from changes in drainage areas and the delivery of different mineral suites into the sedimentary basin. Long transport could have also played a role in 'cleaning up' of the detrital material, as transport can be responsible for sorting of compositionally distinct grains, resulting in preferential enrichment/depletion in some mineral constituents (e.g. Whitmore et al., 2004). Furthermore, quartz is much more durable than K-feldspars and plagioclase (Nesbitt et al., 1997) and therefore long transport and weathering may result in feldspar removal and deposition of clean, quarzitic sandstones. In case of heavy, tropical weathering of quartz rich crystalline rock, the final product may be a pure quartz arenite, as is for example in the case of the modern Amazon River (Franzinelli and Potter, 1983). Similar tropical conditions to the modern Amazon region occurred in the Southern North Sea basin during the Late Carboniferous times, and feldspar, if present at the source, could have been eliminated through the intensive tropical weathering.

The differences in composition and proportions of lithic fragments, and the initial mount of feldspar in analysed wells imply an addition of detritus from a different source for the material in wells 43/19a-4Z and possibly 44/16-2, compared to wells 49/19-1, 43/19-2 and 44/16-1. Detrital composition of sandstones from well 43/19a-4Z further stands out, due to its highest quartz content, the highest proportion of metamorphic fragments and smallest proportion of igneous fragments. This suggests that this well might have benefited from the addition of yet another source of detritus, possibly the southerly quartz-rich source suggested by Bristow (1988). The coarser size of quartz grains in well 43/19a-4Z might also point to a different source, which has coarser quartz crystals than the sources supplying other wells (see e.g. Franzinelli and Potter, 1983). Different provenance therefore appears to be a major factor controlling the origin of quartz rich sandstones in well 43/19a-4Z, but an increasing mineralogical maturity resulting from progressive feldspar removal during sediment transport has most likely aided in cleaning up of those sands.

Due to the lack of accurate stratigraphy data for the analysed wells it is difficult to say how the provenance had changed through time or whether it is geographically controlled.

The sources of detritus active during the Namurian times have been a subject of numerous studies. A primary northern source of Upper Namurian sediments onshore and offshore UK is well established (e.g. Collinson, 1988; Collinson et al., 1993; Hallsworth and Chisholm, 2008), with inputs from a northwestern source (Collinson, 1988) and from the Wales–Brabant High to the south (Bristow, 1988; Collinson et al., 1993; Chisholm and Hallsworth, 2005; Hallsworth and Chisholm, 2008) also proposed, on the basis of petrography, palaeocurrent and heavy mineral data. There is also evidence for the mixing of more local sediment supplies (Hallsworth and Chisholm, 2008). Our petrography data, which suggests multiple sources of sedimentary material, matches well the established provenance data.

3.6 Conclusions

-Sandstones from the Copernicus discovery and the Cavendish field show extremely variable reservoir quality, however most of them are classified as 'tight', which means that hydraulic fracturing, multilateral wellbores or horizontal drilling in order to produce economic quantities of gas. Exceptionally high permeabilities are preserved in medium and coarse grained, quartz rich sandstones deposited as multi-storey fluvial channels in well 43/19a-4Z

-The depositional environment is a fundamental factor controlling reservoir quality in the analysed Copernicus and Cavendish fields, due to the differences in detrital composition, grain size and different pore water chemistries leading to varying digenetic pathways. Porosity in marine sandstones is typically pervasively occluded by detrital clay and carbonate cements, rendering them ineffective as potential reservoirs. Sandstones from continental settings, and fluvial channels in particular, contain little early diagenetic cements leading to better porosity preservation until deep burial.

- Whilst some of the medium and coarse grained multi-storey fluvial channels might be infills of incised valleys, which form some of the best reservoirs in the area, the majority of the cored sandstones are too fine grained and too thin to meet the criteria of an incised valley fills. They have most likely been deposited on a fluvial braidplain, thorough vertical and horizontal stacking on multiple channels.

-The next most important factor in porosity preservation after depositional environment is sandstone composition during deposition. Mineralogically mature, quartz rich sandstones are less prone to adverse effects of diagenesis than the more feldspathic sandstones. In the latter, feldspars are typically altered to kaolinite, which has a detrimental effect on reservoir quality.

-Differences in quartz and feldspar content, grain size, and composition of lithic fragments result from delivering of detrital material from multiple sources. The exceptionally permeable sandstones from well 43/19a-4Z have likely been derived from a different, more quartz rich source, than sandstones from other wells. Provenance therefore appears to be one of the most important factors controlling reservoir quality in the fluvial sandstones.

CHAPTER 4:
Burial modelling and petroleum system development in Copernicus discovery and Cavendish field, Southern, North Sea

4.1 Introduction

The Southern North Sea (SNS) is a mature gas province that has been explored since the 1960s. 50 trillion cubic feet (tcf) of gas were produced to this day (OGA, 2019), with an estimated 3.8 tcf of remaining accessible gas (Oil & Gas Authority, 2017). The active Carboniferous petroleum system of the SNS consists of widespread Carboniferous aged gas-prone source rocks, excellent-quality regional top seal provided by the Upper Permian (Zechstein) salts, as well as intra-Carboniferous seals, and reservoirs found within fluvial channel sand bodies. The burial history of the Southern North Sea basin is long and complex, involving multiple phases of burial and uplift, which all had a big impact on petroleum generation history and reservoir quality preservation. Hydrocarbon generation started as early as the Late Carboniferous in some deeply buried areas, but ceased due to the Variscan uplift, to be later renewed in the Jurassic or Cretaceous times (Besly, 2018) and continues until the present day in many areas.

Basin inversion can significantly modify the tectonic structure, impact the thermal history of the basin, and significantly influence the diagenetic pathway, all of which have fundamental effects on petroleum system development. Inversion can, for example, lead to the exposure of previously deeply buried rocks to meteoric water influence, reduce the effectiveness of sealing horizons, cause hydrocarbon leakage or cooling of source rock and cessation of hydrocarbon generation (Besly et al., 1993; Corcoran and Doré, 2002; Turner and Williams, 2004). The assessment of burial histories of sedimentary basins is therefore crucial for predicting the presence of active petroleum systems and assessment of their quality (Botor et al., 2019). The biggest difficulty lies in the correct estimation of the amount of material that is missing from the rock record due to erosion.

The previous chapters discussed the impact of depositional environment and sedimentary processes on the reservoir quality, sandstone provenance, diagenetic history, and how all these aspects are closely tied together leading to specific diagenetic pathways within the different sedimentary and provenance realms. However, the diagenetic evolution of the basing would not be complete without looking into the burial history of the basin, particularly where said history is as complex as in the Carboniferous system of Southern North Sea. Multiple phases of basin burial and uplift of varying degrees of intensity across the area that could lead to trap formation, while also having the capability to breach the thick seal rock, combined with the presence of widespread source rocks, have all the makings of either

excellent reservoirs or unrealised petroleum systems, regardless of even the most favourable sedimentological and provenance conditions. Therefore, the aim of this chapter is to reconstruct the burial history of two wells from Cavendish and Copernicus fields, in order to unravel the major phases of the burial evolution and understand basin's thermal evolution, hydrocarbon maturation and emplacement, changes to pore fluid chemistry, and ultimately deciphering diagenetic history. These are central to finding the key as to what factors control the reservoir quality of those tightly cemented sandstones. Studying individual stages of basin evolution helps in recognising major temperature thresholds and faulting events, both of which have fundamental impact of reservoir quality preservation.

By studying the burial history of the two wells of interest and combining it with detailed diagenetic study (see chapter 6) and hydrocarbon maturation and emplacement history, it is possible to upscale our understanding of diagenetic events. While most diagenetic studies concentrate on paragenetic relationships between minerals within small samples (thin section scale or core plug scale in the best scenario) that only allows recognition of the relative evolution of the diagenetic system on a small scale, basin modelling, can put a much wider perspective on diagenetic events and help place diagenetic evolution into a time framework.

Both the Cavendish field and Copernicus discovery contain gas, yet Cavendish field produced gas for 11 years (Wasielka et al., 2020), while Copernicus was never commercially developed and the licence was relinquished by the operator after a decision was made that it would not result in an economically viable development (ENGIE, 2015). Although both fields are located on the same major tectonic structure, they experienced different burial histories which resulted in different hydrocarbon generation histories. This chapter sheds some light on why this is the case.

4.2 Geological setting and hydrocarbon system

The Copernicus discovery and Cavendish field are located in the Southern North Sea, in blocks 44/16 and 43/19 respectively about 150 km east of the UK coast. SNS is a mature gas basin, which has been producing gas for several decades, primarily from the Lower Permian and Upper Carboniferous aged reservoirs. Cavendish field produced 98 bcf of gas from Namurian and Westphalian aged reservoirs between 2007 and 2018, when it ceased production (Wasielka et al., 2020). Copernicus discovery, on the other hand, flowed gas during drill stem tests (DST), yet it was assessed as economically non-viable (ENGIE, 2015) and was never developed. Both Copernicus and Cavendish lie on the same tectonic structure, a west northwest-east southeast

orientated, dip and fault closed anticline (Figure 4.1), with its crest eroded by the Base Permian Unconformity (BPU). The anticline is cross cut by numerous NW-SE and WSW-ENE faults giving a series of tilted fault blocks and grabens (ENGIE, 2015), with Copernicus and Cavendish fields located on different blocks.

The tectonic evolution of the Southern North Sea basin comprises several stages of burial and uplift, which led to inversion of the tectonic structures (Figure 4.2). Basin subsidence was first interrupted at the end of Carboniferous by the Variscan orogeny, then in the Jurassic by updoming in the Central North Sea (Glennie and Boegner, 1981; Leeder and Hardman, 1990; Cameron et al., 1993; Arfai and Lutz, 2017; Besly, 2018;), and lastly in the Cenozoic due to Alpine collision (van Hoorn, 1987; de Lugt et al., 2003; Vincent, 2015) and the opening of the Atlantic Ocean (Hillis et al., 2008; Pharaoh et al., 2010).

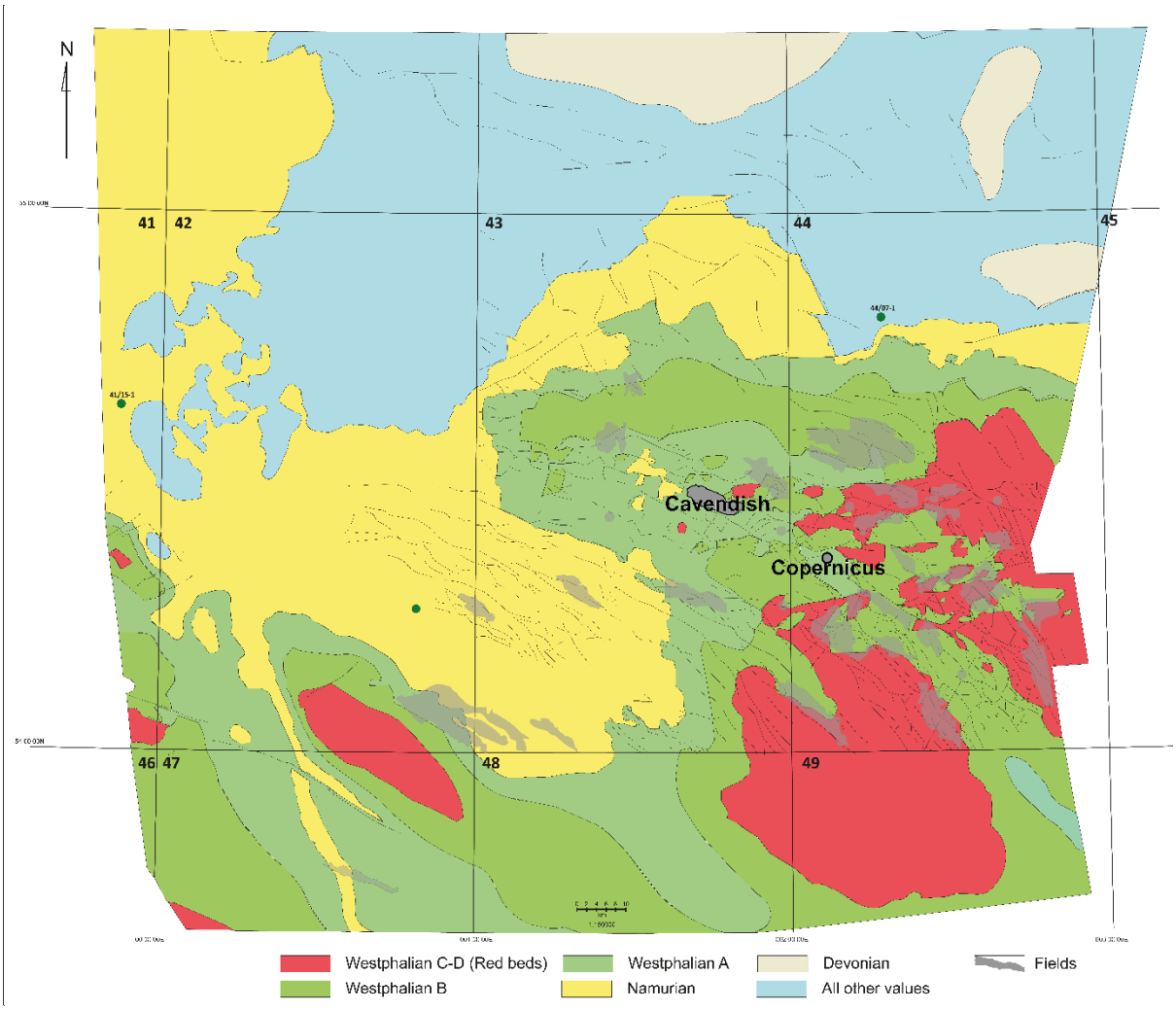

Figure 4.1 Pre-Permian subcrop map. Adapted by Gluyas from Underhill (2003).

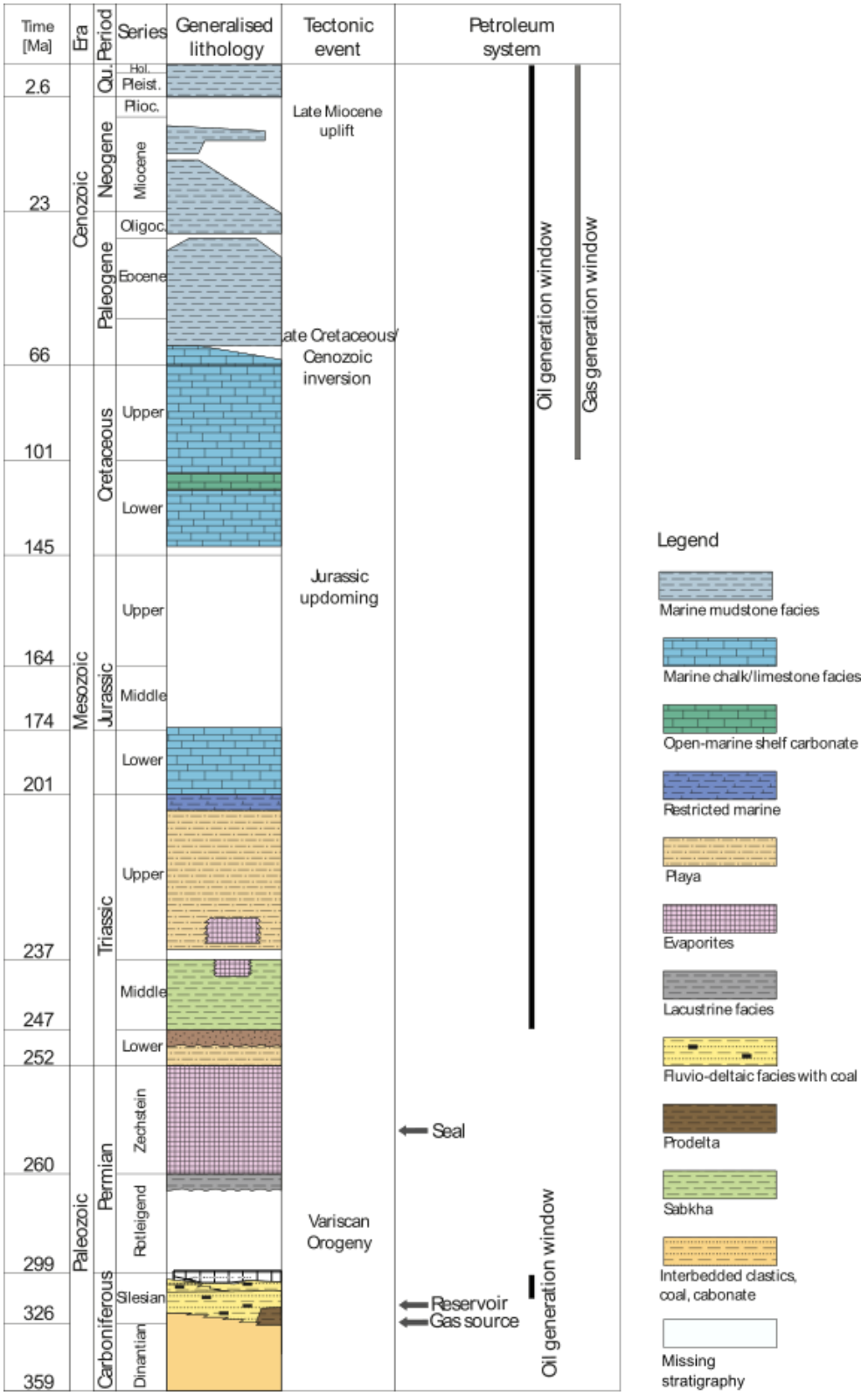

Figure 4.2. Generalized stratigraphy, tectonic evolution and petroleum system elements of the Cavendish and Copernicus area. Timing of hydrocarbon generation varies significantly between areas and for different burial depths. Oil and gas generation windows demonstrated on this figure are true for Copernicus discovery. Stratigraphy and lithology modified from (Doornenbal and Stevenson, 2010). The geological time scale after Cohen et al. (2013, updated).

The Carboniferous succession originally may have been >6 km thick, but much of it has been eroded during Variscan inversion at the end of Carboniferous (Besly, 2018). The preserved Namurian and Westphalian deposits form both the reservoir and source rocks. The best reservoirs are found within multi-storey fluvial channel facies and incised valley fills (Besly, 2018; O'Mara et al., 1999). Variscan structures provide the traps and the top and lateral seals are provided by the mudstones of the Silverpit Formation and Zechstein salts (Besly, 2018). Intra-Carboniferous seals are also found in some fields (e.g. Cavendish (Wasielka et al., 2020), Boulton (Conway and Valvatne, 2003a), Murdoch (Conway and Valvatne, 2003b)). The main gas source rocks are coal seams that occur throughout most of the Carboniferous succession. Westphalian coals act as the major source rocks, along with the Visean and Namurian coals (Cornford, 1998; Gerling et al., 1999; Pletsch et al., 2010; Besly, 2018). Minor oil source potential is also present. Oil in Carboniferous aged reservoirs is well documented in the onshore areas of the UK, e.g. East Midlands, (Fraser et al., 1990; Cameron and Ziegler, 1997; Gluyas and Bowman, 1997; Doornenbal and Stevenson, 2010) and Midland Valley of Scotland (Cornford, 1998; Waters et al., 2011), but uncommon offshore in the Southern North Sea. Potential oil source rocks in the Southern North Sea include e.g. lacustrine deposits of Westphalian age in Quadrants 48, 49, 53 and 54 (Cameron and Ziegler, 1997) and Westphalian coals in West Netherlands Basin (de Jager et al., 1996). Dinantian to Namurian aged oil source rocks comprise deepwater black-shales, which extend directly underneath and to the S-E of the area of our interest, and could provide minor volumes of oil (Cameron and Ziegler, 1997; Cornford, 1998; Schroot et al., 2006; Doornenbal and Stevenson, 2010). Silurian clastic deposits, although initially having high TOC, were overcooked and metamorphosed in the entire area having passes through the gas window already during the early and mid-Devonian (Cameron and Ziegler, 1997) and are thus deemed unimportant for the petroleum system of the SNS. The scarcity of oil shows offshore suggests that oil-prone source rocks are not widespread and require specific palaeogeographical circumstances to form (Fraser et al., 1990; Cameron and Ziegler, 1997; Besly, 2018).

Oil generation onshore and offshore started during late Carboniferous (Cornford, 1998; Schroot et al., 2006; Vincent, 2015; Besly, 2018). The produced oil however was not retained for long, as the subsequent Variscan inversion caused most of it to escape. It is estimated that Lower Carboniferous sediments were buried down to over 4000 m onshore, (e.g. Weeton 1 well, Kerr-McGee York Limited (2002)) and about 2000 – 4000 m offshore (based on wells 43/19-1 (Wasielka et al., 2020) and 43/17-02 (Vincent, 2015) prior to uplift. Although the good quality Rotliegend reservoirs and Zechstein salts

had not been formed by then, some oil was entrapped in the Carboniferous deposits sealed by intra-Carboniferous marine bands and interdistributary muds (Fraser et al., 1990). A second phase of oil generation occurred during Mesozoic burial, followed by gas generation which started between the end of Triassic, in the deeper parts of Carboniferous sequence, and Cretaceous times (Bailey et al., 1993; Robinson et al., 1993; Besly, 2018; Wasielka et al., 2020).

4.3 One-dimensional basin modelling method

Burial histories of two wells 44/16-1 from the Copernicus discovery and 43/19-1 from the Cavendish Field were modelled using Schlumberger's PetroMod (v. 2015.1) software. One dimensional modelling was used to reconstruct burial depths, temperatures and vitrinite reflectance. The stratigraphic profile drilled in two wells provided the record of the depositional history. The lithological unit types used in the models are PetroMod default lithology types or mixed default lithology types, chosen on the basis of well log descriptions. The geological time scale is from the International Chronostratigraphic Chart (v 2017/02; (Cohen et al., 2013, updated). The input model consists of 24 layers in Copernicus (Table 4.1) and 23 layers in Cavendish (Table 4.2), which were constructed based on operators' composite logs (Britoil, 1989; LASMO North Sea PLC, 1991). Modelled intervals cover deposits from Upper Carboniferous to Neogene. Four erosional episodes are included in the model: Late Carboniferous, Mid-Upper Jurassic, Early Palaeogene and Mid Miocene. Determining the amount of erosion is problematic, as erosional events are only indicated by the presence of unconformities. The amount of erosion was estimated based on regional data from Hillis (1995a), Japsen (2000), Cameron et al. (2005), Green, (2005), Green et al. (2017), and Vincent, (2015). Chemical compaction porosity loss is calculated using an integrated software tool that uses Walderhaug's quartz cementation model (Walderhaug, 2000). Hydrocarbon generation was modelled for the Carboniferous source rocks, with TOC values from Vane et al. (2015), and with kinetics and organofacies after Pepper and Corvi (1995).

End time [Ma]	Age	Layer name/event	Layer top depth [m]	Event type	Palaeo-deposition/ erosion [m]
	Mid Paleogene to Quaternary	Mid Paleogene to Quaternary, erosion event	32	E	-500
5.3	Mid Paleogene to Quaternary	Mid Paleogene to Quaternary	32	D	500
33.9	Early-Mid Paleogene	Early-Mid Paleogene	150	D	
40	Early-Mid Paleogene	Early-Mid Paleogene	421	D	
59.2	Early Paleocene	Early Paleocene, erosion event	606	E	-200
64	Early Paleocene	Early Paleocene	606	D	200
72	Upper Cretaceous	Chalk Group	606	D	
100.51	Lower Cretaceous	Cromer Knoll Group	1021	D	
145.01	Middle-Upper Jurassic	Top Lias-Upper Jurassic, erosion event	1131	E	-300
171	Middle-Upper Jurassic	Top Lias-Upper Jurassic	1131	D	300
190	Lower Jurassic	Lias	1131	D	
201.31	Middle-Upper Triassic	Haisborough Gp	1260	D	
243.01	Middle Triassic	Haisborough Gp, Lower Rot Halite Member	1624	D	

244.01	Middle Triassic	Haisborough Gp, Lower Rot Halite Member	1682	D	
245.51	Middle Triassic	Haisborough Gp, Lower Rot Halite Member	1876	D	
247.21	Lower Triassic	Bacton Gp, Bunter Sandstone Fm	1982	D	
251.21	Lower Triassic	Bacton Gp, Bunter Shale Fm	2130	D	
252.17	Upper Permian	Zechstein	2510	D	
256.21	Upper Permian	Zechstein	3298	D	
258.51	Lower Permian	Rotliegend	3349	D	
290	Upper Carboniferous, Westph – Steph.	Westphalian - Stephanian, erosion event	3638	E	-1550
307.2	Upper Carboniferous, Westph – Steph	Westphalian - Stephanian	3638	D	1550
312.71	Upper Carboniferous, Nam-Westph A	Namurian-Westphalian	3638	D	
318.01	Upper Carboniferous, Nam	Upper Carboniferous, Namurian	4670		

Table 4.1. Input data for 1D burial history model of well 44/16-1, Copernicus discovery. Abbreviations: Nam: Namurian, Westph: Westphalian, Steph: Stephanian, Fm: Formation, Gp: Group, D: deposition, E: erosion. Ages and layer names are based on Composite log data (LASMO, 1991).

End time [Ma]	Age	Layer name/event	Layer top depth [m]	Event type	Palaeo-deposition/ erosion [m]
0	Mid-Late Eocene - Quaternary	Mid-Late Eocene - Quaternary	19	E	-150
5.3	Mid-Late Eocene - Quaternary	Mid-Late Eocene - Quaternary	19	D	150
33.9	Early - Mid Eocene	Early - Mid Eocene	50	D	
54.01	Paleocene-Early Eocene	Paleocene- Early Eocene	322	E	0
64	Paleocene-Early Eocene	Paleocene- Early Eocene	322	D	0
72	Lower-Upper Cretaceous	Chalk + Cromer Knoll	451	D	
145.01	Middle - Upper Jurassic	Middle - Upper Jurassic, erosion event	742	E	-50
171	Middle - Upper Jurassic	Middle - Upper Jurassic	742	D	50
190	Lower Jurassic	Lias	742	D	
201.31	Middle-Upper Triassic	Penarth Gp	1058	D	
208.51	Middle-Upper Triassic	Haisborough Gp Triton Fm	1080	D	

227.01	Middle-Upper Triassic	Haisborough Gp Dudgeon & Dowsing Fm	1223	D	
243.01	Middle Triassic	Haisborough Gp Muschelkalk Halite Member	1411	D	
244.01	Middle Triassic	Haisborough Gp Dowsing Dolomitic Fm	1461	D	
245.51	Middle Triassic	Haisborough Gp Dowsing Dolomitic Fm, Lower Rot Halite Member	1610	D	
246.51	Lower Triassic	Bacton Gp Bunter Sandstone Fm	1727	D	
251.21	Lower Triassic	Bacton Gp Bunter Shale Fm	1905	D	
251.91	Upper Permian	Zechstein	2274	D	
258.51	Lower Permian	Rotliegend	3247	D	
298.91	Upper Carboniferous Westph - Steph	Westphalian - Stephanian, erosion event	3497	E	-1500
307.2	Upper Carboniferous Westph - Steph	Westphalian - Stephanian	3497	D	1500

312.71	Upper Carboniferous Nam - Westph A	Namurian-Westphalian	3497	D
318.01	Upper Carboniferous Namurian	Upper Carboniferous, Namurian	3941	

Table 4.2. Input data for 1D burial history model of well 43/19-1, Cavendish field. Abbreviations: Nam: Namurian, Westph: Westphalian, Steph: Stephanian, Fm: Formation, Gp: Group, D: deposition, E: erosion. Ages and layer names are based on Composite log data (Britoil, 1989).

Boundary conditions. The palaeowater depths (PWD) are inferred from the preserved lithology type and eustatic curves by Haq et al. (1988) and Haq and Schutter (2008) (Figure 4.3 a & b). Sediment water interface temperature (SWIT) was calculated with an integrated software tool based on the present-day geographic location and paleo latitude (Wygrala, 1989; Figure 4.3c). Heat flow (HF) values (Figure 4.3 d & e) for the different stages of tectonic development were initially assigned based on regional data from Vincent (2015), Arfai and Lutz (2017), Andrews-Speed et al. (1984), (Kubala et al. (2003) and Oxburgh and Andrews-Speed (1981) and then carefully adjusted against the available calibration data (Figure 4.4).

Basal heat flow and the amount of erosion were adjusted for the burial model to match the bottom hole temperatures (BHT) from well reports (including Horner-corrected temperatures where available and uncorrected temperatures; from (Burchell, 1989; LASMO North Sea PLC, n.d.), vitrinite reflectance data (from Vane et al. 2015), available fluid inclusion data (Smalley and Oxtoby, 1990) and measured porosity values. Best-fit burial model has been used to predict the quartz cementation and porosity evolution in the studied wells.

Source rock properties. Kerogen transformation and hydrocarbon generation was calculated by PetroMod software using the kinetics based on Pepper and Corvi (1995) organofacies F, that is terrigenous, wax-poor organofacies, that is associated with Palaeozoic terrestrial sedimentary organic matter.

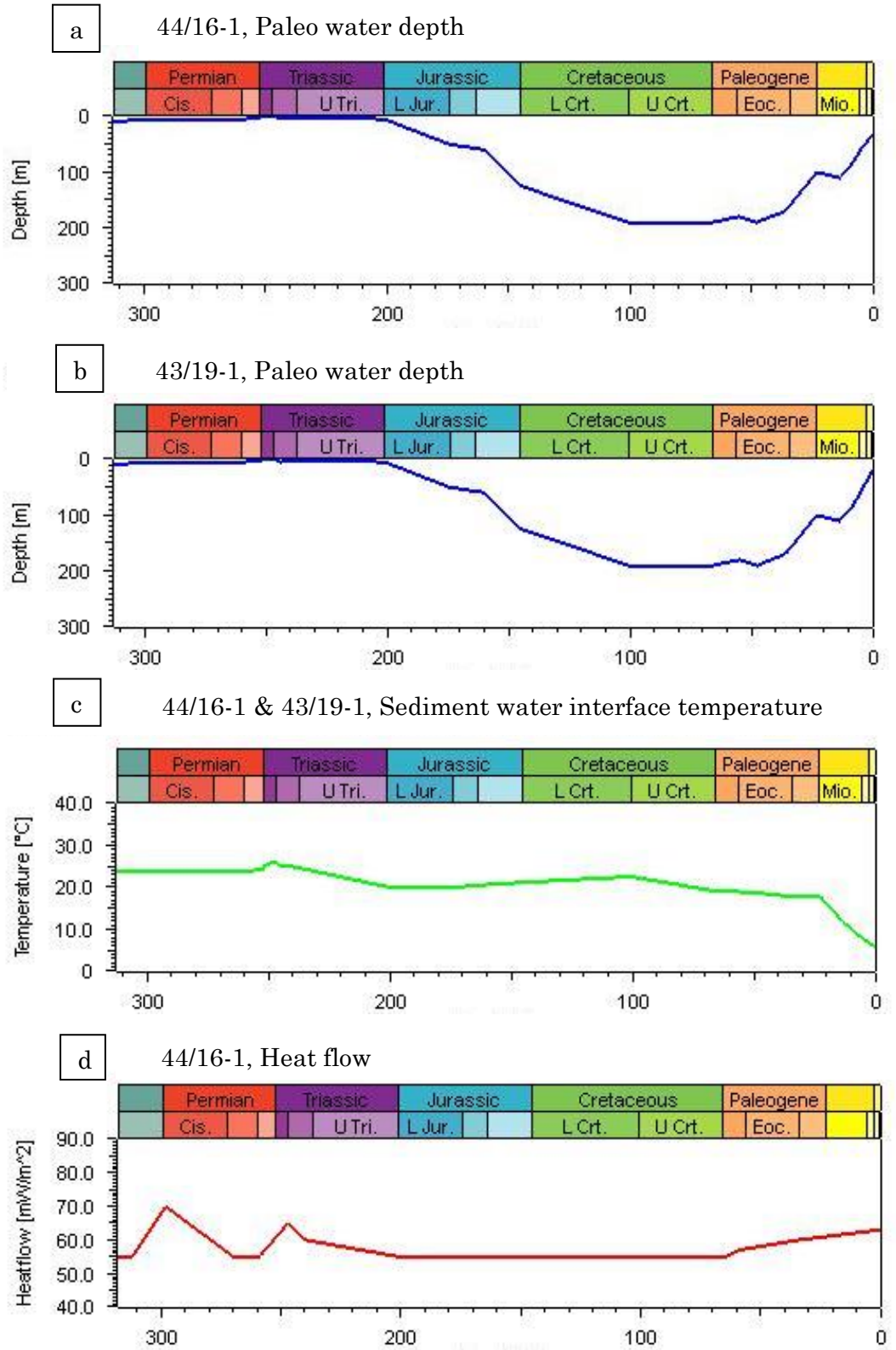

Figure 4.3. Boundary conditions the basin modelling; a, b) Paleo water depth in wells 44/16-1 and 43/19-1. Paleo water depth in both wells is the same from Carboniferous until 5Ma, and reaches 32 m at present day in well 44/16-1 and 190 m in well 43/19-1; c) Sediment water interface temperature was calculated with an integrated software tool and is the same for both modelled wells; d, heat flow values in well 44/16-1.

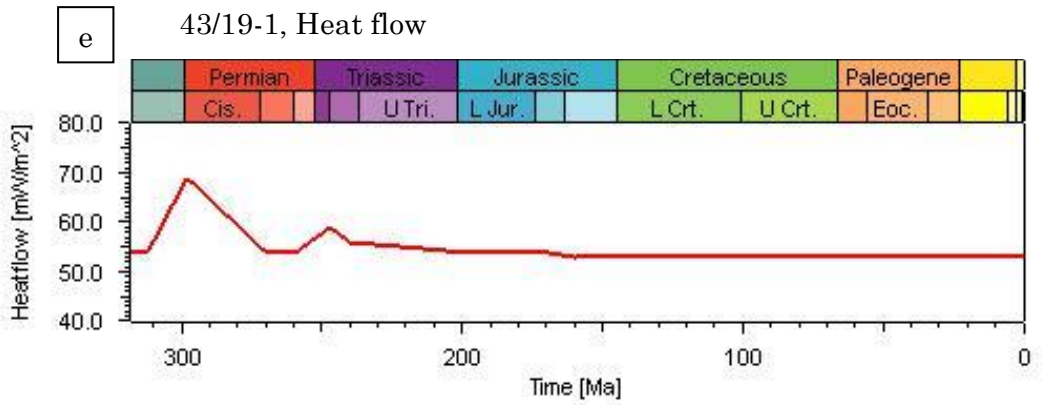

Figure 4.3 continued. e) heat flow values in well 43/19-1. Heat flow values are slightly higher in well 44/16-1 and increase since Palaeocene, whilst remaining constant in well 43/19-1.

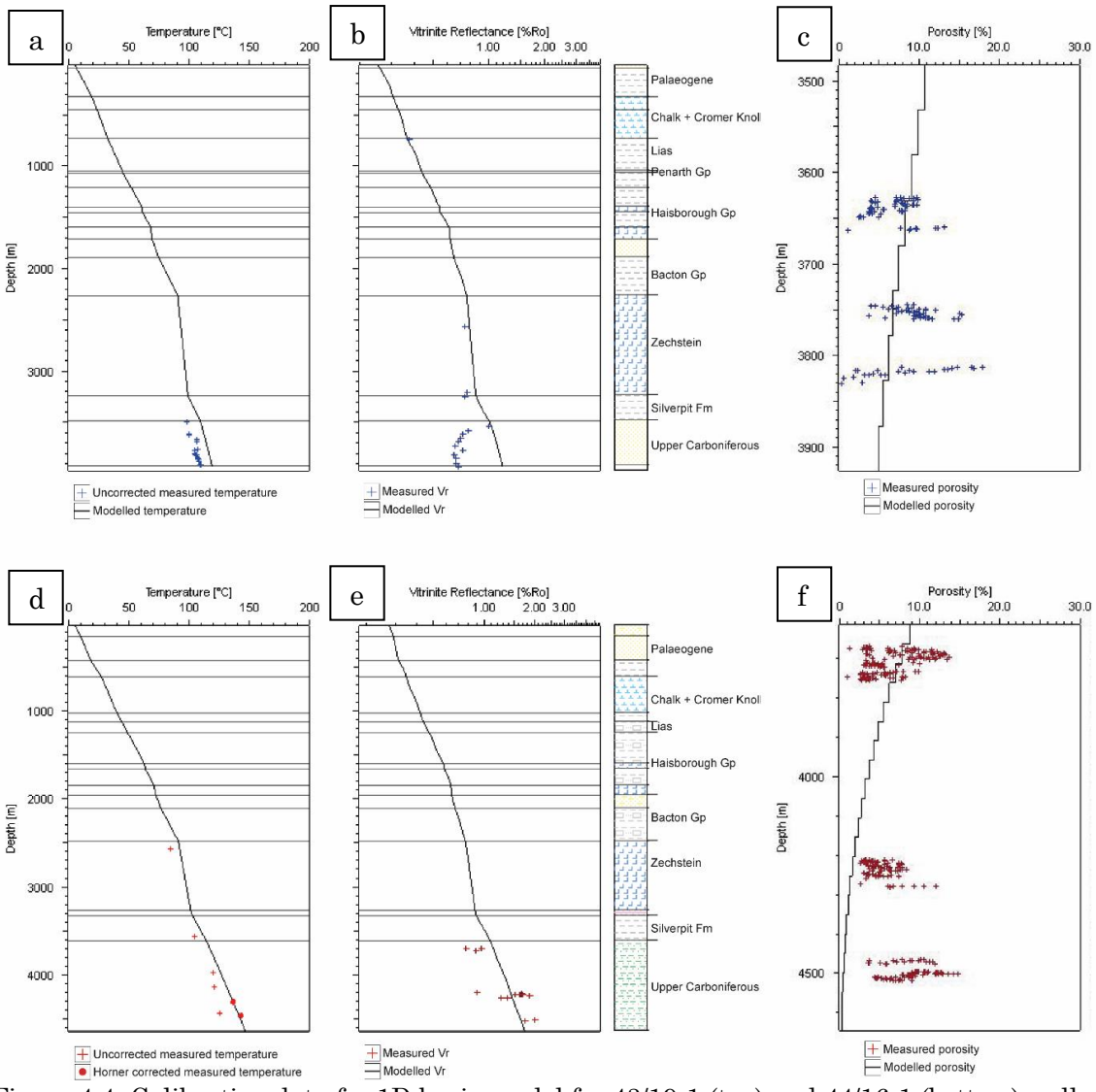

Figure 4.4. Calibration data for 1D basin model for 43/19-1 (top) and 44/16-1 (bottom) wells. a & d) Plot of modelled formation temperature and measured bottom hole temperature against depth for Carboniferous to Neogene deposits; b & e) Plot of modelled and measured Vr values against depth for Carboniferous to Neogene deposits; c & f) Plot of modelled and measured Carboniferous porosity values against depth. Note the significant discrepancy between the measured and modelled Vr values in well 43/19-1: the likely reasons for this are explained in section 4.5.2.

4.4 Burial modelling results

4.4.1 Burial history

Burial histories of the Cavendish field and Copernicus discovery are long and complex. Major subsidence phases during the Late Carboniferous, throughout the Permian until the Jurassic, and a slower subsidence in the Cretaceous and Cenozoic times were interrupted by four uplift episodes in Copernicus area (Figure 4.5a) and three episodes in Cavendish (Figure 4.5b). The Copernicus discovery has undergone more burial than Cavendish and was subjected to higher heat flow values at times (see Figures 4.3 d and e). During the first phase of rapid subsidence at the end of Carboniferous times, the Upper Carboniferous interval in Copernicus reached a maximum temperature of 123°C and c. 2700 m of burial, whilst Cavendish field underwent about 2000 m of burial bringing it to a maximum temperature of 85°C. Uplift of 1500-1550 m at the end of Carboniferous times brought the Namurian strata close to the surface and eroded the overlying Stephanian and much of the Westphalian deposits. Following this was a long-lasting phase of subsidence, which was interrupted by the Jurassic updoming event that caused an uplift and erosion of the Middle and Upper Jurassic deposits. This uplift event was perhaps more pronounced in the Copernicus area (about 300 m), whilst only minor uplift occurred in the Cavendish (50 m). The maximum burial depth and temperatures in Cavendish were reached at 35 Ma during the Eocene, whilst Copernicus experienced its deepest burial and highest temperatures in the late Miocene at about 5.3 Ma, prior to the late Miocene uplift event, that affected both fields to varying degrees. The maximum modelled burial temperature in the Namurian sequence was 140°C and 170°C in Cavendish and Copernicus respectively at depths of 4195 m and 5170 m. A hiatus recorded in biostratigraphy data (LASMO North Sea PLC, n.d.) indicates that an extra phase of erosion took place between deposition of Chalk and Palaeogene deposits in well 44/16-1. Due to lack of biostratigraphy data in well 43/19-1 there is no record of hiatus at the same time, however best match between modelling results and calibration data is achieved when none or very minor Palaeogene erosion is assumed.

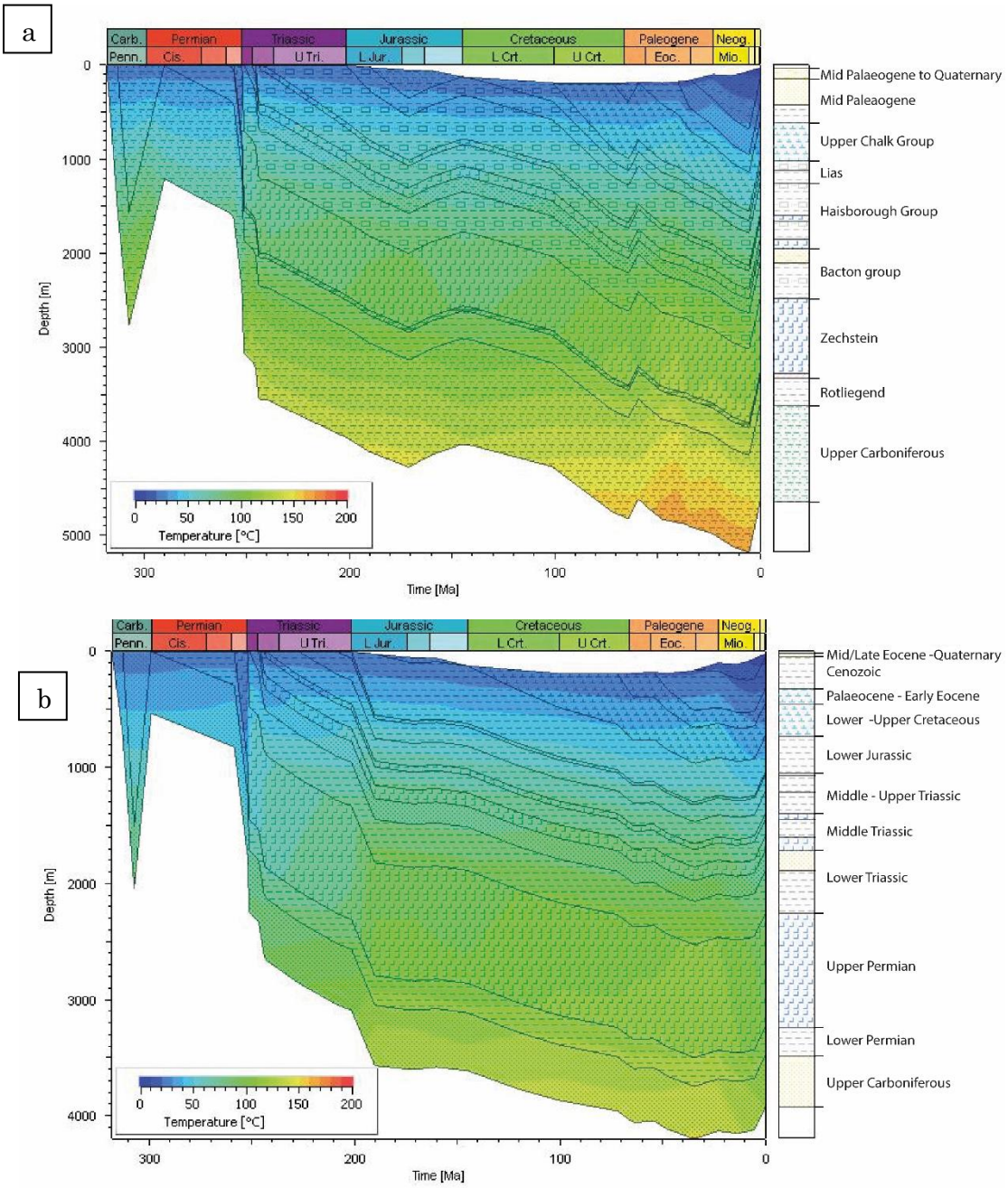

Figure 4.5. a) 1D burial history plot of 44/16-1 well (Copernicus discovery). b) 1D burial history plot of 43/19-1 well (Cavendish field). Colour overlay denotes formation temperature through time.

4.4.2 Hydrocarbon maturation

Hydrocarbon maturation history was modelled for the Upper Carboniferous interval, which contains primarily gas prone source rocks and potential minor oil-prone source rocks. The maturation history shows that well 44/16-1 from the Copernicus field entered the early oil generation window already during the late Carboniferous phase of deep burial, and the deepest buried units entered the main oil generation window for a brief period of time before the Variscan uplift (Figure 4.6 a). Well 43/19-1 from

the Cavendish field, however, did not reach the early oil generation window until the Middle Triassic, and the main oil generation window until the latest Triassic or Earliest Jurassic (Figure 4.6). Gas generation started in the Late Cretaceous in well 44/16-1, while well 43/19-1 remained within the late oil generation window even at its deepest burial in the Palaeogene times (Figures 4.6a and 4.6b respectively). At present day well 44/16-1 remains within the gas generation window, while well 43/19-1 remains oil mature.

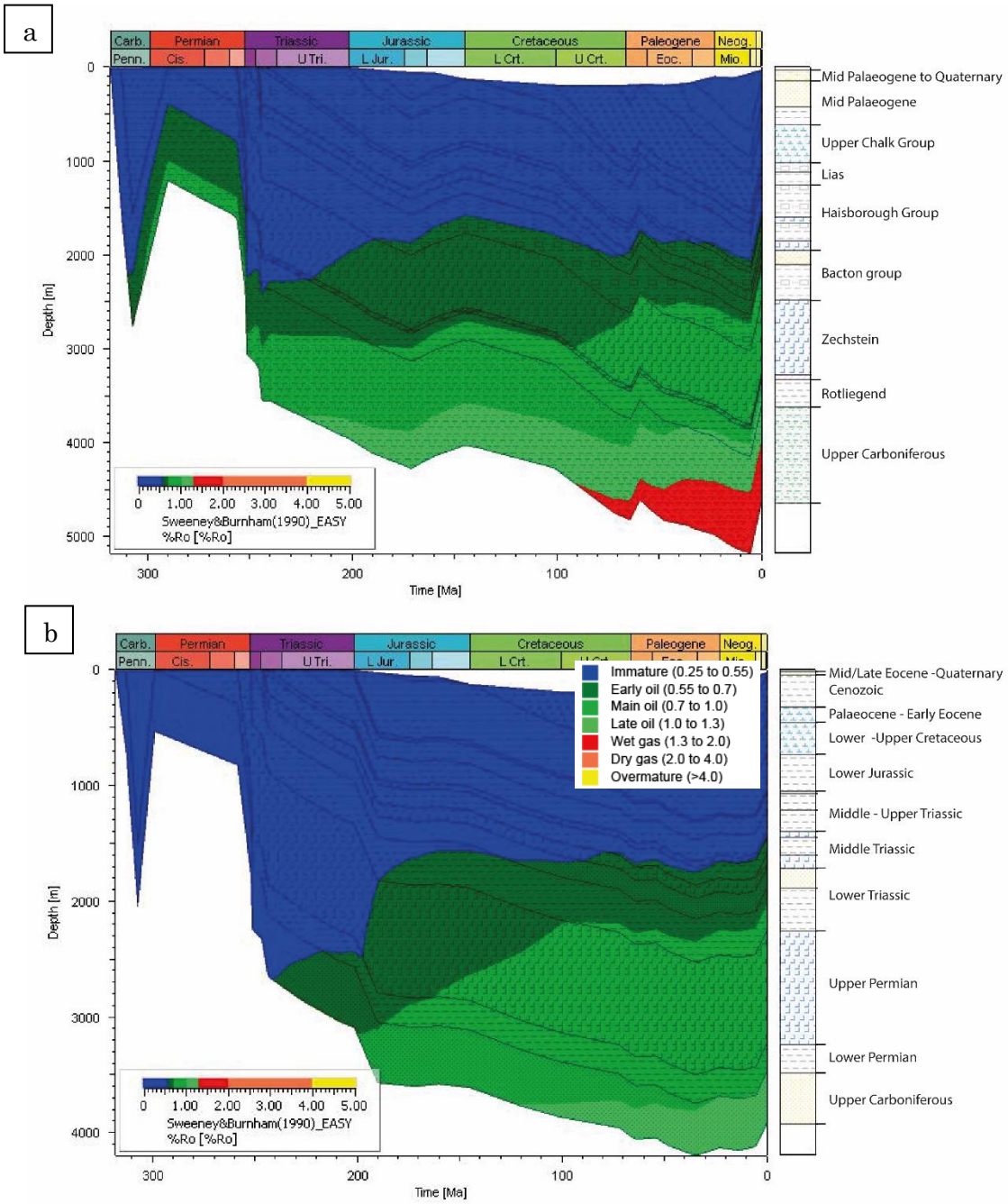

Figure 4.6. a) Modelled maturity evolution in well 44/16-1 (Copernicus discovery). b) Modelled maturity evolution in well 43/19-1 (Cavendish field). The modelled maturity colour scale is based on Sweeney and Burnham's (1990) kinetic model.

4.5 Discussion

4.5.1 Modelled burial stages

When modelling burial histories of basins with polyphase histories of burial and uplift, where the youngest burial depth exceeds that of the earlier times, the most significant uncertainties in the modelling process are the amount of eroded material and the paleo heat flow values, associated with the tectonic evolution of the basin (Schwarzer and Littke, 2007). The elevated paleo heat values remain untested, as heat flow values during early subsidence stages leave no measurable effect if later subsidence has caused higher temperatures than those attained during the early stages (Bray et al., 1992). Equally, all episodes of burial and uplift that occurred before the maximum burial of the basin will be overprinted, and cannot be resolved with absolute certainty. Additionally, effects of secondary thickening/thinning of the Zechstein salts due to post-depositional halokinesis triggered by enhanced differential loading are impossible to assess. Yet, the presence of thick salts has important consequence for thermal modelling (cf. Cedeño et al., 2019). Being aware of these limitations, the most probable burial model can be obtained by finding the best possible fit with the available calibration data and known basin history by fine-tuning the paleo heat flow and erosion values.

The modelled scenarios for Copernicus and Cavendish wells are consistent with the known tectonic evolution of the Southern North Sea. Seven significant stages of geological evolution were distinguished in the analysed wells. Each stage is described below, with significant events that lead to their development, heat flow values and reasons for the estimated erosion values explained in detail.

1. *Carboniferous subsidence:* It is estimated that over 6 km of sediments were deposited during the Upper Carboniferous in the Southern North Sea (Besly, 2018). Basin subsidence was caused by post thermal re-equilibration of the thinned lithosphere (Leeder and Hardman, 1990), while the high sedimentation rate owes to the development of large fluvial systems, that can be compared with the size of modern Amazon river (Leeder, 1988). Heat flow value was set at 55 mW/m^2 at this time.

The model shows that the Namurian source rocks in Copernicus entered the early oil window during the Late Carboniferous, with the most deeply buried Namurian and underlying Dinantian source rocks entering the main oil generation window. Burial depth reached at the time would have been around 2700 m in Copernicus with

concurrent temperatures of around 120°C. Cavendish, in the meantime, was buried down to about 2000 m, reaching temperatures up to 85°C, and was too shallow at the time for hydrocarbon generation to occur. Oil generation window ranges from 95°C to 175°C for organofacies A – F (Pepper and Corvi, 1995). Copernicus field remained at temperatures of over 100°C for about 13 My, therefore even with the higher estimates of oil generation temperatures, it had enough time to generate some oil. Additionally, the underlying Dinantian rocks, which are not included in the model, could have acted as an additional minor source for oil, active during Carboniferous burial. Temperatures modelled in Cavendish are lower, therefore condition for oil generation would have been much less favourable. The model is corroborated by petrographic observations: early oil (prior to main phase of quartz generation) is observed in thin sections in Copernicus, while no evidence of oil emplacement in the Cavendish field is recognised.

2. *Variscan uplift*: Compression during the Variscan orogenic event caused an inversion of tectonic structures in the basin and erosion of much of the deposited Carboniferous sediment. The amount of Variscan uplift is difficult to estimate; erosion maps by various authors indicate that this amount could be as low as 0 m for Copernicus area and 500 m for Cavendish (Cope, 1986), or significantly more: 900 m was proposed by (Glennie and Boegner, 1981) in the vicinity of Sole Pit, 400 to 1400 m was proposed by Vincent (2015) for nearby wells in blocks 42/20, 42/10B and 43/17 (1400 m in well 43/17-2, which is closest to the Cavendish 43/19-1 well from this study). Quirk and Aitken (1997) estimated that about 1700 m of Westphalian – early Stephanian had been deposited in the Copernicus and Cavendish area. Drilling data show that around 330-410 m of Westphalian and no Stephanian is preserved today in Copernicus and Cavendish, indicating that erosion reached 1290 - 1370 m. Estimates of the deposited Westphalian thickness in the area by Ziegler (1990) are much higher than those by Quirk and Aitken (1997) , consisting of 3000 – 3200 m of sediment, which would require 2590 – 2870 m of the Westphalian to be eroded. The amount of erosion used in this study in Copernicus and Cavendish fields is 1550 and 1500 m respectively, which is within the range suggested by other authors, and matches the available well calibration data. It must be borne in mind though, that Mesozoic burial, which was deeper than the pre-Variscan maximum depth, overprinted the effects of Variscan burial therefore the accurate amount of uplift is difficult to estimate.

Elevated heat flow values of 69 – 70 mW/m2 were assigned to this stage, consistent with values proposed by Vincent (2015; proposed heat flow: 56.5 – 82 mW/m^2) and Arfai and Lutz (2017; 80 mW/m^2) in the surrounding areas.

3. *Late Permian and Mesozoic burial.* Subsidence continued initially slowly in the Early Permian after cessation of Variscan orogenesis, as a result of lithosphere-wide cooling, and became very rapid during Late Permian – Early Triassic, when the cooling subsidence was superimposed by crustal stretching and major regional Triassic rifting (Sørensen, 1986; Zijerveld et al., 1992) or due to thermal reequilibration of the lithospheric after the Permo-Carboniferous wrench faulting (McCann et al., 2006; Van Wees et al., 2000). This phase was followed by period of smoother, thermally controlled subsidence until Jurassic times.

A continuous sedimentary sequence of 2507 m in Copernicus and 2755 m in Cavendish are preserved from this stage in the analysed wells, allowing to reconstruct the amount of burial. Average heat flow of 53-55 mW/m^2 was used throughout most of this period, however a slightly elevated heat flow in the Triassic, caused by first post-Variscan rifting phases, was suggested by Arfai and Lutz (2017), and values of 59 and 63 mW/m^2 were used for Cavendish and Copernicus respectively in the Early Triassic.

4. *Jurassic updoming*. The exact effects of the updoming that occurred in Central North Sea are not known in the analysed areas. Different authors proposed varying estimates of Jurassic erosion, ranging from 200 m in block 43/17 (Vincent, 2015) to about 900 m on the flanks of Leman Bank structure (Glennie and Boegner, 1981). In the modelled wells Lower Jurassic (Lias) is directly overlain by Cretaceous Cromer Knoll deposits, indicating significant erosion. Although heat flow was elevated in some areas of the North Sea as a result of the updoming (e.g. Cornford, 1998; Arfai and Lutz, 2017), modelling results indicate that these effects apparently did not impact Quadrants 43 and 44. Increased Jurassic heat flow or a large amount of erosion would have caused modelled Vr values to exceed the measured values, so the best match with the calibration values was obtained when Jurassic heat flow values remained at the same level as the one that persisted from the late Triassic through to the Cretaceous (53 - 55mW/m^2). Erosion of no more than 50 m took place in Cavendish, and was potentially higher in Copernicus, however the latter is not certain due to Paleogene deep burial and overprinting.

5. *Continued Mesozoic burial*. The infilling of the Southern North Sea continued after the Jurassic updoming, however at a slightly lower rate as indicated by the preserved sedimentary sequence. Heat flow rates remained unchanged until the next phase of inversion.

6. *Late Cretaceous/Cenozoic inversion*: Compression forces associated with the Alpine collision (van Hoorn, 1987; de Lugt et al., 2003; Vincent, 2015) and the opening of the Atlantic Ocean (Hillis et al., 2008; Pharaoh et al., 2010) caused an inversion of tectonic structures during the Cenozoic times. A number of studies have attempted to quantify the amount of the Late Cretaceous/Cenozoic erosion in the Southern North Sea using sonic velocities, apatite fission track analysis and vitrinite reflectance data (e.g. Bray et al., 1992; Hillis, 1995a; Hillis, 1995b; Japsen, 1998; Hillis et al., 2008) Japsen (1998) calculated that Chalk burial anomaly is about 500 – 600 m between the Copernicus and Cavendish area. Between 400 and 600 m of Cenozoic exhumation is calculated for area neighbouring with Copernicus by Hillis et al., (2008). Slightly higher values derived from sonic velocity data from numerous wells in the SNS are shown on mean apparent exhumation map by Hillis (1995a), reaching about 800 and 900 m in Copernicus and Cavendish area respectively. Some authors proposed two stages of Cenozoic exhumation: Palaeogene and as well as an earlier phase of mid or early Cretaceous episode (e.g. Hillis et al., 2008, Green et al., 2017). Exhumation episodes were dated by Green (2005) to have started in the Palaeocene (between 65 and 55 Ma) and a later one in Neogene times.

A hiatus indicated by biostratigraphy data between the Chalk (Early Maastrichtian) and Palaeocene (Latest Palaeocene) in 44/16-1 well confirms that the Copernicus area experienced Early Cretaceous or Early Cenozoic uplift (LASMO North Sea PLC, n.d.). Biostratigraphy data for this period are not available from Cavendish wells, however modelling results show that there is little or no capacity for extra burial and erosion at that time. Any additional burial would have resulted in higher Vr and maximum burial temperatures than allowed by the measured Vr and fluid inclusion data (maximum measured fluid inclusion temperature was 129°C; (Smalley and Oxtoby, 1990). The top of the drilled interval is not described in either of the modelled areas, therefore the models assumed the presence of a Neogene erosion phase, based on regional data. To find the best fit with calibration data, two different Neogene uplift scenarios were necessary in Copernicus and Cavendish, with a significantly lower amount of erosion in Cavendish, combined with lower heat flow values in Cavendish. Heat flow values applied in this study were 65 mW/m^2 in Copernicus and 57 mW/m^2 in Cavendish. The value of 57 mW/m^2 is lower than the present day heat flow value suggested by various authors for that area (65mW/m^2 based on heat flow maps by Andrews-Speed et al., (1984), 60 – 75 mW/m^2 based on Kubala et al. (2003) and 67 mW/m^2 (Cavendish) to 74 mW/m^2 (Copernicus) based on heat flow map by Oxburgh

and Andrews-Speed (1981)), however such adjustment was necessary in order to match calibration data.

4.5.2 Vitrinite reflectance interpretation and hydrocarbon generation

Vitrinite reflectance (Vr) data are widely used for assessing thermal maturity in sedimentary rocks in oil and gas exploration (Sweeney and Burnham, 1990; Carr, 2000). However, under certain conditions suppression or retardation of reflectance values might occur, potentially leading to underestimation of thermal maturity of the source rocks. Vr suppression might be related to lithology, depositional environment, high liptinite contents or presence of aliphatic lipids and bitumens derived from associated liptinites. It has also been proposed that Vr values can be supressed below thick salt layers due to the high thermal conductivity of the salt. Vr retardation results from development of overpressure during burial (Carr, 2000). Both Vr suppression and retardation lead to reflectance values lower than expected at given depth.

+/-0.1% spread of Vr values can be attributed to polishing blemishes, random instrument error, bireflectance and type of vitrinite (see Carr, 2000) and does not indicate suppression or retardation. However, a large divergence from normal Vr-depth trends indicate that Vr values are likely either suppressed or retarded.

A large divergence between measured and modelled Vr values is observed in the Cavendish well 43/19-1 and Copernicus well 44/16-1 (Figure 4.4 b & e). The divergence in well 43/19-1 is particularly conspicuous, as Vr values in the Carboniferous interval decrease with depth, showing an opposite trend to what is normally expected (Figure 4.4b). The largest observed divergence is 50% at ~3920 m in 43/19-1 well and about 45% at 4254 m in 44/16-1. Such substantial difference indicates that Vr values in both wells are very likely to be significantly suppressed or retarded.

Numerous processes discussed by (Carr, 2000) could be responsible for those reduced Vr values, including overpressure, variable depositional environmental, or presence of thick salt horizon. In both wells the reduced Vr values occur below Zechstein salt intervals that are 840 - 970 m thick, which could be responsible for Vr suppression, or overpressure build up and Vr retardation.

The maximum measured Vr value in well 43/19-1 is 1 %Ro, which is the transition value between the main and late oil generation window. The maximum modelled Vr value is 1.19%Ro, which sits within the late oil generation window. It can therefore

be safely assumed that Cavendish well 43/19-1 never entered gas generation window, even if the Vr values are significantly supressed or retarded.

Modelling results of Copernicus well 44/16-1 show that the well entered the gas generation window in Late Cretaceous times. This result is corroborated by Vane et al. (2015) who showed that some Tmax values in this well indicate gas window maturity, with the possibility of some gas generated, and HI values are indicative of a gas-prone sequence.

4.5.3 Comparison of Copernicus and Cavendish burial histories

Although both analysed fields are located on the same major tectonic structure, have reservoirs of the same age, and benefit from widespread presence of source rocks and seals, one was developed as a commercial gas field and produced gas for eleven years, while the other was abandoned due to no commercial potential. While many factors are responsible for this (see chapter 3 and 5), the differences in burial history played a role in this. The significantly deeper maximum burial depth and temperature in Copernicus were responsible for more extensive cementation and reservoir quality loss. On top of this, it is possible that the substantial Cenozoic uplift experienced solely by Copernicus, could have caused trap breaching and redistribution of gas. Despite having entered gas generation window about 90 Ma, Copernicus does not form an attractive gas reservoir. Cavendish, on the other hand, despite only ever reaching oil generation window, formed a valuable gas reservoir, owing to its shallower burial and less cementation (amongst other factors). Importantly, Cavendish gas was generated either deeper than in the Namurian and Westphalian coals (however gas source rocks below Namurian are limited), or migrated into the reservoir laterally, therefore an active gas conduit must have existed.

Higher than expected for present burial depth maturities are a consequence of Cenozoic uplift, which brought the Namurian strata from their maximum to present burial depths. The presence of oil recorded in Copernicus is likely a result of deep Carboniferous burial that brought the sequence into the oil generation window (however a later oil generation age cannot be excluded). Shallower Carboniferous burial in Cavendish field meant that no oil formation was possible prior to Triassic times.

4.6 Conclusions and implication for hydrocarbon prospectivity

The timing of formation of trapping structures, seal deposition, hydrocarbon generation and fracturing are important elements which play a role in the formation

of a successful reservoir. Results of this study show how important is the reconstruction of accurate burial histories of apparently similar reservoirs, in order to understand hydrocarbon generation, migration and retention, for a successful exploration.

This study analysed and compared the palaeoburial histories of two gas prospects, Copernicus discovery and Cavendish field. Our study demonstrates that three phases of exhumation occurred: Variscan, Jurassic and Cenozoic, the latter consisting of two stages in the Copernicus area, compatible with regional models from the Southern North Sea. The main findings of the modelling results are:

-Copernicus area experienced deeper maximum burial and temperatures, with the Namurian deposits reaching 170°C at 5170 m, compared to Cavendish, which was buried to 4195 m and subjected to maximum temperature of 140°C (at the bottom of modelled interval, base of Namurian was not drilled in either of the analysed wells);

-Copernicus discovery underwent about 2700 m of burial in late Carboniferous times bringing it into oil generation window. Cavendish experienced shallower burial at that time and did not enter HC generation window;

-The subsequent Variscan uplift brought the Namurian deposits in both areas close to the surface, subjecting them to the influence of meteoric waters;

-Namurian deposits in Copernicus discovery entered gas generation window in Late Cretaceous, and the deeply buried units remain in gas generation window up to the present day;

-Namurian deposits in Cavendish field entered oil generation window in Middle Triassic and never entered gas generation window, therefore gas present in the reservoir must have migrated upwards from deeper lying units or laterally from a different kitchen area. The latter scenario is more likely, as the most prolific source rocks are the Westphalian coals, which lie in oil generation window in the Cavendish.

CHAPTER 5:
Diagenetic evolution and reservoir quality of Upper Carboniferous fluviodeltaic systems

5.1 Introduction

The previous chapters have shown the importance of depositional factors for reservoir quality and briefly remarked on the effects of burial and uplift history on cementation and porosity preservation. Depositional elements, such as the initial sediment composition, grain size, textural homogeneity, and chemistry of initial pore waters control initial porosity and permeability and determine the path of early diagenetic processes (Ajdukiewicz and Lander, 2010; Morad et al., 2010). Burial related diagenesis is also partially dependent on those depositional factors and can further destroy or enhance porosity and permeability. Burial diagenesis becomes particularly important in reservoirs which were subjected to temperatures >100°C, as some of the most detrimental cements for the reservoir quality precipitate in those temperatures, including quartz and illite (Taylor et al., 2010; Wilkinson and Haszeldine, 2002). Telogenesis, or uplift diagenesis, on the other hand, brings sediments closer to the surface potentially subjecting them to the influence of meteoric waters (Worden and Burley, 2003) thus causing secondary porosity development or oxidation, or can cause fracturing and faulting creating conduits for fluid flow. Assessing reservoir quality risk is especially important in prospects where sandstones have been exposed to elevated temperatures for significant periods of geologic time (Taylor et al., 2010), and those that experienced inversion and uplift.

As discussed in Chapter 1, the Upper Carboniferous reservoirs of the Southern North Sea are a focus of renewed interest for exploration in the UK offshore area, and are already an important petroleum hydrocarbon producing interval (Moscariello, 2003; O'Mara et al. 2003a; O'Mara, 2003b, Oil & Gas Authority, 2017; Wasielka et al., 2020). However, reservoir quality within those sandstones is strongly variable, making them risky and expensive to develop.

The quality of the Copernicus and Cavendish sandstones is strongly controlled by sedimentary facies and initial composition of the detrital minerals, which is provenance dependent and further modified by weathering and diagenesis (O'Mara et al., 1999; Wasielka et al., 2020). Quality of sandstones deposited in marine environments is typically negatively affected by the presence of abundant detrital clay or early diagenetic carbonate cements, whilst the sandstones deposited in continental settings avoided early cementation and preserved the porosity until deeper burial. Of all the continental facies associations, the quartz rich, multi-storey fluvial channel sandstones form the best reservoirs, as they are less prone to kaolinite formation, which has a destructive effect on permeability. Nevertheless, reservoir quality in

those sandstones can vary significantly, as other diagenetic events further modify pore architecture and connectivity. The complicated burial history experienced by the Southern North Sea reservoirs is reflected by multiple phases of cement precipitation and mineral dissolution. Authigenic quartz is volumetrically the most important cement in the analysed sandstones, kaolin, illite, and late diagenetic carbonates further reduce permeability, whilst unstable grain dissolution somewhat increases reservoir quality (O'Mara et al., 2003; Wasielka et al., 2020)

This chapter discusses the evolution of the diagenetic alterations in a sequential order throughout the burial history of the Copernicus and Cavendish fields. Changes in diagenetic minerals, which with time fill increasingly more pore space, are important in understanding the evolution of the tight sandstone systems.

5.2 Methods

5.2.1 Optical microscopy

One hundred and eighteen sandstone samples were collected from six wells (Appendix 3) from the Copernicus discovery and Cavendish Field. Samples from five wells were selected to be statistically random representing the porosity distribution for the whole set of measured core plugs. Sampling in well 43/19a-4Z was targeted at the most permeable intervals. All samples were impregnated with blue resin before petrographic thin sections were made. Carbonate minerals were stained with Alizarin Red S and Potassium ferricyanide to identify varieties of calcite and dolomite. Thin sections were examined with polarizing microscopes (Leica DM2500 P) with a Leica MC170 HD digital camera attached. Some post-capture enhancement of digital images was carried out using Photoshop. One hundred point grain size measurements and three hundred point counts were undertaken on all thin sections using Conwy Valley Consultants stepping StageTM connected to PETROG software. Pettijohn's (Pettijohn et al., 1987) sandstone classification and Wentworth`s (Wentworth, 1922) particle-size classification for clastic sediments were used for the basic description of grain size and mineralogy. Point count analysis quantifies the detrital components, authigenic components and macroporosity. The information obtained was used to calculate compactional and cementational porosity loss, based on the methodology of (Lundegard, 1992), and to assess pore type (primary vs. secondary pores), cement distribution, and ultimately to assess basic controls on reservoir quality. The point counting and grain size data are presented in Appendix 3.

5.2.2 Scanning electron microscope (SEM) and Energy-dispersive X-ray spectroscopy (SEM-EDS)

After initial petrographic analysis a subset of samples representing a range of diagenetic patterns was selected for SEM, SEM-EDS and SEM-CL analyses to investigate authigenic mineral development and to describe relationships between various authigenic phases in order to constrain the relative timing of their precipitation. The selected samples contain the most important cements observed in optical microscope and described in the literature as having effect on reservoir quality in Upper Carboniferous sandstones (e.g. by Cowan, 1989; Cowan and Shaw, 1991; O'Mara et al., 1999; O'Mara et al., 2003), such as quartz overgrowths, dolomite, kaolin, illite. For cathodoluminescence only samples with abundant quartz cementation were selected, and those with pervasive carbonate cement were removed to ensure quartz luminescence is not obscured by the bright luminescence of carbonates.

Rock fragments were coated with 35 μm layer of gold, whilst thin sections were coated with 30 μm of carbon, and then analysed using a Hitachi SU-70 field emission gun scanning electron microscope equipped with an energy-dispersive detector (EDS). Mineral and elemental maps were created from uncovered thin sections coated by 30 nm layer of carbon. Compositional data was collected and processed using AZtecEnergy EDS Microanalysis software. Scanning electron microscope analyses of rock chips and thin sections were conducted at 5 to 15 keV acceleration voltage with beam currents of 1 and 0.6 nA, respectively. Magnifications used were between x100 and x10,000. For EDS elemental and mineral mapping 3 samples were selected. Areas of 1.56 to 10.1 mm^2 was mapped in each sample. Settings used for each site on the map were 35-300 μs dwell time, 12 kV accelerating voltage, with 12-96 frames recorded for each area. The acquired elemental maps were processed using Aztec Energy software to create mineral maps.

5.2.3 SEM-Cathodoluminescence (SEM-CL)

A subset of samples with quartz cements was selected for SEM-CL analysis after initial petrographic observations, in order to differentiate authigenic quartz from detrital quartz and to identify potential multiple generations of quartz cements. Cathodoluminescence analysis was undertaken using a Gatan MonoCL system with panchromatic imaging mode, with blue, red, green or no filter, operated at 12 kV. Three samples, which were used for mineral mapping, were also selected for large

area CL-mapping. 96 frames were recorded for each sample, of a total area of 10.1 mm^2. This was done at x300 magnification, 1024 by 1024 resolution, and 45 µs dwell time.

5.2.4 Processing and quantification

The obtained frames of mineral maps, SEM-EDX and CL were processed using Aztec software. All acquired frames were initially automatically aligned by the software and the alignment was then manually enhanced for best results. The aligned frames were montaged to form large area maps for each sample: chemical map, CL and SEM-EDS (Appendix 7).

For quantification of quartz cement and quartz dissolution along grain-to-grain contacts a technique used by Oye (2019) was applied here. This technique is an improved method of estimating petrographic variables from CL data by Sibley and Blatt 1976; Houseknecht 1991. The chemical map was used for mineral identification, while the CL image was used for detrital and authigenic quartz determination and their quantification, and SEM-EDX image aided in texture characterisation.

A grid of 1600 and 1681 (40x40 and 41x41) boxes was created in Adobe Illustrator software and placed on the CL image. The features of interest (quartz cement, detrital quartz grains, points of quartz to quartz grain dissolution and other detrital /authigenic phases) are counted at centre points of the grid, a procedure similar to the usual point counting operation with a statistically robust data generated for 1600 or 1681 point counts per sample over an of 10.1 mm^2.

5.3 Results

5.3.1 Detrital mineralogy and textures

Detrital mineralogy has been described in more detail in chapter 3 where sedimentary controls on the composition and diagenesis of analysed sandstones were discussed. However, the primary framework components such as detrital quartz, feldspars, rock fragments, as well detrital clays have an important effect on the reservoir quality evolution and are thus briefly summarised in this subsection.

Detrital mineralogy is dominated by quartz, averaging 56.6% (ranging from 20.3% to 78%, and one pedogenically modified sample with 1% detrital quartz) (Appendices 3 and 4). Quartz comprises monocrystalline (mean 47.1%) and polycrystalline grains (mean 9.5%). Rigid rock fragments form on average 4.2% of the analysed sandstones

(range 0 – 15.0%) and are primarily of igneous origin, with occasional metamorphic and sedimentary grains. Metamorphic grains comprise schistose quartz ± mica grains. Feldspars are only a minor component, averaging 3.9% and comprise both plagioclase (average 2.9%) and K-feldspar grains (average 1.1%). Where present, feldspar grains are typically well preserved or only weakly dissolved. Plagioclase feldspars show lamellar twinning and are weakly sericitised. Micas form on average 1.6% of the sandstones (range 0 - 9.7%), with muscovite being the dominant component, and biotite occurring in trace amounts. Mica flakes range from pristine where early carbonate cementation allowed their preservation, to strongly degraded and replaced by kaolin and other clays (Figure 5.1a). Organic fragments, ductile rock fragments and heavy minerals each form <1% of the sandstones. Ductile rock fragments comprise degraded igneous fragments and mudclasts. Mudclasts are, however, commonly strongly compacted between rigid grains and filling intergranular areas, resulting in the formation of pseudomatrix (Figure 5.1b), which accounts on average for 2.0% (up to 11.7%). Heavy mineral assemblage comprises apatite, monazite, rutile, tourmaline, zircon, opaque minerals, and garnet. Detrital clays on average account for 4.9% of the analysed sandstones (range 0 - 48.3%). SEM EDS data suggest illitic or illitic-smecititc composition on detrital clays.

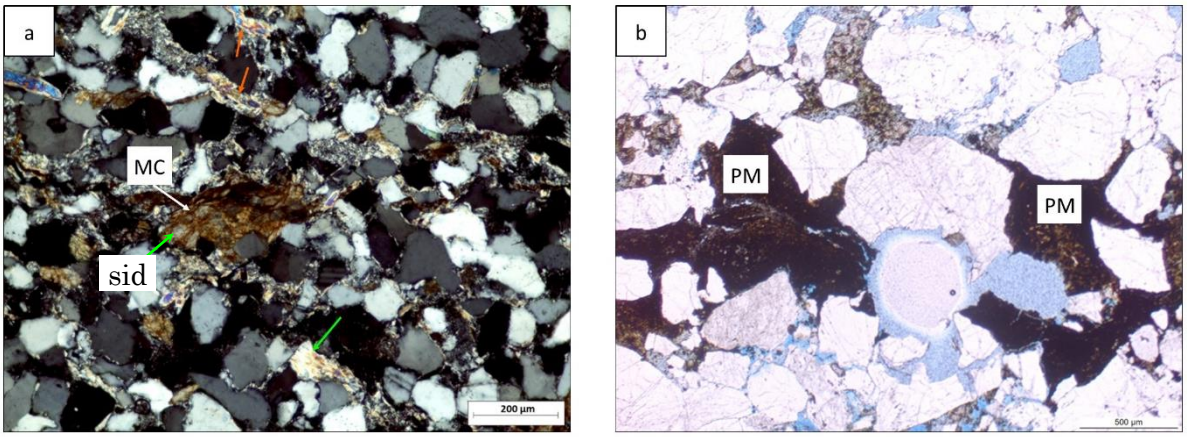

Figure 5.1. Ductile detrital components: a) Deformed muscovite mica flakes (orange arrows), partially kaolinitised muscovite (green arrow) and a deformed mudclast (MC) partially replaced by siderite (sid); b) Pseudomatrix (PM) composed of strongly deformed mudclasts compacted between rigid grains.

5.3.2 Mechanical compaction

Contacts between detrital grains are highly variable, ranging from grains 'floating' in carbonate cement, to concave-convex and sutured contacts (Figure 5.2). Point and long contacts are most common in samples containing early carbonates and abundant detrital clay, and are indicative of weak to moderate levels of compaction, whilst long and concave-convex contacts prevail in samples lacking early carbonates and

containing late quartz cement instead, and indicate strong levels of compaction. Strong mechanical compaction led to fracturing of rigid quartz grains and deformation of ductile grains (Figure 5.1). To calculate porosity loss by mechanical compaction and by cementation method of (Lundegard, 1992) was used with assumed initial (depositional) porosity of 45% (Lundegard, 1992). In the studied suite of samples most of the initial porosity was lost by mechanical compaction (for details see section 3.4.3.1). Samples with dominant cementation porosity loss are mainly those with abundant early carbonate cements (dolomite and siderite). Sandstones where early diagenetic cements did not stabilize grain framework prior to significant burial lost most of their initial porosity to mechanical compaction before the onset of quartz cementation at greater depths.

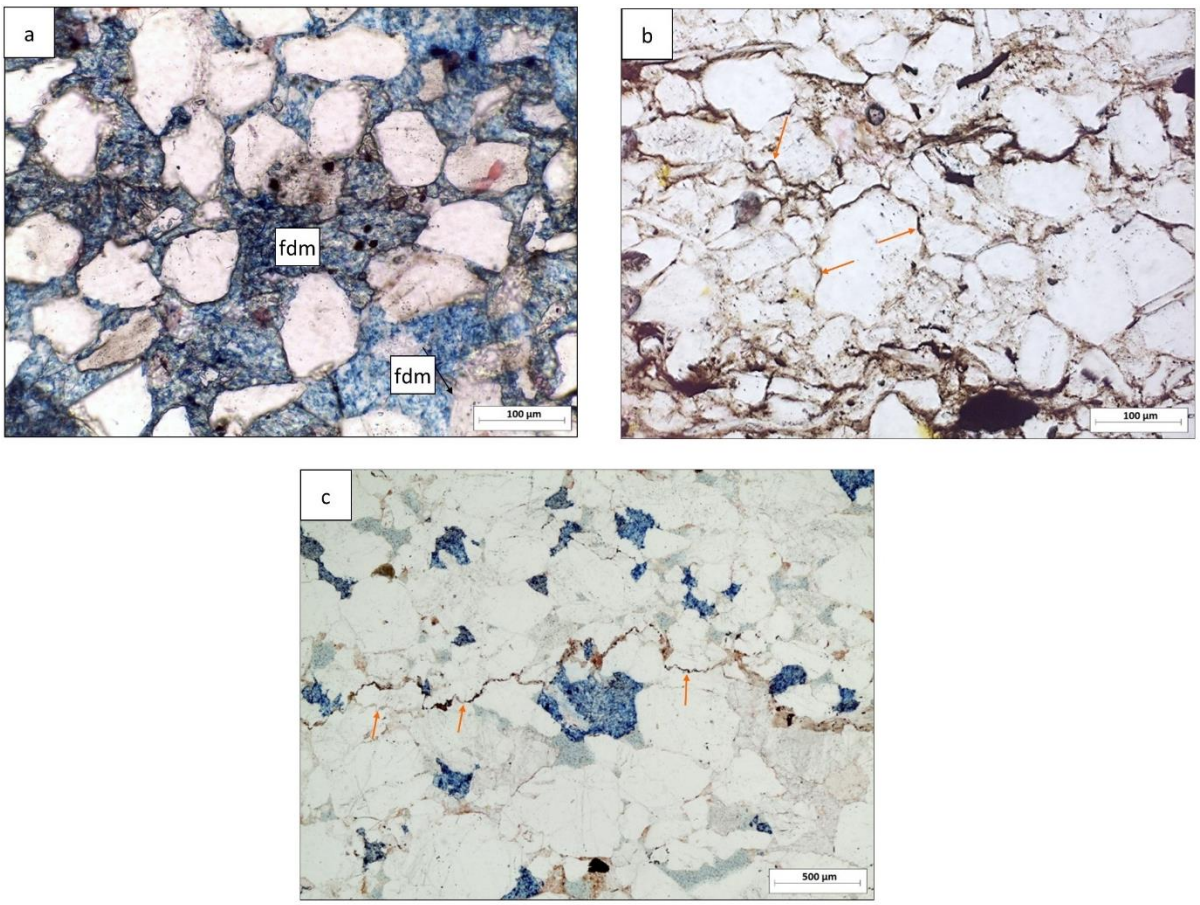

Figure 5.2. Grain contacts observed in the analysed samples: a) 'Floating' grains surrounded by early ferroan dolomite (fdm); b) Concave-convex grain contacts observed where grain dissolution occurred on grains coated by a thin layer of detrital clays (arrowed); c) Sutured grain contacts (arrowed) where pressure solution occurred, forming incipient stylolite. Note the thin layer of detrital clay where the stylolite formed.

5.3.3 Authigenic mineralogy

Authigenic mineralogy has been described briefly in Chapter 3 but is described in more detail here. For the ease of description 'blocky' cements such as quartz,

carbonates, pyrite, barite, anatase etc. are here referred to as 'cements' and are separate from authigenic clays.

The analysed sandstones comprise abundant authigenic minerals due to their long and complicated burial history (see section 2.1.2 and chapter 4). Cements, which on average form 16.7% of the analysed sandstones, are volumetrically far more important components than authigenic clays, which form 5% of these rocks (Appendix 4). This predominance of cements over authigenic clays is true for all wells and facies associations, however the types and proportions of the authigenic minerals vary significantly. In the following section authigenic minerals are described in order of decreasing average modal abundance.

5.3.3.1 *Quartz overgrowths and quartz dissolution*

Quartz overgrowths are the most common authigenic mineral in the analysed sandstones, recognised in all but five samples analysed, forming on average 8.9% of the sandstone (range 0 – 21.7%, based on point counting results). Locally, quartz overgrowths are delineated from their host grain by a line of micron-scale fluid inclusions, however commonly the boundary between detrital grains and overgrowths can only be precisely identified on CL images, therefore the amount of quartz overgrowths was also quantified on large area CL maps on three selected samples (see Appendix 7). In each sample the amount of quartz overgrowths quantified on the CL map was about 40% higher than that from the optical petrographic point counting.

Syntaxial quartz cements typically form continuous overgrowths around detrital quartz grains and, where abundant, they form a tight, interlocking structure isolating some pores from the pore network (Figure 5.3a). Quartz is preferentially precipitated in sandstones with low detrital clay content, which can inhibit quartz nucleation where present (Figure 5.3b and 5.4). The overgrowths reach up to 100 µm in samples where primary pores are 'clean' and detrital and authigenic clays are absent. Quartz overgrowths enclose earlier kaolin booklets (Figure 5.3c), siderite, pyrite and some of the illite (Figure 5.3d) and dolomite (Figure 5.3f), however they are also locally observed enclosed by dolomite (Figure 5.3e) and draped by illite (Figure 3.8f). Two clear generations of quartz overgrowths are identified with cathodoluminescence in both Copernicus and Cavendish (Figure 5.3 h-j). However, a complex pattern observed within the overgrowths might result from more than two phases of quartz formation, or changing fluid chemistry during quartz growth. As seen under CL, the first phase is almost non-luminescent and thin, reaching up to 30 µm. It shows a complex growth pattern and is discontinuous around the detrital grains (Figure 5.3 i-j). The second

phase has a 'stripy' appearance with parallel zonation, comprising red-luminescent and non-luminescent zones. This phase is generally thicker than the previous phase, reaching 50-70 µm. The second phase is precipitated upon the first one fully enclosing it, or upon detrital grains where the first phase is missing. The two generations of quartz overgrowths are also observed under optical microscope in some samples from the Copernicus discovery, where they are separated by a thin layer of residual oil. Locally, quartz surfaces observed in SEM are weakly etched.

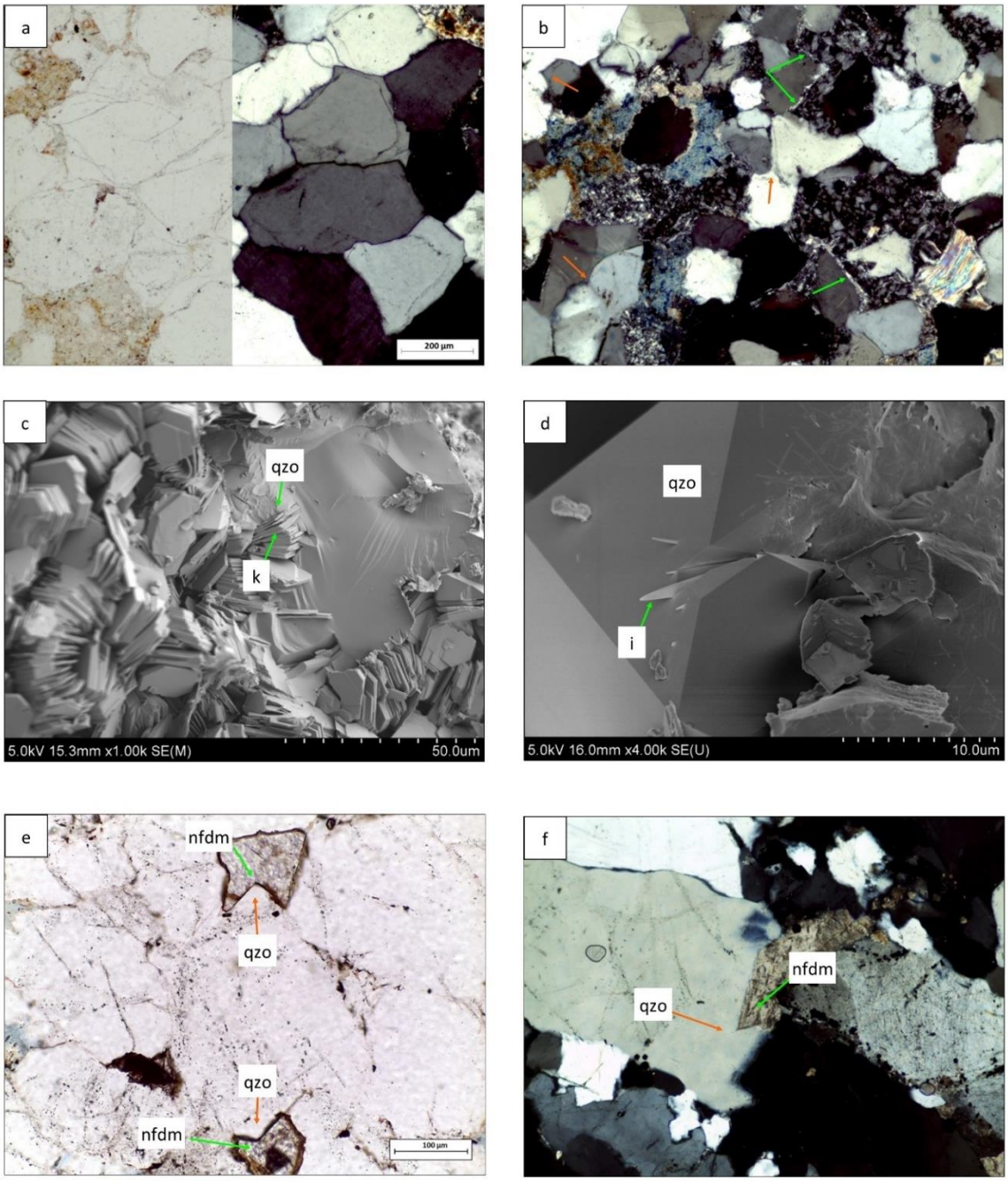

Figure 5.3. Quartz overgrowths and its habit in the analysed samples: a) Interlocking quartz overgrowths in a tightly cemented sample, PPL/XPL; b) Quartz overgrowths (orange arrows) precipitated on surfaces free from detrital and authigenic clay (clay coated surfaces indicated by green arrows); c) Kaolin booklets (k) enclosed by quartz overgrowths (qzo); SEM image, d) Ribbon-like illite crystals (i) enclosed by quartz overgrowths (qzo); SEM image, e) Euhedral quartz overgrowths (qzo) are enclosed by late non-ferroan dolomite (nfdm); f) Quartz overgrowth (qzo) enclosing euhedral non-ferroan dolomite crystal (nfdm).

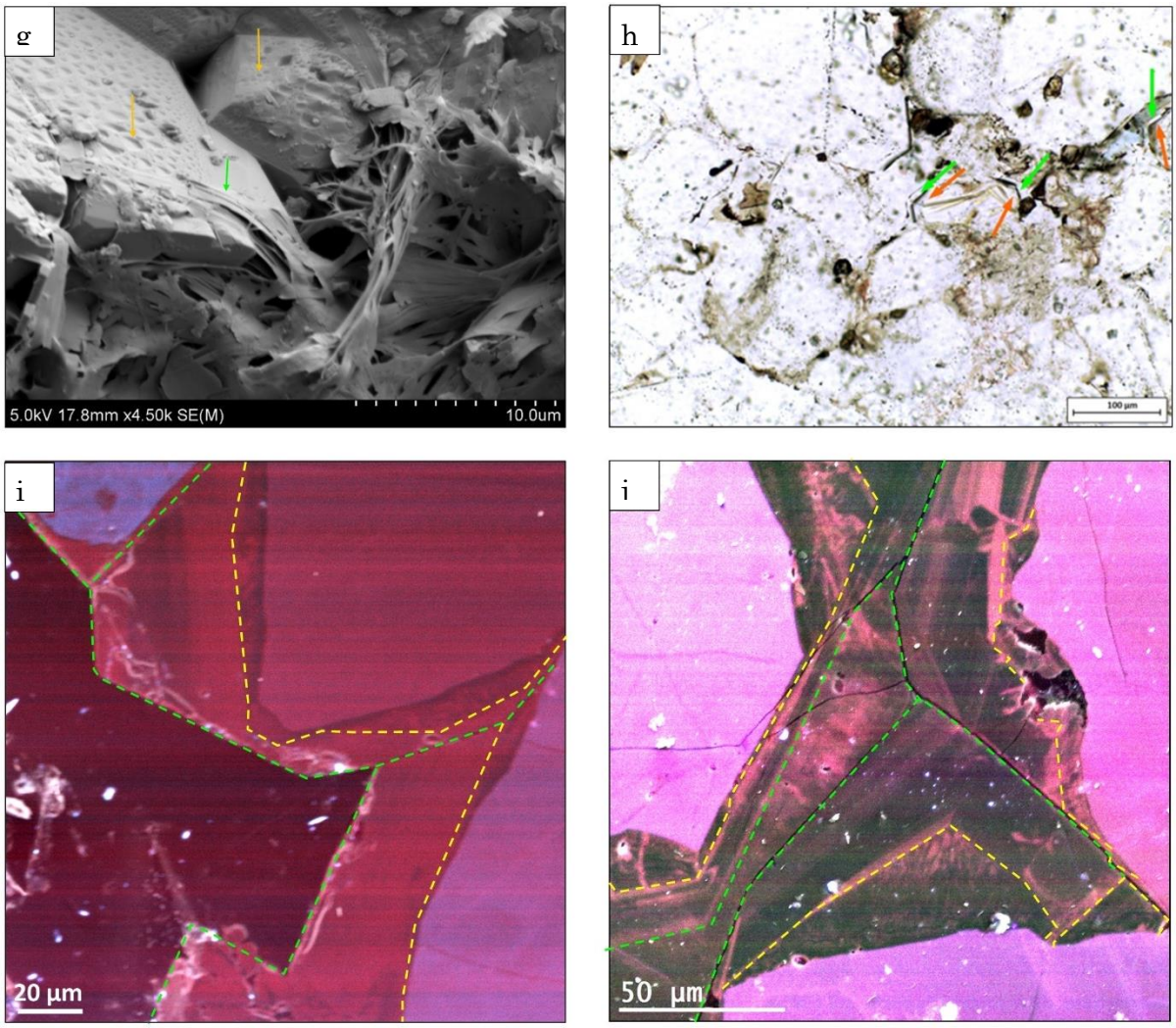

Figure 5.3 continued. g) Quartz overgrowths, which locally show pitted surfaces (orange arrows) are draped over by authigenic illite (green arrows); SEM image; h) Multiple episodes of quartz cementation have occurred during the diagenesis diagenetic history. Two generations of quartz overgrowths can be observed in the thin sections (see green and orange arrows) separated by a black layer of residual oil; photomicrograph; i & j) CL images showing two phases of quartz cementation. First phase is outlined in yellow, second in green; CL images.

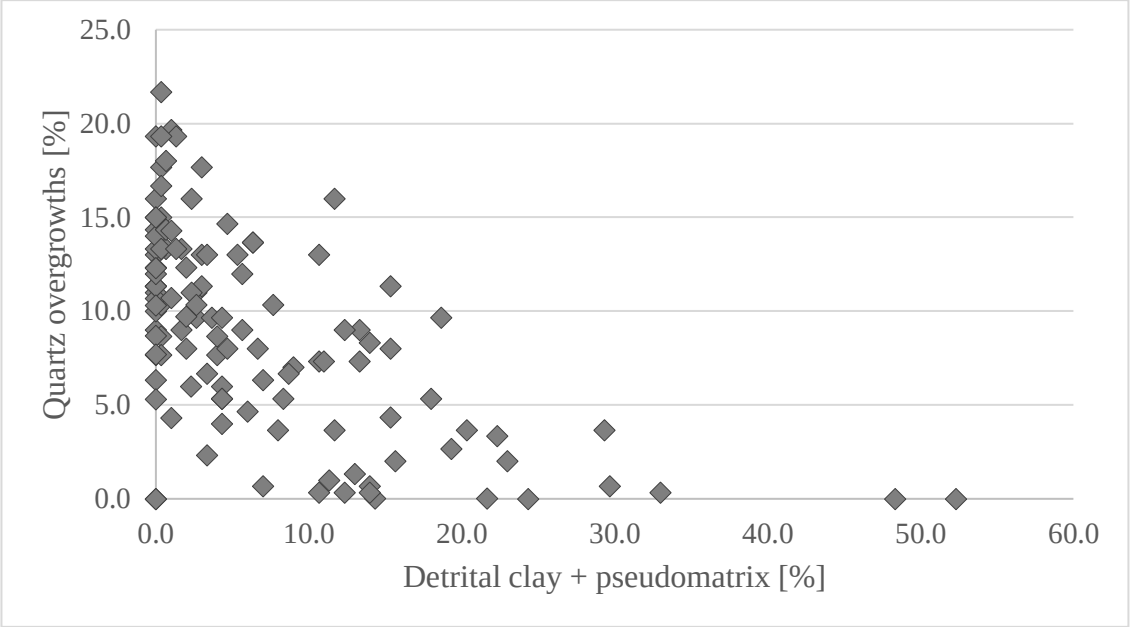

Figure 5.4. Plot showing a weak negative correlation between the amount of detrital clays plus pseudomatrix and quartz overgrowths.

5.3.3.2 Dolomite

Overall dolomite forms 3.8% of the analysed sandstones and comprises primarily ferroan dolomite (3.1%) and lesser non-ferroan dolomite (0.7%). Most of the ferroan dolomite occurs within primary pores (2.8%) and a lesser amount in secondary pores (0.3%). Non-ferroan dolomite is also primarily found in primary pores (0.6%), with a minor amount in secondary pores (0.1%). Dolomite forms rhomb-shaped crystals, locally showing darker cores (Figure 5.5a) or occurs as pore-filling patches or pervasive cement (Figure 5.2a). Textural observations suggest that much of the dolomite in those marine sandstones precipitated during eogenesis, prior to mechanical compaction, as detrital grains show point contacts or locally appear to be floating in the dolomite cement (Figure 5.2a). This early cement is primarily composed of ferroan dolomite, but non-ferroan dolomite is also present. Some of the ferroan and non-ferroan dolomite, however, formed later during diagenesis, as suggested by the fact that it encloses euhedral quartz overgrowths (Figure 5.3e). Ferroan dolomite also locally occurs as lozenge-shaped crystals resembling siderite; this form likely developed from siderite replacement by dolomite.

5.3.3.3 Kaolin

Kaolin (average 3.6%, range 0 – 13.7%) comprises replacive kaolin (average 2.0%, up to 10.7%) and a primary pore-filling phase (average 1.7%, up to 11.3%) and shows a patchy distribution throughout the samples. In Copernicus discovery most of the recorded kaolin occurs as a replacive phase (average 2.3% vs 0.6% in primary pores),

whilst in Cavendish field most of the kaolin occurs within primary pores (average 2.8% vs 1.5% in secondary pores). Replacive kaolin occurs as grain-sized patches locally outlined by detrital clay, separating it from pores or other grains, and is most likely replacing feldspar grains. There are two morphologies of vermicular kaolin seen in thin section and SEM. The first morphology comprises 20 - 50 µm wide, thin to blocky booklets (Figure 5.5b) The second comprises finely crystalline, thin to commonly blocky booklets which are 5 - 15 µm wide (Figure 5.5c). Kaolin is also observed replacing muscovite or splaying muscovite ends. Kaolin booklets are enclosed by later quartz overgrowths (Figure 5.3c) and locally weakly illitised. Residual hydrocarbons are observed staining kaolinite booklets in all Copernicus wells, but not in Cavendish. Kaolin is more common in continental facies than in marine ones (Appendix 5). The recorded kaolin likely consists of kaolinite and dickite polytypes, which could not be quantified separately with the techniques used in this study.

5.3.3.4 *Siderite*

Siderite (average 3.4%, range 0 – 48.7%) fills primary pores and is commonly associated with early dolomite. Siderite occurs in three different morphologies. The first comprises fine, lozenge-shaped crystals; the second comprises finely crystalline siderite concentrated in nodules and patches filling primary pores, replacing ductile grains or expanding mica flakes, particularly common in detrital clay-rich, fine grained marine sandstones. In laminated samples these patches follow the lamination (Figure 5.5d). The third morphology comprises sphaerosiderite crystals, which occur in pedogenically modified deposits (Figure 5.5e).

5.3.3.5 *Optically non-resolvable clay*

Optically-non resolvable clay comprises pore-lining clay (average 0.8%, range 0-9.3%) and replacive clay (average 0.4%, range 0 – 3.7%). Based on SEM and EDX, these clays are composed of illite, illitised kaolin and possible illite-smectite. XRD data from the Upper Carboniferous samples in the operator's reports shows kaolin and illite content in the clay fraction in the Copernicus and Cavendish, as well as traces of chlorite in wells 44/16-2 and 43/19-1 and illite-smectite in well 43/19-1 (Southon, 1991; Geochem Group Limited, 1993). Replacive clay is seen altering degraded ductile grains and is composed of illite, suggested by its high birefringence in XPL and EDS data, and illitised kaolin.

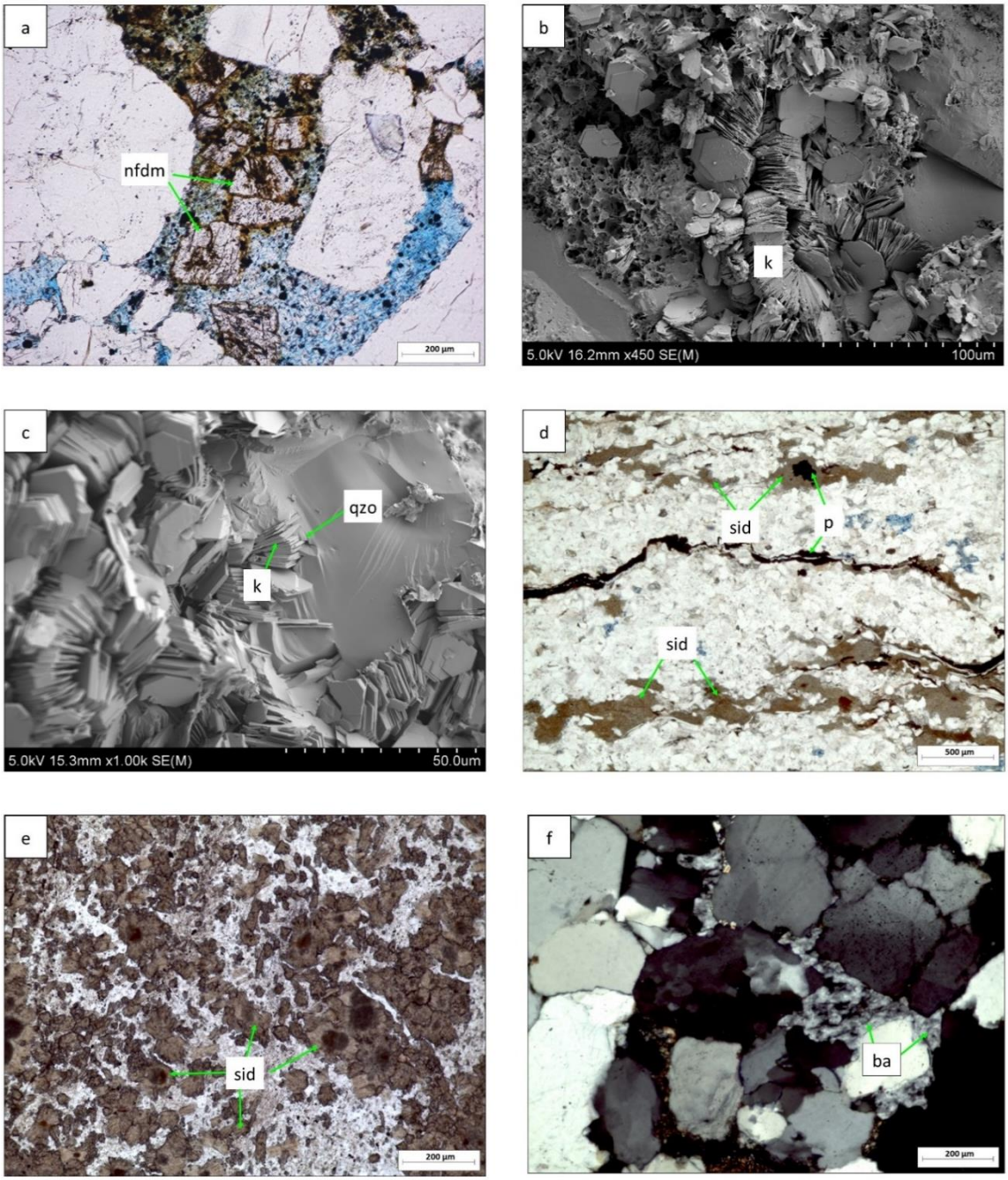

Figure 5.5. Rhomb-shaped dolomite crystals locally show darker cores (arrowed); b) Large (20-30 µm wide), thin kaolin booklets; c) Fine, blocky kaolin booklets, 5 - 15 µm wide; d) Siderite patches (sid) and pyrite (p) often form laminae associated with detrital clay and organic matter; e) Sphaerosiderite crystals associated with delta plain environments; f) Primary pore-filling barite cement.

5.3.3.6 *Illite and illite-smectite*

Illite (average 0.1%, up to 2.7%) mainly forms ribbon-like and bladed strands that developed as primary pore-filling phase and as grain-replacing phase. Occasional illite-smectite is recognised in Cavendish field, based on its boxwork morphology and chemical composition (operators internal reports). SEM examination reveals that illite strands drape over quartz overgrowths (Figure 3.8f), but it is locally also enclosed by quartz (Figure 3.8d). Illite formation at least partially results in part from

illitisation of precursor smectite and illitisation of mudclasts and pseudomatrix. Illite fibres are also commonly nucleated upon kaolin booklets.

5.3.3.7 *Pyrite*

Pyrite (average 0.2%, up to 3.3%) forms framboids and cubic crystals which occur within primary pores or replacing mudclasts and organic fragments. In laminated samples pyrite is more abundant within clay-rich and organic-rich laminae (Figure 5.5d), some of which are incipient stylolite sites. Pyrite is also seen outlining root traces in samples from delta plain facies association. Pyrite generally only occurs in minor amounts and is slightly more common in marine facies.

5.3.3.8 *Other cements*

Other cements are volumetrically insignificant and have little effect on reservoir quality. These comprise Na-feldspar overgrowths, K-feldspar overgrowths, barite, anhydrite, anatase, possible zeolite and iron oxides.

Na-feldspar overgrowths are rare and thin. Small anatase crystals occur in both primary pores and in secondary after feldspar dissolution. Barite (Figure 5.5f) and anhydrite occur as primary pore-filling patches that enclose earlier quartz overgrowths and ferroan dolomite. Trace amounts of rod-shaped crystals are observed in SEM, which are likely zeolite, however EDAX analysis was not possible. These crystals are slightly enclosed by quartz overgrowths, therefore have likely precipitated toward the end of quartz cementation phase. Iron oxides, presumably haematite, form framboids in primary pores, replace degraded ductile grains or appear to be replacing siderite edges.

5.3.4 Residual oil

Residual oil (average 0.1%, up to 3.7%, in Copernicus discovery only) occurs in the form of black fill enclosed within isolated primary pores, as coating between quartz overgrowth layers (Figure 5.3h) and staining kaolin booklets. Residual oil is observed at depths 14065.8 - 14917 ft.

5.3.5 Porosity

Modal porosity comprises primary porosity (modal porosity average 1.7%, range 0 – 14.3%), secondary porosity (average 1.6%, range 0- 24.3%) and microporosity (average 4.7%, range 0-13.3%) (Appendices 3 and 4). Secondary pores are divided into intragranular porosity (which forms on average 0.2% of the samples) and the more common 'oversized' porosity (average 1.4%). Intragranular porosity occurs within

degraded ductile grains and partially dissolved rigid rock fragments and feldspars. 'Oversized' porosity results from a complete dissolution of grains, presumably feldspars, leading to a formation of large pores exceeding the size of grains and primary pores.

Microporosity was calculated as the difference between helium porosity and point counted macroporosity, and it is likely to be largely located within clays and degraded grains. While microporosity might be considered largely ineffective in oil reservoirs, in gas reservoirs it might at least partially contribute towards the effective porosity. Microporosity values in the Copernicus range from 0 – 11.8% (mean 4.1%), and 0 – 13.3% (mean 5.5%) in Cavendish.

5.3.6 Grain fracturing and pressure solution

Stylolites occur primarily, but not exclusively, in delta plain, distributary channels, multi-storey fluvial channel facies and shoreface facies. Stylolite densities range from 0 to ca. 25/m in these facies. They are observed where clay is concentrated along thin laminae and are commonly also associated with higher abundances of pyrite and organic fragments. They are typically very thin with a 'wispy' appearance (Figure 5.6a), but occasional 1 mm-thick stylolites are developed on thicker detrital clay laminae (Figure 5.6b).

The analysis of the relationship between the amount of porosity and distance from stylolite for sandstone samples that are <100 cm from a stylolite shows that there is a weak positive trend between the distance to the stylolite and porosity (Figure 5.7a). To eliminate the impact of detrital clay inhibition on quartz cementation and other cements occluding potential quartz nucleation sites, only samples that contain <15% of detrital clay, siderite plus dolomite combined were used for the analysis. The correlation between the distance from stylolite and permeability or amount of quartz overgrowths does not show a clear trend (Figure 5.7 b and c). Also grain size does not seem to have any effect on porosity preservation with increasing distance from stylolites (Figures 5.7 a-c).

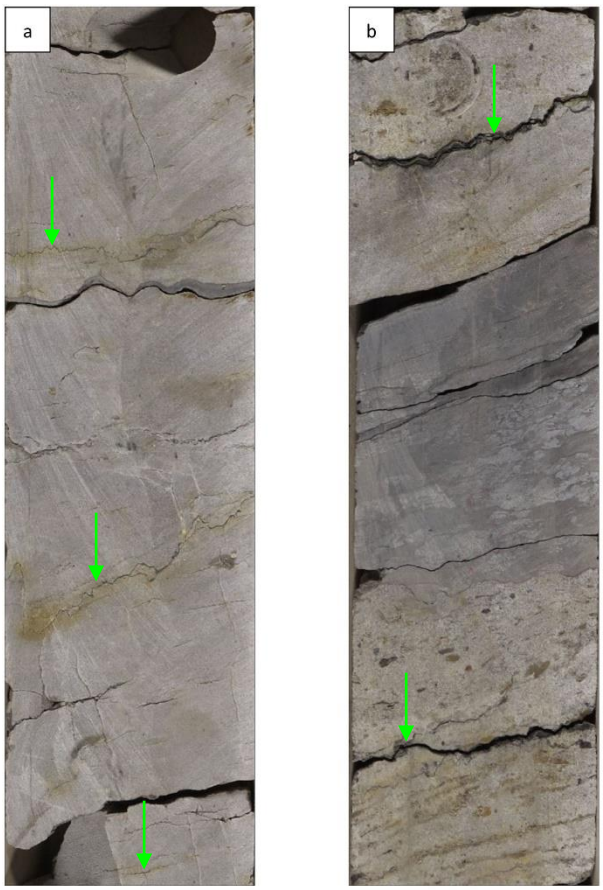

Figure 5.6. Stylolite development in well 44/16-2; a) thin and wispy stylolites; b) thick stylolites developed on thicker clay laminae.

CL images show that extensive fracturing occurred in some detrital quartz grains (Figure 5.8 a-c) and in quartz overgrowths (Figure 5.8c). Most intragranular fractures are sealed by the weakly-luminescent quartz that appears to belong to the second generation of authigenic quartz, but rare fractures filled by non-luminescent quartz are also present. There is no dislocation of grain fragments along fractures, which means that fracturing was most likely coincidental with quartz cement precipitation. Two phases of grain fracturing are interpreted: an early phase coincidental with precipitation of the first generation of authigenic quartz or the second generation during the non-luminescent stage, and a second, perhaps more intensive one, coincidental with precipitation of the second generation of quartz. No fracturing is seen under the optical microscope within other blocky cements, such as dolomite, anhydrite and barite, implying that quartz cementation stopped mechanical compaction before precipitation of later cements.

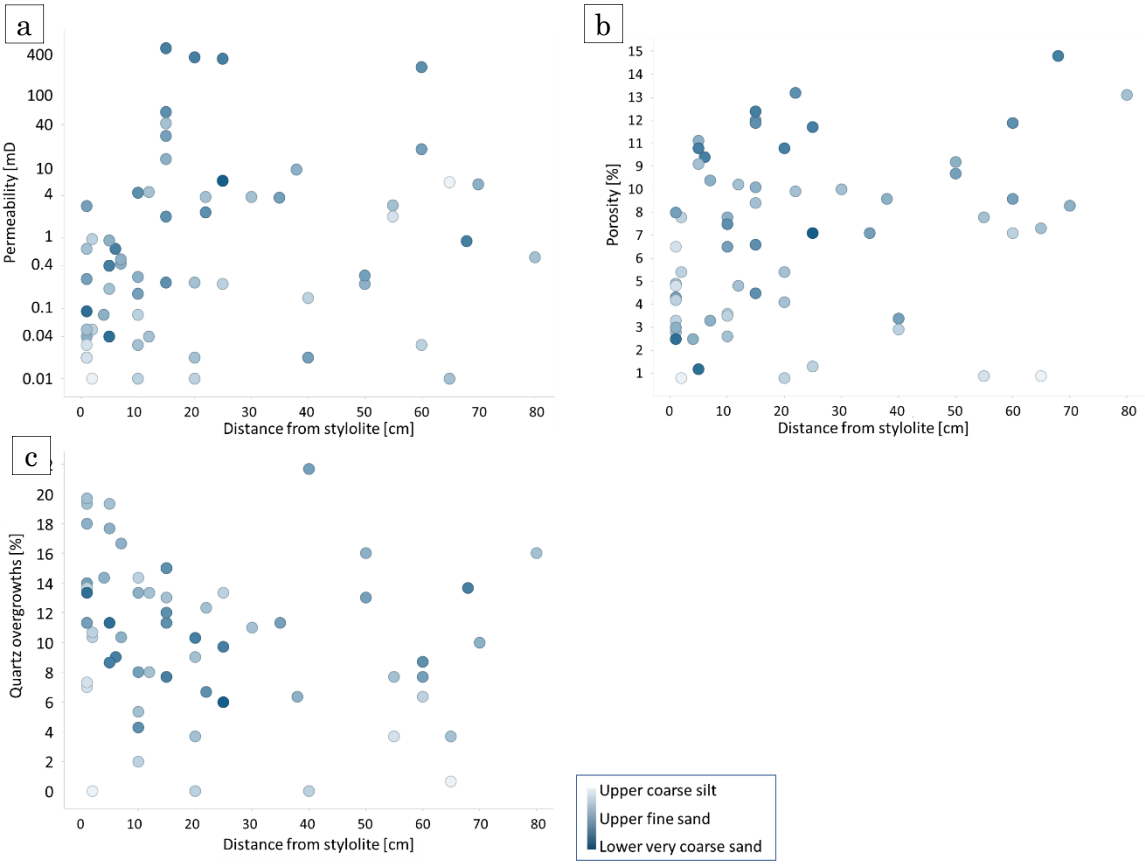

Figure 5.7 Distance to stylolite vs a) helium porosity; b) permeability, and c) quartz overgrowth content, colour-coded by grain size.

Cathodoluminescence revealed the presence of areas of interpenetrating detrital quartz grains, which is a result of pressure solution on grain contacts. The amount of quartz dissolved through the process of pressure dissolution was quantified using a method of Sibley and Blatt (1976) and Houseknecht (1991), improved by Oye (2019). The estimation of volumes of silica dissolved by intergranular pressure dissolution estimated from CL point counting (Appendix 7) shows that 0.2 – 2.4% of silica was released into the system by pressure dissolution in some of the strongly quartz cemented samples (with volume of quartz cement estimated by CL image analysis ranging from 12.4-21.5%).

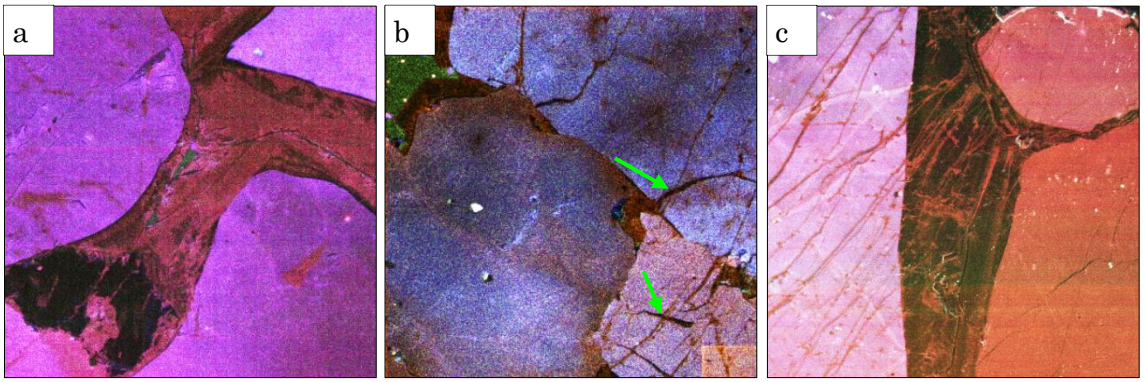

Figure 5.8. Healed fractures in detrital quartz grains (a, b & c) and quartz overgrowths (c). A few fractures within detrital grains are filled by non-luminescent quartz and are cross-cut by later fractures filled by red-luminescent quartz (green arrows).

5.4 Discussion

5.4.1 Diagenesis

5.4.1.1 *Introduction*

The diagenetic sequence in the analysed Namurian sandstones is a complicated one, owing to different environmental conditions during deposition and early diagenesis, and a complex burial history. This led to an extremely variable reservoir quality between different facies and within each facies. Permeabilities of 0.01 mD, which is the lower detection limit, are common where detrital clay and early carbonate cement are abundant, generally in marine facies associations, but are also recorded in fluvial facies, which are overall the best reservoir rocks in the analysed sequence (see Chapter 3). The highest recorded permeability values (up to 691 mD) occur without multi-storey fluvial channel facies. Although provenance and sedimentology are fundamental controls on reservoir quality (see Chapter 3), the large variability within the fluvial facies cannot be explained by those elements alone. Diagenesis in the deeply buried basins plays a fundamental role in porosity and permeability evolution, both their reduction through cement precipitation and compaction, and enhancement through mineral dissolution. In order to understand what controls reservoir quality, it is necessary to analyse the diagenetic evolution, which is inherently connected with the burial history of the basin, its temperatures, fluid flow, and pore water chemistry at every stage of geological evolution.

5.4.1.2 *Paragenetic sequence*

This section presents post-depositional alterations of Namurian Millstone Grit sandstones from Copernicus and Cavendish fields. The paragenetic sequence (Figure 5.9) was developed based on petrographic observations of detrital grain compaction

levels, authigenic mineral relationships, and fracture analysis. While all main diagenetic alterations are included on Figure 5.9, it must be borne in mind that diagenesis in the studied samples was strongly facies related, therefore not all alterations are observed in all samples. Diagenetic sequence in both Copernicus and Cavendish advanced in a similar way, except for lack of residual oil layer between two generations of quartz in Cavendish.

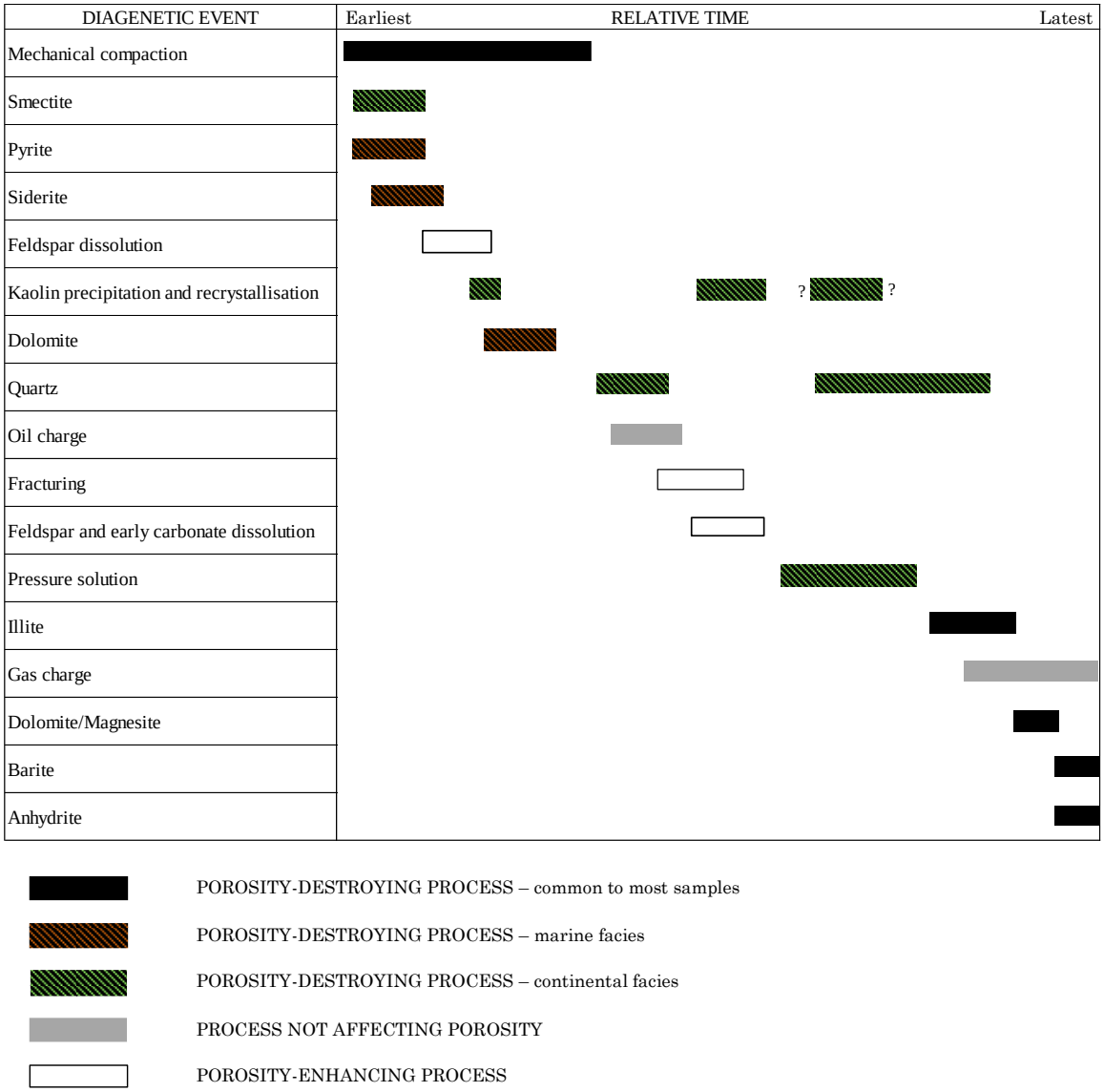

Figure 5.9. Paragenetic sequence of key diagenetic processes in the Upper Carboniferous sandstones from Cavendish and Copernicus fields. Blue fields show processes that occurred primarily in marine facies, and green in continental.

5.4.1.3 *Diagenetic evolution throughout burial history*

This section discusses diagenetic processes of Namurian Millstone Grit sandstones and explains how they are related to the burial phases. The main diagenetic events are presented on a burial history plot on Figure 5.10.

5.4.1.3.1 Eogenesis

Eogenetic, i.e. early diagenetic events, are defined as those taking place under influence of meteoric pore waters. In clastic sediments this zone can extend from a few metres below the surface in low permeability mudstones to several thousand metres in highly permeable sandstones, depending on connectivity of sedimentary unit to the surface (Worden and Burley, 2003). In the studied sandstones the eogenetic stage took place during the early stages of Carboniferous subsidence when the deposited sequence was still close to the surface, before reaching high temperatures characterising the mesogenetic realm (see section 4.5.1, Chapter 4).

Petrographic observations show that the earliest precipitated cements are pyrite (FeS_2) and siderite ($FeCO_3$), however their distribution is strongly facies related (see section 3.4.4 and Figure 3.14 e & f, Chapter 3). Both siderite and pyrite require Fe^{2+}, SO_4^{2-}, HCO_3^- and reducing condition to precipitate, which are commonly found in the marine environments (Worden and Burley, 2003). The formation of pyrite is associated with bacterial sulphate reduction in anaerobic environment (Bottrell et al., 2000; Schwertmann and Fitzpatrick, 1992), which occurs under very shallow burial – starting in the top 1 metre of sediment and continues at high rate in the top c. 10 m (Sass et al., 1997; Bottrell et al. 2000). The H_2S released through the bacterial activity reacts with available Fe^{2+} and forms pyrite (Huggett et al., 2010). Siderite formation may pre- or post-date pyrite precipitation, also occurring at very shallow burial depths, either in the sulphate reduction zone, which stretches between the first metre to tens of metres, or deeper methanogenesis zone (Bojanowski and Clarkson, 2012). In contrast, pyrite and siderite are rarely observed in continental environments in the Copernicus and Cavendish sandstones. Sphaerosiderite is occasionally present in shallow marine and continental deposits of delta plain and interdistributary bay deposits and is associated with soil formation (Ludvigson et al., 1998).

Boxwork-like illite-smectite is occasionally found in Cavendish field in fluvial channels, formed from a precursor smectite. Although not clear from its morphology and relationship with other minerals whether smectite is of a detrital origin or early diagenetic, based on its preference to form during weathering under arid climatic conditions, and it being a common weathering product in modern desert environments (McKinley et al., 2003), the diagenetic origin is likely to be the case here given the rather hot and humid Namurian climate (Leeder, 1988).

Continued early diagenesis in marine settings resulted in slowly using up available Fe ions leading to formation of ferroan dolomite ($Ca(Mg,Fe)(CO_3)_2$) lesser amounts of

non-ferroan dolomite. Its very early diagenetic origin is inferred from the strongly inhibited compaction in sandstones with abundant dolomite in places resulting in what appears to be grains 'floating' in dolomite cement. Based on its habit but with lack of isotopic evidence, it can only be speculated that dolomite formed from ions present in seawater, dissolution of carbonate bioclasts (Morad et al., 2000) or bacterial fermentation reaction in surrounding mudrocks (Cowan, 1989). It must be borne in mind that this ferroan dolomite could have initially formed as aragonite or Mg calcite and was dolomitised at a later stage of diagenesis.

Dolomite is also present in continental facies associations, but in significantly smaller amounts. Fresh, diluted pore waters are unfavourable for authigenic carbonate precipitation, therefore porosity was preserved until deeper burial in fluvial and delta plain deposits. Mechanical compaction, on the other hand, was the dominant process in continental facies, while in marine facies, where early cements stabilised grain framework before significant burial occurred, cementational porosity loss dominated over compactional porosity loss in some of the samples (see Figure 3.10, Chapter 3 and paragraph 3.4.3.1, Chapter 3).

5.4.1.3.2 Mesogenesis and telogenesis

As burial increased and temperature rose the Namurian sequence entered the realm of mesogenesis, defined as processes occurring after the influence of the depositional environment ceases through to the earliest stages of low-grade metamorphism with temperatures of up to 200–250°C (Worden and Burley, 2003).

The basin model presented in Chapter 4 shows that with rapidly progressing burial of the Namurian sequence, the temperatures increased to above 80°C during the late Carboniferous times, when reaching depth of ~1550 and 1800 m in Cavendish and Copernicus respectively (Figure 4.5, Chapter 4). The removal from the influence of depositional waters and changing physico-chemical conditions initiated diagenetic reactions of the unstable components. There is evidence of early carbonate and feldspar dissolution which led to secondary porosity formation, however where dolomite is pervasive it prevented local access to minerals and dolomite and was preserved. Mineral dissolution could have been caused by an increased pore water acidity generated by increasing temperature. Lundegard and Kharaka (1990) and Surdam et al. (1984) have shown that temperatures above 80°C cause bacterial activity to cease increasing organic acids concentration. Cowan (1989) postulated that the 80°C isotherm marks the temperature at which the pore fluids in Carboniferous

sediments changed from being carbonate saturated to being acidic and carbonate and silicate aggressive.

The temperature of around 80°C corresponds also to the onset of quartz precipitation (Walderhaug, 1996; Worden and Morad, 2000), smectite to illite transformation (~70°C proposed by Jennings and Thompson (1986), to ~100°C according to Inoue et al. (1992), and hydrocarbon generation (80°C in Cowan (1989), >100°C in Sajgó (2000), 95°C for marine and 120°C for terrigenous organofacies in Pepper and Corvi (1995) (the maximum temperatures reached by the Namurian sequences of the Copernicus and Cavendish fields reached 123°C and 80°C respectively; see section 4.5.1, Chapter 4). The onset of quartz precipitation allowed for stabilisation of grain framework by ceasing mechanical compaction thus preserving some of the initial porosity, simultaneously infilling primary pore spaces and reducing reservoir quality.

CL analysis has shown the presence of two generations of quartz, the first of which was thinner than the second, locally reaching 30 μm. A layer of residual oil is seen in Copernicus wells coating first generation of quartz in thin section. Based on these observations and analysis of basin's burial history, it is proposed that the first phase of quartz precipitation and oil entrapment occurred during the Carboniferous subsidence phase. Minor oil source rocks in the form of Dinantian to Namurian black shales and Westphalian lacustrine deposits, with Visean to Westphalian coal seams were the sources of oil (Cameron and Ziegler, 1997; Cornford, 1998; Gerling et al., 1999; Schroot et al., 2006; Doornenbal and Stevenson, 2010; Pletsch et al., 2010; Besly, 2018;). According to the burial model, the Namurian rocks in Copernicus well 44/16-1 spent about 20 My in temperatures >80°C during the first phase of burial (see Chapter 4) allowing for quartz cementation and hydrocarbon generation (and migration), until Variscan orogenic event caused rapid uplift of the Carboniferous strata sequence.

The maximum temperature reached by the Upper Carboniferous deposits during this first burial phase was 123°C in Copernicus field. Temperatures modelled in Cavendish are lower, reaching up to 85°C, therefore conditions for oil generation would have been less favourable, however Dinantian sediments underlying the Namurian sequence and subjected to higher temperatures could have acted as an additional minor source of oil during Carboniferous burial. Oil generation in Copernicus field is estimated to have started around 312 Ma, when the Namurian formation entered oil window. Given that source rocks are interbedded with reservoir

rocks, and directly underlying and overlying them, hydrocarbons were trapped in the reservoir concurrently with hydrocarbon generation.

Fracturing of quartz grains observed in CL presumably also happened during this phase of rapid burial and uplift, with near simultaneous healing with authigenic quartz, as is evidenced by non-luminescent quartz-healed fractures observed in detrital grains (see Figure 5.8).

The first phase of burial did not last long, as the Variscan orogenic event, which commenced ca. 307 Ma in the area (see Chapter 4), caused a rapid uplift and erosion of most of the Westphalian sequence in the Copernicus and Cavendish areas, bringing the Namurian deposits close to surface, where the top layers experienced the influence of meteoric waters once again (see Figure 5.10 this chapter and Figure 4.5, Chapter 4). At this time, the fluvial sandstones still would have been very permeable, having experienced only mechanical compaction and weak quartz cementation. Meteoric waters were likely to have penetrated quite deep into the sequence, also aided by faults and fractures formed at the time. In some areas, this meteoric influence and secondary oxidization reached over 500 m below the Base Permian Unconformity (Ruffell et al., 2006). Moreover, the meteoric flushing through the emerged Namurian sandstones led to kaolinite development at the expense of feldspars (Glasmann, 1992; Morad et al., 2000; Ketzer et al., 2003; Busch et al., 2019;). Continued dissolution of feldspar provided ions that were utilised for the formation of kaolinite in primary pores and in the feldspar dissolution pores. The minor amounts of haematite observed in some samples result from oxidation of iron during this period. Furthermore, faulting and fracturing caused by the tectonic movement broke the intra-Carboniferous seals allowing for most of the previously generated hydrocarbons to escape (Besly, 1990, 2018; Hollis, 1998).

Subsidence slowly continued again from the Early Permian after cessation of Variscan orogenesis and significantly sped up in early Triassic due to the onset of Triassic-Jurassic rifting (Figure 5.10 this chapter and Figure 4.5, Chapter 4). This period of burial brought the Carboniferous sequence again into the realm of high temperatures, reaching 80°C ca. 255-251 Ma in the late Permian-Early Triassic times, and the conditions for quartz precipitation and illitisation of smectite were favourable once again. Ions necessary for quartz and kaolinite formation were released during feldspar dissolution, illitisation of smectite in the surrounding mudstones and through pressure dissolution.

The second quartz cement phase is seen enclosing oil rims that are coating the first quartz generation, therefore they must have formed after the oil emplacement. While the effect of oil inhibiting quartz cementation is well documented in the literature (Gluyas et al. 1993a; Worden et al. 1998; Worden et al. 2018; Wilkinson and Haszeldine, 2011), the occurrence of oil between quartz generations in analysed samples indicates that oil did not play such a role in the Namurian sandstones. In general, in highly oil saturated sandstones import of silica would be entirely halted due to low two-phase relative permeability to water (Worden and Morad, 2000), but because in these reservoirs most oil was lost shortly after its generation during the Variscan uplift, quartz nucleation was possible.

A blocky form of kaolin observed in SEM suggests the presence of dickite in the analysed samples (Beaufort et al., 1998; McAulay et al., 1994), but the accurate discrimination between the minerals of the kaolin group (kaolinite, dickite, nacrite) should be based on XRD patterns on randomly oriented powders or FTRI spectra (Lanson et al., 2002), which are unavailable in this study. However, kaolinite-dickite transformation is considered an indicator of palaeotemperature, as multiple studies have shown that blocky dickite results from the diagenetic evolution of early kaolinite with increasing temperature (Beaufort et al., 1998; Lanson et al., 2002). Ehrenberg et al. (1993) observed that this transformation occurred at approximately 120°C in sandstones from Norwegian Continental shelf, which is below the maximum burial temperatures experienced by the studied sequence. Using this temperature as a paleothermometer, kaolinite-dickite transformation in the analysed Namurian sequence in the Copernicus and Cavendish fields would have started in the early Triassic times when the temperature of 120°C was reached.

The Jurassic uplift did not leave a conspicuous diagenetic imprint on the Namurian sandstones. The temperature of over 100°C persisted within the reservoir, and thick Zechstein salt seals likely remained impermeable. Gradual development of quartz cements up to this point resulted in tightening of the reservoir and occluding of some of the pore throats, thus isolating some of the pores and a restricted fluid flow (see Chapter 6). Minor amounts of illite that are observed in SEM enclosed by surrounding quartz overgrowths formed following the major phase of quartz development (Figure 5.3d). Illite development may be an indicator of changing fluid chemistry with pore waters becoming more alkaline (Cowan, 1989), and K^+/H^+ ratio becoming favourable for illite precipitation and illitisation of kaolin. Despite the prolonged period of high temperatures (with maximum temperature reaching 140°C at depth of ~4000 m), minor quantities of illite-smectite remain in the Cavendish sandstones. This is not

unlikely though, as deeply buried smectite was previously reported by other authors. As reported by van de Kamp (2008), transformation of smectite to ~95% illite occurs in the temperature range 20-200ºC, while Chamley (1994) reported smectite-rich layers occurring down to 5500 m. Without detailed XRD data in this study it is not possible to determine illite crystallinity, although most smectite layers are probably replaced by illite.

According to the burial model, Namurian rocks entered gas generation window 90 Ma in the Late Cretaceous times, however gas migration into the reservoir did not have a visible impact on diagenetic processes,

A late phase of ferroan and non-ferroan dolomite, which encloses quartz cement and illite, required supply of Ca, Mg and Fe ions. Considerable amounts of the necessary ions might have been released during conversion of smectite to illite in the surrounding mudstones (Bertier et al., 2008; McKinley et al., 2003; Worden and Morad, 2003). An alternative source could have been the alkaline fluids transported through faults that formed during the last recorded tectonic event, the Palaeogene uplift, as in the Belgian Carboniferous sandstones, where late ankerite formation was concluded to be related to illitisation of smectite based on isotope and fluid inclusion data (Bertier et al. 2008). The latest minerals that formed were barite and anhydrite, which are seen enclosing quartz and the late dolomite. Barite and anhydrite most likely precipitated from fluids derived from Zechstein evaporites (Cowan, 1989) during with the Palaeogene tectonic event. Cowan (1989) also proposed an alternative way of the formation of barite and anhydrite, from fluids derived from a more local source through oxidation of sulphides in surrounding mudstones, however did not propose a possible source of oxidants that would be required for the reaction to take place.

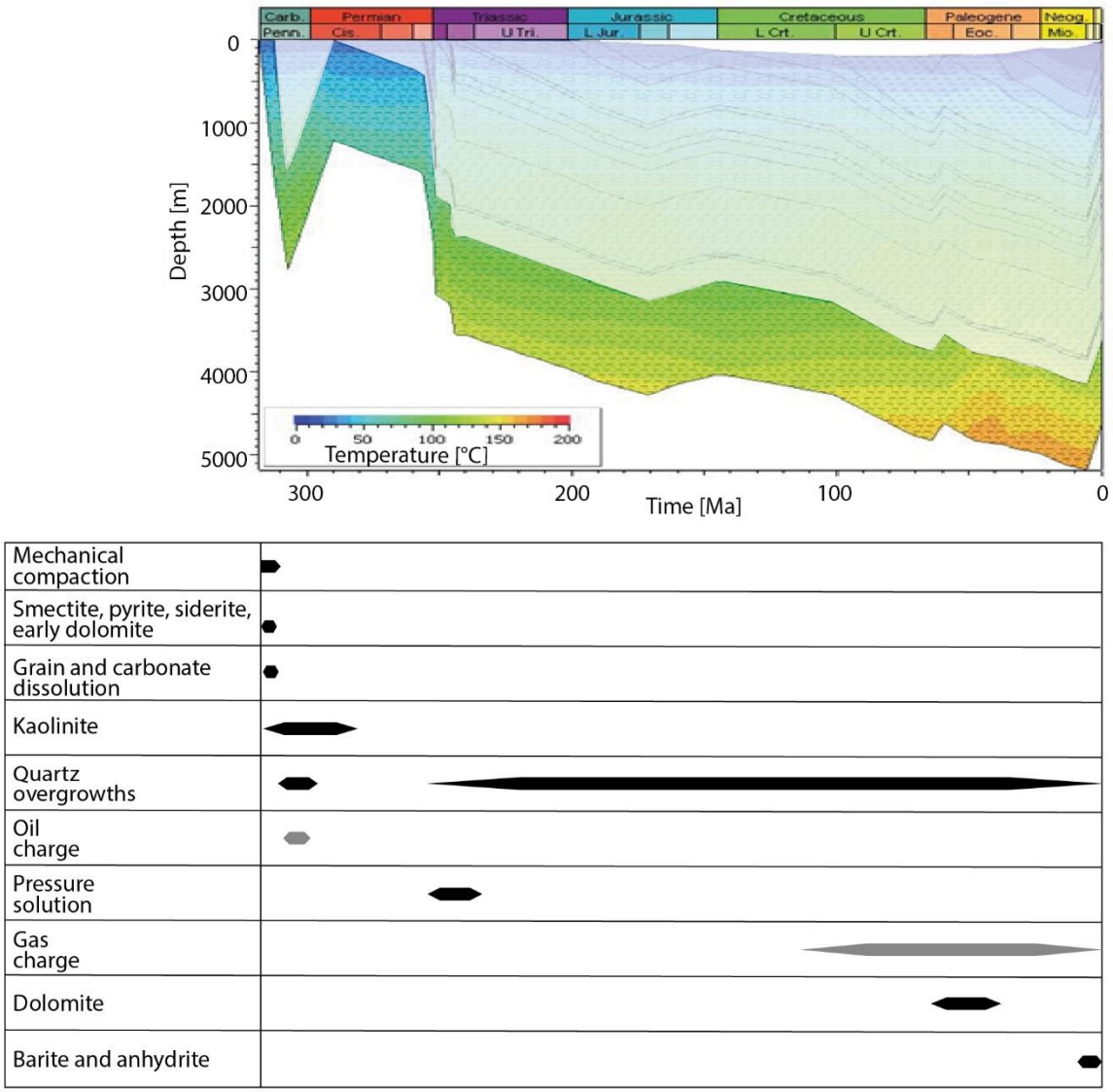

Figure 5.10. Hydrocarbon generation, burial and thermal history, and key diagenetic events of the Millstone Grit sandstones from Cavendish and Copernicus fields.

5.4.2 Quartz cementation

5.4.2.1 *Quartz precipitation kinetics*

Temperature-controlled quartz precipitation kinetics proposed by (Walderhaug, 1994a; Walderhaug, 1996) are a dominant hypothesis for the quartz cement formation in deeply buried sandstones. It assumes that quartz formation starts at the temperature of ca. 80°C and grows exponentially with temperature increase. The volume of precipitated quartz is further a function the available surface area and time spent in the adequate temperatures. This mechanism does not take into account the effect of vertical stress. Based on Walderhaug's approach, conditions favourable for quartz precipitation lasted in both studied reservoirs throughout most of their burial

history, occurring in two stages. A short episode of temperatures >80°C took place at the end of the Carboniferous times, followed by a long period of about 250 million years from the Jurassic till now. Sources of silica ions were abundant as documented by the abundant quartz overgrowths observed.

Despite decades of research on quartz cementation, questions still remain about the duration of quartz cementation. Two scenarios exist, that propose either continuous cementation at slow rates over a long time, or over short bursts of higher intensity (Worden and Morad, 2000). Walderhaug's (1994a) quartz cementation model assumes a continuous process rather than as episodic cementation events separated by periods of little or no cementation. In contrast, Grant and Oxtoby (1992), Robinson and Gluyas (1992), Gluyas et al. (2000) proposed faster rates of quartz precipitation over short periods of time. The analysis of quartz overgrowths in Copernicus and Cavendish fields with cathodoluminescence reveals two distinct quartz generations, a thin early phase of up to 30 µm, and a thicker second phase up to 70 µm displaying a complex internal pattern. In conjunction with the modelled burial history of the basin it is proposed here that the first generation of quartz formed over a short period of about 20 Ma during the Carboniferous subsidence phase (see section 4.5.1, Chapter 4). The maximum temperature reached at the time in the Copernicus field was 123°C. For 30 µm of quartz to form over 20 Ma quartz would have to precipitate on average at a rate of 1.5 µm per million years. By converting equation 5.1:

$$r=1.98*10^{-22}*10^{0.022T}$$

Equation 5.1. Quartz precipitation rate expressed as temperature dependant function (Walderhaug, 1994b), where r is precipitation rate in moles/cm^2*s and T is temperature in °C.

to a linear outwards growth rate for quartz overgrowths in cm/s, Walderhaug (1994b) calculated that in order to precipitate 4 µm at 120°C it would take 6 million years, giving a rate of 0.67 µm/year. This is 2.2 times slower than the rate calculated for the Copernicus sandstones so for quartz cement to precipitate during the Carboniferous subsidence, quartz precipitation rates would have to have been much higher than those proposed by (Walderhaug, 1994b). On the other hand, for the second generation of quartz, that reaches up to 70 µm in thickness, to form over the period on 250 million years, it would have to be precipitating significantly slower than the rate proposed by Walderhaug (1994b), meaning that episodes of non-precipitation likely occurred

throughout the diagenetic history. The stripy appearance of quartz overgrowths can be an effect of such separate episodes of precipitation, however SIMS analysis would be required to confirm whether there indeed is a relationship between $\delta^{18}O$ isotopes and CL zonation (Harwood et al., 2013).

5.4.2.2 *Silica sources*

Quartz cement in the Namurian reservoirs if the Copernicus and Cavendish fields in undoubtedly the most important phase responsible for reservoir tightening and porosity loss. Two distinct phases of quartz cementation occurred, with the second possibly encompassing several episodes of changing chemistry or conditions, as evidenced by its 'stripy' appearance and precipitation rates. Sources of silica ions must have been abundant during quartz precipitation, which accounts for 10.7% and 9.5% rock volume on average in fluvial sandstones in Copernicus and Cavendish fields respectively, and up to 21.7% (based on petrographic point counting).

Multiple sources of silica for quartz cementation are available in deeply buried sandstones, that can be broadly divided into external and internal sources. The internal sources include feldspar dissolution and alteration, illitization or chloritization of smectite, pressure dissolution and stylolitisation, dissolution of biogenic silica and unstable volcanic rock fragments (Bjørlykke & Egeberg, 1993; Worden & Morad, 2000; Xi et al., 2015). The external sources are those outside the cemented sandbody, e.g. from neighbouring mudrocks (Worden and Morad, 2000). Multiple mechanisms responsible for silica transport were proposed by various authors (McBride, 1989; Aplin et al., 1993; Bjørlykke and Egeberg, 1993; Aplin and Warren, 1994; Giles et al., 2000;), including meteoric recharge, compaction-driven flow, fluid-flow by advection, thermal convection, and diffusion. Each of these mechanisms requires different volumes of water to transport the same volume of dissolved silica, some of which requiring large scale fluid movements that are unattainable in deeply buried reservoirs. Therefore, diffusive transport over short distance (<10-100 m) is regarded to be the most important process of silica transportation in deeply buried sandstones (Aplin and Warren, 1994; Bjørlykke and Egeberg, 1993).

Detailed analysis of the Copernicus and Cavendish sandstones revealed that silica that was utilised for quartz cementation was released from a range of potential sources that were available at different times, however the contribution of each of the sources is difficult to quantify. These sources are presented in detail below:

(i) Stylolitisation and pressure solution: Stylolites are a common feature observed in core and in thin section (Figure 5.6 and 5.11 b-d; Appendix 2; see also Figure 3.9 c and d in Chapter 3), most commonly in fluvial and delta plain and shoreface facies. Their distribution varies, from millimetres apart to several metres apart. Stylolites are rich in clay and mica, which are known to enhance pressure dissolution on quartz grain contacts (Bjørkum et al. 1998; Aharonov and Katsman 2009; Fisher et al. 2000) and in pyrite which is associated with organic matter that occurs with clays.

Stylolites certainly are an important source of silica in the analysed sandstones, however quantification of their contribution for quartz cement is difficult to assess. It has been proposed that distance from the stylolites is one of the controls on quartz distribution (Bjørkum et al., 1998; Oelkers et al., 1996), yet such relationship is not observed here (Figure 5.7). This is due to the fact that multiple sources acted as silica sources therefore silica distribution is dependent on multiple other factors. One of such additional sources is quartz dissolution on grain-to-grain contacts. COPL/CEPL plots show that mechanical compaction was an important contributor to porosity loss and CL images show that indented grain contacts indeed occur in the analysed sandstones, indicating pressure dissolution. Point counting of quartz overgrowth and dissolved grain contacts in three quartz cemented samples from fluvial and delta plain sandstones shows that the volume of quartz cement exceeds the volume of quartz which could have been supplied locally from intergranular pressure solution. Dissolved grain contacts account for only 0.2-2.4% of rock volume, which is only a small fraction of all quartz cement (average 8.9% in all analysed samples; Appendix 4). While quantification of the amount of silica released through stylolitisation is more challenging, the wide spacing between stylolites (several metres between stylolites in some areas) imply that stylolites could not have been the only other source of silica to grain-to-grain dissolution. Walderhaug and Bjørkum (2003) observed very good correlation between the distance to the nearest stylolite and amount of quartz cement in the zone of 20 cm from the nearest stylolite, and markedly less quartz cement in samples located more than 20 cm from the nearest stylolite, albeit the analysed sandstones were buried to a maximum of 125°C. Nevertheless, they have shown that transport of silica from the stylolite occurred in a significantly shorter distance than would have been required to cement the Millstone Grit. Furthermore, some quartz-cemented sandstones in the analysed Millstone Grit interval are separated vertically from stylolitised beds by very low permeability mudstones, so the amount of silica transported from those beds would have been negligible.

(ii) Feldspar alteration and dissolution: Optical microscopy observations indicate that feldspars present in sandstones at the time of deposition were completely dissolved or replaced by kaolinite during diagenesis (Figure 5.11a), except where pervasive early carbonate cementation prevented pore fluids from reaching the grains. Since feldspars have higher Si/Al ratio than kaolinite, K-feldspar replacement by kaolinite leads to silica release (Worden and Morad, 2000), as per reaction below:

$$2KAlSi_3O_8 + 2H^+ + H_2O = Al_2Si_2O_5(OH)_4 + 4SiO_2 + 2K^{+}$$

K-feldspar kaolinite quartz

Equation 5.2. Replacement of K-feldspar by kaolinite leading to silica and potassium release (Worden & Morad, 2000).

This reaction produces 0.43 unit volumes of quartz for one unit volume of reacted K-feldspar (Worden and Morad, 2000). Replacive kaolin, which corresponds to the volume originally occupied by K-feldspar, forms 2.3% and 1.5% volume in Copernicus and Cavendish respectively (see Appendix 4), therefore it could be responsible for formation of only 1.0% and 0.6% of quartz cement in the two fields respectively, compared to the 9.1 and 8.6% that is present in these two fields (Appendix 4).

Locally K-feldspar was completely dissolved without precipitation of clays at the site of dissolution. The reason for this might be that the aluminium freed from the feldspar diffused to the site of clay mineral growth determined by the distribution of preferred nucleation sites, while silica diffused to open surface of quartz grains (Giles and De Boer, 1990). In Copernicus and Cavendish fields secondary porosity accounts for 0.6% and 2.8% respectively and it is likely to be largely formed by dissolution of feldspars. Even if this whole volume were occupied by feldspars and no silica export occurred, the silica released from its dissolution would only result in precipitation of minor amounts of quartz cement.

(iii) Illitisation of smectite: Minor amounts of authigenic grain-coating illite are present in fluvial sandstones, some of which likely comes from smectite alteration to illite through the mixed illite-smectite series (Elliott and Matisoff 1996; McKinley, et al., 2003). Detrital clay occurring within the fluvial and other facies, as well as clay forming mudclasts, that at the time of deposition consisted at least partially of

smectite (Figure 5.11e), was altered to illite with increasing temperatures, and contributed as silica source as per reaction below:

$$KAlSi_3O_8 + 2K_{0.3}Al_{1.9}Si_4O_{10}(OH)^2 = 2K_{0.8}Al_{1.9(}Al_{0.5}Si_{3.5})O_{10}(OH)_2 + 4SiO_{2(aq)} \quad (3)$$

K-feldspar K-smectite illite quartz

Equation 5.3. Illitisation of smectite reaction.

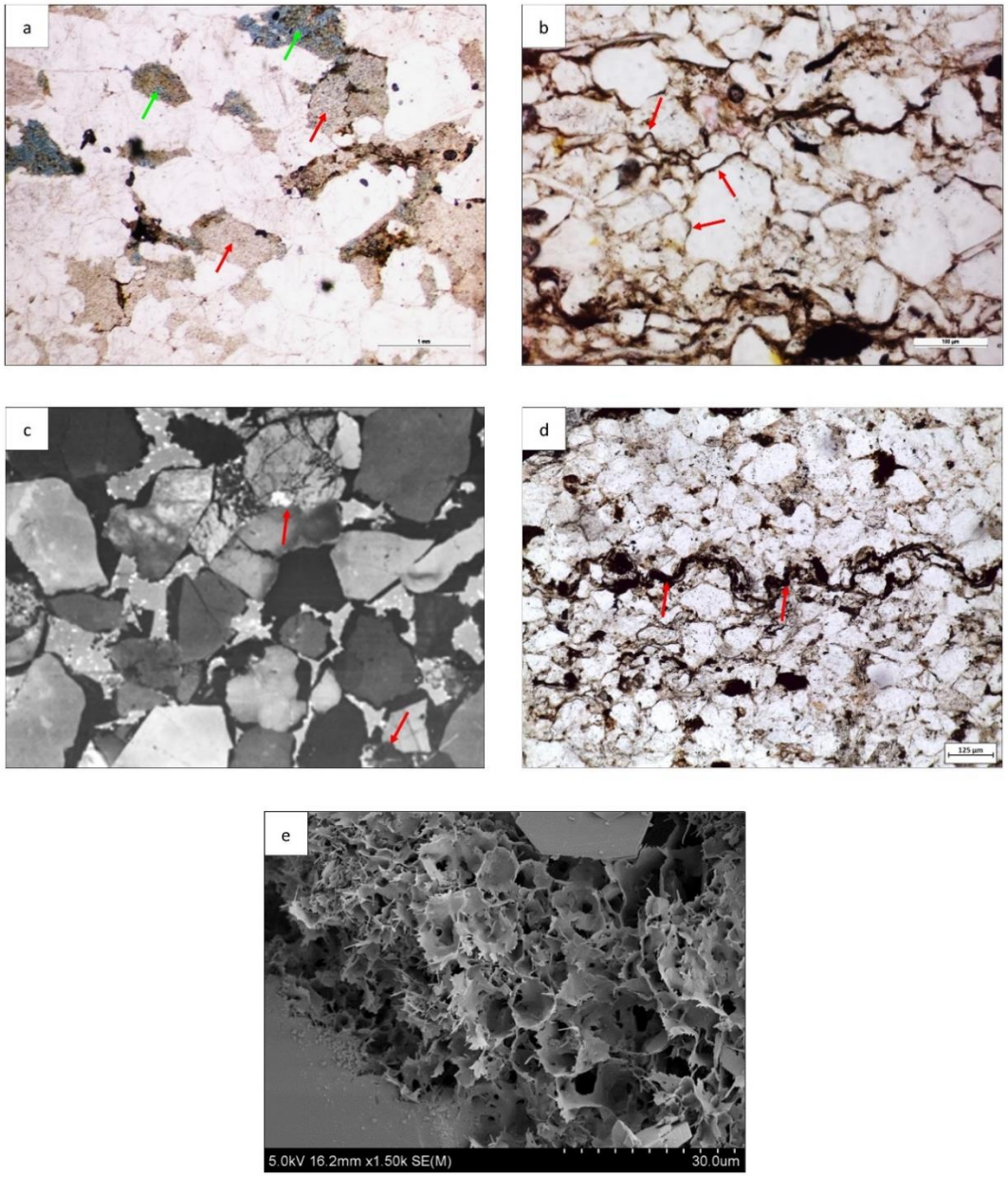

Figure 5.11. Multiple sources of silica were active during diagenesis of Copernicus and Cavendish sandstones: a) feldspar dissolution (green arrows) and kaolinite replacement (red arrows); b & c) detrital quartz dissolution caused by pressure solution; d) stylolite formation; e) illitisation of smectite.

Yet, the amount of illite recorded in the fluvial facies is negligible compared with the amount of quartz cement. The total amount of illite, k-feldspar dissolution, stylolitisation and pressure solution combined cannot account for the amount of quartz cement found in the strongly cemented Millstone Grit sandstones, which implies that silica has been imported into the sandstone. Illitisation of smectite in mudstones encasing sandbodies in this highly heterolithic sequence might have contributed to a local enrichment of quartz cement, without the need for large scale reservoir fluids movement. Further analysis of those mudstones would be required to confirm whether they were silica exporters, or whether silica was precipitated in situ. Although mass transfer in mudstones is very low (Bjørlykke, 1994; Thyberg and Jahren, 2011) ion diffusion between sandstones and mudstones is well documented in some basins (e.g. Haszeldine et al., 2000). In case of Copernicus and Cavendish, silica export from surrounding mudstones into sandstones would have been required in order to account for the high volumes of quartz encountered in the analysed sandstones, as other sources do not account for the quartz amount needed. Models by (Giles et al., 2000) have shown that silica exported from mudstones does not penetrate far into the sandstones before reacting with detrital quartz therefore numerous, thin, interbedded mudstones (as is the case in the analysed Millstone Grit formation in Cavendish and Copernicus, with net:gross from 17% to 36%) would be more efficient exporters of silica into sandstones than thick mudstone sequences.

5.4.3 Diagenetic differences between Copernicus and Cavendish field

The Namurian sequence of Cavendish and Copernicus fields experienced a similar, polyphase tectonic history. Both areas experienced rapid burial in the Namurian times, which resulted in strong mechanical compaction associated with rapid porosity loss, and heating over 80°C, leading to quartz cementation. Sandstones from Copernicus field contain more quartz overgrowths caused by larger maximum burial temperature during Carboniferous burial phase, also leading to higher burial depths during later stages. Unlike the Cavendish, the Copernicus field shows signs of early oil emplacement, indicating that its Namurian sequence entered oil generation window early in the burial history. Despite the fact that the deepest parts of the Namurian sequence of the Copernicus field were buried several hundred metres lower than that of the Cavendish field, telogenetic alterations in both fields followed a similar path suggesting that meteoric waters penetrated through the entire Carboniferous sequence. Such large extent of meteoric telogenesis was possible due to high sandstone permeability and presence of faults, which could have acted as

conduits for meteoric water, despite the presence of interbedded impermeable mudstones (Morad et al., 2000). Feldspar kaolinitisation was one of the most important diagenetic alterations for the whole reservoir, most of which took place during this first phase of burial and uplift. The significance of kaolin presence is discussed in Chapter 3.

The next stage of burial which commenced in the late Permian times and accelerated in the Mesozoic era was characterised by a similar diagenesis style in both regions. Quartz cementation continued in both fields, however at a higher rate in Copernicus than in Cavendish field, since the former was subjected to higher temperatures during the whole of Mesozoic and Cenozoic era. The final diagenetic minerals: barite and anhydrite, are only encountered in Cavendish field, but their influence on reservoir quality loss is negligible.

5.5 Conclusions

-Namurian sandstones from Cavendish and Copernicus fields are characterised by a complex diagenesis caused by their polyphase tectonic history. At least three major stages in the diagenetic history can be inferred from the microscope and CL analysis when examined in close conjunction with basin's burial history.

-The final diagenetic fate of the studied sandstones was chiefly controlled by their depositional composition and texture of the sediment, and burial depths. Sedimentary environment provided initial heterogeneity, which in turn controlled the degree of the meteoric fluid flow in the shallowest eodiagenetic phase, and controlled initial fluid composition, that lead to precipitation of carbonate cements and clay infiltration largely restricted to marine environments.

-Rapid burial caused by the development of a thick sedimentary sequence at the foot of the approaching Variscan front was responsible for significant mechanical porosity reduction in uncemented continental sandstones. Upon reaching the temperature of about 80°C mechanical compaction was impeded by the development of quartz overgrowths with silica sourced locally mainly from the dissolution of liable minerals such as feldspars and lithic fragments to a lesser degree, and from pressure dissolution of quartz grains.

-Once the sandstones and neighbouring organic-rich source rocks entered oil window, the short-lived hydrocarbon generation phase occurred with subsequent migration and local hydrocarbon emplacement in the relatively permeable sandstone intervals. The subsequent uplift which occurred in early Permian brought Namurian sequence

near the surface allowing meteoric waters to percolate. These conditions led to generation of secondary porosity and feldspar kaolinitisation while reactivated faults facilitated fluid transport and hydrocarbon discharge.

-The late Permian and Triassic subsidence led to re-entering of high temperature regimes and yet another phase of quartz cementation and clay transformation. Grain framework had already been stabilised by earlier quartz formation therefore mechanical compaction was insignificant at this time and chemical compaction became a much more important factor in the evolution of the poroperm system. Stylolite formation presumably occurred at this stage. Chemical cementation, led primarily by quartz precipitation, likely became pervasive enough to form tight reservoirs already in the Jurassic times, therefore the Jurassic updoming and elevated thermal flux has only limited impact on the diagenetic parasequence.

-The Namurian sequence entered oil and then gas window in the Cretaceous times but HC emplacement at this time had little effect on diagenesis as cementation had virtually closed the effective pore system.

-The final cements are represented by dolomite, anhydrite and barite sourced from local mineral transformation or transported in solution by faults associated with Alpine orogenesis.

-Burial and uplift diagenesis in the Copernicus and Cavendish fields was controlled by the major tectonic events that included Variscan and, Alpine orogeneses as well as early Triassic rifting related to opening of the Atlantic Ocean.

-In general, the porosity of the analysed sandstones was reduced significantly during the first stage of burial through mechanical compaction, whereas chemical cementation dominated throughout the rest of the basin history. Reservoir quality reduction at the burial stage was primarily controlled by the burial depth and associated temperature, and time spent in quartz generation window.

-Availability of silica sources was unlikely a limiting factor for quartz cementation as multiple sources have been active throughout the time. Silica sources were however highly dependent on the initial composition and the stage of the basin history. Stylolitisation and pressure solution, feldspar dissolution and kaolinitisation, and illitisation of smectite were the main silica generating mechanisms. These mechanisms operated in the Cavendish and Copernicus fields at different magnitudes and took place in various basin burial stages, resulting in highly heterogenous

reservoir quality in the study area. Thus, a thorough analysis of basin subsidence is a prerequisite for reliable paragenetic reconstructions.

-This study shows that the best reservoirs for hydrocarbons in the Southern North existed after the late Carboniferous burial phase when the mechanical compaction was the dominant process responsible for porosity reduction in clean fluvial sandstones, and prior to the second, pervading quartz cementation phase. The intra-Carboniferous sealing horizons were provided by the low-permeability interbedded mudstones, however, the thick regional seal and traps had not yet existed at the time. Furthermore, the late Carboniferous/Permian uplift lead to the hydrocarbon release.

-Oil and gas exploration should therefore focus on areas where burial was quick in the Namurian/Westphalian times with none or greatly reduced uplift in Permian, potentially leading to preservation of oil in high quality sandstones, followed by relatively shallow Mesozoic burial. Such areas would yield highest potential for reservoir quality preservation. With current production technologies oil and gas may be successfully recovered from such reservoirs.

CHAPTER 6:
Characterization and quantitative analysis of pore architecture and permeability modelling in tight gas sandstones utilizing X-ray computed microtomography

6.1 Introduction

X-ray computed tomography (XCT) is widely used in geosciences to map oil saturation, characterise mineral and porosity distribution, and simulate permeability and fluid flow (eg. (Wang et al., 1985; Wellington and Vinegar, 1987; Hunt et al., 1988; Cnudde and Boone, 2013; Bultreys et al., 2016). The advantage of XCT is that the method is non-destructive, meaning that the same material can be used for other purposes. X-ray computed microtomography (XMT) analysis can also reduce the volume of material that needs to be collected, thus reducing high costs of data collection, especially from boreholes. Where suitable core material for lab testing like core plugs is not available, or plugs are damaged, XMT allows to build digital models out of small volumes that can be used in numerical simulations to measure porosity and permeability (Arns et al., 2004; Algive et al., 2012).

Digitisation of rock pore-spaces also allows to model oil relative permeability, fluid flow velocity or drainage capillary pressure (e.g. Caubit et al., 2009; Mostaghimi et al., 2013; Noiriel et al., 2016). These digitally derived petrophysical properties can be an important tool in petroleum exploration, CO_2 sequestration, geothermal energy production, in hydrology, or soil science, where traditional determinations are challenging.

In oil and gas exploration permeability is the key petrophysical property, as it ultimately controls fluid flow through the porous media (reservoir). Permeability is highly sensitive to the architecture of the porous microstructure, i.e. numbers and sizes of pores, specific surface area, size of pore throats, and pore connectivity (e.g. Ehrlich et al., 1991; Martys et al., 1994; Golab et al., 2010). In contrast to well-known relationships between porosity evolution and progressive burial and quartz cement precipitation (e.g. Robinson and Gluyas, 1992; Walderhaug, 1996; Gluyas and Cade, 1997) such relationship for permeability is not well established. There is also no direct relationship between permeability and well-log response, as is observed with porosity (Archie, (1942); Ellis and Singer, 2008). Empirical and theoretical methods that relate permeability reduction directly to porosity reduction generally assume idealized geometries, and do not capture reflect the changes in natural pore microstructures. These models fail to account for the heterogeneity that arises from sedimentological development or non-uniform diagenetic mineralisation, both of which will have a significant impact on permeability (Yue et al., 2018). The ability of XMT to capture and quantify the variability in pore microstructure in 3D, allows us to develop models

that do reflect the non-idealised heterogenous structures, and to accurately measure the pore throat sizes, pore connectivity and tortuosity of the flow path.

We use XMT to construct the pore network architecture at high resolution, characterise the heterogeneity and assess the absolute permeability of a series of sandstones, to determine the most important control on reservoir quality. This study also assesses the usability of XMT method to characterise rock properties.

6.2 Method

The sandstone samples were collected from Copernicus discovery and Cavendish field, Southern North Sea. One set of five 2.5 cm (1 inch) core plugs was taken from the depth of interest and a second set from above or below the location of interest to allow assessment of heterogeneity. This second set was from the same sandstone bed as the first one. The first set of plugs was used for thin sections analysis, XMT analysis, and laboratory-based helium porosity and permeability measurement. The second set was analysed for helium porosity and permeability during the routine conventional core analysis (CCA) by the operator. Thin sections, core plugs and XMT samples were all cut parallel to core length. The five samples selected for XMT analysis were selected after initial petrography screening and after obtaining CCA data, based on their variable porosity, permeability and cement distribution

6.2.1 Sampling and petrography

All samples from the first set of plugs were initially thin sectioned and point counted. Thin sections were examined with polarizing microscopes (Leica DM2500 P), and 100 point grain size measurements and 300 point counts were performed using Conwy Valley Consultants stepping StageTM connected to PETROG software. SEM analysis was performed using a Hitachi SU-70 field emission gun scanning electron microscope equipped with an energy-dispersive detector (EDS) to analyse compositional data. Compositional data processed using AZtecEnergy EDS Microanalysis software. Cathodoluminescence analysis was performed on a Gatan MonoCL system with a panchromatic imaging mode, and with blue, red, green or no filter.

The sandstones were deposited by multi-storey fluvial channels or delta plain facies associations and at the core scale display cross stratification (lithofacies Sx) or pedogenic modification (lithofacies S(M)ped) (see Chapter 3). They are all quartz-cemented and contain varying proportions of kaolin, dolomite, siderite, pyrite and minor other clays. They differ in grain size and sorting, ranging from upper fine to upper coarse and from moderately to moderately well sorted (Table 6.1). Selected

samples have a range of porosities and permeabilities, showing negligible to high reservoir quality. Mineralogy of the samples was determined by optical microscopy and SEM-EDS, and SEM-cathodoluminescence was used to map the distribution of detrital and authigenic quartz.

Depth [ft]	Modal grain size, Mean size [mm]	Sorting	Facies association	Litho-facies	XMT Extracted sub-volume shape	XMT dimensions (x x y x z) [mm]	XMT Volume [mm^3]
14189.1	upper fine 0.22	moderately well	delta plain	S(M) ped	square cuboid	2.5x2.5x2.0	12.5
14262.8	lower medium 0.21	moderately well	multi-storey fluvial channel	Sx	cylinder	4.4x4.4x3.0	45.1
14270.9	upper medium 0.33	moderately well	multi-storey fluvial channel	Sx	cylinder	4.4x4.4x3.0	45.1
16271.8	upper coarse 0.81	moderately well	multi-storey fluvial channel	Sx	cylinder	4.4x4.4x3.0	45.1
16276.4	upper coarse 0.89	moderately	multi-storey fluvial channel	Sx	cylinder	4.4x4.4x3.0	45.1

Table 6.1. Sample database. Abbreviations: Sx – Clean cross-bedded sandstone; S(M)ped – slightly silty pedogenically modified sandstone.

6.2.2 Laboratory permeability measurement

CCA (porosity and permeability) data of the second set of core plugs that were located a few centimetres away from petrography samples were available for this study. New set of plugs which was used for petrography analysis was also used for direct porosity and permeability measurements to assess differences between the two sets caused by heterogeneity. 2.54 cm wide and 2.54-5.1 cm long core plugs were obtained from the core and analysed for porosity and permeability at Wolfson Multiphase Flow Laboratory at Leeds University using methods described by McPhee et al. (2015). Porosity was measured using Helium porosimeter. Permeability was measured using steady state method under 500, 1500 and 5000 psi confining pressure and 500 psi net stress for the more permeable samples (14189.1 ft (4324.8 m), well 44/16-1; 14262.8 ft (4347.3 m), well 44/16-2; 16271.8 ft (4959.6 m) and 16276.4 ft (4961 m) well 43/19a-4Z) and pulse decay under 1500, 2500 and 5000 psi confining pressure and 500 psi net stress for the less permeable one (14270.9 ft (4349.8 m), well 44/16-2).

6.2.3 X-ray microtomography

The 0.5 cm diameter, 1 cm long cores were cut from the offcuts from the thin section preparation, from the depth of interested. The axis of the cores is perpendicular to bedding and parallel to original drill core. These cores were scanned with an XRadia VersaXRM 410 XCT scanner (Durham University), operating at 120 kV and 10 W with 3201 projections collected at a 12 s exposure time for sample 14189.1, and at 100 kV, 10 W with 3201 projections collected at a 12 s exposure time for all other samples. The data were then reconstructed using the proprietary Xradia (filter back projection) software, to give a volume with an isotropic voxel (3D equivalent to a pixel) resolution of 2.5 μm in all samples. Additional CT data were acquired at lower resolution on core plugs at Leeds University to check sample homogeneity (Figure 6.1 (ii)).

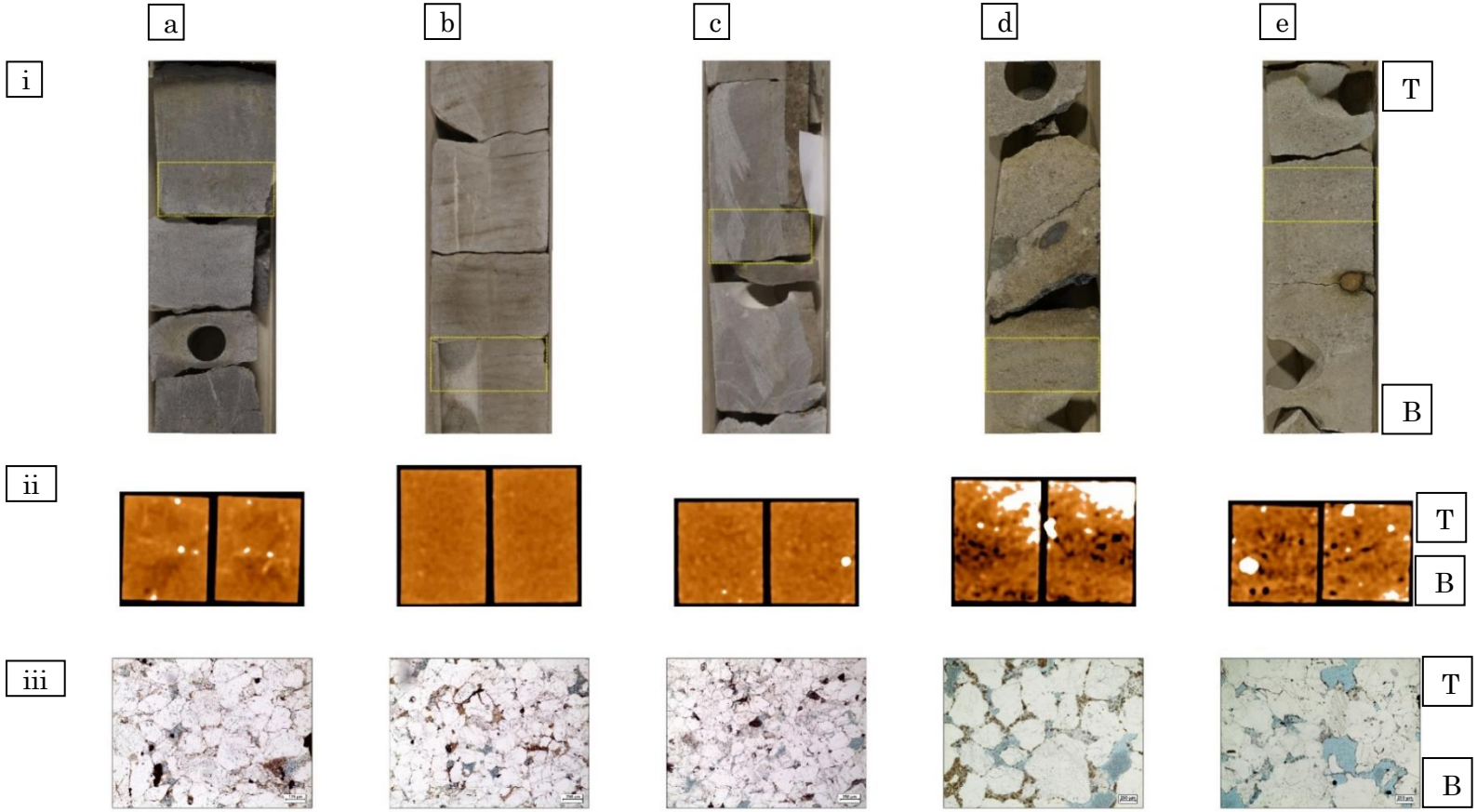

Figure 6.1. Top row shows 1 ft long core section with the location of core plug shown in yellow box, middle row shows low resolution CT image on 2.5 cm wide core plug, and the bottom row shows thin section photograph from the same area. a) sample depth 14189.1, well 44/16-1, b) sample depth 14262.8, well 44/16-2, c) sample depth 14270.9, well 44/16-2, d) sample depth 16271.8, well 43/19a-4Z, e) sample depth 16276.4, well 43/19a-4Z. darker colour on CT scan indicates lower density material, whilst lighter colour indicates high density. Note the very high heterogeneity apparent on a low-resolution CT scan in sample 16271.8. 'T' for top and 'B' for bottom are indicated to show how different sample types are oriented to each other. These also correspond to sample orientation on Figure 6.2.

6.2.4 3D image processing and analysis

The data visualisation and analysis were performed using Avizo™ (ThermoFisher©) (Figure 6.2). After an initial assessment to confirm limited heterogeneity across the scan volume, cubic sub-volumes (sizes indicated in Table 6.1) were extracted to allow efficient computation and analysis. Images were filtered using an edge-preserving anisotropic diffusion filter before segmentation (see Figure 7.1, Chapter 7 for workflow) to map the distribution of mineral phases and porosity (Figure 6.2; binary image showing the pore network and mineral phases as segmented from the original greyscale XCT image in sample 14189.1 are available as an electronic appendix: Wasielka and Dobson (2019). Some minerals have similar densities and x-ray attenuation and therefore similar greyscale values in the reconstructed data. Segmenting these phases was non-trivial and some manual segmentation was needed to improve segmentation of quartz and clays, while different types of clays and different carbonate phases were grouped into 'clays' and 'carbonates' phases.

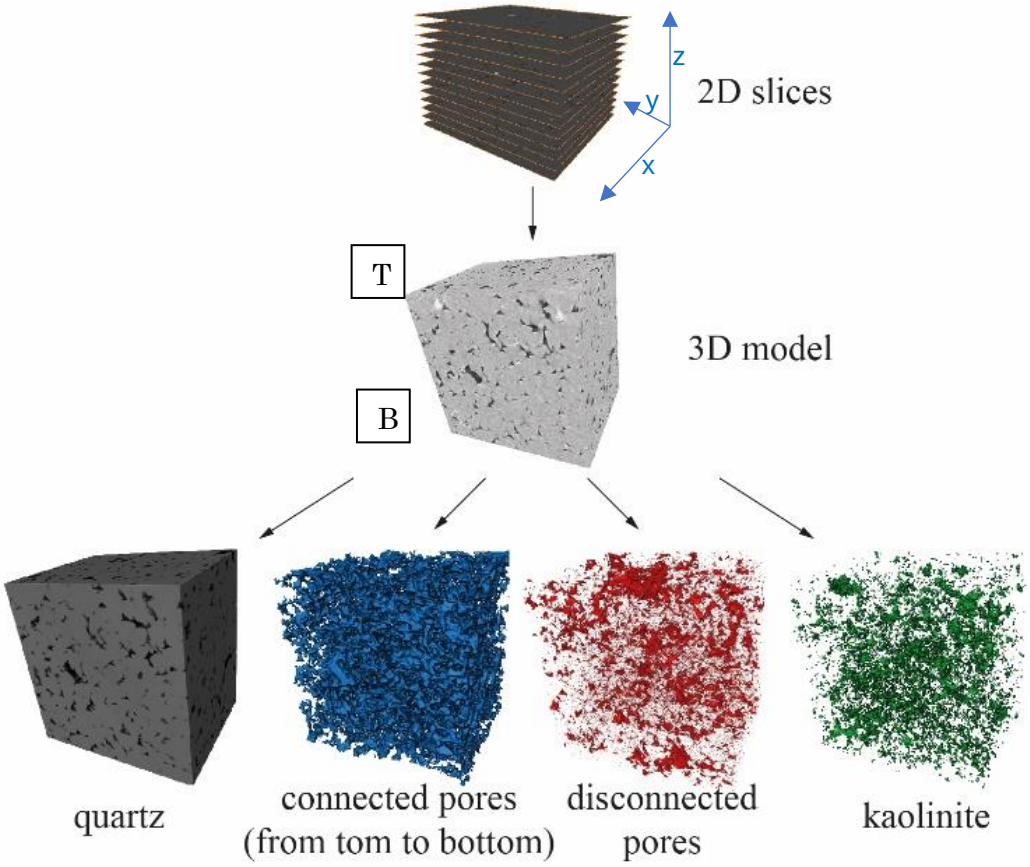

Figure 6.2. 3D image processing methodology and segmented phases in sample 14189.1, well 44/16-1. X, Y and Z axes are shown on 2D model. T' for top and 'B' for bottom are indicated on 3D model to show sample orientation relative to core and thin section on Figure 6.1

As the sample mineralogy and mineral densities are known (thin sections, SEM-EDS), and the expected differences in attenuation in a XMT scan correspond to differences in phase densities, the mineralogy corresponding to the greyscale values in the XMT is defined. The lowest density phase identified in petrography was porosity, which corresponds to the darkest material on XMT images, and the densest phase was pyrite, corresponding to the brightest material in XMT.

After separating the pores from the solid phases, the pores forming part of the throughgoing connected volume in the Z orientation were extracted from the complete pore volume, leaving 3D representations of the "connected" and "disconnected" pores (i.e. connected/not connected in a single throughgoing volume). A Pore Network Model (PNM) was then generated, using the 'Separate objects' algorithm to define the pore throats between the connected pores. In the PNM, the pores are represented by the largest inscribed sphere in that individual pore volume and the pore throat as a rod with diameter scaled to the pore throat (see Blunt et al., 2013; Dong et al., 2008; Silin and Patzek, 2006 for details) (Figure 6.3). A numerical permeability simulation was then calculated assuming Navier-Stokes flow using the Avizo™ XPoreNetworkModeling Extension.

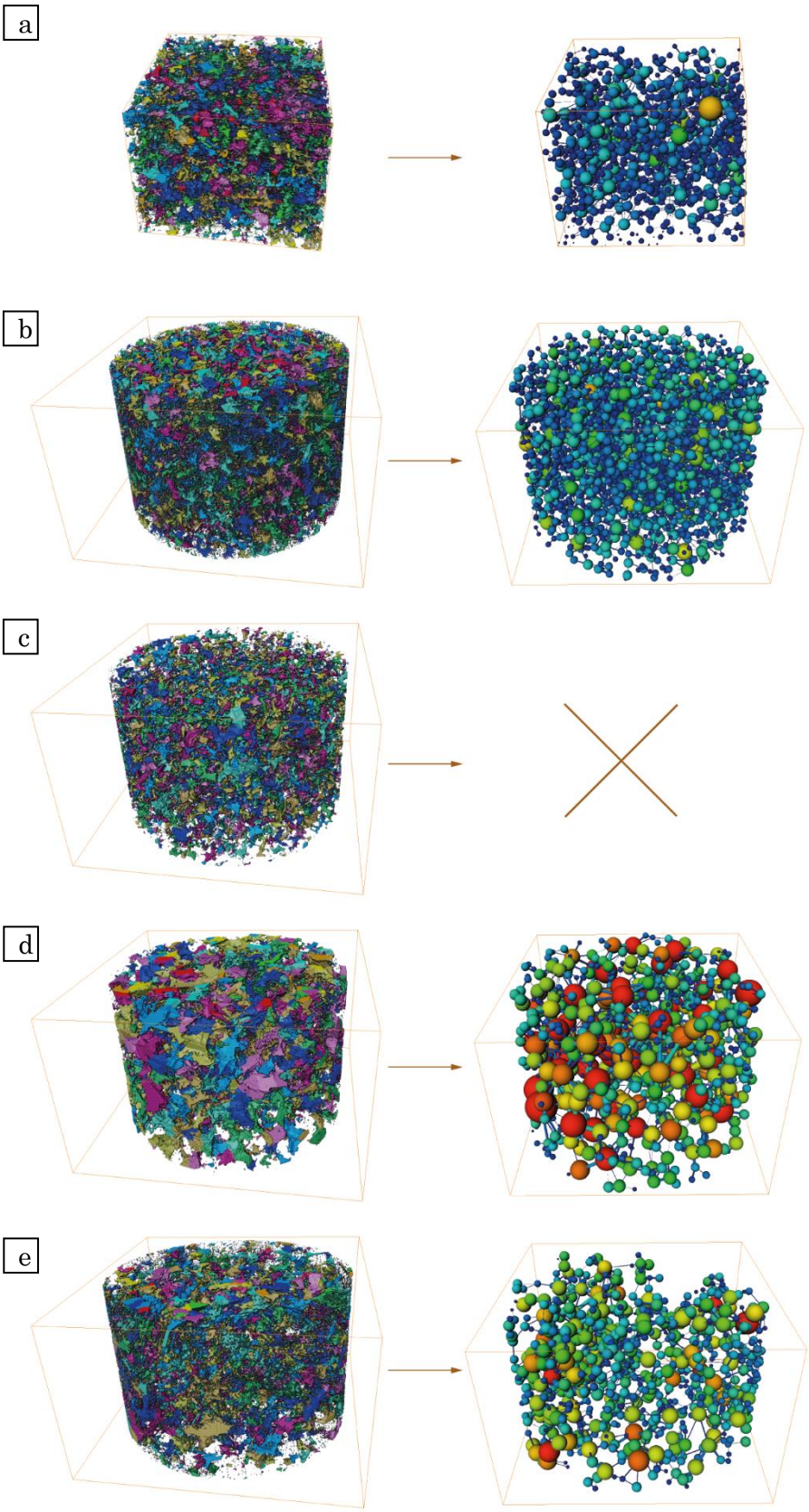

Figure 6.3. Separated pore model (left) was used to generate Pore Network Model (right), on which permeability simulation was then performed. No PNM was generated for sample 14270.9 where no pore connectivity was found. a) sample 14189.1, well 44/16-1, b) sample 14262.8, well 44/16-2, c) sample 14270.9, well 44/16-2, d) sample 16271.8, well 43/19a-4Z, e) depth 16276.4, well 43/19a-4Z. Blue colour in the PNM indicates the smallest pores and red the biggest.

6.3 Results

6.3.1 Heterogeneity analysis

Phase analysis in 3D allows to identify heterogeneity in mineral distribution or in pore network geometry. Figure 6.1 shows the analysed sandstones in different scales, from core (i), to CT (ii) and thin section (iii). The dark colours on low resolution CT scans on Figure 6.1(ii) indicate higher porosity, while lighter colours indicate dense material. Based on the core and CT images it appears that samples 14189.1 and 14270.9 (Figure 6.1 (i), (ii) a & c) are very homogenous along the Z axis, while samples 14262.8, 16271.8 and 16276.4 (Figure 6.1 (i), (ii) b, d & e) show some heterogeneity either in core (14262.8) or on CT image (16271.8 and 16276.4) on a mm- to cm-scale. Sample 14262.8 shows mm-scale lamination on the surface of the core; however, the CT scan reveals that the sample is internally homogenous. Using XMT, heterogeneity of all samples can be quantified on a micron scale, by analysing each slice (or projection) of the model individually. Figure 6.4 shows heterogeneity analysis on the

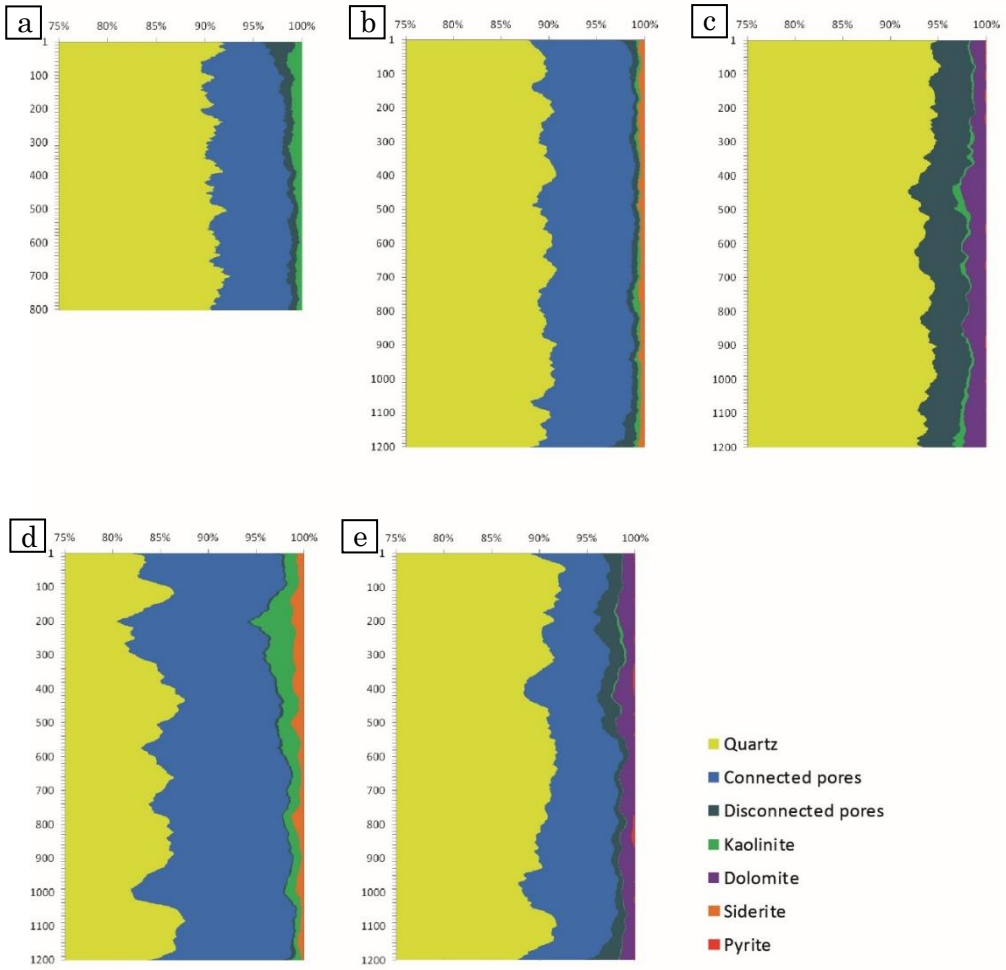

Figure 6.4. Area fraction analysis on all slices in vertical direction on *xz* plane. a) 14189.1, well 44/16-1, b) 14262.8, well 44/16-2, c) 14270.9, well 44/16-2, d) 16271.8, well 43/19a-4Z, e) 16276.4, well 43/19a-4Z. X axis starts on value 75% for better visibility. The area between 0-75% is occupied by quartz.

xz plane. Each analysed slice (see Figure 6.2) is 2.5 μm thick and area occupied by each segmented phase measured on every slide is shown on Figure 6.4. The content of each phase present in samples 14189.1, 14262.8 and 14270.9 is rather uniform, never showing more than 4.6% variation. In samples 16271.8 and 16276.4, however, content of quartz and connected pores ranges throughout the slices by 5.5-7.6%.

Analysis of connected porosity on each slice shows that standard deviation values are the highest in the coarse-grained samples 16271.8 and 16276.4 ft (Table 6.2). Sample 12462.8, despite showing lamination on core surface (Figure 6.1b), does not show any heterogeneity on the CT scan or in the slice analysis, having the lowest standard deviation of porosity values of all samples.

	14189.1	14262.8	16271.8	16276.4
min [%]	4.1	7.7	9.9	4.4
max [%]	8.7	10.3	15.6	10.3
mean [%]	7.3	8.9	12.7	6.7
standard deviation [%]	0.8	0.6	1.3	1.3

Table 6.2. Connected porosity statistics through all slices as shown on Figure 6.4: min = lowest porosity registered on one slice, max = highest porosity registered on slice, mean = mean porosity from all slides. Sample 14270.9 is not shown as no connected porosity exists in the model.

6.3.2 Phase analysis

Based on the knowledge of the mineral phases occurring in petrographic thin sections (Table 6.3), and the densities of those identified phases, the same minerals were identified on the 3D XMT models.

Well	44/16-1	44/16-2	44/16-2	43/19a-4Z	43/19a-4Z
Depth (ftDD)	14189.1	14262.8	14270.90	16271.8	16276.4
Quartz	74.0	73.3	75.3	62.7	60.6
Feldspar	2.0	2.0	0.3	1.7	0.7
Rigid rock fragments	1.0	9.3	6.3	0.7	1.3
Heavy minerals	1.3	0.7	0.7	0.0	tr
Optically non-resolvable detrital clay	0.7	0.3	0.0	0.0	0.0
Quartz overgrowths	13.3	7.7	12.0	5.3	12.3
K-feldspar overgrowths	0.0	0.3	0.0	0.0	tr
Dolomite cement	0.0	0.7	1.0	1.0	2.6
Siderite	0.0	0.0	0.3	17.3	0.3
Pyrite cement	tr	0.3	0.3	0.0	2.0
Residual oil	tr	tr	0.3	0.0	0.0
Optically non-resolvable pore-lining clay	0.0	0.0	0.0	0.0	2.0
Kaolin	1.0	1.0	0.3	5.7	3.0
Macroporosity	6.7	4.3	3.0	5.6	15.0
primary intergranular porosity	5.3	4.3	3.0	2.3	7.7
secondary porosity	1.3	0.0	0.0	3.3	7.3
calculated microporosity	1.1	4.3	1.5	7.0	0.0
Horizontal He porosity (%)	7.80	8.60	4.50	12.6	8.7
Horizontal permeability (mD)	0.28	18.00	0.23	691	59.6

Table 6.3. Point counting results. tr = trace.

However, some simplifications had to be applied; because of (a) the similar densities of kaolin and illite (2.63 and 2.8 g/cm^3), (b) small individual crystal thickness that is often below scanning resolution, (c) the co-occurrence of kaolin and illite in the same areas, and (d) the fact that microporosity is present between clay crystals, the density for voxels in the area of kaolin and illite co-occurrence is a mean value of kaolin, illite and microporosity. This makes it difficult to distinguish kaolin and illite, and therefore they grouped together into one 'clays' phase in the model in those samples where both types of clay are present. Due to the fine nature of illite strands and their wispy shape, some of the illite might have been lost during scanning and processing, as the strands can be smaller than scanning resolution of 2.5 µm. Carbonate phases, which include non-ferroan dolomite (specific gravity 2.84 – 2.86 g/cm^3), ferroan dolomite/ankerite (specific gravity of ankerite 2.93 – 3.10 g/cm^3) and dolomitised

siderite to pure siderite (specific gravity of pure siderite: 3.96 g/cm^3), were also combined in XMT models due to the overlap between their densities. Petrographic analysis shows that siderite is only a very minor constituent of sample 16276.4 (0.3%) and is absent in 14262.8, and in sample 16271.8 no dolomite was recorded. Table 6.4 and Figure 6.5 show the results of XMT phase analysis, compared to point counting data on thin sections.

	Sample depth [ft]	Petrography [%]	XMT [%]
Pores	14189.1	7.8	8.2
(connected pores)			(7.3)
	14262.8	8.6	9.5
			(8.9)
	14270.9	4.5	4
			(0)
	16271.8	12.6	12.9
			(12.7)
	16276.4	15	7.9
			(6.7)
Quartz	14189.1	90.3	89.8
	14262.8	92.3	88.8
	14270.9	93.9	92.8
	16271.8	70.4	83.2
	16276.4	74.9	89.8
Kaolin	14189.1	1	0.8
	14262.8	1	0.3

	14270.9	0.3	0.3
	16271.8	5.7	1.4
	16276.4	3	0.1
Dolomite + siderite	14189.1	-	-
	14262.8	0.7	0.5
	14270.9	1.3	1.7
	16271.8	18.3	0.7
	16276.4	2.9	1.3
Pyrite	14189.1	trace	0
	14262.8	0.3	-
	14270.9	trace	0.3
	16271.8	-	-
	16276.4	2	0.1

Table 6.4. Comparison between XMT phase analysis and petrographic point counting.

The minor amounts of feldspars that were observed in thin sections were not distinguished in XMT due to their densities being similar to quartz; feldspars and quartz were therefore grouped together. Because phase recognition on XMT images is based purely on differences in mineral densities, it is not possible to distinguish between detrital and authigenic quartz.

Pores were easily distinguished from all mineral phases; however, the smallest pore throats, that are the size of scanning resolution (2.5 μm) and smaller, might not always have been accurately resolved.

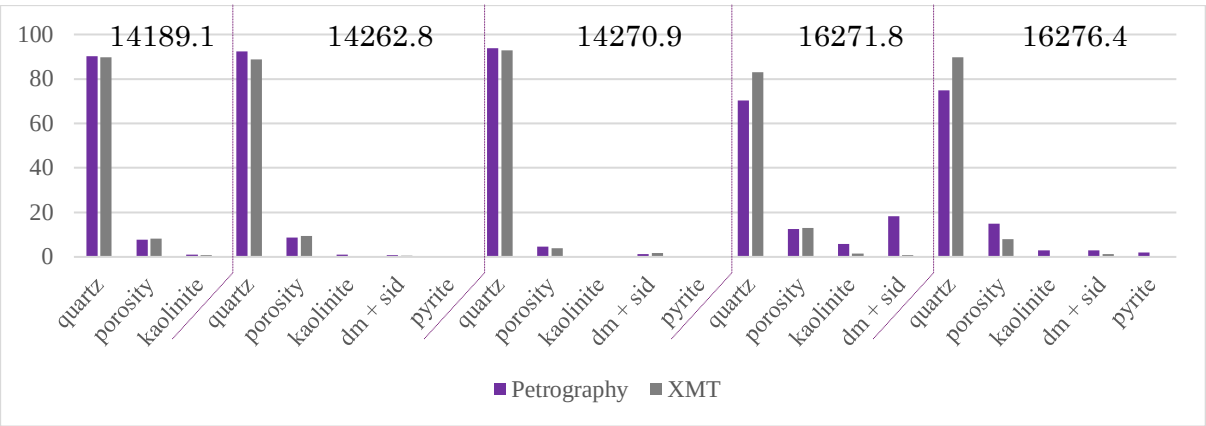

Figure 6.5. Comparison between XMT and petrography phase analysis.

Comparison of results obtained from XMT and petrography shows that XMT is in a very good agreement with petrographic results in those samples that display high homogeneity (14189.1, 14262.8 and 14270.9). Differences of up to two orders of magnitude are however observed in heterogenous samples (16271.8 and 16276.4). The largest difference is observed in carbonate distribution in 14271.8, where petrography shows 18.3% of dolomite, while XMT shows only 0.7%, clearly indication that thin section was slices through a dolomite patch that was not crossed by the XMT sample material.

6.3.3 Porosity and permeability modelling and measurements

The specific advantage of XMT over methods such as petrography of SEM is that XMT allows to reconstruct models in 3D, which allows to look at pore connectivity, that would not be captured on a 2D image. The modelling software allows to separate the all-important connected pore network from isolated pores, which are ineffective for any fluid transport. Both connected and disconnected pores can then be quantified, and the connectivity of the pore network analysed.

Separating all pores connected along Z axis into individual objects allows to generate a pore network model where pores are represented as balls and throats are represented by sticks connecting the pores (Figure 6.3). An algorithm inbuilt in Avizo™ allows for properties generation during pore network modelling, where the output are permeability values for the analysed pore networks. These Avizo modelled permeabilities were compared to laboratory measured values in order to verify their accuracy and/or determine how sandstone heterogeneity affects fluid flow through these sandstones. Table 6.5 and Figure 6.6 show the comparison of porosity and permeability results from different methods. In addition, permeability and porosity

values from nearby core plugs are shown to verify whether the core is heterogeneous on a cm-scale.

	Porosity [%]					Permeability [mD]		
Depth [ft]	Meas.	XMT (all porosity)	XMT (connected porosity)	Meas. nearby plug	Point counted macro-porosity	Meas.	XMT	Meas. on nearby plug
14189.1	8.4	8.2	7.3	7.8	6.7	3.8	19.2	0.3
14262.8	10.0	9.5	8.9	8.6	4.3	11.5	33.2	18.0
14270.9	6.2	4.0	0.0	4.5	3.0	0.37	0.0	0.2
16271.8	13.0	12.9	12.7	12.6	5.6	13.4	1456	691
16276.4	12.1	7.9	6.7	8.7	15.0	20.5	126	59.6

Table 6.5. Comparison of porosity and permeability values obtained through different methods: He porosity and permeability measured on core plugs, porosity and permeability modelled on 3D XMT volumes, measured on plugs located a few centimetres away from the XMT plugs, and point counted on thin sections. Plugs measured in this study and corresponding XMT models are shown in bold. Meas = measured.

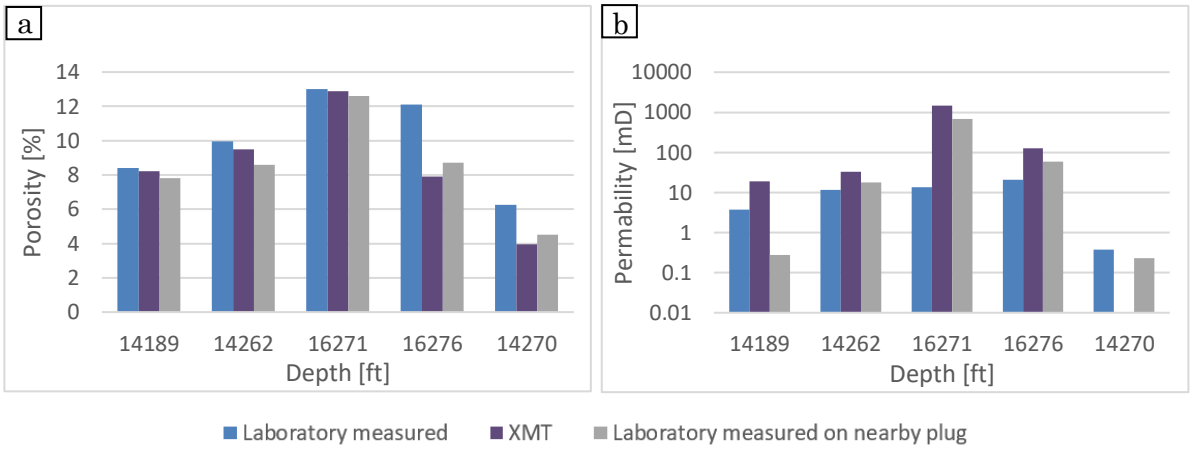

Figure 6.6. Comparison of a) porosity and b) permeability values measured on core plugs, modelled on 3D XMT volumes and measured on plugs located a few centimetres away from the XMT plugs.

The porosity results are largely consistent across the different measurement methods, and similar between the core plugs analysed in this study and those a few centimetres away from our material. The laboratory measured porosity is consistently better matched to the total porosity modelled in XMT (Table 6.5, in bold), rather than the connected porosity, as helium will readily move through pore throats much smaller than those resolvable using XMT.

Macroporosity measured by point counting of thin sections typically displays lower than He porosity values, but it does not take into account microporosity, which is included in other methods. The plugs measured in this study and the nearby plugs vary slightly, showing that there is some cm-scale variation in porosity. The highest

difference in porosity (3.4%) in plugs is recorded in sample 16276.4, which also had one of the highest standard deviation values on a μm- to cm-scale (CT sample size, Table 6.2).

Modelled and measured permeability values are within reasonable agreement, within the same order of magnitude of within one order of magnitude difference, with the difference between two methods ranging from 0.38 mD to 106 mD. The only exception is sample 16271.8, where the difference between the two methods is two orders of magnitude, (13.4 mD vs.1456 mD). Such a large difference is caused by heterogeneity which is clearly seen on low-resolution CT scan of core plug (Figure 6.1d) and is indicated by the highest standard deviation value on the slice area analysis (Table 6.2). Modelled permeability in sample 14270.9 is 0 mD, as no connectivity through the pore network was found in the generated model. This is not in exact agreement with laboratory measurement, which shows that poor pore connectivity exists through the sample, the result is not distant from the measured value that shows only 0.38 mD of permeability.

The knowledge of anisotropy in analysed deposits is important in reservoir characterisation. While area fraction analysis (see section 6.3.1) gives an indication of homogeneity of the material in vertical direction, it does not show how much this can affect permeability and fluid flow in other directions. To investigate this, we ran permeability simulations in three directions: x, y and z in two of the samples, 14270.9 and 14189.1. Permeability values are similar in all directions in sample 14189.1 and are 0 mD in all directions in sample 14270.9, showing that both samples are isotropic.

6.3.4 Pore network microstructure

After segmenting all mineral phases and pores, the pore network microstructures were analysed in each sample. Pore radius, volume, area, location, coordination number (number of throats connected to a pore body), throat radius, length and flow rate per second can all be extracted using the pore network model. Table 6.6 summarises the numbers of pores and throats identified in each sample, and shows the minimum, maximum and mean coordination number. Because the analysed volume of sample 14189.1 is 3.6 times smaller than that of all other samples (see Table 6.1), results of the analysis have been 'normalised' to the same volume (i.e. multiplied by a factor of 3.6). Plots displaying the pore, throat and coordination number distribution are shown on Figure 6.7.

		14189.1	14262.8	16271.8	16276.4
Pores	Number of pores	1341 (4838)	2977	933	965
	Mean pore radius [µm]	43.1	63.9	95.4	82.9
	Max pore radius [µm]	155.7	163.0	307.7	216
	Connected porosity [%]	7.3	8.9	12.7	6.7
Throats	Number of throats	1530 (5520)	4799	1819	1347
	Mean throat radius [µm]	11.7	15.2	36.5	33.8
	Max throat radius [µm]	81.6	120.4	234.2	207.7
	Most frequent throat size [µm]	5-7.5	5-7.5	7.5-10	10-12.5
Coordination number	Mean coordination number	2.3	3.2	3.9	2.8
	Max coordination number	12	16	16	11

Table 6.6. Pore, throat and coordination number statistics in the extracted pore network models. Numbers in brackets in sample 14189.1 are normalised to the same volume size as in the remaining samples. Sample 14270.9 is not included as no connected pores were detected in any direction, and a pore network model cannot be generated

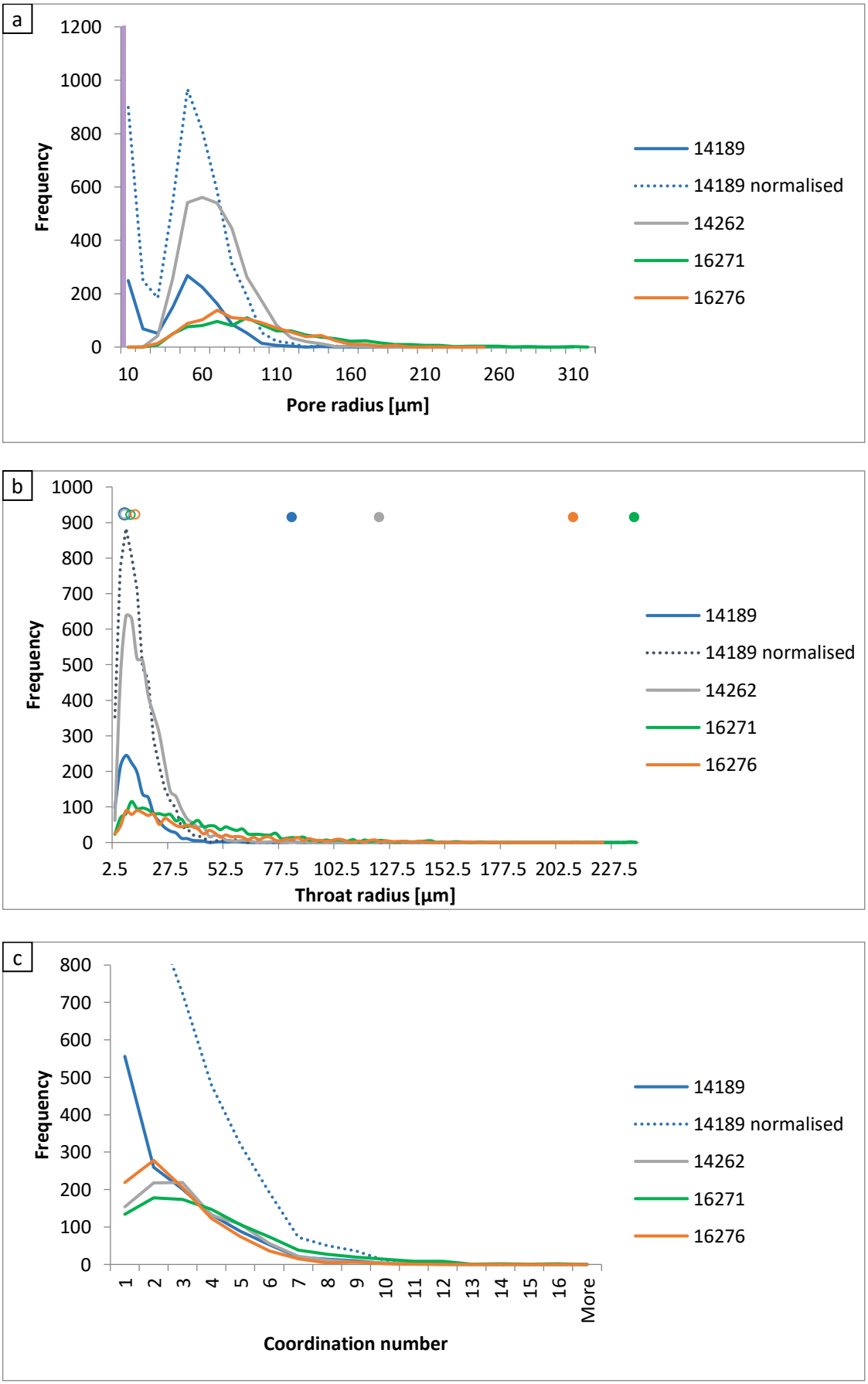

Figure 6.7. a) Pore radius, b) throat radius and c) coordination number distribution. Thin purple area in the low values of pore and throat radii (plots a & b) shows an area of potentially poorly resolved properties, caused by scanning resolution limitations. Open circles on plot b show most frequent throat size and full circles show maximum throat size.

Small pore throats of >5 to 12 μm are dominant in analysed samples, but all samples show skewness towards larger pores and throats. It must be borne in mind, that with an imaging resolution of 2.5 μm, pores and pore throats that are <~5 μm diameter will be underestimated. Sample 14189.1 shows a bimodal distribution of pores. The two samples with the finest grain size are characterised, unsurprisingly, by the smallest pores and throats, but also contain a considerably higher number of pores. It is important to point out is that samples with volumetrically highest porosity are the upper coarse-grained sample 16271.8 and the lower medium-grained sample 14262.8. Both are also characterised by the highest coordination number (Table 6.6). Yet, this does not necessarily translate into better pore connectivity and permeability. While permeability of sample 16271.8 is 1456 mD, the highest of all modelled values, sample 14262.8 has permeability of 33 mD, significantly less than another coarse-grained sample (16276.4), which is characterised by lower mean and maximum coordination numbers (Table 6). Neither is the high permeability of samples 16271.8 and 16276.4 caused by less cementation or lower amount of clays (Table 6.7).

	14189.1	14262.8	14270.9	16271.8	16276.4
Quartz overgrowths	13.3	7.7	12	5.3	12.3
Dolomite + siderite + pyrite	-	0.5	2	0.7	1.2
Clays	0.8	0.3	0.3	1.4	0.1
SUM	14.1	8.5	14.3	7.4	13.6

Table 6.7. Cement distribution. Values of dolomite, siderite, pyrite, and clays are from XMT analysis. Quartz overgrowths cannot be distinguished from detrital quartz by XMT, therefore values shown here are from petrographic measurements.

The common features that characterise the two high permeability samples are their upper-coarse grain size, and the widest pore throats, 2-3 times the size of the fine and medium grained samples. Yet, the modelled permeability in 16271.8 is an order of magnitude higher than for 16276.4 (see Table 6.5), despite its most frequent throat size being smaller and its mean throat radius being similar (Table 6.6). Helium porosities are almost the same but modelled connected porosities are very different. Table 6.6 and Figure 6.7c reveal that the reason behind the large difference in permeabilities in the two samples is pore throat distribution, specifically a larger overall number of throats in 16271.8, larger throat radia overall, aided by a higher

coordination numer. Sample 16276.4 has a higher overall quartz content (Table 6.4), therefore quartz cement is likely the reason for smaller pore throats in this sample.

6.4 Discussion

With increasing access to computed microtomography and its improving resolution, more researchers turn towards this technique to gain better understanding of pore microstructures, spatial distribution of cements, or how these factors affect permeability (e.g. Algive et al., 2012; Van Stappen et al., 2014; Kareem et al., 2017). XMT, unlike SEM or optical microscopy, allows to study material properties in three dimensions. Thin sections, or even SEM stubs, are not representative in heterogeneous material, only showing surfaces of small rock fragments. Even if thin section cuts across lamination and captures vertical variability in e.g. grain sizes or clay distribution within laminae, it cannot capture pore connectivity or distribution of what appear to be patchy cements in 2D. Some researchers attempted to simulate petrophysical properties based on the reconstruction of the 3D architecture of the rock sample from two-dimensional images (e.g. Wu et al., 2007; Van der Land et al., 2013). The advantage of this is wide accessibility and the possibility of achieving a nm-scale resolution (e.g. Sun et al., 2017), but the approach is subject to many assumptions and therefore fails to accurately represent the real rock. Computed tomography overcomes these issues and allows to visualise and numerically analyse rock properties on a micron scale, allowing for the most accurate analysis of internal characteristics of analysed material. Factors controlling permeability, a characteristic that is highly sensitive to the architecture of the porous microstructure, i.e. specific surface area, tortuosity, sizes of pore throats, numbers and sizes of pores, and the connectivity between pores (e.g. (Ehrlich et al., 1991; Martys et al., 1994; Golab et al., 2010; Gouze and Luquot, 2011) can only be accurately identified and assessed when a pore structure is imaged and analysed in 3D.

The technique obviously also has its limitations. These include for example operator dependency for the 3D image analysis from the reconstructed data, the discretations effects and possible imaging artefacts (Cnudde and Boone, 2013), as well as sample size which is critical for accurate representation of sample parameters (Botha and Sheppard, 2016; Ma et al., 2017a).

The results of this chapter show that an interplay of multiple elements controls permeability in the analysed sandstones. However, two factors stand out as the main elements responsible for reservoir quality variation. One is heterogeneity, caused by

the formation of thin, cemented horizons that form baffles for vertical fluid flow; the second is pore throat size distribution. These factors are discussed in more detail below.

6.4.1 Phase analysis

Computed microtomography was successfully applied to separate porosity and various minerals occurring in the analysed sandstones. The generated numerical models are an excellent base for further analyses e.g. of sample heterogeneity or computation of phase connectivity and phase evolution (see Chapter 7). Comparison of results from petrography, porosity, and permeability measurements and XMT modelling in homogenous samples are in very good agreement. At the same time, because XMT models can be analysed in three dimensions, they allow to analyse material heterogeneity which is the cause of the strong variability of reservoir quality in these tight sandstones.

6.4.2 Heterogeneity and cement distribution

When analysing micron-scale rock properties with computed microtomography care must be taken when upscaling the results from mm-scale samples into a core plug (cm-scale) or core scale (m-scale). In heterogeneous systems sample size is critical for accurate representation of sample parameters (Botha and Sheppard, 2016; Ma et al., 2017a). While larger samples are more representative of a heterogeneous system by providing greater sample coverage, a single measurement on such sample cannot indicate heterogeneity in any way, nor does it allow to measure it. Smaller samples can be analysed at higher resolution thus allowing for better representation of pore microstructure, however they are not representative of a heterogeneous system (Botha and Sheppard, 2016). Therefore, methods that complement each other are often utilised, allowing to obtain representative measurements on micro to macro scale and measure variability within the system (e.g. Pamukcu and Gualda, 2010; Ma et al., 2017a, 2017b; Lin et al., 2019). The importance of analysed volume size has also been shown by Auzerais et al. (1996) who analysed multiple subvolumes of different sizes of the same sample to show how inadequate sample size affects the porosity and permeability results.

To capture sandstone heterogeneity in this study several analytical methods were applied and samples from two neighbouring sites in the same sandstone bed were analysed. The results show that permeability values in the analysed tight Carboniferous sandstones from the Southern North Sea are highly variable. On a cm-

scale, differences of two orders of magnitude were found, owing to the heterogeneous distribution of siderite cement in sample 16271.8. While previous chapters (see Chapters 3 and 5) show that siderite overall is only a volumetrically minor cement, and highly subordinate to ubiquitous quartz overgrowths, its presence in thin horizons in those already tightly cemented sandstones forms a flow baffle that can turn very high quality reservoir (1456 mD) into a rather poor one (13.4 mD) over a distance of less than 10 cm (see sample 16271.8, Table 6.5). In this sample the sideritic horizon is associated with organic matter occurring at the top of a fining upward fluvial sandstone bed. Such high heterogeneity occurring on a cm-scale has tremendous implications for permeability distribution and reservoir quality on a reservoir scale. The obvious destructive impact this has on transport properties in vertical direction can turn any promising prospects into extremely risky and difficult one. However, a careful analysis of siderite and other cements distribution in the fluvial and delta plain sandstones, their origin and lateral connectivity, can give an invaluable insight into the system's vertical connectivity.

In texturally homogenous samples, such as e.g. the lower medium grained sample 14262.8 and upper medium grained sample 14270.9, the total amount of cement is crucial for preservation or destruction of reservoir quality. These two samples show similar cementation patterns, with predominant quartz cement and minor amounts of dolomite, siderite and kaolin (see Appendix 3) and very similar values of cementational porosity loss and compactional porosity loss (see Chapter 3). Yet, one of them shows a reasonably good reservoir quality (sample 14262.8 with 33.2 mD and 11.5 mD modelled and measured permeability respectively) and the other has negligible reservoir quality (sample 14270.9, 0 mD and 0.37 mD modelled and measured permeability respectively), despite its slightly coarser grain size. The main difference between these two samples is in the amount of quartz overgrowths which is 7.7% in the former and 12.0% in the latter (petrography values), largely occluding pore throats in the more cemented sample (14270.9) and leading to significant reservoir quality reduction. As a result of stronger quartz cementation, recorded porosity values are lower in 14270.9 than in 14262.8 (9.5% and 4.0% respectively XMT modelled total porosity) and coordination number is 0 (compared to mean coordination number of 3.2 in 14262.8) as no throughout connected porosity is detected.

6.4.3 Pore network analysis

Results of this study show that XMT images can be successfully used to model pore network and mineral phase distribution and to compute effective permeability. To

minimize the errors associated with textural heterogeneity a set of samples of different sizes is required to capture the heterogeneity, and needs to be imaged at low to high resolution in order to capture a full range of structures and pores (e.g. Botha and Sheppard, 2016). Capturing and understanding reservoir heterogeneity from micron to metre scale is crucial for successful development of any potential prospect. Results of this study show that using samples of different sizes scanned at different resolutions is well-suited for the purpose. The measured and modelled permeabilities and porosities are similar in homogenous samples, showing that the applied scanning resolution was sufficiently high to capture the pore throats that are critical for fluid flow. The only exception to this is sample 14270.9, where pores are connected from top to bottom, as proven by laboratory permeability measurements, which is not captured on the XMT model. This implies, that pores are connected through throats that are beyond the imaging capability. Furthermore, the laboratory measured porosity shows a better match with the total modelled porosity rather than modelled connected porosity, implying that the narrowest pore throats were not detected. In heterogenous samples, by analysing samples on different scales it is possible to first, show that heterogeneity exits and secondly, recognize its cause.

With scanning resolution of 2.5 μm, pores and throats below 5 μm in diameter might be poorly resolved. Permeability of 0 mD in the model of homogenous sample 14270.9 which does not match the laboratory measured value of 0.37 mD can be thus be explained by the fact that the fluid is either carried by throats that are below 2.5 μm wide, and possibly some that are >2.5 μm and <5 μm, or perhaps indeed no connectivity exists in this small size sample and that a larger volume is required to capture the flow pathways. In most conventional reservoirs, and unconventional reservoirs with permeabilities of at least a few milliDarcies as in this study, the resolution of 2.5 μm would suffice to accurately resolve the detailed pore microstructures. Beckingham et al. (2013) have shown that for samples analysed with a scanning resolution between 1.8 and 4 μm was the best to obtain most accurate permeability predictions, in samples of permeabilities in the Darcy range. Importantly, when applying a high resolution of 0.4 μm obtained by reconstructing pore network from 2D images, the models resulted in underestimation of permeability by four orders of magnitude, showing that applying adequate scanning resolution is crucial to obtaining accurate results. The good match between the modelled and measured permeabilities in this study indicates that the applied resolution was adequate for the more permeable samples. While channels <2.5 μm still exist in the more permeable samples, their contribution to the overall flow is minimal, so that not

detecting them does not significantly impact the modelled permeability values, as fluid flow is controlled by the largest connected channels (Auzerais et al., 1996; Zhang et al., 2018). However, the low permeability sample 14270.9 requires a higher resolution to capture the fluid conducting pathways. In tight gas reservoirs and other unconventional reservoirs, where pore throats are much narrower than in conventional reservoirs, very high scanning resolution is required to capture the smallest pores and throats. With oil molecule size being 0.01 - >0.001 μm (10 - 1 nm) and gas molecules of <0.001 μm (Nelson, 2009) a method that can characterise pores of that size would be required to accurately resolve possible fluid flow paths in tight and other unconventional reservoirs. Such methods could include synchrotron tomography (resolution limit 10 nm; Boller et al., 2017), mercury injection (lower resolution limit of 3.5 nm), or small-angle neutron scattering (lower resolution limit of 1 nm), computational chemistry (lower resolution limit of 0.1 nm) (Nelson, 2009) or focused ion beam scanning electron microscopy (FIB-SEM) (nanometre resolution, e.g. Gu et al. (2015)). These methods are typically applied to characterise shale reservoirs and seals.

Factors such as overall porosity, number of pores, mean and maximum pore size, mean, maximum and most common throat size, and mean and maximum coordination numbers were all analysed in this study. The highest permeability was found in the most porous sample (16271.8, ϕ 12.9%, k: 1456 mD); however, the results have shown that the overall porosity is not the most significant control on permeability. The example of samples 14189.1 and 16276.4, which have very similar porosities of 7.9% and 8.2% respectively, and permeabilities of different orders of magnitude: 19.2 mD and 126 mD, shows that factors other than overall porosity are more important. The volume of cements is very similar in both samples (Table 6.7). The clear difference between these samples is their grain size (see Table 6.1; 14189.1 is upper fine-grained, while 16276.4 is upper coarse-grained). This is accompanied by larger pore sizes and, as shown in Table 6.6 and Figure 6.3, also by wider pore throats and thus higher permeability (14189.1: avg. pore radius: 43.1 μm, avg. throat radius: 11.7 μm, perm.: 19.2 mD; 16276.4: avg. pore radius: 82.9 μm, avg. throat radius: 33.8 μm, perm.: 126 mD). Similarly, a comparison between two upper coarse-grained samples: 16271.8 and 16276.4 shows that the one with overall higher number of larger pore throats (16271.8; Figure 6.7b), has permeability value an order of magnitude higher, owing to a lower content of quartz cement.

In the analysed samples factors paramount for high permeability are the high number of the largest pore throats, rather than the size of the most frequent throat size

(compare samples 16271.8 and 16276.4, Table 6.6). Interestingly, higher pore coordination number, i.e. the number of throats connected to each pore, is not associated with increased permeability values, if not accompanied by larger throat sizes (see samples 14262.8 and 16276.4, Table 6.6). These results corroborate findings of other authors who argue that pore architecture is an important control on permeability (Ehrlich et al., 1991; Golab et al., 2010; Martys et al., 1994) and imply that standard methods directly relating permeability to porosity are not enough to envisage permeability values will be for a given porosity. Grain size and quartz cement volume determine the final pore throat size distribution, however other cements, connected porosity volume and coordination number also play a role, therefore the relating permeability to one single element is not sufficient to determine reservoir quality controls.

This chapter focused on porosity and blocky cement distribution (quartz overgrowths, siderite, dolomite. Yet, from the previous chapters (Chapters 3 and 5), it is known that detrital and authigenic clays are also very important controls on permeability in Copernicus and Cavendish sandstones. However, in the samples analysed in this chapter the volume of clay does not exceed 1.4% in any of the samples, therefore its effect on pore network and fluid flow cannot be accurately evaluated, and further work would be required to understand how clay distribution affects fluid flow on a micron scale.

6.5 Conclusions

-X-ray computed microtomography (XMT) is a useful tool in geosciences that grants the capability to accurately characterise and measure the 3D rock structure at resolutions down to a few microns. As the digital images processed by the 3D modelling software are numerical models, they are available for numerical computation of the material properties such as e.g. permeability.

-In homogenous materials XMT can be used to predict rock properties where direct measurements are not possible e.g. when the quality or amount of available material is not suitable for laboratory analysis .

-Mineral distribution, porosity and permeability can be predicted from XMT models within an accuracy of a few percent in case of phase distribution, and an order of magnitude for permeability even for the fine-grained samples with very narrow pore throats, as long as the analysed phases are above the resolution limit.

-In some tight sandstones where pore throats, which are crucial for accurate determining of permeability, are below the scanning resolution fluid flow paths cannot be imaged and permeability modelling is not possible.

-The largest the difficulty of understanding and thus predicting permeability problems are posed by material heterogeneity, rather than modelling accuracy. Due to a small sample sizes that can be scanned at high resolution and computational power required for processing only very homogenous material can be well represented by 3D models of small samples. However, combining quantitative petrography and pore network analysis allows to unravel controls on permeability that can be observed on a micron to cm-scale.

-XMT allows to capture and measure material heterogeneity on μm- to cm-scale when XMT results of one sample are compared with measurements on a nearby sample or compared with parameters measured on larger sample using other methods (such as Helium porosimetry, permeametry, petrographic modal analysis)

-The results of this study show that in the analysed suite of samples from the Copernicus gas discovery and Cavendish gas field samples with nearly identical porosity can vary extensively in their internal microstructure resulting in permeability differences varying be orders of magnitude over a small area (even on cm-scale) due to cementation heterogeneity of volumetrically minor cements, such as siderite. Distribution of these volumetrically minor cements is critical for reservoir quality therefore their spatial continuity should be assessed. If such cements form laterally widespread horizons, they can lead to internal vertical compartmentalisation of reservoirs, rendering the reservoir virtually ineffective. This chapter shows how a sideritic horizon associated with organic matter occurring at the top of a fining upward sandstone bed changes permeability of this bed from 1456 mD to 13.4 mD over a distance of less than 10 cm, having tremendous implications for permeability distribution and reservoir quality on a reservoir scale. XMT analysis of cement distribution gives an invaluable insight into the system's vertical connectivity.

-Factors such as overall and connected porosity, number of pores, mean and maximum pore size, mean, maximum and most common throat size, and mean and maximum coordination numbers were all analysed in this study. Of these, pore throat size distribution, which is generally associated with grain size, is the most important aspect controlling permeability, rather than coordination number or connected porosity volume, although all elements contribute to permeability value.

-Major differences in permeability values are recorded in samples that are similar in terms of grain size, but where pore throat radius is reduced by significant quartz cementation.

CHAPTER 7:

Permeability evolution of sandstones using X-ray tomography and quartz cement modelling

7.1 Introduction

Pore architecture and networks control fluid flow in porous media, and changes in pore structure and connectivity as a function of time or changing temperature exert a critical influence on the evolution of permeability in natural and human-made materials including rocks, building materials and ceramics (Gallé and Sercombe, 2001; Cheadle et al., 2004; Ashwell et al., 2015). For sandstones, the focus of this study, permeability and pore geometries are of interest in the context of a range of applications including the effectiveness of water, hydrocarbon, geothermal and CO_2 storage reservoirs (e.g. Medina et al., 2011; Bertoncello, 2013; Regenspurg et al., 2015).

Whilst recent technological advances in X-ray micro-tomography (XMT) make direct 4D observations (3D + time) of pore network evolution possible in certain circumstances (Bultreys et al., 2016a; Dobson et al., 2016; Powierza et al., 2019), most geological processes are far too slow to be observed in the laboratory. In these cases, modelling approaches are therefore required to generate insights into the likely temporal changes in porosity, pore networks and permeability.

Standard, empirical or theoretical methods that relate permeability reduction directly to porosity loss work with large suites of samples or idealized geometries but are limited in that they do not capture real, detailed pore microstructure in a single location. Nevertheless, permeability is highly sensitive to the architecture of the porous microstructure, i.e. specific surface area, sizes of pore throats, numbers and sizes of pores, and the relationships between pores and throats (e.g. Ehrlich et al., 1991; Martys et al., 1994). Current models which attempt to constrain the temporal evolution of permeability in rocks use synthetic, highly simplified pore or crystal architectures, either derived from 2D images (e.g. Van der Land et al., 2013; Prajapati et al., 2020) or developed using computer algorithms which simulate crystallization (Cheadle et al., 2004), or are purely theoretical (Wadsworth et al., 2016). Such models fail to capture the complex interaction between flow, pore geometry, cement growth and permeability evolution in natural systems.

Here, we exploit the capability of X-ray micro-tomography to quantify complex pore structures as inputs for pore-scale modelling of present-day transport properties. Next, we recognize that quartz is often the main pore-occluding cement in deeply-buried sandstones, developing on geological timescales at rates which increase predictably as well-constrained functions of temperature and quartz grain surface area (Lander et al., 2008; Walderhaug, 2000). Finally, by forward-modelling quartz

cementation, and simulating changes in the pore network as a function of the amount of quartz cement, we enable an estimation of the sandstone permeability development through geological time.

7.2 Present-day pore network and permeability

We define the present-day pore system of a fine-grained, quartz-rich sandstone with minor kaolin from an undeveloped tight gas discovery (Southern North Sea (SNS), depth of 4325 m). using an Xradia Versa 410 scanner. Operating at 120 kV and 10 W with a 12 s exposure time, the 3D image volume was reconstructed from 3201 projections with a voxel (3D pixel) resolution of 2.5 μm, before processing using Avizo™ software (ThermoFisher©). The mineralogy of the sample was determined by optical microscopy and SEM-EDS, and SEM-cathodoluminescence was used to map the distribution of detrital and authigenic quartz. Standard thresholding algorithms (Figure 7.1) were used to map the distribution of quartz, kaolin and porosity, and the connected and isolated porosity quantified. The permeability simulation was conducted using a Pore Network Model in which both pore body and throat networks are extracted from a representation of the pore space (Blunt et al., 2013) using the Avizo™ XPoreNetworkModeling Extension. A constant pressure gradient of 0.01 Pa/m is applied, and the simulation is run until steady state flow is achieved. Flow is laminar and slow compared with the sound speed in the simulated fluid, such that the flow is creeping and viscous, and Darcy's law is strictly valid. Permeability was then calculated with Darcy's law assuming laminar, steady-state flow of a single phase, incompressible fluid. Since computational limitations make it infeasible to perform permeability simulations on the entire (2000x2000x2000 voxel) XMT data set using a standard office workstation, a representative volume (same porosity as the bulk sample) of 1000x1000x800 voxel (or 2500x2500x2000 μm) of the pore network was defined. The segmented pore networks are provided as an electronic appendix (Wasielka and Dobson, 2019). Permeability derived from the XMT data is 0.019 μm^2 (19 mD), compared to the measured Klinkenberg-corrected permeability of 0.0038 μm^2 (3.8 mD; measured at 3.45 MPa (500 psi) net stress, using a steady-state permeameter at Leeds University, UK; see McPhee et al., 2015). The relationship between fluid flow rates and driving fluid pressure gradients was found to be linear over a wide range of pressure gradients, and so no Forchheimer correction was necessary, and Darcy's law applies. Our measurements show a weak positive relationship between calculated apparent permeability and the inverse mean pore fluid pressure, which implies that Klinkenberg effects may play a role. We therefore applied a Klinkenberg correction to

our data, but note that it is a minor correction (0.3 mD) in our case. The small difference (15.2 mD) between simulated and measured permeability values most likely arises from the effect of simplifications in the model (nodes represent pores, links represent throats) and the different volume over which the permeability is assessed, although the image processing methodology, imaging resolution, and the effect of confining pressure for the measured permeability may also have small effects. The model was also validated using the lattice-Boltzmann method (see Wadsworth et al., 2017), which was in very good agreement with XMT modelling results, yielding values of 0.022 μm^2 (22 mD).

Maximum voxel size should be at least half the size of a feature that needs to be resolved: with an image resolution of 2.5 µm, pores and pore throats < ~5 µm diameter might be poorly determined. While it is possible to acquire XMT data at higher spatial resolution, the associated reduction in scan volume means the pore network would not be representative. Gas molecule diameters are < 1 nm and will therefore pass through pore throats beyond the resolution of any imaging method. However, since permeability is largely controlled by the widest pore throats (Zhang et al., 2018) and occurs through pore throats that are > 4 voxels in diameter (11-15 µm wide), image resolution does not have a significant effect on the image-based permeability determination in the presented sample.

For the purpose of this study, a uniform layer of quartz cement was backstripped around the detrital grains to simulate reversed quartz cementation, however it is acknowledged that this is a simplification of natural quartz cement growth habit. Quartz overgrowths grow rapidly on noneuhedral c-axis surfaces until they each reach euhedral termination, at which point the growth rate slows down (Lander et al., 2008).

.

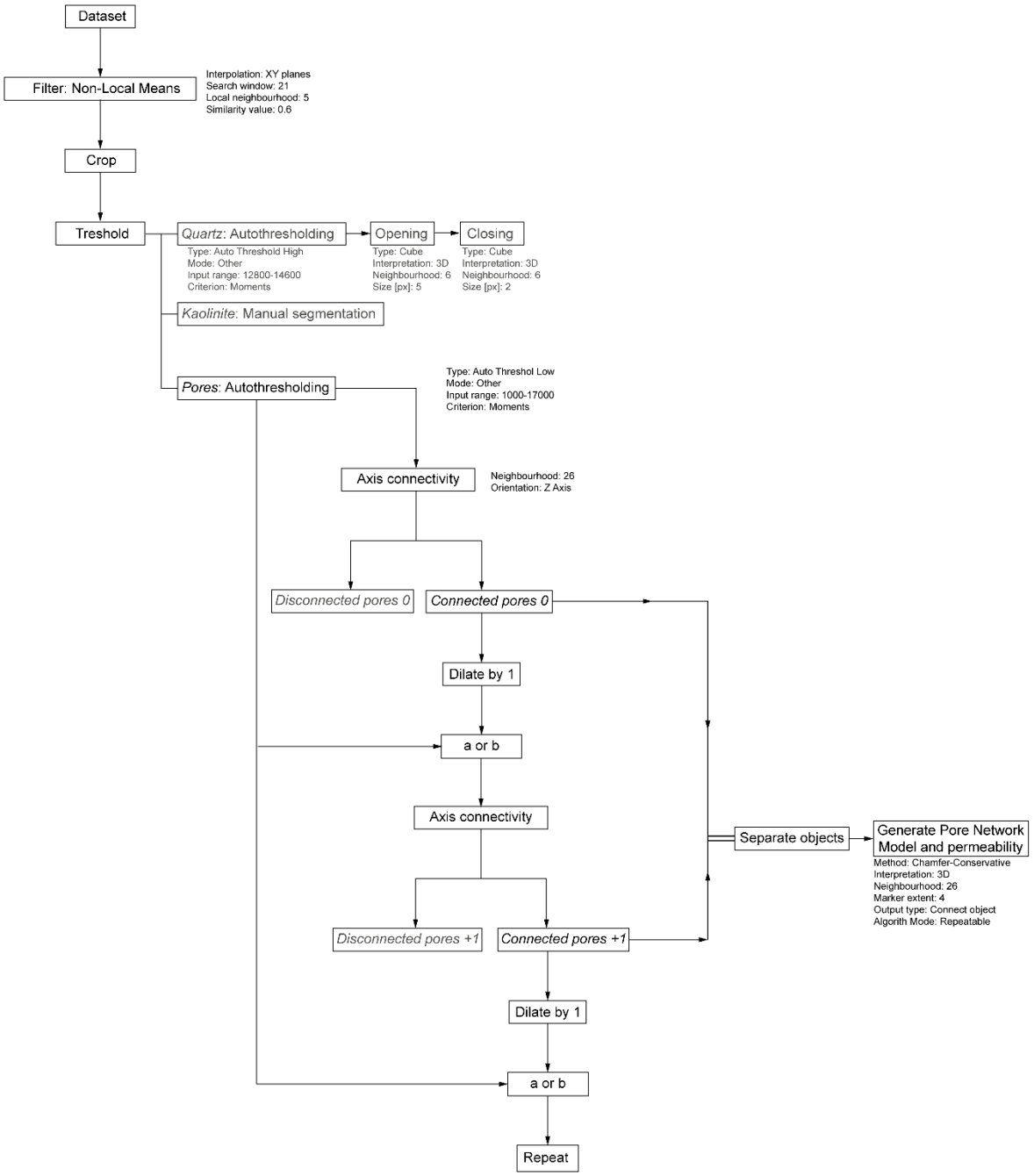

Figure **7**.1. Avizo processing workflow.

Since the orientation of crystallographic axes in individual grains cannot be extracted from XMT data, the results of this simulation are only approximations. Additionally, the type of detrital quartz grain: monocrystalline or polycrystalline, has been shown to impact the cement textures and volume (Lander et al., 2008), but distinguishing the two types cannot be achieved with XMT. However, petrographic observations show that monocrystalline quartz forms 91% of all detrital quartz grains, therefore the effect of type of quartz grain on the presented sample is insignificant.

7.3 Palaeo-permeability

The sample selected for this analysis is a 'clean', quartz-rich sandstone with minor amounts of feldspar, kaolinite and pyrite. It was selected because it is a good representation of fluvial and delta plain samples analysed in this study, and because of its simple composition with quartz, which is the cement of interest in this part of the study, being the dominant control on fluid flow, with little interference from other cements. The XMT model shows that quartz forms 91 vol.% of the sample, kaolin 0.8 vol.% and connected porosity 7.3 vol.%, which is in agreement with the petrographic analysis which shows 87.3 vol.%, 1.0 vol.% and 7.8 vol.% for quartz, kaolin and total porosity, respectively (Table 7.1; Figure 7.2). Having defined a representative sub-region of the present-day pore network and identified the connected and isolated pores within that network, we next perform a stepwise numerical removal of the quartz overgrowths through numerical dilation of the 3D pore volume (Figure 7.1). Cathodoluminescence analysis shows that quartz overgrowths are 7 - 100 μm thick where facing open pores and are continuous on all detrital grain surfaces (no gaps in quartz overgrowths were observed; Figure 7.3).

	Quartz [%]	**Kaolin [%]**	**Porosity %**	**Other [%]**
Point counting	**87.3** 74 detrital 13.3 cement	**1**	**7.8** 6.7 macroporosity 1.1 microporosity	**3.9**
CT	**91**	**0.8**	**8.2** 7.3 connected 0.9 disconnected	

Table 7.1. Comparison between point counting and XMT phase analysis. Category 'Other' includes feldspar, quartz-rich lithic fragments, heavy minerals, and detrital clay.

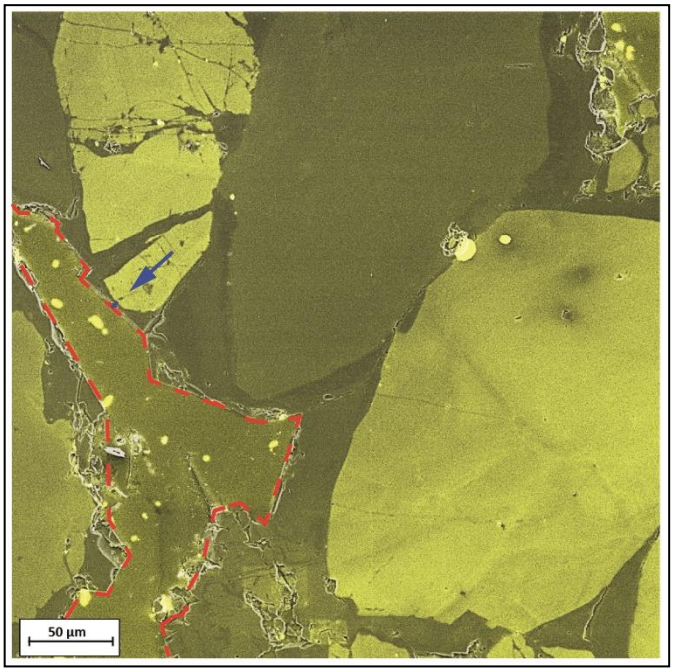

Figure 7.2. CL image showing quartz overgrowths (dashed red line) precipitated upon detrital quartz grains. The overgrowths are continuous around the grains and are 7 – 100 µm thick. The blue line (arrowed) is about 7 µm long.

Four steps of quartz erosion (or pore dilation) were applied, with each step removing a uniform layer 2.5 µm thick (Figure 7.4). Detrital and authigenic quartz cannot be distinguished by XMT, so in the final step some parts of the network might, locally, experience erosion of the detrital grains; however, the effect of this on permeability will be small. At each step the erosion is applied only along the surfaces of the connected pore network: the quartz-pore interfaces of the disconnected porosity remain unchanged. If the erosion captures a disconnected pore volume, erosion also occurs along that newly connected surface in the subsequent steps. Although quartz precipitation from solution in disconnected pores is still possible if the p-T-conditions change during burial or exhumation, the volumes formed are likely negligible given the available amounts of reactants. Kaolin evolution was omitted in this simulation due to its insignificant amount (0.8%) and different precipitation rates to quartz, however backstripping of multiple cements can be implemented in future models if called for in a sample with more complex composition. The results of gradual back-stripping of quartz cement show how the pores and pore throats widen with each step and how isolated pores eventually reconnect to the pore network (Figure 7.4).

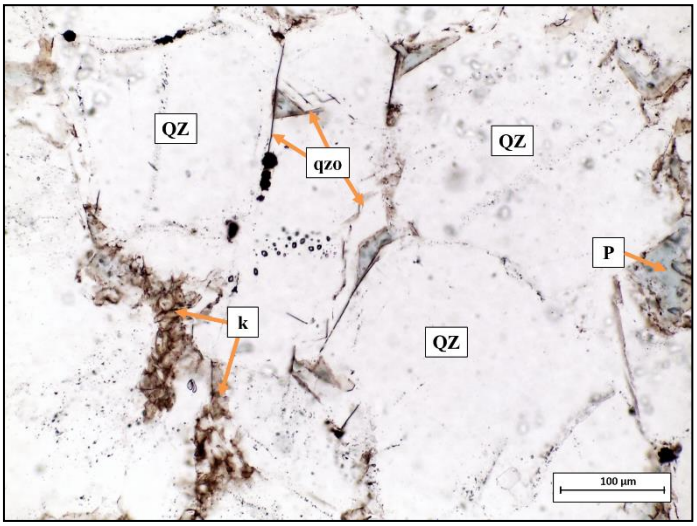

Figure 7.3 Thin section micrograph showing detrital quartz grains (QZ), quartz overgrowths (qzo), kaolin (k) and pores (P).

Analysis of the pore networks after each of the four steps shows the evolving pore architecture and pore connectivity. Simulation of fluid flow through the pore network at each step results in a backwards-stepping permeability evolution of the sandstone through time. The specific advantage of using 3D XMT models for this method rather than traditional 2D thin section-based imaging, is that it more accurately identifies the connected and disconnected porosity at each step and captures new pore volumes during the erosion. With complex and tortuous pore geometries, erosion on a 2D model will often fail to reconnect a pore volume which becomes connected during a 3D erosion.

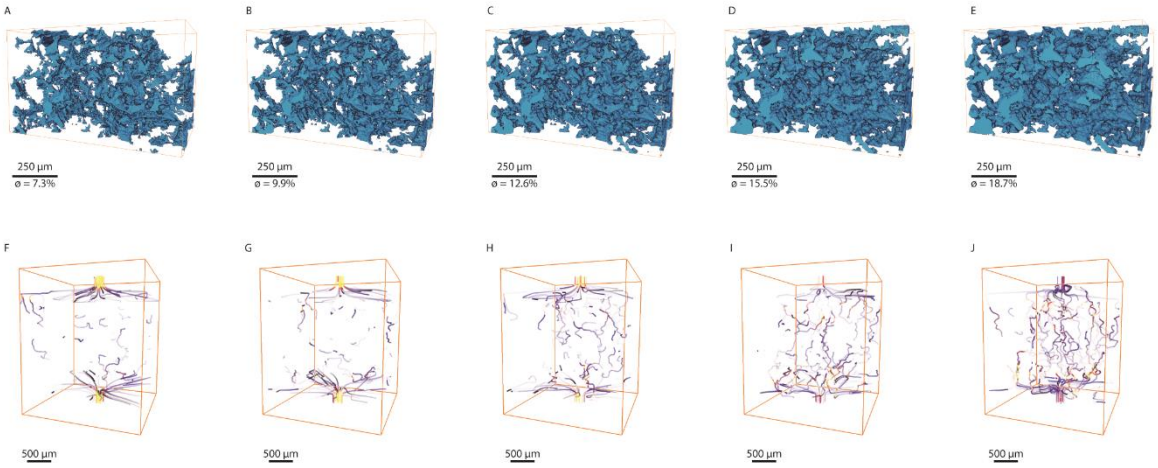

Figure 7.4. Rendered 3D sub-volumes of the SNS sandstone porosity and fluid flow paths. (A). The sub-volume as-scanned showing present-day connected porosity; (B-E) the sub-volumes showing connected porosity after the cement has been back-stripped to increasing degrees; (F) steady-state fluid flow paths through the present-day pore network; (G-J) steady-state fluid flow paths through the expanded pore networks. Flow line colours indicate velocity magnitude, with increasing magnitude from blue to yellow.

Over the four steps of the experiment, the connected pore volume increases from 7.3 vol. % (plus 0.9% disconnected) with a mean pore diameter of 43 μm, to 18.7 vol. % (plus 0.4% disconnected), with a mean pore diameter of 57 μm (step 4) (Table 7.2). The number of pore throats and the mean and modal pore throat radii also increase (see Table 7.2), as does the mean coordination number (the number of pore throats connected to a specific pore), which increases from 2.3 to 3.6. As a result, the total connected pore volume increases by approximately 26% with each step, and the average pore throat size increases by 14% (Table 7.2). These changes are reflected in the calculated permeability and flow rates. The permeability increase is most substantial over the first three erosion steps (7.5 μm erosion) from initial values of 19.2 mD, to 46.5 mD (143% increase) at step 1, 124 mD (167%) at step 2 and 359 mD (189%) at step 3 (Table 7.2). After step 4 permeability continues to increase, but by a slightly lower amount (150 %), showing that while a uniform reduction in the quartz cement thickness may result in only a small change in the total and connected porosity, it can have a significant impact on the permeability as pore throats widen and tortuosity reduces.

	0	**+1**	**+2**	**+3**	**+4**	**Average increase**
Porosity						
Number of pores	1341	1459	1580	1648	1706	N.A.*
Average pore size [μm]	43	47	50	54	57	N.A.*
Connected porosity [%]	7.3	9.9	12.6	15.5	18.7	N.A.*
Connected porosity increase compared to previous step	N.A.*	34	28	23	20	26.4
Disconnected porosity	0.9	0.7	0.6	0.5	0.4	N.A.*
Pore throats						
Number of throats	1530	1830	2176	2637	3047	N.A.*
Average throat size	12	13	15	17	20	14.1
Most frequent throat size [μm]	7	8	12	12	14	N.A.*

Coordination number						
Average coordination number	2.3	2.5	2.8	3.3	3.6	N.A.*
Permeability						
Permeability [mD]	19.2	46.5	124	359	899	N.A.*
Permeability increase compared to previous step	N.A.*	143	167	189	150	162

*N.A. = not applicable.

Table 7.2. Modelling results: porosity, pore throats, coordination number and permeability increase with each modelling step. 0 is the present-day porosity model, +1 is the model after porosity expansion by one step, +2 is after two steps, etc.

This magnitude of the change in permeability for a modest change in total porosity agrees with the highly variable permeability of low porosity sandstones at in situ conditions, as small variations in diagenetic style and cement thickness can result in permeability differences of several orders of magnitude (Cade et al., 1994; Nelson, 2009).

We performed a second simulation in which we grew the quartz layer by 2.5 μm, which effectively simulates precipitation and further porosity reduction. The results were compared with laboratory-measured porosity and permeability values of low permeability samples of similar grain size and cementation style from the same sandstone unit (Figure 7.5).

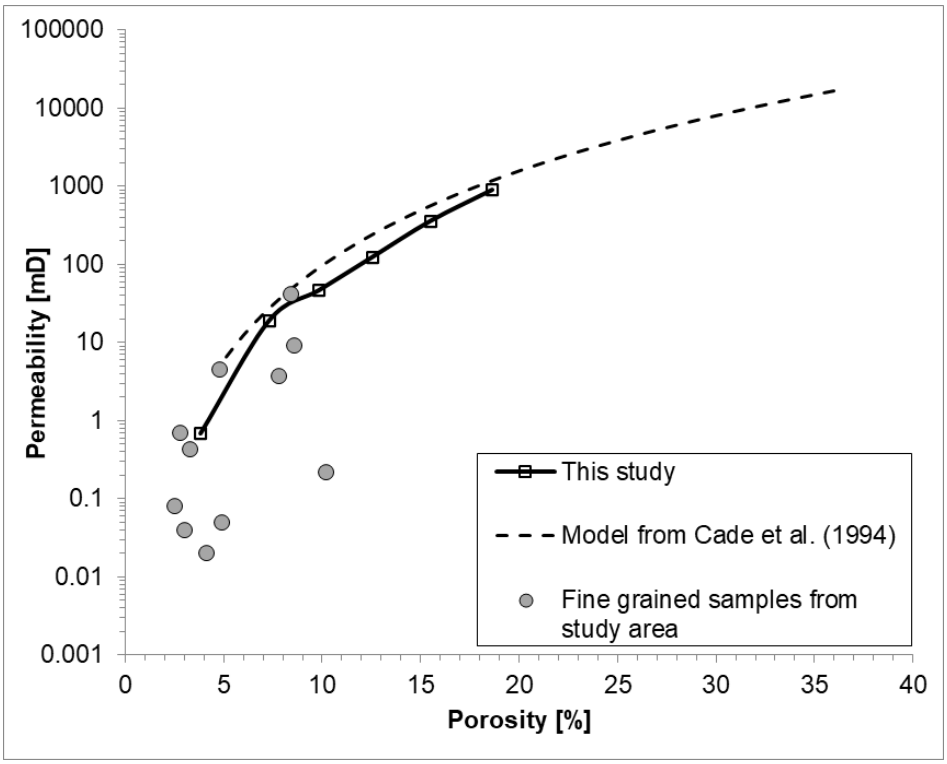

Figure 7.5. Comparison of XMT-derived poroperm curve with porosity and permeability values of similar fine grain-sized, quartz cemented samples from the same area, and with poroperm curve for fine grained samples based on data from Cade et al. (1994). The six points shown on the curve from this study include the original sample, four back-stripped models, and one model with added quartz).

The XMT derived porosity-permeability curve shows a very good fit with the measured samples and, for porosities above 5 vol. %, with the empirically derived porosity-permeability trend for clean, fine-grained sandstones suggested by Cade et al. (1994). The XMT model, which considers detailed pore microstructures of those specific sandstones, allows reconstruction of pore networks and permeability even for very low permeability sandstones. The method can be advanced further to build or strip

cements in more complex ways, depending for example on their mineralogy, morphology and growth patterns.

7.4 Permeability evolution through geological time

As in many sandstones, quartz is the main porosity-occluding cement in the studied sample. Quartz cementation in sandstones is commonly considered to be controlled by the temperature-related kinetics of silica precipitation (Lander and Walderhaug, 1999; Walderhaug, 2000). Quartz precipitation rates are negligible until a thermally-limited barrier is surpassed around 70 – 80°C. Quartz precipitation rate increases with temperature and quartz surface area (Lander and Walderhaug, 1999; Walderhaug, 2000). By linking (a) the evolution of quartz cementation as a function of temperature and time and (b) the way in which the pore network and permeability developed as a function of quartz cementation, we now determine the way in which permeability has evolved through geological time. Thermal and quartz cementation histories were both modelled within the 1D PetroMod software, using a burial history based on Green et al. (2017) and Walderhaug's (2000) quartz cementation model. Both models were calibrated with present-day temperature, organic matter maturity (V_R) and quartz cement data. Assuming even and radial growth of secondary quartz, the model defines the quartz overgrowth thickness through time, and the 3D pore network analysis (above) is then used to determine the evolution of permeability through time (Figure 7.6).

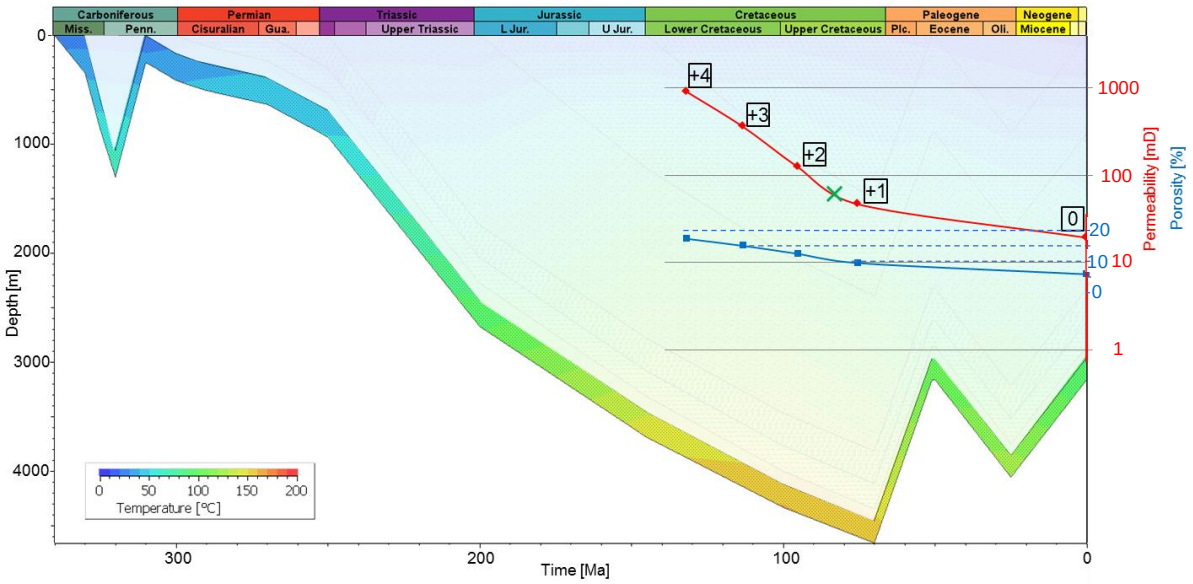

Figure 7.6. Burial history data for the modelled Southern North Sea sandstone. Colour overlay denotes formation temperature through time (see key). Tomography data have been placed at corresponding time points, with numbers in squares (0, +1, +2 etc.) corresponding to model numbers in Table 2. Blue and red lines show porosity and permeability respectively, based on XMT data, and tipping point in permeability evolution is marked with X. Beyond this point most of the permeability is lost and further quartz cementation significantly impeded due to limited fluid flow.

Figure 7.6 shows that through the Cretaceous, porosity decreased from 18.7% to 9.9 %, and then to 7.3% at present-day. Modelled permeability decreased rapidly from 900 to 46 mD through the Cretaceous, before slowly declining to 19 mD over the last 80 Ma. The main reason for the limited change in permeability since the late Cretaceous is uplift and cooling, resulting in much lower rates of quartz cementation.

We have not modelled permeability evolution prior to the Cretaceous because below *ca*. 100°C, rates of quartz cementation are low and close to zero at temperatures below 70-80°C. Under these conditions, porosity loss is mainly by mechanical processes, and permeability is primarily a function of grain size and sorting.

From a practical perspective, the importance of predicting the evolution of sandstone porosity and permeability includes the risking of petroleum reservoir quality. The emplacement of hydrocarbons into sandstones is thought to reduce the rate of quartz cementation (e.g. Worden et al., 2018). The ability to predict porosity and permeability at the time of hydrocarbon migration and entrapment, and generally throughout the reservoir history, may therefore be crucial in order to successfully predict reservoir quality, especially in prospects where sandstones have been exposed to elevated temperatures (>~100°C) for significant periods of geologic time (Taylor et al., 2010).

7.5 Concluding remarks

The results of the presented workflow can be interpreted as a first approach to reconstructing palaeo-permeability throughout the geological history of a reservoir. By applying a theoretical backstripping of quartz cement on a real pore network morphology and linking that to a burial history, we can reconstruct permeability evolution and the timing and mechanisms of reservoir tightening. Our method offers a tool for predicting the timing of the tipping points during diagenesis, beyond which reservoir quality is too low to form a viable reservoir. While this calculated porosity-permeability-time relationship is highly dependent on the precision of the burial model and the quartz precipitation model used, this method for extracting the permeability-time evolution of a porous system can be applied with any model combination (e.g. other cement precipitation models) and parameter set, and can also quantify behavior in systems where cement volumes either increase and decrease depending on factors such as temperature, stress and fluid flow. The modelled porosity-permeability curve shows a close match to measured porosity and permeability values and closely captures porosity-permeability trends. This is even the case for very low permeability sandstone samples, as the method captures detailed pore microstructures.

The permeability reconstruction method can be applied to a wide range of geologic media, not only in sedimentary rocks but also for example to reconstruct permeability changes during the growth of bubbles and crystals in magma, or in manufacturing for permeability modelling in porous ceramics and curing of concrete.

CHAPTER 8:
Conclusions

8.1 Summary of Thesis Objectives

Tight reservoirs are major resource of gas worldwide, successfully producing in multiple countries, including e.g. USA, Canada, Australia and Mexico. However, tight reservoirs are commonly heterogenous, production from tight gas wells is low compared to conventional reservoir wells, and they require stimulation in order to produce economic volumes of gas, making the production from tight gas reservoirs more expensive than from conventional reservoirs. It is therefore important to be able to identify sandstones with sufficient reservoir quality to optimize the drilling and gas recovery process.

The UK Continental Shelf, although it is one of the most mature offshore basins in the world, comprises still largely unexplored Carboniferous tight gas reservoirs in the Southern North Sea (Wood, 2014) despite the fact that their gas potential has been proven by a number of wells that successfully produce gas. Reassessing the potential of the Upper Carboniferous deposits of the North Sea in terms of oil and gas exploration may bring new, recoverable resources to the UK enhance the security of energy supply. This study, therefore, focuses on those poorly documented, low porosity, low permeability Carboniferous sandstones in which small variations in depositional and diagenetic style can result in permeability differences of several orders of magnitude over small areas of reservoir in order to understand main controls on reservoir quality and develop permeability and porosity distribution models. Two fields with reservoirs in the Namurian Millstone Grit formation were analysed in this study: Copernicus discovery (block 44/16) and Cavendish Field (block 43/19), both located about 140-150 km north-east of the Lincolnshire coast in the Silverpit Basin. The Cavendish Field was discovered in 1989 and was in production from 2007 until 2018 and throughout its lifetime produced 98 bcf of gas plus associated condensate (Wasielka et al., 2020). Copernicus discovery on the other hand, after it was drilled in 1991 was classed as gas discovery, however it was assessed as economically non-viable and was never put into production (ENGIE, 2015).

8.2 Conclusions

Chapter-specific conclusions are contained within Chapter 3, 4, 5, 6, and 7. Here a more general summary is provided.

-The depositional environment is a fundamental factor controlling reservoir quality in the analysed Copernicus and Cavendish fields, due to the differences in detrital composition, grain size and different pore water chemistries leading to varying

digenetic pathways. Porosity in marine sandstones is typically pervasively occluded by detrital clay and carbonate cements, rendering them ineffective as potential reservoirs. Sandstones from continental settings, and fluvial channels in particular, form the best reservoirs, as they contain little early diagenetic cements leading to better porosity preservation until deep burial.

-Differences in quartz and feldspar content, grain size, and composition of lithic fragments result from delivering of detrital material from multiple sources. The exceptionally permeable sandstones from well 43/19a-4Z have likely been derived from a different, more quartz rich source, than sandstones from other wells. Mineralogically mature, quartz rich sandstones are less prone to adverse effects of diagenesis than the more feldspathic sandstones. In the latter, feldspars are typically altered to kaolinite, which has a detrimental effect on reservoir quality. Provenance therefore, appears to be one of the most important factors controlling reservoir quality in the fluvial sandstones.

-Reconstruction of accurate burial histories of apparently similar reservoirs is crucial in order to understand cement precipitation, hydrocarbon generation, migration and retention, for a successful exploration. The higher burial depth in Copernicus discovery than in Cavendish field render the former an economically non-viable resource, despite the presence of clean, fluvial sandstones with high reservoir quality potential.

-Authigenic quartz is volumetrically the most important cement in the analysed sandstones. Higher burial temperature and longer time spent in quartz generation window are responsible for most porosity loss during burial diagenesis.

-X-ray computed microtomography results show that samples with nearly identical porosity can vary extensively in their internal microstructure resulting in permeability differences varying be orders of magnitude over a small area (even on cm-scale) due to cementation heterogeneity. Major differences in permeability values are recorded in samples that are similar in terms of grain size, but where pore throat radius is reduced by significant quartz cementation.

-X-ray computed microtomography results show that pore throat size distribution, which is generally associated with grain size, is the most important aspect controlling permeability, rather than coordination number or connected porosity volume, although all elements contribute to permeability value.

-An integrated approach utilising burial history modelling, analysis of diagenetic processes, and 3D modelling of pore architecture, and changes in pore structure and connectivity as a function of time, offer a tool that allows reconstructing permeability evolution throughout the geological history of the reservoir, and the timing and mechanisms of reservoir tightening.

-Material heterogeneity and sample representativity pose a big challenge to successful permeability prediction. Due to a small sample sizes that can be scanned at high resolution with X-ray computed microtomography (XMT), and computational power required for processing, only very homogenous material can be well represented by 3D models of small samples. However, combining quantitative petrography and 3D (XMT) pore network analysis allows to unravel controls on permeability that can be observed on a micron to cm-scale.

8.3 Further work

Results from this research have shown the importance of an integrated, multi-disciplinary approach in characterising tight reservoirs. Only by piecing together results of detailed analysis on micron to basin scale can one see the whole picture necessary for a successful exploration of the often risky and expensive tight reservoirs.

To specifically build upon the work undertaken in this thesis further work has been identified involving developing on the methods applied in this study and expanded by new approaches.

-Detailed provenance analysis is recommended for the Namurian sandstones in the studied area in order to further investigate the sources of the detritus, which is crucial for the reservoir potential. Heavy mineral assemblage or chemostratigraphy have proven to be useful methods to analyse the stratigraphy and provenance of the Westphalian deposits from the Southern North Sea (Pearce et al., 2010, 2005) and could be applied to the Namurian strata.

-Results of this study show that presence of even minor amounts of accessory cements such as siderite can be critical for reservoir quality loss, therefore careful analysis of the causes of their development is fundamental for understanding of vertical flow paths in the analysed sandstones. Their position within the facies (e.g. top/base of the bed, or fining/coarsening upward sequence) and in the sequence stratigraphic system (e.g. are they associated with high stands, transgressive surfaces, etc.) should be considered.

-Fluid inclusion data, clumped isotopes, and stable oxygen isotope data from high resolution, in situ secondary ion mass spectrometry (SIMS) could help to refine the diagenetic and burial history of the analysed wells by adding new information about quartz and carbonate cementation history. These can be compared with chemical porosity loss history generated from 1D basin models and petrographic analysis. Additionally, XRD analysis would result in more accurate qualitative and quantitative data about clay composition thus allowing for more detailed analysis of clay authigenesis and its influence on reservoir quality.

-Numerous fractures were observed and recorded on sedimentary logs, with the material filling the fractures assessed visually during logging. Since fracture network may increase reservoir permeability where it forms active fluid conduits, or decrease it when forming baffles for fluid flow, detailed analysis of fracture connectivity, orientation, and fill would allow to for a better assessment of permeability anisotropy and reservoir quality distribution.

References

Aharonov, E., Katsman, R., 2009. Interaction between pressure solution and clays in stylolite development: Insights from modeling. Am. J. Sci. 309, 607–632. https://doi.org/10.2475/07.2009.04

Ajdukiewicz, J.M., Lander, R.H., 2010. Sandstone reservoir quality prediction : The state of the art. Am. Assoc. Pet. Geol. Bull. 94, 1083–1091. https://doi.org/10.1306/intro060110

Algive, L., Békri, S., Nader, F.H., Lerat, O., Vizika, O., 2012. Impact of Diagenetic Alterations on the Petrophysical and Multiphase Flow Properties of Carbonate Rocks Using a Reactive Pore Network Modeling Approach. Oil Gas Sci. Technol. 67, 147–160. https://doi.org/10.2516/ogst/2011171

Amoco (U.K.), 1990. 43/19-2A Post Drilling Appraisal.

Amoco (U.K.), 1989. 43/19-1 Post Drilling Appraisal.

Andrews-Speed, C.P., Oxburgh, E.R., Cooper, B.A., 1984. Temperatures and Depth-Dependent Heat Flow in Western North Sea. Am. Assoc. Pet. Geol. Bull. 68, 1764–1781. https://doi.org/10.1306/ad461999-16f7-11d7-8645000102c1865d

Aplin, A.C., Warren, E.A., 1994. Oxygen isotopic indications of the mechanisms of silica transport and quartz cementation in deeply buried sandstones. Geology 22, 847–850.

Aplin, A.C., Warren, E.A., Grant, S.M., Robinson, A.G., 1993. Mechanisms of quartz cementation in North Sea reservoir sandstones: constraints from fluid compositions, in: Horbury, A., Robinson, A.G. (Eds.), Diagenesis and Basin Development. AAPG Studies in Geology 36, pp. 7–22.

Archie, G.E., 1942. The Electrical Resistivity Log as an Aid in Determining Some Reservoir Characteristics. Pet. Technol. 54–62. https://doi.org/10.2118/942054-g

Arfai, J., Lutz, R., 2017. 3D basin and petroleum system modelling of the NW German North Sea (Entenschnabel), in: Bowman, M., Levell, B. (Eds.), Petroleum Geology of NW Europe: 50 Years of Learning - Proceedings of the 8th Petroleum Geology Conference. Geological Society, London, pp. 67–86. https://doi.org/https://doi.org/10.1144/PGC8.35

Arns, C.H., Knackstedt, M.A., Pinczewski, W.V., Martys, N.S., 2004. Virtual permeametry on microtomographic images. J. Pet. Sci. Eng. 45, 41–46.

Ashwell, P., Kendrick, J., Lavallée, Y., Kennedy, B., Hess, K., von Aulock, F., Wadsworth, F., Vasseur, J., Dingwell, D., 2015. Permeability of compacting porous lavas. J. Geophys. Res. Solid Earth 120, 1605–1622. https://doi.org/10.1002/2014JB011519

Auzerais, F.M., Dunsmuir, J., Ferréol, B., Martys, N., Olson, J., Ramakrishnan, T., Rothman, D., Schwartz, L., 1996. Transport in sandstone: a study based on three dimensional microtomography. Geophys. Res. Lett. 23, 705–708. https://doi.org/10.1029/96GL00776

Bailey, J.B., Arbin, P., Daffinoti, O., Gibson, P., Ritchie, J.S., 1993. Permo-Carboniferous plays of the Silver Pit Basin, in: Parker, J.R. (Ed.), Petroleum Geology of Northwest Europe: Proceedings of the 4th Conference. The Geological Society, London, pp. 707–715. https://doi.org/https://doi.org/10.1144/0040707

Beaufort, D., Cassagnabere, A., Petit, S., Lanson, B., Berger, G., Lacharpagne, J., Johansen, H., 1998. Kaolinite-to-dickite reaction in sandstone reservoirs. Clay Miner. 33, 297–316. https://doi.org/10.1180/claymin.1998.033.2.12

Becker, I., Wüstefeld, P., Koehrer, B., Felder, M., Hilgers, C., 2017. Porosity and permeability variations in a tight gas sandstone reservoir analogue, Westphalian D ,Lower Saxony basin , NW Germany : Influence of depositional setting and diagenesis. J. Pet. Geol. Vol 40, 363–389. https://doi.org/10.1111/jpg.12685

Beckingham, L.E., Peters, C.A., Um, W., Jones, K.W., Lindquist, W.B., 2013. 2D and 3D imaging resolution trade-offs in quantifying pore throats for prediction of permeability. Adv. Water Resour. 62, 1–12. https://doi.org/10.1016/j.advwatres.2013.08.010

Bertier, P., Swennen, R., Lagrou, D., Laenen, B., Kemps, R., 2008. Palaeo-climate controlled diagenesis of the Westphalian C & D fluvial sandstones in the Campine Basin (north-east Belgium). Sedimentology 55, 1375–1417. https://doi.org/10.1111/j.1365-3091.2008.00950.x

Bertoncello, A., Honarpour, M., 2013. Standards for Characterization of Rock Properties in Unconventional Reservoirs: SPE Annu. Tech. Conf. … SPE 166470, 1–17.

Besly, B., 2018. Exploration and development in the Carboniferous of the Southern North Sea : a 30-year retrospective, in: Monaghan, A.A., Underhill, J.R., Hewett, A.J., Marshall, J.E.A. (Eds.), Paleozoic Plays of NW Europe. Geological Society, London, Special Publications, 471, London, pp. 17–64. https://doi.org/https://doi.org/10.1144/SP471.10

Besly, B., 1990. Carboniferous, in: Glennie, K.W. (Ed.), Introduction to the Petroleum Geology of the North Sea. Blackwell Scientific Publications, Oxford, pp. 90–119.

Besly, B.M., Burley, S.D., Turner, P., 1993. The late Carboniferous "Barren Red Bed" play of the Silver Pit area, southern north sea, in: Parker, J. (Ed.), Petroleum Geology of Northwest Europe: Proceedings of the 4th Conference. The Geological Society, London, pp. 727–740. https://doi.org/10.1144/0040727

Bhattacharya, J.P., Davies, R.K., 2004. Sedimentology and Structure of Growth Faults at the Base of the Ferron Sandstone Member Along Muddy Creek, Utah Analog for Fluvial-Deltaic Reservoir Modeling: Ferron Sandstone of Utah, in: Chidsey, T.C.J., Adams, R.D., Morris, T. (Eds.), Analog for Fluvial– Deltaic Reservoir Modeling: The Ferron Sandstone of Utah. American Association of Petroleum Geologists, Studies in Geology, no. 50, pp. 279–304.

Bjørkum, P.A., Oelkers, E.H., Nadeau, P.H., Walderhaug, O., Murphy, W.M., 1998. Porosity prediction in quartzose sandstones as a function of time, temperature, depth, stylolite frequency, and hydrocarbon saturation. Am. Assoc. Pet. Geol. Bull. 82, 637–647. https://doi.org/10.1306/1d9bc5cf-172d-11d7-8645000102c1865d

Bjørlykke, K., 2014. Relationships between depositional environments, burial history and rock properties. Some principal aspects of diagenetic process in sedimentary basins. Sediment. Geol. 301, 1–14. https://doi.org/10.1016/j.sedgeo.2013.12.002

Bjørlykke, K., 1994. Pore-water flow and mass transfer of solids in solution in sedimentary basins, in: Parker, A., Sellwood, B.W. (Eds.), Quantitative Diagenesis: Recent Developments and Applications to Reservoir Geology. Springer Netherlands, Dordrecht, pp. 189–221. https://doi.org/10.1007/978-94-011-0189-9_6

Bjørlykke, K., Egeberg, P.K., 1993a. Quartz cementation in sedimentary basins. Am. Assoc. Pet. Geol. Bull. 77, 1538–1548.

Bjørlykke, K., Egeberg, P.K., 1993b. Quartz cementation in sedimentary basins. Am.

Assoc. Pet. Geol. Bull. 77, 1538–1548.

Blunt, M.J., Bijeljic, B., Dong, H., Gharbi, O., Iglauer, S., Mostaghimi, P., Paluszny, A., Pentland, C., 2013. Pore-scale imaging and modelling. Adv. Water Resour. 51, 197–216. https://doi.org/10.1016/j.advwatres.2012.03.003

Bojanowski, M.J., Clarkson, E.N.K., 2012. Origin of siderite concretionsiIn microenvironments of methanogenesis developed in a sulfate reduction zone: an exception or a rule? J. Sediment. Res. 82, 585–598. https://doi.org/10.2110/jsr.2012.50

Boller, E., Tafforeau, P., Rack, A., Fernandez, V., Helfen, L., Rénier, M., Valade, J.P., Vitoux, H., Villanova, J., Cloetens, P., Fayard, B., Guiraud, O., Latil, P., 2017. Synchrotron-Tomography With Micro, Nano and High Temporal Resolution for Industrial and Academic Use, in: 3rd International Conference on Tomography of Materials and Structures. Lund, Sweden.

Botha, P.W.S.K., Sheppard, A.P., 2016. Mapping permeability in low-resolution micro-CT images: A multiscale statistical approach. Water Resour. Res. 52, 4377–4398,. https://doi.org/10.1002/2015WR018454

Botor, D., Golonka, J., Anczkiewicz, A.A., Dunkl, I., Papiernik, B., Zając, J., Guzy, P., 2019. Burial and thermal history of the Lower Palaeozoic petroleum source rocks at the sw margin of the east european craton (Poland). Ann. Soc. Geol. Pol. 89, 121–152. https://doi.org/10.14241/asgp.2019.12

Bottrell, S.H., Parkes, R.J., Cragg, B.A., Raiswell, R., 2000. Isotopic evidence for anoxic pyrite oxidation and stimulation of bacterial sulphate reduction in marine sediments. J. Geol. Soc. London. 157, 711–714. https://doi.org/10.1144/jgs.157.4.711

Bray, R.J., Green, P.F., Duddy, I.R., 1992. Thermal history reconstruction using apatite fission track analysis and vitrinite reflectance: A case study from the UK East Midlands and Southern North Sea, in: Hardman, R.F. (Ed.), Exploration Britain: Geological Insights for the next Decade. Geological Society Special Publication No. 67, pp. 3–25. https://doi.org/10.1144/GSL.SP.1992.067.01.01

Bristow, C.S., 1993. Sedimentology of the Rough Rock: a Carboniferous braided river sheet sandstone in northern England, in: Best, J.L., Bristow, C.S. (Eds.), Braided Rivers. Geological Society of London, Special Publication, London, pp. 291–304. https://doi.org/10.1144/GSL.SP.1993.075.01.18

Bristow, C.S., 1988. Controls on the sedimentation of the Rough Rock Group (Namurian) from the Pennine Basin of northern England, in: Besly, B.M., Kelling, G. (Eds.), Sedimentation in a Synorogenic Basin Complex. The Upper Carboniferous of Northwest Europe. Blackie, Glasgow and London, pp. 114–131.

British Geological Survey, 2019. The BGS Lexicon of Named Rock Units [WWW Document]. URL https://www.bgs.ac.uk/lexicon/ (accessed 5.13.19).

Britoil, 1989. Composite well log 43/19-1.

Buatois, L.A., Santiago, N., Parra, K., Steel, R., 2008. Animal-Substrate Interactions in an Early Miocene Wave-Dominated Tropical Delta: Delineating Environmental Stresses and Depositional Dynamics (Tacata Field, Eastern Venezuela). J. Sediment. Res. 78, 458–479. https://doi.org/10.2110/jsr.2008.053

Bultreys, T., Boone, M.A., Boone, M.N., De Schryver, T., Masschaele, B., Van Hoorebeke, L., Cnudde, V., 2016a. Fast laboratory-based micro-computed tomography for pore-scale research: Illustrative experiments and perspectives on the future. Adv. Water Resour. 95, 341–351. https://doi.org/10.1016/j.advwatres.2015.05.012

Bultreys, T., De Boever, W., Cnudde, V., 2016b. Imaging and image-based fluid transport modeling at the pore scale in geological materials: A practical introduction to the current state-of-the-art. Earth-Science Rev. 155, 93–128. https://doi.org/10.1016/j.earscirev.2016.02.001

Burchell, M., 1989. Geological completion report well 43/19-1.

Busch, B., Becker, I., Koehrer, B., Adelmann, D., Hilgers, C., 2019. Porosity evolution of two Upper Carboniferous tight-gas-fluvial sandstone reservoirs: Impact of fractures and total cement volumes on reservoir quality. Mar. Pet. Geol. 100, 376–390. https://doi.org/10.1016/j.marpetgeo.2018.10.051

Cade, C., Evans, I., Bryant, S., 1994. Analysis of permeability controls: A new approach. Clay Miner. 29, 491–501. https://doi.org/https://doi.org/10.1180/claymin.1994.029.4.08

Cameron, D., Munns, J., Stoker, S., 2005. Remaining exploration potential of the Carboniferous fairway, UK southern North Sea, in: Collinson, J.D., Evans, D.J., Holliday, D.W., Jones, N.S. (Eds.), Carboniferous Hydrocarbon Geology, the Southern North Sea and Surrounding Onshore Areas. Yorkshire Geological

Society, Occasional Publication 7, pp. 209–224.

Cameron, D., van Doorn, D., Laban, C., Streif, H., 1993. Geology of the Southern North Sea Basin, in: Coastlines of the Southern North Sea. New Orleans, pp. 14–26. https://doi.org/10.1144/pygs.36.1.1

Cameron, N., Ziegler, T., 1997. Probing the lower limits of a fairway : further pre-Permian potential in the southern North Sea, in: Ziegler, K., Turner, P., Daines, S.R. (Eds.), Petroleum Geology of the Southern North Sea: Future Potential. Geological Society Special Publication No.123, pp. 123–141.

Cameron, T.D.J., 1993. Carboniferous and Devonian of the Southern North Sea, in: Knox, R.W.O., Cordey, W.G. (Eds.), Lithostratigraphic Nomenclature of the UK North Sea. British Geological Survey, Nottingham, pp. 1–93.

Carmona, N.B., Buatois, L.A., Ponce, J.J., Mángano, M.G., 2009. Ichnology and sedimentology of a tide-influenced delta, Lower Miocene Chenque Formation, Patagonia, Argentina: Trace-fossil distribution and response to environmental stresses. Palaeogeogr. Palaeoclimatol. Palaeoecol. 273, 75–86. https://doi.org/10.1016/j.palaeo.2008.12.003

Carr, A.D., 2000. Suppression and retardation of vitrinite reflectance, Part 1. Formation and significance for hydrocarbon generation. J. Pet. Geol. 23, 313–343. https://doi.org/10.1111/j.1747-5457.2000.tb01022.x

Caubit, C., Hamon, G., Sheppard, A.P., Øren, P.E., 2009. Evaluation of the reliability of prediction of petrophysical data through imagery and pore network modelling. Petrophysics 50, 322–334.

Cedeño, A., Rojo, L.A., Cardozo, N., Centeno, L., Escalona, A., 2019. The Impact of Salt Tectonics on the Thermal Evolution and the Petroleum System of Confined Rift Basins: Insights from Basin Modeling of the Nordkapp Basin, Norwegian Barents Sea. Geosciences 9, 1–25. https://doi.org/10.3390/geosciences9070316

Chamley, H., 1994. Clay Mineral Diagenesis, in: Parker, A., Sellwood, B.W. (Eds.), Quantitative Diagenesis: Recent Developments and Applications to Reservoir Geology. Springer Science+Business Media, Dordrecht, pp. 161–188. https://doi.org/10.1016/0264-8172(96)88337-1

Cheadle, M.J., Elliott, M.T., McKenzie, D., 2004. Percolation threshold and permeability of crystallizing igneous rocks: The importance of textural

equilibrium. Geology 32, 757–760. https://doi.org/10.1130/G20495.1

Chisholm, J.I., Hallsworth, C.R., 2005. Provenance of Upper Carboniferous sandstones in east Derbyshire: Role of the Wales-Brabant High. Proc. Yorksh. Geol. Soc. 55, 209–233. https://doi.org/10.1144/pygs.55.3.209

Cnudde, V., Boone, M.N., 2013. High-resolution X-ray computed tomography in geosciences : A review of the current technology and applications. Earth Sci. Rev. 123, 1–17. https://doi.org/10.1016/j.earscirev.2013.04.003

Cohen, K.M., Finney, S.C., Gibbard, P.L., Fan, J.-X., n.d. The International Stratigraphic Chart. Episodes 36.

Collinson, J.D., 2005. Dinantian and Namurian depositional systems in the southern North Sea, in: Collinson, J.D., Evans, D., Holliday, D., Jones, N. (Eds.), Carboniferous Hydrocarbon Geology: The Southern North Sea and Surrounding Onshore Areas. Yorkshire Geological Society Occasional Publication 7, pp. 35–56.

Collinson, J.D., 1988. Controls on Namurian sedimentation in the Central Province basins of northern England, in: Besly, B.M., Kelling, G. (Eds.), Sedimentation in a Synorogenic Basin Complex. The Upper Carboniferous of Northwest Europe. Blackie, Glasgow and London, pp. 85–101.

Collinson, J.D., Jones, C.M., Blackbourn, G.A., Besly, B.M., Archard, G.M., McMahon, A.H., 1993. Carboniferous depositional systems of the Southern North Sea, in: Parker, J.R. (Ed.), Petroleum Geology of Northwest Europe: Proceedings of the 4th Conference. The Geological Society, London, pp. 677–687.

Collinson, J.D., Martinsen, O., Bakken, B., Kloster, A., 1991. Early fill of the Western Irish Namurian Basin: A complex relationship between turbidites and deltas. Basin Res. 3, 223–242. https://doi.org/10.1111/j.1365-2117.1991.tb00131.x

Conway, A.M., Valvatne, C., 2003a. The Boulton Field, Block 44/21a, UK North Sea, in: Gluyas, J.G., Hichens, H.M. (Eds.), United Kingdom Oil and Gas Fields. Geological Society, London, pp. 671–680. https://doi.org/10.1144/gsl.mem.2003.020.01.53

Conway, A.M., Valvatne, C., 2003b. The Murdoch Gas Field, Block 44/22a, UK Southern North Sea. Geol. Soc. Mem. 20, 789–798. https://doi.org/10.1144/GSL.MEM.2003.020.01.66

Cope, M.J., 1986. An Interpretation of Vitrinite Reflectance Data From the Southern North Sea Basin, in: Brooks, J, Goff, J. C., van Hoon, B. (Ed.), Habitat of Palaeozoic Gas in N.W. Europe. Geological Society Special Publication, pp. 85–98.

Corcoran, D. V., Doré, A.G., 2002. Top seal assessment in exhumed basin settings - some insights from atlantic margin and borderland basins, in: Koestler, A., Hunsdale, R. (Eds.), Hydrocarbon Seal Quantification. Norwegian Petroleum Society Special Publication, Amsterdam, pp. 89–107. https://doi.org/10.1016/S0928-8937(02)80009-1

Cornford, C., 1998. Source rocks and hydrocarbons of the North Sea, in: Glennie, K. (Ed.), Introduction to Petroleum Geology of the North Sea. Basic Concepts and Recent Advances. Blackwell Science, Oxford, pp. 376–462.

Cowan, G., 1989. Diagenesis of Upper Carboniferous sandstones : southern North Sea Basin, in: Whateley, M.K.G. & Pickering, K.T. (Ed.), Deltas: Sites and Traps for Fossil Fuels. Geological Society Special Publication, London, pp. 57–73.

Cowan, G., Shaw, H., 1991. Diagenesis of Namurian fluvio-deltaic sandstones from the Trumfleet Field , South Yorkshire. Mar. Pet. Geol. 8, 212–224.

Dahraj, N.U.H., Aziz, T., Asghar, A., Aslam, A., Rashid, K., Hashmi, S., 2018. Production Strategy of a Tight Gas Carbonate Reservoir in Pakistan, in: PAPG/SPE Pakistan Section Annual Technical Conference and Exhibition. Society of Petroleum Engineers, pp. 1–17. https://doi.org/10.2118/195666-MS

de Jager, J., Doyle, M.A., Grantham, P.J., Mabillard, J.E., 1996. Hydrocarbon habitat of the West Netherlands Basin, in: Rondeel, H.E., Batjes, D.A.J., Nieuwenhuijs, W.H. (Eds.), Geology of Gas and Oil under the Netherlands: Selection of Papers Presented at the 1983 Iternational Conference of the American Association of Petroleum Geologists, Held in The Hague. Springer Netherlands, Dordrecht, pp. 191–209. https://doi.org/10.1007/978-94-009-0121-6_17

de Lugt, I.R., van Wees, J.D., Wong, T.E., 2003. The tectonic evolution of the southern Dutch North Sea during the Palaeogene: Basin inversion in distinct pulses. Tectonophysics 373, 141–159. https://doi.org/10.1016/S0040-1951(03)00284-1

Discovery Digest United Kingdom, 2019. Released & Completed Well Reviews [WWW Document]. URL https://ukdigest.canadiandiscovery.com/?q=articles-search&field_computed_search_terms_value=&tabs_one=group-

location&field_quad_tid=All&field_regions_or_topics_tid=All&field_ages_tid=All&field_product_tid[]=13715&field_article_type_tid[]=11787&field_artic (accessed 4.4.19).

Dobson, K., Coban, S., McDonald, S., Walsh, J., Atwood, R., Withers, P., 2016. 4-D imaging of sub-second dynamics in pore-scale processes using real-time synchrotron X-ray tomography. Solid Earth 7, 1059–1073. https://doi.org/10.5194/se-7-1059-2016

Dong, H., Fjeldstad, S., Roth, S., Bakke, S., Øren, P., 2008. Pore Network Modelling on Carbonate: A comparative Study of Different Micro-CT Network Extraction Methods. Proc. Int. Symp. Soc. Core Anal. 2008–2031.

Doornenbal, H., Stevenson, A., 2010. Petroleum Geological Atlas of the Southern Permian Basin Area. EAGE Publications b.v., Houten.

Ehrenberg, S.N., Aagaard, P., Wilson, M.J., Fraser, A.R., Duthie, D.M.L., 1993. Depth-dependent transformation of kaolinite to dickite in sandstones of the Norwegian continental shelf. Clay Miner. 28, 325–352. https://doi.org/10.1180/claymin.1993.028.3.01

Ehrlich, R., Etris, E.L., Brumfield, D., Yuan, L.P., Crabtree, S.J., 1991. Petrography and reservoir physics III: physical models for permeability and formation factor. Am. Assoc. Pet. Geol. Bull. https://doi.org/10.1016/0148-9062(92)93815-2

Elliott, T., 1976. The morphology, magnitude and regime of a Carboniferous fluvial-distributary channel. J. Sediment. Petrol. 46, 70–76.

Elliott, T., 1974. Interdistributary bay sequences and their genesis. Sedimentology 21, 611–622. https://doi.org/10.1111/j.1365-3091.1974.tb01793.x

Elliott, W.C., Matisoff, G., 1996. Evaluation of kinetic models for the smectite to illite transformation. Clays Clay Miner. 44, 77–87. https://doi.org/10.1346/CCMN.1996.0440107

Ellis, D. V., Singer, J.M., 2008. Well Logging for Earth Scientists. Springer, Springer.

ENGIE, 2015. Relinquishment Report (Copernicus) Licence P2102 - Block 44/16b.

Fisher, Q.J., Knipe, R.J., Worden, R.H., 2000. Microstructures of deformed and non-deformed sandstones from the North Sea: implications for the origins of quartz cement in sandstones, in: Worden, R.H., Morad, S. (Eds.), Quartz Cementation

in Sandstones. Blackwell Publishing Ltd., Oxford, UK, pp. 129–146. https://doi.org/10.1002/9781444304237.ch10

Folk, R.L., 1980. Petrology of Sedimentary Rocks. Hemphill Publishing Company, Austin.

Franzinelli, E., Potter, P.E., 1983. Petrology , Chemistry , and Texture of Modern River Sands , Amazon River System Author (s): Elena Franzinelli and Paul Edwin Potter Source : The Journal of Geology , Vol . 91 , No . 1 (Jan ., 1983), pp . 23-39 Published by : The University of Chicago. J. Geol. 91, 23–39.

Fraser, A.J., Gawthorpe, R.L., 1990. Tectono-stratigraphic development and hydrocarbon habitat of the Carboniferous in northern England, in: Hardman, R.F.P., Brooks, J. (Eds.), Tectonic Events Responsible for Britain's Oil and Gas Reserves. Geological Society London Special Publication, pp. 49–86. https://doi.org/10.1144/GSL.SP.1990.055.01.03

Fraser, A.J., Nash, D.F., Steele, R.P., Ebdon, C.C., 1990. A regional assessment of the intra-Carboniferous play of Northern England, in: Brooks, J. (Ed.), Classic Petroleum Provinces. Geological Society London Special Publication, pp. 417–440. https://doi.org/10.1144/gsl.sp.1990.050.01.26

Gallé, C., Sercombe, J., 2001. Permeability and pore structure evolution of silico-calcareous and hematite high-strength concretes submitted to high temperatures. Mater. Struct. Constr. 34, 619–628. https://doi.org/10.1617/13695

Gautier, D.L., 2003. Carboniferous-Rotliegend Total Petroleum System Description and Assessment Results Summary. U.S. Geol. Surv. Bull. 2211.

Geochem Group Limited, 1993. Sedimentological and petrographical evaluation of 363.30 feet of core from the Permian and Carboniferous intervals in well 44/16-2. Southern North Sea, UKCS.

Gerling, P., Geluk, M., Kockel, F., Lokhorst, A., Lott, G.K., Nicholson, R.A., 1999. NW European Gas Atlas - new implications for the Carboniferous gas plays in the western part of the Southern Permian Basin, in: Fleet, A.J., Boldy, S.A.R. (Eds.), Petroleum Geology of Northwest Europe: Proceedings of the 5th Conference. Geological Society, London, pp. 799–808.

Giles, M.R., De Boer, R.B., 1990. Origin and significance of redistributional secondary porosity. Mar. Pet. Geol. 7, 378–397.

Giles, M.R., Indrelid, S.L., Beynon, G. V., Amthor, J., 2000. The origin of large-scale quartz cementation: evidence from large data sets and coupled heat-fluid mass transport modelling, in: Worden, R.H., Morad, S. (Eds.), Quartz Cementation in Sandstones. International As-sociation of Sedimentologists Special Publication 29, pp. 21–38. https://doi.org/10.1002/9781444304237.ch2

Glasmann, J.R., 1992. The fate of feldspar in Brent Group reservoirs, North Sea: a regional synthesis of diagenesis in shallow, intermediate, and deep burial environments, in: Morton, A., Haszeldine, R.S., Giles, M.R., Brown, S. (Eds.), Geology of the Brent Group. Geological Society Special Publication No. 61, pp. 329–350. https://doi.org/10.1144/GSL.SP.1992.061.01.17

Glennie, K., Boegner, P.L., 1981. Sole Pit inversion tectonics, in: Illing, L.V., Hobson, G. (Eds.), Petroleum Geology of the Continental Shelf of North-West Europe. Institute of Petroleum, Heyden, London, pp. 110–120.

Gluyas, J., Bowman, M., 1997. Edale no. 1 oilwell, Derbyshire, UK, 1938. Mar. Pet. Geol. 14, 191–199. https://doi.org/10.1016/S0264-8172(96)00066-9

Gluyas, J., Cade, C.A., 1997. Prediction of porosity in compacted sands, in: Kupecz, J.A., Gluyas, J, Bloch, S. (Eds.), Reservoir Quality Prediction in Sand- Stones and Carbonates. AAPG Memoir 69, pp. 19–28.

Gluyas, J., Garland, C., Oxtoby, N.H., Hogg, A.J.C., 2000. Quartz Cement: The Miller's Tale, in: Worden, R.H., mor (Eds.), Quartz Cementation in Sandstones. nternational Association of Sedimentologists, Special Publication 29, Oxford, UK, pp. 199–218. https://doi.org/10.1002/9781444304237.ch14

Gluyas, J.G., Robinson, A.G., Emery, D., Grant, S.M., Oxtoby, N.H., 1993. The link between petroleum emplacement and sandstone cementation, in: Petroleum Geology of Northwest Europe: Proceedings of the 4th Conference. The Geological Society, London, pp. 1395–1402. https://doi.org/10.1144/0041395

Golab, A.N., Knackstedt, M.A., Averdunk, H., Senden, T., Butcher, A.R., Jaime, P., 2010. 3D porosity and mineralogy characterization in tight gas sandstones. Lead. edge 29, 1476–1483.

Gouze, P., Luquot, L., 2011. X-ray microtomography characterization of porosity, permeability and reactive surface changes during dissolution. J. Contam. Hydrol. 120–121, 45–55. https://doi.org/10.1016/j.jconhyd.2010.07.004

Grant, S.M., Oxtoby, N.H., 1992. The timing of quartz cementation in Mesozoic sandstones from Haltenbanken, offshore mid-Norway: fluid inclusion evidence. J. Geol. Soc. London. 149, 479–482. https://doi.org/10.1144/gsjgs.149.4.0479

Grant, R.J., Underhill, J.R., Hernández-Casado, J., Barker, S.M. and Jamieson, R.J., 2019. Upper Permian Zechstein Supergroup carbonate-evaporite platform palaeomorphology in the UK Southern North Sea. *Mar. Pet. Geol.*, 100, 484–518.

Gray, J., 2013. Petroleum prospectivity of the principal sedimentary basins on the United Kingdom Continental Shelf, Petroleum Prospectivity, UKCS.

Green, P.F., 2005. Post-Carboniferous burial and exhumation histories of Carboniferous rocks of the southern North Sea and adjacent onshore UK, in: Collinson, J.D., Evans, D.J., Holliday, D.W., Jones, N.S. (Eds.), Carboniferous Hydrocarbon Geology: The Southern North Sea and Surrounding Onshore Areas. Occasional Publications of the Yorkshire Geological Society, pp. 25–34.

Green, P.F., Duddy, I.R., Japsen, P., 2017. Multiple episodes of regional exhumation and inversion identified in the UK Southern North Sea based on integration of palaeothermal and palaeoburial indicators, in: Bowman, M, Levell, B. (Ed.), Petroleum Geology of NW Europe: 50 Years of Learning - Proceedings of the 8th Petroleum Geology Conference. Geological Society, London, pp. 47–65. https://doi.org/https://doi.org/10.1144/PGC8.21

Gu, X., Cole, D.R., Rother, G., Mildner, D.F.R., Brantley, S.L., 2015. Pores in marcellus shale: A neutron scattering and FIB-SEM study. Energy and Fuels 29, 1295–1308. https://doi.org/10.1021/acs.energyfuels.5b00033

Hallsworth, C.R., Chisholm, J.I., 2008. Provenance of late Carboniferous sandstones in the Pennine Basin (UK) from combined heavy mineral, garnet geochemistry and palaeocurrent studies. Sediment. Geol. 203, 196–212. https://doi.org/10.1016/j.sedgeo.2007.11.002

Hallsworth, C.R., Chisholm, J.I., 2000. Stratigraphic evolution of provenance characteristics in Westphalian sandstones of the Yorkshire Coalfield. Proc. Yorksh. Geol. Soc. 53, 43–72. https://doi.org/10.1144/pygs.53.1.43

Hampson, G., 1995. Discrimination of regionally extensive coals in the Upper Carboniferous of the Pennine Basin, UK using high resolution sequence stratigraphic concepts, in: Whateley, M.K.G., Spears, D.A. (Eds.), European Coal

Geology. Geological Society Special Publications, London, pp. 79–97. https://doi.org/10.1144/gsl.sp.1995.082.01.04

Hampson, G., Elliott, T., Davies, S.J., 1997. The application of sequence stratigraphy to Upper Carboniferous fluvio-deltaic strata of the onshore UK and Ireland: implications for the southern North Sea. J. Geol. Soc. London. 154, 719–733. https://doi.org/10.1144/gsjgs.154.4.0719

Hampson, G.J., 1998. Evidence for relative sea-level falls during deposition of the Upper Carboniferous Millstone Grit, South Wales. Geol. J. 33, 243–266. https://doi.org/10.1002/(SICI)1099-1034(199810/12)33:4<243::AID-GJ800>3.0.CO;2-4

Hampson, G.J., Davies, S.J., Elliott, T., Flint, S.S., Stollhofen, H., 1999. Incised valley fill sandstone bodies in Upper Carboniferous fluvio–deltaic strata: recognition and reservoir characterization of Southern North Sea analogues, in: Fleet, A.J., Boldy, S.A.R. (Eds.), Petroleum Geology of Northwest Europe: Proceedings of the 5th Conference. Geological Society, London, pp. 771–788. https://doi.org/10.1144/0050771

Haq, B.U., Hardenbol, J., Vail, P.R., 1988. Mesozoic and Cenozoic chronostatigraphy and cycles of sea-level change, in: Wilgus, C.K., Hastings, B.S., Kendall, C.G.S.C., Posamentier, H.W., Ross, C.A., Van Wagoner, J.C. (Eds.), Sea Level Changes- An Integrated Approach. The Society of Economic Paleontologists and Mineralogists Special Publication 42, Tulsa, pp. 71–108.

Haq, B.U., Schutter, S.R., 2008. A Chronology of Paleozoic Sea-Level Changes. Science (80-.). 322, 64–68.

Harwood, J., Aplin, A.C., Fialips, C.I., Iliffe, J.E., Kozdon, R., Ushikubo, T., Valley, J.W., 2013. Quartz cementation history of sandstones revealed by high-resolution SIMS oxygen isotope analysis. J. Sediment. Res. 522–530. https://doi.org/10.2110/jsr.2013.29

Haszeldine, R.S., MacAulay, C.I., Marchand, A., Wilkinson, M., Graham, C.M., Cavanagh, A., Fallick, A.E., Couples, G.D., 2000. Sandstone cementation and fluids in hydrocarbon basins. J. Geochemical Explor. 69–70, 195–200. https://doi.org/10.1016/S0375-6742(00)00126-6

Hillis, R.R., 1995a. Quantification of Tertiary exhumation in the United Kingdom southern North Sea using sonic velocity data. Am. Assoc. Pet. Geol. Bull. 79, 130–

152.

Hillis, R.R., 1995b. Regional Tertiary Exhumation in and around the United Kingdom, in: Buchanan, J., P.G, B. (Eds.), Basin Inversion. Geological Society Special Publication No. 88, pp. 167–190. https://doi.org/10.1144/GSL.SP.1995.088.01.11

Hillis, R.R., Holford, S.P., Green, P.F., Doré, A.G., Gatliff, R.W., Stoker, M.S., Thomson, K., Turner, J.P., Underhill, J.R., Williams, G.A., 2008. Cenozoic exhumation of the southern British Isles. Geology 36, 371–374. https://doi.org/10.1130/G24699A.1

Holditch, S.A., 2006. Tight Gas Sands. J. Pet. Technol. 58, 86–93. https://doi.org/10.2118/103356-JPT

Holditch, S.A., 2003. The Increasing Role of Unconventional Reservoirs in the Future of the Oil and Gas Business. J. Pet. Technol. 55, 34-37 + 79.

Hollis, C., 1998. Reconstructing fluid history: an integrated approach to timing fluid expulsion and migration on the Carboniferous Derbyshire Platform, England, in: Parnell, J. (Ed.), Dating and Duration of FluidFlow and Fluid-Rock Interaction. Geological Society Special Publication, Londin, pp. 153–159. https://doi.org/10.1144/GSL.SP.1998.144.01.12

Houseknecht, D.W., 1991. Use of Cathodoluminescence Petrography for Understanding Compaction, Quartz Cementation, and Porosity in Sandstones, in: Barker, C.E., Burruss, R.C., Kopp, O.C., Machel, H.G., Marshall, D.J., Wright, P., Colbum, H.Y. (Eds.), Luminescence Microscopy and Spectroscopy: Qualitative and Quantitative Applications. SEPM Society for Sedimentary Geology, pp. 59–66. https://doi.org/10.2110/scn.91.25

Houseknecht, D.W., 1987. Assessing the Relative Importance of Compaction Processes and Cementation to Reduction of Porosity in Sandstones:Discussion; Compaction and Porosity Evolution of Pliocene Sandstones, Ventura Basin, California: Discussion. Am. Assoc. Pet. Geol. Bull. 71, 633–642.

Huggett, J.M., Gale, A.S., McCarty, D., 2010. Petrology and palaeoenvironmental significance of authigenic iron-rich clays, carbonates and apatite in the Claiborne Group, Middle Eocene, NE Texas. Sediment. Geol. 228, 119–139. https://doi.org/10.1016/j.sedgeo.2010.04.005

Hunt, P.K., Engler, P., Bajsarowicz, C., 1988. Computed Tomography as a Core Analysis Tool: Applications, Instrument Evaluation, and Image Improvement Techniques. Soc. Pet. Eng. 40, 1203–1210. https://doi.org/10.2118/16952-PA

Ielpi, A., Ghinassi, M., 2015. Planview style and palaeodrainage of Torridonian channel belts: Applecross Formation, Stoer Peninsula, Scotland. Sediment. Geol. 325, 1–16. https://doi.org/10.1016/j.sedgeo.2015.05.002

Inoue, A., Utada, M., Wakita, K., 1992. Smectite-to-illite conversion in natural hydrothermal systems. Appl. Clay Sci. 7, 131–145. https://doi.org/10.1016/0169-1317(92)90035-L

Japsen, P., 2000. Investigation of multi-phase erosion using reconstructed shale trends based on sonic data. Sole Pit axis, North Sea. Glob. Planet. Change 24, 189–210.

Japsen, P., 1998. Regional velocity-depth anomalies, North Sea Chalk: A record of overpressure and Neogene uplift and erosion. Am. Assoc. Pet. Geol. Bull. 82, 2031–2074.

Jennings, S., Thompson, G.R., 1986. Diagenesis of Plio-Pleistocene sediments of the Colorado River delta, southern California. J. Sediment. Petrol. 56, 89–98. https://doi.org/10.1306/212f8891-2b24-11d7-8648000102c1865d

Jolly, R.J.H., Lonergan, L., 2002. Mechanisms and controls on the formation of sand intrusions. J. Geol. Soc. London. 159, 605–617.

Kareem, R., Cubillas, P., Gluyas, J., Bowen, L., Hillier, S., Greenwell, H.C., 2017. Multi-technique approach to the petrophysical characterization of Berea sandstone core plugs (Cleveland Quarries, USA). J. Pet. Sci. Eng. 149, 436–455. https://doi.org/10.1016/j.petrol.2016.09.029

Kawata, Y., Fujita, K., 2001. SPE 68755 Some Predictions of Possible Unconventional Hydrocarbons Availability Until 2100. Soc. Pet. Eng. 1–10.

Kearsey, T., Ellen, R., Millward, D., Monaghan, A., 2015. Devonian and Carboniferous stratigraphical correlation and interpretation in the Central North Sea, Quadrants 25 –44.

Kerr-McGee York Limited, 2002. Carboniferous opportunities in the Bowland-Craven Basin.

Ketzer, J.M., Morad, S., Nystuen, J.P., De Ros, L.F., 2003. The Role of the Cimmerian Unconformity (Early Cretaceous) in the kaolinitization and related reservoir-quality evolution in Triassic sandstones of the Snorre Field, North Sea, in: Worden, R.H., Morad, S. (Eds.), Clay Mineral Cements in Sandstones. International Association of Sedimentologists, Oxford, UK, pp. 361–382. https://doi.org/10.1002/9781444304336.ch16

Khlaifat, A., Qutob, H., Barakat, N., 2011. Tight Gas Sands Development is Critical to Future World Energy Resources. Soc. Pet. Eng. 1–12. https://doi.org/https://doi.org/10.2118/142049-MS

Kiersnowski, H., Buniak, A., Kuberska, M., Srokowska-Okoñska, A., 2010. Występowanie gazu ziemnego zamkniętego w piaskowcach czerwonego spągowca Polski. Przegląd Geol. 58, 335–346.

Kombrink, H., Besly, B.M., Collinson, J.D., Den Hartog Jager, D.G., Drozdzewski, G., Dusar, M., Hoth, P., Pagnier, H.J.M., Stemmerik, L., Waksmundzka, M.I., Wrede, V., 2010. Carboniferous, in: Doornenbal, J.C., Stevenson, A.G. (Eds.), Petroleum Geological Atlas of the Southern Permian Basin Area. EAGE Publications b.v. (Houten), pp. 81–99.

Kubala, M., Bastow, M., Thompson, S., Scotchman, I., Oygard, K., 2003. Geothermal regime, petroleum generation and migration, in: Evans, D., Graham, C., Armour, A., Bathurst, P. (Eds.), The Millenium Atlas: Petroleum Geology of the Central and Northern North Sea. The Geological Society, London, pp. 285–315.

Lander, R.H., Larese, R.E., Bonnell, L.M., 2008. Toward more accurate quartz cement models: The importance of euhedral versus noneuhedral growth rates. Am. Assoc. Pet. Geol. Bull. 92, 1537–1563. https://doi.org/10.1306/07160808037

Lander, R.H., Walderhaug, O., 1999. Predicting porosity through simulating sandstone compaction and quartz cementation. AAPG Bull. (American Assoc. Pet. Geol. 83, 433–449. https://doi.org/10.1306/00aa9bc4-1730-11d7-8645000102c1865d

Lanson, B., Beaufort, D., Berger, G., Bauer, A., Cassagnabère, A., Meunier, A., 2002. Authigenic kaolin and illitic minerals during burial diagenesis of sandstones: a review. Clay Miner. 37, 1–22. https://doi.org/10.1180/0009855023710014

LASMO North Sea PLC, 1991. Composite log well 44/16-1.

LASMO North Sea PLC, n.d. Final well report. Well 44/16-1, Well 44/16-1ST, Volume one: Geology.

Law, B.E., Curtis, J.B., 2002. Introduction to Unconventional Petroleum Systems. Am. Assoc. Pet. Geol. Bull. 86, 1851–1852.

Leeder, M., Hardman, M., 1990. Carboniferous geology of the Southern North Sea Basin and controls on hydrocarbon prospectivity, in: Hardman, R.F.P., Brooks, J. (Eds.), Tectonic Events Responsible for Britain's Oil and Gas Reserves. Geological Society Special Publication, pp. 87–105.

Leeder, M.R., 1988. Recent developments in Carboniferous geology: a critical review with implications for the British Isles and N. W. Europe, in: Proceedings of the Geologists' Association. The Geologists' Association, pp. 73–100. https://doi.org/10.1016/S0016-7878(88)80001-4

Lin, W., Li, X., Yang, Z., Manga, M., Fu, X., Xiong, S., Gong, A., Chen, G., Li, H., Pei, L., Li, S., Zhao, X., Wang, X., 2019. Multiscale Digital Porous Rock Reconstruction Using Template Matching. Water Resour. Res. 55, 6911–6922. https://doi.org/10.1029/2019WR025219

Ludvigson, G.A., González, L.A., Metzger, R.A., Witzke, B.J., Brenner, R.L., Murillo, A.P., White, T.S., 1998. Meteoric sphaerosiderite lines and their use for paleohydrology and paleoclimatology. Geology 26, 1039–1042. https://doi.org/10.1130/0091-7613(1998)026<1039:MSLATU>2.3.CO;2

Lundegard, P.D., 1992. Sandstone porosity loss; a 'big picture' view of the importance of compaction. J. Sediment. Petrol. 62, 250–260.

Lundegard, P.D., Kharaka, Y.K., 1990. Geochemistry of Organic Acids in Subsurface Waters, in: Melchior, D., Bassett, R. (Eds.), Chemical Modeling of Aqueous Systems II. American Chemical Society Symposium Series 416, pp. 169–189. https://doi.org/10.1021/bk-1990-0416.ch013

Ma, L., Fauchille, A.L., Dowey, P.J., Pilz, F.F., Courtois, L., Taylor, K.G., Lee, P.D., 2017a. Correlative multi-scale imaging of shales: A review and future perspectives, in: Rutter, E., Mecklenburgh, J., Taylor, K.G (Eds.), Geomechanical and Petrophysical Properties of Mudrocks. Geological Society Special Publication, London, pp. 175–199. https://doi.org/10.1144/SP454.11

Ma, L., Taylor, K.G., Dowey, P.J., Courtois, L., Gholinia, A., Lee, P.D., 2017b. Multi-

scale 3D characterisation of porosity and organic matter in shales with variable TOC content and thermal maturity: Examples from the Lublin and Baltic Basins, Poland and Lithuania. Int. J. Coal Geol. 180, 100–112. https://doi.org/10.1016/j.coal.2017.08.002

MacEachern, J.A., Pemberton, S.G., 1994. Ichnological aspects of incised-valley fill systems from the Viking Formation of the western Canada sedimentary basin, Alberta, Canada. SEPM Spec. Publ. No. 51, Soc. Sediment. Geol. 51, 129–157. https://doi.org/10.2110/pec.94.12.0129

Martys, N., Torquato, S., Bentz, D., 1994. Universal scaling of fluid permeability for sphere packings. Phys. Rev. E 50, 403–4008. https://doi.org/10.1103/PhysRevE.50.403

McAulay, G.E., Burley, S.D., Fallick, A.E., Kusznir, N.J., 1994. Palaeohydrodynamic fluid flow regimes during diagenesis of the Brent Group in the Hutton-NW Hutton reservoirs: constraints from oxygen isotope studies of authigenic kaolin and reverse flexural modelling. Clay Miner. 29, 609–625. https://doi.org/10.1180/claymin.1994.029.4.16

McBride, E.F., 1989. Quartz cement in sandstones: a review. Earth Sci. Rev. 26, 69–112. https://doi.org/10.1016/0012-8252(89)90019-6

McCann, T., Pascal, C., Timmerman, M.J., Krzywiec, P., López-Gómez, J., Wetzel, A., Krawczyk, C.M., Rieke, H., Lamarche, J., 2006. Post-Variscan (end Carboniferous-Early Permian) basin evolution in Western and Central Europe, in: Glee, D., Stephenson, R. (Eds.), European Lithosphere Dynamic. Geological Society, Memoirs, 32, London, pp. 355–388. https://doi.org/10.1144/GSL.MEM.2006.032.01.22

McKinley, J.M., Worden, R.H., Ruffel, A.H., 2003. Smectite in sandstones: a review of the controls on occurrence and behaviour during diagenesis, in: Worden, R.H., Morad, S. (Eds.), Clay Mineral Cements in Sandstones. International Association of Sedimentologists, Special Publication Number 34, Blackwell Publishing, pp. 109–128. https://doi.org/10.1017/CBO9781107415324.004

McPhee, C., Reed, J., Zubizarreta, I., 2015. Core analysis: a best practice guide. Elsevier, Amsterdam. https://doi.org/10.1016/B978-0-444-63533-4.09989-3

Medina, C.R., Rupp, J.A., Barnes, D.A., 2011. Effects of reduction in porosity and permeability with depth on storage capacity and injectivity in deep saline

aquifers: A case study from the Mount Simon Sandstone aquifer. Int. J. Greenh. Gas Control 5, 146–156. https://doi.org/10.1016/j.ijggc.2010.03.001

Miall, A.D., 1996. The Geology of Fluvial Deposits: Sedimentary Facies, Basin Analysis, and Petroleum Geology. Springer, New York.

Monaghan, A.A., Arsenikos, S., Quinn, M.F., Johnson, K.R., Vincent, C.J., Vane, C.H., Kim, A.W., Uguna, C.N., Hannis, S.D., Gent, C.M.A., Millward, D., Kearsey, T.I., Williamson, J.P., 2017. Carboniferous petroleum systems around the Mid North Sea High , UK. Mar. Pet. Geol. 88, 282–302. https://doi.org/http://dx.doi.org/10.1016/j.marpetgeo.2017.08.019

Morad, S., Al-ramadan, K., Ketzer, J.M., De Ros, L.F., 2010. The impact of diagenesis on the heterogeneity of sandstone reservoirs : A review of the role of depositional facies and sequence stratigraphy. Am. Assoc. Pet. Geol. Bull. 94, 1267–1309. https://doi.org/10.1306/04211009178

Morad, S., Ketzer, J.M., De Ros, L.R., 2000. Spatial and temporal distribution of diagenetic alterations in siliciclastic rocks: Implications for mass transfer in sedimentary basins. Sedimentology 47, 95–120. https://doi.org/10.1046/j.1365-3091.2000.00007.x

Moscariello, A., 2003. The Schooner Field, Blocks 44/26a, 43/30a, UK North Sea, in: Gluyas, J., Hitchens, H.M. (Eds.), United Kingdom Oil and Gas Fields, Commemorative Millennium Volume. London, pp. 811–824. https://doi.org/10.1144/GSL.MEM.2003.020.01.68

Mostaghimi, P., Blunt, M.J., Bijeljic, B., 2013. Computations of Absolute Permeability on Micro-CT Images. Math. Geosci. 45, 103–125. https://doi.org/10.1007/s11004-012-9431-4

Nelson, P.H., 2009. Pore-throat sizes in sandstones, tight sandstones, and shales. Am. Assoc. Pet. Geol. Bull. 93, 329–340. https://doi.org/10.1306/10240808059

Nesbitt, H.W., Fedo, C.M., Young, G.M., 1997. Quartz and Feldspar Stability, Steady and Non-steady-State Weathering, and Petrogenesis of Siliciclastic Sands and Muds. J. Geol. 105, 173–192.

Noiriel, C., Steefel, C.I., Yang, L., Bernard, D., 2016. Effects of pore-scale precipitation on permeability and flow. Adv. Water Resour. 95, 125–137. https://doi.org/10.1016/j.advwatres.2015.11.013

Nygaard Hansen, H., Løvstad, K., Müller, R., Jahren, J., 2017. Clay coating preserving high porosities in deeply buried intervals of the Stø Formation. Mar. Pet. Geol. 88, 648–658. https://doi.org/10.1016/j.marpetgeo.2017.09.011

O'Mara, P. T., Merryweather, M., Cooper, D.S., 2003. The Tyne Gas Fields, Block 44/18a, UK North Sea, in: Gluyas, J.G., Hichens, H. (Eds.), United Kingdom Oil and Gas Fields, Commemorative Millennium Volume. Geological Society, London, Memoir 20, pp. 851–860. https://doi.org/10.1144/GSL.MEM.2003.020.01.71

O'Mara, P. T, Merryweather, M., Stockwell, M., Bowler, M.M., 2003. The Trent Gas Field, Block 43/24a, UK North Sea, in: Gluyas, J.G., Hichens, H. (Eds.), United Kingdom Oil and Gas Fields, Commemorative Millennium Volume. Geological Society, London, Memoir 20, pp. 835–849.

O'Mara, P.T., Merryweather, M., Stockwell, M., Bowler, M.M., 1999. The Trent Gas Field: correlation and reservoir quality within a complex Carboniferous stratigraphy, in: Fleet, A., Boldy, S.A. (Eds.), Petroleum Geology of Northwest Europe: Proceedings of the 5th Conference. Geological Society, London, pp. 809–821. https://doi.org/10.1144/0050809

Oelkers, E.H., Bjørkum, P.A., Murphy, W.M., 1996. A petrographic and computational investigation of quartz cementation and porosity reduction in North Sea sandstones. Am. J. Sci. 296, 420–452. https://doi.org/10.2475/ajs.296.4.420

OGA, 2019. Sign up for NorEX 2019 – Southern North Sea Exploration Conference [online] [WWW Document]. URL https://www.ogauthority.co.uk/news-publications/news/2019/norex-2019-southern-north-sea-exploration-conference/ (accessed 12.4.20).

Oil & Gas Authority, 2017. Southern North Sea Tight Gas Strategy, Oil and Gas Authority.

Oluwadebi, A.G., Taylor, K.G., Dowey, P.J., 2018. Diagenetic controls on the reservoir quality of the tight gas Collyhurst Sandstone Formation , Lower Permian , East Irish Sea Basin , United Kingdom. Sediment. Geol. 371, 55–74. https://doi.org/10.1016/j.sedgeo.2018.04.006

Oxburgh, E., Andrews-Speed, C.P., 1981. Temperature, thermal gradients and heat flow in the southwestern North Sea, in: Illing, L., Hobson, G. (Eds.), Petroleum Geology of the Continental Shelf of North-West Europe. Heyden & Son, pp. 141–200

151.

Oye, O.J., 2019. Influence of Fluid Pressure and Effective Stress on Quartz Cementation in Clastic Reservoirs. Durham University.

Pamukcu, A.S., Gualda, G.A.R., 2010. Quantitative 3D petrography using X-ray tomography 2: Combining information at various resolutions. Geosphere 6, 775–781. https://doi.org/10.1130/GES00565.1

Pattison, S.A.J., 2005. Storm-influenced prodelta turbidite complex in the Lower Kenilworth Member at Hatch Mesa, Book Cliffs, Utah, U.S.A.: Implications for shallow marine facies models. J. Sediment. Res. 75, 420–439. https://doi.org/10.2110/jsr.2005.033

Paxton, S.T., Szabo, J.O., Ajdukiewicz, J.M., Klimentidis, R.E., 2002. Construction of an intergranular volume compaction curve for evaluating and predicting compaction and porosity loss in rigid-grain sandstone reservoirs. Am. Assoc. Pet. Geol. Bull. 86, 2047–2067.

Pearce, T.J., Martin, J.H., Cooper, D., Wray, D.S., 2010. Chemostratigraphy of Upper Carboniferous (Pennsylvanian) Sequences from the Southern North Sea (United Kingdom), in: Ratcliffe, K.T., Zaitlin, B.A. (Eds.), Application of Modern Stratigraphic Techniques: Theory and Case Histories. Special Publication 94: SEPM (Society for Sedimentary Geology), Tulsa, Oklahoma, pp. 109–127. https://doi.org/10.2110/sepmsp.094.109

Pearce, T.J., McLean, D., Wray, D., Wright, D.K., Jeans, C.J., Mearns, E.W., 2005. Stratigraphy of the Upper Carboniferous Schooner Formation, southern North Sea: chemostratigraphy, mineralogy, palynology and Sm-Nd isotope analysis, in: Collinson, D., Evans, D.J., Holliday, D.W., Jones, N.S. (Eds.), Carboniferous Hydrocarbon Resources: The Southern North Sea and Surrounding Onshore Areas. Occasional Publications, Yorkshire Geological Society, pp. 165–182.

Pepper, A.S., Corvi, P.J., 1995. Simple kinetic models of petroleum formation. Part I : oil and gas generation from kerogen. Mar. Pet. Geol. 12, 291–319.

Percival, C.J., 1992. The Harthope Ganister - A transgressive barrier island to shallow-marine sand-ridge from the Namurian of Northern England. J. Sediment. Petrol. Vol. 62, 442–454. https://doi.org/10.1306/d426791f-2b26-11d7-8648000102c1865d

Pettijohn, F., Potter, P., Siever, R., 1987. Sand and sandstone. Springer-Verlag, new York. https://doi.org/10.2475/ajs.275.5.607

Pharaoh, T., Dusar, M., Geluk, M., Kockel, F., Krawczyk, C., Krzywiec, P., Scheck-Wenderoth, M., Thybo, H., Vejbaek, O., van Wees, J., 2010. Tectonic evolution, in: Doornenbal, H., Stevenson, A. (Eds.), Petroleum Geological Atlas of the Southern Permian Basin Area. EAGE Publications b.v., Houten, pp. 25–57.

Pletsch, T., Appel, J., Botor, D., Clayton, C., Duin, E., Faber, E., Gorecki, W., Kombrink, H., Kosakowski, P., Kuper, G., Kus, J., Lutz, R., Mathiesen, A., Ostertag-Henning, C., Papiernik, B., van Bergen, F., 2010. Petroleum generation and migration, in: Doornenbal, H., Stevenson, A. (Eds.), Petroleum Geological Atlas of the Southern Permian Basin Area. EAGE Publications b.v., Houten, pp. 225–253.

Polish Geological Institute, 2015. How much tight gas is in Poland. [Press release]. [WWW Document]. URL https://www.pgi.gov.pl/en/docman-tree-all/prasa/2962-press-release-tight-gas-poland/file.html (accessed 8.20.19).

Porten, K.W., Warchoł, M.J., Kane, I.A., 2019. Formation of detrital clay grain coats by dewatering of deep-water sands and significance for reservoir quality. J. Sediment. Res. 89, 1231–1249. https://doi.org/10.2110/jsr.2019.65

Powierza, B., Stelzner, L., Oesch, T., Gollwitzer, C., Weise, F., Bruno, G., 2019. Water Migration in One-Side Heated Concrete: 4D In-Situ CT Monitoring of the Moisture-Clog-Effect. J. Nondestruct. Eval. 38, 1–11. https://doi.org/10.1007/s10921-018-0552-7

Prajapati, N., Abad Gonzalez, A., Selzer, M., Nestler, B., Busch, B., Hilgers, C., 2020. Quartz Cementation in Polycrystalline Sandstone: Insights From Phase-Field Simulations. J. Geophys. Res. Solid Earth 125, 1–23. https://doi.org/10.1029/2019JB019137

Quirk, D.G., Aitken, J., 1997. The structure of the Westphalian in the northern oart of the southern North Sea, in: Petroleum Geology of the Southern North Sea: Future Potential. Geological Society Special Publication No.123, pp. 143–152. https://doi.org/10.1144/GSL.SP.1997.123.01.10

Ramm, M., 2000. Reservoir quality and its relationship to facies and provenance in Middle to Upper Jurassic sequences, northeastern North Sea. Clay Miner. 35, 77–94. https://doi.org/10.1180/000985500546747

Ramsbottom, W.H., 1977. Major cycles of transgression and regression (mesothems) in the Namurian. Proc. Yorksh. Geol. Soc. 41, 261–291.

Reading, H., 1995. Sedimentary Environments and Facies, 2nd ed. Blackwell Science Ltd, Oxford.

Regenspurg, S., Feldbusch, E., Byrne, J., Deon, F., Driba, D.L., Henninges, J., Kappler, A., Naumann, R., Reinsch, T., Schubert, C., 2015. Mineral precipitation during production of geothermal fluid from a Permian Rotliegend reservoir. Geothermics 54, 122–135. https://doi.org/10.1016/j.geothermics.2015.01.003

Robinson, A., Gluyas, J., 1992a. Duration of quartz cementation in sandstones, North Sea and Haltenbanken Basins. Mar. Pet. Geol. 9, 324–327.

Robinson, A., Gluyas, J., 1992b. Model calculations of loss of porosity in sandstones as a result of compaction and quartz cementation. Mar. Pet. Geol. 9, 319–323.

Robinson, A.G., Coleman, M.L., Gluyas, J.G., 1993. The age of illite cement growth, Village Fields area, Southern North Sea: evidence from K-Ar ages and 18O/16O ratios. Am. Assoc. Pet. Geol. Bull. 77, 68–80. https://doi.org/10.1306/BDFF8B64-1718-11D7-8645000102C1865D

Ruffell, A., Holliday, D., Smith, D., 2006. Permian: arid basins and hypersaline seas, in: Brenchley, P., Rawson, P.F. (Eds.), The Geology of England and Wales. Geological Society, London, pp. 269–293.

Sajgó, C., 2000. Assessment of generation temperatures of crude oils. Org. Geochem. 31, 1301–1323. https://doi.org/10.1016/S0146-6380(00)00097-8

Sass, H., Cypionka, H., Babenzien, H.D., 1997. Vertical distribution of sulfate-reducing bacteria at the oxic-anoxic interface in sediments of the oligotrophic Lake Stechlin. FEMS Microbiol. Ecol. 22, 245–255. https://doi.org/10.1016/S0168-6496(96)00096-7

Schroot, B.M., V.Bergen, F., Abbink, O.A., David, P., V.Eijs, R., Veld, H., 2006. Hydrocarbon potential of the Pre-Westphalian in the Netherlands on- and offshore - report of the PETROPLAY project, TNO report. Utrecht.

Schwarzer, D., Littke, R., 2007. Petroleum generation and migration in the "Tight Gas" area of the German Rotliegend natural gas play: A basin modelling study. Pet. Geosci. 13, 37–62. https://doi.org/10.1144/1354-079306-703

Schwertmann, U., Fitzpatrick, R.W., 1992. Iron minerals in surface environments, in: Skinner, H.C.W., Fitzpatrick, R.W. (Eds.), Biomineralization Processes of Iron and Manganese: Modern and Ancient Environments. Catena Verlag, pp. 7–30.

Sibley, D.F., Blatt, H., 1976. Intergranula pressure solution and cementation of the Tuscarora orthoquartzite. J. Sediment. Petrol. 46, 881–896.

Silin, D., Patzek, T., 2006. Pore space morphology analysis using maximal inscribed spheres. Phys. A Stat. Mech. its Appl. 371, 336–360. https://doi.org/10.1016/j.physa.2006.04.048

Smalley, P. C., Oxtoby, N., 1990. Diagenesis of Carboniferous channel sands from well 43/19-1, SNS: evidence for poroperm modification during the last 70 M.Y.

Sørensen, K., 1986. Danish Basin subsidence by Triassic rifting on a lithosphere cooling background. Lett. to Nat. 319, 660–663.

Southern, S.J., Mountney, N.P., Pringle, J.K., 2014. The Carboniferous Southern Pennine Basin, UK. Geol. Today 30, 71–78. https://doi.org/10.1111/gto.12044

Southon, L.A., 1991. Special core analysis study, Cavendish (well 43/19-2A) part I: Petrography.

Sultan, L., Plink-Björklund, P., 2006. Depositional environments at a Palaeoproterozoic continental margin, Västervik Basin, SE Sweden. Precambrian Res. 145, 243–271. https://doi.org/10.1016/j.precamres.2005.12.005

Sun, H., Yao, J., Cao, Y. chang, Fan, D. yan, Zhang, L., 2017. Characterization of gas transport behaviors in shale gas and tight gas reservoirs by digital rock analysis. Int. J. Heat Mass Transf. 104, 227–239. https://doi.org/10.1016/j.ijheatmasstransfer.2016.07.083

Surdam, R.C., Boese, S.W., Crossey, L.J., 1984. The Chemistry of Secondary Porosity: Part 2. Aspects of Porosity Modification, in: McDonald, D., Surdam, Ronald C. (Eds.), Clastic Diagenesis. AAPG Memoir 37, pp. 127–149.

Survey, B.G., 2016. Mid North Sea High/Central North Sea files [WWW Document]. 21st Century Explor. Roadmap Palaeoz. Proj. URL https://www.bgs.ac.uk/research/energy/petroleumGeoscience/explorationRoadmap.html (accessed 5.13.19).

Sweeney, J., Burnham, A., 1990. Evaluation of a simple model of vitrinite reflectance

based on chemical kinetics. Am. Assoc. Pet. Geol. Bultetin 74, 1559–1570.

Taylor, A.M., Goldring, R., 1993. Description and analysis of bioturbation and ichnofabric. J. Geol. Soc. London. 150, 141–148. https://doi.org/10.1144/gsjgs.150.1.0141

Taylor, J.M., 1950. Pore-space reduction in sandstones. Bull. Am. Assoc. Pet. Geol. 34, 701–716.

Taylor, T.R., Giles, M.R., Hathon, L.A., Diggs, T.N., Braunsdorf, N.R., Birbiglia, G. V, Kittridge, M.G., Macaulay, C.I., Espejo, I.S., 2010. Sandstone diagenesis and reservoir quality prediction: Models, myths, and reality. Am. Assoc. Pet. Geol. Bull. 94, 1093–1132. https://doi.org/10.1306/04211009123

Thyberg, B., Jahren, J., 2011. Quartz cementation in mudstones: sheet-like quartz cement from clay mineral reactions during burial. Pet. Geosci. 17, 53–63. https://doi.org/10.1144/1354-079310-028

Turner, J.P., Williams, G.A., 2004. Sedimentary basin inversion and intra-plate shortening. Earth-Science Rev. 65, 277–304. https://doi.org/10.1016/j.earscirev.2003.10.002

Underhill, J.R., 2003. The tectonic and stratigraphic framework of the United Kingdom's oil and gas fields, in: Gluyas, J.G., Hichens, H. (Eds.), United Kingdom Oil and Gas Fields, Commemorative Millennium Volume. Geological Society Memoir, pp. 17–59. https://doi.org/10.1144/GSL.MEM.2003.020.01.04

Unknown, n.d. Well 44/16-1 and 44/16-1ST Final Well Report.

van de Kamp, P.C., 2008. Smectite-illite-muscovite transformations, quartz dissolution, and silica release in shales. Clays Clay Miner. 56, 66–81. https://doi.org/10.1346/CCMN.2008.0560106

Van der Land, C., Wood, R., Wu, K., van Dijke, M.I., Jiang, Z., Corbett, P.W.M., Couples, G., 2013. Modelling the permeability evolution of carbonate rocks. Mar. Pet. Geol. 48, 1–7. https://doi.org/10.1016/j.marpetgeo.2013.07.006

van Hoorn, B., 1987. Structural evolution, timing and tectonic style of the Sole Pit inversion. Tectonophysics 137, 239–284. https://doi.org/10.1144/GSL.SP.1989.044.01.24

Van Stappen, J., De Kock, T., Boone, M.A., Olaussen, S., Cnudde, V., 2014. Pore-scale

characterisation and modelling of CO2 flow in tight sandstones using X-ray micro-CT; knorringfjellet formation of the longyearbyen CO2 lab, Svalbard. Nor. J. Geol. 94, 201–215.

Van Wees, J.-D., Stephenson, R.A., Ziegler, P.A., Bayer, U., McCann, T., Dadlez, R., Gaupp, R., Narkiewicz, M., Bitzer, F., Scheck, M., 2000. On the origin of the Southern Permian Basin, Central Europe. Mar. Pet. Geol. 17, 43–59. https://doi.org/10.1016/S0264-8172(99)00052-5

Vane, C., Uguna, C., Kim, A., Johnson, K., Monaghan, A., 2015. Palaeozoic Source Rock Organic Geochemistry of the Central North Sea (CNS).

Vincent, C.J., 2015. Maturity modelling of selected wells in the Central North Sea. Keyworth, Nottingham.

Wadsworth, F.B., Vasseur, J., Llewellin, E.W., Dobson, K., Colombier, M., Von Aulock, F.W., Fife, J.L., Wiesmaier, S., Hess, K.U., Scheu, B., Lavallée, Y., Dingwell, D.B., 2017. Topological inversions in coalescing granular media control fluid-flow regimes. Phys. Rev. E 96, 1–6. https://doi.org/10.1103/PhysRevE.96.033113

Wadsworth, F.B., Vasseur, J., Scheu, B., Kendrick, J.E., Lavallée, Y., Dingwell, D.B., 2016. Universal scaling of fluid permeability during volcanic welding and sediment diagenesis. Geology 44, 219–222. https://doi.org/10.1130/G37559.1

Walderhaug, O., 2000. Modeling Quartz Cementation and Porosity in Middle Jurassic Brent Group Sandstones of the Kvitebjørn Field, Northern North Sea. Am. Assoc. Pet. Geol. Bull. 84, 1325–1339.

Walderhaug, O., 1996. Kinetic modeling of quartz cementation and porosity loss in deeply buried sandstone reservoirs. Am. Assoc. Pet. Geol. Bull. 80, 731–745.

Walderhaug, O, 1994. Precipitation rates for quartz cement in sandstones determined by fluid-inclusion microthermometry and temperature-history modeling. J. Sediment. Res. 64, 324–333. https://doi.org/10.2110/jsr.64.324

Walderhaug, O., 1994. Temperatures of quartz cementation in Jurassic sandstones from the Norwegian continental shelf - evidence from fluid inclusions. J. Sediment. Res. A64, 311–323. https://doi.org/10.1306/d4267d89-2b26-11d7-8648000102c1865d

Walderhaug, O., Bjørkum, P.A., 2003. The effect of stylolite spacing on quartz

cementation in the Lower Jurassic Sto Formation, Southern Barents Sea. J. Sediment. Res. 73, 146–156. https://doi.org/10.1306/090502730146

Wang, S.Y., Huang, Y.B., Pereira, V., Gryte, C.C., 1985. Application of computed tomography to oil recovery from porous media. Appl. Opt. 24, 4021–4027.

Wang, Y., Liu, L., Li, S., Ji, H., Xu, Z., Luo, Z., Xu, T., Li, L., 2017. The forming mechanism and process of tight oil sand reservoirs : A case study of Chang 8 oil layers of the Upper Triassic Yanchang Formation in the western Jiyuan area of the Ordos Basin, China. J. Pet. Sci. Eng. 158, 29–46. https://doi.org/10.1016/j.petrol.2017.08.026

Warr, L.N., 2012. The Variscan Orogeny: the Welding of Pangaea, in: Woodcock, N., Strachan, R. (Eds.), Geological History of Britain and Ireland. John Wiley & Sons, Ltd, Oxford, pp. 274–298. https://doi.org/10.1002/9781118274064.ch15

Wasielka, N., Dobson, K., 2019. Permeability evolution using X-ray backstripping [WWW Document]. Durham Res. Data Repos. https://doi.org/10.15128/r237720c72p

Wasielka, N., Gluyas, J.G., Breese, H., Symonds, R., 2020. The Cavendish Field, Block 43/19, UK North Sea, in: Goffey, G., Gluyas, J.G. (Eds.), United Kingdom Oil and Gas Fields: 50th Anniversary Commemorative Volume. Geological Society, London, Memoirs, 52, pp. 131–141. https://doi.org/https://doi.org/10.1144/M52-2019-10

Waters, C., Browne, M.A., Jones, N., Somerville, I., 2011. Midland Valley of Scotland, in: Waters, C.N., Somerville, I.D., Jones, N.S., Cleal;, C.J., Collinson;, J.D., Waters;, R.A., Besly;, B.M., Dean, M.T., Stephenson, M.H., Davies, J.R., Freshney, E.C., Jackson, D.I., Mitchell, W.I., Powell;, J.H., Barclay, W.J., Browne, M.A.E., Leveridge, B.E., Long, S.L., McLean, D. (Eds.), A Revised Correlation of Carboniferous Rocks in the British Isles. Geological Society of London, London, pp. 96–102. https://doi.org/10.1144/SR26.14

Waters, C.N., Davies, S., 2006. Carboniferous: extensional basins, advancing deltas and coal swamps, in: Brenchley, P.J., Rawson, P.F. (Eds.), The Geology of England and Wales. The Geological Society, London, pp. 173–223.

Wellington, S.L., Vinegar, H.J., 1987. X-Ray Computerized Tomography. Soc. Pet. Eng. 39, 885–898. https://doi.org/10.2118/16983-PA

Weltje, G.J., von Eynatten, H., 2004. Quantitative provenance analysis of sediments: Review and outlook. Sediment. Geol. 171, 1–11. https://doi.org/10.1016/j.sedgeo.2004.05.007

Wentworth, C., 1922. A scale of grade and class terms for clastic sediments. J. Geol. 30, 377–392.

Whitmore, G.P., Crook, K.A.W., Johnson, D.P., 2004. Grain size control of mineralogy and geochemistry in modern river sediment, New Guinea collision, Papua New Guinea. Sediment. Geol. 171, 129–157. https://doi.org/10.1016/j.sedgeo.2004.03.011

Wilkinson, M., Haszeldine, R.S., 2011. Oil charge preserves exceptional porosity in deeply buried, overpressured, sandstones: Central North Sea, UK. J. Geol. Soc. London. 168, 1285–1295. https://doi.org/10.1144/0016-76492011-007

Wilkinson, M., Haszeldine, R.S., 2002. Fibrous illite in oilfield sandstones - a nucleation kinetic theory of growth. Terra Nov. 14, 56–60. https://doi.org/10.1046/j.1365-3121.2002.00388.x

Wood, I., 2014. UKCS Maximising Economic Recovery Review: Final Report 'The Wood Review' [WWW Document]. URL https://www.gov.uk/government/uploads/system/uploads/attachment_data/file/471452/UKCS_Maximising_Recovery_Review_FINAL_72pp_locked.pdf (accessed 12.16.19).

Worden, R.H., Bukar, M., Shell, P., 2018. The effect of oil emplacement on quartz cementation in a deeply buried sandstone reservoir. Am. Assoc. Pet. Geol. Bull. 102, 49–75. https://doi.org/10.1306/02071716001

Worden, R. H., Burley, S.D., 2003. Sandstone diagenesis: the evolution of sand to stone, in: Burley, S.D., Worden, R.H. (Eds.), Sandstone Diagenesis: Recent and Ancient. International Association of Sedimentologists, pp. 1–44. https://doi.org/10.1002/9781444304459.ch

Worden, Richard H, Burley, S.D., 2003. Sandstone diagenesis: the evolution of sand to stone, in: Burley, S.D., Worden, R.H. (Eds.), Sandstone Diagenesis: Recent and Ancient. International Association of Sedimentologists, vol. 4, Blackwell Publishing Ltd., Oxford, UK, pp. 3–44. https://doi.org/10.1002/9781444304459

Worden, R.H., Morad, S., 2003. Clay minerals in sandstones: controls on formation,

distribution and evolution, in: Worden, R.H., Morad, S. (Eds.), Clay Mineral Cements in Sandstones. International Association of Sedimentologists, Special Publication Number 34, Blackwell Publishing, pp. 3–41.

Worden, R.H., Morad, S., 2000. Quartz Cementation in Oil Field Sandstones: A Review of the Key Controversies, in: Worden, Richard H., Morad, S. (Eds.), Quartz Cementation in Sandstones. Blackwell Publishing Ltd., Oxford, UK, pp. 1–20. https://doi.org/10.1002/9781444304237.ch1

Worden, R.H., Oxtoby, N.H., Smalley, P.C., 1998. Can oil emplacement prevent quartz cementation in sandstones? Pet. Geosci. 4, 129–137. https://doi.org/10.1144/petgeo.4.2.129

Wu, K., Jiang, Z., Couples, G., Van Dijke, M.I.J., Sorbie, K.S., 2007. Reconstruction of Multi-Scale Heterogeneous Porous Media and Their Flow Prediction, in: International Symposium of the Society of Core Analysts. Calgary, Canada, pp. 1–12.

Wulandari, R., Elie, M., Rajhi, M., Morad, K., 2018. Complex Fluid Characterization of Tight Gas Field in Sultanate of Oman; The Success Story of Subsurface Data Integration. Soc. Pet. Eng. 1–14. https://doi.org/https://doi.org/10.2118/193337-MS

Wygrala, B., 1989. Integrated study of an oil field in the southern Po basin, Northern Italy. Köln University, Jülich Research Centre.

Xi, K., Cao, Y., Jahren, J., Zhu, R., Bjørlykke, K., Zhang, X., Cai, L., Hellevang, H., 2015a. Quartz cement and its origin in tight sandstone reservoirs of the Cretaceous Quantou formation in the southern Songliao basin, China. Mar. Pet. Geol. 66, 748–763. https://doi.org/10.1016/j.marpetgeo.2015.07.017

Xi, K., Cao, Y., Jahren, J., Zhu, R., Bjørlykke, K., Zhang, X., Cai, L., Hellevang, H., 2015b. Quartz cement and its origin in tight sandstone reservoirs of the Cretaceous Quantou formation in the southern Songliao basin , China. Mar. Pet. Geol. 66, 748–763. https://doi.org/10.1016/j.marpetgeo.2015.07.017

Yue, D., Wu, S., Xu, Z., Xiong, L., Chen, D., Ji, Y., Zhou, Y., 2018. Reservoir quality, natural fractures, and gas productivity of upper Triassic Xujiahe tight gas sandstones in western Sichuan Basin, China. Mar. Pet. Geol. 89, 370–386. https://doi.org/10.1016/j.marpetgeo.2017.10.007

Zhang, Y., Bao, Z., Yang, F., Mao, S., Song, J., Jiang, L., 2018. The controls of pore-throat structure on fluid performance in tight clastic rock reservoir: A case from the Upper Triassic of Chang 7 member, Ordos Basin, China. Geofluids 2018, 1–17. https://doi.org/10.1155/2018/3403026

Ziegler, P., 1990. Geological Atlas of Western and Central Europe, 2nd Editio. ed. Shell Internationale Petroleum Mij. B.V. and Geological Society, London.

Zijerveld, L., Stephenson, R., Cloetingh, S., Duin, E., van den Berg, M.W., 1992. Subsidence analysis and modelling of the Roer Valley Graben (SE Netherlands). Tectonophysics 208, 159–171. https://doi.org/10.1016/0040-1951(92)90342-4

Appendix 1

Logged core database

Field	Well	Lat/long	Core run number	Core top depth [ft]	Core base depth [ft]	Core thickness [ft]
Copernicus	44/16-1	54.361569, 2.118242	6	13950	14009.7	59
			7	14009	14087.5	78.5
			8	14090	14160	70.0
			9	14162	14199.6	37.6
			10	14806	14838.6	32.60
			11	14900	14986.6	86.6
						SUM: 364.3
	44/16-1Z	54.361569, 2.118242	2	14175	14191.5	16.5
			3	14191.5	14210.1	18.6
			4	14210.1	14263.4	53.3
						SUM: 88.4
	44/16-2	54.375677, 2.10941	5	14252	14286.5	34.5
			6	14764	14771	7.0
			7	14772	14840	68.0
						SUM: 109.5
Cavendish	43/19-1	54.478111, 1.754167	1	12044	12104.8	60.8
			2	12105	12164	59
			3	12429	12489	60
			4	12654	12717	63
						SUM: 242.8
	43/19-2	54.481944, 1.706194	2	11892.8	11949.1	56.3
			3	11987.0	12048.3	61.3
			4	12049.0	12077.2	28.2
			5	13188.7	13224.9	36.3
			6	13300.2	13361.2	61.0
			7	13408.4	13469.5	61.1
			8	13910.4	13971.9	61.5
						SUM: 365.7
	43/19a-4Z	54.481928, 1.706165	10	16180	16248.6	68.6
			11	16252	16294	42
			11	16500	16520.5	20.5
			12	16520.5	16608.8	88.3
						SUM: 219.4

Appendix 2

Sedimentary logs

NATALIA WASIELKA
CORE DESCRIPTION CHART
SCALE 1:100
10 ft

43/19-1

Durham University

CORE DESCRIPTION | INTERPRETATION | CORE ANALYSIS

AGE | CORE | DRILLERS DEPTH (FEET) | FRACTURES (GEOMETRY) | FRACTURES (FILL) | PERCENT SAND | LITHOLOGY

GRAIN SIZE, SEDIMENTARY STRUCTURES AND PALAEONTOLOGY

CLAY | SAND: SILT, VERY FINE, FINE, MEDIUM, COARSE, VERY COARSE | GRANULE | PEBBLE | COBBLE | TRENDS

SORTING | BIOTURBATION INDEX | VISUAL CEMENTS | VISUAL POROSITY IN HAND SPECIMEN | LITHOFACIES

FACIES ASSOCIATION

SAMPLE | POROSITY & PERMEABILITY

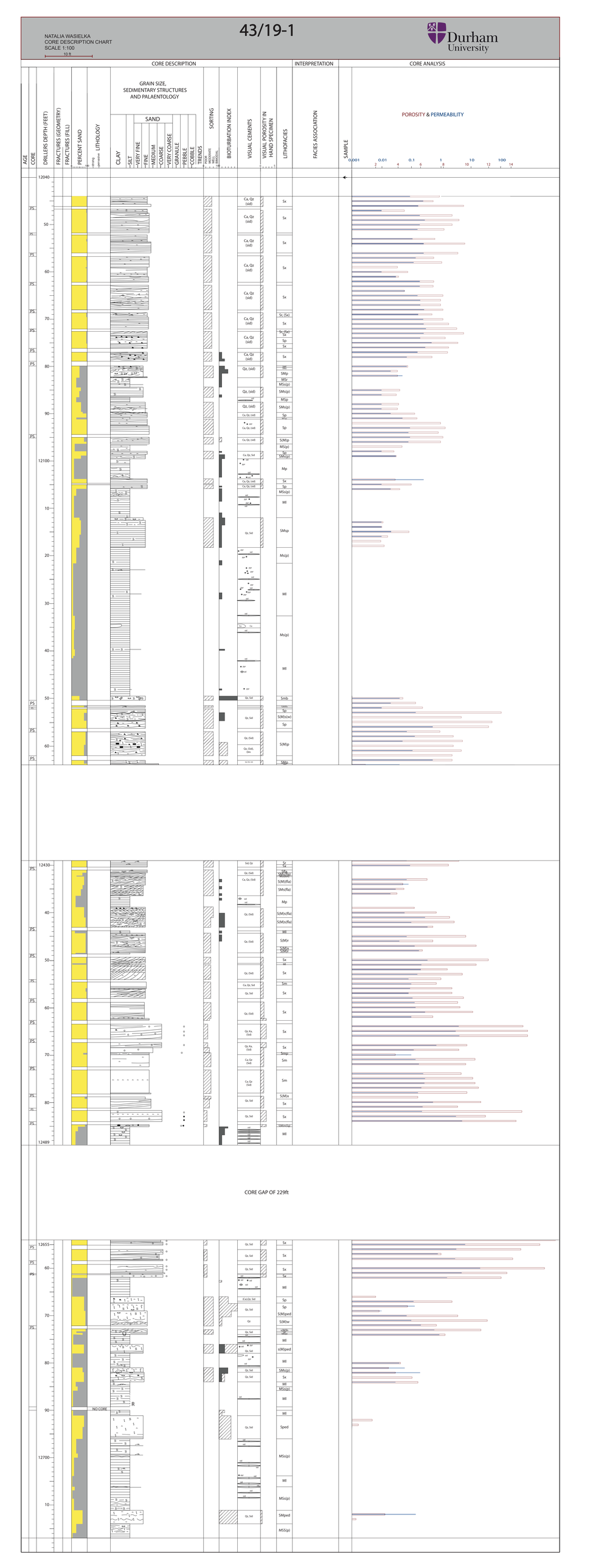

43/19-2

NATALIA WASIELKA
CORE DESCRIPTION CHART
SCALE 1:100
10 ft

CORE DESCRIPTION | INTERPRETATION | CORE ANALYSIS

LITHOSTRATIGRAPHY | CORE | DRILLERS DEPTH (METERS) | FRACTURES (GEOMETRY) | FRACTURES (FILL) | PERCENT SAND | LITHOLOGY | GRAIN SIZE, SEDIMENTARY STRUCTURES AND PALAEONTOLOGY | SORTING | BIOTURBATION INDEX | VISUAL CEMENTS | VISUAL POROSITY IN HAND SPECIMEN | LITHOFACIES | FACIES ASSOCIATION | SAMPLE | POROSITY & PERMEABILITY

Coal Measures

Millstone Grit

MULTI-STOREY FLUVIAL CHANNEL

MULTI-STOREY FLUVIAL CHANNEL

INTERDISTRIBUTARY BAY

NON-SCALED CORE GAP OF 12 M

INTERDISTRIBUTARY BAY

SHOREFACE

INTERDISTRIBUTARY BAY

DELTA PLAIN

SHOREFACE

INTERDISTRIBUTARY BAY

NON-SCALED CORE GAP OF 339 M

Millstone Grit

MULTI-STOREY FLUVIAL CHANNEL

NATALIA WASIELKA
CORE DESCRIPTION CHART
SCALE 1:100

44/16-1

Durham University

CORE DESCRIPTION | INTERPRETATION | CORE ANALYSIS

GRAIN SIZE, SEDIMENTARY STRUCTURES AND PALAEONTOLOGY

SAND

AGE | CORE | DRILLERS DEPTH (FEET) | FRACTURES (GEOMETRY) | FRACTURES (FULL) | PERCENT SAND | LITHOLOGY | CLAY | SILT | VERY FINE | FINE | MEDIUM | COARSE | VERY COARSE | GRANULE | PEBBLE | COBBLE | TRENDS | SORTING | BIOTURBATION INDEX | VISUAL CEMENTS | VISUAL POROSITY IN HAND SPECIMEN | LITHOFACIES | FACIES ASSOCIATION | SAMPLE | POROSITY & PERMEABILITY

KINDERSCOUTIAN

DISTAL PRODELTA
OFFSHORE TRANSITION (heterolithic shelf)
DISTAL DELTA FRONT
PROXIMAL PRODELTA TURBIDITE COMPLEX
DISTAL PRODELTA TURBIDITE COMPLEX
CORE GAP OF 2.5 FT
PROXIMAL PRODELTA TURBIDITE COMPLEX
DISTAL PRODELTA TURBIDITE COMPLEX
OPEN SHELF
DISTAL PRODELTA
CORE GAP OF 2 FT
DISTAL PRODELTA
OPEN SHELF
DELTA PLAIN
INTERDISTRIBUTARY BAY
NON-SCALED CORE GAP OF 605 FT
DISTRIBUTARY CHANNEL
INTERDISTRIBUTARY BAY
DELTA PLAIN
NON-SCALED CORE GAP OF 61.4 FT

1:100 SCALE LOGGING SHEET

WELL:
DATE:
LOGGED BY:

CORE DESCRIPTION
COMMENTS
DEPOSITIONAL INTERPRETATION
FACIES
FACIES ASSOC.
ENVIRONMENT
KEY STRATAL SURFACES
SHEET

PROXIMAL PRODELTA
DISTAL DELTA FRONT
PROXIMAL DELTA FRONT
DISTAL PRODELTA

44/16-1Z

NATALIA WASIELKA
CORE DESCRIPTION CHART
SCALE 1:100
10 ft

Durham University

CORE DESCRIPTION | INTERPRETATION | CORE ANALYSIS

AGE | CORE | DRILLERS DEPTH (FEET) | FRACTURES (GEOMETRY) | FRACTURES (FILL) | PERCENT SAND (0–100) | LITHOLOGY (strong, pervasive) | GRAIN SIZE, SEDIMENTARY STRUCTURES AND PALAEONTOLOGY (CLAY, SILT, SAND: VERY FINE, FINE, MEDIUM, COARSE, VERY COARSE, GRANULE, PEBBLE, COBBLE, TRENDS) | SORTING (0–100: POOR, MODERATE, WELL, BIMODAL) | BIOTURBATION INDEX | VISUAL CEMENTS | VISUAL POROSITY IN HAND SPECIMEN (0–5) | LITHOFACIES | FACIES ASSOCIATION | SAMPLE | POROSITY & PERMEABILITY (0.001, 0.01, 0.1, 1, 10, 100; 2, 4, 6, 8, 10, 12, 14)

DRILLERS DEPTH (FEET)	CORE	LITHOFACIES	VISUAL CEMENTS	FACIES ASSOCIATION
14175	2	S(M)x	Qz (Dm)	DELTA PLAIN
		S(M)p		DISTRIBUTARY CHANNEL
80	PS	SMr		
	2	SM(s/r)	Qz (Dm)	INTERISTRIBUTARY BAY (tidally influenced)
		Mm		
		SMr		
		SMp	sid	
90		Sm?	Qz (Dm)	DELTA PLAIN
	PS			
	2	Sp?	Qz (Dm)	
	PS			
		Sp	Qz (Dm)	
	3	SM(p)		
		MI	pyr sid	INTERISTRIBUTARY BAY
		SMr	Qz (Dm)	
	PS	S(M)p		
14200		MSs(r,p)	Qz (Dm) sid	
	3	Ms(p)		
		Sm	Qz (Dm) + goet sid	DELTA PLAIN
	PS			
	3	SM(p)		
10		Sm	Qz (Dm)	
	PS			
		S(M)p	Qz (Dm)	
	4		Qz (Dm) goet	
		S(M)ped	Qz (Dm)	
	PS			
20		Sp?	Qz (Dm)	
	4	S(M)p	Qz (Dm) Goet	
	PS			
		MI		
		coal	Qz (Dm)	
	4	S(M)	Qz (Dm) Goet	
30		Sped	Qz (Dm)	
	PS			
		MSsP		INTERISTRIBUTARY BAY/LAGOON (tidally influenced)
		Ms(p)		
	4	S(M)r	Qz (Dm)	
		Ms(l)		
		S(M)w	Qz (Dm) Qz, sid (Dm) Qz (Dm)	
	PS	MI		
40		Msp	sid	
	4	SMs(r)	Qz (Dm)	
	PS	MSsp		
50				
	4	MI	sid sid py sid sid sid sid sid	
60		SMsp	Qz	
		MI	sid	
		S(M)d	Qz (Dm)	

NATALIA WASIELKA
CORE DESCRIPTION CHART
SCALE 1:100
10 ft

44/16-2

Durham University

CORE DESCRIPTION | INTERPRETATION | CORE ANALYSIS

AGE | CORE | DRILLERS DEPTH (FEET) | FRACTURES (GEOMETRY) | FRACTURES (FILL) | PERCENT SAND (0–100) | LITHOLOGY (strong – pervasive)

GRAIN SIZE, SEDIMENTARY STRUCTURES AND PALAEONTOLOGY: CLAY | SILT | SAND (VERY FINE | FINE | MEDIUM | COARSE | VERY COARSE) | GRANULE | PEBBLE | COBBLE | TRENDS

SORTING (POOR – MODERATE – WELL – BIMODAL) | BIOTURBATION INDEX (0–100) | VISUAL CEMENTS | VISUAL POROSITY IN HAND SPECIMEN (0–5) | LITHOFACIES | FACIES ASSOCIATION

CORE ANALYSIS: SAMPLE | POROSITY & PERMEABILITY (0.001 – 0.01 – 0.1 – 1 – 10 – 100; 2 – 4 – 6 – 8 – 10 – 12 – 14)

AGE	CORE	DRILLERS DEPTH (FEET)	LITHOLOGY	GRAIN SIZE	BIOTURBATION INDEX	VISUAL CEMENTS	LITHOFACIES	FACIES ASSOCIATION
KINDERSCOUTIAN	5	14255				Qz, Dm	MI	
							S(I)ped	DELTA PLAIN
		60					S(M)x	MULTI-STOREY FLUVIAL CHANNEL
	PS	70				Qz, Dm, He	Sx	
	5					Qz, Dm	MSl	
						sid	S(M)x	
		80				sid	MI	INTERDISTRIBUTARY BAY/LAGOON
						Qz, Dm	S(M)ped	DELTA PLAIN
		NON-SCALED CORE GAP OF 477.5 FT						
	6	14765				Qz, Dm	Sx	DISTRIBUTARY CHANNEL
	PS	70						
	6					Qz, Dm	Sp	PROXIMAL DELTA FRONT (tidally-influenced sand flat)
							S(M)x	
							S(M)fla	
							Smdfla	
							Smd	
							SMs(fla)	
		80					MS(len)	PROXIMAL PRODELTA
						µpy	MI	DISTAL PRODELTA
		90				µpy		OPEN SHELF
						µpy		
						µpy		
						µpy		DISTAL PRODELTA
	7	14800				µpy		
		10						OPEN SHELF
		20				Qz, (Ca,Dm)	Sx	PROXIMAL DELTA FRONT (tidally-influenced sand flat)
							Sr	
							S(M)r	
							MI	DELTA PLAIN (with distributary channels)
		30				Qz, (Dm) Sid	Sped	
							Sp	
							Sp(Sr)	
						Sid	Sp	
		40					MI	

LEGEND

LITHOLOGY

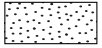

sandstone

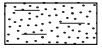

silty sandstone

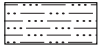

sandy siltstone

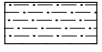

siltstone

LITHOCLASTS

- Coarse sand/granule
- Mudclast
- Coal fragment

STRUCTURES

Horizontal stratification

Tabular stratification

Wavy stratification

Flaser stratification

Lenticular bedding

Flame structure

Ripples

Sand injection

Synaeresis cracks

Roots

BODY FOSSILS

Ammonites

Bioclast

Plant debris

TRACE FOSSILS

Chondrites

Escape burrow

General bioturbation

Ophiomorpha

Phycosiphon

Planolites

Resting trace

Teichichnus

Zoophycos

DIAGENESIS

Nodule

Filled fracture

Open fracture

Stylolite

- Ca — Calcite
- Dm — Dolomite
- He — Haematite
- Ka — Kaolinite
- Py — Pyrite
- Qz — Quartz
- Sd — Sand
- Si — Siderite
- St — Silt

Well defined cements
e.g. Qz, Ca

Possible cements
e.g. (Qz), (Ca)

VISUAL POROSITY

0	Negligible
1	Very low
2	Low
3	Moderate
4	High
5	Very high

Appendix 3

Modal table

WELL	44/16-1	44/16-1	44/16-1	44/16-1	44/16-1	44/16-1	44/16-1	44/16-1	44/16-1	44/16-1	44/16-1	44/16-1	44/16-1	44/16-1	44/16-1	44/16-1	44/16-1
DEPTH (m/ftDD)	13969.5	13969.9	13985.20	13993.90	13995.90	14002.20	14023.70	14033.30	14048.20	14062.10	14065.80	14094.90	14107.20	14189.10	14190.00	14806.90	14832.20
UNIT	ft	ft	ft	ft	ft	ft	ft	ft	ft	ft	ft	ft	ft	ft	ft	ft	ft
LITHOSTRATIGRAPHY	Millstone Grit Fm	Millstone Grit Fm	Millstone Grit Fm	Millstone Grit Fm	Millstone Grit Fm	Millstone Grit Fm	Millstone Grit Fm	Millstone Grit Fm	Millstone Grit Fm	Millstone Grit Fm	Millstone Grit Fm	Millstone Grit Fm	Millstone Grit Fm	Millstone Grit Fm	Millstone Grit Fm	Millstone Grit Fm	Millstone Grit Fm
LITHOFACIES	SMd	SMp	SMs(p)	SMs(p)	SMs(p)	Sm	S(M)s(p,r)	Sx	MSs(p,d)	SMs(p)	Sm	MSs(r)	Sp	S(M)ped	S(M)m	Sm	S(M)ped
SANDSTONE CLASSIFICATION	dFA	dFA	sidLW	LW	sidFA	dFA	d/sidFA	FA	sidLA	sid/dFA	dSFA	sidLA	dSLA	sQA	sQA	sQA	SLW
FACIES ASSOCIATION	Proximal prodelta	Proximal prodelta	Proximal prodelta	Proximal prodelta	Proximal prodelta	Distal delta front	Distal delta front	Distal delta front	Prodelta turbidite complex	Prodelta turbidite complex	Prodelta turbidite complex	Prodelta turbidite complex	Prodelta turbidite complex	Delta plain	Delta plain	Distributary channel	Delta plain
MODAL GRAIN SIZE	lower very fine sand	upper very fine sand	lower coarse silt	upper coarse silt	lower very fine sand	lower medium sand	upper medium sand	lower fine sand	upper coarse silt	lower very fine sand	upper fine sand	upper coarse silt	upper very fine sand	upper fine sand	lower medium sand	upper fine sand	upper very fine sand
SORTING	moderately well sorted	moderately well sorted	moderately well sorted	moderately sorted	moderately well sorted	moderately well sorted	poorly sorted	moderately well sorted	moderately well sorted	moderately well sorted	moderately well sorted	moderately sorted	moderately well sorted	moderately well sorted	well sorted	moderately well sorted	moderately sorted
DETRITAL MINERALOGY																	
QUARTZ	20.3	28.3	24.3	26.7	29.0	38.0	28.7	40.7	26.7	24.0	47.0	28.0	36.3	74.0	65.3	71.7	53.7
monocrystalline	17.0	25.3	22.0	24.3	23.0	29.0	24.7	34.0	24.3	20.0	36.7	26.0	32.7	67.3	63.0	65.3	48.3
polycrystalline	3.3	3.0	2.3	2.3	6.0	9.0	4.0	6.7	2.3	4.0	10.3	2.0	3.7	6.7	2.3	6.3	5.3
FELDSPAR	22.0	20.0	16.3	13.0	18.3	20.0	20.7	19.0	17.7	24.3	13.7	15.0	12.0	2.0	3.7	3.0	4.0
K-feldspar	3.3	3.7	1.7	2.3	3.7	3.0	2.3	3.7	3.0	5.7	4.0	2.3	3.0	1.7	3.3	2.3	0.0
plagioclase	18.7	16.3	14.7	10.7	14.7	17.0	18.3	15.3	14.7	18.7	9.7	12.7	9.0	0.3	0.3	0.7	4.0
RIGID ROCK FRAGMENTS	2.7	5.7	5.7	7.0	3.0	4.0	3.7	4.0	5.3	1.0	5.0	3.7	6.7	1.0	3.0	2.3	7.0
igneous	2.7	5.7	5.7	7.0	2.3	4.0	3.7	4.0	5.3	1.0	3.7	3.7	6.0	1.0	3.0	2.3	7.0
metamorphic	0.0	0.0	0.0	0.0	0.7	tr	0.0	0.0	0.0	0.0	1.3	0.0	0.7	0.0	0.0	0.0	0.0
sedimentary	0.0	0.0	0.0	0.0	0.0	0.0	0.0	0.0	0.0	0.0	0.0	0.0	0.0	0.0	0.0	0.0	0.0
HEAVY MINERALS	0.3	0.0	0.7	0.3	0.3	1.0	0.3	0.7	tr	0.7	0.3	1.0	tr	1.3	tr	0.7	tr
heavy mineral types	A,Z	M,R,Z		O,T	R	M,O,R,T	R	R,Z	R	R,Z	O,T,Z	O,R,Z	Z	M,O,R,T	R,T	A,M,R,T,Z	R,T,Z
DUCTILE ROCK FRAGMENTS	0.0	0.7	0.3	0.0	0.7	1.0	1.7	2.0	1.7	0.7	2.7	1.0	1.7	0.0	0.0	0.0	0.0
degraded igneous	0.0	0.0	0.0	0.0	0.7	1.0	1.3	1.7	1.7	0.7	2.7	1.0	1.7	0.0	0.0	0.0	0.0
sedimentary	0.0	0.7	0.3	0.0	0.0	0.0	0.3	0.3	0.0	0.0	0.0	0.0	0.0	0.0	0.0	0.0	0.0
MICA	4.7	6.3	6.0	10.7	5.7	3.0	5.7	3.3	1.7	5.0	2.0	5.0	4.7	0.0	0.0	tr	5.3
muscovite	4.7	6.3	6.0	9.7	5.3	3.0	5.7	3.3	1.7	4.7	2.0	4.0	4.7	0.0	0.0	tr	5.3
biotite	0.0	0.0	0.0	1.0	0.3	0.0	0.0	0.0	0.0	0.3	0.0	1.0	0.0	0.0	0.0	0.0	tr
CHLORITE	0.0	0.0	0.0	0.3	0.0	0.0	0.0	0.0	0.0	0.0	0.0	0.0	0.0	0.0	0.0	0.0	0.0
ORGANIC FRAGMENTS	7.7	4.7	6.0	8.0	6.3	0.3	0.7	0.3	16.0	9.3	0.0	5.3	0.0	0.0	0.0	0.0	2.7
OPTICALLY NON-RESOLVABLE CLAY	10.7	14.3	21.7	24.3	12.3	4.0	6.0	8.0	14.0	7.0	4.3	11.3	8.3	0.7	0.3	0.0	23.0
detrital	8.0	10.3	16.3	21.0	9.7	0.0	2.3	3.3	5.7	4.7	2.3	8.7	4.7	0.0	0.3	0.0	20.7
pseudomatrix	2.7	4.0	5.3	3.3	2.7	4.0	3.7	4.7	8.3	2.3	2.0	2.7	3.7	0.7	0.0	0.0	2.3
AUTHIGENIC MINERALOGY																	
QUARTZ OVERGROWTHS	0.3	tr	tr	0.0	0.3	7.7	4.7	3.7	0.7	0.7	6.0	1.0	5.3	13.3	15.0	16.0	2.0
Na-FELDSPAR OVERGROWTHS	0.0	0.0	0.0	0.0	0.0	1.0	1.3	1.0	0.7	0.7	2.0	0.0	0.0	0.0	0.0	0.0	0.0
K-FELDSPAR OVERGROWTHS	0.0	0.0	0.0	0.0	0.0	0.0	0.0	0.0	0.0	0.0	0.0	0.0	0.0	0.0	0.0	0.0	0.0
CALCITE CEMENT	0.0	0.0	0.0	0.0	0.0	0.0	0.0	0.0	0.0	0.0	0.0	0.0	0.0	0.0	0.0	0.0	0.0
ferroan	0.0	0.0	0.0	0.0	0.0	0.0	0.0	0.0	0.0	0.0	0.0	0.0	0.0	0.0	0.0	0.0	0.0
non-ferroan	0.0	0.0	0.0	0.0	0.0	0.0	0.0	0.0	0.0	0.0	0.0	0.0	0.0	0.0	0.0	0.0	0.0
DOLOMITE CEMENT	21.0	10.3	1.7	0.7	5.3	13.0	14.3	7.7	0.7	11.3	12.7	6.7	14.7	0.0	0.0	tr	0.0
ferroan - primary pore-filling	11.7	8.3	0.0	0.0	1.0	9.7	9.3	4.0	0.0	2.0	9.7	0.0	4.7	0.0	0.0	tr	0.0
ferroan - replacive	5.3	0.0	0.0	tr	2.7	2.3	0.7	0.0	0.7	0.7	1.7	0.3	5.0	0.0	0.0	0.0	0.0
non-ferroan - primary pore-filling	2.7	1.3	1.3	0.3	0.7	1.0	4.0	3.7	0.0	8.3	1.0	6.3	3.0	0.0	0.0	0.0	0.0
non-ferroan - replacive	1.3	0.7	0.3	0.3	1.0	0.0	0.3	0.0	0.0	0.3	0.3	0.0	2.0	0.0	0.0	tr	0.0
SIDERITE	10.3	9.0	17.0	8.7	17.7	1.7	11.0	8.3	13.7	12.3	2.3	22.0	9.7	0.0	0.0	0.3	0.0
BARITE	0.0	0.0	0.0	0.0	0.0	0.0	0.0	0.0	0.0	0.0	0.0	0.0	0.0	0.0	0.0	0.0	0.0
ANHYDRITE	0.0	0.0	0.0	0.0	0.0	0.0	0.0	0.0	0.0	0.0	0.0	0.0	0.0	0.0	0.0	0.0	0.0
IRON OXIDE	0.0	0.0	0.0	0.0	0.0	0.0	0.0	0.0	0.0	0.0	0.0	0.0	0.0	0.0	0.0	0.0	0.0
PYRITE CEMENT	tr	0.0	0.0	0.0	0.0	0.0	0.0	0.0	0.0	2.3	0.0	tr	0.0	tr	0.3	0.0	0.0
ANATASE	0.0	0.0	0.0	tr	1.3	0.3	0.3	0.0	0.0	0.7	0.0	0.0	0.0	tr	0.7	0.3	tr
ZEOLITE	0.0	0.0	0.0	0.0	0.0	0.0	0.0	0.0	0.0	0.0	0.0	0.0	0.0	0.0	0.0	0.0	0.0
RESIDUAL OIL	0.0	0.0	0.0	0.0	0.0	0.0	0.0	0.0	0.0	0.0	tr	0.0	0.0	tr	tr	0.0	0.0
OPTICALLY NON-RESOLVABLE REPLACIVE CLAY	0.0	0.0	0.0	0.0	0.0	0.0	0.3	0.3	0.0	0.0	0.0	0.0	0.0	0.0	0.0	0.3	0.0
OPTICALLY NON-RESOLVABLE PORE-LINING CLAY	0.0	0.0	0.0	0.0	0.0	0.0	0.0	0.0	0.0	0.0	0.0	0.0	0.0	0.0	0.0	0.7	0.0
KAOLINITE	0.0	0.7	0.3	0.3	1.0	4.0	0.7	0.7	1.3	0.7	1.3	0.0	0.7	1.0	3.7	2.0	2.3
primary pore-filling	0.0	0.0	0.0	0.0	0.0	1.0	0.7	0.0	0.0	0.0	0.7	0.0	0.0	0.7	2.7	1.0	0.0
replacive	0.0	0.7	0.3	0.3	1.0	3.0	0.0	0.7	1.3	0.7	0.7	0.0	0.7	0.3	1.0	1.0	2.3
ILLITE	0.0	tr	0.0	0.0	0.0	tr	tr	0.0	0.0	0.0	0.0	0.0	0.0	0.0	0.0	0.0	0.0
ILLITE-SMECTITE	0.0	0.0	0.0	0.0	0.0	0.0	0.0	0.0	0.0	0.0	0.0	0.0	0.0	0.0	0.0	0.0	0.0
CHLORITE	0.0	0.0	0.0	0.0	0.0	0.0	0.0	0.0	0.0	0.0	0.0	0.0	0.0	0.0	0.0	0.0	0.0
MACROPOROSITY	0.0	tr	0.0	0.0	0.0	0.0	0.0	0.0	0.0	0.0	0.0	0.0	0.0	6.7	8.0	2.7	0.0
primary intergranular porosity	0.0	0.0	0.0	0.0	0.0	0.0	0.0	0.0	0.0	0.0	0.0	0.0	0.0	5.3	6.3	1.3	0.0
secondary intragranular porosity	0.0	tr	0.0	0.0	0.0	0.0	0.0	0.0	0.0	0.0	0.0	0.0	0.0	0.0	0.0	0.3	0.0
secondary 'oversized' porosity	0.0	0.0	0.0	0.0	0.0	0.0	0.0	0.0	0.0	0.0	0.0	0.0	0.0	1.3	1.7	1.0	0.0
calculated microporosity	6.6	5.6	2.8	3.1	3.3	7.4	4.2	7.3	5.7	4.2	6.3	3.6	6.1	1.1	4.0	7.5	3.6
TOTALS																	
Detrital grains	57.7	65.7	59.3	66.0	63.3	67.3	61.3	70.0	69.0	65.0	70.7	59.0	61.3	78.3	72.0	77.7	72.7
Detrital clay and pseudomatrix	10.7	14.3	21.7	24.3	12.3	4.0	6.0	8.0	14.0	7.0	4.3	11.3	8.3	0.7	0.3	0.0	23.0
Blocky Cements	31.7	19.3	18.7	9.3	23.3	24.7	31.7	21.0	15.7	27.3	23.7	29.7	29.7	13.4	16.0	16.7	2.0
Authigenic clays	0.0	0.7	0.3	0.3	1.0	4.0	1.0	1.0	1.3	0.7	1.3	0.0	0.7	1.0	3.7	3.0	2.3
Porosity	0.0	0.0	0.0	0.0	0.0	0.0	0.0	0.0	0.0	0.0	0.0	0.0	0.0	6.7	8.0	2.7	0.0
	100.0	*100.0*	*100.0*	*100.0*	*100.0*	*100.0*	*100.0*	*100.0*	*100.0*	*100.0*	*100.0*	*100.0*	*100.0*	*100.0*	*100.0*	*100.0*	*100.0*
SUMMARY CATEGORIES																	
Ductile grains	12.3	11.7	12.3	19.0	12.7	4.3	8.0	5.7	19.3	15.0	4.7	11.3	6.3	0.0	0.0	0.0	8.0
Ductiles	23.0	26.0	34.0	43.3	25.0	8.3	14.0	13.7	33.3	22.0	9.0	22.7	14.7	0.7	0.3	0.0	31.0
Authigenic minerals	31.7	20.0	19.0	9.6	24.3	28.7	32.7	22.0	17.0	28.0	25.0	29.7	30.3	14.4	19.7	19.7	4.3
Authigenic minerals - intergranular	25.0	18.7	18.3	9.0	19.7	23.3	31.3	21.0	15.0	26.3	22.3	29.3	22.7	14.0	18.7	18.3	2.0
Authigenic minerals - replacive	6.7	1.3	0.6	0.6	4.7	5.3	1.3	1.0	2.0	1.7	2.7	0.3	7.7	0.3	1.0	1.3	2.3
QUARTZ	0.41	0.46	0.46	0.46	0.51	0.57	0.47	0.58	0.50	0.43	0.67	0.52	0.59	0.94	0.91	0.92	0.77
FELDSPAR	0.44	0.33	0.31	0.22	0.32	0.30	0.34	0.27	0.33	0.44	0.19	0.28	0.20	0.03	0.05	0.04	0.06
LITHICS	0.15	0.21	0.24	0.32	0.17	0.13	0.19	0.14	0.16	0.13	0.14	0.20	0.21	0.03	0.04	0.04	0.18
MATRIX	10.67	14.33	21.67	24.33	12.33	4.00	6.00	8.00	14.00	7.00	4.33	11.33	8.33	0.67	0.33	0.00	23.00
Horizontal helium porosity (%)	6.6	5.6	2.8	3.1	3.3	7.4	4.20	7.30	5.70	4.20	6.30	3.60	6.10	7.80	12.00	10.20	3.60
Horizontal permeability (Kg) (mD)	0.01	44	0.08	0.32	0.01	0.02	0.02	0.01	3.30	0.12	0.02	3.90	0.01	0.28	28.00	0.22	0.01
Estimated initial porosity (Beard & Weyl 1973)	45.00	45.00	45.00	45.00	45.00	45.00	45.00	45.00	45.00	45.00	45.00	45.00	45.00	45.00	45.00	45.00	45.00
Compactional porosity loss (COPL	26.66	32.36	32.65	39.56	31.53	28.25	24.14	30.38	35.29	25.34	29.17	22.16	28.88	31.79	26.66	31.53	43.87
Cementational porosity loss (CEPL)	18.34	12.64	12.35	5.44	13.47	16.75	20.86	14.62	9.71	19.66	15.83	22.84	16.12	9.57	13.70	12.56	1.13
Compaction index (ICOMPACT)	0.59	0.72	0.73	0.88	0.70	0.63	0.54	0.68	0.78	0.56	0.65	0.49	0.64	0.77	0.66	0.72	0.97
Pmc (minus-cement porosity or intergranular volume)	25.01	18.69	18.34	9.00	19.68	23.34	27.50	21.00	15.00	26.33	22.34	29.34	22.67	19.36	25.01	19.68	2.01
Po (observed intergranular porosity)	0.00	0.00	0.00	0.00	0.00	0.00	0.00	0.00	0.00	0.00	0.00	0.00	0.00	5.33	6.33	1.33	0.00
C (intergranular cement volume)	25.01	18.69	18.34	9.00	19.68	23.34	27.50	21.00	15.00	26.33	22.34	29.34	22.67	14.03	18.68	18.34	2.01
Depositional feldspar (feldspar + replacive kaolinite + secondary pores)	0.44	0.34	0.31	0.23	0.33	0.33	0.34	0.28	0.35	0.44	0.20	0.28	0.20	0.05	0.08	0.07	0.09

KEY

Sandstone classification
LA = lithic arenite
SLA = sublithic arenite
FA=feldspathic arenite
SFA=subfeldspathic arenite
QA=quarta arenite
LW = lithic wackes
SLW=sublithic wacke

Traces
tr - thin section
scanning electron microscopy
tr - X-ray diffraction

Cement qualifiers
dm = dolomitic
sid = sideritic
s = siliceous

Heavy minerals
A = apatite
O = opaques
M = monazite
R = rutile
T = tourmaline
Z = zircon

WELL	44/16-1	44/16-1	44/16-1	44/16-1	44/16-1	44/16-1	44/16-1	44/16-1	44/16-1	44/16-1	44/16-1Z	44/16-1Z	44/16-1Z	44/16-1Z	44/16-1Z	44/16-1Z	44/16-1Z
DEPTH (m/ftDD)	14837.90	14917.00	14922.80	14926.10	14927.90	14931.00	14935.10	14945.00	14963.20	14977.00	14175.00	14177.10	14181.20	14188.00	14194.00	14203.10	14204.00
UNIT	ft	ft	ft	ft	ft	ft	ft	ft	ft	ft	ft	ft	ft	ft	ft	ft	ft
LITHOSTRATIGRAPHY	Millstone Grit Fm	Millstone Grit Fm	Millstone Grit Fm	Millstone Grit Fm	Millstone Grit Fm	Millstone Grit Fm	Millstone Grit Fm	Millstone Grit Fm	Millstone Grit Fm	Millstone Grit Fm	Millstone Grit Fm	Millstone Grit Fm	Millstone Grit Fm	Millstone Grit Fm	Millstone Grit Fm	Millstone Grit Fm	Millstone Grit Fm
LITHOFACIES	Sm	Sx	Sx	Sx	Sp	Sx	Sm	Sx	S(M)d	S(M)x	S(M)x	S(M)x	S(M)p	Sm	Sp	Sm	Sm
SANDSTONE CLASSIFICATION	sQA	sQA	sSLA	sSLA	SLA	sSLW	dSLA	SLA	SLW	SLW	sQA	sSLA	QA	QA	sQA	sQA	sQA
FACIES ASSOCIATION	Delta plain	Multi-storey fluvial channel	Multi-storey fluvial channel	Multi-storey fluvial channel	Multi-storey fluvial channel	Multi-storey fluvial channel	Multi-storey fluvial channel	Multi-storey fluvial channel	Distal delta front	Proximal delta front	Delta plain	Delta plain	Distributary channel	Delta plain	Delta plain	Delta plain	Delta plain
MODAL GRAIN SIZE	upper medium sand	upper medium sand	lower coarse sand	lower coarse sand	lower coarse sand	lower medium sand	upper fine sand	upper fine sand	upper very fine sand	lower fine sand	lower fine sand	lower fine sand	lower fine sand	upper fine sand	lower fine sand	upper fine sand	lower fine sand
SORTING	moderately well sorted	moderately sorted	moderately well sorted	moderately well sorted	moderately sorted	moderately well sorted	well sorted	moderately well sorted	moderately well sorted	moderately well sorted	moderately well sorted	moderately well sorted	moderately well sorted	moderately well sorted	well sorted	moderately well sorted	moderately well sorted
DETRITAL MINERALOGY																	
QUARTZ	71.0	61.0	57.0	54.7	46.7	51.3	51.7	53.3	50.0	59.3	68.0	66.3	75.0	76.3	73.3	69.7	70.7
monocrystalline	63.7	47.7	41.0	37.3	27.3	39.0	45.0	47.7	46.7	52.0	63.0	61.0	67.3	68.0	65.3	60.0	64.0
polycrystalline	7.3	13.3	16.0	17.3	19.3	12.3	6.7	5.7	3.3	7.3	5.0	5.3	7.7	8.3	8.0	9.7	6.7
FELDSPAR	3.0	1.0	4.0	3.0	2.3	1.0	4.0	3.0	5.0	5.7	2.3	3.7	1.7	1.0	0.7	0.3	4.0
K-feldspar	2.0	0.0	3.7	2.7	2.3	1.0	2.0	2.0	0.3	1.0	2.0	2.0	0.7	0.7	0.7	0.3	4.0
plagioclase	1.0	1.0	0.3	0.3	0.0	0.0	2.0	1.0	4.7	4.7	0.3	1.7	1.0	0.3	0.0	0.0	0.0
RIGID ROCK FRAGMENTS	3.3	5.0	7.7	10.0	13.3	5.7	4.3	3.3	8.7	5.0	3.7	5.7	0.7	2.3	3.7	4.0	3.7
igneous	3.3	4.3	7.3	9.7	11.3	5.0	4.3	3.3	8.7	5.0	3.7	5.7	0.7	2.0	3.0	3.3	3.7
metamorphic	tr	0.7	0.3	0.3	2.0	0.7	0.0	tr	0.0	0.0	0.0	0.0	0.0	0.3	0.7	0.7	tr
sedimentary	0.0	0.0	0.0	0.0	0.0	0.0	0.0	0.0	0.0	0.0	0.0	0.0	0.0	0.0	tr	0.0	0.0
HEAVY MINERALS	0.3	0.0	0.0	0.3	tr	0.0	0.7	0.3	0.7	0.3	0.3	2.0	0.7	0.0	0.7	1.7	0.7
heavy mineral types	T,Z			A,R	Z		M,O,R,T,Z	?A,?M,O,T,Z	R,Z	O,R,T,Z	O,R,T,Z	A,O,T,Z	R,T,Z	A,R,T,Z	O,T,Z	G,O,R,T,Z	M,O,R,T,Z
DUCTILE ROCK FRAGMENTS	0.3	0.7	1.0	0.3	1.0	0.0	0.3	1.3	0.0	0.0	0.0	0.0	0.0	0.0	0.3	0.0	0.0
degraded igneous	0.3	0.7	1.0	0.3	1.0	0.0	0.0	1.3	0.0	0.0	0.0	0.0	0.0	0.0	0.3	0.0	0.0
sedimentary	0.0	0.0	0.0	0.0	0.0	0.0	0.3	0.0	0.0	0.0	0.0	0.0	0.0	0.0	0.0	0.0	0.0
MICA	0.3	0.0	0.3	tr	0.3	0.7	2.7	2.3	2.3	2.0	0.7	0.0	0.3	tr	0.0	0.0	0.0
muscovite	0.3	0.0	0.3	tr	0.3	0.7	2.7	2.3	2.3	2.0	0.7	0.0	0.3	tr	0.0	0.0	0.0
biotite	0.0	0.0	0.0	0.0	0.0	0.0	0.0	0.0	0.0	0.0	0.0	0.0	0.0	0.0	0.0	0.0	0.0
CHLORITE	0.0	0.0	0.0	0.0	0.0	0.0	0.0	0.0	0.0	0.0	0.0	0.0	0.0	0.0	0.0	0.0	0.0
ORGANIC FRAGMENTS	0.0	0.0	0.0	0.3	0.0	7.3	0.0	0.0	2.0	0.0	0.0	0.0	0.0	2.3	0.0	0.7	0.0
OPTICALLY NON-RESOLVABLE CLAY	tr	10.7	7.7	6.3	13.3	15.3	10.7	14.0	15.3	15.7	0.0	0.0	0.0	0.0	0.0	0.0	0.0
detrital	0.0	5.3	0.3	0.0	1.7	10.3	7.0	4.7	6.3	4.7	0.0	0.0	0.0	0.0	0.0	0.0	0.0
pseudomatrix	tr	5.3	7.3	6.3	11.7	5.0	3.7	9.3	9.0	11.0	0.0	0.0	0.0	0.0	0.0	0.0	0.0
AUTHIGENIC MINERALOGY																	
QUARTZ OVERGROWTHS	11.3	13.0	10.3	13.7	9.0	11.3	7.3	8.3	8.0	2.0	13.0	11.0	9.0	10.0	19.3	15.0	12.3
Na-FELDSPAR OVERGROWTHS	0.0	0.0	0.0	0.0	0.0	0.0	0.0	0.0	0.0	0.0	0.0	0.0	0.0	0.0	0.0	0.0	0.0
K-FELDSPAR OVERGROWTHS	0.0	0.0	0.0	0.0	0.0	0.0	0.0	0.0	0.0	0.0	0.0	tr	0.0	0.0	0.0	0.0	0.0
CALCITE CEMENT	0.0	0.0	0.0	0.0	0.0	0.0	0.0	0.0	0.0	0.0	0.0	0.0	0.0	0.0	0.0	0.0	0.0
ferroan	0.0	0.0	0.0	0.0	0.0	0.0	0.0	0.0	0.0	0.0	0.0	0.0	0.0	0.0	0.0	0.0	0.0
non-ferroan	0.0	0.0	0.0	0.0	0.0	0.0	0.0	0.0	0.0	0.0	0.0	0.0	0.0	0.0	0.0	0.0	0.0
DOLOMITE CEMENT	tr	1.0	2.0	0.0	0.0	0.0	16.0	5.0	0.0	0.3	0.0	0.7	3.7	0.0	0.0	0.0	0.0
ferroan - primary pore-filling	tr	0.0	1.7	0.0	0.0	0.0	13.7	3.3	0.0	0.3	0.0	0.0	0.0	0.0	0.0	0.0	0.0
ferroan - replacive	0.0	1.0	0.0	0.0	0.0	0.0	1.3	0.3	0.0	0.0	0.0	0.0	0.0	0.0	0.0	0.0	0.0
non-ferroan - primary pore-filling	0.0	0.0	0.3	0.0	0.0	0.0	1.0	1.3	0.0	0.0	0.0	0.7	3.7	0.0	0.0	0.0	0.0
non-ferroan - replacive	tr	0.0	0.0	0.0	0.0	0.0	0.0	0.0	0.0	0.0	0.0	0.0	0.0	0.0	0.0	0.0	0.0
SIDERITE	0.0	tr	tr	0.0	0.0	0.3	0.0	1.7	4.3	5.7	4.3	3.3	2.0	0.0	0.7	0.0	0.0
BARITE	0.0	0.0	0.0	0.0	0.0	0.0	0.0	0.0	0.0	0.0	0.0	tr	0.0	0.3	0.0	0.0	0.0
ANHYDRITE	0.0	0.0	0.0	0.0	0.0	0.0	0.0	0.0	0.0	0.0	0.0	0.0	0.0	0.0	0.0	0.0	0.0
IRON OXIDE	tr	0.0	0.0	0.0	0.0	0.0	0.0	0.0	0.0	0.0	0.0	0.0	0.0	0.0	0.0	0.0	0.0
PYRITE CEMENT	tr	tr	0.0	tr	tr	0.7	0.0	tr	2.7	0.0	0.0	0.3	tr	tr	tr	tr	0.7
ANATASE	tr	0.0	0.0	0.3	0.0	0.0	0.0	0.0	0.0	0.0	tr	tr	0.0	0.3	tr	0.3	0.3
ZEOLITE	0.0	0.0	0.0	0.0	0.0	0.0	0.0	0.0	0.0	0.0	0.0	0.0	0.0	0.0	0.0	0.0	0.0
RESIDUAL OIL	tr	tr	0.0	0.0	0.0	0.0	0.0	0.0	0.0	0.0	tr	tr	tr	tr	tr	tr	tr
OPTICALLY NON-RESOLVABLE REPLACIVE CLAY	0.0	0.3	0.0	3.7	0.0	0.3	0.0	0.7	0.0	0.0	0.0	0.0	0.3	0.0	0.0	0.0	0.0
OPTICALLY NON-RESOLVABLE PORE-LINING CLAY	0.7	0.0	0.7	0.7	0.7	0.0	0.0	0.0	0.0	0.3	0.0	0.0	0.3	0.0	0.0	0.0	0.0
KAOLINITE	1.7	4.7	6.7	3.7	8.0	5.7	2.3	6.0	1.0	3.7	4.3	1.3	4.0	2.0	1.0	1.0	1.3
primary pore-filling	0.7	1.0	1.0	1.0	0.7	0.0	0.3	0.7	0.0	0.0	1.0	1.0	1.3	1.0	0.7	0.7	0.7
replacive	1.0	3.7	5.7	2.7	7.3	5.7	2.0	5.3	1.0	3.7	3.3	0.3	2.7	1.0	0.3	0.3	0.7
ILLITE	tr	0.3	0.3	tr	tr	0.0	0.0	0.7	0.0	0.0	0.0	0.0	0.0	0.0	0.0	0.0	0.0
ILLITE-SMECTITE	0.0	0.0	0.0	0.0	0.0	0.0	0.0	0.0	0.0	0.0	0.0	0.0	0.0	0.0	0.0	0.0	0.0
CHLORITE	0.0	0.0	0.0	0.0	0.0	0.0	0.0	0.0	0.0	0.0	0.0	0.0	0.0	0.0	0.0	0.0	0.0
MACROPOROSITY	8.0	2.3	2.3	3.0	5.3	0.3	0.0	0.0	0.0	0.0	3.3	5.7	2.3	5.3	0.3	7.3	6.3
primary intergranular porosity	6.0	tr	tr	0.3	0.0	0.0	0.0	0.0	0.0	0.0	2.3	3.7	1.7	3.7	0.0	6.7	6.3
secondary intragranular porosity	0.0	1.0	2.0	2.7	0.3	0.3	0.0	0.0	0.0	0.0	0.7	0.0	0.0	0.0	0.0	0.0	0.0
secondary 'oversized' porosity	2.0	1.3	0.3	0.0	5.0	0.0	0.0	0.0	0.0	0.0	0.3	2.0	0.7	1.7	0.3	0.7	0.0
calculated microporosity	3.9	10.1	10.6	11.8	5.1	7.7	8.6	8.8	5.8	9.1	5.1	3.3	1.8	3.0	2.5	1.8	2.6
TOTALS																	
Detrital grains	78.3	67.7	70.0	68.7	63.7	66.0	63.7	63.7	68.7	72.3	75.0	77.7	78.3	82.0	78.7	76.3	79.0
Detrital clay and pseudomatrix	tr	10.7	7.7	6.3	13.3	15.3	10.7	14.0	15.3	15.7	0.0	0.0	0.0	0.0	0.0	0.0	0.0
Blocky Cements	11.4	14.0	12.3	14.0	9.0	12.3	23.3	15.0	15.0	8.0	17.4	15.4	14.7	10.7	20.0	15.4	13.3
Authigenic clays	2.3	5.3	7.7	8.0	8.7	6.0	2.3	7.3	1.0	4.0	4.3	1.3	4.7	2.0	1.0	1.0	1.3
Porosity	8.0	2.3	2.3	3.0	5.3	0.3	0.0	0.0	0.0	0.0	3.3	5.7	2.3	5.3	0.3	7.3	6.3
	100.1	*100.0*	*100.0*	*100.0*	*100.0*	*100.0*	*100.0*	*100.0*	*100.0*	*100.0*	*100.0*	*100.0*	*100.0*	*100.0*	*100.0*	*100.0*	*100.0*
SUMMARY CATEGORIES																	
Ductile grains	0.7	0.7	1.3	0.7	1.3	8.0	3.0	3.7	4.3	2.0	0.7	0.0	0.3	2.3	0.3	0.7	0.0
Ductiles	0.7	11.3	9.0	7.0	14.7	23.3	13.7	17.7	19.7	17.7	0.7	0.0	0.3	2.3	0.3	0.7	0.0
Authigenic minerals	13.7	19.4	20.0	22.0	17.7	18.3	25.7	22.3	16.0	12.0	21.7	16.7	19.4	12.7	21.0	16.4	14.7
Authigenic minerals - intergranular	12.7	14.4	14.3	15.7	10.4	12.3	22.3	16.0	15.0	8.3	18.4	16.4	16.4	11.7	20.7	16.0	14.0
Authigenic minerals - replacive	1.0	5.0	5.7	6.3	7.3	6.0	3.3	6.3	1.0	3.7	3.3	0.3	3.0	1.0	0.3	0.3	0.7
QUARTZ	0.91	0.90	0.81	0.80	0.73	0.87	0.81	0.84	0.75	0.82	0.91	0.85	0.96	0.96	0.93	0.92	0.89
FELDSPAR	0.04	0.01	0.06	0.04	0.04	0.02	0.06	0.05	0.07	0.08	0.03	0.05	0.02	0.01	0.01	0.00	0.05
LITHICS	0.06	0.08	0.13	0.16	0.23	0.11	0.13	0.12	0.18	0.10	0.06	0.10	0.02	0.03	0.06	0.07	0.05
MATRIX	0.01	10.67	7.67	6.33	13.33	15.33	10.67	14.00	15.33	15.67	0.00	0.00	0.00	0.00	0.00	0.00	0.00
Horizontal helium porosity (%)	11.90	12.40	12.90	14.80	10.40	8.00	8.60	8.80	5.80	9.10	8.40	9.00	4.10	8.30	2.80	9.10	8.90
Horizontal permeability (Kg) (mD)	61.00	0.32	0.51	0.90	0.70	2.80	0.07	0.11	0.03	0.03	42.00	3.80	0.02	5.70	0.70	13.00	3.80
Estimated initial porosity (Beard & Weyl 1973)	45.00	45.00	45.00	45.00	45.00	45.00	45.00	45.00	45.00	45.00	45.00	45.00	45.00	45.00	45.00	45.00	45.00
Compactional porosity loss (COPL	32.33	35.77	35.78	34.51	38.65	37.26	29.18	34.52	35.29	40.00	30.66	31.22	32.91	35.02	30.65	28.86	30.95
Cementational porosity loss (CEPL)	8.61	9.23	9.21	10.27	6.35	7.74	15.82	10.48	9.71	5.00	12.73	11.26	10.97	7.59	14.35	11.40	9.67
Compaction index (ICOMPACT)	0.79	0.79	0.80	0.77	0.86	0.83	0.65	0.77	0.78	0.89	0.71	0.73	0.75	0.82	0.68	0.72	0.76
Pmc (minus-cement porosity or intergranular volume)	18.73	14.37	14.35	16.02	10.35	12.33	22.33	16.01	15.00	8.33	20.69	20.04	18.02	15.35	20.70	22.69	20.34
Po (observed intergranular porosity)	6.00	0.01	0.01	0.33	0.00	0.00	0.00	0.00	0.00	0.00	2.33	3.67	1.67	3.67	0.00	6.67	6.33
C (intergranular cement volume)	12.73	14.36	14.34	15.69	10.35	12.33	22.33	16.01	15.00	8.33	18.35	16.37	16.35	11.69	20.70	16.02	14.01
Depositional feldspar (feldspar + replacive kaolinite + secondary pores)	0.07	0.10	0.15	0.11	0.20	0.11	0.09	0.12	0.09	0.12	0.08	0.08	0.06	0.04	0.02	0.02	0.06

WELL	44/16-1Z	44/16-1Z	44/16-1Z	44/16-1Z	44/16-1Z	44/16-1Z	44/16-1Z	44/16-1Z	44/16-1Z	44/16-1Z	44/16-1Z	44/16-2	44/16-2	44/16-2	44/16-2	44/16-2	44/16-2
DEPTH (m/ftDD)	14205.90	14210.15	14215.00	14221.00	14224.15	14229.00	14231.10	14235.90	14244.90	14258.90	14260.90	14258.80	14262.10	14262.8	14264.80	14268.00	14270.90
UNIT	ft	ft	ft	ft	ft	ft	ft	ft	ft	ft	ft	ft	ft	ft	ft	ft	ft
LITHOSTRATIGRAPHY	Millstone Grit Fm	Millstone Grit Fm	Millstone Grit Fm	Millstone Grit Fm	Millstone Grit Fm	Millstone Grit Fm	Millstone Grit Fm	Millstone Grit Fm	Millstone Grit Fm	Millstone Grit Fm	Millstone Grit Fm	Millstone Grit Fm	Millstone Grit Fm	Millstone Grit Fm	Millstone Grit Fm	Millstone Grit Fm	Millstone Grit Fm
LITHOFACIES	Sm	Sm	S(M)p	Sp	S(M)p	Sped	S(M)p	S(M)r	SMs(r)	Ml	Ml	S(M)ped	Sx	Sx	Sx	Sx	Sx
SANDSTONE CLASSIFICATION	sSLA	QA	sQA	sQA	sQA	sQA	sQA	sQA	sidSLA	sidSLW	SLW	sQA	QA	SLA	sQA	sQA	sQA
FACIES ASSOCIATION	Delta plain	Delta plain	Delta plain	Delta plain	Delta plain	Delta plain	Delta plain	Interdistributary bay	Interdistributary bay	Interdistributary bay	Interdistributary bay	Delta plain	Multi-storey fluvial channel	Multi-storey fluvial channel	Multi-storey fluvial channel	Multi-storey fluvial channel	Multi-storey fluvial channel
MODAL GRAIN SIZE	upper very fine sand	lower fine sand	lower fine sand	upper very fine sand	upper very fine sand	upper fine sand	lower medium sand	upper very fine sand	lower very fine sand		upper coarse silt	upper very fine sand	upper fine sand	lower medium sand	lower medium sand	upper medium sand	upper medium sand
SORTING	moderately sorted	moderately well sorted	moderately well sorted	moderately well sorted	well sorted	well sorted	moderately well sorted	moderately well sorted	moderately well sorted		moderately well sorted	moderately well sorted	moderately well sorted	moderately well sorted	moderately well sorted	moderately well sorted	moderately well sorted
DETRITAL MINERALOGY																	
QUARTZ	72.7	71.3	78.0	70.3	69.0	70.7	75.3	69.0	64.0	1.0	49.3	68.0	77.0	73.3	74.3	73.7	75.3
monocrystalline	61.7	64.3	69.0	66.3	63.0	61.0	64.0	58.7	60.7	1.0	43.3	58.7	67.7	62.3	64.0	65.3	67.3
polycrystalline	11.0	7.0	9.0	4.0	6.0	9.7	11.3	10.3	3.3	0.0	6.0	9.3	9.3	11.0	10.3	8.3	8.0
FELDSPAR	2.0	1.0	1.3	3.7	0.3	0.7	0.0	1.3	1.0	0.0	4.0	5.7	3.7	2.0	4.0	1.0	0.3
K-feldspar	1.0	1.0	1.0	3.0	0.3	0.7	0.0	0.7	0.3	0.0	3.0	5.0	3.3	2.0	3.7	1.0	0.3
plagioclase	1.0	0.0	0.3	0.7	0.0	0.0	0.0	0.7	0.7	0.0	1.0	0.7	0.3	0.0	0.3	0.0	0.0
RIGID ROCK FRAGMENTS	5.0	4.0	2.3	1.7	1.3	3.7	1.3	0.7	0.7	0.0	2.0	4.0	3.0	9.3	5.3	1.0	6.3
igneous	5.0	3.7	2.3	1.7	1.3	3.7	0.7	0.7	0.7	0.0	2.0	4.0	3.0	9.3	4.7	1.0	6.3
metamorphic	tr	tr	0.0	tr	0.0	tr	0.7	0.0	0.0	0.0	0.0	0.0	tr	tr	0.7	0.0	0.0
sedimentary	0.0	0.3	0.0	0.0	0.0	0.0	0.0	tr	0.0	0.0	0.0	0.0	0.0	0.0	0.0	tr	0.0
HEAVY MINERALS	3.0	0.3	1.0	0.3	tr	0.3	0.3	2.0	0.3	0.0	1.3	tr	0.3	0.7	0.3	0.7	0.7
heavy mineral types	A,M,O,R,T,Z	O,R,T,Z	A,O,R,T,Z	M,R,T	T,Z	R,T,Z	?G,O,R	A,O,R,T,Z	?G,R,T,Z	-	M,O,R,T,Z	G,O,R,T,Z	A,O,R,T	A,O,T	A,M,O,R,T	M,O,R,T,Z	O,R,T,Z
DUCTILE ROCK FRAGMENTS	0.0	tr	0.0	0.7	0.0	0.0	0.0	0.3	0.7	0.0	0.0	0.0	0.0	0.0	0.0	0.0	0.0
degraded igneous	0.0	0.0	0.0	0.7	0.0	0.0	0.0	0.0	0.7	0.0	0.0	0.0	0.0	0.0	0.0	0.0	0.0
sedimentary	0.0	tr	0.0	0.0	0.0	0.0	0.0	0.3	0.0	0.0	0.0	0.0	0.0	0.0	0.0	0.0	0.0
MICA	1.3	0.0	0.7	1.3	3.3	0.3	0.7	tr	1.0	0.3	8.0	0.7	0.3	tr	0.3	0.0	0.0
muscovite	1.3	0.0	0.7	1.3	3.3	0.3	0.7	tr	1.0	0.3	7.7	0.7	0.3	tr	0.3	0.0	0.0
biotite	0.0	0.0	0.0	0.0	0.0	0.0	0.0	0.0	0.0	0.0	0.3	0.0	0.0	0.0	0.0	0.0	0.0
CHLORITE	0.0	0.0	0.0	0.0	0.0	0.0	0.0	0.0	0.0	0.0	0.0	0.0	0.0	0.0	0.0	0.0	0.0
ORGANIC FRAGMENTS	0.0	0.0	0.0	0.0	1.0	0.7	0.0	0.7	5.0	1.0	2.3	0.0	0.0		0.0	0.0	0.0
OPTICALLY NON-RESOLVABLE CLAY	0.3	tr	0.0	0.0	0.0	0.0	0.0	0.3	0.3	48.3	29.7	0.7	0.0	0.3	0.0	0.0	0.0
detrital	0.3	tr	0.0	0.0	0.0	0.0	0.0	0.3	0.3	48.3	21.7	0.7	0.0	0.3	0.0	0.0	0.0
pseudomatrix	0.0	0.0	0.0	0.0	0.0	0.0	0.0	0.0	0.0	0.0	8.0	0.0	0.0	0.0	0.0	0.0	0.0
AUTHIGENIC MINERALOGY																	
QUARTZ OVERGROWTHS	10.3	7.7	13.3	10.7	11.3	14.3	14.0	17.7	8.7	0.0	0.7	14.3	6.3	7.7	11.3	15.0	12.0
Na-FELDSPAR OVERGROWTHS	0.0	0.0	0.0	0.0	0.0	0.0	0.0	0.0	0.0	0.0	0.0	0.0	0.0	0.0	0.0	0.0	0.0
K-FELDSPAR OVERGROWTHS	0.0	0.0	0.0	0.0	0.0	0.0	0.0	0.0	0.0	0.0	0.0	0.0	0.3	0.3	0.3	0.0	0.0
CALCITE CEMENT	0.0	0.0	0.0	0.0	0.0	0.0	0.0	0.0	0.0	0.0	0.0	0.0	0.0	0.0	0.0	0.0	0.0
ferroan	0.0	0.0	0.0	0.0	0.0	0.0	0.0	0.0	0.0	0.0	0.0	0.0	0.0	0.0	0.0	0.0	0.0
non-ferroan	0.0	0.0	0.0	0.0	0.0	0.0	0.0	0.0	0.0	0.0	0.0	0.0	0.0	0.0	0.0	0.0	0.0
DOLOMITE CEMENT	0.0	8.3	0.0	0.0	0.3	0.0	1.0	1.0	0.0	0.0	0.0	0.0	0.3	0.7	0.3	0.0	1.0
ferroan - primary pore-filling	0.0	0.0	0.0	0.0	0.0	0.0	0.0	0.0	0.0	tr	0.0	0.0	0.0	0.0	0.0	0.0	0.0
ferroan - replacive	0.0	0.0	0.0	0.0	0.0	0.0	0.0	0.0	0.0	0.0	0.0	0.0	0.0	0.0	0.0	0.0	0.0
non-ferroan - primary pore-filling	0.0	8.3	0.0	0.0	0.3	0.0	0.3	1.0	0.0	0.0	0.0	0.0	0.3	0.7	0.3	0.0	1.0
non-ferroan - replacive	0.0	0.0	0.0	0.0	0.0	0.0	0.7	0.0	0.0	tr	0.0	0.0	0.0	0.0	0.0	0.0	0.0
SIDERITE	0.0	tr	0.0	0.0	3.3	0.0	0.0	1.3	14.3	48.7	0.7	0.0	0.0	0.0	0.3	0.3	0.3
BARITE	0.0	0.0	0.0	0.0	0.0	0.0	0.0	0.0	0.0	0.0	0.0	0.0	0.0	0.0	0.0	0.0	0.0
ANHYDRITE	0.0	0.0	0.0	0.0	0.0	0.0	0.0	0.0	0.0	0.0	0.0	0.0	0.0	0.0	0.0	0.0	0.0
IRON OXIDE	0.0	0.0	0.0	0.0	0.0	0.0	0.0	0.0	0.0	0.0	0.0	0.0	0.0	0.0	0.0	0.0	0.0
PYRITE CEMENT	0.7	tr	0.0	0.0	0.0	tr	0.0	0.0	0.0	0.0	0.0	0.7	0.3	0.3	0.0	0.0	0.3
ANATASE	tr	tr	0.3	tr	0.3	tr	0.0	tr	0.0	0.0	0.0	0.3	0.3	0.0	tr	tr	0.0
ZEOLITE	0.0	tr	0.0	0.0	0.0	0.0	0.0	0.0	0.0	0.0	0.0	0.0	0.0	0.0	0.0	0.0	0.0
RESIDUAL OIL	tr	tr	tr	tr	0.0	0.0	3.7	0.0	0.0	0.0	0.0	0.0	tr	tr	tr	tr	0.3
OPTICALLY NON-RESOLVABLE REPLACIVE CLAY	0.0	0.3	0.0	0.0	0.0	0.0	0.0	0.0	0.7	0.0	0.0	0.3	0.0	0.0	0.0	0.0	0.0
OPTICALLY NON-RESOLVABLE PORE-LINING CLAY	0.0	0.0	0.0	0.3	0.0	0.0	0.0	0.0	0.0	0.0	0.0	0.3	0.0	0.0	0.0	0.0	0.0
KAOLINITE	3.3	2.7	1.3	7.3	9.3	8.7	2.7	5.7	3.3	0.7	2.0	4.3	1.0	1.0	0.0	0.7	0.3
primary pore-filling	0.3	1.7	0.7	2.0	1.3	1.0	0.3	1.3	0.3	0.0	0.0	0.7	0.0	1.0	0.0	0.3	0.3
replacive	3.0	1.0	0.7	5.3	8.0	7.7	2.3	4.3	3.0	0.7	2.0	3.7	1.0	0.0	0.0	0.3	0.0
ILLITE	0.0	0.0	0.0	0.0	0.0	0.0	0.0	0.0	0.0	0.0	0.0	0.0	0.0	tr	0.0	0.0	0.0
ILLITE-SMECTITE	0.0	0.0	0.0	0.0	0.0	0.0	0.0	0.0	0.0	0.0	0.0	0.0	0.0	0.0	0.0	0.0	0.0
CHLORITE	0.0	0.0	0.0	0.0	0.0	0.0	0.0	0.0	0.0	0.0	0.0	0.0	0.0	0.0	0.0	0.0	0.0
MACROPOROSITY	1.3	4.3	1.7	3.0	0.3	0.7	1.0	0.0	0.0	0.0	0.0	0.7	7.0	4.3	3.3	7.7	3.0
primary intergranular porosity	0.7	4.3	0.3	2.0	0.0	0.3	0.0	0.0	0.0	0.0	0.0	0.7	6.7	4.3	3.0	6.0	3.0
secondary intragranular porosity	0.3	0.0	1.0	0.3	0.0	0.0	0.3	0.0	0.0	0.0	0.0	0.0	0.0	tr	0.3	0.7	0.0
secondary 'oversized' porosity	0.3	0.0	0.3	0.7	0.3	0.3	0.7	0.0	0.0	0.0	0.0	0.0	0.3	0.0	0.0	1.0	0.0
calculated microporosity	6.5	3.5	3.1	2.4	3.0	1.8	3.3	2.0	1.8	0.8	0.9	2.8	1.6	4.3	3.8	0.0	1.5
TOTALS																	
Detrital grains	84.0	76.7	83.3	78.0	75.0	76.3	77.7	74.0	72.7	2.3	67.0	78.4	84.3	85.4	84.3	76.3	82.7
Detrital clay and pseudomatrix	0.3	0.0	0.0	0.0	0.0	0.0	0.0	0.3	0.3	48.3	29.7	0.7	0.0	0.3	0.0	0.0	0.0
Blocky Cements	11.0	16.1	13.7	10.7	15.3	14.4	18.7	20.0	23.0	48.7	1.3	15.3	7.7	9.0	12.4	15.4	14.0
Authigenic clays	3.3	3.0	1.3	7.7	9.3	8.7	2.7	5.7	4.0	0.7	2.0	5.0	1.0	1.0	0.0	0.7	0.3
Porosity	1.3	4.3	1.7	3.0	0.3	0.7	1.0	0.0	0.0	0.0	0.0	0.7	7.0	4.3	3.3	7.7	3.0
	100.0	*100.0*	*100.0*	*100.0*	*100.0*	*100.0*	*100.0*	*100.0*	*100.0*	*100.0*	*100.0*	*100.0*	*100.0*	*100.0*	*100.0*	*100.0*	*100.0*
SUMMARY CATEGORIES																	
Ductile grains	1.3	0.0	0.7	2.0	4.3	1.0	0.7	1.0	6.7	1.3	10.3	0.7	0.3	0.0	0.3	0.0	0.0
Ductiles	1.7	0.0	0.7	2.0	4.3	1.0	0.7	1.3	7.0	49.7	40.0	1.3	0.3	0.3	0.3	0.0	0.0
Authigenic minerals	14.4	19.1	15.0	18.4	24.7	23.0	21.3	25.7	27.0	49.4	3.3	20.3	8.7	10.0	12.4	16.0	14.3
Authigenic minerals - intergranular	11.4	17.7	14.3	13.0	16.7	15.4	18.3	21.3	23.3	48.7	1.3	16.3	7.7	10.0	12.4	15.7	14.3
Authigenic minerals - replacive	3.0	1.3	0.7	5.3	8.0	7.7	3.0	4.3	3.7	0.7	2.0	4.0	1.0	0.0	0.0	0.3	0.0
QUARTZ	0.86	0.93	0.94	0.90	0.93	0.93	0.97	0.94	0.95	0.75	0.76	0.87	0.91	0.86	0.88	0.96	0.91
FELDSPAR	0.02	0.01	0.02	0.05	0.00	0.01	0.00	0.02	0.01	0.00	0.06	0.07	0.04	0.02	0.05	0.01	0.00
LITHICS	0.11	0.06	0.05	0.05	0.06	0.06	0.03	0.04	0.04	0.25	0.18	0.06	0.04	0.12	0.07	0.02	0.08
MATRIX	0.33	0.01	0.00	0.00	0.00	0.00	0.00	0.33	0.33	48.33	29.67	0.67	0.00	0.33	0.00	0.00	0.00
Horizontal helium porosity (%)	7.80	7.80	4.80	5.40	3.30	2.50	4.30	2.00	1.80	0.80	0.90	3.50	8.60	8.60	7.10	6.60	4.50
Horizontal permeability (Kg) (mD)	0.95	2.90	4.50	0.05	0.02	0.08	0.26	0.01	0.05	0.01	6.10	0.08	9.30	18.00	3.70	2.00	0.23
Estimated initial porosity (Beard & Weyl 1973)	45.00	45.00	45.00	45.00	45.00	45.00	45.00	45.00	45.00	45.00	45.00	45.00	45.00	45.00	45.00	45.00	45.00
Compactional porosity loss (COPL	37.49	29.44	35.54	35.28	34.00	34.77	32.65	30.08	28.26	-7.16	44.26	33.73	35.79	35.78	35.03	29.77	33.47
Cementational porosity loss (CEPL)	7.10	12.50	9.25	8.43	11.00	10.02	12.35	14.92	16.74	52.16	0.74	10.82	4.93	6.43	8.03	11.02	9.54
Compaction index (ICOMPACT)	0.84	0.70	0.79	0.81	0.76	0.78	0.73	0.67	0.63	-0.16	0.98	0.76	0.88	0.85	0.81	0.73	0.78
Pmc (minus-cement porosity or intergranular volume)	12.02	22.05	14.68	15.02	16.67	15.69	18.33	21.34	23.33	48.68	1.33	17.00	14.34	14.35	15.35	21.69	17.33
Po (observed intergranular porosity)	0.67	4.33	0.33	2.00	0.00	0.33	0.00	0.00	0.00	0.00	0.00	0.67	6.67	4.33	3.00	6.00	3.00
C (intergranular cement volume)	11.35	17.72	14.34	13.02	16.67	15.35	18.33	21.34	23.33	48.68	1.33	16.33	7.68	10.02	12.35	15.69	14.33
Depositional feldspar (feldspar + replacive kaolinite + secondary pores)	0.06	0.03	0.04	0.12	0.11	0.10	0.04	0.07	0.06	0.33	0.09	0.11	0.06	0.02	0.05	0.04	0.00

WELL	44/16-2	44/16-2	44/16-2	44/16-2	44/16-2	44/16-2	44/16-2	44/16-2	44/16-2	44/16-2	44/16-2	44/16-2	43/19-1	43/19-1	43/19-1	43/19-1	43/19-1
DEPTH (m/ftDD)	14274.10	14282.90	14764.30	14769.00	14774.80	14817.90	14822.90	14824.10	14828.10	14831.00	14837.00	14838.70	12049.0	12064.9	12075.1	12092.7	12116.1
UNIT	ft	ft	ft	ft	ft	ft	ft	ft	ft	ft	ft	ft	ft	ft	ft	ft	ft
LITHOSTRATIGRAPHY	Millstone Grit Fm	Millstone Grit Fm	Millstone Grit Fm	Millstone Grit Fm	Millstone Grit Fm	Millstone Grit Fm	Millstone Grit Fm	Millstone Grit Fm	Millstone Grit Fm	Millstone Grit Fm	Millstone Grit Fm	Millstone Grit Fm	Millstone Grit Fm	Millstone Grit Fm	Millstone Grit Fm	Millstone Grit Fm	Millstone Grit Fm
LITHOFACIES	Sx	S(M)ped	Sx	Sx	S(M)x	Sx	S(M)r	S(M)r	Sped	Sp	Sp	Sp	Sx	Sx	Sp	Sp	SMs(p)
SANDSTONE CLASSIFICATION	sQA	sQA	sQA	sQA	sQA	sidQA	dQA	SLW	sQA	sQA	QA	QA	sSLA	sSLA	dSLA	d/sSLA	dSLA
FACIES ASSOCIATION	Multi-storey fluvial channel	Delta plain	Distributary channel	Distributary channel	Proximal delta front	Proximal delta front	Proximal delta front	Proximal delta front	Delta plain	Delta plain	Delta plain	Delta plain	Multi-storey fluvial channel	Multi-storey fluvial channel	Multi-storey fluvial channel	Distributary channel	Distal delta front
MODAL GRAIN SIZE	upper coarse sand	upper fine sand	lower medium sand	upper fine sand	upper very fine sand	lower fine sand	upper very fine sand	lower very fine sand	lower fine sand	upper very fine sand	lower very fine sand	lower very fine sand	upper fine sand	upper fine sand	upper fine sand	lower fine sand	upper very fine sand
SORTING	moderately sorted	moderately well sorted	moderately well sorted	moderately well sorted	moderately well sorted	moderately well sorted	well sorted	well sorted	moderately well sorted	well sorted	moderately well sorted	moderately well sorted	moderately well sorted	moderately well sorted	moderately well sorted	moderately well sorted	moderately well sorted
DETRITAL MINERALOGY																	
QUARTZ	76.3	75.7	66.3	72.3	71.7	53.3	39.7	49.0	74.7	64.3	71.0	69.3	40.7	41.3	41.0	38.3	31.7
monocrystalline	61.0	70.3	61.0	65.3	66.3	48.3	35.3	45.0	67.7	60.7	67.3	66.3	28.3	32.3	29.0	33.7	29.0
polycrystalline	15.3	5.3	5.3	7.0	5.3	5.0	4.3	4.0	7.0	3.7	3.7	3.0	12.3	9.0	12.0	4.7	2.7
FELDSPAR	0.3	0.0	0.3	0.0	1.7	1.7	1.0	3.0	0.0	2.3	1.7	2.7	9.0	10.0	8.3	8.0	9.0
K-feldspar	0.3	0.0	0.3	0.0	0.0	0.0	0.0	0.0	tr	1.7	0.7	1.0	2.0	1.3	0.7	1.0	0.0
plagioclase	0.0	0.0	0.0	0.0	1.7	1.7	1.0	3.0	tr	0.7	1.0	1.7	7.0	8.7	7.7	7.0	9.0
RIGID ROCK FRAGMENTS	4.0	0.3	2.0	0.3	0.7	1.7	0.7	1.7	1.3	2.3	0.3	0.3	9.0	9.7	6.7	7.7	4.0
igneous	4.0	0.3	2.0	0.3	0.7	1.7	0.7	1.7	1.3	2.3	0.3	0.3	8.7	9.3	6.3	7.0	4.0
metamorphic	tr	0.0	0.0	tr	0.0	0.0	0.0	0.0	0.0	0.0	0.0	0.0	0.3	0.3	0.3	0.0	0.0
sedimentary	0.0	0.0	0.0	0.0	0.0	0.0	0.0	0.0	0.0	0.0	0.0	0.0	0.0	0.0	0.0	0.0	0.0
HEAVY MINERALS	tr	tr	tr	0.7	0.3	tr	0.3	0.3	0.3	1.3	3.0	2.0	tr	0.3	0.7	1.0	0.7
heavy mineral types	T,Z	O,R,T,Z	T	M,O,R,T,Z	O,R,T,Z	A,T	R,T,Z	M,O,T,Z	M,O,R,T,Z	R,T,Z	M,O,R,T,Z	O,R,T	Z	UNDIFF	R,T,Z	R,T,Z	O,Z
DUCTILE ROCK FRAGMENTS	0.0	0.0	0.3	0.0	0.0	0.3	0.3	0.0	0.0	0.3	1.7	0.7	2.3	1.7	3.3	1.0	0.0
degraded igneous	0.0	0.0	0.0	0.0	0.0	0.3	0.3	0.0	0.0	0.3	1.3	0.7	0.0	0.3	1.0	1.0	0.0
sedimentary	0.0	0.0	0.3	0.0	0.0	0.0	0.0	0.0	0.0	0.0	0.3	0.0	2.3	1.3	2.3	0.0	0.0
MICA	0.0	0.0	0.0	0.7	1.3	3.3	1.7	3.0	0.0	0.3	2.0	1.0	3.7	2.0	1.7	2.7	6.3
muscovite	0.0	0.0	0.0	0.7	1.3	3.3	1.7	3.0	0.0	0.3	2.0	1.0	3.7	2.0	1.7	2.7	6.3
biotite	0.0	0.0	tr	0.0	0.0	0.0	0.0	0.0	0.0	0.0	0.0	0.0	0.0	0.0	0.0	0.0	0.0
CHLORITE	0.0	0.0	0.0	0.0	0.0	0.0	0.0	0.0	0.0	0.0	0.0	0.0	0.0	0.0	0.0	0.0	0.0
ORGANIC FRAGMENTS	0.0	0.3	0.0	0.0	0.0	0.0	0.0	1.3	0.0	0.0	1.0	0.3	0.0	0.0	0.0	0.0	6.7
OPTICALLY NON-RESOLVABLE CLAY	0.3	0.7	0.3	0.3	1.7	4.3	0.0	20.3	1.0	6.3	9.0	11.0	5.7	2.0	2.7	2.7	13.0
detrital	0.3	0.7	0.0	0.0	0.0	0.3	0.0	12.0	1.0	5.3	7.3	8.0	0.0	0.0	0.0	0.3	8.0
pseudomatrix	0.0	0.0	0.3	0.3	1.7	4.0	0.0	8.3	0.0	1.0	1.7	3.0	5.7	2.0	2.7	2.3	5.0
AUTHIGENIC MINERALOGY																	
QUARTZ OVERGROWTHS	13.3	18.0	21.7	16.7	13.3	5.3	0.0	3.7	19.7	13.7	7.0	7.3	12.0	12.3	9.7	11.0	1.3
Na-FELDSPAR OVERGROWTHS	0.0	0.0	0.0	0.0	0.0	0.0	0.0	0.0	0.0	0.0	0.0	0.0	0.0	0.0	1.3	1.7	0.0
K-FELDSPAR OVERGROWTHS	0.0	0.0	0.0	0.0	0.0	0.0	0.0	0.0	0.0	0.0	0.0	0.0	0.0	0.0	0.0	0.0	0.0
CALCITE CEMENT	0.0	0.0	0.0	0.0	0.0	0.0	0.0	0.0	0.0	0.0	0.0	0.0	0.0	0.0	0.0	0.0	0.0
ferroan	0.0	0.0	0.0	0.0	0.0	0.0	0.0	0.0	0.0	0.0	0.0	0.0	0.0	0.0	0.0	0.0	0.0
non-ferroan	0.0	0.0	0.0	0.0	0.0	0.0	0.0	0.0	0.0	0.0	0.0	0.0	0.0	0.0	0.0	0.0	0.0
DOLOMITE CEMENT	0.7	0.0	0.7	0.3	2.7	2.0	52.0	1.0	0.0	0.0	0.0	0.0	4.7	9.3	12.0	17.7	19.7
ferroan - primary pore-filling	0.0	0.0	0.0	0.0	0.0	0.0	50.3	0.0	0.0	0.0	0.0	0.0	2.7	6.0	9.0	15.0	18.3
ferroan - replacive	0.0	0.0	0.0	0.0	0.3	tr	0.0	0.0	0.0	0.0	0.0	0.0	2.0	2.7	2.7	2.0	1.0
non-ferroan - primary pore-filling	0.7	0.0	0.7	0.3	2.3	2.0	1.7	1.0	0.0	0.0	0.0	0.0	0.0	0.3	0.3	0.7	0.3
non-ferroan - replacive	0.0	0.0	0.0	0.0	0.0	0.0	0.0	0.0	0.0	0.0	tr	0.0	0.0	0.3	0.0	0.0	0.0
SIDERITE	0.3	0.0	3.3	3.3	2.0	13.7	0.3	9.0	0.0	0.0	tr	1.7	2.3	1.7	0.7	2.7	7.0
BARITE	0.0	0.0	tr	0.0	0.0	0.0	0.0	0.0	0.0	0.0	0.0	0.0	0.0	0.0	0.0	0.0	0.0
ANHYDRITE	0.0	0.0	0.0	0.0	0.0	0.0	0.0	0.0	0.0	0.0	0.0	0.0	0.0	0.0	0.0	0.0	0.0
IRON OXIDE	0.0	0.0	0.0	0.0	0.0	0.0	0.0	0.0	0.0	0.0	0.0	0.0	0.0	0.0	0.0	0.0	0.0
PYRITE CEMENT	0.0	0.7	0.0	0.3	0.0	0.3	0.3	1.0	0.3	1.0	0.0	0.0	0.0	0.0	tr	0.0	0.0
ANATASE	0.0	tr	0.0	0.0	0.0	0.0	0.0	0.0	0.0	0.0	tr	0.0	1.0	0.7	tr	0.3	0.3
ZEOLITE	0.0	0.0	0.0	0.0	0.0	0.0	0.0	0.0	0.0	0.0	0.0	0.0	0.0	0.0	0.0	0.0	0.0
RESIDUAL OIL	0.0	0.0	0.0	0.0	0.0	0.0	0.0	0.0	tr	0.0	0.0	0.0	0.0	0.0	0.0	0.0	0.0
OPTICALLY NON-RESOLVABLE REPLACIVE CLAY	0.0	0.0	0.0	0.3	0.0	0.3	0.0	0.3	0.0	0.0	0.0	0.0	1.3	1.7	2.3	1.0	0.3
OPTICALLY NON-RESOLVABLE PORE-LINING CLAY	0.0	0.0	0.0	0.0	0.0	0.0	0.0	0.0	0.0	0.0	0.0	0.0	0.0	0.0	0.7	0.0	0.0
KAOLINITE	3.7	1.3	3.0	3.3	3.3	13.0	3.7	6.3	2.7	8.0	3.0	3.7	7.7	6.3	8.3	4.0	0.0
primary pore-filling	1.7	0.3	0.7	0.7	1.0	2.3	0.0	0.0	1.7	2.0	0.0	0.3	3.3	2.7	3.7	3.7	0.0
replacive	2.0	1.0	2.3	2.7	2.3	10.7	3.7	6.3	1.0	6.0	3.0	3.3	4.3	3.7	4.7	0.3	0.0
ILLITE	0.0	0.0	0.0	0.0	1.3	0.7	0.0	0.0	0.0	0.0	0.0	0.0	0.7	1.0	0.3	0.0	0.0
ILLITE-SMECTITE	0.0	0.0	0.0	0.0	0.0	0.0	0.0	0.0	0.0	0.0	0.0	0.0	0.0	0.0	0.0	0.0	0.0
CHLORITE	0.0	0.0	0.0	0.0	0.0	0.0	0.0	0.0	0.0	0.0	0.0	0.0	0.0	0.0	0.0	0.0	0.0
MACROPOROSITY	1.0	3.0	2.0	1.3	0.0	0.0	0.0	0.0	0.0	0.0	0.3	0.0	0.0	0.0	0.3	0.3	0.0
primary intergranular porosity	0.7	3.0	1.7	0.0	0.0	0.0	0.0	0.0	0.0	0.0	0.0	0.0	0.0	0.0	0.0	0.0	0.0
secondary intragranular porosity	0.0	0.0	0.3	0.3	0.0	0.0	0.0	0.0	0.0	0.0	0.3	0.0	0.0	0.0	0.3	0.3	0.0
secondary 'oversized' porosity	0.3	0.0	0.0	1.0	0.0	0.0	0.0	0.0	0.0	0.0	0.0	0.0	0.0	0.0	0.0	0.0	0.0
calculated microporosity	1.5	0.0	1.4	2.0	1.3	2.6	0.8	0.9	4.9	4.2	6.2	4.8	9.4	8.0	9.0	7.9	3.1
TOTALS																	
Detrital grains	80.7	76.3	69.0	74.0	75.7	60.3	43.7	58.3	76.4	71.0	80.7	76.3	64.7	65.0	61.7	58.7	58.3
Detrital clay and pseudomatrix	0.3	0.7	0.3	0.3	1.7	4.3	0.0	20.3	1.0	6.3	9.0	11.0	5.7	2.0	2.7	2.7	13.0
Blocky Cements	14.3	18.7	25.7	20.7	18.0	21.3	52.7	14.7	20.0	14.7	7.0	9.0	20.0	24.0	23.7	33.3	28.3
Authigenic clays	3.7	1.3	3.0	3.7	4.7	14.0	3.7	6.7	2.7	8.0	3.0	3.7	9.7	9.0	11.7	5.0	0.3
Porosity	1.0	3.0	2.0	1.3	0.0	0.0	0.0	0.0	0.0	0.0	0.3	0.0	0.0	0.0	0.3	0.3	0.0
	100.0	*100.0*	*100.0*	*100.0*	*100.0*	*100.0*	*100.0*	*100.0*	*100.0*	*100.0*	*100.0*	*100.0*	*100.0*	*100.0*	*100.0*	*100.0*	*100.0*
SUMMARY CATEGORIES																	
Ductile grains	0.0	0.3	0.3	0.7	1.3	3.7	2.0	4.3	0.0	0.7	4.7	2.0	6.0	3.7	5.0	3.7	13.0
Ductiles	0.3	1.0	0.7	1.0	3.0	8.0	2.0	24.7	1.0	7.0	13.7	13.0	11.7	5.7	7.7	6.3	26.0
Authigenic minerals	18.0	20.0	28.7	24.3	22.7	35.3	56.3	21.3	22.7	22.7	10.0	12.7	29.7	33.0	35.4	38.3	28.7
Authigenic minerals - intergranular	16.0	19.0	26.3	21.3	20.0	24.3	52.7	14.7	21.7	16.7	7.0	9.3	22.0	24.7	25.7	35.0	27.3
Authigenic minerals - replacive	2.0	1.0	2.3	3.0	2.7	11.0	3.7	6.7	1.0	6.0	3.0	3.3	7.7	8.3	9.7	3.3	1.3
QUARTZ	0.95	1.00	0.96	0.98	0.95	0.88	0.91	0.86	0.98	0.91	0.89	0.91	0.63	0.64	0.66	0.65	0.61
FELDSPAR	0.00	0.00	0.00	0.00	0.02	0.03	0.02	0.05	0.00	0.03	0.02	0.04	0.14	0.15	0.14	0.14	0.17
LITHICS	0.05	0.00	0.03	0.02	0.03	0.09	0.07	0.09	0.02	0.06	0.09	0.05	0.23	0.21	0.20	0.21	0.21
MATRIX	0.33	0.67	0.33	0.33	1.67	4.33	0.00	20.33	1.00	6.33	9.00	11.00	5.7	2.0	2.7	2.7	13.0
Horizontal helium porosity (%)	2.50	3.00	3.40	3.30	1.30	2.60	0.80	0.90	4.90	4.20	6.50	4.80	9.4	8	9.3	8.2	3.1
Horizontal permeability (Kg) (mD)	0.09	0.04	0.02	0.43	0.22	0.03	0.01	2.00	0.05	0.02	0.03	0.02	0.28	0.16	0.48	0.09	0.01
Estimated initial porosity (Beard & Weyl 1973)	45.00	45.00	45.00	45.00	45.00	45.00	45.00	45.00	45.00	45.00	45.00	45.00	45.00	45.00	45.00	45.00	45.00
Compactional porosity loss (COPL	34.00	29.48	23.60	30.09	31.25	27.31	0.00	35.55	29.78	34.00	40.85	39.34	29.49	26.99	25.99	15.38	24.31
Cementational porosity loss (CEPL)	10.56	13.41	20.13	14.91	13.75	17.69	45.00	9.45	15.22	11.00	4.15	5.66	15.51	18.01	19.01	29.62	20.69
Compaction index (ICOMPACT)	0.76	0.69	0.54	0.67	0.69	0.61	0.00	0.79	0.66	0.76	0.91	0.87	0.66	0.60	0.58	0.34	0.54
Pmc (minus-cement porosity or intergranular volume)	16.67	22.01	28.01	21.33	20.00	24.33	45.00	14.67	21.68	16.67	7.02	9.33	22.0	24.7	25.7	35.0	27.3
Po (observed intergranular porosity)	0.67	3.00	1.67	0.00	0.00	0.00	0.00	0.00	0.00	0.00	0.00	0.00	0.0	0.0	0.0	0.0	0.0
C (intergranular cement volume)	16.00	19.01	26.34	21.33	20.00	24.33	45.00	14.67	21.68	16.67	7.02	9.33	22.00	24.67	25.69	35.00	27.33
Depositional feldspar (feldspar + replacive kaolinite + secondary pores)	0.03	0.01	0.04	0.05	0.05	0.17	0.10	0.15	0.01	0.11	0.06	0.08	0.2	0.2	0.2	0.1	0.2

WELL	43/19-1	43/19-1	43/19-1	43/19-1	43/19-1	43/19-1	43/19-1	43/19-1	43/19-1	43/19-1	43/19-1	43/19-1	43/19-1	43/19-1	43/19-1	43/19-2	43/19-2
DEPTH (m/ftDD)	12152.9	12155.9	12164.0	12434.9	12445.8	12453.8	12465.9	12475.9	12482.1	12654.0	12658.3	12659.5	12673.0	12682.3	12711.2	3625.56	3631.94
UNIT	ft	ft	ft	ft	ft	ft	ft	ft	ft	ft	ft	ft	ft	ft	ft	m	m
LITHOSTRATIGRAPHY	Millstone Grit Fm	Millstone Grit Fm	Millstone Grit Fm	Millstone Grit Fm	Millstone Grit Fm	Millstone Grit Fm	Millstone Grit Fm	Millstone Grit Fm	Millstone Grit Fm	Millstone Grit Fm	Millstone Grit Fm	Millstone Grit Fm	Millstone Grit Fm	Millstone Grit Fm	Millstone Grit Fm	Millstone Grit Fm	Millstone Grit Fm
LITHOFACIES	Sp	Sp	Sm	SMs(fla)	S(M)r	Sx	Sx	Sm	Sx	Sx	Sx	Sx	S(M)w	Sx	SMped	Sx	Sm
SANDSTONE CLASSIFICATION	QA	sSLA	sQA	dSLA	QA	sQA	sQA	dSLA	SLA	sSLA	sQA	QA	QA	SLA	SLA	sQA	sQA
FACIES ASSOCIATION	Proximal delta front	Proximal delta front	Multi-storey fluvial channel	Shoreface	Shoreface	Multi-storey fluvial channel	Multi-storey fluvial channel	Multi-storey fluvial channel	Multi-storey fluvial channel	Multi-storey fluvial channel	Multi-storey fluvial channel	Multi-storey fluvial channel	Interdistributary bay	Interdistributary bay	Interdistributary bay	Multi-storey fluvial channel	Multi-storey fluvial channel
MODAL GRAIN SIZE	upper very fine sand	upper very fine sand	upper coarse sand	upper very fine sand	lower fine sand	upper fine sand	upper medium sand	upper fine sand	upper coarse sand	upper medium sand	upper coarse sand	lower coarse sand	upper very fine sand	lower very fine sand	upper very fine sand	upper fine sand	lower fine sand
SORTING	moderately well sorted	moderately well sorted	moderately sorted	moderately well sorted	well sorted	well sorted	moderately sorted	moderately well sorted	moderately sorted	moderately sorted	moderately sorted	moderately sorted	moderately well sorted	moderately well sorted	moderately sorted	moderately well sorted	moderately well sorted
DETRITAL MINERALOGY																	
QUARTZ	60.0	50.7	62.7	43.0	52.3	49.7	53.3	50.3	51.7	53.3	60.7	64.7	56.3	52.3	31.0	58.7	62.0
monocrystalline	49.3	45.0	40.7	36.7	46.7	40.7	35.7	41.0	31.3	36.3	38.0	51.7	50.3	46.7	27.7	50.7	51.3
polycrystalline	10.7	5.7	22.0	6.3	5.7	9.0	17.7	9.3	20.3	17.0	22.7	13.0	6.0	5.7	3.3	8.0	10.7
FELDSPAR	2.7	3.7	0.0	3.7	0.3	0.0	0.0	0.3	0.0	0.0	0.0	0.0	1.0	2.3	2.0	0.0	0.0
K-feldspar	0.3	0.0	0.0	0.0	0.0	0.0	0.0	0.0	0.0	0.0	0.0	0.0	0.0	0.0	0.0	0.0	0.0
plagioclase	2.3	3.7	0.0	3.7	0.3	0.0	0.0	0.3	0.0	0.0	0.0	0.0	1.0	2.3	2.0	0.0	0.0
RIGID ROCK FRAGMENTS	3.0	2.7	2.7	2.3	2.7	1.3	4.7	4.7	10.0	6.3	5.7	3.0	3.3	2.7	4.3	2.3	2.3
igneous	2.7	2.3	2.3	2.3	2.7	1.0	4.7	4.7	9.0	6.3	4.7	3.0	3.3	2.7	4.3	2.3	2.3
metamorphic	0.3	0.3	0.3	0.0	0.0	0.3	0.0	0.0	1.0	0.0	1.0	0.0	0.0	0.0	0.0	0.0	0.0
sedimentary	0.0	0.0	0.0	0.0	0.0	0.0	0.0	0.0	0.0	0.0	0.0	0.0	0.0	0.0	0.0	0.0	0.0
HEAVY MINERALS	tr	0.3	tr	0.3	0.7	tr	tr	tr	0.0	0.0	0.0	0.0	0.3	1.3	tr	0.3	0.3
heavy mineral types	T,Z	O,T,Z	Z	T,Z	O,Z	O,Z	A,?M,Z	T					A,?M,R,T,Z	?M,R,T,Z	R,Z	A,O,T,Z	A,O,R
DUCTILE ROCK FRAGMENTS	0.3	1.7	0.0	0.7	0.0	1.3	0.0	0.0	0.0	0.3	0.0	0.3	0.7	0.3	2.0	0.3	0.7
degraded igneous	0.3	1.7	0.0	0.7	0.0	1.3	0.0	0.0	0.0	0.3	0.0	0.3	0.7	0.3	2.0	0.3	0.7
sedimentary	0.0	0.0	0.0	0.0	0.0	0.0	0.0	0.0	0.0	0.0	0.0	0.0	0.0	0.0	0.0	0.0	0.0
MICA	2.3	2.7	0.0	4.3	1.3	2.3	0.7	1.3	0.0	0.3	0.0	0.0	2.0	3.0	2.3	1.0	1.3
muscovite	2.0	2.7	0.0	4.3	1.3	2.3	0.7	1.3	0.0	0.3	0.0	0.0	2.0	3.0	2.3	1.0	1.3
biotite	0.3	0.0	0.0	0.0	0.0	0.0	0.0	0.0	0.0	0.0	0.0	0.0	tr	0.0	0.0	0.0	0.0
CHLORITE	0.0	0.0	0.0	0.0	0.0	0.0	0.0	0.0	0.0	0.0	0.0	0.0	0.0	0.0	0.0	0.0	0.0
ORGANIC FRAGMENTS	0.0	0.0	0.0	2.7	0.0	0.0	0.0	0.0	0.0	0.0	0.0	0.0	0.0	0.7	2.3	0.0	0.0
OPTICALLY NON-RESOLVABLE CLAY	18.0	11.7	3.0	22.3	12.3	1.3	1.3	2.3	3.7	3.0	4.7	1.7	18.7	33.0	52.3	3.0	2.3
detrital	14.3	9.0	2.7	18.7	10.0	0.0	0.0	1.3	2.7	2.3	2.3	1.7	18.0	31.3	47.3	1.3	1.0
pseudomatrix	3.7	2.7	0.3	3.7	2.3	1.3	1.3	1.0	1.0	0.7	2.3	0.0	0.7	1.7	5.0	1.7	1.3
AUTHIGENIC MINERALOGY																	
QUARTZ OVERGROWTHS	5.3	16.0	11.3	3.3	9.0	19.3	13.3	11.0	9.7	13.0	14.7	9.0	9.7	0.3	0.0	17.7	16.0
Na-FELDSPAR OVERGROWTHS	0.0	0.0	0.0	0.0	0.0	0.0	0.0	0.0	0.0	0.0	0.0	0.0	0.0	0.0	0.0	0.0	0.0
K-FELDSPAR OVERGROWTHS	tr	0.0	0.0	0.0	0.0	0.0	0.0	0.0	0.0	0.0	0.0	0.0	0.0	0.0	0.0	0.0	0.0
CALCITE CEMENT	0.0	0.0	0.0	0.0	0.0	0.0	0.0	0.0	0.0	0.0	0.0	0.0	0.0	0.0	0.0	0.0	0.0
ferroan	0.0	0.0	0.0	0.0	0.0	0.0	0.0	0.0	0.0	0.0	0.0	0.0	0.0	0.0	0.0	0.0	0.0
non-ferroan	0.0	0.0	0.0	0.0	0.0	0.0	0.0	0.0	0.0	0.0	0.0	0.0	0.0	0.0	0.0	0.0	0.0
DOLOMITE CEMENT	4.7	5.7	8.0	1.0	4.0	2.0	0.0	12.0	0.0	0.0	0.0	0.3	1.0	0.0	0.0	0.0	3.0
ferroan - primary pore-filling	4.3	5.3	7.7	0.0	4.0	1.3	0.0	11.3	0.0	0.0	tr	0.3	1.0	0.0	0.0	0.0	2.3
ferroan - replacive	0.0	0.0	0.0	0.0	0.0	0.7	0.0	0.0	0.0	0.0	tr	0.0	0.0	0.0	0.0	0.0	0.0
non-ferroan - primary pore-filling	0.0	0.3	0.3	1.0	0.0	tr	0.0	0.7	0.0	0.0	tr	0.0	0.0	0.0	0.0	0.0	0.7
non-ferroan - replacive	0.3	0.0	0.0	0.0	0.0	tr	0.0	0.0	0.0	0.0	0.0	tr	0.0	0.0	0.0	0.0	0.0
SIDERITE	0.3	0.3	0.3	15.0	7.0	1.3	0.0	0.0	3.3	1.3	1.3	0.3	0.0	0.0	0.3	2.3	1.7
BARITE	tr	0.0	0.0	0.0	0.0	0.0	0.0	0.0	tr	tr	0.0	0.0	0.3	0.0	0.0	0.0	0.0
ANHYDRITE	tr	0.0	0.0	0.0	0.0	0.0	0.0	0.0	tr	tr	0.0	0.0	0.0	0.0	0.0	0.7	0.3
IRON OXIDE	0.3	tr	0.0	0.0	0.0	0.0	0.3	0.0	0.3	0.0	0.0	0.0	0.0	0.0	0.0	0.0	1.0
PYRITE CEMENT	0.3	tr	0.0	tr	0.0	tr	tr	0.3	0.3	tr	0.0	0.0	tr	2.0	3.3	0.0	0.0
ANATASE	0.0	0.0	0.0	0.3	0.7	0.7	0.0	0.0	tr	0.0	0.0	0.0	tr	tr	0.0	0.3	tr
ZEOLITE	0.3	0.0	0.0	0.0	0.0	0.0	0.0	0.0	0.0	0.0	0.0	0.0	0.0	0.0	0.0	0.0	0.0
RESIDUAL OIL	0.0	0.0	0.0	0.0	0.0	0.0	0.0	0.0	0.0	0.0	0.0	0.0	0.0	0.0	0.0	0.0	0.0
OPTICALLY NON-RESOLVABLE REPLACIVE CLAY	1.3	2.3	0.3	0.3	1.3	1.0	0.0	1.0	0.7	2.0	0.7	0.0	0.0	0.0	0.0	0.0	0.7
OPTICALLY NON-RESOLVABLE PORE-LINING CLAY	0.7	0.0	1.3	0.0	0.0	3.0	1.0	2.3	1.7	2.0	1.7	2.7	2.0	0.0	0.0	0.7	2.7
KAOLINITE	0.3	2.0	4.7	0.7	7.7	13.7	10.3	11.0	11.0	12.3	7.0	12.0	2.0	1.7	0.0	9.0	3.7
primary pore-filling	0.0	0.0	3.7	0.0	3.3	8.3	9.0	6.3	5.3	6.7	5.7	10.3	0.7	0.0	0.0	6.7	3.7
replacive	0.3	2.0	1.0	0.7	4.3	5.3	1.3	4.7	5.7	5.7	1.3	1.7	1.3	1.7	0.0	2.3	0.0
ILLITE	0.0	0.0	tr	0.0	0.0	2.7	0.3	0.3	tr	0.0	0.0	0.7	0.0	0.0	0.0	0.0	0.0
ILLITE-SMECTITE	0.0	0.0	0.0	0.0	0.0	0.0	0.0	tr	tr	0.0	0.0	tr	0.0	0.0	0.0	0.0	0.0
CHLORITE	0.0	0.0	0.0	0.0	0.0	0.0	0.0	0.0	0.0	0.0	0.0	0.0	0.0	0.0	0.0	0.0	0.0
MACROPOROSITY	0.0	0.3	5.7	0.0	0.7	0.3	14.7	3.0	7.7	6.0	3.7	5.3	2.7	0.3	0.0	3.7	2.0
primary intergranular porosity	0.0	0.0	3.0	0.0	0.0	0.0	3.3	1.3	1.7	3.3	3.0	3.7	0.0	0.0	0.0	1.0	1.3
secondary intragranular porosity	0.0	0.3	0.3	0.0	0.7	0.3	0.0	0.3	0.0	0.0	0.0	0.0	0.0	0.0	0.0	0.0	0.0
secondary 'oversized' porosity	0.0	0.0	2.3	0.0	0.0	0.0	11.3	1.3	6.0	2.7	0.7	1.7	2.7	0.3	0.0	2.7	0.7
calculated microporosity	13.1	11.7	0.0	4.6	6.4	7.5	0.7	7.8	4.0	11.9	10.4	11.6	5.5	3.5	2.9	7.4	11.1
TOTALS																	
Detrital grains	68.3	61.7	65.3	57.0	57.3	54.7	58.7	56.7	61.7	60.3	66.3	68.0	63.7	62.7	44.0	62.7	66.7
Detrital clay and pseudomatrix	18.0	11.7	3.0	22.3	12.3	1.3	1.3	2.3	3.7	3.0	4.7	1.7	18.7	33.0	52.3	3.0	2.3
Blocky Cements	11.4	22.0	19.7	19.7	20.7	23.4	13.7	23.3	13.7	14.4	16.0	9.7	11.0	2.3	3.7	21.0	22.0
Authigenic clays	2.3	4.3	6.3	1.0	9.0	20.3	11.7	14.7	13.4	16.3	9.3	15.3	4.0	1.7	0.0	9.7	7.0
Porosity	0.0	0.3	5.7	0.0	0.7	0.3	14.7	3.0	7.7	6.0	3.7	5.3	2.7	0.3	0.0	3.7	2.0
	100.0	*100.0*	*100.0*	*100.0*	*100.0*	*100.0*	*100.0*	*100.0*	*100.0*	*100.0*	*100.0*	*100.0*	*100.0*	*100.0*	*100.0*	*100.0*	*100.0*
SUMMARY CATEGORIES																	
Ductile grains	2.7	4.3	0.0	7.7	1.3	3.7	0.7	1.3	0.0	0.7	0.0	0.3	2.7	4.0	6.7	1.3	2.0
Ductiles	20.7	16.0	3.0	30.0	13.7	5.0	2.0	3.7	3.7	3.7	4.7	2.0	21.3	37.0	59.0	4.3	4.3
Authigenic minerals	13.7	26.4	26.0	20.7	29.7	43.7	25.3	38.0	27.1	30.7	25.4	25.0	15.0	4.0	3.7	30.7	29.0
Authigenic minerals - intergranular	11.7	22.0	24.7	19.7	24.0	36.7	24.0	32.3	20.7	23.0	23.4	23.3	13.7	2.3	3.7	28.4	28.3
Authigenic minerals - replacive	2.0	4.3	1.3	1.0	5.7	7.0	1.3	5.7	6.3	7.7	2.0	1.7	1.3	1.7	0.0	2.3	0.7
QUARTZ	0.88	0.82	0.96	0.79	0.91	0.91	0.91	0.89	0.84	0.88	0.91	0.95	0.88	0.84	0.74	0.94	0.93
FELDSPAR	0.04	0.06	0.00	0.07	0.01	0.00	0.00	0.01	0.00	0.00	0.00	0.00	0.02	0.04	0.05	0.00	0.00
LITHICS	0.08	0.12	0.04	0.14	0.08	0.09	0.09	0.11	0.16	0.12	0.09	0.05	0.10	0.12	0.21	0.06	0.07
MATRIX	18.00	11.67	3.00	22.33	12.33	1.33	1.33	2.33	3.67	3.00	4.67	1.67	18.67	33.00	52.33	3.00	2.33
Horizontal helium porosity (%)	13.1	12	1.2	4.6	7.1	7.8	15.4	10.8	11.7	17.9	14.1	16.9	8.2	3.8	2.9	11.1	13.1
Horizontal permeability (Kg) (mD)	0.14	0.52	0.04	0.03	0.04	0.08	4.1	0.28	3.2	15	3	21	0.9	0.2	0.14	0.91	0.53
Estimated initial porosity (Beard & Weyl 1973)	45.00	45.00	45.00	45.00	45.00	45.00	45.00	45.00	45.00	45.00	45.00	45.00	45.00	45.00	45.00	45.00	45.00
Compactional porosity loss (COPL	37.72	29.47	23.95	31.53	27.63	13.13	24.30	17.08	29.14	25.31	25.32	24.65	36.28	43.68	42.91	22.13	21.79
Cementational porosity loss (CEPL)	7.28	15.53	18.77	13.47	17.37	31.87	18.17	26.82	14.68	17.20	17.44	17.59	8.72	1.32	2.09	22.09	22.17
Compaction index (ICOMPACT)	0.84	0.65	0.56	0.70	0.61	0.29	0.57	0.39	0.66	0.60	0.59	0.58	0.81	0.97	0.95	0.50	0.50
Pmc (minus-cement porosity or intergranular volume)	11.70	22.02	27.68	19.68	24.00	36.69	27.34	33.68	22.38	26.36	26.35	27.01	13.69	2.34	3.67	29.37	29.68
Po (observed intergranular porosity)	0.00	0.00	3.00	0.00	0.00	0.00	3.33	1.33	1.67	3.33	3.00	3.67	0.00	0.00	0.00	1.00	1.33
C (intergranular cement volume)	11.70	22.02	24.68	19.68	24.00	36.69	24.01	32.34	20.72	23.03	23.35	23.34	13.69	2.34	3.67	28.37	28.34
Depositional feldspar (feldspar + replacive kaolinite + secondary pores)	0.04	0.09	0.05	0.08	0.09	0.09	0.18	0.11	0.16	0.12	0.03	0.05	0.07	0.07	0.05	0.07	0.01

WELL	43/19-2	43/19-2	43/19-2	43/19-2	43/19-2	43/19-2	43/19-2	43/19-2	43/19-2	43/19-2	43/19-2	43/19-2	43/19-2	43/19-2	43/19-2	43/19-2	43/19-2
DEPTH (m/ftDD)	3635.01	3635.37	3639.98	3655.42	3661.92	3667.19	3670.15	3672.92	3676.96	4024.17	4027.90	4056.68	4059.20	4063.05	4064.99	4067.26	4087.18
UNIT	m	m	m	m	m	m	m	m	m	m	m	m	m	m	m	m	m
LITHOSTRATIGRAPHY	Millstone Grit Fm	Millstone Grit Fm	Millstone Grit Fm	Millstone Grit Fm	Millstone Grit Fm	Millstone Grit Fm	Millstone Grit Fm	Millstone Grit Fm	Millstone Grit Fm	Millstone Grit Fm	Millstone Grit Fm	Millstone Grit Fm	Millstone Grit Fm	Millstone Grit Fm	Millstone Grit Fm	Millstone Grit Fm	Millstone Grit Fm
LITHOFACIES	Sx	Sx	Sx	S(M)fla	Sx	Sped	Sx	Sx	Sx	Sr	Sx	S(M)ped	Sx	Sx	Sx	Sx	Sx
SANDSTONE CLASSIFICATION	dSLA	SLA	sQA	sidSLA	SLA	SLA	SLA	SLA	sQA	QA	QA	sidSLA	SLA	SLA	QA	SLA	SLA
FACIES ASSOCIATION	Multi-storey fluvial channel	Multi-storey fluvial channel	Multi-storey fluvial channel	Interistributary bay	Multi-storey fluvial channel	Delta plain	Multi-storey fluvial channel	Multi-storey fluvial channel	Multi-storey fluvial channel	Multi-storey fluvial channel	Multi-storey fluvial channel	Delta plain	Multi-storey fluvial channel	Multi-storey fluvial channel	Multi-storey fluvial channel	Multi-storey fluvial channel	Multi-storey fluvial channel
MODAL GRAIN SIZE	upper very fine sand	upper very fine sand	lower fine sand	lower very fine sand	lower fine sand	upper very fine sand	lower fine sand	upper very fine sand	upper fine sand	upper fine sand	upper coarse sand	lower fine sand	upper fine sand	upper medium sand	lower coarse sand	lower coarse sand	lower medium sand
SORTING	moderately well sorted	moderately well sorted	moderately well sorted	moderately well sorted	moderately well sorted	moderately well sorted	moderately well sorted	moderately well sorted	moderately well sorted	moderately well sorted	moderately sorted	moderately well sorted	moderately well sorted	moderately sorted	moderately sorted	moderately sorted	moderately well sorted
DETRITAL MINERALOGY																	
QUARTZ	36.0	52.7	59.0	40.7	53.7	56.7	64.0	57.0	61.0	56.7	65.3	57.7	62.0	59.3	58.7	58.7	50.7
monocrystalline	30.3	46.3	53.0	36.7	37.3	49.7	55.0	50.3	50.3	50.3	30.7	46.0	51.3	41.3	38.3	50.7	38.3
polycrystalline	5.7	6.3	6.0	4.0	16.3	7.0	9.0	6.7	10.7	6.3	34.7	11.7	10.7	18.0	20.3	8.0	12.3
FELDSPAR	2.7	1.3	0.0	3.7	6.7	4.0	2.3	5.7	1.0	1.3	0.0	0.7	0.3	0.0	0.0	0.7	1.0
K-feldspar	1.7	0.7	0.0	1.0	1.0	1.3	0.7	0.7	0.3	0.3	0.0	0.0	0.0	0.0	0.0	0.0	0.7
plagioclase	1.0	0.7	0.0	2.7	5.7	2.7	1.7	5.0	0.7	1.0	0.0	0.7	0.3	0.0	0.0	0.7	0.3
RIGID ROCK FRAGMENTS	4.7	5.3	3.3	7.7	8.7	3.3	7.0	3.0	3.7	3.7	5.7	3.0	5.0	7.0	6.0	5.0	6.7
igneous	4.7	5.3	3.3	7.7	8.7	3.3	7.0	3.0	3.7	3.7	4.3	3.0	5.0	7.0	6.0	5.0	6.3
metamorphic	0.0	0.0	tr	0.0	0.0	0.0	0.0	0.0	0.0	tr	1.3	0.0	0.0	0.0	0.0	0.0	0.3
sedimentary	0.0	0.0	0.0	0.0	0.0	0.0	0.0	0.0	0.0	0.0	0.0	0.0	0.0	tr	0.0	0.0	0.0
HEAVY MINERALS	0.7	tr	tr	0.3	0.3	1.3	tr	0.3	1.0	0.3	0.0	tr	2.0	tr	0.0	0.3	tr
heavy mineral types	A,R,T,Z	A,M,R,T,Z	A,R,T,Z	O,R,T,Z	?A,R	?M,O,R,T,Z	A,M,R,T,Z	T	Z	Z		T,Z	O,R,T,Z	Z		A,M,T,Z	Z
DUCTILE ROCK FRAGMENTS	0.0	0.3	0.3	1.3	1.3	1.0	0.0	2.3	0.3	0.7	0.0	0.0	0.3	0.7	0.0	0.3	2.3
degraded igneous	0.0	0.3	0.3	1.0	1.3	0.3	0.0	2.3	0.3	0.7	0.0	0.0	0.0	0.0	0.0	0.3	2.3
sedimentary	0.0	0.0	0.0	0.3	0.0	0.7	0.0	0.0	0.0	0.0	0.0	0.0	0.3	0.7	0.0	0.0	0.0
MICA	1.7	2.3	0.7	4.3	2.7	2.7	2.7	1.7	0.7	0.3	0.3	2.0	0.7	0.3	0.0	0.7	0.3
muscovite	1.7	2.3	0.7	4.3	2.7	2.7	2.7	1.7	0.7	0.3	0.3	2.0	0.7	0.3	0.0	0.7	0.3
biotite	0.0	0.0	0.0	0.0	0.0	0.0	0.0	0.0	0.0	0.0	0.0	0.0	0.0	0.0	0.0	0.0	0.0
CHLORITE	0.0	0.0	0.0	0.0	0.0	0.0	0.0	0.0	0.0	0.0	0.0	0.0	0.0	0.0	0.0	0.0	0.0
ORGANIC FRAGMENTS	0.0	0.0	0.3	2.0	0.0	0.3	0.0	0.0	0.0	0.0	0.0	1.7	0.0	0.3	0.0	0.3	0.0
OPTICALLY NON-RESOLVABLE CLAY	0.0	5.7	0.3	15.3	14.0	19.3	4.7	7.0	2.7	4.3	3.3	11.7	6.7	3.3	4.3	4.0	8.7
detrital	0.0	4.7	0.0	12.0	10.7	17.7	3.7	5.3	1.7	3.3	3.0	10.0	5.0	1.7	2.0	3.3	3.7
pseudomatrix	0.0	1.0	0.3	3.3	3.3	1.7	1.0	1.7	1.0	1.0	0.3	1.7	1.7	1.7	2.3	0.7	5.0
AUTHIGENIC MINERALOGY																	
QUARTZ OVERGROWTHS	0.0	9.0	19.3	4.3	0.3	2.7	8.0	6.3	10.3	4.0	2.3	3.7	8.0	6.7	9.7	8.7	6.7
Na-FELDSPAR OVERGROWTHS	0.0	0.0	0.0	0.0	0.0	0.0	0.0	0.0	0.0	0.0	0.0	0.0	0.0	0.0	0.0	0.0	0.0
K-FELDSPAR OVERGROWTHS	0.0	0.0	0.0	0.0	0.0	0.0	0.0	0.0	0.0	0.0	0.0	0.0	0.0	0.0	0.0	0.0	0.0
CALCITE CEMENT	0.0	0.0	0.0	0.0	0.0	0.0	0.0	0.0	0.0	0.0	0.0	0.0	0.0	0.0	0.0	0.0	0.0
ferroan	0.0	0.0	0.0	0.0	0.0	0.0	0.0	0.0	0.0	0.0	0.0	0.0	0.0	0.0	0.0	0.0	0.0
non-ferroan	0.0	0.0	0.0	0.0	0.0	0.0	0.0	0.0	0.0	0.0	0.0	0.0	0.0	0.0	0.0	0.0	0.0
DOLOMITE CEMENT	51.3	0.7	2.7	3.7	4.0	0.3	0.7	9.0	1.3	1.7	0.0	0.3	2.0	0.0	1.0	3.7	7.3
ferroan - primary pore-filling	47.7	0.7	1.7	0.7	3.7	0.3	0.7	8.3	1.3	1.7	tr	0.3	2.0	0.0	1.0	3.3	7.0
ferroan - replacive	0.0	0.0	0.7	0.0	0.3	0.0	0.0	0.0	0.0	0.0	0.0	0.0	0.0	0.0	0.0	0.3	0.3
non-ferroan - primary pore-filling	3.7	tr	0.3	3.0	0.0	0.0	0.0	0.7	0.0	0.0	0.0	0.0	0.0	0.0	0.0	0.0	0.0
non-ferroan - replacive	0.0	0.0	0.0	0.0	0.0	0.0	0.0	0.0	0.0	0.0	0.0	0.0	0.0	0.0	0.0	0.0	0.0
SIDERITE	tr	0.3	tr	14.3	4.0	2.7	1.7	0.0	2.3	3.0	1.3	12.3	0.7	1.0	0.3	1.0	0.0
BARITE	0.0	0.0	tr	0.0	0.3	0.7	0.0	1.3	0.0	0.0	1.0	0.0	0.0	0.0	0.0	0.0	0.0
ANHYDRITE	0.0	1.3	0.3	0.0	tr	0.0	0.0	0.0	0.0	0.0	0.0	0.0	0.0	0.0	0.0	0.0	0.0
IRON OXIDE	3.0	3.7	0.3	0.0	0.0	0.0	0.0	0.0	0.0	0.3	0.0	tr	0.0	0.0	0.0	0.0	0.0
PYRITE CEMENT	0.0	0.0	tr	tr	0.0	0.0	0.0	0.0	0.7	0.0	0.0	tr	0.0	0.3	tr	0.0	0.0
ANATASE	0.0	tr	0.7	0.0	tr	0.3	tr	0.3	0.3	0.0	0.0	0.0	0.0	0.0	0.0	0.0	0.0
ZEOLITE	0.0	0.0	0.0	0.0	0.0	0.0	0.0	0.0	0.0	0.0	0.0	0.0	0.0	0.0	0.0	0.0	0.0
RESIDUAL OIL	0.0	0.0	0.0	0.0	0.0	0.0	0.0	0.0	0.0	0.0	0.0	0.0	0.0	0.0	0.0	0.0	0.0
OPTICALLY NON-RESOLVABLE REPLACIVE CLAY	0.0	2.0	1.3	0.0	0.0	0.0	0.7	0.3	0.3	0.0	0.0	0.3	0.7	2.0	0.3	0.7	1.0
OPTICALLY NON-RESOLVABLE PORE-LINING CLAY	0.0	2.7	1.3	1.3	0.0	1.3	1.7	1.3	1.0	0.3	1.7	3.7	2.0	4.3	6.3	4.0	1.7
KAOLINITE	0.0	9.7	9.0	1.0	4.0	2.3	5.3	4.3	5.0	1.7	11.7	2.7	8.7	5.0	4.0	6.7	0.0
primary pore-filling	0.0	6.7	6.3	0.0	1.7	0.3	2.3	2.3	3.3	1.7	11.3	0.0	5.7	4.3	3.0	4.0	0.0
replacive	0.0	3.0	2.7	1.0	2.3	2.0	3.0	2.0	1.7	0.0	0.3	2.7	3.0	0.7	1.0	2.7	0.0
ILLITE	0.0	1.0	0.0	0.0	0.0	0.0	0.0	0.0	0.0	tr	2.0	0.0	0.3	1.0	0.3	0.3	0.0
ILLITE-SMECTITE	0.0	0.0	0.0	0.0	0.0	0.0	0.0	0.0	0.0	0.0	0.0	0.0	0.0	0.0	0.0	0.0	0.0
CHLORITE	0.0	0.0	0.0	0.0	0.0	0.0	0.0	0.0	0.0	0.0	0.0	0.0	0.0	0.0	0.0	0.0	0.0
MACROPOROSITY	0.0	2.0	1.0	0.0	0.0	1.0	1.3	0.0	8.3	21.7	5.3	0.3	0.7	8.7	9.0	5.0	13.7
primary intergranular porosity	0.0	0.0	1.0	0.0	0.0	0.3	0.7	0.0	1.3	0.0	1.0	0.0	0.3	2.3	1.3	0.3	2.0
secondary intragranular porosity	0.0	0.7	0.0	0.0	0.0	0.0	0.7	0.0	0.7	0.0	0.0	0.3	0.0	0.7	0.0	0.3	0.7
secondary 'oversized' porosity	0.0	1.3	0.0	0.0	0.0	0.7	0.0	0.0	6.3	21.7	4.3	0.0	0.3	5.7	7.7	4.3	11.0
calculated microporosity	2.4	6.6	9.1	5.5	8.1	10.7	7.9	7.1	1.1	0.0	10.2	4.9	13.3	4.5	10.1	5.8	0.0
TOTALS																	
Detrital grains	45.7	62.0	63.7	60.0	73.3	69.3	76.0	70.0	67.7	63.0	71.3	65.0	70.3	67.7	64.7	66.0	61.0
Detrital clay and pseudomatrix	0.0	5.7	0.3	15.3	14.0	19.3	4.7	7.0	2.7	4.3	3.3	11.7	6.7	3.3	4.3	4.0	8.7
Blocky Cements	54.3	15.0	23.4	22.3	8.7	6.7	10.3	17.0	15.0	9.0	4.7	16.4	10.7	8.0	11.0	13.3	14.0
Authigenic clays	0.0	15.3	11.7	2.3	4.0	3.7	7.7	6.0	6.3	2.0	15.3	6.7	11.7	12.3	11.0	11.7	2.7
Porosity	0.0	2.0	1.0	0.0	0.0	1.0	1.3	0.0	8.3	21.7	5.3	0.3	0.7	8.7	9.0	5.0	13.7
	100.0	*100.0*	*100.0*	*100.0*	*100.0*	*100.0*	*100.0*	*100.0*	*100.0*	*100.0*	*100.0*	*100.0*	*100.0*	*100.0*	*100.0*	*100.0*	*100.0*
SUMMARY CATEGORIES																	
Ductile grains	1.7	2.7	1.3	7.7	4.0	4.0	2.7	4.0	1.0	1.0	0.3	3.7	1.0	1.3	0.0	1.3	2.7
Ductiles	1.7	8.3	1.7	23.0	18.0	23.3	7.3	11.0	3.7	5.3	3.7	15.3	7.7	4.7	4.3	5.3	11.3
Authigenic minerals	54.3	30.3	35.0	24.7	12.7	10.3	18.0	23.0	21.3	11.0	20.0	23.0	22.3	20.3	22.0	25.0	16.7
Authigenic minerals - intergranular	54.3	25.3	30.4	23.7	10.0	8.3	14.3	20.7	19.3	11.0	19.7	20.0	18.7	17.7	20.7	21.3	15.3
Authigenic minerals - replacive	0.0	5.0	4.7	1.0	2.7	2.0	3.7	2.3	2.0	0.0	0.3	3.0	3.7	2.7	1.3	3.7	1.3
QUARTZ	0.79	0.85	0.93	0.70	0.73	0.82	0.84	0.81	0.90	0.90	0.92	0.91	0.88	0.88	0.91	0.89	0.83
FELDSPAR	0.06	0.02	0.00	0.06	0.09	0.06	0.03	0.08	0.01	0.02	0.00	0.01	0.00	0.00	0.00	0.01	0.02
LITHICS	0.15	0.13	0.07	0.24	0.18	0.12	0.13	0.10	0.08	0.08	0.08	0.08	0.11	0.12	0.09	0.10	0.15
MATRIX	0.00	5.67	0.33	15.33	14.00	19.33	4.67	7.00	2.67	4.33	3.33	11.67	6.67	3.33	4.33	4.00	8.67
Horizontal helium porosity (%)	2.4	8.6	10.1	5.5	8.1	11.7	9.2	7.1	9.4	10.2	15.5	5.2	14	13.2	19.1	10.8	11.6
Horizontal permeability (Kg) (mD)	0.01	0.01	0.19	0.05	0.05	0.09	0.04	0.03	0.49	0.16	7	0.02	0.24	2.3	5	0.4	0.21
Estimated initial porosity (Beard & Weyl 1973)	45.00	45.00	45.00	45.00	45.00	45.00	45.00	45.00	45.00	45.00	45.00	45.00	45.00	45.00	45.00	45.00	45.00
Compactional porosity loss (COPL	0.00	26.33	19.87	27.94	38.88	39.78	35.29	30.67	30.67	38.20	30.66	31.23	32.10	31.25	29.48	29.79	33.47
Cementational porosity loss (CEPL)	45.00	18.67	24.33	17.06	6.12	5.02	9.28	14.33	13.40	6.80	13.64	13.77	12.68	12.15	14.58	14.98	10.20
Compaction index (ICOMPACT)	0.00	0.59	0.45	0.62	0.86	0.89	0.79	0.68	0.70	0.85	0.69	0.69	0.72	0.72	0.67	0.67	0.77
Pmc (minus-cement porosity or intergranular volume)	45.00	25.34	31.36	23.68	10.02	8.67	15.01	20.67	20.66	11.01	20.68	20.02	19.00	20.00	22.01	21.67	17.33
Po (observed intergranular porosity)	0.00	0.00	1.00	0.00	0.00	0.33	0.67	0.00	1.33	0.00	1.00	0.00	0.33	2.33	1.33	0.33	2.00
C (intergranular cement volume)	45.00	25.34	30.36	23.68	10.02	8.33	14.34	20.67	19.33	11.01	19.68	20.02	18.67	17.67	20.68	21.33	15.33
Depositional feldspar (feldspar + replacive kaolinite + secondary pores)	0.06	0.09	0.04	0.08	0.12	0.09	0.08	0.11	0.13	0.27	0.06	0.06	0.05	0.09	0.12	0.11	0.17

WELL	43/19-2	43/19-2	43/19-2	43/19-2	43/19-2	43/19-2	43/19a-4Z	43/19a-4Z	43/19a-4Z	43/19a-4Z	43/19a-4Z	43/19a-4Z	43/19a-4Z	43/19a-4Z	43/19a-4Z	43/19a-4Z
DEPTH (m/ftDD)	4091.75	4097.32	4100.43	4101.91	4241.30	4246.47	15868.65	15872	15874	16263.6	16266.6	16274.4	16539.1	16540.75	16271.8	16276.4
UNIT	m	m	m	m	m	m	ft	ft	ft	ft	ft	ft	ft	ft	ft	ft
LITHOSTRATIGRAPHY	Millstone Grit Fm	Millstone Grit Fm	Millstone Grit Fm	Millstone Grit Fm	Millstone Grit Fm	Millstone Grit Fm	Millstone Grit Fm	Millstone Grit Fm	Millstone Grit Fm	Millstone Grit Fm	Millstone Grit Fm	Millstone Grit Fm	Millstone Grit Fm	Millstone Grit Fm	Millstone Grit Fm	Millstone Grit Fm
LITHOFACIES	Sx	SMp	Sx	Sx	Sx	Sx	Sx	Sx	Sx	Sx	Sx	Sx	Sx	Sx	Sx	Sx
SANDSTONE CLASSIFICATION	sQA	sQA	SLA	SLA	SLA	SLA	sQA	QA	QA	QA	QA	QA	sQA	sQA	sidQA	sQA
FACIES ASSOCIATION	Multi-storey fluvial channel	Multi-storey fluvial channel	Multi-storey fluvial channel	Multi-storey fluvial channel	Multi-storey fluvial channel	Multi-storey fluvial channel	Multi-storey fluvial channel	Multi-storey fluvial channel	Multi-storey fluvial channel	Multi-storey fluvial channel	Multi-storey fluvial channel	Multi-storey fluvial channel	Multi-storey fluvial channel	Multi-storey fluvial channel	Multi-storey fluvial channel	Multi-storey fluvial channel
MODAL GRAIN SIZE	lower medium sand	upper fine sand	lower fine sand	upper fine sand	lower medium sand	upper fine sand	lower coarse sand	upper medium sand	upper medium sand	lower coarse sand	lower coarse sand	lower very coarse sand	upper coarse sand	upper medium sand	upper coarse sand	upper coarse sand
SORTING	moderately well sorted	moderately well sorted	moderately well sorted	well sorted	moderately well sorted	moderately well sorted	moderately well sorted	moderately well sorted	moderately sorted	moderately well sorted	moderately well sorted	poorly sorted	moderately sorted	moderately sorted	moderately well sorted	moderately sorted
DETRITAL MINERALOGY																
QUARTZ	63.7	60.0	44.7	60.7	51.3	44.7	61.0	76.3	71.7	69.6	67.3	72.3	61.3	63.7	62.7	60.6
monocrystalline	48.3	50.0	36.7	46.7	34.3	28.3	47.7	65.3	58.7	49.3	51.3	41.0	38.0	54.0	44.7	45.3
polycrystalline	15.3	10.0	8.0	14.0	17.0	16.3	13.3	11.0	13.0	20.3	16.0	31.3	23.3	9.7	18.0	15.3
FELDSPAR	0.7	1.0	2.0	0.3	9.3	16.0	1.3	0.0	0.0	0.0	0.7	0.0	0.0	0.0	1.7	0.7
K-feldspar	0.3	0.3	0.3	0.0	0.0	0.3	1.3	0.0	0.0	0.0	0.7	0.0	0.0	0.0	1.7	0.7
plagioclase	0.3	0.7	1.7	0.3	9.3	15.7	0.0	0.0	0.0	0.0	0.0	0.0	0.0	0.0	0.0	0.0
RIGID ROCK FRAGMENTS	6.0	3.7	3.3	4.7	15.0	14.0	5.0	1.6	1.3	3.0	2.0	5.3	3.0	2.7	0.7	1.3
igneous	6.0	3.7	3.3	4.7	14.7	13.7	5.0	1.3	1.3	2.3	1.7	3.0	1.3	1.0	0.7	1.0
metamorphic	0.0	0.0	0.0	tr	0.3	0.3	0.0	0.3	0.0	0.7	0.3	2.3	1.7	1.7	0.0	0.3
sedimentary	0.0	0.0	0.0	0.0	0.0	0.0	0.0	0.0	0.0	0.0	0.0	0.0	0.0	0.0	0.0	0.0
HEAVY MINERALS	0.0	tr	tr	0.3	tr	0.3	0.0	0.0	0.0	0.0	0.3	0.3	0.3	0.0	0.0	tr
heavy mineral types		M,R,Z	R,T,Z	O	Z	T										R,Z
DUCTILE ROCK FRAGMENTS	0.3	0.3	0.3	0.3	2.0	1.7	0.0	0.0	0.0	0.0	0.0	0.0	0.3	0.3	0.0	0.0
degraded igneous	0.3	0.3	0.3	0.3	1.0	1.7	0.0	0.0	0.0	0.0	0.0	0.0	0.0	0.0	0.0	0.0
sedimentary	0.0	0.0	0.0	0.0	1.0	0.0	0.0	0.0	0.0	0.0	0.0	0.0	0.3	0.3	0.0	0.0
MICA	0.0	1.0	5.7	1.7	2.3	2.7	0.0	0.0	0.0	0.0	0.0	0.0	0.3	0.7	0.0	0.0
muscovite	0.0	1.0	5.7	1.7	2.3	2.7	0.0	0.0	0.0	0.0	0.0	0.0	0.3	0.7	0.0	0.0
biotite	0.0	0.0	0.0	0.0	0.0	0.0	0.0	0.0	0.0	0.0	0.0	0.0	0.0	0.0	0.0	0.0
CHLORITE	0.0	0.0	0.0	0.0	0.0	0.0	0.0	0.0	0.0	0.0	0.0	0.0	0.0	0.0	0.0	0.0
ORGANIC FRAGMENTS	0.0	0.0	0.7	0.0	0.0	0.0	0.0	0.0	0.0	0.0	0.0	0.0	0.0	0.0	0.0	0.0
OPTICALLY NON-RESOLVABLE CLAY	3.3	5.3	29.3	13.3	2.0	4.3	0.0	0.0	1.0	2.0	0.0	2.3	1.0	1.0	0.0	0.0
detrital	2.3	3.3	27.3	12.0	0.3	3.3	0.0	0.0	1.0	2.0	0.0	2.3	0.7	0.0	0.0	0.0
pseudomatrix	1.0	2.0	2.0	1.3	1.7	1.0	0.0	0.0	0.0	0.0	0.0	0.0	0.3	1.0	0.0	0.0
AUTHIGENIC MINERALOGY																
QUARTZ OVERGROWTHS	13.0	13.0	3.7	7.3	8.0	5.3	10.3	8.7	4.3	9.7	7.7	6.0	10.7	14.3	5.3	12.3
Na-FELDSPAR OVERGROWTHS	0.0	0.0	0.0	0.0	0.3	0.3	0.0	0.0	0.0	0.0	0.0	0.0	0.0	0.0	0.0	0.0
K-FELDSPAR OVERGROWTHS	0.0	0.0	0.0	0.0	0.0	0.0	0.0	0.0	0.0	0.0	0.0	0.0	0.0	0.0	0.0	tr
CALCITE CEMENT	0.0	0.0	0.0	0.0	0.0	0.0	0.0	0.0	0.0	0.0	0.0	0.0	0.0	0.0	0.0	0.0
ferroan	0.0	0.0	0.0	0.0	0.0	0.0	0.0	0.0	0.0	0.0	0.0	0.0	0.0	0.0	0.0	0.0
non-ferroan	0.0	0.0	0.0	0.0	0.0	0.0	0.0	0.0	0.0	0.0	0.0	0.0	0.0	0.0	0.0	0.0
DOLOMITE CEMENT	0.3	1.7	6.0	0.7	4.7	3.0	0.0	2.7	9.0	0.0	0.7	1.0	0.0	0.0	1.0	2.6
ferroan - primary pore-filling	0.0	1.7	6.0	0.7	0.7	3.0	0.0	2.7	9.0	0.0	0.0	1.0	0.0	0.0	1.0	2.3
ferroan - replacive	0.3	0.0	0.0	0.0	0.0	0.0	0.0	0.0	0.0	0.0	0.0	0.0	0.0	0.0	0.0	0.3
non-ferroan - primary pore-filling	0.0	0.0	0.0	0.0	1.0	0.0	0.0	0.0	0.0	0.0	0.7	0.0	0.0	0.0	0.0	0.0
non-ferroan - replacive	0.0	0.0	0.0	0.0	3.0	tr	0.0	0.0	0.0	0.0	0.0	0.0	0.0	0.0	0.0	0.0
SIDERITE	0.7	tr	1.0	1.3	0.7	5.0	0.0	0.0	0.0	3.7	1.7	0.0	0.0	0.0	17.3	0.3
BARITE	0.0	0.0	0.0	0.0	0.0	0.0	0.3	2.0	1.0	0.0	0.0	0.0	0.0	0.0	0.0	0.0
ANHYDRITE	0.0	0.0	0.0	0.0	0.0	0.0	0.0	0.0	0.0	0.0	0.0	0.0	0.0	0.0	0.0	0.0
IRON OXIDE	0.0	0.0	0.0	0.0	0.0	0.0	0.0	0.0	0.0	0.0	0.0	0.0	0.0	0.0	0.0	0.0
PYRITE CEMENT	0.0	0.0	tr	tr	0.0	0.0	0.0	0.0	0.3	0.0	0.0	0.0	0.0	0.0	0.0	2.0
ANATASE	0.0	tr	0.3	0.3	0.0	0.0	0.0	0.0	0.0	0.0	0.0	0.0	1.0	0.3	0.0	0.0
ZEOLITE	0.0	0.0	0.0	0.0	0.0	0.0	0.0	0.0	0.0	0.0	0.0	0.0	0.0	0.0	0.0	0.0
RESIDUAL OIL	0.0	0.0	0.0	0.0	0.0	0.0	0.0	0.0	0.0	0.0	0.0	0.0	0.0	0.0	0.0	0.0
OPTICALLY NON-RESOLVABLE REPLACIVE CLAY	1.0	3.3	0.7	3.3	2.0	0.7	0.0	0.0	0.3	0.0	0.0	0.0	0.0	0.0	0.0	0.0
OPTICALLY NON-RESOLVABLE PORE-LINING CLAY	2.0	6.3	0.0	2.7	0.7	0.3	1.6	0.0	2.0	0.0	1.4	0.7	9.3	4.6	0.0	2.0
KAOLINITE	0.0	0.0	2.0	0.3	0.0	0.0	0.0	0.0	2.0	0.3	0.0	0.3	5.3	4.3	5.7	3.0
primary pore-filling	tr	tr	0.0	0.0	0.0	0.0	0.0	0.0	2.0	0.3	0.0	0.3	5.0	3.3	5.0	2.7
replacive	tr	tr	2.0	0.3	0.0	0.0	0.0	0.0	0.0	0.0	0.0	0.0	0.3	1.0	0.7	0.3
ILLITE	0.0	tr	0.0	0.0	0.0	0.0	0.0	0.0	0.0	0.0	0.0	0.0	0.0	0.0	0.0	0.0
ILLITE-SMECTITE	0.0	0.0	0.0	0.0	0.0	0.0	0.0	0.0	0.0	0.0	0.0	0.0	0.0	0.0	0.0	0.0
CHLORITE	0.0	0.0	0.0	0.0	0.0	0.0	0.0	0.0	0.0	0.0	0.0	0.0	0.0	0.0	0.0	0.0
MACROPOROSITY	9.0	4.3	0.3	2.7	1.7	1.7	20.4	8.7	7.0	11.6	18.3	11.6	7.3	8.0	5.6	15.0
primary intergranular porosity	0.7	1.0	0.0	1.0	0.7	0.3	13.7	7.7	6.7	10.3	14.3	10.3	5.3	3.7	2.3	7.7
secondary intragranular porosity	1.3	0.0	0.0	1.0	1.0	0.0	0	0	0.3	0	0	0.3	0.3	1	0	0
secondary 'oversized' porosity	7.0	3.3	0.3	0.7	0.0	1.3	6.7	1		1.3	4	1	1.7	3.3	3.3	7.3
calculated microporosity	0.7	0.0	5.1	6.3	4.8	6.6	0.0	3.2	0.5	0.1	0.0	0.0	0.2	3.8	7.0	0.0
TOTALS																
Detrital grains	70.7	66.0	56.7	68.0	80.0	79.3	67.3	77.9	73.0	72.6	70.3	77.9	65.2	67.4	65.1	62.6
Detrital clay and pseudomatrix	3.3	5.3	29.3	13.3	2.0	4.3	0.0	0.0	1.0	2.0	0.0	2.3	1.0	1.0	0.0	0.0
Blocky Cements	14.0	14.7	11.0	9.7	13.7	13.7	10.6	13.4	14.6	13.4	10.1	7.0	11.7	14.6	23.6	17.2
Authigenic clays	3.0	9.7	2.7	6.3	2.7	1.0	1.6	0.0	4.3	0.3	1.4	1.0	14.6	8.9	5.7	5.0
Porosity	9.0	4.3	0.3	2.7	1.7	1.7	20.4	8.7	7.0	11.6	18.3	11.6	7.3	8.0	5.6	15.0
	100.0	*100.0*	*100.0*	*100.0*	*100.0*	*100.0*	*100.0*	*100.0*	*100.0*	*100.0*	*100.0*	*100.0*	*100.0*	*100.0*	*100.0*	*100.0*
SUMMARY CATEGORIES																
Ductile grains	0.3	1.3	6.7	2.0	4.3	4.3	0.0	0.0	0.0	0.0	0.0	0.0	0.6	1.0	0.0	0.0
Ductiles	3.7	6.7	36.0	15.3	6.3	8.7	0.0	0.0	1.0	2.0	0.0	2.3	1.6	2.0	0.0	0.0
Authigenic minerals	17.0	24.4	13.7	16.0	16.3	14.7	12.2	13.4	18.9	13.7	11.5	8.0	26.3	23.5	29.3	22.2
Authigenic minerals - intergranular	15.7	21.0	11.0	12.3	11.3	14.0	12.2	13.4	18.6	13.7	11.5	8.0	26.0	22.5	28.6	21.6
Authigenic minerals - replacive	1.3	3.3	2.7	3.7	5.0	0.7	0.0	0.0	0.3	0.0	0.0	0.0	0.3	1.0	0.7	0.6
QUARTZ	0.90	0.91	0.80	0.89	0.64	0.56	0.91	0.98	0.98	0.96	0.96	0.93	0.94	0.95	0.96	0.97
FELDSPAR	0.01	0.02	0.04	0.00	0.12	0.20	0.02	0.00	0.00	0.00	0.01	0.00	0.00	0.00	0.03	0.01
LITHICS	0.09	0.08	0.17	0.10	0.24	0.24	0.07	0.02	0.02	0.04	0.03	0.07	0.06	0.05	0.01	0.02
MATRIX	3.33	5.33	29.33	13.33	2.00	4.33	0.00	0.00	1.00	2.00	0.00	2.30	1.00	1.00	0.00	0.00
Horizontal helium porosity (%)	9.7	2.6	5.4	9	6.5	8.3	10.8	11.9	7.5	11.7	12.4	7.1	7.5	11.8	12.6	8.7
Horizontal permeability (Kg) (mD)	0.29	0.07	0.23	1.8	0.16	0.12	365	267	4.39	350	492	6.51	0.51	19.4	691	59.6
Estimated initial porosity (Beard & Weyl 1973)	45.00	45.00	45.00	45.00	45.00	45.00	45.00	45.00	45.00	45.00	45.00	45.00	45.00	45.00	45.00	45.00
Compactional porosity loss (COPL	34.25	29.45	38.20	36.53	37.50	35.80	25.78	30.29	26.37	27.63	25.88	32.68	19.94	25.47	20.41	22.20
Cementational porosity loss (CEPL)	10.31	14.84	6.80	7.83	7.08	8.99	9.06	9.34	13.69	9.91	8.52	5.39	20.82	16.77	22.76	16.81
Compaction index (ICOMPACT)	0.77	0.66	0.85	0.82	0.84	0.80	0.74	0.76	0.66	0.74	0.75	0.86	0.49	0.60	0.47	0.57
Pmc (minus-cement porosity or intergranular volume)	16.34	22.04	11.01	13.34	12.00	14.33	25.90	21.10	25.30	24.00	25.80	18.30	31.30	26.20	30.90	29.31
Po (observed intergranular porosity)	0.67	1.00	0.00	1.00	0.67	0.33	13.70	7.70	6.70	10.30	14.30	10.30	5.30	3.70	2.30	7.70
C (intergranular cement volume)	15.68	21.04	11.01	12.34	11.33	14.00	12.20	13.40	18.60	13.70	11.50	8.00	26.00	22.50	28.60	21.61
Depositional feldspar (feldspar + replacive kaolinite + secondary pores)	0.11	0.06	0.07	0.03	0.13	0.21	0.11	0.01	0.00	0.02	0.06	0.02	0.03	0.07	0.08	0.12

Appendix 4

Modal tables, averages by well and field

	44/16-1			44/16-1Z			44/16-2			All samples Copernicus		
	Average	Min	Max	Average	Min	Max	Average	Min	Max	Average	Min	Max
DETRITAL MINERALOGY												
QUARTZ	45.1	20.3	74.0	66.1	1.0	78.0	68.1	39.7	77.0	57.7	1.0	78.0
monocrystalline	38.2	17.0	67.3	59.0	1.0	69.0	61.1	35.3	70.3	50.7	1.0	70.3
polycrystalline	7.0	2.0	19.3	7.1	0.0	11.3	7.0	3.0	15.3	7.0	0.0	19.3
FELDSPAR	10.2	1.0	24.3	1.6	0.0	4.0	1.7	0.0	5.7	5.3	0.0	24.3
K-feldspar	2.4	0.0	5.7	1.2	0.0	4.0	1.1	0.0	5.0	1.7	0.0	5.7
plagioclase	7.8	0.0	18.7	0.4	0.0	1.7	0.7	0.0	3.0	3.7	0.0	18.7
RIGID ROCK FRAGMENTS	5.1	1.0	13.3	2.6	0.0	5.7	2.5	0.3	9.3	3.6	0.0	13.3
igneous	4.8	1.0	11.3	2.4	0.0	5.7	2.4	0.3	9.3	3.5	0.0	11.3
metamorphic	0.2	0.0	2.0	0.1	0.0	0.7	0.0	0.0	0.7	0.2	0.0	2.0
sedimentary	0.0	0.0	0.0	0.0	0.0	0.3	0.0	0.0	0.0	0.0	0.0	0.3
HEAVY MINERALS	0.4	0.0	1.3	0.8	0.0	3.0	0.6	0.0	3.0	0.6	0.0	3.0
DUCTILE ROCK FRAGMENTS	0.7	0.0	2.7	0.1	0.0	0.7	0.2	0.0	1.7	0.4	0.0	2.7
degraded igneous	0.6	0.0	2.7	0.1	0.0	0.7	0.2	0.0	1.3	0.3	0.0	2.7
sedimentary	0.1	0.0	0.7	0.0	0.0	0.3	0.0	0.0	0.3	0.0	0.0	0.7
MICA	3.0	0.0	10.7	1.0	0.0	8.0	0.8	0.0	3.3	1.8	0.0	10.7
muscovite	2.9	0.0	9.7	1.0	0.0	7.7	0.8	0.0	3.3	1.7	0.0	9.7
biotite	0.1	0.0	1.0	0.0	0.0	0.3	0.0	0.0	0.0	0.0	0.0	1.0
CHLORITE	0.0	0.0	0.3	0.0	0.0	0.0	0.0	0.0	0.0	0.0	0.0	0.3
ORGANIC FRAGMENTS	2.9	0.0	16.0	0.8	0.0	5.0	0.2	0.0	1.3	1.5	0.0	16.0
OPTICALLY NON-RESOLVABLE CLAY	10.3	0.0	24.3	4.4	0.0	48.3	3.1	0.0	20.3	6.6	0.0	48.3
detrital	5.9	0.0	21.0	3.9	0.0	48.3	2.0	0.0	12.0	4.2	0.0	48.3
pseudomatrix	4.5	0.0	11.7	0.4	0.0	8.0	1.1	0.0	8.3	2.4	0.0	11.7
AUTHIGENIC MINERALOGY												
QUARTZ OVERGROWTHS	6.3	0.0	16.0	11.0	0.0	19.3	11.5	0.0	21.7	9.1	0.0	21.7
Na-FELDSPAR OVERGROWTHS	0.2	0.0	2.0	0.0	0.0	0.0	0.0	0.0	0.0	0.1	0.0	2.0
K-FELDSPAR OVERGROWTHS	0.0	0.0	0.0	0.0	0.0	tr	0.1	0.0	0.3	0.0	0.0	0.3
CALCITE CEMENT	0.0	0.0	0.0	0.0	0.0	0.0	0.0	0.0	0.0	0.0	0.0	0.0
ferroan	0.0	0.0	0.0	0.0	0.0	0.0	0.0	0.0	0.0	0.0	0.0	0.0
non-ferroan	0.0	0.0	0.0	0.0	0.0	0.0	0.0	0.0	0.0	0.0	0.0	0.0
DOLOMITE CEMENT	5.3	0.0	21.0	0.8	0.0	8.3	3.4	0.0	52.0	3.5	0.0	52.0
ferroan - primary pore-filling	2.9	0.0	13.7	0.0	0.0	0.0	2.8	0.0	50.3	2.1	0.0	50.3
ferroan - replacive	0.8	0.0	5.3	0.0	0.0	0.0	0.0	0.0	0.3	0.4	0.0	5.3
non-ferroan - primary pore-filling												
non-ferroan - replacive	0.2	0.0	2.0	0.0	0.0	0.7	0.0	0.0	0.0	0.1	0.0	2.0
SIDERITE	5.8	0.0	22.0	4.4	0.0	48.7	1.9	0.0	13.7	4.3	0.0	48.7
BARITE	0.0	0.0	0.0	0.0	0.0	0.3	0.0	0.0	0.0	0.0	0.0	0.3
ANHYDRITE	0.0	0.0	0.0	0.0	0.0	0.0	0.0	0.0	0.0	0.0	0.0	0.0
IRON OXIDE	0.0	0.0	0.0	0.0	0.0	0.0	0.0	0.0	0.0	0.0	0.0	0.0
PYRITE CEMENT	0.2	0.0	2.7	0.1	0.0	0.7	0.3	0.0	1.0	0.2	0.0	2.7
ANATASE	0.1	0.0	1.3	0.1	0.0	0.3	0.0	0.0	0.3	0.1	0.0	1.3
ZEOLITE	0.0	0.0	0.0	0.0	0.0	tr	0.0	0.0	0.0	0.0	0.0	0.0
RESIDUAL OIL	0.0	0.0	tr	0.2	0.0	3.7	tr	0.0	0.3	0.1	0.0	3.7
OPTICALLY NON-RESOLVABLE REPLACIVE CLAY	0.2	0.0	3.7	0.1	0.0	0.7	0.1	0.0	0.3	0.1	0.0	3.7
OPTICALLY NON-RESOLVABLE PORE-LINING CLAY	0.1	0.0	0.7	0.0	0.0	0.3	0.0	0.0	0.3	0.1	0.0	0.7
KAOLINITE	2.4	0.0	8.0	3.4	0.7	9.3	3.5	0.0	13.0	3.0	0.0	13.0
primary pore-filling	0.4	0.0	2.7	0.9	0.0	2.0	0.7	0.0	2.3	0.6	0.0	2.7
replacive	1.9	0.0	7.3	2.6	0.3	8.0	2.7	0.0	10.7	2.3	0.0	10.7
ILLITE	0.1	0.0	0.7	0.0	0.0	0.0	0.1	0.0	1.3	0.1	0.0	1.3
ILLITE-SMECTITE	0.0	0.0	0.0	0.0	0.0	0.0	0.0	0.0	0.0	0.0	0.0	0.0
CHLORITE	0.0	0.0	0.0	0.0	0.0	0.0	0.0	0.0	0.0	0.0	0.0	0.0
MACROPOROSITY	1.4	0.0	8.0	2.4	0.0	7.3	1.9	0.0	7.7	1.8	0.0	8.0
primary intergranular porosity	0.7	0.0	6.3	1.8	0.0	6.7	1.6	0.0	6.7	1.3	0.0	6.7
secondary intragranular porosity	0.2	0.0	2.7	0.1	0.0	1.0	0.1	0.0	0.7	0.2	0.0	2.7
secondary 'oversized' porosity	0.5	0.0	5.0	0.5	0.0	2.0	0.1	0.0	1.0	0.4	0.0	5.0
calculated microporosity	6.1	1.1	11.8	2.7	0.8	6.5	2.4	0.0	6.2	4.1	0.0	11.8
TOTALS												
Detrital grains	67.4	57.7	78.3	73.0	2.3	84.0	74.1	43.7	85.4	70.9	2.3	85.4
Detrital clay and pseudomatrix	10.3	0.0	24.3	4.4	0.0	48.3	3.1	0.0	20.3	6.6	0.0	48.3
Blocky Cements	18.1	2.0	31.7	16.6	1.3	48.7	17.2	7.0	52.7	17.4	1.3	52.7
Authigenic clays	2.8	0.0	8.7	3.6	0.7	9.3	3.7	0.0	14.0	3.3	0.0	14.0
Porosity	1.4	0.0	8.0	2.4	0.0	7.3	1.9	0.0	7.7	1.8	0.0	8.0
SUMMARY CATEGORIES												
Ductile grains	6.5	0.0	19.3	1.9	0.0	10.3	1.2	0.0	4.7	3.7	0.0	19.3
Ductiles	16.9	0.0	43.3	6.3	0.0	49.7	4.3	0.0	24.7	10.3	0.0	49.7
Authigenic minerals	20.9	4.3	32.7	20.2	3.3	49.4	20.9	8.7	56.3	20.7	3.3	56.3
Authigenic minerals - intergranular	17.7	2.0	31.3	17.5	1.3	48.7	18.1	7.0	52.7	17.7	1.3	52.7
Authigenic minerals - replacive	3.2	0.3	7.7	2.7	0.3	8.0	2.8	0.0	11.0	3.0	0.0	11.0
											0.0	0.0
QUARTZ	0.7	0.4	0.9	0.9	0.8	1.0	0.9	0.9	1.0	0.8	0.4	1.0
FELDSPAR	0.2	0.0	0.4	0.0	0.0	0.1	0.0	0.0	0.1	0.1	0.0	0.4
LITHICS	0.1	0.0	0.3	0.1	0.0	0.2	0.1	0.0	0.1	0.1	0.0	0.3
MATRIX	10.3	0.0	24.3	4.4	0.0	48.3	3.1	0.0	20.3	6.6	0.0	48.3
Horizontal helium porosity (%)	7.5	2.8	14.8	5.1	0.8	9.1	4.3	0.8	8.6	5.9	0.8	14.8
Horizontal permeability (Kg) (mD)	5.4	0.01	61.0	4.7	0.01	42.0	2.0	0.01	18.0	4.2	0.01	61.0
	0.21 (geomean perm.)			0.51 (geomean perm.)			0.18 (geomean perm.)			0.26 (geoeman perm.)		
Estimated initial porosity (Beard & Weyl 1973)	38.4	27.5	41.0	39.2	37.0	41.0	39.1	35.5	41.5	38.8	27.5	41.5
Compactional porosity loss (COPL	24.2	0.0	35.7	26.0	20.5	39.2	24.0	0.0	34.9	24.7	0.0	39.2
Cementational porosity loss (CEPL)	13.6	1.3	27.5	11.8	0.8	18.4	14.4	4.6	52.7	13.4	0.8	52.7
Compaction index (ICOMPACT)	0.6	0.0	1.0	0.7	0.5	1.0	0.6	0.0	0.9	0.7	0.0	1.0
Pmc (minus-cement porosity or intergranular volume)	18.2	2.0	29.3	19.3	1.3	48.7	19.0	7.0	41.0	18.8	1.3	48.7
Po (observed intergranular porosity)	0.7	0.0	6.3	1.8	0.0	6.7	1.6	0.0	6.7	1.3	0.0	6.7
C (intergranular cement volume)	17.5	2.0	29.3	17.5	1.3	48.7	18.1	7.0	52.7	17.7	1.3	52.7
Depositional feldspar (feldspar + replacive kaolinite + secondary pores)	0.2	0.0	0.4	0.1	0.0	0.3	0.1	0.0	0.2	0.1	0.0	0.4
Number of samples	*27*			*18*			*18*			*63*		

	43/19-1			43/19-2			43/19a-4Z			Cavendish all samples			All samples		
	Average	Min	Max	Average	Min	Max	Average	Min	Max	Average	Min	Max	Average	Min	Max
DETRITAL MINERALOGY															
QUARTZ	49.3	31.0	64.7	55.8	36.0	65.3	66.7	60.6	76.3	55.4	31.0	76.3	56.6	1.0	78.0
monocrystalline	38.5	27.7	51.7	44.1	28.3	55.0	49.5	38.0	65.3	43.0	27.7	65.3	47.1	1.0	70.3
polycrystalline	10.8	2.7	22.7	11.7	4.0	34.7	17.1	9.7	31.3	12.3	2.7	34.7	9.5	0.0	34.7
FELDSPAR	3.0	0.0	10.0	2.4	0.0	16.0	0.4	0.0	1.7	2.3	0.0	16.0	3.9	0.0	24.3
K-feldspar	0.3	0.0	2.0	0.4	0.0	1.7	0.4	0.0	1.7	0.4	0.0	2.0	1.1	0.0	5.7
plagioclase	2.8	0.0	9.0	2.0	0.0	15.7	0.0	0.0	0.0	1.9	0.0	15.7	2.9	0.0	18.7
RIGID ROCK FRAGMENTS	4.8	1.3	10.0	5.6	2.3	15.0	2.6	0.7	5.3	4.8	0.7	15.0	4.2	0.0	15.0
igneous	4.6	1.0	9.3	5.5	2.3	14.7	1.9	0.7	5.0	4.5	0.7	14.7	3.9	0.0	14.7
metamorphic	0.2	0.0	1.0	0.1	0.0	1.3	0.7	0.0	2.3	0.3	0.0	2.3	0.2	0.0	2.3
sedimentary	0.0	0.0	0.7	0.0	0.0	tr	0.0	0.0	0.0	0.0	0.0	0.7	0.0	0.0	0.7
HEAVY MINERALS	0.3	0.0	1.3	0.3	0.0	2.0	0.1	0.0	0.3	0.3	0.0	2.0	0.4	0.0	3.0
DUCTILE ROCK FRAGMENTS	0.8	0.0	3.3	0.7	0.0	2.3	0.1	0.0	0.3	0.6	0.0	3.3	0.5	0.0	3.3
degraded igneous	0.5	0.0	2.0	0.6	0.0	2.3	0.0	0.0	0.0	0.4	0.0	2.3	0.4	0.0	2.7
sedimentary	0.3	0.0	2.3	0.1	0.0	1.0	0.1	0.0	0.3	0.2	0.0	2.3	0.1	0.0	2.3
MICA	2.0	0.0	6.3	1.6	0.0	5.7	0.1	0.0	0.7	1.4	0.0	6.3	1.6	0.0	10.7
muscovite	1.9	0.0	6.3	1.6	0.0	5.7	0.1	0.0	0.7	1.4	0.0	6.3	1.6	0.0	9.7
biotite	0.0	0.0	0.3	0.0	0.0	0.0	0.0	0.0	0.0	0.0	0.0	0.3	0.0	0.0	1.0
CHLORITE	0.0	0.0	0.0	0.0	0.0	0.0	0.0	0.0	0.0	0.0	0.0	0.0	0.0	0.0	0.3
ORGANIC FRAGMENTS	0.6	0.0	6.7	0.2	0.0	2.0	0.0	0.0	0.0	0.3	0.0	6.7	0.9	0.0	16.0
OPTICALLY NON-RESOLVABLE CLAY	10.8	1.3	52.3	7.1	0.0	29.3	0.7	0.0	2.3	7.3	0.0	52.3	6.9	0.0	52.3
detrital	8.5	0.0	47.3	5.5	0.0	27.3	0.6	0.0	2.3	5.7	0.0	47.3	4.9	0.0	48.3
pseudomatrix	2.3	0.0	5.7	1.6	0.0	5.0	0.1	0.0	1.0	1.6	0.0	5.7	2.0	0.0	11.7
AUTHIGENIC MINERALOGY															
QUARTZ OVERGROWTHS	9.6	0.0	19.3	7.8	0.0	19.3	8.9	4.3	14.3	8.6	0.0	19.3	8.9	0.0	21.7
Na-FELDSPAR OVERGROWTHS	0.2	0.0	1.7	0.0	0.0	0.3	0.0	0.0	0.0	0.1	0.0	1.7	0.1	0.0	2.0
K-FELDSPAR OVERGROWTHS	0.0	0.0	tr	0.0	0.0	0.0	0.0	0.0	tr	0.0	0.0	0.0	0.0	0.0	0.3
CALCITE CEMENT	0.0	0.0	0.0	0.0	0.0	0.0	0.0	0.0	0.0	0.0	0.0	0.0	0.0	0.0	0.0
ferroan	0.0	0.0	0.0	0.0	0.0	0.0	0.0	0.0	0.0	0.0	0.0	0.0	0.0	0.0	0.0
non-ferroan	0.0	0.0	0.0	0.0	0.0	0.0	0.0	0.0	0.0	0.0	0.0	0.0	0.0	0.0	0.0
DOLOMITE CEMENT	5.1	0.0	19.7	4.4	0.0	51.3	1.7	0.0	9.0	4.1	0.0	51.3	3.8	0.0	52.0
ferroan - primary pore-filling	4.3	0.0	18.3	3.8	0.0	47.7	1.6	0.0	9.0	3.6	0.0	47.7	2.8	0.0	50.3
ferroan - replacive	0.6	0.0	2.7	0.1	0.0	0.7	0.0	0.0	0.3	0.2	0.0	2.7	0.3	0.0	5.3
non-ferroan - primary pore-filling							0.1	0.0	0.7	0.3	0.0	3.7	0.6	0.0	8.3
non-ferroan - replacive	0.0	0.0	0.3	0.1	0.0	3.0	0.0	0.0	0.0	0.1	0.0	3.0	0.1	0.0	3.0
SIDERITE	2.3	0.0	15.0	2.3	0.0	14.3	2.3	0.0	17.3	2.3	0.0	17.3	3.4	0.0	48.7
BARITE	0.0	0.0	0.3	0.1	0.0	1.3	0.3	0.0	2.0	0.1	0.0	2.0	0.1	0.0	2.0
ANHYDRITE	0.0	0.0	tr	0.1	0.0	1.3	0.0	0.0	0.0	0.0	0.0	1.3	0.0	0.0	1.3
IRON OXIDE	0.1	0.0	0.3	0.3	0.0	3.7	0.0	0.0	0.0	0.2	0.0	3.7	0.1	0.0	3.7
PYRITE CEMENT	0.3	0.0	3.3	0.0	0.0	0.7	0.2	0.0	2.0	0.2	0.0	3.3	0.2	0.0	3.3
ANATASE	0.2	0.0	1.0	0.1	0.0	0.7	0.1	0.0	1.0	0.1	0.0	1.0	0.1	0.0	1.3
ZEOLITE	0.0	0.0	0.3	0.0	0.0	0.0	0.0	0.0	0.0	0.0	0.0	0.3	0.0	0.0	0.3
RESIDUAL OIL	0.0	0.0	0.0	0.0	0.0	0.0	0.0	0.0	0.0	0.0	0.0	0.0	0.0	0.0	3.7
OPTICALLY NON-RESOLVABLE REPLACIVE CLAY	0.9	0.0	2.3	0.9	0.0	3.3	0.0	0.0	0.3	0.7	0.0	3.3	0.4	0.0	3.7
OPTICALLY NON-RESOLVABLE PORE-LINING CLAY	1.0	0.0	3.0	2.0	0.0	6.3	2.2	0.0	9.3	1.6	0.0	9.3	0.8	0.0	9.3
KAOLINITE	6.1	0.0	13.7	3.8	0.0	11.7	2.1	0.0	5.7	4.4	0.0	13.7	3.6	0.0	13.7
primary pore-filling	3.6	0.0	10.3	2.5	0.0	11.3	1.9	0.0	5.0	2.8	0.0	11.3	1.7	0.0	11.3
replacive	2.5	0.0	5.7	1.3	0.0	3.0	0.2	0.0	1.0	1.5	0.0	5.7	2.0	0.0	10.7
ILLITE	0.3	0.0	2.7	0.2	0.0	2.0	0.0	0.0	0.0	0.2	0.0	2.7	0.1	0.0	2.7
ILLITE-SMECTITE	0.0	0.0	tr	0.0	0.0	0.0	0.0	0.0	0.0	0.0	0.0	0.0	0.0	0.0	0.0
CHLORITE	0.0	0.0	0.0	0.0	0.0	0.0	0.0	0.0	0.0	0.0	0.0	0.0	0.0	0.0	0.0
MACROPOROSITY	2.5	0.0	14.7	4.1	0.0	21.7	11.4	5.6	20.4	4.9	0.0	21.7	3.2	0.0	21.7
primary intergranular porosity	1.0	0.0	3.7	0.7	0.0	2.3	8.2	2.3	14.3	2.1	0.0	14.3	1.7	0.0	14.3
secondary intragranular porosity	0.1	0.0	0.7	0.3	0.0	1.3	0.2	0.0	1.0	0.2	0.0	1.3	0.2	0.0	2.7
secondary 'oversized' porosity	1.5	0.0	11.3	3.2	0.0	21.7	3.3	1.0	7.3	2.6	0.0	21.7	1.4	0.0	21.7
calculated microporosity	6.7	0.0	13.1	5.4	0.0	13.3	-1.2	0.0	7.0	4.7	0.0	13.3	4.4	0.0	13.3
TOTALS															
Detrital grains	60.7	44.0	68.3	66.7	45.7	80.0	69.9	62.6	77.9	65.1	44.0	80.0	68.2	2.3	85.4
Detrital clay and pseudomatrix	10.8	1.3	52.3	7.1	0.0	29.3	0.7	0.0	2.3	7.3	0.0	52.3	6.9	0.0	52.3
Blocky Cements	17.7	2.3	33.3	15.2	4.7	54.3	13.6	7.0	23.6	15.8	2.3	54.3	16.7	1.3	54.3
Authigenic clays	8.3	0.0	20.3	6.9	0.0	15.3	4.3	0.0	14.6	6.9	0.0	20.3	5.0	0.0	20.3
Porosity	2.5	0.0	14.7	4.1	0.0	21.7	11.4	5.6	20.4	4.9	0.0	21.7	3.2	0.0	21.7
SUMMARY CATEGORIES															
Ductile grains	3.4	0.0	13.0	2.5	0.0	7.7	0.2	0.0	1.0	2.4	0.0	13.0	3.1	0.0	19.3
Ductiles	14.1	2.0	59.0	9.6	1.7	36.0	0.9	0.0	2.3	9.7	0.0	59.0	10.0	0.0	59.0
Authigenic minerals	26.0	3.7	43.7	22.1	10.3	54.3	17.9	8.0	29.3	22.7	3.7	54.3	21.6	3.3	56.3
Authigenic minerals - intergranular	22.0	2.3	36.7	19.7	8.3	54.3	17.6	8.0	28.6	20.2	2.3	54.3	18.9	1.3	54.3
Authigenic minerals - replacive	4.0	0.0	9.7	2.4	0.0	5.0	0.3	0.0	1.0	2.6	0.0	9.7	2.8	0.0	11.0
QUARTZ	0.8	0.6	1.0	0.8	0.6	0.9	1.0	0.9	1.0	0.9	0.6	1.0	0.8	0.4	1.0
FELDSPAR	0.1	0.0	0.2	0.0	0.0	0.2	0.0	0.0	0.0	0.0	0.0	0.2	0.1	0.0	0.4
LITHICS	0.1	0.0	0.2	0.1	0.1	0.2	0.0	0.0	0.1	0.1	0.0	0.2	0.1	0.0	0.3
MATRIX	10.8	1.3	52.3	7.1	0.0	29.3	0.7	0.0	2.3	7.3	0.0	52.3	6.9	0.0	52.3
Horizontal helium porosity (%)	9.3	1.2	17.9	9.5	2.4	19.1	10.2	7.1	12.6	9.5	1.2	19.1	7.6	0.8	19.1
Horizontal permeability (Kg) (mD)	2.5	0.01	21.0	0.8	0.01	7.0	225.5	0.5	691.0	42.3	0.0	691.0	22.0	0.0	691.0
	0.34 (geomean perm.)			0.19 (geomean perm.)			53.59 (geomean perm.)			0.66 (geomean perm.)			0.40 (geomean perm.)		
Estimated initial porosity (Beard & Weyl 1973)	37.9	35.5	40.5	38.4	35.5	40.5	36.5	27.0	39.0	37.9	27.0	40.5	38.4	27.0	41.5
Compactional porosity loss (COPL	18.4	6.0	38.0	22.5	0.0	33.2	14.2	6.1	22.7	19.5	0.0	38.0	22.2	0.0	39.2
Cementational porosity loss (CEPL)	18.7	1.5	34.5	15.3	5.6	39.0	15.3	7.1	25.5	16.5	1.5	39.0	14.9	0.8	52.7
Compaction index (ICOMPACT)	0.5	0.1	1.0	0.6	0.0	0.9	0.5	0.2	0.7	0.5	0.0	1.0	0.6	0.0	1.0
Pmc (minus-cement porosity or intergranular volume)	23.0	2.3	36.7	19.8	8.7	39.0	25.8	18.3	31.3	22.0	2.3	39.0	20.3	1.3	48.7
Po (observed intergranular porosity)	1.0	0.0	3.7	0.7	0.0	2.3	8.2	2.3	14.3	2.1	0.0	14.3	1.7	0.0	14.3
C (intergranular cement volume)	22.0	2.3	36.7	19.1	8.3	39.0	17.6	8.0	28.6	19.9	2.3	39.0	18.7	1.3	52.7
Depositional feldspar (feldspar + replacive kaolinite + secondary pores)	0.1	0.0	0.2	0.1	0.0	0.3	0.1	0.0	0.1	0.1	0.0	0.3	0.1	0.0	0.4
Number of samples	*20*			*25*			*10*			*55*			*118*		

Appendix 5

Modal tables, averages by facies association split by field;

Copernicus discovery

	Delta plain			Distal delta front			Distributary channel			Interdistributary bay			Multi-storey fluvial channel		
	Average	Min	Max	Average	Min	Max	Average	Min	Max	Average	Min	Max	Average	Min	Max
DETRITAL MINERALOGY															
QUARTZ	70.4	53.7	78.0	39.3	28.7	50.0	71.3	66.3	75.0	45.8	1.0	69.0	63.5	46.7	77.0
monocrystalline	63.7	48.3	70.3	33.6	24.7	46.7	64.7	61.0	67.3	40.9	1.0	60.7	51.7	27.3	67.7
polycrystalline	6.7	2.3	11.3	5.8	3.3	9.0	6.6	5.3	7.7	4.9	0.0	10.3	11.8	5.7	19.3
FELDSPAR	2.0	0.0	5.7	16.2	5.0	20.7	1.3	0.0	3.0	1.6	0.0	4.0	2.3	0.3	4.0
K-feldspar	1.4	0.0	5.0	2.3	0.3	3.7	0.8	0.0	2.3	1.0	0.0	3.0	1.9	0.0	3.7
microcline															
plagioclase	0.6	0.0	4.0	13.8	4.7	18.3	0.4	0.0	1.0	0.6	0.0	1.0	0.4	0.0	2.0
RIGID ROCK FRAGMENTS	2.8	0.3	7.0	5.1	3.7	8.7	1.3	0.3	2.3	0.8	0.0	2.0	6.0	1.0	13.3
igneous	2.7	0.3	7.0	5.1	3.7	8.7	1.3	0.3	2.3	0.8	0.0	2.0	5.7	1.0	11.3
metamorphic	0.1	0.0	0.7	0.0	0.0	0.0	0.0	0.0	tr	0.0	0.0	0.0	0.4	0.0	2.0
sedimentary	0.0	0.0	0.3	0.0	0.0	0.0	0.0	0	0.0	0.0	0.0	0.0	0.0	0.0	0.0
HEAVY MINERALS	0.8	0.0	3.0	0.7	0.3	1.0	0.5	tr	0.7	0.9	0.0	2.0	0.3	0.0	0.7
DUCTILE ROCK FRAGMENTS	0.2	0.0	1.7	1.2	0.0	2.0	0.1	0.0	0.3	0.3	0.0	0.7	0.4	0.0	1.3
degraded igneous	0.2	0.0	1.3	1.0	0.0	1.7	0.0	0.0	0.0	0.2	0.0	0.7	0.3	0.0	1.3
sedimentary	0.0	0.0	0.3	0.2	0.0	0.3	0.1	0.0	0.3	0.1	0.0	0.3	0.0	0.0	0.3
MICA	0.8	0.0	5.3	3.6	2.3	5.7	0.3	0.0	0.7	2.3	tr	8.0	0.5	0.0	2.7
muscovite	0.8	0.0	5.3	3.6	2.3	5.7	0.3	0.0	0.7	2.3	tr	7.7	0.5	0.0	2.7
biotite	0.0	0.0	0.0	0.0	0.0	0.0	0.0	0.0	tr	0.1	0.0	0.3	0.0	0.0	0.0
CHLORITE	0.0	0.0	0.0	0.0	0.0	0.0	0.0	0.0	0.0	0.0	0.0	0.0	0.0	0.0	0.0
ORGANIC FRAGMENTS	0.4	0.0	2.7	0.8	0.3	2.0	0.0	0.0	0.0	2.3	0.7	5.0	0.6	0.0	7.3
OPTICALLY NON-RESOLVABLE CLAY	2.3	0.0	23.0	8.3	4.0	15.3	0.2	0.0	0.3	19.7	0.3	48.3	6.1	0.0	15.3
detrital	1.9	0.0	20.7	3.0	0.0	6.3	0.0	0.0	0.0	17.7	0.3	48.3	2.3	0.0	10.3
pseudomatrix	0.4	0.0	3.0	5.3	3.7	9.0	0.2	0.0	0.3	2.0	0.0	8.0	3.7	0.0	11.7
AUTHIGENIC MINERALOGY															
QUARTZ OVERGROWTHS	12.3	2.0	19.7	6.0	3.7	8.0	15.8	9.0	21.7	6.8	0.0	17.7	10.7	6.3	15.0
MICROCRYSTALLINE QUARTZ	0.0	0.0	0.0	0.0	0.0	0.0	0.0	0.0	0.0	0.0	0.0	0.0	0.0	0.0	0.0
Na-FELDSPAR OVERGROWTHS	0.0	0.0	0.0	0.8	0.0	1.3	0.0	0.0	0.0	0.0	0.0	0.0	0.0	0.0	0.0
K-FELDSPAR OVERGROWTHS	0.0	0.0	tr	0.0	0.0	0.0	0.0	0.0	0.0	0.0	0.0	0.0	0.1	0.0	0.3
CALCITE CEMENT	0.0	0.0	0.0	0.0	0.0	0.0	0.0	0.0	0.0	0.0	0.0	0.0	0.0	0.0	0.0
ferroan	0.0	0.0	0.0	0.0	0.0	0.0	0.0	0.0	0.0	0.0	0.0	0.0	0.0	0.0	0.0
non-ferroan	0.0	0.0	0.0	0.0	0.0	0.0	0.0	0.0	0.0	0.0	0.0	0.0	0.0	0.0	0.0
DOLOMITE CEMENT	0.5	0.0	8.3	8.8	0.0	14.3	1.2	tr	3.7	0.3	0.0	1.0	2.1	0.0	16.0
ferroan - primary pore-filling	0.0	0.0	tr	5.8	0.0	9.7	0.0	0.0	tr	0.0	0.0	tr	1.4	0.0	13.7
ferroan - replacive	0.0	0.0	0.0	0.8	0.0	2.3	0.0	0.0	0.0	0.0	0.0	0.0	0.2	0.0	1.3
non-ferroan - primary pore-filling	0.4	0.0	8.3	2.2	0.0	4.0	1.2	0.0	3.7	0.3	0.0	1.0	0.4	0.0	1.3
non-ferroan - replacive	0.0	0.0	0.7	0.1	0.0	0.3	0.0	0.0	tr	0.0	0.0	tr	0.0	0.0	0.0
SIDERITE	0.6	0.0	4.3	6.3	1.7	11.0	2.2	0.3	3.3	16.3	0.7	48.7	0.3	0.0	1.7
BARITE	0.0	0.0	0.3	0.0	0.0	0.0	0.0	0.0	0.0	0.0	0.0	0.0	0.0	0.0	0.0
ANHYDRITE	0.0	0.0	0.0	0.0	0.0	0.0	0.0	0.0	0.0	0.0	0.0	0.0	0.0	0.0	0.0
IRON OXIDE	0.0	0.0	tr	0.0	0.0	0.0	0.0	0.0	0.0	0.0	0.0	0.0	0.0	0.0	0.0
PYRITE CEMENT	0.2	0.0	1.0	0.7	0.0	2.7	0.1	0.0	0.3	0.0	0.0	0.0	0.1	0.0	0.7
ANATASE	0.1	0.0	0.7	0.5	0.0	1.3	0.1	0.0	0.3	0.0	0.0	tr	0.1	0.0	0.3
ZEOLITE	0.0	0.0	tr	0.0	0.0	0.0	0.0	0.0	0.0	0.0	0.0	0.0	0.0	0.0	0.0
RESIDUAL OIL	0.2	0.0	3.7	0.0	0.0	0.0	0.0	0.0	tr	0.0	0.0	0.0	0.0	0.0	0.3
OPTICALLY NON-RESOLVABLE REPLACIVE CLAY	0.0	0.0	0.3	0.2	0.0	0.3	0.2	0.0	0.3	0.2	0.0	0.7	0.4	0.0	3.7
OPTICALLY NON-RESOLVABLE PORE-LINING CLAY	0.1	0.0	0.7	0.0	0.0	0.0	0.3	0.0	0.7	0.0	0.0	0.0	0.2	0.0	0.7
KAOLINITE	3.4	1.0	9.3	1.6	0.7	4.0	3.1	2.0	4.0	2.9	0.7	5.7	3.4	0.0	8.0
primary pore-filling	0.9	0.0	2.7	0.4	0.0	1.0	0.9	0.7	1.3	0.4	0.0	1.3	0.6	0.0	1.7
replacive	2.5	0.3	8.0	1.2	0.0	3.0	2.2	1.0	2.7	2.5	0.7	4.3	2.7	0.0	7.3
ILLITE	0.0	0.0	tr	0.0	0.0	tr	0.0	0.0	0.0	0.0	0.0	0.0	0.1	0.0	0.7
ILLITE-SMECTITE	0.0	0.0	0.0	0.0	0.0	0.0	0.0	0.0	0.0	0.0	0.0	0.0	0.0	0.0	0.0
CHLORITE	0.0	0.0	0.0	0.0	0.0	0.0	0.0	0.0	0.0	0.0	0.0	0.0	0.0	0.0	0.0
MACROPOROSITY	2.9	0.0	8.0	0.0	0.0	0.0	2.1	1.3	2.7	0.0	0.0	0.0	3.1	0.0	7.7
primary intergranular porosity	2.2	0.0	6.7	0.0	0.0	0.0	1.2	0.0	1.7	0.0	0.0	0.0	1.8	0.0	6.7
secondary intragranular porosity	0.1	0.0	1.0	0.0	0.0	0.0	0.2	0.0	0.3	0.0	0.0	0.0	0.6	0.0	2.7
secondary 'oversized' porosity	0.6	0.0	2.0	0.0	0.0	0.0	0.7	0.0	1.0	0.0	0.0	0.0	0.6	0.0	5.0
calculated microporosity	3.4	0.0	6.5	6.2	4.2	7.4	3.2	1.4	7.5	1.4	0.8	2.0	5.7	0.0	11.8
TOTALS															
Detrital grains	77.4	71.0	84.0	66.8	61.3	70.0	74.8	69.0	78.3	54.0	2.3	74.0	73.6	63.7	85.4
Detrital clay and pseudomatrix	2.3	0.0	23.0	8.3	4.0	15.3	0.2	0.0	0.3	19.7	0.3	48.3	6.1	0.0	15.3
Blocky Cements	13.9	2.0	20.0	23.1	15.0	31.7	19.4	14.7	25.7	23.3	1.3	48.7	13.3	7.7	23.3
Authigenic clays	3.5	1.0	9.3	1.8	1.0	4.0	3.6	3.0	4.7	3.1	0.7	5.7	4.0	0.0	8.7
Porosity	2.9	0.0	8.0	0.0	0.0	0.0	2.1	1.3	2.7	0.0	0.0	0.0	3.1	0.0	7.7
SUMMARY CATEGORIES															
Ductile grains	1.4	0.0	8.0	5.6	4.3	8.0	0.3	0.0	0.7	4.8	1.0	10.3	1.5	0.0	8.0
Ductiles	3.7	0.0	31.0	13.9	8.3	19.7	0.5	0.0	1.0	24.5	1.3	49.7	7.5	0.0	23.3
Authigenic minerals	17.4	4.3	24.7	24.8	16.0	32.7	23.0	19.4	28.7	26.3	3.3	49.4	17.3	8.7	25.7
Authigenic minerals - intergranular	14.8	2.0	21.7	22.7	15.0	31.3	20.6	16.4	26.3	23.7	1.3	48.7	14.0	7.7	22.3
Authigenic minerals - replacive	2.5	0.3	8.0	2.2	1.0	5.3	2.4	1.3	3.0	2.7	0.7	4.3	3.3	0.0	7.3
QUARTZ	0.9	0.8	1.0	0.6	0.5	0.7	1.0	0.9	1.0	0.8	0.8	0.9	0.9	0.7	1.0
FELDSPAR	0.0	0.0	0.1	0.2	0.1	0.3	0.0	0.0	0.0	0.0	0.0	0.1	0.0	0.0	0.1
LITHICS	0.1	0.0	0.2	0.2	0.1	0.2	0.0	0.0	0.0	0.1	0.0	0.2	0.1	0.0	0.2
MATRIX	2.3	0.0	23.0	8.3	4.0	15.3	0.2	0.0	0.3	19.7	0.3	48.3	6.1	0.0	15.3
Horizontal helium porosity (%)	6.3	2.5	12.0	6.2	4.2	7.4	5.3	3.3	10.2	1.4	0.8	2.0	8.8	2.5	14.8
Horizontal permeability (Kg) (mD)	7.3	0.0	61.0	0.0	0.0	0.0	0.2	0.0	0.4	1.5	0.0	6.1	3.0	0.1	18.0
Depositional feldspar (feldspar + replacive kaolinite + secondary pores)	5.1	1.0	10.0	17.3	6.0	23.0	4.3	3.0	5.3	4.1	0.7	6.0	6.2	0.3	15.0
Number of samples	*23*			*4*			*4*			*4*			*13*		

	Prodelta turbidite complex			Proximal delta front			Proximal prodelta			Continental facies			Marine facies		
	Average	Min	Max	Average	Min	Max	Average	Min	Max	Average	Min	Max	Average	Min	Max
DETRITAL MINERALOGY															
QUARTZ	32.4	24.0	47.0	54.6	39.7	71.7	25.7	20.3	29.0	68.2	46.7	78.0	39.3	1.0	71.7
monocrystalline	27.9	20.0	36.7	49.4	35.3	66.3	22.3	17.0	25.3	59.9	27.3	70.3	34.6	1.0	66.3
polycrystalline	4.5	2.0	10.3	5.2	4.0	7.3	3.4	2.3	6.0	8.3	2.3	19.3	4.7	0.0	10.3
FELDSPAR	16.5	12.0	24.3	2.6	1.0	5.7	17.9	13.0	22.0	2.0	0.0	5.7	11.1	0.0	24.3
K-feldspar	3.6	2.3	5.7	0.2	0.0	1.0	2.9	1.7	3.7	1.5	0.0	5.0	2.0	0.0	5.7
microcline															
plagioclase	12.9	9.0	18.7	2.4	1.0	4.7	15.0	10.7	18.7	0.5	0.0	4.0	9.1	0.0	18.7
RIGID ROCK FRAGMENTS	4.3	1.0	6.7	1.9	0.7	5.0	4.8	2.7	7.0	3.7	0.3	13.3	3.4	0.0	8.7
igneous	3.9	1.0	6.0	1.9	0.7	5.0	4.7	2.3	7.0	3.5	0.3	11.3	3.3	0.0	8.7
metamorphic	0.4	0.0	1.3	0.0	0.0	0.0	0.1	0.0	0.7	0.2	0.0	2.0	0.1	0.0	1.3
sedimentary	0.0	0.0	0.0	0.0	0.0	0.0	0.0	0.0	0.0	0.0	0.0	0.3	0.0	0.0	0.0
HEAVY MINERALS	0.4	tr	1.0	0.3	tr	0.3	0.3	0.0	0.7	0.6	0.0	3.0	0.5	0.0	2.0
DUCTILE ROCK FRAGMENTS	1.5	0.7	2.7	0.1	0.0	0.3	0.3	0.0	0.7	0.2	0.0	1.7	0.7	0.0	2.7
degraded igneous	1.5	0.7	2.7	0.1	0.0	0.3	0.1	0.0	0.7	0.2	0.0	1.3	0.6	0.0	2.7
sedimentary	0.0	0.0	0.0	0.0	0.0	0.0	0.2	0.0	0.7	0.0	0.0	0.3	0.1	0.0	0.7
MICA	3.7	1.7	5.0	2.3	1.3	3.3	6.7	4.7	10.7	0.7	0.0	5.3	3.8	0.0	10.7
muscovite	3.4	1.7	4.7	2.3	1.3	3.3	6.4	4.7	9.7	0.7	0.0	5.3	3.6	0.0	9.7
biotite	0.3	0.0	1.0	0.0	0.0	0.0	0.3	0.0	1.0	0.0	0.0	0.0	0.1	0.0	1.0
CHLORITE	0.0	0.0	0.0	0.0	0.0	0.0	0.1	0.0	0.3	0.0	0.0	0.0	0.0	0.0	0.3
ORGANIC FRAGMENTS	6.1	0.0	16.0	0.3	0.0	1.3	6.5	4.7	8.0	0.4	0.0	7.3	3.3	0.0	16.0
OPTICALLY NON-RESOLVABLE CLAY	9.0	4.3	14.0	8.4	0.0	20.3	16.7	10.7	24.3	3.3	0.0	23.0	12.3	0.0	48.3
detrital	5.2	2.3	8.7	3.4	0.0	12.0	13.1	8.0	21.0	1.9	0.0	20.7	8.3	0.0	48.3
pseudomatrix	3.8	2.0	8.3	5.0	0.0	11.0	3.6	2.7	5.3	1.5	0.0	11.7	4.0	0.0	11.0
AUTHIGENIC MINERALOGY															
QUARTZ OVERGROWTHS	2.7	0.7	6.0	4.9	0.0	13.3	0.1	0.0	0.3	12.1	2.0	21.7	3.9	0.0	17.7
MICROCRYSTALLINE QUARTZ	0.0	0.0	0.0	0.0	0.0	0.0	0.0	0.0	0.0	0.0	0.0	0.0	0.0	0.0	0.0
Na-FELDSPAR OVERGROWTHS	0.7	0.0	2.0	0.0	0.0	0.0	0.0	0.0	0.0	0.0	0.0	0.0	0.3	0.0	2.0
K-FELDSPAR OVERGROWTHS	0.0	0.0	0.0	0.0	0.0	0.0	0.0	0.0	0.0	0.0	0.0	0.3	0.0	0.0	0.0
CALCITE CEMENT	0.0	0.0	0.0	0.0	0.0	0.0	0.0	0.0	0.0	0.0	0.0	0.0	0.0	0.0	0.0
ferroan	0.0	0.0	0.0	0.0	0.0	0.0	0.0	0.0	0.0	0.0	0.0	0.0	0.0	0.0	0.0
non-ferroan	0.0	0.0	0.0	0.0	0.0	0.0	0.0	0.0	0.0	0.0	0.0	0.0	0.0	0.0	0.0
DOLOMITE CEMENT	9.2	0.7	14.7	11.6	0.3	52.0	7.8	0.7	21.0	1.1	0.0	16.0	7.8	0.0	52.0
ferroan - primary pore-filling	3.3	0.0	9.7	10.1	0.0	50.3	4.2	0.0	11.7	0.5	0.0	13.7	4.8	0.0	50.3
ferroan - replacive	1.7	0.3	5.0	0.1	0.0	0.3	1.6	0.0	5.3	0.1	0.0	1.3	0.9	0.0	5.3
non-ferroan - primary pore-filling	3.7	0.0	8.3	1.4	0.0	2.3	1.3	0.3	2.7	0.5	0.0	8.3	1.8	0.0	8.3
non-ferroan - replacive	0.5	0.0	2.0	0.0	0.0	0.0	0.7	0.3	1.3	0.0	0.0	0.7	0.3	0.0	2.0
SIDERITE	12.0	2.3	22.0	6.1	0.3	13.7	12.5	8.7	17.7	0.6	0.0	4.3	10.6	0.3	48.7
BARITE	0.0	0.0	0.0	0.0	0.0	0.0	0.0	0.0	0.0	0.0	0.0	0.3	0.0	0.0	0.0
ANHYDRITE	0.0	0.0	0.0	0.0	0.0	0.0	0.0	0.0	0.0	0.0	0.0	0.0	0.0	0.0	0.0
IRON OXIDE	0.0	0.0	0.0	0.0	0.0	0.0	0.0	0.0	0.0	0.0	0.0	0.0	0.0	0.0	0.0
PYRITE CEMENT	0.5	0.0	2.3	0.3	0.0	1.0	0.0	0.0	0.0	0.2	0.0	1.0	0.3	0.0	2.7
ANATASE	0.1	0.0	0.7	0.0	0.0	0.0	0.0	0.0	tr	0.1	0.0	0.7	0.1	0.0	1.3
ZEOLITE	0.0	0.0	0.0	0.0	0.0	0.0	0.0	0.0	0.0	0.0	0.0	0.0	0.0	0.0	0.0
RESIDUAL OIL	0.0	0.0	tr	0.0	0.0	0.0	0.0	0.0	0.0	0.1	0.0	3.7	0.0	0.0	tr
OPTICALLY NON-RESOLVABLE REPLACIVE CLAY	0.0	0.0	0.0	0.1	0.0	0.3	0.0	0.0	0.0	0.2	0.0	3.7	0.1	0.0	0.7
OPTICALLY NON-RESOLVABLE PORE-LINING CLAY	0.0	0.0	0.0	0.1	0.0	0.3	0.0	0.0	0.0	0.1	0.0	0.7	0.0	0.0	0.3
KAOLINITE	0.8	0.0	1.3	6.0	3.3	13.0	0.5	0.0	1.0	3.4	0.0	9.3	2.4	0.0	13.0
primary pore-filling	0.1	0.0	0.7	0.7	0.0	2.3	0.0	0.0	0.0	0.8	0.0	2.7	0.3	0.0	2.3
replacive	0.7	0.0	1.3	5.3	2.3	10.7	0.5	0.0	1.0	2.5	0.0	8.0	2.0	0.0	10.7
ILLITE	0.0	0.0	0.0	0.4	0.0	1.3	0.0	0.0	tr	0.0	0.0	0.7	0.1	0.0	1.3
ILLITE-SMECTITE	0.0	0.0	0.0	0.0	0.0	0.0	0.0	0.0	0.0	0.0	0.0	0.0	0.0	0.0	0.0
CHLORITE	0.0	0.0	0.0	0.0	0.0	0.0	0.0	0.0	0.0	0.0	0.0	0.0	0.0	0.0	0.0
MACROPOROSITY	0.0	0.0	0.0	0.0	0.0	0.0	0.0	0.0	tr	2.9	0.0	8.0	0.0	0.0	tr
primary intergranular porosity	0.0	0.0	0.0	0.0	0.0	0.0	0.0	0.0	0.0	2.0	0.0	6.7	0.0	0.0	0.0
secondary intragranular porosity	0.0	0.0	0.0	0.0	0.0	0.0	0.0	0.0	tr	0.3	0.0	2.7	0.0	0.0	tr
secondary 'oversized' porosity	0.0	0.0	0.0	0.0	0.0	0.0	0.0	0.0	0.0	0.6	0.0	5.0	0.0	0.0	0.0
calculated microporosity	5.2	3.6	6.3	2.9	0.8	9.1	4.3	2.8	6.6	4.1	0.0	11.8	4.0	0.8	9.1
TOTALS															
Detrital grains	65.0	59.0	70.7	62.1	43.7	75.7	62.4	57.7	66.0	75.9	63.7	85.4	62.2	2.3	75.7
Detrital clay and pseudomatrix	9.0	4.3	14.0	8.4	0.0	20.3	16.7	10.7	24.3	3.3	0.0	23.0	12.3	0.0	48.3
Blocky Cements	25.2	15.7	29.7	22.9	8.0	52.7	20.5	9.3	31.7	14.2	2.0	25.7	23.0	1.3	52.7
Authigenic clays	0.8	0.0	1.3	6.6	3.7	14.0	0.5	0.0	1.0	3.7	0.0	9.3	2.5	0.0	14.0
Porosity	0.0	0.0	0.0	0.0	0.0	0.0	0.0	0.0	0.0	2.9	0.0	8.0	0.0	0.0	0.0
SUMMARY CATEGORIES															
Ductile grains	11.3	4.7	19.3	2.7	1.3	4.3	13.6	11.7	19.0	1.3	0.0	8.0	7.8	1.0	19.3
Ductiles	20.3	9.0	33.3	11.1	2.0	24.7	30.3	23.0	43.3	4.6	0.0	31.0	20.1	1.3	49.7
Authigenic minerals	26.0	17.0	30.3	29.5	12.0	56.3	20.9	9.6	31.7	17.9	4.3	28.7	25.5	3.3	56.3
Authigenic minerals - intergranular	23.1	15.0	29.3	24.0	8.3	52.7	18.1	9.0	25.0	15.1	2.0	26.3	22.3	1.3	52.7
Authigenic minerals - replacive	2.9	0.3	7.7	5.5	2.7	11.0	2.8	0.6	6.7	2.8	0.0	8.0	3.3	0.3	11.0
QUARTZ	0.5	0.4	0.7	0.9	0.8	0.9	0.5	0.4	0.5	0.9	0.7	1.0	0.7	0.4	0.9
FELDSPAR	0.3	0.2	0.4	0.0	0.0	0.1	0.3	0.2	0.4	0.0	0.0	0.1	0.2	0.0	0.4
LITHICS	0.2	0.1	0.2	0.1	0.0	0.1	0.2	0.2	0.3	0.1	0.0	0.2	0.2	0.0	0.3
MATRIX	9.0	4.3	14.0	8.4	0.0	20.3	16.7	10.7	24.3	3.3	0.0	23.0	12.3	0.0	48.3
Horizontal helium porosity (%)	5.2	3.6	6.3	2.9	0.8	9.1	4.3	2.8	6.6	7.0	2.5	14.8	4.0	0.8	9.1
Horizontal permeability (Kg) (mD)	1.5	0.0	3.9	0.5	0.0	2.0	0.3	0.0	1.0	5.2	0.0	61.0	0.8	0.0	6.1
Depositional feldspar (feldspar + replacive kaolinite + secondary pores)	17.2	12.7	25.0	7.9	4.0	12.3	18.4	13.3	22.0	5.4	0.3	15.0	13.2	0.7	25.0
Number of samples	*5*			*5*			*5*			*40*			*23*		

Appendix 5

Modal tables, averages by facies association split by field;

Cavendish field

	Delta plain			Distal delta front			Distributary channel			Interdistributary bay			Multi-storey fluvial channel		
	Average	Min	Max	Average	Min	Max	Average	Min	Max	Average	Min	Max	Average	Min	Max
DETRITAL MINERALOGY															
QUARTZ	57.2	56.7	57.7	31.7	31.7	31.7	38.3	38.3	38.3	45.1	31.0	56.3	57.6	36.0	76.3
monocrystalline	47.8	46.0	49.7	29.0	29.0	29.0	33.7	33.7	33.7	40.3	27.7	50.3	43.5	28.3	65.3
polycrystalline	9.3	7.0	11.7	2.7	2.7	2.7	4.7	4.7	4.7	4.8	3.3	6.0	14.1	5.7	34.7
FELDSPAR	2.3	0.7	4.0	9.0	9.0	9.0	8.0	8.0	8.0	2.3	1.0	3.7	2.0	0.0	16.0
K-feldspar	1.3	1.3	1.3	0.0	0.0	0.0	1.0	1.0	1.0	0.3	0.0	1.0	0.5	0.0	2.0
plagioclase	1.7	0.7	2.7	9.0	9.0	9.0	7.0	7.0	7.0	2.0	1.0	2.7	1.9	0.0	15.7
RIGID ROCK FRAGMENTS	3.2	3.0	3.3	4.0	4.0	4.0	7.7	7.7	7.7	4.5	2.7	7.7	5.0	0.7	15.0
igneous	3.2	3.0	3.3	4.0	4.0	4.0	7.0	7.0	7.0	4.5	2.7	7.7	4.7	0.7	14.7
metamorphic	0.0	0.0	0.0	0.0	0.0	0.0	0.0	0.0	0.0	0.0	0.0	0.0	0.3	0.0	2.3
sedimentary	0.0	0.0	0.0	0.0	0.0	0.0	0.7	0.7	0.7	0.0	0.0	0.0	0.0	0.0	tr
HEAVY MINERALS	0.7	tr	1.3	0.7	0.7	0.7	1.0	1.0	1.0	0.5	tr	1.3	0.2	0.0	2.0
DUCTILE ROCK FRAGMENTS	0.5	0.0	1.0	0.0	0.0	0.0	1.0	1.0	1.0	1.1	0.3	2.0	0.6	0.0	3.3
degraded igneous	0.2	0.0	0.3	0.0	0.0	0.0	1.0	1.0	1.0	1.0	0.3	2.0	0.4	0.0	2.3
sedimentary	0.3	0.0	0.7	0.0	0.0	0.0	0.0	0.0	0.0	0.1	0.0	0.3	0.2	0.0	2.3
MICA	2.3	2.0	2.7	6.3	6.3	6.3	2.7	2.7	2.7	2.9	2.0	4.3	1.0	0.0	5.7
muscovite	2.3	2.0	2.7	6.3	6.3	6.3	2.7	2.7	2.7	2.9	2.0	4.3	1.0	0.0	5.7
biotite	0.0	0.0	0.0	0.0	0.0	0.0	0.0	0.0	0.0	0.0	0.0	tr	0.0	0.0	0.0
CHLORITE	0.0	0.0	0.0	0.0	0.0	0.0	0.0	0.0	0.0	0.0	0.0	0.0	0.0	0.0	0.0
ORGANIC FRAGMENTS	1.0	0.3	1.7	6.7	6.7	6.7	0.0	0.0	0.0	1.3	0.0	2.3	0.0	0.0	0.7
GLAUCONITIC PELLETS	0.0	0.0	0.0	0.0	0.0	0.0	0.0	0.0	0.0	0.0	0.0	0.0	0.0	0.0	0.0
OPTICALLY NON-RESOLVABLE CLAY	15.5	11.7	19.3	13.0	13.0	13.0	2.7	2.7	2.7	29.8	15.3	52.3	4.0	0.0	29.3
detrital	13.8	10.0	17.7	8.0	8.0	8.0	0.3	0.3	0.3	27.2	12.0	47.3	2.7	0.0	27.3
pseudomatrix	1.7	1.7	1.7	5.0	5.0	5.0	2.3	2.3	2.3	2.7	0.7	5.0	1.2	0.0	5.7
AUTHIGENIC MINERALOGY															
QUARTZ OVERGROWTHS	3.2	2.7	3.7	1.3	1.3	1.3	11.0	11.0	11.0	3.6	0.0	9.7	9.5	0.0	19.3
Na-FELDSPAR OVERGROWTHS	0.0	0.0	0.0	0.0	0.0	0.0	1.7	1.7	1.7	0.0	0.0	0.0	0.0	0.0	1.3
K-FELDSPAR OVERGROWTHS	0.0	0.0	0.0	0.0	0.0	0.0	0.0	0.0	0.0	0.0	0.0	0.0	0.0	0.0	tr
CALCITE CEMENT	0.0	0.0	0.0	0.0	0.0	0.0	0.0	0.0	0.0	0.0	0.0	0.0	0.0	0.0	0.0
ferroan	0.0	0.0	0.0	0.0	0.0	0.0	0.0	0.0	0.0	0.0	0.0	0.0	0.0	0.0	0.0
non-ferroan	0.0	0.0	0.0	0.0	0.0	0.0	0.0	0.0	0.0	0.0	0.0	0.0	0.0	0.0	0.0
DOLOMITE CEMENT	0.3	0.3	0.3	19.7	19.7	19.7	17.7	17.7	17.7	1.2	0.0	3.7	4.0	0.0	51.3
ferroan - primary pore-filling	0.3	0.3	0.3	18.3	18.3	18.3	15.0	15.0	15.0	0.4	0.0	1.0	3.4	0.0	47.7
ferroan - replacive	0.0	0.0	0.0	1.0	1.0	1.0	2.0	2.0	2.0	0.0	0.0	0.0	0.2	0.0	2.7
non-ferroan - primary pore-filling	0.0	0.0	0.0	0.3	0.3	0.3	0.7	0.7	0.7	0.8	0.0	3.0	0.2	0.0	3.7
non-ferroan - replacive	0.0	0.0	0.0	0.0	0.0	0.0	0.0	0.0	0.0	0.0	0.0	0.0	0.1	0.0	3.0
SIDERITE	7.5	2.7	12.3	7.0	7.0	7.0	2.7	2.7	2.7	3.7	0.0	14.3	1.5	0.0	17.3
BARITE	0.3	0.0	0.7	0.0	0.0	0.0	0.0	0.0	0.0	0.1	0.0	0.3	0.1	0.0	2.0
ANHYDRITE	0.0	0.0	0.0	0.0	0.0	0.0	0.0	0.0	0.0	0.0	0.0	0.0	0.1	0.0	1.3
IRON OXIDE	0.0	0.0	tr	0.0	0.0	0.0	0.0	0.0	0.0	0.0	0.0	0.0	0.2	0.0	3.7
PYRITE CEMENT	0.0	0.0	tr	0.0	0.0	0.0	0.0	0.0	0.0	1.3	tr	3.3	0.1	0.0	2.0
ANATASE	0.2	0.0	0.3	0.3	0.3	0.3	0.3	0.3	0.3	0.0	0.0	tr	0.1	0.0	1.0
ZEOLITE	0.0	0.0	0.0	0.0	0.0	0.0	0.0	0.0	0.0	0.0	0.0	0.0	0.0	0.0	0.0
RESIDUAL OIL	0.0	0.0	0.0	0.0	0.0	0.0	0.0	0.0	0.0	0.0	0.0	0.0	0.0	0.0	0.0
OPTICALLY NON-RESOLVABLE REPLACIVE CLAY	0.2	0.0	0.3	0.3	0.3	0.3	1.0	1.0	1.0	0.0	0.0	0.0	0.8	0.0	3.3
OPTICALLY NON-RESOLVABLE PORE-LINING CLAY	2.5	1.3	3.7	0.0	0.0	0.0	0.0	0.0	0.0	0.8	0.0	2.0	1.9	0.0	9.3
KAOLINITE	2.5	2.3	2.7	0.0	0.0	0.0	4.0	4.0	4.0	1.2	0.0	2.0	5.0	0.0	13.7
primary pore-filling	0.2	0.0	0.3	0.0	0.0	0.0	3.7	3.7	3.7	0.2	0.0	0.7	3.4	0.0	11.3
replacive	2.3	2.0	2.7	0.0	0.0	0.0	0.3	0.3	0.3	1.0	0.0	1.7	1.6	0.0	5.7
ILLITE	0.0	0.0	0.0	0.0	0.0	0.0	0.0	0.0	0.0	0.0	0.0	0.0	0.3	0.0	2.7
ILLITE-SMECTITE	0.0	0.0	0.0	0.0	0.0	0.0	0.0	0.0	0.0	0.0	0.0	0.0	0.0	0.0	tr
CHLORITE	0.0	0.0	0.0	0.0	0.0	0.0	0.0	0.0	0.0	0.0	0.0	0.0	0.0	0.0	0.0
MACROPOROSITY	0.7	0.3	1.0	0.0	0.0	0.0	0.3	0.3	0.3	0.8	0.0	2.7	6.1	0.0	21.7
primary intergranular porosity	0.2	0.0	0.3	0.0	0.0	0.0	0.0	0.0	0.0	0.0	0.0	0.0	2.7	0.0	14.3
secondary intragranular porosity	0.2	0.0	0.3	0.0	0.0	0.0	0.3	0.3	0.3	0.0	0.0	0.0	0.2	0.0	1.3
secondary 'oversized' porosity	0.3	0.0	0.7	0.0	0.0	0.0	0.0	0.0	0.0	0.8	0.0	2.7	3.2	0.0	21.7
calculated microporosity	7.8	4.9	10.7	3.1	3.1	3.1	7.9	7.9	7.9	4.4	2.9	5.5	4.1	0.0	13.3
TOTALS															
Detrital grains	67.2	65.0	69.3	58.3	58.3	58.3	58.7	58.7	58.7	57.6	44.0	63.7	66.4	45.7	80.0
Detrital clay and pseudomatrix	15.5	11.7	19.3	13.0	13.0	13.0	2.7	2.7	2.7	29.8	15.3	52.3	4.0	0.0	29.3
Blocky Cements	11.5	6.7	16.4	28.3	28.3	28.3	33.3	33.3	33.3	9.8	2.3	22.3	15.6	4.7	54.3
Authigenic clays	5.2	3.7	6.7	0.3	0.3	0.3	5.0	5.0	5.0	2.0	0.0	4.0	7.9	0.0	20.3
Porosity	0.7	0.3	1.0	0.0	0.0	0.0	0.3	0.3	0.3	0.8	0.0	2.7	6.1	0.0	21.7
SUMMARY CATEGORIES															
Ductile grains	3.8	3.7	4.0	13.0	13.0	13.0	3.7	3.7	3.7	5.3	2.7	7.7	1.6	0.0	6.7
Ductiles	19.3	15.3	23.3	26.0	26.0	26.0	6.3	6.3	6.3	35.1	21.3	59.0	5.6	0.0	36.0
Authigenic minerals	16.7	10.3	23.0	28.7	28.7	28.7	38.3	38.3	38.3	11.8	3.7	24.7	23.5	8.0	54.3
Authigenic minerals - intergranular	14.2	8.3	20.0	27.3	27.3	27.3	35.0	35.0	35.0	10.8	2.3	23.7	20.9	8.0	54.3
Authigenic minerals - replacive	2.5	2.0	3.0	1.3	1.3	1.3	3.3	3.3	3.3	1.0	0.0	1.7	2.7	0.0	9.7
QUARTZ	0.9	0.8	0.9	0.6	0.6	0.6	0.7	0.7	0.7	0.8	0.7	0.9	0.9	0.6	1.0
FELDSPAR	0.0	0.0	0.1	0.2	0.2	0.2	0.1	0.1	0.1	0.0	0.0	0.1	0.0	0.0	0.2
LITHICS	0.1	0.1	0.1	0.2	0.2	0.2	0.2	0.2	0.2	0.2	0.1	0.2	0.1	0.0	0.2
MATRIX	15.5	11.7	19.3	13.0	13.0	13.0	2.7	2.7	2.7	29.8	15.3	52.3	4.0	0.0	29.3
									0.0						
Horizontal helium porosity (%)	8.5	5.2	11.7	3.1	3.1	3.1	8.2	8.2	8.2	5.1	2.9	8.2	10.2	1.2	19.1
Horizontal permeability (Kg) (mD)	0.06	0.02	0.09	0.01	0.01	0.01	0.09	0.09	0.09	0.32	0.05	0.90	54.03	0.01	691.00
Depositional feldspar (feldspar + replacive kaolinite + secondary pores)	5.2	3.7	6.7	9.0	9.0	9.0	8.7	8.7	8.7	4.0	2.0	5.0	6.9	0.3	23.0
Number of samples	*2*			*1*			*1*			*4*			*43*		

	Proximal delta front			Shoreface			Continetal facies			Marine facies		
	Average	Min	Max	Average	Min	Max	Average	Min	Max	Average	Min	Max
DETRITAL MINERALOGY												
QUARTZ	55.3	50.7	60.0	47.7	43.0	52.3	57.1	36.0	76.3	46.4	31.0	60.0
monocrystalline	47.2	45.0	49.3	41.7	36.7	46.7	43.5	28.3	65.3	40.9	27.7	50.3
polycrystalline	8.2	5.7	10.7	6.0	5.7	6.3	13.7	4.7	34.7	5.6	2.7	10.7
FELDSPAR	3.2	2.7	3.7	2.0	0.3	3.7	2.1	0.0	16.0	3.1	0.3	9.0
K-feldspar	0.2	0.0	0.3	0.0	0.0	0.0	0.5	0.0	2.0	0.1	0.0	1.0
plagioclase	3.0	2.3	3.7	2.0	0.3	3.7	2.0	0.0	15.7	3.0	0.3	9.0
RIGID ROCK FRAGMENTS	2.8	2.7	3.0	2.5	2.3	2.7	5.0	0.7	15.0	3.6	2.3	7.7
igneous	2.5	2.3	2.7	2.5	2.3	2.7	4.7	0.7	14.7	3.6	2.3	7.7
metamorphic	0.3	0.3	0.3	0.0	0.0	0.0	0.3	0.0	2.3	0.1	0.0	0.3
sedimentary	0.0	0.0	0.0	0.0	0.0	0.0	0.0	0.0	0.7	0.0	0.0	0.0
HEAVY MINERALS	0.2	tr	0.3	0.5	0.3	0.7	0.2	0.0	2.0	0.4	0.0	1.3
DUCTILE ROCK FRAGMENTS	1.0	0.3	1.7	0.3	0.0	0.7	0.6	0.0	3.3	0.8	0.0	2.0
degraded igneous	1.0	0.3	1.7	0.3	0.0	0.7	0.4	0.0	2.3	0.7	0.0	2.0
sedimentary	0.0	0.0	0.0	0.0	0.0	0.0	0.2	0.0	2.3	0.0	0.0	0.3
MICA	2.5	2.3	2.7	2.8	1.3	4.3	1.1	0.0	5.7	3.2	1.3	6.3
muscovite	2.3	2.0	2.7	2.8	1.3	4.3	1.1	0.0	5.7	3.1	1.3	6.3
biotite	0.2	0.0	0.3	0.0	0.0	0.0	0.0	0.0	0.0	0.0	0.0	0.3
CHLORITE	0.0	0.0	0.0	0.0	0.0	0.0	0.0	0.0	0.0	0.0	0.0	0.0
ORGANIC FRAGMENTS	0.0	0.0	tr	1.3	0.0	2.7	0.1	0.0	1.7	1.6	0.0	6.7
GLAUCONITIC PELLETS	0.0	0.0	0.0	0.0	0.0	0.0	0.0	0.0	0.0	0.0	0.0	0.0
OPTICALLY NON-RESOLVABLE CLAY	14.8	11.7	18.0	17.3	12.3	22.3	4.4	0.0	29.3	21.9	11.7	52.3
detrital	11.7	9.0	14.3	14.3	10.0	18.7	3.2	0.0	27.3	18.7	8.0	47.3
pseudomatrix	3.2	2.7	3.7	3.0	2.3	3.7	1.3	0.0	5.7	3.1	0.7	5.0
		0.0	0.0									
AUTHIGENIC MINERALOGY		0.0	0.0									
QUARTZ OVERGROWTHS	10.7	5.3	16.0	6.2	3.3	9.0	9.2	0.0	19.3	5.5	0.0	16.0
Na-FELDSPAR OVERGROWTHS	0.0	0.0	0.0	0.0	0.0	0.0	0.1	0.0	1.7	0.0	0.0	0.0
K-FELDSPAR OVERGROWTHS	0.0	0.0	tr	0.0	0.0	0.0	0.0	0.0	0.0	0.0	0.0	0.0
CALCITE CEMENT	0.0	0.0	0.0	0.0	0.0	0.0	0.0	0.0	0.0	0.0	0.0	0.0
ferroan	0.0	0.0	0.0	0.0	0.0	0.0	0.0	0.0	0.0	0.0	0.0	0.0
non-ferroan	0.0	0.0	0.0	0.0	0.0	0.0	0.0	0.0	0.0	0.0	0.0	0.0
DOLOMITE CEMENT	5.2	4.7	5.7	2.5	1.0	4.0	4.1	0.0	51.3	4.4	0.0	19.7
ferroan - primary pore-filling	4.8	4.3	5.3	2.0	0.0	4.0	3.6	0.0	47.7	3.7	0.0	18.3
ferroan - replacive	0.0	0.0	0.0	0.0	0.0	0.0	0.3	0.0	2.7	0.1	0.0	1.0
non-ferroan - primary pore-filling	0.2	0.0	0.3	0.5	0.0	1.0	0.2	0.0	3.7	0.5	0.0	3.0
non-ferroan - replacive	0.2	0.0	0.3	0.0	0.0	0.0	0.1	0.0	3.0	0.0	0.0	0.3
SIDERITE	0.3	0.3	0.3	11.0	7.0	15.0	1.8	0.0	17.3	4.9	0.0	15.0
BARITE	0.0	0.0	tr	0.0	0.0	0.0	0.1	0.0	2.0	0.0	0.0	0.3
ANHYDRITE	0.0	0.0	tr	0.0	0.0	0.0	0.1	0.0	1.3	0.0	0.0	0.0
IRON OXIDE	0.2	tr	0.3	0.0	0.0	0.0	0.2	0.0	3.7	0.0	0.0	0.3
PYRITE CEMENT	0.2	tr	0.3	0.0	0.0	tr	0.1	0.0	2.0	0.6	0.0	3.3
ANATASE	0.0	0.0	0.0	0.5	0.3	0.7	0.1	0.0	1.0	0.2	0.0	0.7
ZEOLITE	0.2	0.0	0.3	0.0	0.0	0.0	0.0	0.0	0.0	0.0	0.0	0.3
RESIDUAL OIL	0.0	0.0	0.0	0.0	0.0	0.0	0.0	0.0	0.0	0.0	0.0	0.0
OPTICALLY NON-RESOLVABLE REPLACIVE CLAY	1.8	1.3	2.3	0.8	0.3	1.3	0.7	0.0	3.3	0.6	0.0	2.3
OPTICALLY NON-RESOLVABLE PORE-LINING CLAY	0.3	0.0	0.7	0.0	0.0	0.0	1.9	0.0	9.3	0.4	0.0	2.0
KAOLINITE	1.2	0.3	2.0	4.2	0.7	7.7	4.9	0.0	13.7	1.7	0.0	7.7
primary pore-filling	0.0	0.0	0.0	1.7	0.0	3.3	3.3	0.0	11.3	0.4	0.0	3.3
replacive	1.2	0.3	2.0	2.5	0.7	4.3	1.6	0.0	5.7	1.3	0.0	4.3
ILLITE	0.0	0.0	0.0	0.0	0.0	0.0	0.2	0.0	2.7	0.0	0.0	0.0
ILLITE-SMECTITE	0.0	0.0	0.0	0.0	0.0	0.0	0.0	0.0	0.0	0.0	0.0	0.0
CHLORITE	0.0	0.0	0.0	0.0	0.0	0.0	0.0	0.0	0.0	0.0	0.0	0.0
MACROPOROSITY	0.2	0.0	0.3	0.3	0.0	0.7	5.7	0.0	21.7	0.4	0.0	2.7
primary intergranular porosity	0.0	0.0	0.0	0.0	0.0	0.0	2.6	0.0	14.3	0.0	0.0	0.0
secondary intragranular porosity	0.2	0.0	0.3	0.3	0.0	0.7	0.2	0.0	1.3	0.1	0.0	0.7
secondary 'oversized' porosity	0.0	0.0	0.0	0.0	0.0	0.0	3.0	0.0	21.7	0.3	0.0	2.7
calculated microporosity	12.4	11.7	13.1	5.5	4.6	6.4	4.4	0.0	13.3	6.3	2.9	13.1
TOTALS												
Detrital grains	65.0	61.7	68.3	57.2	57.0	57.3	66.3	45.7	80.0	59.2	44.0	68.3
Detrital clay and pseudomatrix	14.8	11.7	18.0	17.3	12.3	22.3	4.4	0.0	29.3	21.9	11.7	52.3
Blocky Cements	16.7	11.4	22.0	20.2	19.7	20.7	15.8	4.7	54.3	15.7	2.3	28.3
Authigenic clays	3.3	2.3	4.3	5.0	1.0	9.0	7.7	0.0	20.3	2.8	0.0	9.0
Porosity	0.2	0.0	0.3	0.3	0.0	0.7	5.7	0.0	21.7	0.4	0.0	2.7
SUMMARY CATEGORIES												
Ductile grains	3.5	2.7	4.3	4.5	1.3	7.7	1.8	0.0	6.7	5.6	1.3	13.0
Ductiles	18.3	16.0	20.7	21.8	13.7	30.0	6.2	0.0	36.0	27.4	13.7	59.0
Authigenic minerals	20.0	13.7	26.4	25.2	20.7	29.7	23.6	8.0	54.3	18.5	3.7	29.7
Authigenic minerals - intergranular	16.9	11.7	22.0	21.8	19.7	24.0	20.9	8.0	54.3	16.5	2.3	27.3
Authigenic minerals - replacive	3.2	2.0	4.3	3.3	1.0	5.7	2.7	0.0	9.7	2.0	0.0	5.7
QUARTZ	0.8	0.8	0.9	0.9	0.8	0.9	0.9	0.6	1.0	0.8	0.6	0.9
FELDSPAR	0.0	0.0	0.1	0.0	0.0	0.1	0.0	0.0	0.2	0.1	0.0	0.2
LITHICS	0.1	0.1	0.1	0.1	0.1	0.1	0.1	0.0	0.2	0.1	0.1	0.2
MATRIX	14.8	11.7	18.0	17.3	12.3	22.3	4.4	0.0	29.3	21.9	11.7	52.3
Horizontal helium porosity (%)	12.6	12.0	13.1	5.9	4.6	7.1	10.1	1.2	19.1	6.7	2.9	13.1
Horizontal permeability (Kg) (mD)	0.33	0.14	0.52	0.04	0.03	0.04	50.51	0.01	691.00	0.23	0.01	0.90
Depositional feldspar (feldspar + replacive kaolinite + secondary pores)	4.5	3.0	6.0	4.8	4.3	5.3	6.9	0.3	23.0	4.9	2.0	9.0
Number of samples	*2*			*2*			*46*			*9*		

Appendix 6

Modal tables, averages for multi-storey fluvial channel split by field; Copernicus discovery

	44/16-1			44/16-2		
	Average	Min	Max	Average	Min	Max
DETRITAL MINERALOGY						
QUARTZ	53.7	46.7	61.0	75.0	73.3	77.0
monocrystalline	40.7	27.3	47.7	64.6	61.0	67.7
polycrystalline	13.0	5.7	19.3	10.4	8.0	15.3
FELDSPAR	2.6	1.0	4.0	1.9	0.3	4.0
K-feldspar	2.0	0	3.7	1.8	0.3	3.7
plagioclase	0.7	0	2.0	0.1	0	0.3
RIGID ROCK FRAGMENTS	7.0	3.3	13.3	4.8	1.0	9.3
igneous	6.5	3.3	11.3	4.7	1.0	9.3
metamorphic	0.6	0	2.0	0.1	0	0.7
sedimentary	0	0	0	0	0	0
HEAVY MINERALS	0.2	0	0.7	0.4	0	0.7
DUCTILE ROCK FRAGMENTS	0.7	0	1.3	0	0	0
degraded igneous	0.6	0	1.3	0	0	0
sedimentary	0	0	0.3	0	0	0
MICA	0.9	0	2.7	0.1	0	0.3
muscovite	0.9	0	2.7	0.1	0	0.3
biotite	0	0	0	0	0	0
CHLORITE	0	0	0	0	0	0
ORGANIC FRAGMENTS	1.1	0	7.3	0	0	0
OPTICALLY NON-RESOLVABLE CLAY	11.1	6.3	15.3	0.1	0	0.3
detrital	4.2	0	10.3	0.1	0	0.3
pseudomatrix	7.0	3.7	11.7	0	0	0
AUTHIGENIC MINERALOGY						
QUARTZ OVERGROWTHS	10.4	7.3	13.7	10.9	6.3	15.0
Na-FELDSPAR OVERGROWTHS	0	0	0.0	0	0	0
K-FELDSPAR OVERGROWTHS	0	0	0.0	0.2	0	0.3
CALCITE CEMENT	0	0	0.0	0	0	0
ferroan	0	0	0.0	0	0	0
non-ferroan	0	0	0.0	0	0	0
DOLOMITE CEMENT	3.4	0	16.0	0.5	0	1.0
ferroan - primary pore-filling	2.7	0	13.7	0	0	0
ferroan - replacive	0.4	0	1.3	0	0	0
non-ferroan - primary pore-filling	0.4	0	1.3	0.5	0	1.0
non-ferroan - replacive	0	0	0.0	0.0	0	0
SIDERITE	0.3	0	1.7	0.2	0	0.3
BARITE	0	0	0.0	0	0	0
ANHYDRITE	0	0	0.0	0	0	0
IRON OXIDE	0	0	0.0	0	0	0
PYRITE CEMENT	0.1	0	0.7	0.2	0	0.3
ANATASE	0	0	0.3	0.1	0	0.3
ZEOLITE	0	0	0.0	0	0	0
RESIDUAL OIL	0	0	0.0	0.1	0	0.3
OPTICALLY NON-RESOLVABLE REPLACIVE CLAY	0.7	0	3.7	0	0	0
OPTICALLY NON-RESOLVABLE PORE-LINING CLAY	0.3	0	0.7	0	0	0.0
KAOLINITE	5.3	2.3	8.0	1.1	0	3.7
primary pore-filling	0.7	0	1.0	0.6	0	1.7
replacive	4.6	2.0	7.3	0.6	0	2.0
ILLITE	0.2	0	0.7	0	0	0
ILLITE-SMECTITE	0	0	0	0	0	0
CHLORITE	0	0	0	0	0	0
MACROPOROSITY	1.9	0	5.3	4.4	1.0	7.7
primary intergranular porosity	0.1	0	0.3	3.9	0.7	6.7
secondary intragranular porosity	0.9	0	2.7	0.2	0	0.7
secondary 'oversized' porosity	1.0	0	5.0	0.3	0	1.0
calculated microporosity	8.9	5.1	11.8	1.9	0	4.3
TOTALS						
Detrital grains	66.2	63.7	70.0	82.3	76.3	85.4
Detrital clay and pseudomatrix	11.1	6.3	15.3	0.1	0	0.3
Blocky Cements	14.3	9.0	23.3	12.1	7.7	15.4
Authigenic clays	6.5	2.3	8.7	1.1	0	3.7
Porosity	1.9	0	5.3	4.4	1.0	7.7
SUMMARY CATEGORIES						
Ductile grains	2.7	0.7	8.0	0.1	0	0.3
Ductiles	13.8	7.0	23.3	0.2	0	0.3
Authigenic minerals	20.8	17.7	25.7	13.2	8.7	18.0
Authigenic minerals - intergranular	15.1	10.4	22.3	12.7	7.7	16.0
Authigenic minerals - replacive	5.7	3.3	7.3	0.6	0	2.0
QUARTZ	0.8	0.7	0.9	0.9	0.9	1.0
FELDSPAR	0	0	0.1	0	0	0
LITHICS	0.1	0.1	0.2	0.1	0	0.1
MATRIX	11.1	6.3	15.3	0.1	0	0.3
Horizontal helium porosity (%)	10.8	8.0	14.8	6.3	2.5	8.6
Horizontal permeability (Kg) (mD)	0.8	0.1	2.8	5.6	0.1	18.0
	0.42 (geomean perm.)			1.72 (geomean perm.)		
Depositional feldspar (feldspar + replacive kaolinite +secondary pores	9.1	6.0	15.0	2.9	0.3	5.0
Number of samples	*23*			*4*		

Appendix 6

Modal tables, averages for multi-storey fluvial channel split by field;

Cavendish field

	43/19-1			43/19-2			43/19a-4Z		
	Average	Min	Max	Average	Min	Max	Average	Min	Max
DETRITAL MINERALOGY									
QUARTZ	51.8	40.7	64.7	56.4	36.0	65.3	66.7	60.6	76.3
monocrystalline	36.8	28.3	51.7	44.1	28.3	55.0	49.5	38.0	65.3
polycrystalline	14.9	9.0	22.7	12.3	5.7	34.7	17.1	9.7	31.3
FELDSPAR	2.5	0	10.0	2.4	0	16.0	0.4	0	1.7
K-feldspar	0.4	0	2.0	0.6	0.3	1.7	0.4	0	1.7
plagioclase	2.2	0	8.7	2.8	0.3	15.7	0	0	0
RIGID ROCK FRAGMENTS	5.8	1.3	10.0	5.7	2.3	15.0	2.6	0.7	5.3
igneous	5.5	1.0	9.3	5.6	2.3	14.7	1.9	0.7	5.0
metamorphic	0.3	0	1.0	0.1	0	1.3	0.7	0	2.3
sedimentary	0	0	0	0	0	0	0	0	0
HEAVY MINERALS	0.1	0	0.7	0.3	0	2.0	0.1	0	0.3
DUCTILE ROCK FRAGMENTS	0.8	0	3.3	0.7	0	2.3	0.1	0	0.3
degraded igneous	0.3	0	1.3	0.6	0	2.3	0	0	0
sedimentary	0.5	0	2.3	0.1	0	1.0	0.1	0	0.3
MICA	1.1	0	3.7	1.4	0	5.7	0.1	0	0.7
muscovite	1.1	0	3.7	1.4	0	5.7	0.1	0	0.7
biotite	0	0	0	0	0	0	0	0	0
CHLORITE	0	0	0	0	0	0	0	0	0
ORGANIC FRAGMENTS	0	0	0	0.1	0	0.7	0	0	0
OPTICALLY NON-RESOLVABLE CLAY	2.8	1.3	5.7	6.0	0	29.3	0.7	0	2.3
detrital	1.2	0	2.7	4.5	0	27.3	0.6	0	2.3
pseudomatrix	1.7	0	5.7	1.5	0	5.0	0.1	0	1.0
AUTHIGENIC MINERALOGY									
QUARTZ OVERGROWTHS	12.3	9.0	19.3	8.3	0	19.3	8.9	4.3	14.3
MICROCRYSTALLINE QUARTZ	0.0	0	0.0	0	0	0	0	0	0
Na-FELDSPAR OVERGROWTHS	0.1	0	1.3	0	0	0.3	0	0	0
K-FELDSPAR OVERGROWTHS	0	0	0	0	0	0	0	0	0
CALCITE CEMENT	0	0	0	0	0	0	0	0	0
ferroan	0	0	0	0	0	0	0	0	0
non-ferroan	0	0	0	0	0	0	0	0	0
DOLOMITE CEMENT	4.4	0	12.0	4.8	0	51.3	1.7	0	9.0
ferroan - primary pore-filling	3.5	0	11.3	4.2	0	47.7	1.6	0	9.0
ferroan - replacive	0.7	0	2.7	0.1	0	0.7	0	0	0.3
non-ferroan - primary pore-filling	0.2	0	0.7	0.3	0	3.7	0.1	0	0.7
non-ferroan - replacive	0	0	0.3	0.1	0	3.0	0.0	0	0
SIDERITE	1.2	0	3.3	1.3	0	5.0	2.3	0	17.3
BARITE	0	0	0	0.1	0	1.3	0.3	0	2.0
ANHYDRITE	0	0	0	0.1	0	1.3	0	0	0
IRON OXIDE	0.1	0	0.3	0.4	0	3.7	0	0	0
PYRITE CEMENT	0.1	0	0.3	0	0	0.7	0.2	0	2.0
ANATASE	0.2	0	1.0	0.1	0	0.7	0.1	0	1.0
ZEOLITE	0	0	0	0	0	0	0	0	0
RESIDUAL OIL	0	0	0	0	0	0	0	0	0
OPTICALLY NON-RESOLVABLE REPLACIVE CLAY	1.0	0	2.3	1.0	0	3.3	0	0	0.3
OPTICALLY NON-RESOLVABLE PORE-LINING	1.5	0	3.0	2.0	0	6.3	2.2	0	9.3
KAOLINITE	9.5	4.7	13.7	4.1	0	11.7	2.1	0	5.7
primary pore-filling	5.9	2.7	10.3	2.9	0	11.3	1.9	0	5.0
replacive	3.6	1.0	5.7	1.2	0	3.0	0.2	0	1.0
ILLITE	0.5	0	2.7	0.2	0	2.0	0	0	0
ILLITE-SMECTITE	0	0	0	0	0	0	0	0	0
CHLORITE	0	0	0	0	0	0	0	0	0
MACROPOROSITY	4.2	0	14.7	4.6	0	21.7	11.4	5.6	20.4
primary intergranular porosity	1.8	0	3.7	0.7	0	2.3	8.2	2.3	14.3
secondary intragranular porosity	0.1	0	0.3	0.3	0	1.3	0.2	0	1.0
secondary 'oversized' porosity	2.4	0	11.3	3.6	0	21.7	3.3	1.0	7.3
calculated microporosity	7.3	0	11.9	5.8	0	13.3	1.5	0	7.0
TOTALS									
Detrital grains	62.1	54.7	68.0	66.9	45.7	80.0	69.9	62.6	77.9
Detrital clay and pseudomatrix	2.8	1.3	5.7	6.0	0	29.3	0.7	0	2.3
Blocky Cements	18.3	9.7	24.0	15.2	4.7	54.3	13.6	7.0	23.6
Authigenic clays	12.5	6.3	20.3	7.3	0	15.3	4.3	0	14.6
Porosity	4.2	0	14.7	4.6	0	21.7	11.4	5.6	20.4
SUMMARY CATEGORIES									
Ductile grains	1.9	0	6.0	2.2	0	6.7	0.2	0	1.0
Ductiles	4.8	2.0	11.7	8.2	1.7	36.0	0.9	0	2.3
Authigenic minerals	30.8	25.0	43.7	22.5	11.0	54.3	17.9	8.0	29.3
Authigenic minerals - intergranular	25.5	20.7	36.7	20.0	10.0	54.3	17.6	8.0	28.6
Authigenic minerals - replacive	5.3	1.3	9.7	2.4	0	5.0	0.3	0	1.0
QUARTZ	0.8	0.6	1.0	0.8	0.6	0.9	1.0	0.9	1.0
FELDSPAR	0	0	0.2	0	0	0.2	0	0	0
LITHICS	0.1	0.0	0.2	0.1	0.1	0.2	0	0	0.1
MATRIX	2.8	1.3	5.7	6.0	0	29.3	0.7	0	2.3
Horizontal helium porosity (%)	11.1	1.2	17.9	9.8	2.4	19.1	10.2	7.1	12.6
Horizontal permeability (Kg) (mD)	4.3	0.0	21.0	0.9	0.0	7.0	225.5	0.5	691.0
	0.88 (geomean perm.)			0.23 (geomean perm.)			53.59 (geomean perm.)		
Depositional feldspar (feldspar + replacive kaolinite + secondary	8.6	2.0	13.7	7.5	0.7	23.0	3.8	0.3	8.3
Number of samples	*2*			*1*			*1*		

Appendix 7

Cathodoluminescence maps

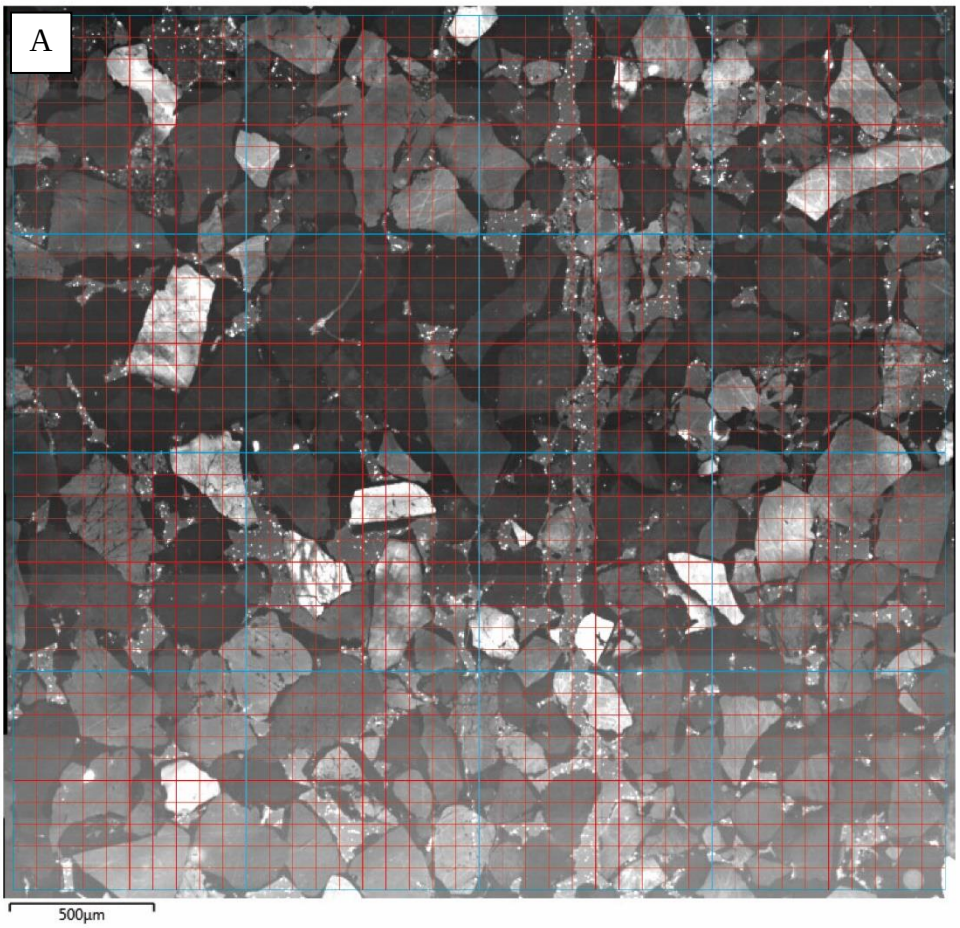

Sample depth 14190.0 ft, well 44/16-1. Large area CL, SEM and chemical maps used for quartz cementation and pressure dissolution quantification. A) CL map for detrital and authigenic quartz discrimination; B) SEM map showing grain and pore distribution; C) Chemical map showing quartz in green and porosity in red.

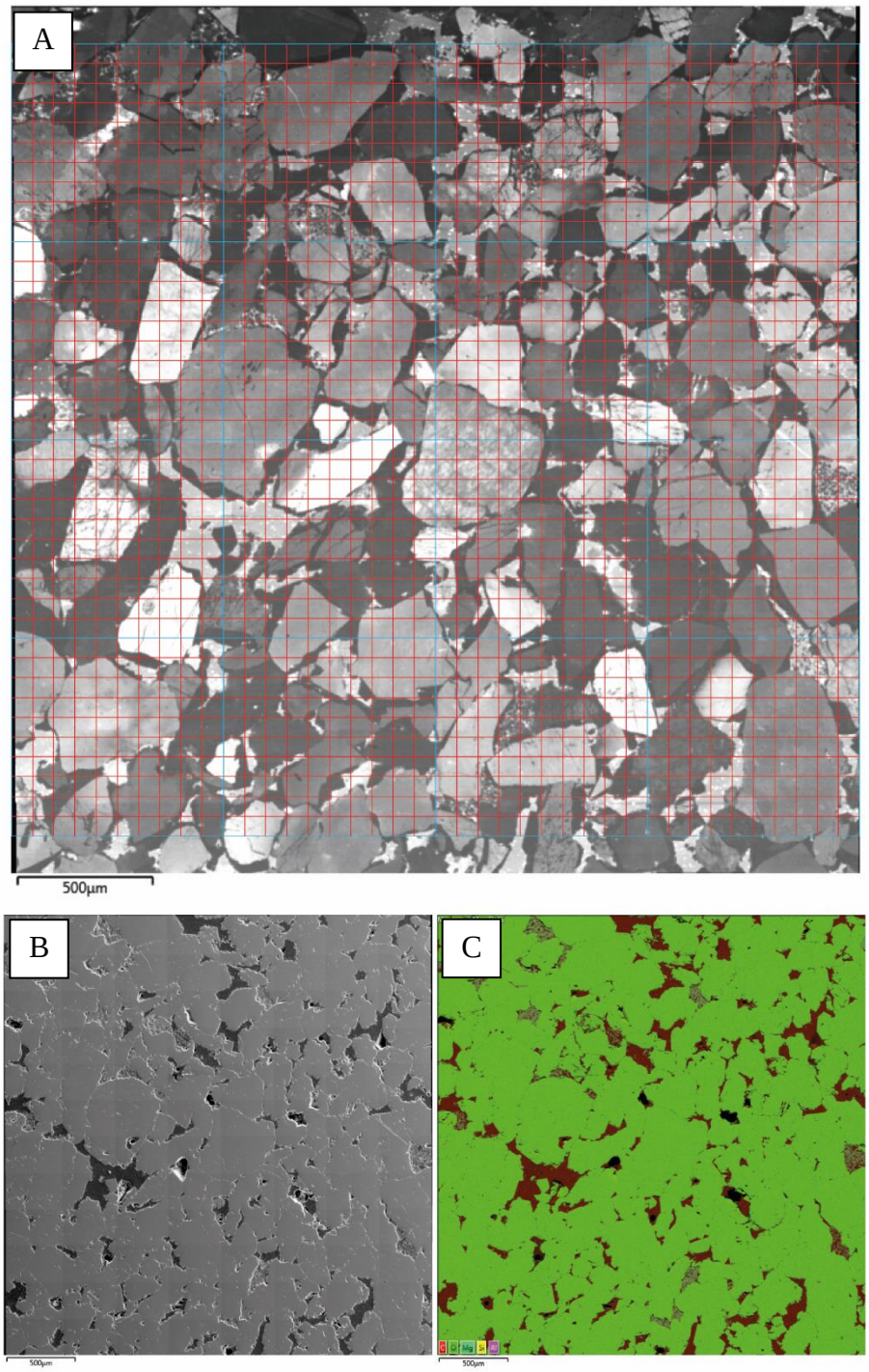

Sample depth 14837.9 ft, well 44/16-1. Large area CL, SEM and chemical maps used for quartz cementation and pressure dissolution quantification. A) CL map for detrital and authigenic quartz discrimination; B) SEM map showing grain and pore distribution; C) Chemical map showing quartz in green and porosity in red.

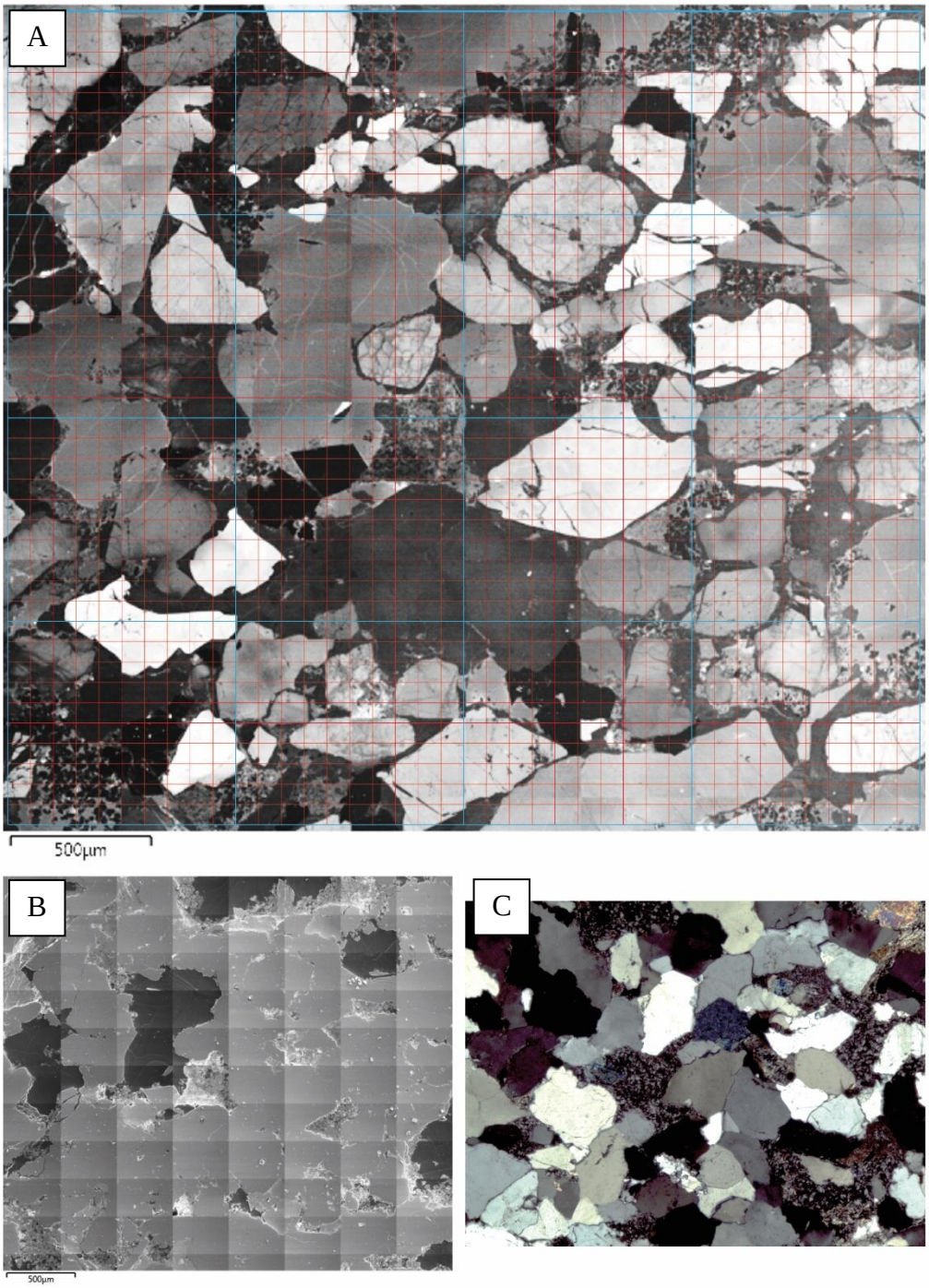

Sample depth 4067.26 m, well 43/19-2. Large area CL and SEM maps, and thin section micrograph used for quartz cementation and pressure dissolution quantification. A) CL map for detrital and authigenic quartz discrimination; B) SEM map showing grain and pore distribution; C) Thin section micrograph.

Appendix 8

Wasielka et al., 2020. The Cavendish Field, Block 43/19, UK North Sea

The Cavendish Field, Block 43/19, UK North Sea

N. WASIELKA[1]*, J. G. GLUYAS[1], H. BREESE[2] & R. SYMONDS[2]

[1]*Durham University, Science Site, Durham DH1 3LE, UK*

[2]*INEOS, UK SNS LIMITED, Anchor House, 15–19 Britten Street, London SW3 3TY, UK*

NW, 0000-0001-9078-4184

**Correspondence:* *natalia.wasielka@durham.ac.uk*

Abstract: The Cavendish Field is located in UK Continental Shelf Block 43/19a on the northern margin of the Outer Silverpit Basin of the Southern North Sea, 87 miles (140 km) NE of the Lincolnshire coast in a water depth of 62 ft (18.9 m). The Cavendish Field is a gas field in the upper Carboniferous Namurian C (Millstone Grit Formation) and Westphalian A (Caister Coal Formation) strata. It was discovered in 1989 by Britoil-operated well 43/19-1. Production started in 2007 and ceased in 2018. Gas initially in place was 184 bcf and at end of field life 98 bcf had been produced. The field was developed by three wells drilled through the normally unmanned platform into fluvio-deltaic sandstone intervals that had sufficiently good reservoir quality to be effective reservoirs. The majority of the formation within closure comprises mudstones, siltstones and low permeability, non-reservoir-quality feldspathic sandstones. The quality of the reservoir is variable and is controlled by grain size, feldspar content and diagenesis. The field is a structural trap, sealed by a combination of intra-Carboniferous mudstones and a thick sequence of Permian mudstones and evaporites.

The Cavendish Field, currently operated by INEOS UK SNS Limited, is located within UK Continental Shelf Block 43/19a (Fig. 1). The block is located on the northern margin of the Outer Silverpit Basin of the Southern North Sea (SNS), 87 miles (140 km) NE of the Lincolnshire coast in a water depth of 62 ft (18.9 m). The field is approximately 7.5 miles (12 km) long and covers an area of 13.7 square miles (35.5 km^2).

History of exploration and appraisal

Block 43/19 was awarded to the Britoil/Amoco Consortium (Britoil 50% as operator, Amoco 50%) as part of the 10th Round of Licensing in 1987, with the commitment to drill two exploratory wells to test for gas expected to be within Upper Carboniferous sandstones, to penetrate at least 300 ft (91.4 m) of the Namurian section, and to acquire 155 miles (250 km) of 2D seismic within the block.

The first well on the block, 43/19-1, was drilled in 1989 by Britoil over the centre of the prospect and slightly downdip of the structural crest. It found Carboniferous strata subcropping beneath the Base Permian Unconformity (BPU) at 11 450 ft (3490 m) TVDSS (true vertical depth subsea). The well successfully tested gas from two intervals in late Carboniferous Westphalian A and Namurian B–C sandstones. Cores were taken in three separate intervals in the Namurian section. Drill stem test (DST) 1 was conducted over two quartzitic sandstones 12 and 20 ft (3.7 and 6 m) thick in the Namurian section and flowed a combined 14.6 MMscfgd of gas and 230 bpd of condensate. DST 2a was conducted on an 18 ft (5.5 m) thick, quartzitic Westphalian A Sandstone (Fig. 2) immediately below the BPU and flowed gas at 32.6 MMscfgd and condensate at 240 bpd. The gas-down-to level in this well

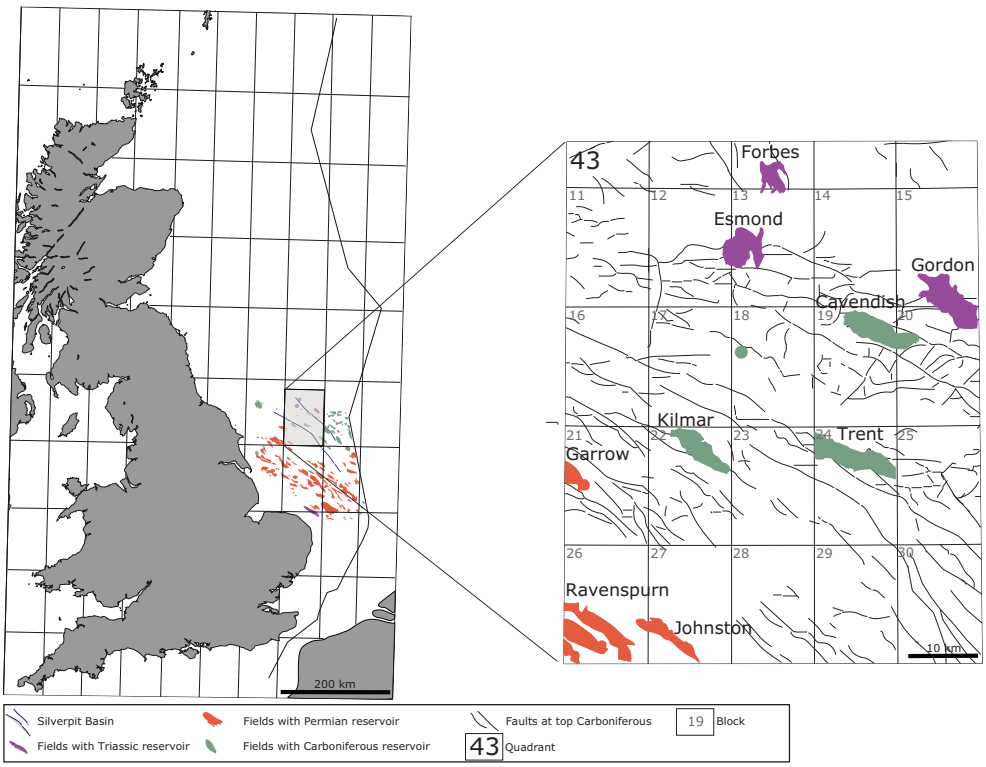

Fig. 1. Location map of Cavendish gas field.

From: Goffey, G. & Gluyas, J. G. (eds) 2020. *United Kingdom Oil and Gas Fields: 50th Anniversary Commemorative Volume*. Geological Society, London, Memoirs, **52**, 131–141, https://doi.org/10.1144/M52-2019-10

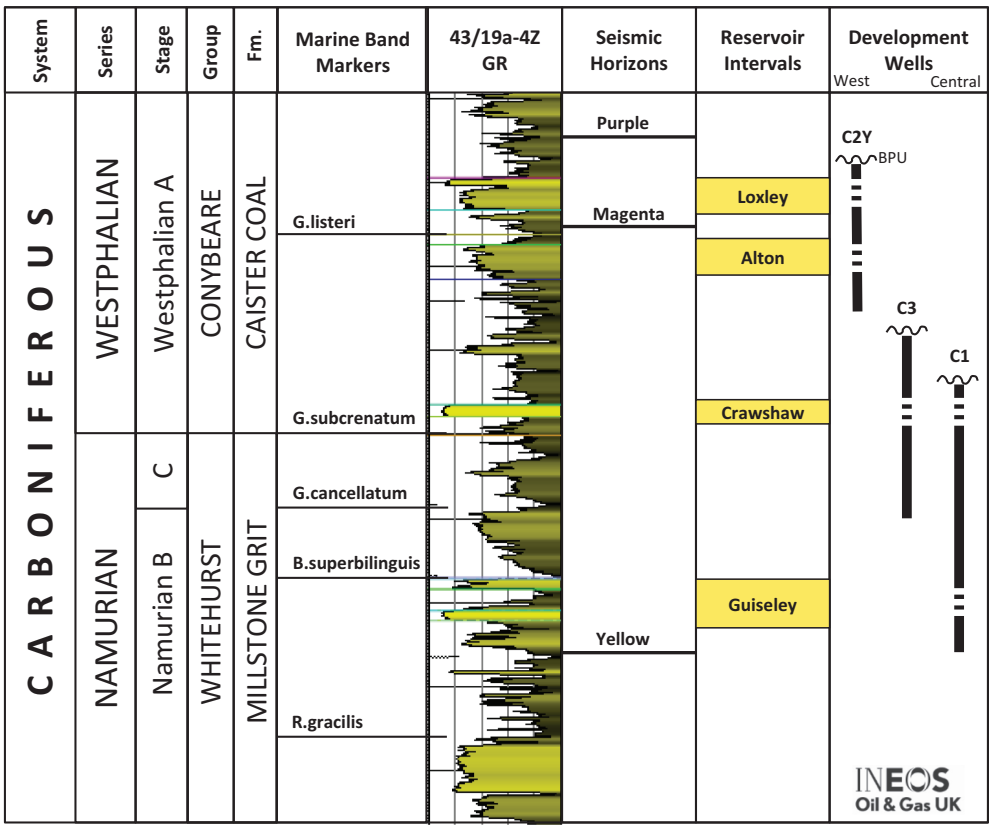

Fig. 2. Cavendish Field stratigraphic column with the position of the reservoir units.

was 11 906 ft (3629 m) TVDSS, proving a minimum gas column height of 456 ft (139 m).

Appraisal well 43/19-2A was drilled in 1990 by Amoco and located 1.4 miles (2.2 km) west of the discovery well. This well encountered a thicker section of Westphalian A below the BPU with two different gas-bearing sandstones stratigraphically younger than those seen in 43/19-1. The quartzitic sandstone (thought to be equivalent to the Crawshaw Sandstone onshore UK) tested in 43/19-1 was water bearing. The well also penetrated an 1800 ft (549 m) Namurian interval ranging in age from Marsdenian to Pendleian. Numerous sandstone intervals were found but most were tight. Out of 90 repeat formation tests (RFTs) attempted, only six were considered valid tests. Three DSTs were conducted on Westphalian sandstones. DSTs 1 and 2 failed to flow on test due to low permeability formation. DST 3 was conducted over a thin Westphalian A quartzitic sandstone, and flowed gas at 17 MMscfgd and 91 bpd of condensate. RFT pressure measurements made in the water leg enable a free water level (FWL) estimate of 11 960 ft TVDSS. This extended the proven gas column height to 510 ft (155 m).

Further delineation of the field occurred in 1996 when Amoco drilled well 43/19a-4Z from the same top-hole location as 43/19-2A, to a bottom-hole location 1.4 miles (2.3 km) further west. This test of the western flank proved a more extensive Westphalian A section below the BPU; however, the permeable Westphalian sandstone intervals were beneath the FWL. In this well, the longest continuously cored section of the Carboniferous yet made in the UK SNS was acquired, from 14 779 ft measured depth below rotary table (MDBRT, 4504.6 m) in the Westphalian A to 16 858 ft MDBRT (5138.3 m) in the Kinderscoutian, totalling 2079 ft (634 m) of continuous coring.

The appraisal programme had proven a gas-bearing structure though the gas composition had inert gas (CO_2 and N_2 combined) >7%. This gas quality alone would be below specification for entry to the National Transmission System (NTS). Commercial production rates had been proven from three separate sandstone intervals but there were a larger number of sandstones that were considered to have permeabilities that were too low to sustain economic gas production. Amoco's interest was acquired by BP in 1998 through the merger of BP and Amoco and in 2000 the licence was sold to Highland Energy, which was then acquired by RWE-Dea in 2002.

Development

A reduction in the calorific value entry specification in the NTS and the availability of low CO_2 blend gas from Saturn and Topaz fields to add to gas from fields produced via the Lincolnshire Offshore Gas Gathering System (LOGGS) and Caister–Murdoch System (CMS) pipelines allowed Cavendish gas to be considered for production through the Theddlethorpe gas terminal. This, combined with rising gas prices in the first decade of the twenty-first century, led to renewed interest in the field by the new operator RWE-Dea. The field development plan (FDP) was for a three-well development from a six slot, normally unattended, remotely operated, minimum facilities platform tied-back with a 28 mile (45 km) 10-inch pipeline to the Murdoch platform to the SE. From Murdoch, gas was to be exported through the CMS trunk pipeline to Theddlethorpe in Lincolnshire. The FDP was approved by the Government in 2005 with the partnership group comprising RWE Dea UK 50% and operator, Dana 25% and Gaz de France 25%.

Three development wells were drilled through the platform slots in 2006 and 2007 (Table 1). Well 43/19a-C1 was located in the centre of the field, twinning exploration well 43/19-1. The well was completed in three intervals, two Westphalian A sandstones and a deeper Marsdenian age sandstone. Well 43/19a-C2 was drilled to the west to develop the thicker but marginal-quality Westphalian sandstones seen in 43/19a-2A. The 43/19a-C2 well did not encounter the same thin high

Table 1. *Gas composition data for the Cavendish Field*

	Reservoir interval	N_2 (%mol)	CO_2 (%mol)	C1 (%mol)
43/19a-C1	Crawshaw and Guiseley	3.792	3.774	85.708
43/19a-C2Y	Loxley and Alton	4.399	1.502	88.163
43/19a-C3	Crawshaw	3.852	3.296	86.842

permeability quartzitic sandstone interval tested on 43/19-2A and was side-tracked downdip as 43/19a-C2Z. However, the side-track also proved unsuccessful. The well was side-tracked a second time in 2010 as 43/19a-C2Y and eventually put on production. Well 43/19a-C3 was drilled to the south of the platform to ensure there was a second producer from the high-quality Crawshaw Sandstone equivalent and to mitigate the risk of any potential fault compartmentalization.

Regional context

Basin evolution

The Southern North Sea Basin experienced a complicated geological history, involving multiple episodes of uplift and subsidence. During Carboniferous times the basin was bounded in the south by the London Brabant Massif and in the north by the Mid North Sea High/Ringkøbing-Fyn High (Cameron *et al.* 1993), with over 19 685 ft (6000 m) of sediments deposited in parts of the basin (Besly 2018). The Variscan Orogeny resulted in faulting and folding of the Carboniferous rocks and subsequent erosion of much of the Upper Carboniferous strata. During Permian times, renewed subsidence of the Variscan foreland resulted in deposition of a thick sequence of mainly clastic and evaporite strata deposited initially in continental and subsequently restricted marine environments, which were for short periods connected to the ocean through constricted seaways, resulting in hypersaline conditions (Ziegler 1990; Cameron *et al.* 1993). Subsidence, with additional extensional faulting, continued into the Triassic, accompanied by regional regression. Deposition in the Southern North Sea Basin was dominated by fine-grained clastics and evaporites with coarse-grained clastics in the Early Triassic, formed within fluvial, sabkha, lacustrine and shallow-marine environments (Johnson *et al.* 1994; Fisher & Mudge 1998). End Triassic to Early Jurassic crustal extension caused rapid subsidence, and a major transgression in Jurassic times marked the onset of deposition of predominantly shallow-marine muds and limestones (Lott & Knox 1994). This period of subsidence was interrupted by thermal doming in the Central North Sea, which caused uplift and erosion of much of the Jurassic sequence in the region. Crustal extension continued after the uplift until Mid-Cretaceous times, providing accommodation space for a thick, predominantly marine sequence. An episode of uplift at the end of the Cretaceous caused basin inversion in many fault-bounded basins, such that Paleogene marine deposits unconformably overlie the Cretaceous Chalk deposits. Miocene tectonic uplift linked to the Alpine Orogeny removed part of the Paleogene sequence, capped by a major Pliocene deltaic system (Cameron *et al.* 1992, 1993).

Stratigraphy

At the time of FDP submission (2005) the three key productive sand intervals were identified as Reservoir Layers '1', '2' and '3' and dated as Mid-Marsdenian (Namurian B–C) to Langsettian (Westphalian A). These layers are part of the Millstone Grit Formation (Namurian) and Caister Coal Formation (Westphalian) and, using onshore stratigraphic terminology (e.g. BGS 2019), were later named the Guiseley Grit (layer 1), Crawshaw Sandstone (layer 2) and Loxley and Alton sandstones (layer 3; Fig. 2). The Loxley Sandstone is an informal abbreviation of the formal Loxley Edge Sandstone and the Alton Sandstone is an informal field name for sandstone that occurs just beneath the *Gastrioceras listeri* Marine Band. These zones were identified through a multi-well biostratigraphy study that included wells outside the development area. Using palynostratigraphic methods a number of likely marine band-equivalent mudstones were identified (Fig. 2) that are recognized over areas of the offshore Carboniferous play and are correlatable to onshore stratigraphic events (Waters *et al.* 2009). The palynostratigraphy is constrained by the cored section from well 43/19a-4Z, from which macropalaeontological data are available. Well correlation based on palynostratigraphy is improved by palaeovegetational analysis, providing a high-resolution framework. The study allows a high level of confidence to be applied to the well correlation (Fig. 3a, b) and is fully consistent with the seismic interpretation and mapping.

The oldest producing horizon on the Cavendish Field is the Mid-Marsdenian age Guiseley Grit equivalent and occurs immediately below the *Bilinguites superbilinguis* Marine Band (Fig. 2). The interval is subdivided into an upper and lower sandstone unit separated by a thin mudstone. The sandstones were probably deposited by a major distributary channel within a shallow-water prograding delta front.

The overlying Yeadonian interval comprises mudstones with sporadic sandstone intervals. These sandstones are of non-reservoir quality and probably originate as minor distributary channels or overbank crevasse splay-type deposits.

The base of the Westphalian interval is marked by the marine band *G. subcrenatum*. Immediately above this marine band is the Crawshaw Sandstone (Fig. 2). These quartzitic sandstones may have originated as the result of a base-level change and been deposited as incised valley fill over a wide area. The origin of quarzitic sandstones in Upper Carboniferous strata has been widely discussed. O'Mara *et al.* (1999 and 2003) suggest that quarzitic sandstones encountered in the nearby Trent Field are a product of tidal reworking. An alternative explanation given by Bristow (1988) for the origin of time-equivalent, quarzitic Rough Rock sandstones in more distal parts of the basin is the proximal to distal degradation of feldspars resulting in quartz enrichment in distal parts, and to sediment supply to the basin by two different river systems. An unpublished proprietary report for the operator proposed the quarzitic sandstones to have a diagenetic origin due to feldspar dissolution and a lesser amount of kaolinite precipitation in intervals near marine bands.

In the early Westphalian interval above the Crawshaw Sandstone, the Loxley Sandstone and Alton Sandstone are separated by the *G. listeri* Marine Band. These sandstones have average thicknesses of 58 ft (17.8 m) and 77 ft (23.4 m), respectively, and are characterized by low-porosity, low-permeability feldspathic sandstones.

Source

Westphalian and Namurian coals and mudstones (Westoe Coal and Caister Coal Formation, Millstone Grit Formation) are considered to be a source rock for many of the fields with Carboniferous reservoirs in the region (Cameron & Ziegler 1997; Cornford 1998). The operator's unpublished proprietary reports propose gas charging probably started in Cretaceous times. This is in agreement with data elsewhere

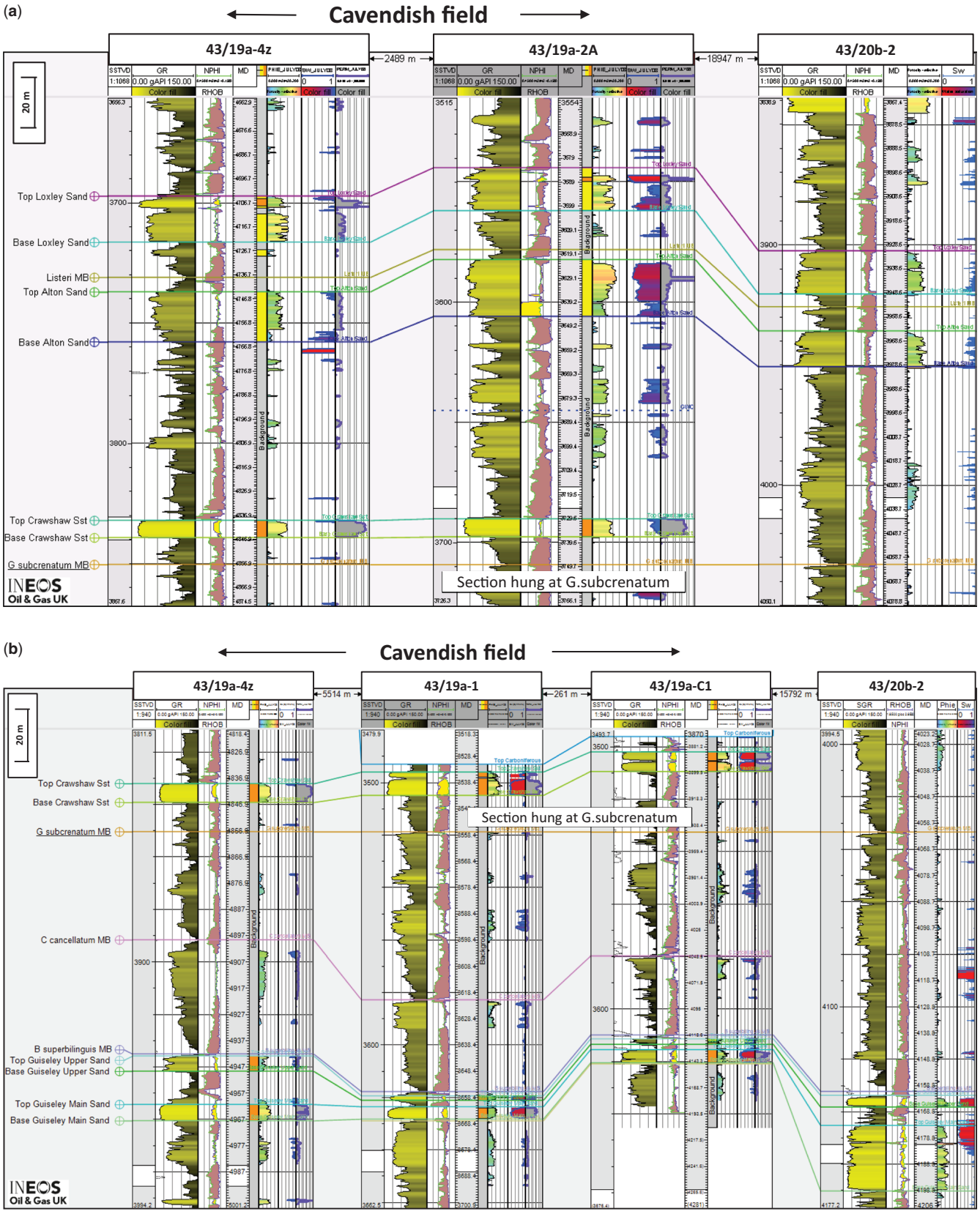

Fig. 3. (**a**) Westphalian A (Caister Coal) well correlation plot datumed on the *G. subcrenatum* Marine Band. (**b**) Namurian B–C (Millstone Grit) well correlation plot datumed on the *G. subcrenatum* Marine Band.

in the SNS area (Middle Jurassic reported by Robinson *et al.* (1993), Jurassic or Cretaceous by Besly (2018)). Thermal maturity data show that the Upper Carboniferous deposits in the Cavendish Field are currently in the oil generation window, with vitrinite reflectance values from 0.65–0.78% Ro.

Database

Well data included exploration and appraisal wells over the field and offset wells that have significant penetration of the Carboniferous interval. Multi-well studies were completed

prior to development that made use of the wireline logs, core and pressure–volume–temperature (PVT) data.

A 529 square mile (1370 km^2) 3D seismic survey was acquired by Geco-Prakla in 1993/94 over the Cavendish Field. Initially the data were processed with a dip move-out (DMO) stack and post-stack 3D phase-shift migration to produce a conventional time-migrated dataset. The dataset was subsequently re-imaged in the post-stack depth domain for Amoco in 1995 resulting in a post-stack depth-migrated (PostSDM) dataset.

This PostSDM volume provides clearer definition of faults within the Carboniferous section, partly at the expense of true amplitude relationships. Both datasets suffer contamination from long-period multiples. During 2004 the dataset was reprocessed in the time domain (pre-stack time migration) in an attempt to reduce the number of multiples. This exercise was only partially successful as the resultant dataset still suffers from some long period multiples.

Seismic interpretation has used both datasets to provide a high level of confidence in the mapping. Below the BPU two intra-Carboniferous horizons were picked and gridded. The deepest horizon is a near equivalent to the Guiseley Grit (Fig. 2). The Crawshaw Sandstone is truncated below the BPU on the crest of the structure. Depth conversion and a combination of error correction and isochore maps were used to produce a set of final top reservoir depth maps.

Trap

The Cavendish structure resulted from multiple deformation phases since late Carboniferous through to early Tertiary times. During late Carboniferous times, NW–SE extension occurred creating a series of normal and listric-style faults with NE–SW trends. Syn-sedimentary faulting produced a series of half-graben which flank the main hanging-wall anticline. At intra-Carboniferous level, the Cavendish structure is a WNW–ESE-orientated anticline. The axis plunges both east and west and is truncated to the east by a WSW–ENE-trending fault. To the north the structure is bounded by a major WNW–ESE-trending reverse fault and the flank to the south is steeply dipping (Fig. 4). At the crest of the anticline the Crawshaw Sandstone is partially eroded by the BPU whilst a thick succession of Westphalian A interval is preserved on the flanks of the structure (Fig. 4). The BPU is characterized as a gently undulating surface with dip to the south and no expression of the underlying structure other than the reverse fault.

Early interpretation of the gas–water contacts (GWCs) based on log and pressure data identified a high and low depth range with a most likely contact at 11 960 ft (3645 m) TVDSS. This GWC was applied across the structure at the field development stage. Post-development further analysis of well data provided the opportunity to review the GWCs of the various reservoir intervals and sealing mechanisms.

The regional seal is formed by the Permian, Silverpit Formation siltstones and mudstones, which are effective over a wide area of the Carboniferous play in the SNS. In the absence of a common BPU closure each reservoir interval has a unique sealing mechanism and consequently they have different GWCs. Gas compositional variations found during well testing demonstrate discreet reservoir intervals not in vertical communication and production subsequently demonstrated that these reservoirs are not in pressure communication.

The interpreted GWCs are summarized:

- a quartzitic interval in the Westphalian A (Loxley Sandstone), 11 910 ft (3630 m) TVDSS;
- the Crawshaw Sandstone equivalent, 12 000 ft (3658 m) TVDSS; and
- productive sandstone within the Marsdenian (Guiseley), 11 950 ft (3642 m) TVDSS.

The Loxley–Alton sandstones are proven on the western flank of the structure where a thick succession of Westphalian A is preserved below the BPU. The trapping mechanism requires a combination seal, and this is provided by the Silverpit Formation where the reservoir units are truncated at the BPU and dip closure from a thick succession of shale in the Westphalian A above the reservoir interval where the structure plunges to the west. The Westphalian A shale interval is proven in well 43/19a-4z located downdip to the west. Closure is mapped down

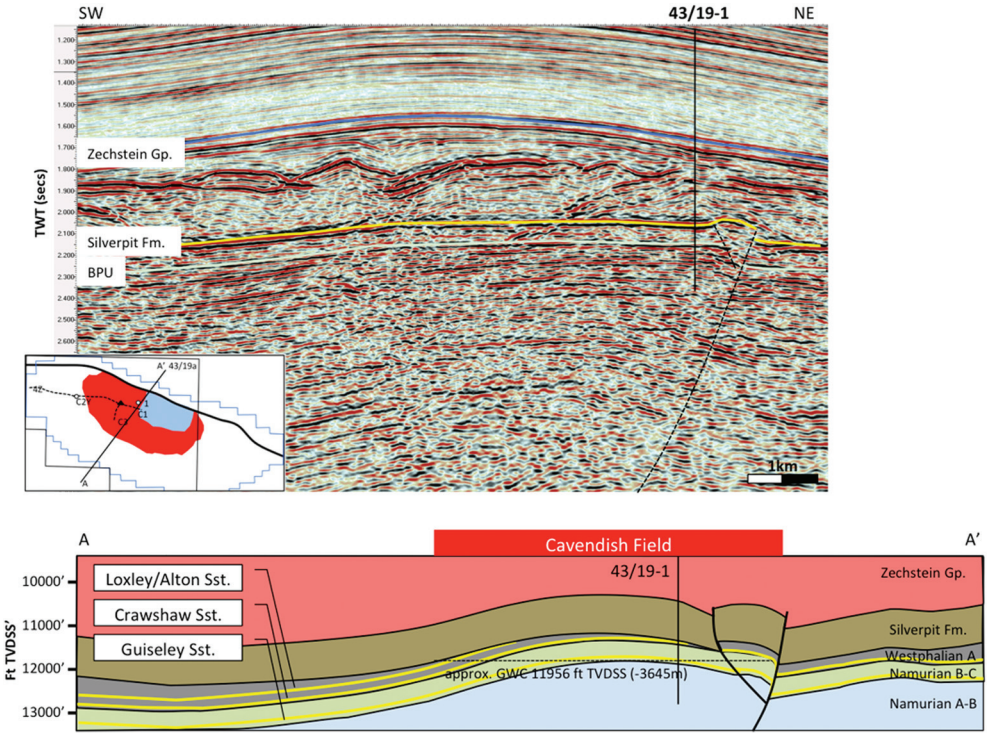

Fig. 4. Cavendish Field 2D time-migrated dip-line BN-43/87-107 (image from seismic data acquired for Britoil in 1982) through discovery well 43/19-1 and schematic depth cross-section along line. Location shown on inset map, where pale blue area denotes crestal absence of Crawshaw Sandstone.

to a spill point at 12 087 ft (3684 m) TVDSS which is *c.* 170 ft deeper than the GWC in the quartzitic sand. It is likely that the spill point is either controlled by a shallower, more effective shale interval in the Westphalian A or there is communication across the main boundary fault to the north with an unidentified sand interval. As the Loxley–Alton reservoir does not share a common GWC with the stratigraphically older but structurally higher Crawshaw Sandstone it may be assumed that an effective seat-seal or barrier is present between the two reservoir intervals.

The Crawshaw Sandstone has a combination seal of the Silverpit Formation where it is truncated at the crest of the structure by the BPU and the shale interval immediately above the reservoir in the Westphalian A and below the Loxley–Alton reservoir units. The GWC is the deepest of the three reservoir intervals at 12 000 ft (3658 m) TVDSS. A significantly deeper closure with a spill point at 12 530 ft (3820 m) TVDSS is located on the plunging axis to the west. A difference between structural closure and GWC of more than 500 ft (152 m) would suggest that the reservoir is in communication with a permeable sand juxtaposed across the reverse fault that potentially has a shallower spill point.

The Guiseley Sandstone reservoir GWC proved more problematic to determine, however, even with a depth range of potential GWC it is shallower (most likely case) at 11 950 ft (3642 m) TVDSS than the Crawshaw Sandstone GWC, although the reservoir interval is structurally deeper. The top Guiseley Sandstone depth structure has similar form to the Crawshaw Sandstone although the crestal area of the structure is smaller and has an elevation that is deeper than the BPU. The intra-Carboniferous seal is most probably associated with shale intervals that are present above the marine bands (*B. superbilinguis* and *G. cancellatum*) that occur between the Guiseley and Crawshaw sandstones. Closure of the structure is greater than the observed GWC and it is assumed that cross-fault seal is the controlling factor of the observed gas column height.

Reservoir and petrophysics

The reservoir rock comprises Namurian to Westphalian A fluvial sandstones deposited by a southward-prograding fluviodeltaic system infilling a deep basin, which originally formed in Dinantian times. The whole Upper Carboniferous sequence consists of multiple cycles of coarsening-upward deposits with marine mudstones (marine bands) at their base and fluvial deposits at the top. The multi-storey fluvial channel sandstones are up to 26 m (85 ft; Kinderscoutian age, well 43-19a-4Z) in thickness, with net:gross ratios of 0.17–0.22. In terms of reservoir continuity, Collinson *et al.* (1993) suggested that the thinner channels (<33 ft; 10 m) have widths of 328 ft (100 m) or less, whilst channel sandbodies, which are about 82 ft (25 m) thick, are <6.2 mile (10 km) wide.

Facies

The Upper Carboniferous sequence penetrated in the three appraisal wells drilled in the Cavendish Field was extensively cored: 25 cores were obtained, 11 of which were described in detail, including grain size, sorting, sedimentary structures, sand/detrital clay content, bioturbation index, cements, lithofacies and facies associations. A number of facies associations have been identified, of which multi-storey fluvial channels and distributary fluvial channels comprise the reservoir. Non-reservoir facies associations include delta plain, shoreface, interdistributary bay, proximal delta front, distal delta front, prodelta and offshore muds.

Fluvial channels, which form the reservoir, are represented by light grey, moderately well-sorted, predominantly upper fine-grained, 'clean' sandstones, interbedded with intervals of mid fine- to upper very coarse-grained sandstones and local conglomerate beds which are up to 0.8 ft (25 cm) thick. Conglomerates are generally matrix supported and composed of rigid clasts and mudclasts of up to cobble grade. Sandstones are stacked in metre-scale intervals (up to 59 ft; 18 m) and locally contain mudclasts and rigid grains of up to pebble grade and scattered fine carbonaceous debris. Crevasse splay deposits are represented by planar-laminated sandy siltstone beds up to 0.4 ft (12 cm) thick, interbedded with the fluvial sandstones. Sandstone bodies are predominantly cross-stratified, with some intervals planar-laminated, structureless or ripple cross-laminated. Stacked sandstone bodies commonly display sharp tops. Sandstones are predominantly quartz cemented, with local dolomite cements.

Depositional model

On a large scale, the Namurian strata record filling of relict Dinantian basin topography, which consisted of a series of highs and graben (Fig. 5), formed as a result of the convergence of Gondwana with Laurussia, the following rifting phase and a subsequent phase of thermal subsidence (Waters & Davies 2006). Large fluviodeltaic systems, mainly fed from the north, progressed southwards filling the accommodation space within the basin (Collinson *et al.* 1993; Collinson 2005). The overall Namurian sequence in a broad sense begins with marine mudstones, followed by deep-water delta-front turbidites, shallow-water sheet-like delta facies and large fluvial channels developed on top, following delta progradation. The huge fluvial system that developed during Namurian times has likely drained continental-scale areas, with the Pennine river-delta system possibly comparable in size to the modern Amazon

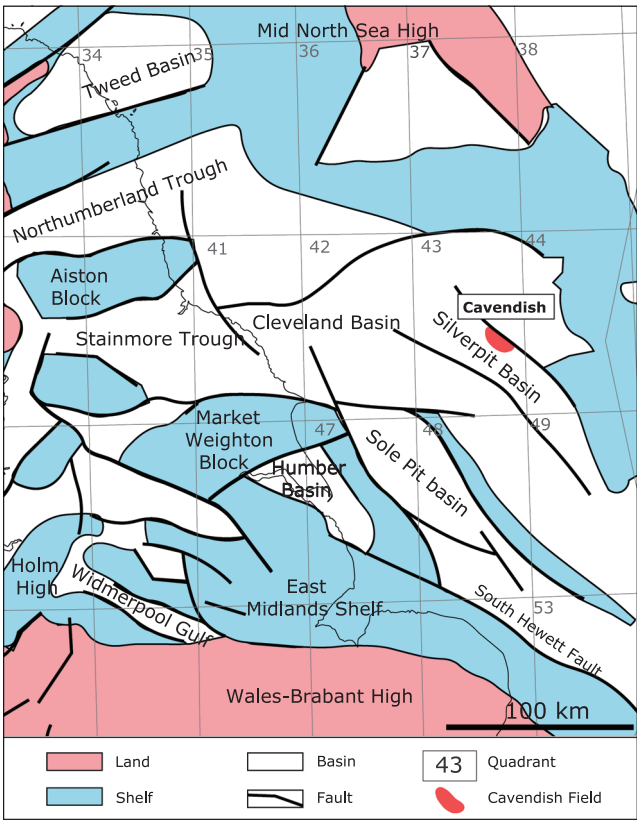

Fig. 5. Dinantian palaeogeography map.

(Leeder 1988). The exposed granite/gneiss Caledonian hinterland was the main source of the sediment transported by extensive river systems. Palaeocurrent analysis in well 43/19-1 shows that the channels in this locality flowed to the NNW and NW during the Namurian C and to the SE during the Namurian B. This NNW–NW trend, contrasting with the larger regional observations, might be explained by a local structural control diverting the flow, as is found in some onshore areas in the UK (e.g. Bristow 1988). As an effect of glacio-eustatic cyclicity (Davies *et al.* 1999), multiple marine transgressions occurred during Namurian times, resulting in stacking of numerous coarsening-upward successions of genetically related facies.

Reservoir quality

Reservoir quality in the sandstones varies from very low (0.01 mD, analysis threshold) to excellent (744 mD in 43/19a-4Z). Porosity (0.4–19.1%) appears to be partially controlled by depositional environment, whilst permeability is largely controlled by diagenetic processes.

The Guiseley Grit interval has an average thickness of 47 ft (14.2 m) and is subdivided into an upper and lower sandstone unit (informally called Guiseley Main) separated by a thin mudstone. The sandstones vary significantly in reservoir character, with the upper sandstone having low porosity in the range of 2–7% and low permeability of less than 1 mD. The Guiseley Main sandstones generally have better reservoir characteristics, with porosity in the range of 7–10% and permeability in the order of 25–400 mD. The Crawshaw Sandstone has an average thickness over the field of 25 ft (7.6 m) and has an average porosity 9.5% and permeability of 88–744 mD (horizontal permeability from analysis of offset core data). This interval is highly productive due to the clean quartzitic sandstone and preservation of high porosity and permeability.

The best reservoir quality is found in plugs taken from multistorey fluvial channel sandstones (Fig. 6). This is, in part, related to detrital clay content and grain size, with plugs taken from those facies being the cleanest and coarsest (lower very fine- to upper coarse-grained) of those cored (Fig. 7a, b). Quartz arenites and sublithic arenites reach higher porosity and permeability values than lithic arenites, feldspathic arenites and sublithic and lithic wackes. Current burial depth, grain sorting and sandstone age do not correlate with permeability.

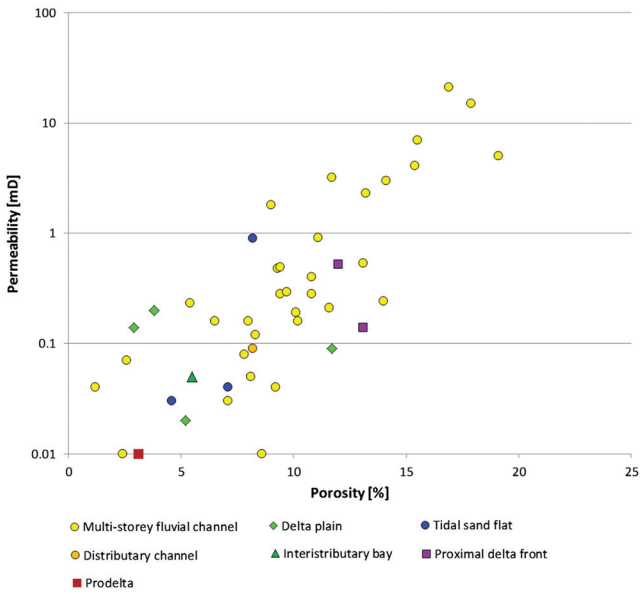

Fig. 6. Porosity v. permeability plot for the cored Namurian deposits in Cavendish Field wells 43/19-1 and 43/19-2A.

Reservoir quality in those tight reservoirs is very variable, locally showing permeability variation of orders of magnitude over small areas of the reservoir (decimetre-scale, within the same facies association). In most samples compactional porosity loss is higher than cementational porosity loss, due to a rapid and deep burial during Carboniferous times (Fig. 8). Early diagenesis exerts a large influence on present-day reservoir quality and it is different in the marine facies associations and continental facies. Primary porosity within the marine facies (shoreface, delta front) is commonly occluded by detrital clay and early diagenetic dolomite and siderite. In some samples, early carbonate formation precedes mechanical compaction, stabilizing the grain framework but at the same time also pervasively occluding porosity, rendering the reservoir largely ineffective. Reservoir quality is better preserved in the continental facies (fluvial channels and delta plain), which were not subject to early marine diagenesis; however, it is highly variable, ranging from 0.01 to 744 mD, mainly owing to later diagenetic processes. After an early period of compaction and cementation, the sandstones experienced a phase of unstable grain dissolution (probably feldspars) and likely also some carbonate dissolution, temporarily increasing reservoir quality. Another phase of deep burial and associated temperature and pressure increase resulted in fracturing, pressure dissolution and precipitation of abundant quartz overgrowths and kaolinite. Quartz overgrowths comprise two generations. Minor illite formed during the later stages of diagenesis during or after quartz formation. A late phase of ferroan dolomite appears to be the latest stage of diagenesis in most samples. Minor amounts of barite and anhydrite are locally observed occluding late dolomite. Late diagenetic dolomite and illite, despite being volumetrically minor, reduce reservoir quality in the already tightly cemented sandstones. Other authigenic phases, such as pyrite and feldspar overgrowths, have very little effect on reservoir quality.

Modal porosity values from analysed thin sections from wells 43/19-1 and 42/19-2A range from 0 to 21.7% (3.4% average), with secondary pores being the dominant type (2.6% average) and primary pores subordinate (0.8%). Secondary pores, which might have led to an improved reservoir quality, probably result from feldspar dissolution.

The Westphalian A pay zone in well 43/19-1 (Crawshaw Sandstone), located just a few feet below the BPU, shows anomalously high permeability values, which might be a result of leaching during the Variscan uplift. This is consistent with the model of reservoir quality enhancement by weathering beneath the exposed Variscan unconformity surface, observed by Bailey *et al.* (1993) and Besly *et al.* (1993), for example. High permeability streaks were also recorded in 43/19-2A Westphalian A and nearby well 43/20b-2 in Namurian B strata, both of which are fractured.

Production history and reserves

The gas initially in place (GIIP) determined at the time of FDP submission had a stochastic range (P90–P10) of 166–403 bcf and a P50 volume of 311 bcf. The expected recovery (P90–P10) was 85–181 bcf with a P50 of 117 bcf. The main volumetric uncertainty affecting GIIP was the net reservoir cut-off and effective GWC.

First gas was produced on 3 July 2007. Well 43/19a-C1 was brought online with an initial rate of 61 MMscfgd. Well 43/19a-C3 came online 9 November 2007 with similar rates and increased to 70 MMscfgd after a couple of months. Three

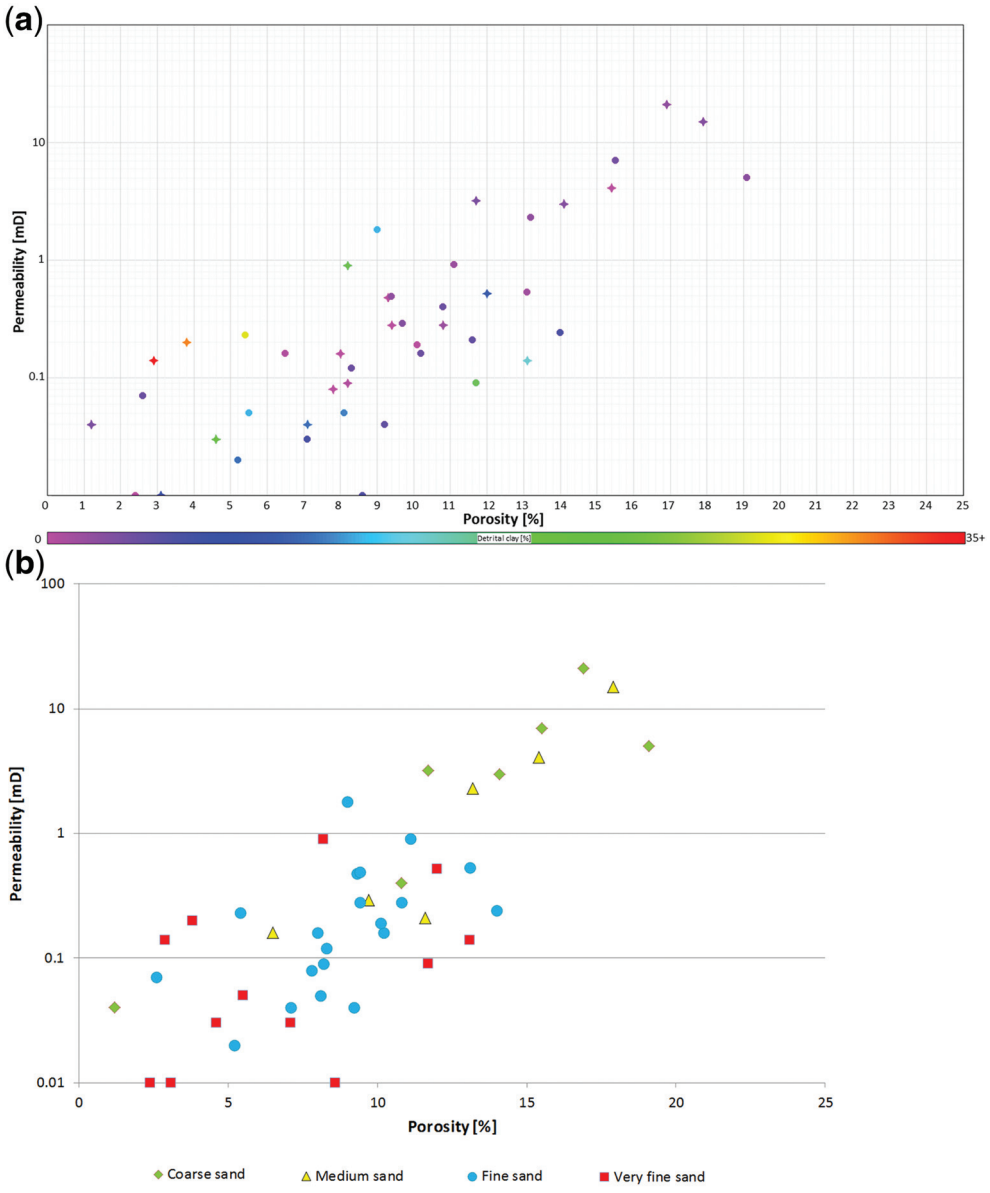

Fig. 7. (**a**) Porosity v. permeability plot coded by detrital clay content, wells 43/19-1 and 43/19-2A. (**b**) Porosity v. permeability plot coded by grain size, wells 43/19-1 and 43/19-2A.

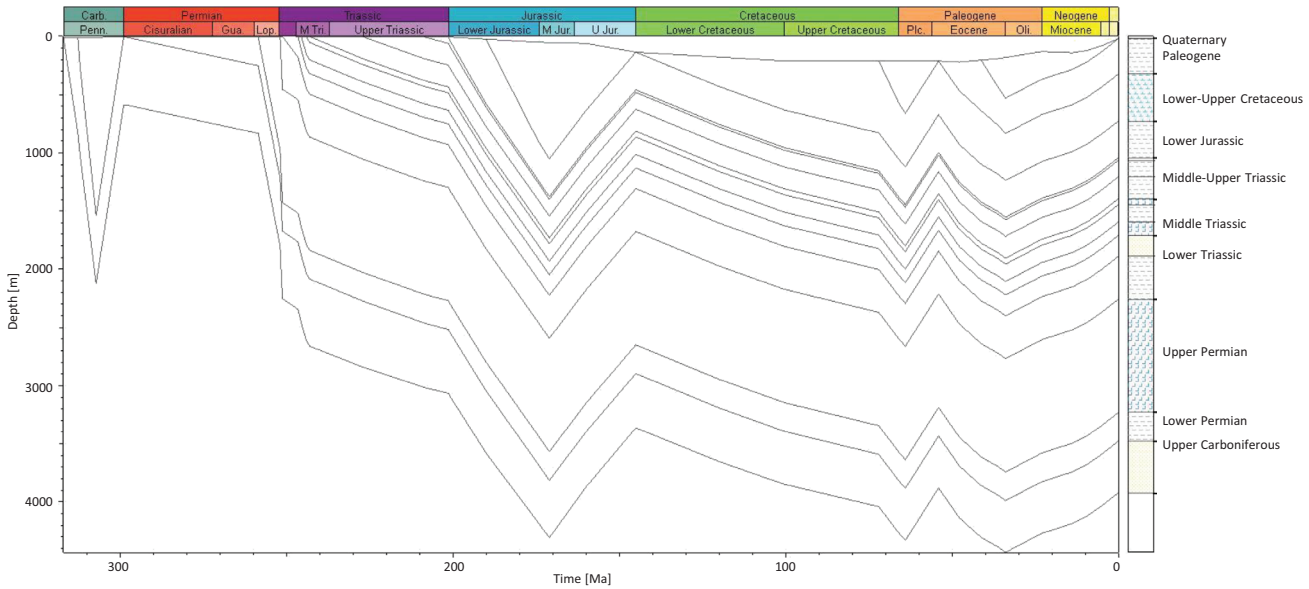

Fig. 8. Burial plot for well 43/19-1, Cavendish Field. A phase of rapid burial during Carboniferous times was responsible for strong compactional porosity loss. Strong chemical compaction occurred during a later phase of deep burial.

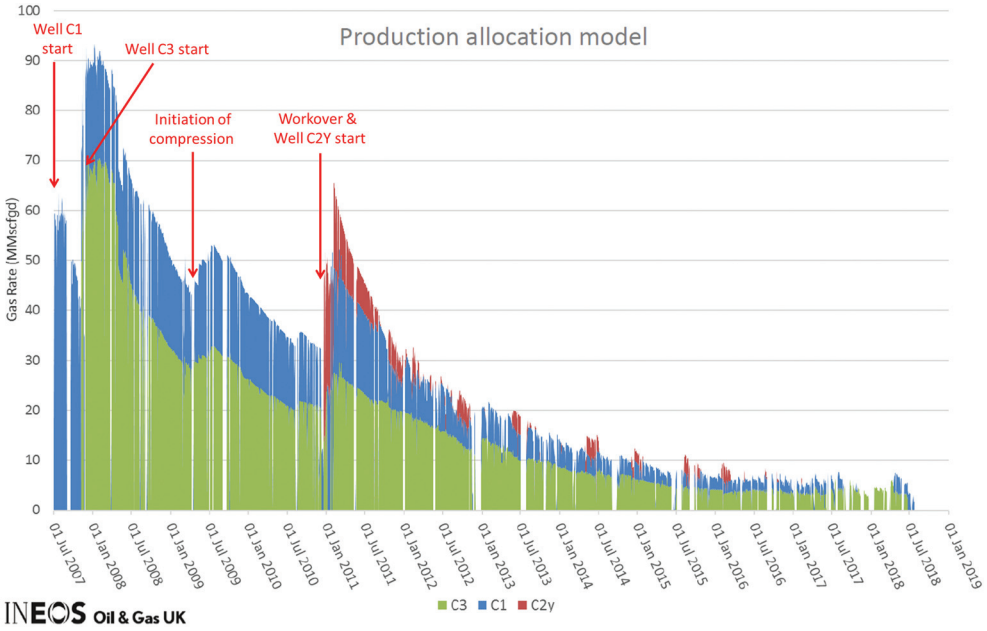

Fig. 9. Production profile for the Cavendish Field.

years elapsed before 43/19a-C2Y was brought online on 19 December 2010, with a maximum rate of 30 MMscfgd (Fig. 9).

The field achieved a plateau rate of around 90 MMscfgd for a period of five months soon after 43/19a-C1 and 43/19a-C3 were both on-stream. Rates then declined until 22 April 2009 when compression was provided through the CMS facilities and this allowed production rates to be increased over a six-month period. A further step-up in production occurred after work-overs on 43/19a-C1 and 43/19a-C3 followed by 43/19a-C2Y on stream in 2010. A maximum field rate of 68 MMscfgd was achieved with all three wells online. All the wells have exhibited steady decline, although 43/19a-C2Y has declined more rapidly in comparison to 43/19a-C1 and 43/19a-C3.

The modelling and understanding of the field at the development planning stage was approached stochastically. A static model build to reflect the various fluvio-deltaic channel facies was modelled using a probabilistic approach with reference to documented examples of UK onshore Carboniferous sandbody geometries. Input parameters for channel thickness, width to thickness ratios, sinuosity, amplitude and net:gross range were applied for the different stratigraphic intervals. Early simulation models developed using this approach did not reflect subsequent production behaviour, which demonstrated good connectivity within the Guiseley Grit and Crawshaw Sandstone whilst the Loxley and Alton sandstones, when eventually developed, proved to have a very low connected volume. Rebuilding of the static model with the Crawshaw Sandstone and Guiseley Grit represented as 'sheet' form geometries provided an improvement but did not completely balance the connected gas volume in the Crawshaw Sandstone. Remapping was required to reduce the level of truncation at the BPU horizon and restore volume to the Crawshaw Sandstone reservoir interval. The final revised GIIP for all the developed reservoir intervals was determined as 184 bcf.

At cessation of production in 2018 the field had produced a total volume of 98 bcf plus associated condensate. The condensate–gas ratio was between 3.5 and 11.0 bbl/MMscf (Kersten *et al.* 2013) and this ratio is used to calculate condensate yield which is not measured independently. Various well tests, pressure data and production logging results were used to determine the produced gas volumes by the various discreet reservoir intervals. The Crawshaw Sandstone near the base of the Westphalian A produced approximately 83 bcf and demonstrated a recovery factor of 80% based on revised GIIP for the developed horizon. The Guiseley Grit produced 11 bcf and recovered 39% of the GIIP volume. The younger, but of marginal reservoir quality, Loxley and Alton sandstones produced a combined total of 4 bcf with recovery factors of 12 and 2%, respectively.

Production from Cavendish Field remained economic at very low levels (5 MMscfgd) achieved through the low operating costs of a minimum facilities, normally unmanned platform. Cessation of production came when the ConocoPhillips-operated Caister–Murdoch export route to LOGGS and the onshore plant at Theddlethorpe as a whole became uneconomic due to low aggregated throughput.

Acknowledgements We wish to thank our reviewers Bernard Besly and Gordon Taylor and the editor Graham Goffey for their helpful comments. We would like to acknowledge the help and support of staff at INEOS UK SNS Ltd and Dana Petroleum (E&P) Ltd in facilitating this paper.

Funding This research received no specific grant from any funding agency in the public, commercial, or not-for-profit sectors.

Author contributions **NW**: writing – original draft (lead); **JGG**: writing – review & editing (lead); **HB**: writing – original draft (supporting); **RS**: writing – original draft (supporting).

Cavendish gas field data summary

Trap	
Type	Dip and fault-closed anticline
Depth to crest (ft TVDSS)	11 550
Hydrocarbon contacts (ft TVDSS)	11 910–2 000
Maximum gas column thickness (ft)	450

Main pay zone		
Formation	Caister Coal Formation, Millstone Grit Formation	
Age	Westphalian A, Namurian B–C	
Depositional setting	Deep basin progressively infilled with fluviodeltaic deposits. Reservoir in fluvial deposits.	
Gross/net thickness (ft)	1475/254	(43/19-1)
	745/166	(43/19-2 A)
Average porosity (range) (%)	7.9 (0.4–19.1)	
Average net/gross ratio (%)	17	19-1
	0.22	19-2 A
Cutoff for net reservoir (% porosity)	7	43/19-1
	8	43/19-2A
Average permeability (range) (mD)	7.72 (arithmetic mean)/ 0.4 (geomean) (0.01–744)	horizontal permeability
Average hydrocarbon saturation (%)	87.9	43/19-1
Hydrocarbons		
Oil gravity (°API)	48.1–48.2	43/19-1 variation in API gravity
Dew point (condensate) (psig)	4800–6450	
Condensate/gas ratio (bbl/MMscf)	3.5–11	
Gas gravity (°API)	0.67	
Gas expansion factor (scf/rcf)	280	
Formation water		
Resistivity (ohm m)	0.0415	
Pressure gradient – water (psi/ft)	0.5	43/19-1 at 12 200 ft TVDSS
Reservoir conditions		
Temperature (°C)	99	at 11 491 ft MDBRT
Initial pressure (psi)	6107.92	at 11 491 ft MD BRT
Field size		
Area ($km^{2)}$	35.5	
Non-associated GIP (bcf)	166–403, most likely 311	
Drive mechanism (primary)	Pressure depletion	
Recovery to date – condensate (boe)	100 500	
Recovery to date – gas (bcf)	98	
Expected ultimate recovery factor/volume – gas (%)/(bcf)	53/98	
Production		
Start-up date	2007	
Number of exploration/appraisal wells	5 including 2 side-tracks	
Number of production wells	5	
Number of injection wells	0	
Development scheme	Gas expansion drive	
Planned abandonment	2018	

References

Bailey, J.B., Arbin, P., Daffinoti, O., Gibson, P. & Ritchie, J.S. 1993. Permo-Carboniferous plays of the Silver Pit Basin. *In*: Parker, J.R. (ed.) *Petroleum Geology of Northwest Europe: Proceedings of the 4th Conference*. Geological Society, London, 707–715, https://doi.org/10.1144/0040707

Besly, B. 2018. Exploration and development in the Carboniferous of the Southern North Sea: a 30-year retrospective. *In*: Monaghan, A.A., Underhill, J.R., Hewett, A.J. & Marshall, J.E.A. (eds) *Paleozoic Plays of NW Europe*. Geological Society, London, Special Publications, **471**, 17–64, https://doi.org/10.1144/SP471.10

Besly, B.M., Burley, S.D. & Turner, P. 1993. The late Carboniferous 'Barren Red Bed' play of the Silver Pit area, Southern North Sea. *In*: Parker, J.R. (ed.) *Petroleum Geology of Northwest Europe: Proceedings of the 4th Conference*. Geological Society, London, 727–740, https://doi.org/10.1144/0040727

BGS 2019. Lexicon of Named Rock Units, https://www.bgs.ac.uk/lexicon/home.cfm [accessed 5 March 2019].

Bristow, C.S. 1988. Controls on the sedimentation of the Rough Rock Group (Namurian) from the Pennine Basin of northern England. *In*: Besly, B.M. & Kelling, G. (eds) *Sedimentation in a Synorogenic Basin Complex: The Upper Carboniferous of Northwest Europe*. Blackie, Glasgow, 114–131.

Cameron, D., van Doorn, D. & Laban, C. & Streif, H.J. 1993. Geology of the Southern North Sea Basin. *In*: Hillen, R. & Verhagen, H. (eds) *Coastlines of the Southern North Sea*. American Society of Civil Engineers, New York, 14–26.

Cameron, N. & Ziegler, T. 1997. Probing the lower limits of a fairway: further pre- Permian potential in the southern North Sea. *In*: Ziegler, K., Turner, P. & Daines, S.R. (eds) *Petroleum Geology of the Southern North Sea: Future Potential*. Geological Society, London, Special Publications, **123**, 123–141, https://doi.org/10.1144/GSL.SP.1997.123.01.08

Cameron, T.D.J., Crosby, A., Balson, P.S., Jeffery, D.H., Lott, G.K., Bulat, J. & Harrison, D.J. 1992. *The Geology of the Southern North Sea*. British Geological Survey, UK Offshore Regional Report, HMSO, London.

Collinson, J.D. 2005. Dinantian and Namurian depositional systems in the southern North Sea. *In*: Collinson, J.D., Evans, D.J., Holliday, D.W. & Jones, N.S. (eds) *Carboniferous Hydrocarbon Geology: The Southern North Sea and Surrounding Onshore Areas*. Yorkshire Geological Society Occasional Publications, **7**, 35–56.

Collinson, J.D., Jones, C.M., Blackbourn, G.A., Besly, B.M., Archard, G.M. & McMahon, A.H. 1993. Carboniferous depositional systems of the Southern North Sea. *In*: Parker, J.R. (ed.) *Petroleum Geology of Northwest Europe: Proceedings of the 4th Conference*. Geological Society, London, 677–687, https://doi.org/10.1144/0040677

Cornford, C. 1998. Source rocks and hydrocarbons of the North Sea. *In*: Glennie, K.W. (ed.) *Petroleum Geology of the North Sea: Basic Concepts and Recent Advances*. Blackwell Science, Oxford, 376–462.

Davies, S., Hampson, G., Flint, S. & Elliott, T. 1999. Continental-scale sequence stratigraphy of the Namurian, Upper Carboniferous and its applications to reservoir prediction. *In*: Fleet, A.J. & Boldy, S.A.R. (eds) *Petroleum Geology of Northwest Europe: Proceedings of the 5th Conference*. Geological Society, London, 757–770, https://doi.org/10.1144/0050757

Fisher, M.J. & Mudge, D.C. 1998. Triassic. *In*: Glennie, K.W. (ed.) *Petroleum Geology of the North Sea: Basic Concepts and Recent Advances*. Blackwell Science, Oxford, 212–244.

Johnson, H., Warrington, G. & Stoker, S.J. 1994. Permian and Triassic of the Southern North Sea. *In*: Knox, R.W.O'B. & Cordey, W.G. (eds) *Lithostratigraphic nomenclature of the North Sea*. British Geological Survey, Nottingham, 1–125.

Kersten, C., Schulze, K., Schroers, F., Mandiwall, D. & Jeffs, P. 2013. Formation damage in the Cavendish gas field – causes, treatment and future measures. Paper SPE 164185, presented at the SPE European Formation Damage Conference, Noordwijk, Netherlands, 5–7 June 2013.

Leeder, M.R. 1988. Recent developments in Carboniferous geology: a critical review with implications for the British Isles and N. W. Europe *Proceedings of the Geologists' Association*, **99**, 73–100.

Lott, G.K. & Knox, R.W.O'B. 1994. 7. Post-Triassic of the Southern North Sea. *In*: Knox, R.W.O'B. & Cordey, W.G. (eds) *Lithostratigraphic nomenclature of the UK North Sea*. British Geological Survey, Nottingham, 1–155.

O'Mara, P.T., Merryweather, M., Stockwell, M. & Bowler, M.M. 1999. The Trent Gas Field; correlation and reservoir quality within a complex Carboniferous stratigraphy *In*: Fleet, A.J. & Boldy, S.A.R. (eds) *Petroleum Geology of Northwest Europe: Proceedings of the 5th Conference*. Geological Society, London, 809–821, https://doi.org/10.1144/0050809

O'Mara, P.T., Merryweather, M., Stockwell, M. & Bowler, M.M. 2003. The Trent Gas Field, Block 43/24a, UK North Sea. *In*: Gluyas, J.G. & Hichens, H.M. (eds) *United Kingdom Oil and Gas Fields, Commemorative Millennium Volume*. Geological Society, London, Memoirs, **20**, 835–849, https://doi.org/10.1144/GSL.MEM.2003.020.01.70

Robinson, A.G., Coleman, M.L. & Gluyas, J.G. 1993. The age of illite cement growth, village fields area, Southern North Sea: evidence from K–Ar ages and 18O/16O isotope ratios. *American Association of Petroleum Geologists Bulletin*, **77**, 68–80.

Waters, C.N. & Davies, S.J. 2006. Carboniferous: extensional basins, advancing deltas and coal swamps. *In*: Brenchley, P.J. & Rawson, P.F. (eds) *The Geology of England and Wales*. Geological Society, London, 173–223.

Waters, C.N., Waters, R.A., Barclay, W.J. & Davies, J.R. 2009. *A lithostratigraphical framework for the Carboniferous successions of the southern Great Britain (onshore)*. British Geological Survey Research Report, **RR/09/01**.

Ziegler, P.A. 1990. *Geological Atlas of Western and Central Europe*. Shell International Petroleum Maatschappij B.V., The Hague.